

Y2018 Annual Report

Site-Directed Research & Development

Strategic Opportunity Research
Exploratory Research

NEVADA NATIONAL SECURITY SITE

Site-Directed Research and Development

Fiscal Year 2018 Annual Report

This work was done by Mission Support and Test Services, LLC, under Contract No. DE-NA0003624, with the U.S. Department of Energy and supported by the Site-Directed Research and Development Program.

Report Date: April 2019



Disclaimer

Reference herein to any specific commercial product, process, or service by trade name, trademark, manufacturer, or otherwise does not necessarily constitute or imply its endorsement, recommendation, or favoring by the United States Government or any agency thereof or its contractors or subcontractors.

Available as a digital download at no charge via the website below:

**U.S. Department of Commerce
National Technical Information Service
5301 Shawnee Road
Alexandria, VA 22312**

Telephone: 1.800.553.6847
Fax: 703.605.6880

E-mail: info@ntis.gov; customerservice@ntis.gov

Downloadable (no charge) at: <https://classic.ntis.gov/search>
Online ordering: <http://www.ntis.gov/help/ordermethods.aspx>
Available electronically at no charge: <http://www.osti.gov>

Available in paper for a processing fee to the
U.S. Department of Energy and its contractors, from:

**U.S. Department of Energy
Office of Scientific and Technical Information
P.O. Box 62
Oak Ridge, TN 37831**

Telephone: 865.576.8401
Fax: 865.576.5728

E-mail: reports@osti.gov

Contents

- V Foreword: “SDRD: Staying True to Our Mission”
- vii Introduction: Nevada National Security Site:
Sustained Investment and Technology Partnerships
Drive Research and Development

Strategic Opportunity Research

- 1 Strategic Studies in Dynamic Material Response of
Weapons-Relevant Materials
Robert S. Hixson
- 17 Drone Video Platform–Collision Avoidance,
Situational Awareness, and Communications
Rusty Trainham

Exploratory Research

Material Studies and Techniques

- 39 Simultaneous Raman and Pyrometric
Temperature Measurements of a Shock Wave–
Compressed Material
Gene Capelle
- 47 A Multi-Axial Time-Resolved Spectroscopic
Technique for Magnetic Field, Electron Density, and
Temperature Measurements in Dense Magnetized
Plasmas
Eric C. Dutra
- 59 Correlation between Hot Spots and 3-D Defect
Structure in Single and Polycrystalline High-
Explosive Materials
Cameron Hawkins
- 65 Quasielastic Plastic Flow in Dynamically
Compressed Materials
Jason Scharff
- 71 Dynamic Measurement of Chemical Composition
and Chemical Reaction with Surrounding Gas of
Shock Wave–Generated Ejecta Particles
Dale Turley

Instruments, Detectors, and Sensors

- 77 Next-Generation Photomultiplier Detectors
Using Transmissive III-Nitride Semiconductor
Electrodes
Robert Buckles
- 85 Adaptive Source Localization Using Augmented
Reality
James Essex
- 91 Man-Portable Dense Plasma Focus for Neutron
Interrogation Applications
Brady Gall
- 101 Silicon Strip Cosmic Muon Detectors for
Homeland Security
J. Andrew Green
- 109 Transient RF and Optical Plasma Signatures
Clare Kimblin
- 123 Triggerable Mode-Locked Laser for Synchronization
with Dynamic Compression Experiments
Brandon La Lone
- 129 Gas-Phase Ion-Neutral Interactions of Cerium
Ions with Deuterium
Manuel J. Manard
- 137 Dark-Fringe Velocimeter for Measuring Fast Transient
Features in Shock Wave profiles with 1 m/s Precision
and 50 ps Time Resolution
E. Kirk Miller
- 145 A Semiconductor-Based High-Yield X-Ray
Photocathode
Kathy Opachich
- 151 Single-Crystal X-Ray Spectropolarimeter
Radu Presura

Computational and Information Sciences

- 159 A Spectral Evaluation of the Application of Super-Resolution to Commercial Satellite Imagery
Chris Burt
- 167 Dynamic Test Prediction and Characterization through Modeling-Informed, Multi-Source Data Fusion
Aaron Luttmann
- 177 Real-Time Modification of a Modulated Wireless Digital Bit Stream
Ryan Martin
- 185 Algorithm Development for Targeted Isotopics
Eric Moore
- 193 Dynamic Algorithms for Aerial Measurements
Rusty Trainham

Photonics

- 201 X-Ray Phase Contrast Imaging for Dynamic Material Mix Experiments
Daniel J. Clayton
- 209 X-Ray Doppler Velocimetry
Jeffrey A. Koch
- 215 Fast Spectroscopic Temperature and Pressure Measurements Using a Time Stretch–Dispersive Fourier Transformation
Jason Mance
- 221 Multi-Frame X-Ray Imaging Using a Streak Camera with a Patterned Photocathode
Daniel Marks

Appendix: SDRD Performance Metrics

Unpublished Summaries
Available from SDRD Program Office,
Las Vegas, NV 89193-8521

Improvised Chemical Device Source Term
Determinations (ICD-STD)
John Di Benedetto

Flexible Intelligent Multi-Node CBRN
Environment Simulator
Richard Hansen

SDRD: Staying True to Our Mission

With an increased sense of national security mission urgency, there is a need for concurrent Nevada National Security Site (NNSS) urgency to develop and deploy the next generation of capabilities that will offset many of the global challenges we face today as a nation. Hence, it is Mission Support and Test Services (MSTS) leadership's intent to continue to grow the Site-Directed Research and Development (SDRD) program so we can continue to meet the challenges of the future. However, increased funding is not the only solution to our challenge. The needs of the nation require our greater focus on specific and impactful mission-germane needs. In response, our scientific efforts require careful study of our future mission requirements and the crafting of innovative solution concepts worthy of taxpayer investment.

In my vision, the SDRD program has three purposes. They are to:

- 1. Identify and pursue technologies of value and importance to our national security mission.*
- 2. Research and develop concepts that have high-value and may be too risky for other program investment.*
- 3. Develop excellence and foster curiosity within our scientific talent pool.*

First, in identifying technologies of value and importance to our national security mission, SDRD-funded research develops capabilities that mature and are ultimately incorporated in experimental work done at the NNSS.

Second, we balance a mission-centric portfolio with a practical process that allows scientists to explore high-value, high-risk scientific endeavors without fear of failure. If we do our jobs well, we will restock the technical cupboards with multiple technical solutions capable of answering emerging issues and challenges to our national security mission.

Third, we encourage the technical workforce to delve into areas of great personal interest in order to stimulate creativity and scientific debate. A clear sign of this engagement is another R&D 100 award for NNSS and continued publication of our fine work in nationally significant scientific journals.

I remain impressed with the competencies and capabilities of our scientific staff and the output of the SDRD program. Your contributions of practical solutions to difficult problems, high-value high-risk exploratory research, prestigious national awards, and publications in relevant scientific journals is greatly appreciated and an indicator of the quality of our program and creativity of our scientists. Congratulations on a continuing job well done!

Mark Martinez
President



This page left blank intentionally

Introduction

NEVADA NATIONAL SECURITY SITE: SUSTAINED INVESTMENT AND TECHNOLOGY PARTNERSHIPS DRIVE RESEARCH AND DEVELOPMENT

Sustained investment and ongoing core innovation are the keys to successful research and development programs. These elements drive the Site-Directed Research and Development (SDRD) Program and provide solutions to some of the most challenging problems our nation and our allies face. Our Nevada enterprise, consisting of both our management and operating entity and our NNSA field office, is aggressively investing in SDRD and injecting innovation through strategic partnerships. Our partnerships with universities, industry, and our sister institutions within the National Nuclear Security Administration (NNSA) build upon our core capabilities and allow us to create innovative solutions to support our mission requirements.

In 2018, we raised the investment level of SDRD for only the second time in the history of the program. Nearly at our congressionally authorized limit, SDRD has substantial resources to successfully address numerous issues. Investment is only one part of the equation; innovation is generated through collaborations that bring discovery and provide the “technical differentiation” and the return on investment we seek. This report demonstrates an enduring theme of how partnerships help us drive the best outcomes and provide the maximum impact possible, while using our resources efficiently.

SCIENCE AND TECHNOLOGY PARTNERSHIPS HARNESS INNOVATION

Although technology partnerships are not new to advanced research and development, they are sometimes viewed as add-on activities, not central parts of an institution’s framework. In our case, we have been transforming the culture of partnerships and collaborations for many years now, with SDRD investment driving change. Most of our multidisciplinary SDRD projects have strong university collaborations that provide an advantage by leveraging talent. With these partnerships applied as a force multiplier, we achieve much more than



traditional independent research. This is evident in many of the projects in this annual report, which also highlights two of our most productive university collaborations in the past few years (see “SDRD and University Collaborations Hit the High Notes,” pages x–xi).

As responsible stewards of government investment, we also strive to support and transition technology in the public interest. We implemented the first SDRD-born CRADA (Cooperative Research and Development Agreement) with a private company to further enhance and develop operational potential for radiation detection equipment (see “NNSA Cooperative Research and Development Agreement (CRADA) Supports Advanced Radiation Sensing,” page xii). This highly successful effort illustrates the power of collaborative R&D and represents a model approach for developing mutually beneficial partnerships.

PROJECT SELECTION PROCESS AND FUTURE PROGRAM DEVELOPMENT

In 2018, we issued another broad site announcement (BSA) proposal call similar to our first one in 2017. This guidance outlined our Strategic Initiatives (SIs)

in three major areas: nuclear event detection, dynamic materials and equation of state studies, and advanced algorithms for sensor networks. This BSA defines our strategic opportunity research areas as well as emphasizes our exploratory research desires backed by our *NNSS Technology Needs Assessment*. We have seen effective responses to the BSA now two years in a row and will continue this for our 2020 cycle and presumably beyond.

Proposal and project selection remains essentially unchanged from the previous year, and we are making adjustments as needed to reflect changing requirements in our mission. The discretionary nature of SDRD is one of the most powerful elements in maintaining an efficient and agile responsive R&D program. The latter cannot be understated, and we have utilized this ability to make important corrections in the strategy and direction of efforts. Our FY 2019 proposal call and project selections benefited from this flexibility and, as mentioned, saw an increased response to the strategic areas with highly focused and targeted proposals. We invited 60 full proposals (based on pre-proposal screening described in previous reports), which was slightly lower than last year; however, program and organizational changes and staffing issues influenced our decisions to focus on certain evaluation criteria. Technical review of proposals also remained

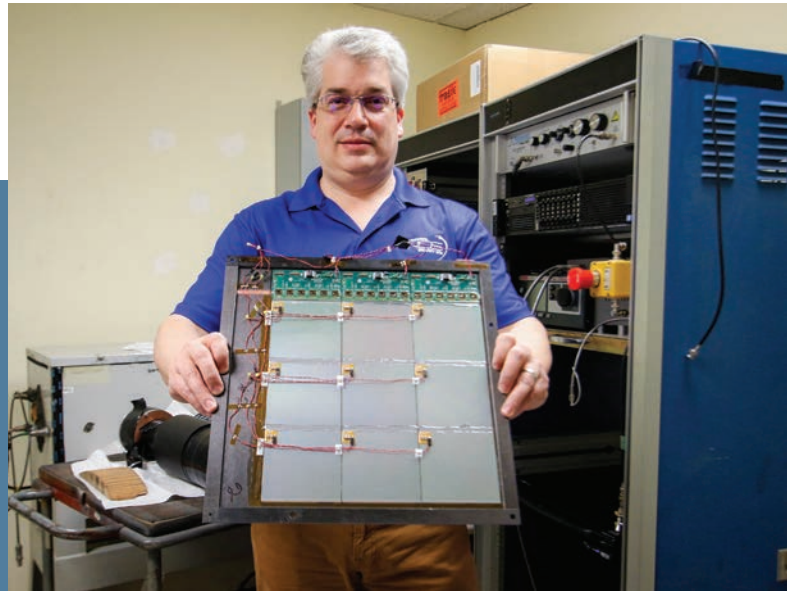
essentially unchanged, with two subcommittees overseeing the pre-proposal process (in our main mission areas) and an integrated team performing the evaluation of the invited proposals. We benefited from a diverse peer review team that encompassed broad technical knowledge and background in program needs and requirements. This balance, coupled with external peer review from our partner laboratories, once again provided a sound and robust assessment that ultimately yielded the best project selection possible.

As mentioned earlier, SDRD took another step forward as we increased the investment rate in 2018 to 3%. This level is nearly at our congressional authorization and, at current NNSS funding levels, the program size is approximately \$14M per annum. A glance back at our previous annual report stated that we would utilize this for furthering our strategic efforts in 2019 and beyond, and this increase is exactly what has been done. As improvements to the program continue, we realize better performance outcomes that are clearly related to prudent decisions. Progressively, we expect to achieve both short- and long-term impacts based on investment choices tied to our mission imperatives. Further enhancements to our research infrastructure, through platform development, equipment investment, and strategic growth in human intellectual capital will be the mainstays in the future.

SDRD Steps to the Future



*SDRD Project
Wins 2018
R&D 100 Award
for Solid-State-
Based Cosmic
Muon Detector
Technology*



Andrew Green holds one plane of silicon microstrip detectors, which have been integrated with their readout electronics. For each detector column, three 10 cm sensors are wire-bonded in series to effectively make ~30 cm sensors. The microstrips cannot be seen individually, but they run vertically in the photo.

The NNS received its sixth R&D 100 Award for the development of silicon strip cosmic muon detectors. The project began as an SDRD in 2016 based on ideas to improve muon detection technology for global security applications. Co-developed with the Fermi National Accelerator Laboratory and Los Alamos National Laboratory, solid-state-based, silicon strip muon detectors are an attractive replacement for drift tube-based systems, which are often cumbersome due to their size and the fact they rely on ionization gases. The very thin and compact muon detector panels can be embedded into structures and assembled into multiple layer arrays. They do not require extensive calibration and are inherently safer without

the risk of high voltage. These detectors enable so-called muon trackers to interrogate shielded nuclear materials, explosives, and other items of interest. The identification process allows threats that could be concealed in different types of materials to be recognized. Various implementation options make the silicon strip muon detectors a potentially paramount advantage to maritime safety and homeland security.

“It is a great accomplishment for the Nevada National Security Site and our multi-laboratory team to receive one of this year’s R&D 100 Awards,” said Robert Koss, Mission Support and Test Services Strategy Development Manager. “The scientists and engineers who developed this award-winning

technology are keeping our nation at the forefront of innovation through contributions to U.S. and global security.”

The NNS has previously won R&D 100 awards for its 2017 Geometrically Enhanced Photocathodes, 2013 KiloPower, 2012 Multiplexed Photonic Doppler Velocimeter, 2010 Movies of eXtreme Imaging Experiments, and 2009 High-Resolution Holography Lens. In each case of these prior awards, partnerships were an important and driving factor in the innovation.

SDRD and University Collaborations Hit the High Notes

Laser-based Microscale Fusion with Record-Setting Efficiency for Neutron Generation

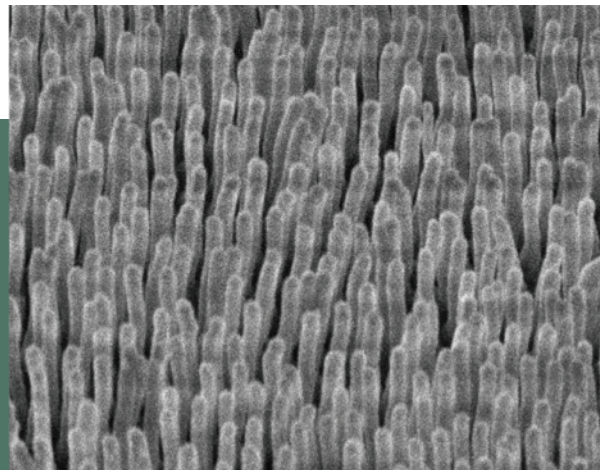


A significant discovery in laser-based microscale fusion was recently featured in the prestigious journal *Nature Communications* (A. Curtis et al., “Microscale fusion in dense relativistic nanowire array plasmas,” *Nat. Comm.* **9** (2018) article 1077). This article was the culmination of a three-year combined NNSS SDRD effort and collaboration with Colorado State University to study neutron production from ultrahigh energy density laser-produced plasmas. The new pulsed neutron source is based on nanowire targets that are irradiated with high intensity, ultrashort pulse terawatt class lasers. In the laser plasma source here, DD fusion is induced with the femtosecond laser drive and produces a very short pulse of energetic (2.45 MeV) neutrons using specially made deuterium nanowire targets.

The collaboration was highly successful due to the teamwork required to overcome many of the several challenges inherent in frontier research.

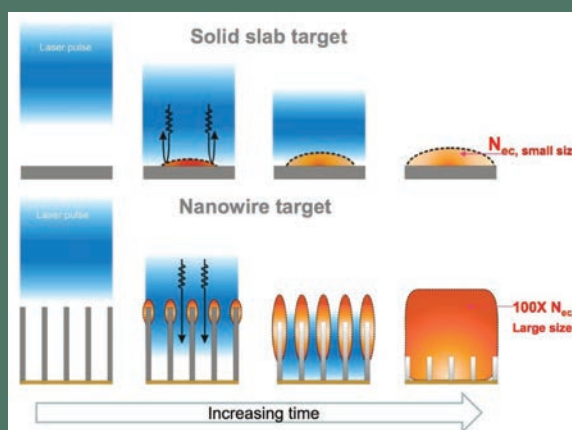
As the article describes, key achievements in target fabrication and plasma modeling and diagnostics were central to the discovery. For instance, building well-formed nanowires out of deuterated polyethylene was crucial, and considerable innovation was needed to make highly ordered structures suitable as targets and ensure the proper plasma conditions. With the very high energy contrast laser pulse, the energy penetrates the target volume and is more completely absorbed than if the laser were incident on a solid target surface. Strong coupling of the incident laser radiation and the target material produces an extremely hot and high-density plasma.

New studies show that as the laser energy increases beyond current achievable levels, the dynamics of the laser–target interaction



Deuterated nanowire array targets for the laser-based microscale fusion experiments

enter a new regime. In these cases, it may be possible to consider new schemes, such as layered target geometries where neutrons are launched and react to produce preferential directional output. This neutron source has the potential to open up new applications related to the NNSS mission, such as advanced neutron-diagnosed subcritical testing and more fundamental studies in dynamic materials.



Neutrons produced by a traditional solid slab target (top) compared to those possible when an ordered nanowire array (bottom) absorbs the incident laser energy

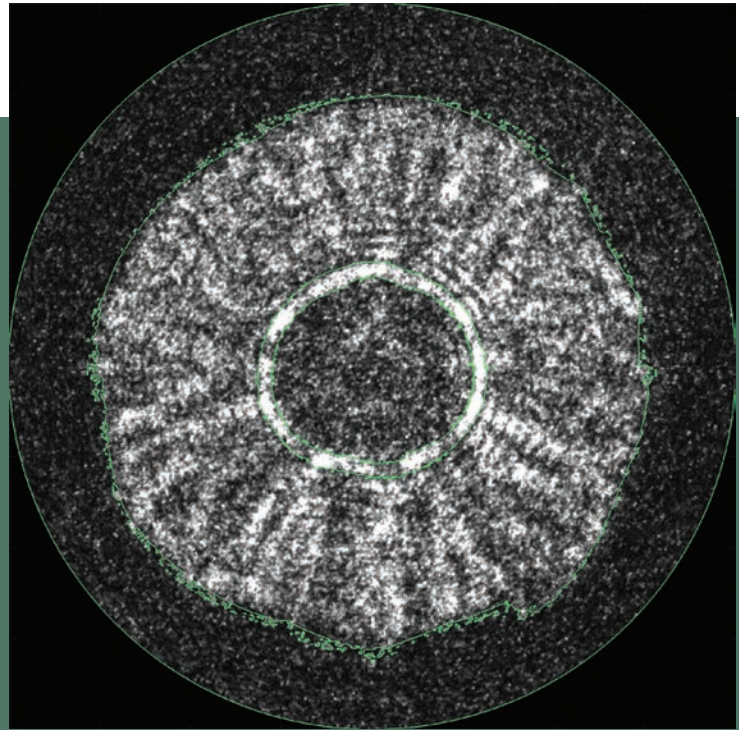
Machine Learning Algorithm for Statistical Image Segmentation Improves Digital Image Analysis

Following up on previous successes, a team of NNSC researchers with their collaborators at MIT and the University of Alabama in Huntsville has published a new article in the *SIAM Journal of Scientific Computing* (*SIAM J. Sci. Comput.*, **40**, 4 B1161–B1179) describing improved extraction of features from x-ray and optical imagery. A core competency within the NNSC, quantitative and statistically reliable analysis of images, is crucial to many of the experiments conducted in support of the stockpile stewardship program and for other national security needs. The techniques developed here, under previous SDRD projects, were meeting a long-standing requirement for uncertainty quantification and robust methods of calculating key features, such as material densities and boundaries. The locally adaptive discriminant analysis (LADA) technique provides a way to train the

machine learning on data classes local and relevant to the image characteristics. This technique allows features to be identified and discriminated against, which would be difficult via other methods and perhaps lead to wrong conclusions about the nature of what is being observed. In addition, repeated use of this method on a large number of images builds a statistical uncertainty with errors attributed to known quantities of interest.

Based on the utility of the LADA technique and statistical quantification, this method has proven to be a highly useful

and effective tool in support of these analysis efforts. New and advanced radiographic machines are being planned for the NNSC, and experiments conducted on these will require quick and accurate analysis of images with minimal subject matter expert interpretation. The use of machine-learned methods will provide a robust and ground-truth component to these efforts and ultimately yield efficient and cost-saving approaches.



Here, ALADA (closely related to LADA) is used to identify boundaries in an image of a laser-induced cylindrically converging shock wave (shock in water). Knowing the exact boundary locations in the image allows for the calculation of quantities such as velocity and pressure. The low resolution and high noise levels in this image cause normal methods to produce unsatisfactory results, but ALADA successfully identifies boundary locations, opening new doors for how we analyze images.

NNSS Cooperative Research and Development Agreement (CRADA) Supports Advanced Radiation Sensing



The Virginia Tech hexacopter carries the Apollo detector and the Raspberry Pi in the pod mounted beneath it, and the 2x2 NaI detector is mounted beneath the pod. This photo was taken in April 2018 at an exercise in Idaho.

A technology partnership and CRADA between the NNSS and H3D, Inc., is improving the ability to detect and identify radioactive sources. The NNSS's Remote Sensing Laboratories at Nellis Air Force Base in Nevada and Joint Base Andrews in Washington, D.C., have responsibility for radiological incident response and rely upon state-of-the-art sensors to detect, measure, and identify radioactive sources. The partnership holds promise for enhancing the NNSS mission using unmanned aerial systems (UASs) to measure radioactivity in places where deploying our manned aircraft may be too challenging or difficult. Initially begun as one of the first strategic SDRD efforts, the project quickly identified key technology that could enhance operational aspects by using special sensors and imagers uniquely adaptable to the compact system requirements. H3D's suite of CZT gamma imagers were a natural possibility for further development on aerial platforms and were already highly

successful tools for radiation detection and surveillance. H3D's technology grew out of research conducted at the nuclear engineering department at the University of Michigan, and the technology was further developed in part by the Defense Threat Reduction Agency.

Our main goal for this CRADA was to implement H3D's high-efficiency radiation detector on UASs provided by the NNSS and prove the concept of remote detection in hazardous environments. As part of the research and development efforts, scientists and engineers from the NNSS integrated the H3D sensors with different UAS platforms, creating flexible and agile systems for measuring radiation. Over the course of the multi-year effort, multiple test flights and operational scenarios were conducted in a multitude of environments. This CRADA has allowed us to leverage commercialized radiation detectors and UAS technology, enabling us to deploy them in entirely new ways and

develop a new asset to respond to nuclear emergencies. The ongoing partnership between H3D and the NNSS will provide research into the trade-offs between sensitivity and resolution of compact radiation detection systems. Integrating the sensor technology with unmanned aerial vehicles has the potential to enhance radiation detection capabilities for our mission and other emergency response agencies. In addition, H3D gained new opportunities for product development for key customers in the nuclear power and waste management industries. CRADAs like this one allow the federal government to partner with private entities, complement NNSA missions, and foster mutually beneficial partnerships to facilitate cutting-edge R&D and economic competitiveness and improve our security and quality of life through innovations in science and technology.



For her outstanding work in research and development, Kathy Opachich was named MVPI in 2018. Her groundbreaking work in x-ray photocathodes garnered an R&D 100 award in 2017. With Kathy is Jeffrey Fuller, Director of Strategic Programs at the NNSS.

Each year the NNSS selects one of its most deserving individuals as the SDRD most valuable principal investigator, the MVPI. This year Dr. Kathy Opachich received the MVPI award for her groundbreaking work in x-ray photocathodes, which also garnered her a 2017 R&D 100 award.

Kathy's seminal contribution that won the R&D 100 began with her FY 2015–FY 2016 SDRD project “High-Yield X-ray Photocathodes for Next-Generation Imaging Detectors.” Her project's hallmark innovation conceived a way to break the limits of detector efficiency and performance in the soft x-ray region for critical diagnostic imaging instruments. The new enhanced photocathodes met a much-needed requirement with improved electron yield, high spatial resolution, picosecond temporal resolution, and low noise coupled with large-area detection. Many of these attributes would be difficult at best to satisfy as sole parameters.

enhanced photocathode that uses microstructure elements lithographically printed and etched onto silicon substrates. These structures are coated with active photoemissive materials such as Au, CsI, and others. Although such structures were previously investigated, they lacked the novel recessed geometry using cone and pillar structures proposed by Opachich. Prior structures introduced noise and did not show stable emission properties. The culminating achievement in Kathy's work was a 3X improvement in quantum efficiency in the 1–12 keV range while maintaining all other desirable properties. Kathy worked with Livermore Operations colleagues, collaborators from Lawrence Livermore and Lawrence Berkeley National Laboratories, and General Atomics and NanoShift, LLC, to develop the photocathode design and produce viable devices.

In two years of research, Kathy invented a new geometrically

In late 2017, a U.S. patent (US9837238B2) was granted for Kathy's photocathode concept; this patent includes many advances and embodiments that could potentially be commercialized in future streak and framing camera systems. The high-yield photocathode can be used for current high energy density physics diagnostics at the National Ignition Facility and other facilities. Such a device, in fact, is beneficial to the U. S. Department of Energy (DOE) Office of Science, the NNSA complex, and to synchrotron facilities worldwide. The successful completion of this project positions the NNSS as one of the few key contributors to next-generation x-ray detectors.

Kathy has also presented her work in multiple talks that elevate the stature of NNSS technical contributions to the broader NNSA community. She has published multiple articles describing her efforts, two in *Review of Scientific Instruments*, and one in *Applied Physics Letters*.

Kathy Opachich, FY 2018 SDRD Most Valuable Principal Investigator

FY 2018 ANNUAL REPORT

SYNOPSIS

This annual report is organized into our two major portfolio elements, Strategic Opportunity Research and Exploratory Research, with the latter grouped into sections by our major science and technology categories. The reports that follow in each are for project activities that occurred from October 2017 through September 2018. Note that project life cycle is indicated under the title as well as the original proposal number (in the following format: site abbreviation--ID #--originating fiscal year, e.g., STL-###-YR).

The SDRD program, now in its 18th year, continues to be the engine for innovation with potential only limited by the imagination of the individuals who contribute their time and talent. Each report contained herein describes the progress, outcomes, and discoveries achieved by the principal investigators and their teams and partners. In many cases, there are clearly recognizable, definitive payoffs. In others, however, there may be considerable uncertainty and/or realization that may not come until many years ahead, which is precisely the definition of high-risk, high-reward research that we have referred to countless times. One of the most satisfying aspects of these efforts is to look back and see the discovery point years before that has led to the transformed world we are experiencing now. This in itself is the critical justification for attempting anything of this nature.

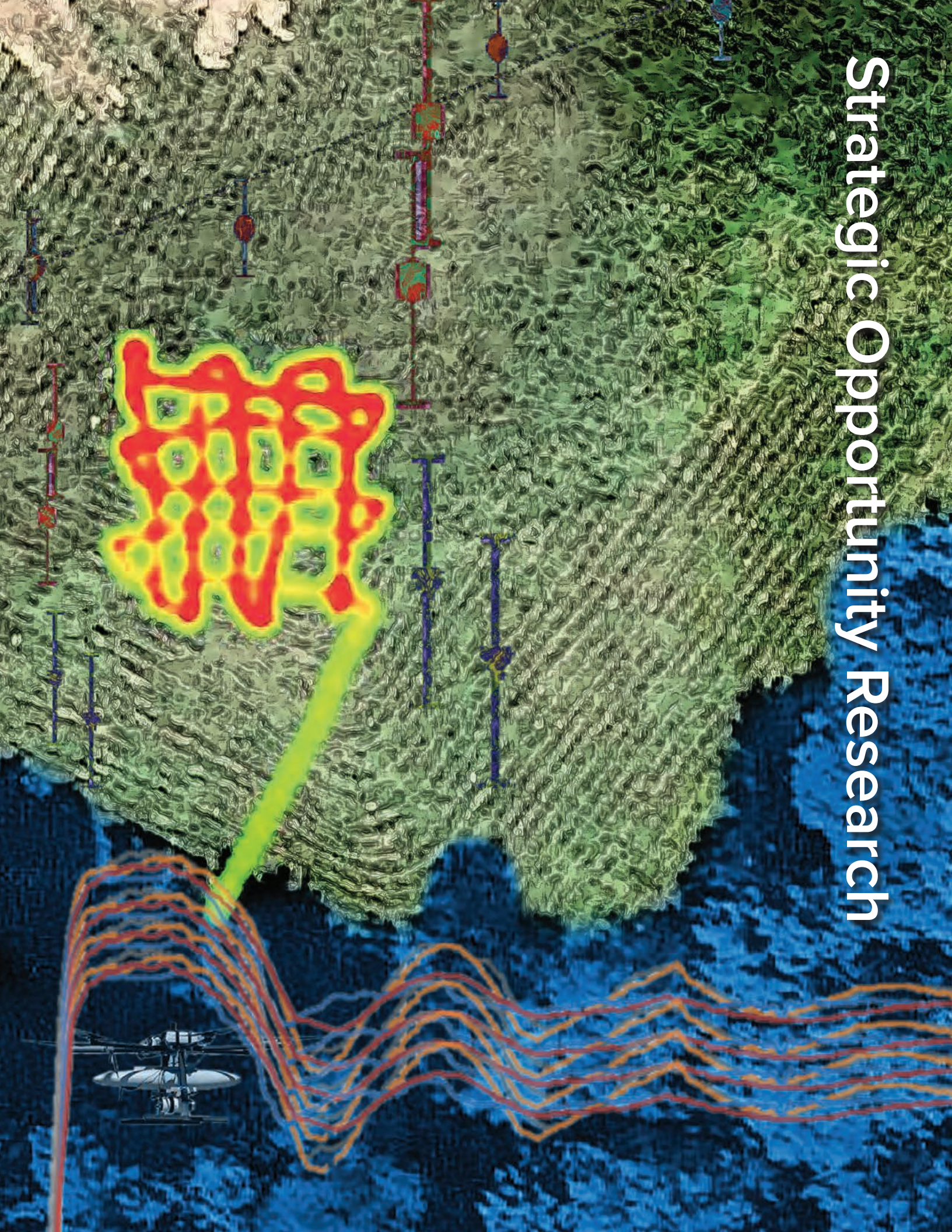
ACKNOWLEDGMENTS

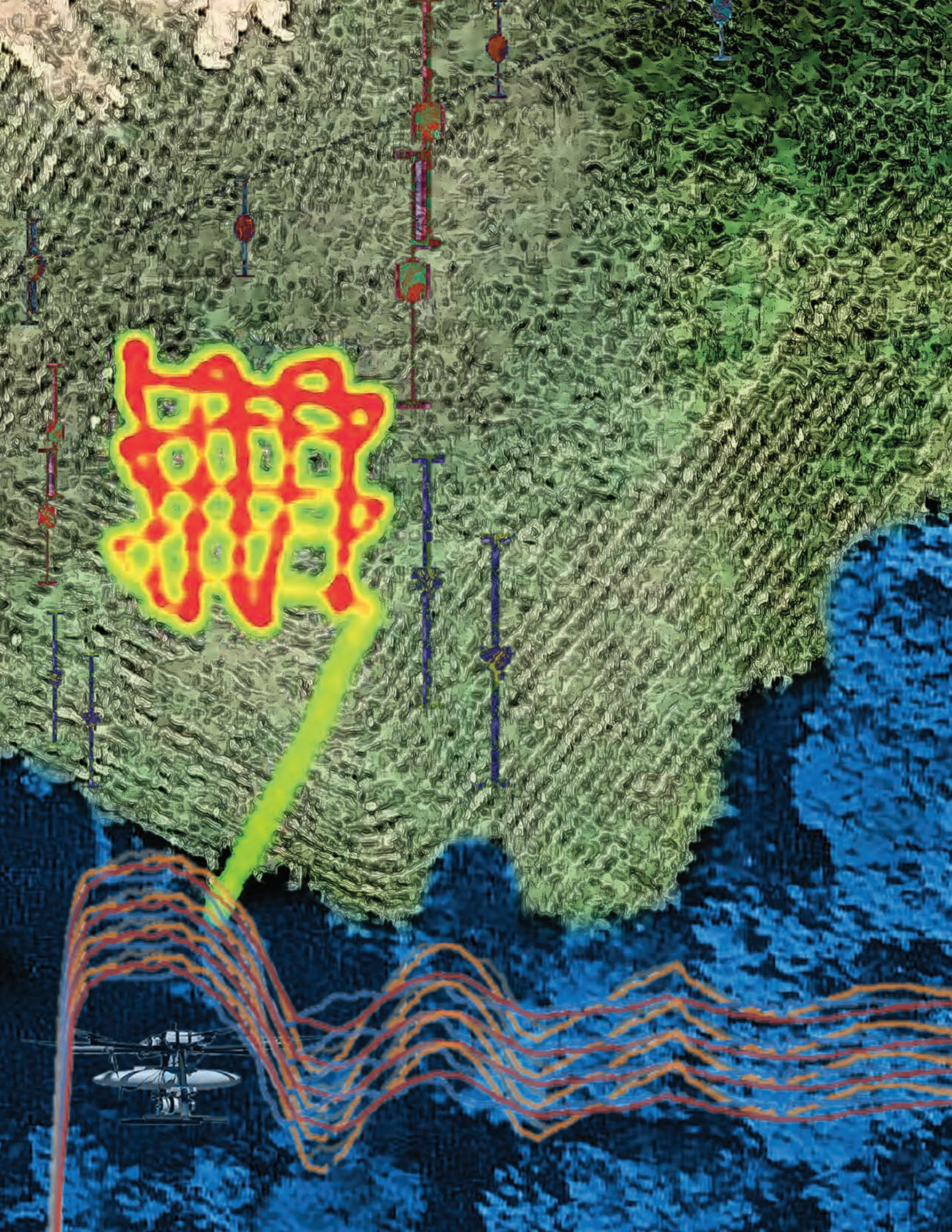
SDRD requires a talented team of individuals to ensure success from year to year. Without their support, none of this would be possible. Special acknowledgment and appreciation goes out to Michele Vochosky, assisted by editors Katsura Rast, Sierra Cory, and Jill Gibson, for technical communications and compiling, editing, and publishing this report; to Katina Loo for providing document design, graphics, and overall book layout; to Tom Graves, Leslie Esquibel, and Emma Gurr for project management and cost accounting efforts; to Newell Ramsey and Kathy Gallegos for information system support; to Eduardo Morales for financial data reporting; to Larry Franks, Rob Hixson, and Lynn Veese for technical guidance and support; and to our SDRD site representatives and technical review committee: Jesse Bonner, Frank Cverna, Daniel Frayer, Paul Guss, Marylesa Howard, Jeff Koch, Craig Kruschwitz, Brandon La Lone, Aaron Luttmann, Mary

O'Neill, Alex Plionis, Patrick Sawyer, Jerry Stevens, and Rusty Trainham. And, finally, special thanks again goes to members of our external advisory board, Larry Franks, Carl Ekdahl, Damon Giovanielli, Ralph James, Paul Rockett, Maurice Sheppard, Ralph Schneider, and Gerry Yonas, who graciously give their time and provide ongoing, valuable recommendations.

Howard A. Bender III
SDRD Program Manager

Strategic Opportunity Research







Strategic Studies in Dynamic Material Response of Weapons-Relevant Materials

LAO-015-18 ■ Year 1 of 3

**Robert S. Hixson,^{1,a} Sarah Thomas,^a Brandon La Lone,^b Dale Turley,^b
Cameron Hawkins,^c Gerald D. Stevens,^b Lynn R. Veaser,^a
Saryu J. Fensin,^d and David Jones^d**

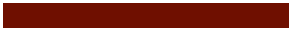
¹hixsonrs@nv.doe.gov, (505) 663-2022

^aNew Mexico Operations—Los Alamos

^bSpecial Technologies Laboratory

^cNevada Operations

^dLos Alamos National Laboratory



We have initiated a research program in dynamic materials properties to understand some key outstanding shock physics issues with regards to certain stockpile materials. Because some of these important materials are difficult to obtain and must be studied in high-hazard facilities, we are exploring relevant physics effects on substitute materials—iron, tin, and cerium. We have chosen to study some materials, cerium and iron, that have dynamic phase transitions, and to study dynamic melting. Because cerium metal has a very low-stress large-volume phase transition, the melting point is low enough to study with single-stage launchers. We are working to better understand both the melting transition and refreezing upon release of stress. We hope to address still-unanswered questions about how melted metals solidify upon release, although this is a challenging goal. In addition, we are exploring how anisotropies in single-crystal metals affect the polycrystalline averages for metals with moderate crystalline anisotropy. Studying the dynamic properties of single-crystal iron this year, we observed clear differences in key dynamic properties such as the elastic limit and spall strength, but more surprising were apparent differences we noted in the shock velocity, which are at least somewhat contradictory to previous results for copper single crystals. This is still a work in progress. We will conduct more rigorous experiments in FY 2019 to better understand these results. We are also focusing on making accurate temperature measurements in dynamic experiments. A key goal is to measure the Hugoniot temperature

and reflectance of cerium up to and above the melting transition in FY 2020. We are uniquely poised to do this with last years' invention of a combined radiance/reflectivity probe. Finalizing a study to map the solid-liquid phase boundary of tin, we believe that we have made the first measurements of sections of the melting curve of tin using dynamic techniques, a very important result. We seek to extend our capability to measure shock temperature (not just radiance) to higher shock stress (50 GPa and beyond) on polycrystalline iron using techniques developed for tin measurements, namely the integrating sphere method developed at the Special Technologies Laboratory. We will continue to test high-entropy alloy materials in FY 2019.

BACKGROUND

There is an outstanding need to explore many dynamic material properties in a quantitative way and use those data to build new generations of physics models. In some cases, experimental techniques do not exist, or are not refined enough to produce high-quality data. For example, to refine multiphase equations of state (EOSs), it is necessary both to measure pure phase thermodynamic properties and to find the location of any phase transitions that cause the fundamental thermodynamic properties to change. Such transitions include both solid-solid and melting. Solid-solid phase changes can be difficult to study, and they are typically measured only on the principal shock Hugoniot, but to map out a phase boundary requires that more points be measured. In shock experiments we can accomplish this by preheating or cooling the sample (not part of the current project). The location of the shock melting point on the principal Hugoniot is also important, as is the complete melt curve. It is well known that shock melting can happen quickly, but less well known is the timescale for solidification. To make these measurements requires complex loading (including loading, unloading, and reloading) methods. We are studying materials with the simplest crystalline structures (iron and tin) and those with complex and anomalous phase diagrams (cerium). We have developed a method to map the melt boundary of tin, and we are now attempting to expand the method to measure shock temperatures of iron at relatively high stress states (tens of GPa). Finally, we are planning to investigate solid-solid, solid-liquid, and liquid-solid phase changes for cerium metal.

What follows is a summary of our research thrusts for FY 2018. First, perform research on single-crystal iron to examine dynamic properties as a function of

orientation. The properties to be studied include shock speeds, Hugoniot elastic limit (HEL), spall strength, and sound speed. Second, finish work to dynamically determine the melt curve for tin. We need to collect more data to publish work done on a predecessor SDRD project (Hixson 2016; La Lone 2017, 2018). We intend to complete and publish the results of this effort in 2019. Third, conduct research on cerium metal to examine the low-stress phase change, shock melting, and solidification using both velocimetry and radiance/reflectivity methods. We will be developing complex loading methods. Fourth, make credible temperature measurements, using a combination of radiometry and dynamic reflectivity, in shock-loaded iron at stress states up to 50–60 GPa. This is a challenging problem for several reasons, including extraneous light caused by the relatively high stress. Fifth, undertake a small, exploratory effort to characterize high-entropy alloy (HEA) materials for shock-compression response. These materials were characterized for mechanical properties by MST-8 Division at Los Alamos National Laboratory (LANL), but shock response is unknown. This is a dynamic research topic of prime interest to the high-pressure physics community. Sixth, execute the first experiments on the 40 mm powder launcher at the Special Technologies Laboratory (STL).

PROJECT

Single-Crystal Metals

Most shock compression research has been done on isotropic materials, which have the same properties in all directions. Anisotropic materials are well known to have different elastic properties as a function of orientation, but it is less clear if shock properties are

also different. In previous projects we have clearly shown that for single-crystal metals with moderate anisotropy, the compressive strength and dynamic tensile (spall) strengths are directionally dependent, and shock velocities were within 1% to 2% of being the same. This was determined for copper metal, a very low strength material. To look more into this issue, we are studying iron (which has higher compressive strength) and are looking at all three principal crystalline orientations, [100], [110], and [111]. Because single-crystal metals are typically anisotropic to some degree, they may respond differently when shocked along different crystal orientations, and if they do this can lead to texture when polycrystalline versions are produced. The most fundamental property to measure to begin to characterize such anisotropic response is the velocity of elastic and plastic shock waves. Other important properties are compressive strength and tensile strength. Finally, for materials with phase transformations such as iron, it is reasonable to ask if the transformation stress depends on shock direction.

The Zener ratio gives the degree of anisotropy of a material, with a value of 1 being isotropic, and can be written in terms of the cubic elastic constants as $A = 2C_{44}/(C_{11} - C_{12})$. To determine the Zener ratio for iron, we used the values of $C_{11} = 2.2809$, $C_{12} = 1.3348$, and $C_{44} = 1.1086$ (Simmons 1971). The calculated Zener ratio was $A = 2.34$, which indicates that iron is moderately anisotropic. In the elastic regime, isotropic materials have the simplest response. Elastic properties are the same in all directions, and the constitutive relation is also simple, described by

$$\begin{bmatrix} \sigma_{xx} \\ \sigma_{yy} \\ \sigma_{zz} \\ \sigma_{yz} \\ \sigma_{zx} \\ \sigma_{xy} \end{bmatrix} = \begin{bmatrix} \lambda + 2\mu & \lambda & \lambda & 0 & 0 & 0 \\ \lambda & \lambda + 2\mu & \lambda & 0 & 0 & 0 \\ \lambda & \lambda & \lambda + 2\mu & 0 & 0 & 0 \\ 0 & 0 & 0 & \mu & 0 & 0 \\ 0 & 0 & 0 & 0 & \mu & 0 \\ 0 & 0 & 0 & 0 & 0 & \mu \end{bmatrix} \begin{bmatrix} \epsilon_{xx} \\ \epsilon_{yy} \\ \epsilon_{zz} \\ \epsilon_{yz} \\ \epsilon_{zx} \\ \epsilon_{xy} \end{bmatrix}, \quad (1)$$

where λ and μ are called the Lamé constants. The elastic response of isotropic solids depends on only these two constants.

Slightly more complex are single-crystal solids with cubic structure (either simple, face-centered cubic or body-centered cubic). For this class of material, the elastic response is governed by three elastic constants, C_{11} , C_{12} , and C_{44} . The constitutive relation is

$$\begin{bmatrix} \sigma_{xx} \\ \sigma_{yy} \\ \sigma_{zz} \\ \sigma_{yz} \\ \sigma_{zx} \\ \sigma_{xy} \end{bmatrix} = \begin{bmatrix} C_{11} & C_{12} & C_{12} & 0 & 0 & 0 \\ C_{12} & C_{11} & C_{12} & 0 & 0 & 0 \\ C_{12} & C_{12} & C_{11} & 0 & 0 & 0 \\ 0 & 0 & 0 & C_{44} & 0 & 0 \\ 0 & 0 & 0 & 0 & C_{44} & 0 \\ 0 & 0 & 0 & 0 & 0 & C_{44} \end{bmatrix} \begin{bmatrix} \epsilon_{xx} \\ \epsilon_{yy} \\ \epsilon_{zz} \\ \epsilon_{yz} \\ \epsilon_{zx} \\ \epsilon_{xy} \end{bmatrix} \quad (2)$$

For solids with less symmetry, the number of required elastic constants increases. For cubic symmetry, the bulk modulus, K , is an invariant of the elastic constant tensor

$$K = \frac{C_{11} + 2C_{12}}{3}. \quad (3)$$

We also know that $K = \rho_0 C_b^2$, where C_b is the bulk sound velocity and ρ_0 is the initial material density. This implies that the bulk sound speed does not depend on direction in crystals with cubic symmetry in the elastic regime. Because the y -intercept of the plastic shock Hugoniot is approximately equal to C_b , the Hugoniot in the various directions might be expected to have close to the same y -intercept in U_s-u_p (shock velocity-particle velocity) space. For materials with linear Hugoniot in U_s-u_p space, the slopes might still be different; this should be looked at in more detail, both theoretically and experimentally. But the directional elastic Hugoniot, as well as the HEL, may still be expected to be different in general.

So it makes sense to carefully measure shock properties in the [100], [110], and [111] directions for a cubic system. We previously studied single-crystal copper (Thomas 2017, 2018b), which has very low strength and no solid-solid phase changes. Now we are looking at iron, which has relatively high compressive strength and a solid-solid phase change at about 13 GPa. Some limited research has been done on single-crystal iron (Jensen 2009), but that research did not examine all the properties we plan to study. Based on the above considerations and our previous research on copper, we expect to observe different elastic wave speeds but plastic wave speeds that fall on the polycrystalline Hugoniot. We also expect to observe different spall and compressive strength responses in the different orientations.

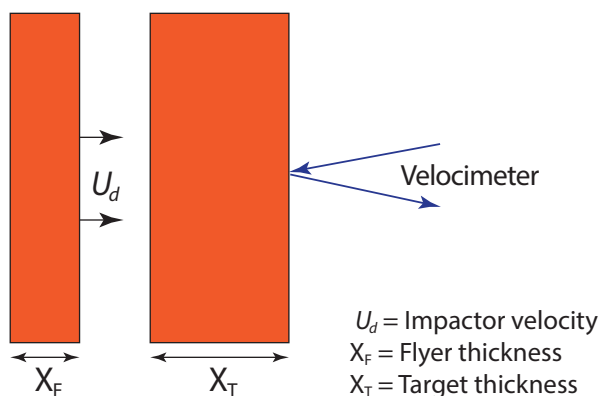


Figure 1. Experiment design used in all experiments

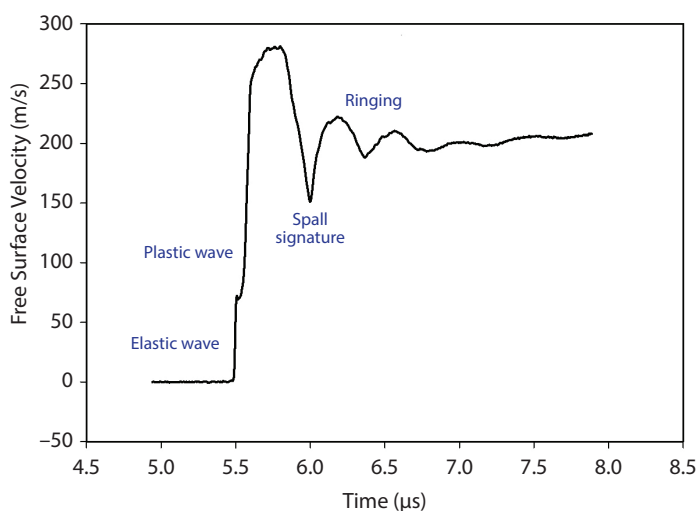


Figure 2. The 1018 steel control shot (experiment 80) had a nominally 2 mm thick target and 1 mm thick impactor. The characteristics of the wave profile, as labeled, appear in all such plots.

Design and Results of Iron Experiments

Several experiments were performed on single-crystal iron in the [100] and [111] orientations.

We used a very simple experimental geometry with a sample free surface so that spall would occur in the target single crystal.

For most experiments, we used samples of polycrystalline iron as the impactor (1018 cold rolled steel) because large single crystals are difficult to procure and very expensive.

However, we conducted a few symmetric impact shots using single-crystal impactors to see if the release wave structures mattered. In addition, we performed a control experiment with polycrystalline iron onto polycrystalline

iron at the same thicknesses and impact velocity. For the first experiments, targets were nominally 14 mm in diameter and 2 mm in thickness, and impactors were 14 mm in diameter and 1 mm in thickness. Because we know that shock waves in iron take a long run distance to become steady, we will be observing some nonequilibrium effects, particularly with regard to the elastic wave amplitude. However, we can compare this amplitude among our experiments to look for systematic differences as a function of orientation.

Because we wished to obtain a broad range of information from these first experiments, we used a simple experimental geometry (Figure 1) that is well suited for spall measurements (with a sample free surface). This design also yields information on compressive strength and shock velocity. Measuring shock velocity in this way yields results that have slightly larger error bars than can be obtained on experiments having a more complex design, which we intend to perform in FY 2019. The NNSS single-stage gas gun in North Las Vegas was used for all experiments.

Metrology was done on all samples tested. Both initial density and sound speeds were measured, as well as flatness and parallelism of sample surfaces. Samples were lapped to be flat and parallel to $\sim 10 \mu\text{m}$. Example results are shown in Table 1.

Impactor velocities were measured with electrical shorting pins and a single channel of photonic Doppler velocimetry (PDV, collimating probe) looking down the barrel. Shown in Table 2 are the impact velocity and thicknesses for all experiments.

All experiments had tilts of a few milliradians, typically from 1 to 2 mrad. Good time-resolved results were obtained for data for polycrystalline steel, and iron in the [100] and [111] orientations. Figure 2 shows one of the polycrystalline 1018 steel control

Table 1. Sample properties and results

MATERIAL	SAMPLE DENSITY ρ_0 (g/cm ³) ±0.04	LONGITUDINAL SOUND SPEED C_L (km/s) ±0.03	SHEAR SOUND SPEED C_S (km/s) ±0.02
1018 steel	7.84	6.02	3.25
[100] iron	7.78	5.47	3.78
[111] iron	7.88	6.33	2.94

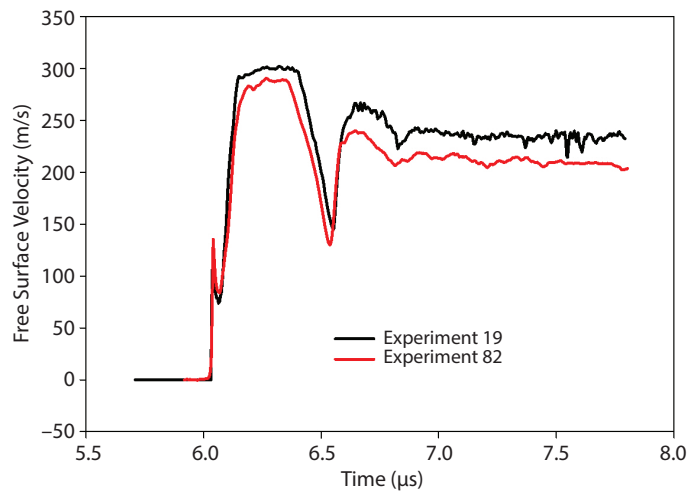


Figure 3. Results for single-crystal [100] iron experiments 19 and 82. Experiment 19 had a [100] iron impactor, and experiment 82 had a 1018 steel impactor.

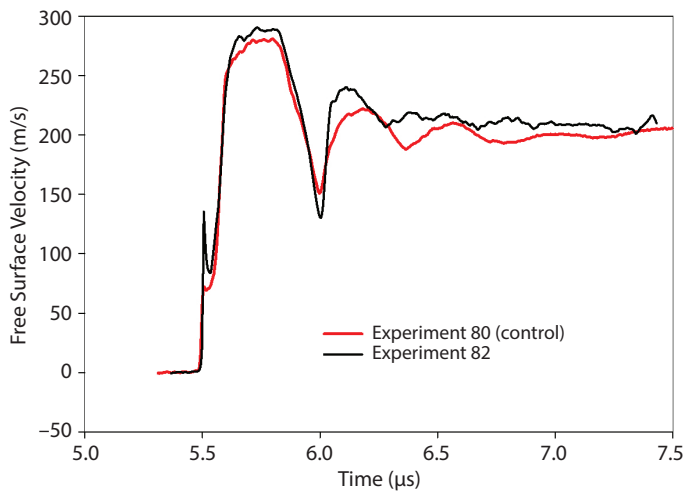


Figure 4. Wave profile comparison of polycrystalline 1018 steel (experiment 80) and [100] iron (experiment 82) results at impact conditions similar to those in Figure 3

experiments. We can use this polycrystalline result as a baseline for comparison with single-crystal iron results.

We performed two single-crystal [100] iron experiments, one using a 1018 steel impactor (experiment 82) and one using a [100] iron impactor (experiment 19). Time-resolved results are shown in Figure 3. We observe reasonable reproducibility given the small difference in impactor velocity. Experiment 19 had a higher impact velocity.

Figure 4 is a plot of the polycrystalline 1018 steel (experiment 80) and [100] iron (experiment 82) results at essentially the same impact condition. Clear differences are observed. We note that the elastic wave amplitudes are very different, and the [100] iron data show a pronounced precursor decay. Reasons for this are not currently understood. In addition, the peak particle velocity states are different, even though the impact speeds are nearly identical (both measured at 0.293 km/s). Spall signatures show that the spall strength for [100] iron is clearly higher than that for polycrystalline 1018 steel. We note that even though the timing of the elastic and plastic wave arrivals are also nearly identical, the measured elastic longitudinal wave speeds are much different. This suggests that there may be a different plastic shock velocity.

For the [100] experiments we note that the very large elastic wave and its triangular shape can cause significant perturbations to the plastic wave before it reaches the free surface. This means that we need to do window experiments before we can draw any quantitative conclusions about shock velocities.

Table 2. Measured parameters

EXPERIMENT NUMBER	FLYER MATERIAL	FLYER VELOCITY (km/s) ± 0.003	TARGET MATERIAL	TARGET THICKNESS (mm) ± 0.005	FLYER THICKNESS (mm) ± 0.005
80 (Control)	1018 steel	0.293	1018 steel	2.024	1.016
81	1018 steel	0.293	1018 steel	2.020	1.014
82	1018 steel	0.293	[100] iron	2.080	1.015
83	1018 steel	0.293	[111] iron	2.073	1.010
19	[100] iron	0.302	[100] iron	1.978	0.982
20	1018 steel	0.303	[111] iron	1.986	0.977

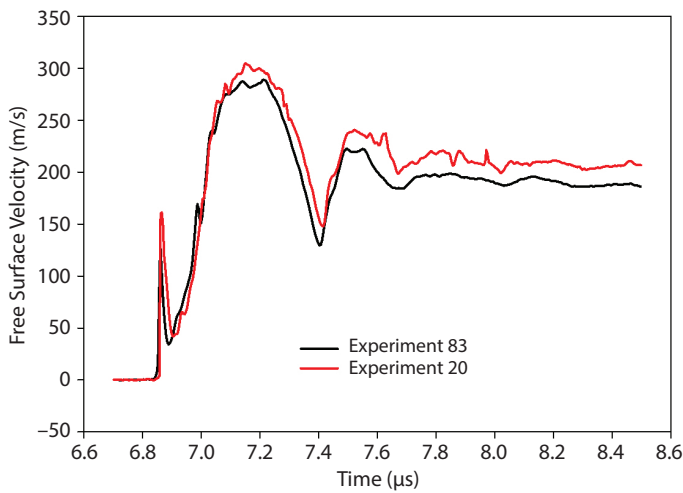


Figure 5. Wave profile comparison of two experiments performed on single-crystal iron in the [111] direction (experiments 83 and 20); both used polycrystalline 1018 steel impactors

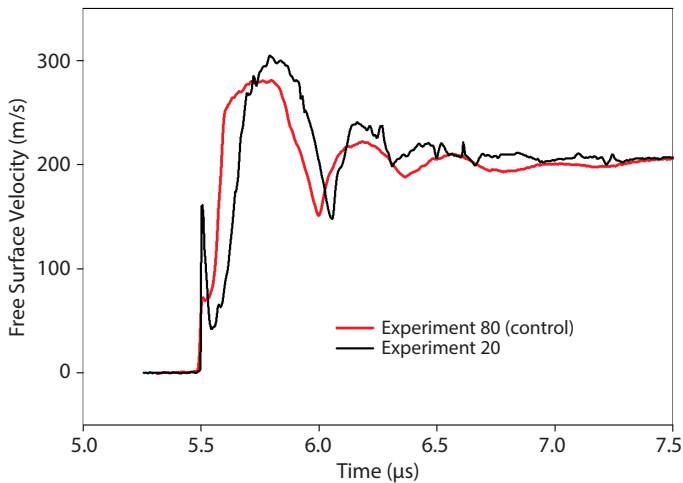


Figure 6. Plot of polycrystalline 1018 steel data (experiment 80) and single-crystal [111] iron data (experiment 20)

Two single-crystal iron experiments using polycrystalline steel impactors were done in the [111] iron orientation as well (experiments 83 and 20), and the time-resolved data are shown in Figure 5. Experiment 20 had a slightly higher impact velocity, so it also had a higher peak free surface velocity. There is a noticeable “glitch” in the plastic wave rise for experiment 83, which may be an analysis artifact, or the glitch may be related to the elastic wave reflecting from the free surface into the oncoming plastic wave. If this artifact is due to the elastic wave reflecting back into the oncoming plastic wave, we must ask why this artifact is not observed in experiment 20. Experiment 20 was very noisy, which may be due to poor signal

level in the experiment. One feature that really stands out in these datasets is the very pronounced elastic precursor decay that occurs immediately after the elastic wave rise. This is not completely understood yet, but is clearly related to the dislocation dynamic processes in this direction. This precursor decay is also observed in the [100] iron data, but to a lesser extent; it is not present in the polycrystalline 1018 steel data.

Next, we compared the polycrystalline 1018 steel data (experiment 80) with [111] iron data (experiment 20), at similar impact velocities (0.293 and 0.303 km/s, respectively), as shown in Figure 6. Here we see significant differences in the amplitude and shapes of the elastic waves, and a large difference in the arrival times of the plastic shock waves even though the sample thicknesses were nearly identical. The elastic wave speed of the [111] iron is higher than that of the polycrystalline 1018 steel, but this does not fully account for the relatively late arrival time of the plastic shock wave. We note that the impact velocities were slightly different, as is observed in the peak free surface velocity as well.

Finally, we plotted representative [100] and [111] iron experiments 82 and 20 (Figure 7) for comparison. We see differences in the structure and amplitude of the elastic waves and the arrival times of the plastic waves. We also note that ringing after spall pullback is much damped for experiment 82 when compared to experiment 20.

The results above are preliminary, and in FY 2019 we will repeat and validate them. We will also develop new methods for measuring elastic wave speed directly.

Calculated Results

We can estimate spall strength by using the momentum shock jump condition

$$\sigma_{spall} \cong \frac{1}{2} \rho_0 C_b \Delta u_{fs}, \quad (4)$$

where u_{fs} is the measured free surface pullback velocity and C_b is the bulk sound speed. To calculate peak stress values, we use the polycrystalline Hugoniot for alpha-phase iron (Thomas 2018a),

$$U_s = 4.477 + 1.620 u_p. \quad (5)$$

Typical uncertainties in velocimetry data are ~1% in velocity and ~1 ns in timing.

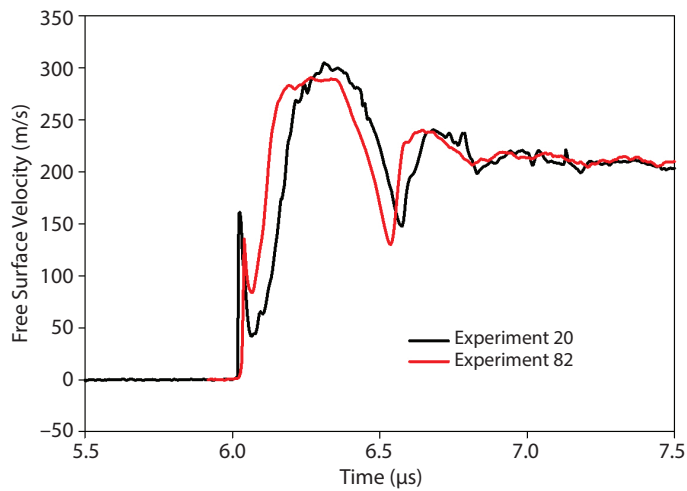


Figure 7. Wave profile comparison of [100] iron (experiment 82) and [111] iron (experiment 20) results

The amplitude of the elastic wave is also found from the momentum jump condition

$$\sigma_E = \frac{1}{2} \rho_0 C_L u_{fs}, \quad (6)$$

where C_L is the longitudinal elastic sound speed. Values determined from these experiments are given in Table 3.

One of the major goals of this project is to determine if plastic shock velocities depend upon crystalline orientation. From ultrasonic sound speed measurements (including our own), it is clear that small amplitude elastic waves travel at different velocities in all of the orientations we have studied. Johnson (1974) predicts that plastic waves at low pressure travel at the same bulk sound speed in the [100] and [111] orientations but at a different velocity

Table 3. Calculated values for precursor amplitude and spall stress

EXPERIMENT NUMBER	PRECUSOR AMPLITUDE σ_E (GPa) ± 0.01	SPALL STRESS σ_{SPALL} (GPa) ± 0.01
80 (Control)	1.70	2.40
81	1.72	2.44
82	2.89	2.02
83	3.37	3.47
19	2.85	1.97
20	4.02	3.25

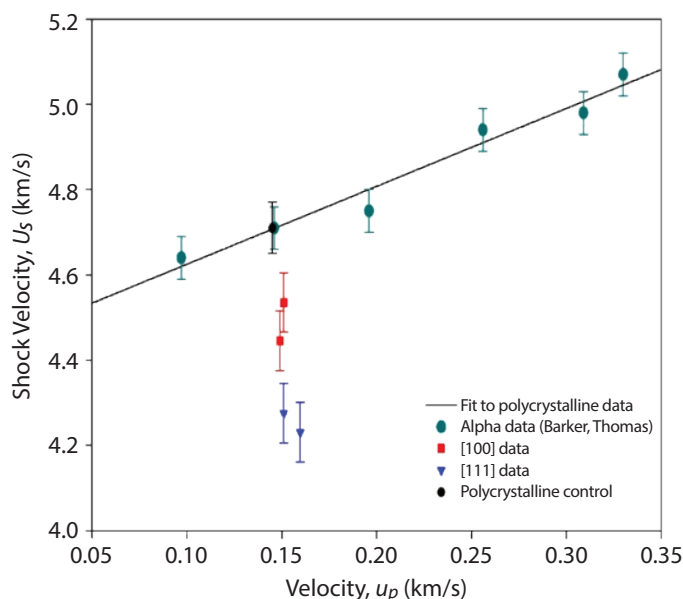
in the [110] orientation (specifically for the sodium chloride structure). The bulk sound speed for many materials is close to the U_s intercept for U_s-u_p Hugoniot, so if the bulk sound speed is different, the shock Hugoniot will be as well. At higher stress, it is less clear what will happen. The work of Chau (2010), which only examined relatively high stress states, concludes that the single-crystal Hugoniot points are the same as the polycrystalline Hugoniot for copper. To our knowledge, no prior research has studied this issue for single-crystal iron.

We applied a technique previously developed for use on polycrystalline iron and steel (Thomas 2018a) to these data to determine shock velocities. We applied the same analysis method to all our data. We note that this method yields good values for shock velocity when elastic wave

amplitudes are small but that other methods may give more accurate values. We will apply one or more of these techniques in the future. Future work includes measuring the velocity of the elastic wave in dynamic experiments to see if our experimental technique increases accuracy. The method applied here assumes that the elastic shock waves travel at the same speed as the known elastic sound speed for each orientation; it uses that sound speed to determine impact time, which is then used to calculate shock speeds. We assume that the toe of the elastic wave is running at this sound speed—that is, the elastic wave has not shocked up enough to make its velocity increase. This assumption seemed to hold in our prior research on iron and steel. We also note that how well this method works depends on how well we can identify the first motion of the elastic wave. This, in turn, can depend on how the PDV data are analyzed (Strand 2006). We have taken all this into account in assigning uncertainties. Table 4 shows our results for shock velocity. The data for shock velocity are plotted in Figure 8. Work is underway to refine error bars. However, even with the conservative error bars shown in Figure 8, there is a variation of measured shock velocity with orientation for roughly the same peak stress state. This result is extremely interesting and warrants further investigation. However, as mentioned above, the large triangular-shaped elastic wave we observe in the single-crystal samples can cause results on calculated shock velocity to be in error. In addition, when this triangular wave reflects from the free surface of the sample, it can cause tension. If this leads to spall damage, shock speed results can be affected. To investigate this we will be performing window experiments in FY 2019.

Table 4. Shock velocity and peak stress

EXPERIMENT NUMBER	PEAK STRESS σ_{PEAK} (GPa) ± 0.02	SHOCK VELOCITY U_S (km/s) ± 0.05	VELOCITY u_p (km/s) ± 0.002
80 (Control)	4.61	4.710	0.145
81	4.62	4.700	0.141
82	4.71	4.445	0.149
83	5.57	4.275	0.151
19	4.89	4.535	0.151
20	5.88	4.230	0.160

**Figure 8.** Hugoniot data as measured in this research for polycrystalline and single-crystal iron. Also shown are data from Baker (1974) and Thomas (2018a).

Tin Temperature Measurements

This research extends that of another SDRD project that concluded in FY 2017 (La Lone 2018). Below we describe the technical need and research approach, along with results from the previous SDRD project.

Measurements of both the beta phase to body-centered tetragonal (bct) phase change and melt of shocked tin over a broad range of shock conditions were made by Mabire (2000). Mabire (2000) shock compressed tin with aluminum or copper impactors and observed the velocities of the sample-window (lithium fluoride) interfaces. By interpreting structure in the velocity during shock release, Mabire (2000) determined the stresses at the times of the phase changes, and by using a theoretical EOS to estimate temperatures,

calculated a temperature versus pressure phase diagram. Given our recent advances in dynamic temperature measurement techniques, we set out to validate the phase diagram calculated by Mabire (2000).

Figure 9 shows results from the predecessor SDRD project (La Lone 2018) and this project. Some of these results were published by La Lone (2013). Experimental techniques and details are described in La Lone (2018).

In FY 2018, the first year of the current project, we conducted one additional experiment, but due to technical issues, it will be repeated in FY 2019. We expect a publication soon afterwards.

Cerium Research

Cerium metal has a complex phase diagram that includes several solid phases, an anomalous melting curve, and very low melting stress on the principal Hugoniot (about 10 GPa). The low melting point is caused by a very low stress (about 0.75 GPa) solid-solid phase transition with a large volume collapse (about 15% to 20%). The volume collapse causes a great deal of PdV (pressure-volume) work to occur, which is responsible for the large temperature rise. By comparison, most metals melt at 100–250 GPa, so cerium has a really low melting stress. This allows us to not only study the low-stress phase change and shock melting at very moderate stress, but also do this research on a single-stage launcher. Previous studies done on cerium include research conducted at LANL (Jensen 2010) and at Arzamas-17 in Russia (Zhernokletov 2011).

Shown in Figure 10 is a well-known phase diagram from static high-pressure research done by Zhao (1997). More recently, Jensen (2010) has drawn a

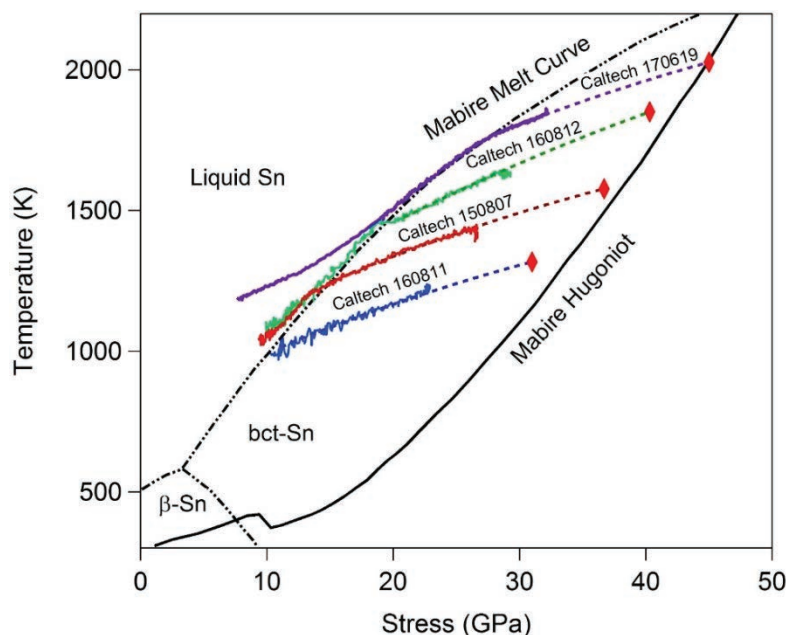


Figure 9. Measured temperature versus stress for the first Caltech radiance-emissivity pair of tin experiments. The brown curve (Caltech 150807) was calculated by the use of the time-independent emissivity (average dynamic data); the green curve (Caltech 160812) used the measured time-dependent emissivity. The black dot-dash lines show the theoretical phase boundaries estimated by Hérelil (2002), and the solid black curve is the Hugoniot and a release curve from the same reference. Hérelil (2002) did not measure the temperatures but instead determined the Hugoniot and phase change stresses from the velocimetry data and a theoretical EOS for temperature data.

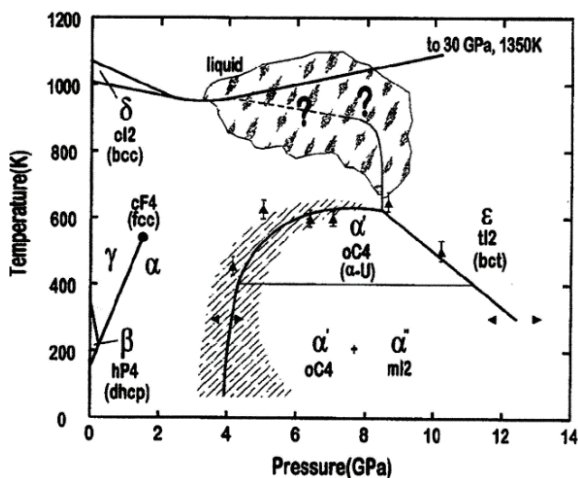


Figure 10. Early static phase diagram for cerium (Zhao 1997)

simplified version of this phase diagram, limited to low stress and states achievable on the principal Hugoniot (Figure 11). Jensen’s phase diagram represents what we

believe is the current state of knowledge of the dynamic response of cerium metal. The inset shows the results of an early low-stress time-resolved experiment, which shows the complex response well. The delta-phase wave is a ramp because of anomalous compressibility in that phase, and the low-stress phase change wave is clearly evident (becoming more compressible with increasing stress). We have obtained the best current SESAME table EOS for cerium, and have been able to successfully simulate experimental geometries using CTH. These models are needed because of the complexity of the Hugoniot and EOS for cerium. In FY 2019 we plan to do two low-stress experiments similar to ones Jensen did to demonstrate that we can safely handle cerium metal. We will obtain appropriate permissions to do experiments on both the NNSS single-stage gas gun in North Las Vegas and the 40 mm powder launcher at STL.

High-Stress Temperature Measurements in Polycrystalline Iron

In the first year of this project (FY 2018), we began to look at the feasibility of extending our ability to make careful temperature measurements to higher stress level. This is an important undertaking because of the need for accurate temperatures over a broad stress regime for better constraining EOSs.

This kind of research is made difficult by several real-world problems. To begin with, we need high stresses to be present to see even moderate ~1500 K temperatures; therefore, thermal radiance is low, and as the stress state increases, sources of extraneous light become brighter. Also, as we expect that glues used to bond window materials to the iron target will decompose at pressures above about 40 GPa, we cannot use them. In addition, sample-window interface features such as gaps or voids can have a dramatic effect on the measured interface temperatures. Finally, we need thermodynamic properties such as heat capacity, thermal conductivity, and window temperatures to accurately relate measured interface temperatures to interior temperatures.

We chose polycrystalline iron as a candidate metal for this research because of its importance as a high-

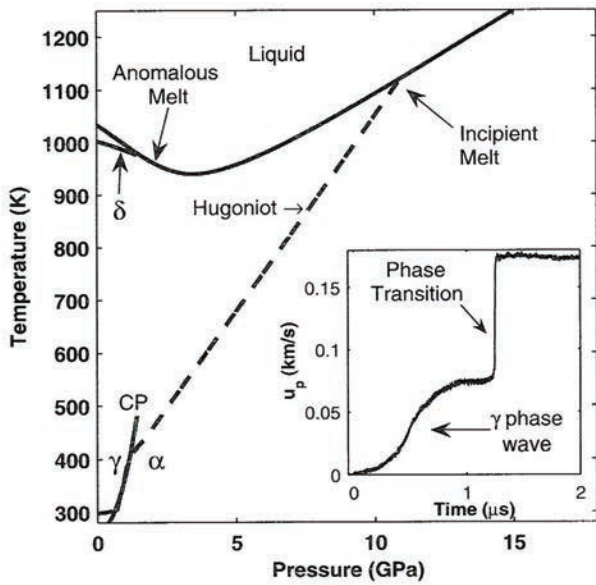


FIG. 1. Partial phase diagram for cerium showing multiple phases at low pressures. The melt boundary, γ - α boundary and the Hugoniot curve (or shock adiabat) were obtained from a multi-phase EOS that was based on available static data (Ref. 13). The δ -phase boundary (Ref. 12) and solid-solid critical point are also indicated. (Inset) Example of shock-wave data (particle velocity vs time) showing the structured wave for cerium samples shocked to stresses in the vicinity of the γ - α phase transition. The large-volume collapse at the γ - α phase boundary is expected to result in a low-pressure melt transition.

Figure 11. Low-stress phase diagram representing the current state of knowledge of the dynamic phase changes of cerium metal (Jensen 2010)

pressure standard and its interest to geophysicists. In addition, it has well-known shock properties, including an accurate Hugoniot. However, there is a great deal of uncertainty in the melting curve of iron. We chose

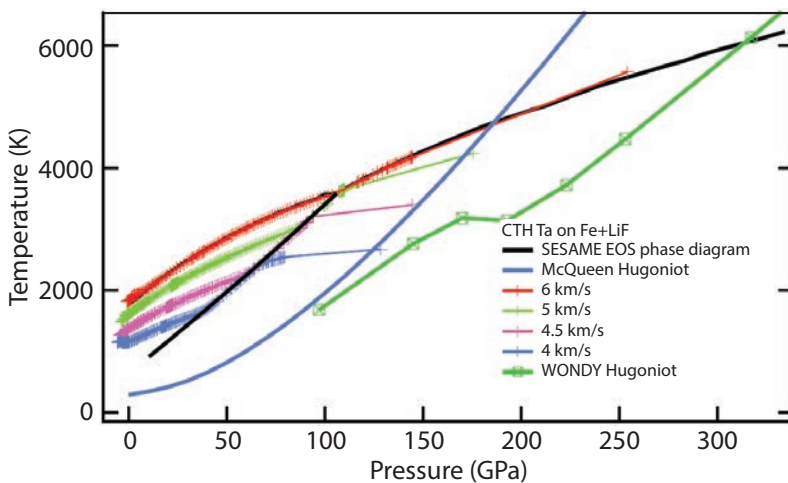


Figure 12. Calculated iron melting curve, Hugoniot, and unloading paths for different projectile velocities with copper impactors

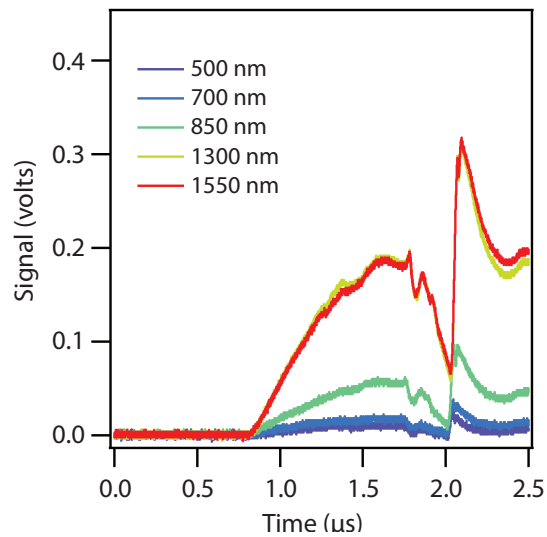


Figure 13. Light emission from shocked sapphire at a shock stress of about 50 GPa indicates that the sapphire would be a poor window for high-stress radiance measurements

the melting curve from the LANL SESAME EOS for iron. We plotted this melting curve and the principal Hugoniot using estimated temperatures (Figure 12). The concave up blue curve is the principal Hugoniot from McQueen (1970), and the black curve is the SESAME melting curve. Shown in other colors are release paths from various initial shock stress states. This plot indicates that we can probably release melt iron, but the initial shock stress will still be high compared to previous work on tin.

Experimental work so far has centered on characterizing light emission of sapphire windows. Figure 13 shows measurements of light emission

from sapphire at several wavelengths to a stress state above the yielding point. As can be seen, there is a lot of light emission at wavelengths relevant for radiance measurements, high enough to interfere with what we are measuring. This would make sapphire a poor choice for window material for our experiments. We will evaluate magnesium oxide windows next.

A Brief Study of the Shock Compression of HEAs

High-entropy alloys show promise for being materials with high compressive strength that have some ductility as well. Such alloys have many potential applications. We conducted

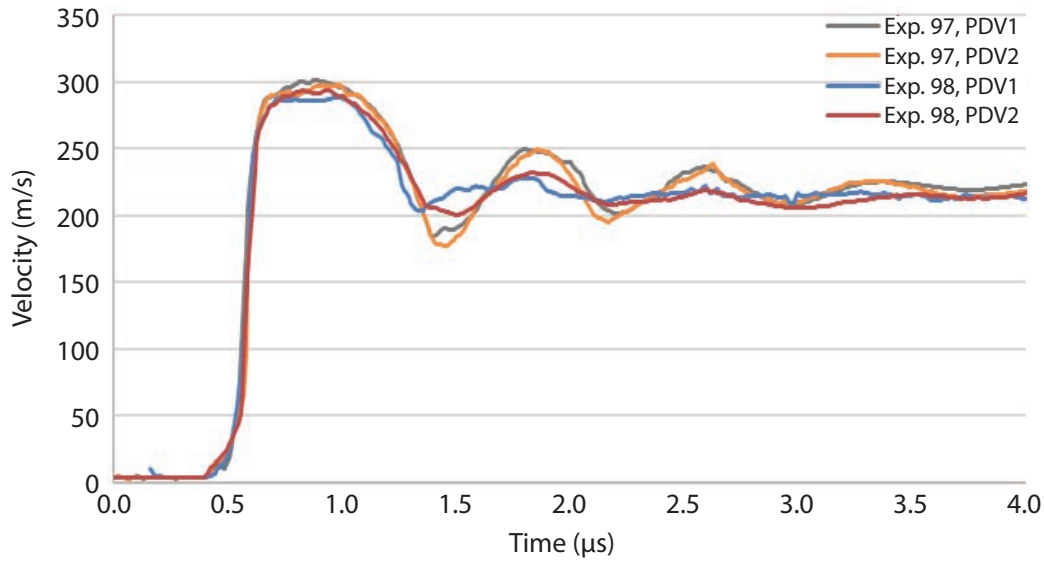


Figure 14. Velocimetry curves of the two experiments on HEA targets (PDV1 is the center probe and PDV2 is the probe offset 4 mm from the center)

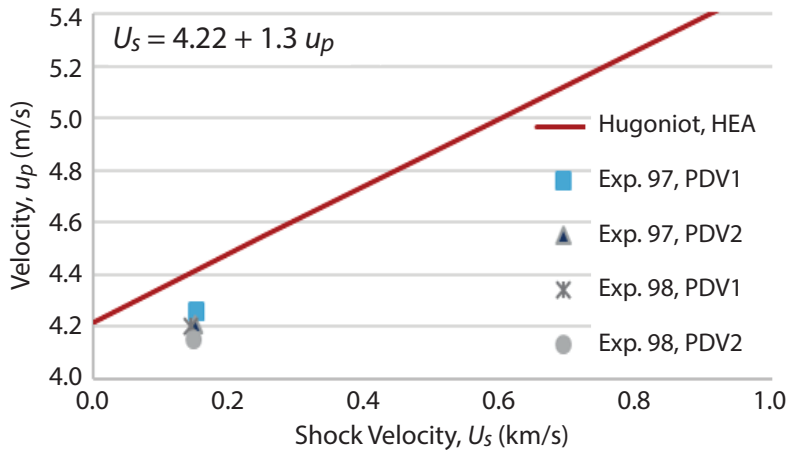


Figure 15. Approximate shock Hugoniot line shown with experimental data

two experiments on a particular HEA material in a symmetric impact configuration to specifically study spall. The HEA used in this study, HEA-T-1, was obtained through LANL and was characterized beforehand by LANL for mechanical properties. It was of mutual interest to measure the high-velocity impact properties of this HEA as well. This particular HEA consists of iron, chromium, manganese, and nickel in

weight percentages of 25.2, 23.5, 24.8, and 26.5, respectively. This study was a first step in characterizing this HEA material for shock-compression response. The experiments yielded two data points that are in reasonable agreement with an estimated Hugoniot for the material.

We performed spall experiments using the NNSS single-stage gas gun in North Las Vegas. We used PDV during the shock experiments to record the movement of the back surface of the target with two-fiber PDV probes. To collect PDV data, we used two locations on the target surface: (1) the center of the target, and (2) offset 4 mm laterally from the center of the target.

Because this material had not been previously characterized for its shock-compression response, the Hugoniot was unknown and additional care was taken in the experimental design. The HEA targets and impactors were both 22 mm in diameter. Target and flyer dimensions are given in Table 5. We chose these dimensions to cause spall to happen about halfway through the target.

Table 5. Experimental parameters for the HEA study

EXPERIMENT NUMBER	IMPACTOR THICKNESS X_F (mm)	TARGET THICKNESS X_T (mm)	IMPACT VELOCITY U_d (km/s)
97	1.75	3.50	0.302
98	1.77	3.53	0.293

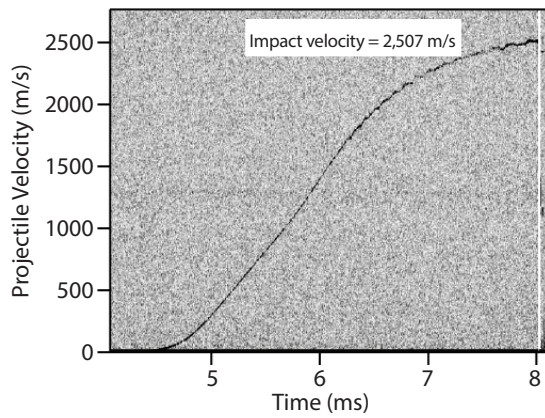


Figure 16. Projectile velocity from a collimating PDV probe looking down the barrel of the new 40 mm powder launcher. Note that a flyer velocity of about 2.5 km/s was achieved.

The sample diameters were relatively small for shock wave experiments, and this limited the observation time in uniaxial strain, so timing was carefully considered in the design of the experiment. We insulated the impactor from the aluminum projectile with syntactic foam; this also allowed a release wave to be reflected from that surface.

The material was first measured for its density (7.52 g/cm^3), longitudinal sound speed (5.40 km/s), and shear sound speed (2.92 km/s). The density of the material was measured via the Archimedes principle with a Mettler Toledo analytical balance, and the longitudinal and shear sound speeds were determined via ultrasonic measurements conducted with an Olympus ultrasonic pulsar/receiver and transducers. We used a Heidenhain gauge to verify the targets and impactors were within $5 \text{ }\mu\text{m}$ of flatness.

Good time-resolved data were obtained for both experiments. Shown in Figure 14 are the velocimetry curves obtained from the two experiments. The first showed a very clear elastic wave that is a ramp, and both curves showed clear evidence of spall by the ringing in the data following the velocity pullback from the peak. Experiment 98 had a smaller spall amplitude, perhaps due to the lower projectile velocity.

Derived quantities from the velocimetry curve were the HEL, which was approximately 0.23 GPa , and the spall strength, which was approximately 1.8 GPa . Quasistatic experiments also showed a small value of compressive strength. Measured wave speeds were close to the estimated Hugoniot ($U_s = 4.22 + 1.3 u_p$) for this HEA, as shown in Figure 15. The plastic wave had a very long rise time ($\sim 150 \text{ ns}$), which led to a large

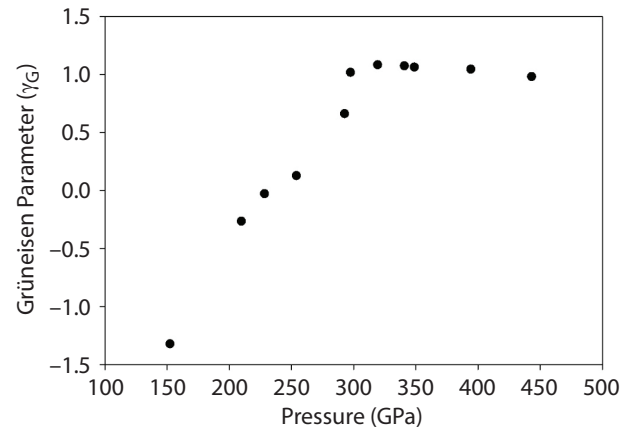


Figure 17. Calculated Grüneisen parameter for tantalum

uncertainty in U_s . The data also revealed that this HEA has a relatively low compressive strength. We plan to conduct further experiments with this material to verify the data obtained from these initial experiments.

First Powder Launcher Experiments

A 40 mm powder launcher was procured under a previous strategic SDRD project (La Lone 2018). Operator training and the first shots were supported by this project. The launcher performed as advertised by the manufacturer. Velocity data from a test shot are shown in Figure 16. This new capability will greatly enhance the ability of research staff in the company to do dynamic experiments.

Grüneisen Parameter

The Grüneisen parameter is a quantity that has roots in the physics of lattice dynamics, but that can also be expressed as a thermodynamic derivative quantity

$$\gamma_G = \left[\frac{\partial P}{\partial E} \right]_V, \quad (7)$$

where P is pressure, E is internal energy, and V is volume. This quantity has turned out to be very useful in defining EOSs, such as the well-known Mie-Grüneisen EOS. Because of this, it has long been of interest to make experimental measurements. One way to do this derives from the Hugoniot differential equation. This fundamental relationship can be arranged in such a way as to express the Grüneisen parameter as a function of certain variables that can be measured experimentally, namely the slope of the Hugoniot at the stress state of interest, P_h , and the slope of the isentrope centered at that stress state, P_s .

The slope of the isentrope is related to sound speed at stress,

$$\gamma_G = \frac{2(1-\varepsilon)}{\varepsilon} \left(\frac{P_h - P_s}{P_h - P_R} \right), \quad (8)$$

where ε is strain, and

$$P_h = \left. \frac{dp}{dv} \right|_H, \quad P_R = -\frac{P}{V_0 - V}, \quad \text{and} \quad P_s = \left. \frac{dp}{dv} \right|_s. \quad (9)$$

We have used the recent sound speed results from Rigg (2014) to see how well this method works. Figure 17 shows results obtained from calculating the Grüneisen parameter over the range studied by Rigg (2014); we also incorporated Hugoniot results from Mitchell (1981) in the plot. Error bars remain to be assigned. The figure shows that unphysical results are obtained (negative values) for the lowest stress states but that as the shock melting point is approached, more reasonable values are derived. From an inspection of Equation 8, we can see that it contains a term that is the difference between two large numbers. This limits how well we can determine the Grüneisen parameter. This also means that bulk sound speeds must be well known. Obtaining bulk sound speed in the solid phase presents many challenges. We are planning to look at ways to reduce uncertainties.

CONCLUSION

We made good progress along a number of research paths in the first year of this project. We extended two efforts from a previous strategic SDRD project, commissioning a new 40 mm powder launcher and finalizing a study to map the solid-liquid phase boundary of tin. We believe that we have made the first time-resolved measurements of sections of the melting curve of tin using dynamic techniques, a very important result. We also initiated four new efforts to (1) measure the dynamic response of single-crystal iron, (2) map the complex phase diagram of cerium, (3) measure the temperature of materials shocked to near 50 GPa, and (4) measure the dynamic response of an HEA.

We have begun to look in detail at the dynamic properties of single-crystal iron, a material of considerable interest to the high-pressure physics and geophysics communities. This research will also help the Stockpile Stewardship program by studying high-pressure material properties of anisotropic

polycrystalline metals. We will develop experimental techniques and obtain data that we can analyze to better understand at a very detailed level how single-crystal properties in the principal crystallographic directions contribute to the average polycrystalline response. We intend to extend this research to stress levels above the 13 GPa solid-solid phase change as well. In our first experiments we are observing a surprising and clear difference in key dynamic properties such as the elastic limit and spall strength. But most surprising are the apparent differences we see in the shock velocity. Such differences are at least a little controversial and at odds with previous results on copper single crystals. Our early results are also surprising in that shock speeds for both the [100] and [111] iron orientations fall below the polycrystalline Hugoniot. This is interesting because, of the three principal orientations, the [111] iron orientation has the highest value for longitudinal elastic sound speed, but the plastic shock speed falls below the polycrystalline Hugoniot in our early experiments. More work is needed here, and there is a clear need to do experiments on the [110] iron orientation, which has the next to highest longitudinal sound speed. Experiments with windows are also needed to verify these results because of the possibility of having large systematic errors due to free surface wave interaction effects. If the large elastic wave causes tension and damage when it reflects from the free surface and then interacts with the oncoming plastic wave, that might cause the differences we are observing. These results must be considered as preliminary. Work for FY 2019 includes defining and executing more rigorous window experiments to validate these tentative results.

Cerium is an f-electron metal with a complex phase diagram. This complexity includes several solid phases, an anomalous melting curve, a large-volume solid-solid phase change at very low pressure, and a very low Hugoniot melting point. These properties make cerium an ideal metal for study of solid-solid phase changes, melting, and solidification. Because only low shock stresses are needed, this research can be done on single-stage launchers. Typically metals melt at very high stress (200–300 GPa), and we need two-stage guns to obtain these stress states. We have designed an initial experiment for the NNSS single-stage gas gun in North Las Vegas to begin the research and to establish procedures and methods to work with this reactive material; approvals for this work are underway. After we establish material handling procedures, we will design additional complex loading experiments to explore melting and solidification, as well as the low-stress isostructural phase change.

The measurement of the dynamic temperature of a material is essential to building a complete EOS. This is because temperature does not appear directly in the shock jump conditions and cannot be directly extracted from velocity measurements. Temperature is subsumed in the energy jump condition, but to calculate temperature from energy measurements requires a knowledge of, or assumption about, how energy is partitioned. Therefore, it is of high interest to the community to make direct measurements of temperature behind a shock wave. Most studies have used the measured radiance from a shock sample to determine temperature. This work has been going on for decades, and with only moderate success because of the difficulty of converting radiance to temperature. One principal problem is that of measuring the emissivity of a shocked surface or interface. With the development of the integrating sphere method at STL, this can now be done with reasonable precision and accuracy. The research on tin discussed above is a good example of doing this at low stress, but there is a need to extend to higher shock stresses. We are beginning to look at how to do this for polycrystalline iron with the intent to create a technique able to measure dynamic temperatures to 50 GPa and beyond. Key technical challenges concern unwanted radiance in the window materials, and we have begun investigating experiments with no glue bonds and new window materials and analysis methods to allow extraction of sample radiance from unwanted optical contamination.

Finally, we have done a short study on a relatively new class of metallic alloys called HEAs, so named for the high entropy of formation in alloys with multiple component metals (typically five to six component metals). These materials hold promise for having high compressive strength and ductility. Currently ceramics are used in many applications where high compressive strength is required (7–8 GPa, for example). However, ceramics are known to fail in a brittle mode, and so can only be impacted once before they lose all strength. A material that fails in a ductile mode would be a better choice for some applications (e.g., armor), but the results of our initial experiments suggest that the HEA we studied is not a good candidate. Although it has a high spall strength, it appears to have a low Hugoniot elastic limit.

ACKNOWLEDGMENTS

We gratefully acknowledge Cheng Liu at LANL for providing the HEA material used for this work. We also appreciate the valuable support from Melissa Matthes, Jeff Cates, and Russ Howe at the NNS North Las Vegas single-stage gas gun facility.

REFERENCES

- Barker, L. M., R. E. Hollenbach, “Shock wave study of the $\alpha \rightleftharpoons \epsilon$ phase transition in iron,” *J. Appl. Phys.* **45** (1974) 4872.
- Barker, L. M., “ α -phase Hugoniot of iron,” *J. Appl. Phys.* **46** (1975) 2544.
- Chau R., J. Stölken, P. Asoka-Kumar, M. Kumar, N. C. Holmes., “Shock Hugoniot of single crystal copper,” *J. Appl. Phys.* **107** (2010) 023506.
- Héreil, P.-L., C. Mabire, “Temperature measurement of tin under shock compression,” *AIP Conf. Proc.* **620** (2002) 1235.
- Hixson, R. S., B. La Lone, G. D. Stevens, D. Turley, L. R. Veerer, “Enhanced dynamic materials research,” in *Site-Directed Research and Development*, FY 2015, National Security Technologies, LLC, Las Vegas, Nevada, 2016, 15–29.
- Jensen, B. J., G. T. Gray III, R. S. Hixson, “Direct measurements of the α - ϵ transition stress and kinetics for shocked iron,” *J. Appl. Phys.* **105** (2009) 103502.
- Jensen, B. J., F. J. Cherne, J. C. Cooley, M. V. Zhernokletov, A. E. Kovalev, “Shock melting of cerium,” *Phys. Rev. B* **81** (2010) 214109.
- Johnson, J. N., “Wave velocities in shock-compressed cubic and hexagonal single crystals above the elastic limit,” *J. Phys. Chem. Solids* **35**, 5 (1974) 609–616.
- La Lone, B. M., G. D. Stevens, W. D. Turley, D. B. Holtkamp, A. J. Iverson, R. S. Hixson, L. R. Veerer, “Release path temperatures of shock-compressed tin from dynamic reflectance and radiance measurements,” *J. Appl. Phys.* **114** (2013) 063506.
- La Lone, B., G. D. Stevens, —D. Turley, L. R. Veerer, R. S. Hixson, “Enhanced dynamic materials research,” in *Site-Directed Research and Development*, FY 2016, National Security Technologies, LLC, Las Vegas, Nevada, 2017, 1–9.
- La Lone, B., G. D. Stevens, D. Turley, L. R. Veerer, R. S. Hixson, “Enhanced dynamic materials research,” in *Site-Directed Research and Development*, FY 2017, National Security Technologies, LLC, and Mission Support and Test Services, LLC, Las Vegas, Nevada, 2018, 1–8.

Mabire, C., P.-L. Hérel, “Shock induced polymorphic transition and melting of tin,” *AIP Conf. Proc.* **505** (2000) 93–96.

McQueen R. G., S. P. Marsh, J. W. Taylor, J. N. Fritz, J. W. Carter, “The Equation of State of Solids from Shock Wave Studies,” chap. VII, in *High-Velocity Impact Phenomena*, R. Kinslow, ed., Academic Press, New York and London, 1970, 294–417.

Mitchell, A. C., W. J. Nellis, “Shock compression of aluminum, copper, and tantalum,” *J. Appl. Phys.* **52** (1981) 3363.

Rigg, P. A., R. J. Scharff, R. S. Hixson, “Sound speed measurements in tantalum using the front surface impact technique,” *J. Phys. Conf. Ser.* **500** (2014) 032018.

Simmons, G., H. Wang, *Single Crystal Elastic Constants and Calculated Aggregate Properties: A Handbook*, 2nd edition, MIT Press, Cambridge, Massachusetts, 1971.

Strand, O. T., D. R. Goosman, C. Martinez, T. L. Whitworth, W. W. Kuhlow, “Compact system for high-speed velocimetry using heterodyne techniques,” *Rev. Sci. Instrum.* **77** (2006) 083108.

Thomas, S. A., R. S. Hixson, “Systematic studies in dynamic material response – Early-career postdoctoral research,” in *Site-Directed Research and Development*, FY 2016, National Security Technologies, LLC, Las Vegas, Nevada, 2017, 53–58.

Thomas, S. A., M. C. Hawkins, M. K. Matthes, G. T. Gray III, R. S. Hixson, “Dynamic strength properties and alpha-phase shock Hugoniot of iron and steel,” *J. Appl. Phys.* **123** (2018a) 175902.

Thomas, S. A., R. S. Hixson, “Systematic studies in dynamic material response – Early-career postdoctoral research,” in *Site-Directed Research and Development*, FY 2017, National Security Technologies, LLC, Las Vegas, Nevada, 2018b, 43–48

Zhao Y., W. B. Holzapfel, “Structural studies on the phase diagram of cerium,” *J. Alloys Compd.* **246**, 1–2 (1997) 216–219.

Zhernokletov, M. V., A. E. Kovalev, V. V. Komissarov, M. G. Novikov, M. A. Zocher, F. J. Cherne, “Study of cerium phase transitions in shock wave experiments,” *J. Exp. Theor. Phys.* **112** (2011) 212.

This page left blank intentionally



Drone Video Platform—Collision Avoidance, Situational Awareness, and Communications

STL-039-17 ■ Year 2 of 2

Rusty Trainham,^{1,a} Paul Guss,^b Manuel J. Manard,^a Lance McLean,^c
Willy Kaye,^d and Kevin Kochersberger^e

¹trainhcr@nv.doe.gov, (805) 681-2248

^aSpecial Technologies Laboratory

^bRemote Sensing Laboratory–Nellis

^cRemote Sensing Laboratory–Andrews

^dH3D Corporation

^eVirginia Polytechnic Institute and State University



We have developed detectors for radiation, chemical, and spectroscopic real-time sensing for use on fixed-wing and rotary-wing unmanned aerial vehicles. Our effort in FY 2018 continued work begun last year using the Sandstorm drone platform, but with a new scope that focused on detector payload development, aircraft integration, and flight testing. The systems have been flight tested in Idaho, Montana, Nevada, and Wisconsin, and they have demonstrated detection of radiation from an aerial asset, mapping of radioactive contamination, real-time chemical sensing, chemical sampling for post-flight analysis, and the capture of optical spectra from small detonations. Although benchtop testing of the systems is essential during development, it is not a replacement for actual flight testing. Operating detectors on aerial platforms is challenging, and we experienced technical problems while testing in difficult environments. The experience gained during flight tests highlights the importance of designing detectors that are low cost and expendable.

BACKGROUND

This project began in FY 2017 as an attempt to implement collision avoidance on the fixed-wing Sandstorm drone platform (Frayer 2018). Unfortunately, feature creep in the design phase resulted in a concept too ambitious for available project

resources. What started as a collision avoidance module morphed into a “core” module—users would be able to insert any detector into any flight platform and interface to an unspecified autopilot. A year into the design it became obvious that the goal was unrealistic. Three circuit boards had been designed, but no firmware or software had been written, and

no package engineering for aircraft integration had been undertaken. Furthermore, the electronic design duplicated what was already commercially available. Consequently, the core module task was put on hold, and the project was redirected into detector payload development, aircraft integration, and flight testing. This year we flew six detectors on four different flight platforms over five missions in Montana, Idaho, Nevada, and Wisconsin. Unexpected issues arose during all of the test flights, and most were successfully mitigated. However, two incidents invoked premature halts to the missions, with one resulting in catastrophic aircraft failure.

Flying detectors on drones is not without risk, and mishaps can occur quickly and unexpectedly. This year we lost an expensive hexacopter during a test flight in Idaho, but fortunately, the more expensive Apollo detector that was on board survived that crash. Other incidents that occurred could have been serious but were not, either because we caught or corrected problems in time, or simply because we were lucky. Where we fly, test conditions can be severe, and replicating the density altitude, temperature, humidity, wind, and dust conditions in the laboratory or at a training field is not always feasible. Because our test flight venues can be brutal—which also makes them particularly valuable—success in those venues is an ultimate test of survivability. From the Idaho crash we learned that the Sandstorm pod, which consists of a suspended tray within a reinforced fiberglass shell, offers robust protection of the instrumentation within. We also learned that the Raspberry Pi is an excellent single-board computing solution for detector operations on a drone. It runs for hours on a small battery, has adequate computing power for our detectors, and is mechanically very robust. It survived another severe crash while on board the Sandstorm in FY 2019; it booted up again after we blew out the sand.

Mapping and characterizing radioactive contamination after a nuclear or radiological accident is a hazardous operation for which drones are ideally suited. In the aftermath of the Fukushima nuclear meltdown, radiation levels in the vicinity of the reactors were lethal, so personnel were unable to make measurements in critical locations. Even aerial surveys had to avoid direct low-altitude overflights of the reactor containment structures to limit personnel exposure. Replicating this sort of environment for testing drone-borne detector operations is challenging because radioactive contamination poses real risks to personnel and equipment. Another scenario for radiation detection is searching, locating, and characterizing a radioactive source. Tests of this

scenario are considerably easier, as the radiation hazards are easily contained and managed.

Factory accidents and refinery fires are compelling use cases for drone-borne chemical detection systems. Smoke sampling for the situational awareness of firefighters is another, and characterizing the chemical composition and lethality of releases from improvised chemical explosive devices is yet another. Two tests useful for drone-borne chemical detecting capability development are single-point sampling of small but lethal releases and plume mapping over large, extensive contaminated areas. The questions we ask are “What is it?”, “Where is it?”, and “How far does it extend?” We have developed two detector systems; one for the fixed-wing Sandstorm, and one for the 3DR Solo quadcopter. They both use the same chemical sensing and sampling technologies, but were scaled for the different platforms; the Sandstorm version weighs 7 lb and the 3DR Solo version is less than 2 lb.

Positioning an optical spectrometer close to a detonation or flame by a drone—useful for situations where direct line of sight with a telescope-based spectrometer is infeasible—is another scenario that we have tested. The optical spectrometer is small and light enough that a drone can also carry a chemical detector along with it to provide more information. This combination could be useful for assessing backcountry wildfires or chemical or petroleum facility fires.

PROJECT

Data and Telemetry from a Raspberry Pi 3B

The Sandstorm fixed-wing drone offers no infrastructure for detector operations; therefore, we consider it to be merely an aerial test bench. All power, telemetry, and communications for a detector on board must be implemented in the detector package itself. Flight tests began while the core module was still being designed, so we improvised a solution to operate the detector from a Raspberry Pi 3B. The Raspberry Pi is single-board computer about the size of a credit card and is housed in a box that is somewhat thicker than a deck of playing cards. Inside the box with the Raspberry Pi is an Adafruit Ultimate GPS receiver, and attached to the outside is an Adafruit ten-degree-of-freedom (10 DOF) card for flight telemetry (acceleration, rotation, altitude, and compass heading).

The GPS receiver has a MediaTek MTK3339 GPS chipset, and is configured to output data five times per

second. It communicates National Marine Electronics Association (NMEA) sentences over a serial connection, and it also outputs a digital strobe marking the top of the second. The one-pulse-per-second (1PPS) strobe is routed to the general purpose input output (GPIO) header of the Raspberry Pi, and is used to lock the Raspberry Pi's system clock to GPS time. The system clock is accurate to within several tens of microseconds absolute time of day, and time stamps from the system clock are used to correlate sensor data to GPS locations and flight telemetry.

The 10 DOF telemetry card consists of a STMicroelectronics L3GD20H gyroscope, a STMicroelectronics LSM303DLHC accelerometer and compass, and a Bosch BMP180 barometer and thermometer. The card communicates over the I2C bus to the Raspberry Pi, and it provides telemetry data five times per second (although it can be configured to nearly kHz sampling rates). The code to query the 10 DOF card is written in C; in addition to streaming data to a log file, it mirrors the current data to a memory-mapped file for real-time queries. The altitude signal produced by the 10 DOF card is actually barometric pressure, so the C code calculates the pressure altitude using the raw barometer and thermometer readings.

Altitude above ground is measured by a LightWare SF11/C single-point lidar range finder. During Sandstorm operation, the lidar range finder is plugged into one of the Raspberry Pi's USB ports and monitored by a program written in C. During 3DR Solo operation, the lidar range finder is connected to the onboard computer via the USB connection shared with the detector, and it is monitored by a program written in Python. For both platforms the lidar readings are merged with the 10 DOF telemetry readings and written to the same log file. The current lidar reading is also separately mirrored by a memory-mapped file for real-time access.

Radio Downlink

Several options exist for communications to the ground station. The Raspberry Pi 3B has onboard Ethernet, Wi-Fi, Bluetooth, USB, and serial ports. For short-range communications, Wi-Fi is very convenient, and it is the most commonly used mode of communication for aircraft on the ground. For longer-range service, a 915 MHz radio has been the most common aerial communication link. Radios such as a 500 mW 3DR SiK or a 1 W RFDesign RFD900x plug into a USB port, and they are routinely used during missions. If the venue of a test flight has 4G LTE cellular service available, then a cellular data link becomes an option. However, most of our test flights have been in areas with poor cellular reception. Finally, we have used the Raspberry Pi's Ethernet interface to connect to the Virginia Polytechnic Institute and State University (Virginia Tech) hexacopter's 2.4 GHz Ubiquiti UniFi hardware to provide both aircraft and payload ground links over the same radio. Communications from the pod to the ground use internet protocol (IP). It is not the most efficient use of bandwidth, but it does offer extraordinary flexibility for data transmission. IP allows us to make extensive use of port programming, Secure Shell (SSH) tunneling, and the web for data streaming.

Real-time access to the pod's data stream from the internet at large is possible by means of a virtual server on the Amazon Elastic Compute Cloud (EC2). The virtual server transparently redirects external client communications through an SSH tunnel to the pod's Raspberry Pi. The client computer does not require any special software or configuration changes; simply directing a web browser to the IP number of the virtual server is sufficient to stream data from the Raspberry Pi. Of course this requires that the pod itself have internet access, either through the ground station or over a cellular link directly from within the pod. Figure 1 shows an example of an SSH tunneling script that runs on the Raspberry Pi during system boot. This

```
#!/bin/bash
# port access to SERVER gets tunneled back to me
SERVER=54.183.239.158
USER=root
KEY=aws_ubuntu_california.pem
TIMEOUT=180
TRIES=3
ssh -fNT -o ServerAliveInterval=${TIMEOUT} -o ServerAliveCountMax=${TRIES} -R *:8080:127.0.0.1:80 -i $KEY ${USER}@${SERVER}
ssh -fNT -o ServerAliveInterval=${TIMEOUT} -o ServerAliveCountMax=${TRIES} -R *:9001:127.0.0.1:9001 -i $KEY ${USER}@${SERVER}
```

Figure 1. This shell script executes during start-up on the Raspberry Pi to set up the SSH reverse tunnel to the Amazon Web Services (AWS) virtual server, which maps IP ports on the virtual server to ports on the Raspberry Pi, permitting external clients to monitor flight data in real time over the internet

Figure 2. The SSH forward tunnel maps port 8080 on the Raspberry Pi to port 80 on the Apollo. The IP number of the USB interface on the Apollo is 192.168.200.200.

script redirects port 8080 from the virtual server to the Raspberry Pi for web page access, and port 9001 on the virtual server is redirected to the same port on the Raspberry Pi for streaming data in real time. Because of the limited bandwidth of the radio link to the pod, this solution is not scalable if numerous clients desire access. A better solution would be for the virtual server on to mirror the pod's real-time data and to handle external clients without redirection.

Communicating with the Apollo Detector

The Apollo detector is a handheld gamma imager commercially available from H3D, Inc., of Ann Arbor, Michigan. The version that we have tested has had its form factor reengineered to fit inside the Sandstorm pod. The Apollo detector, a self-contained unit, has its own battery but does not have built-in GPS or telemetry. Access to the Apollo is through H3D's graphical interface via a redirect from the onboard web server. Although the graphical interface is accessible over Wi-Fi, Ethernet, and cellular data links, its bandwidth requirement is too much for the 915 MHz radio link. Since the 915 MHz radio is the most commonly used communications link to the pod, we had to make some adjustments. Because the Raspberry Pi was already in the pod to provide GPS and telemetry, we configured it to access the Apollo and pull a subset of real-time data to make it available over the low-bandwidth link. Average spectra and region-of-interest gamma intensity readings are accessible in real time through the Raspberry Pi's web server, and the ground station can start and stop Apollo data acquisitions via the Raspberry Pi's web server.

The Apollo communicates with the Raspberry Pi over a USB tether, which provides a full IP interface. Network Time Protocol synchronizes the system clock on the Apollo to the Raspberry Pi's GPS time reference. Access to the Apollo's web interface through the Raspberry Pi is via an SSH tunnel such that an external web browser accessing port 8080 of the Raspberry Pi gets forwarded through the SSH tunnel to port 80 of the Apollo. The SSH tunneling command executes during system start-up, and

because the Raspberry Pi and the Apollo can be restarted arbitrarily, there are start-up shell scripts on both systems. The syntax for the Raspberry Pi is for a forward SSH tunnel, and the syntax for the Apollo is for a reverse SSH tunnel. The syntax for opening an SSH tunnel can be somewhat confusing, but the command is a single line for each forwarded port. Figure 2 shows the command for the SSH forward tunnel executed on the Raspberry Pi.

Drone-Borne Radiation Detection

In the final week of September 2017, we conducted radiation detector test flights at the Unmanned Systems, Inc. (USI), airfield in Kalispell, Montana. Our primary goal was to fly the Apollo detector as a high-resolution gamma spectrometer on the USI Sandstorm electric drone. The test proceeded smoothly, and we were able to accomplish several secondary goals. In addition to the Sandstorm test, the Apollo was flown on a T-Rex 600 helicopter. Also, a 2×2 thallium-doped sodium iodide (NaI(Tl)) detector was flown on a T-28 fixed-wing trainer and on a 3DR Solo quadcopter. A 3×6 NaI(Tl) detector also was flown on the Sandstorm. Radioactive sources cesium-137 (¹³⁷Cs), europium-152 (¹⁵²Eu), and barium-133 (¹³³Ba) were shipped from the Remote Sensing Laboratory at Nellis Air Force Base to the Kalispell airfield. All test flights produced quality data for locating and identifying these millicurie-level sources.

Radiation Sensing with the Apollo Detector on the USI Sandstorm

The redesign of the Apollo detector for the Sandstorm pod is shown in Figure 3. The detector is shock-mounted to a tray that slides into the pod. The batteries and the Raspberry Pi are attached by Velcro to the tray at the nose end of the pod, and the cadmium zinc telluride (CZT) crystals are housed at the aft end of the pod. The Apollo detector has four 20 × 20 × 15 mm CZT crystals mounted on an anode and backed by a Peltier cooler. The anode is an 11 × 11 grid, and it provides x-y positional sensing of gamma absorption or scattering within the CZT

Design Overview

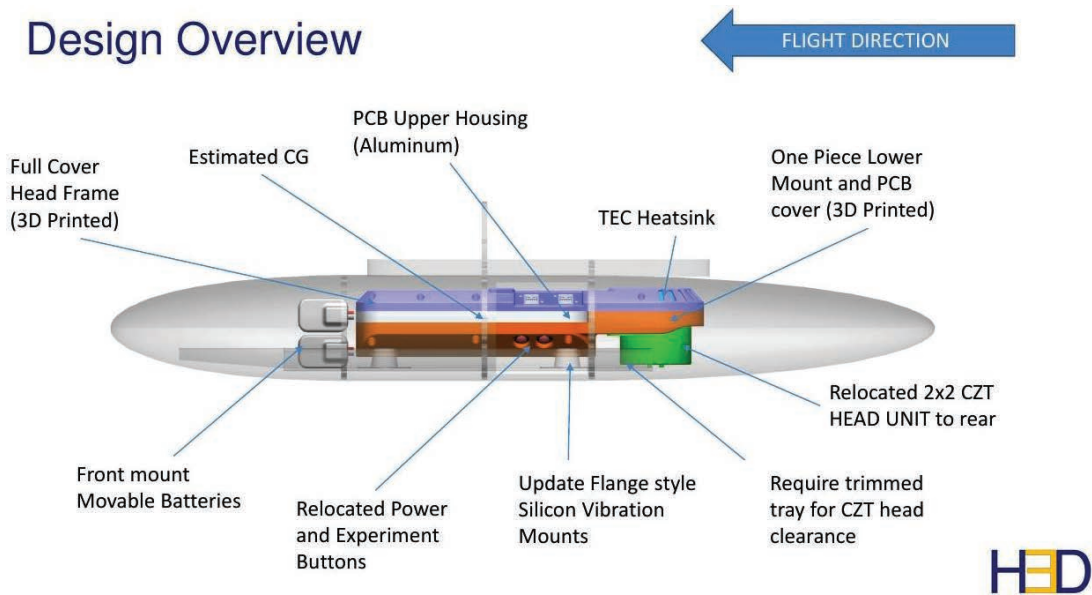


Figure 3. The repackaged Apollo detector mounts on a tray and slides into the Sandstorm pod. Not shown in the solid model is the Raspberry Pi on the tray just ahead of the front mount movable batteries.

crystal. The difference of drift times to the anode vs. cathode of the induced charge carriers in the crystal provides a depth of interaction for a z coordinate. Thus, the CZT crystal is essentially voxelized. The data consist of gamma energy, x-y-z location of the interaction, a time stamp of the interaction, and the number of correlated interactions if they occur within a defined time window. Correlated interactions are primarily from Compton scattering, and the locations of the correlated interactions define vectors for back-projecting to a probable location of the gamma source. Back projection is exploited to construct the gamma image of the radioactive source.

A further advantage of voxelizing a CZT crystal is that individual voxels can be calibrated to improve detector resolution. Gamma energy is inferred from the amount of charge created in the CZT by a gamma photoabsorption. Lattice defects and impurities within the crystal trap some of the charge and consequently smear out the energy calibration of the crystal as a whole. Typically, a $10 \times 10 \times 10$ mm CZT crystal has an energy resolution of about 3% for the 662 keV ^{137}Cs gamma, and the resolution further degrades for larger crystals. Individually calibrating CZT voxels compensates for the range of charge creation throughout the crystal, and sub-percent energy resolution has been achieved by the method. The Apollo detector has an energy resolution of slightly better than 1%.

The commercial, handheld Apollo normally operates on a tripod, and is allowed several minutes to collect data and to compute a gamma image. This mode of operation is simply not possible when the detector is mounted on a fixed-wing drone flying at 40 knots or more. Consequently, we never intended the flight test on the Sandstorm to be a test of the Apollo detector's ability to do aerial gamma imaging, but rather how well it performed as a high-resolution gamma spectrometer when mounted on a flying platform. The 1% energy resolution of the Apollo is superior to the 6.5% energy resolution of the 3×6 NaI(Tl) detector, but the smaller detector volume reduces its sensitivity. The four crystals in the Apollo sum to a detector volume of 24 cm^3 . Compared to the 700 cm^3 of the 3×6 NaI(Tl) detector, the Apollo would be expected to be less sensitive by more than an order of magnitude. The results of the flight tests confirmed that a fast-moving aircraft is not an ideal platform for the Apollo, and this prompted us to fly the Apollo on a radio-controlled (RC) helicopter.

Figure 4a shows the Sandstorm in flight over the Kalispell airfield with the Apollo detector in the belly pod. A 37 mCi ^{137}Cs source was placed at the north end of the runway, and a 9 mCi ^{152}Eu source was placed on the runway 250 m to the south (seen in the lower right corner of the photograph). Figure 4b displays a flight track measured by the Raspberry Pi's GPS receiver in the pod.

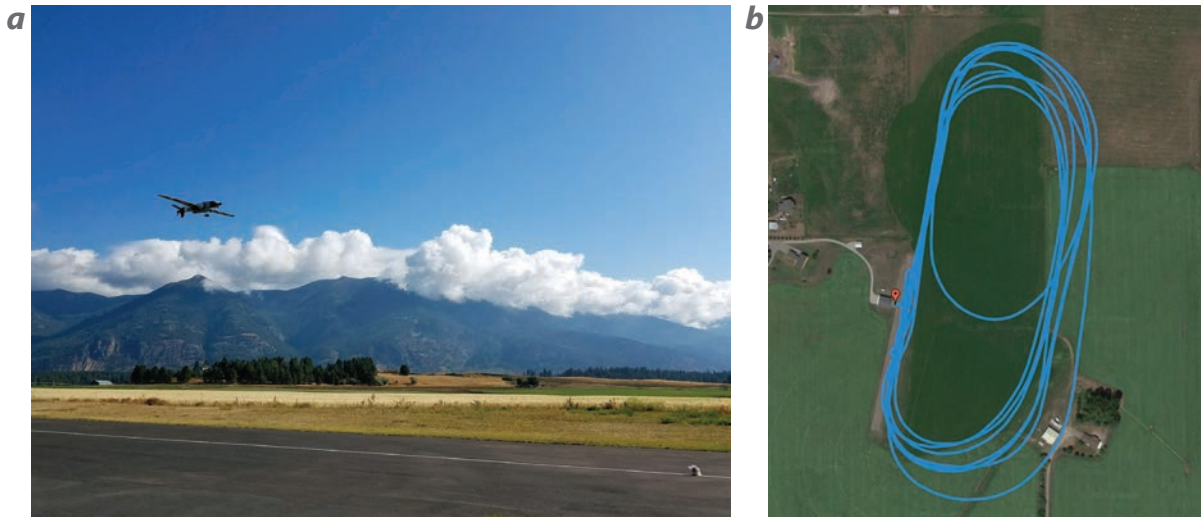


Figure 4. (a) The Sandstorm approaching the ^{152}Eu source (in the lower right corner of the photograph) and (b) the flight path. Flights over the radioactive sources were from north to south. The ^{137}Cs source was located at the north end of the runway, and the ^{152}Eu source was about halfway down the runway. The pin marks the location of the ground station.

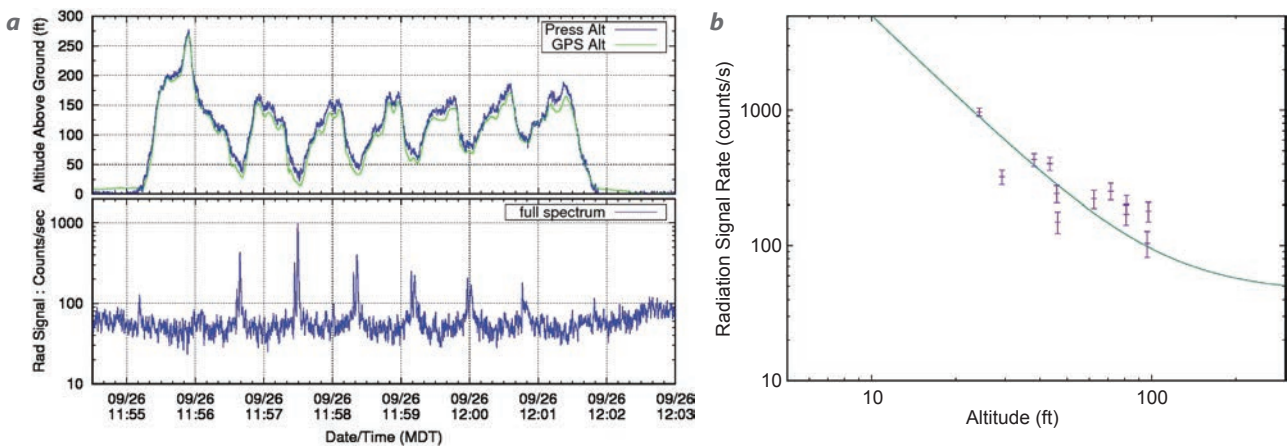


Figure 5. Measurements taken by the Apollo detector on the Sandstorm during the test flight at the Kalispell airfield in Montana on September 26, 2017. We placed two radioactive sources, ^{137}Cs and ^{152}Eu , on the runway and took measurements over a range of altitudes to estimate the sensitivity limit of the Apollo detector on the Sandstorm drone. Shown are (a) the altitude above ground in the upper plot, and the radiation intensity in the lower plot. The double peaks indicate two radioactive sources separated by 250 m along the side of the runway; and (b) the signal as a function of altitude, which suggests a sensitivity limit of about 200 feet.

Figure 5 shows radiation intensity data from a test flight conducted at the Kalispell airfield on September 26, 2017. Figure 5a shows the altitude above ground measured by the barometer and GPS in the upper plot, and the radiation intensity measured by the Apollo detector in the lower plot. The data shown in Figure 5a are from full-scale integrations smoothed by an exponential moving average filter with a one-second time constant.

Radiation measurements were taken at different altitudes, which allowed us to estimate the altitude sensitivity limit of the Apollo detector by extrapolating the data to the noise limit. Figure 5b suggests a sensitivity limit of about 200 feet. The precision of the cross-track offset, however, was no better than 30 feet, so the actual distance to the source is uncertain to that extent. The error bars in the figure represent only the statistical errors of the radiation counting and do not account for uncertainties of altitude and cross-track offset measurements.

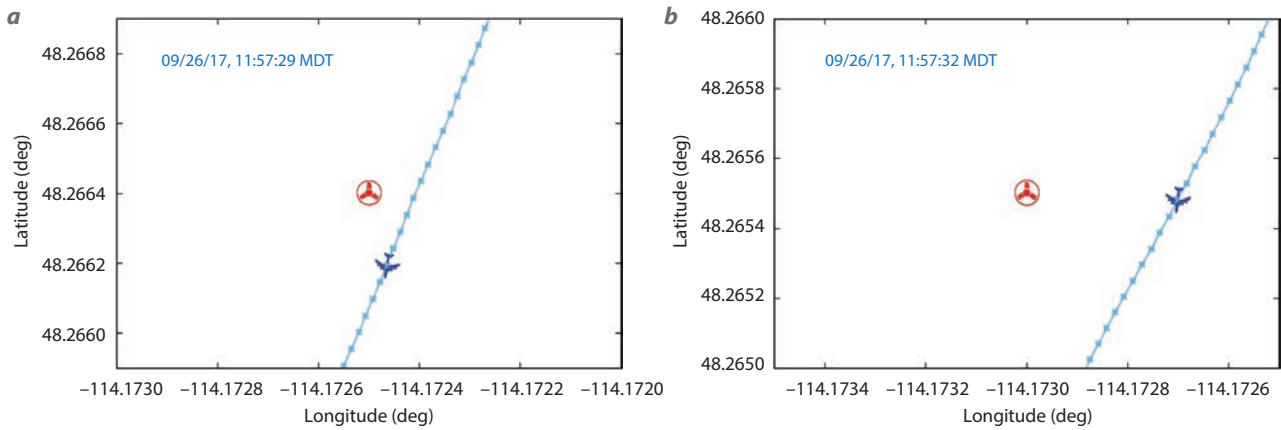


Figure 6. Flight tracks of the Sandstorm over the radioactive sources illustrate uncertainties of positions of the sources on the ground and the aircraft in the sky. The flight paths over (a) the ^{137}Cs source and (b) the ^{152}Eu source are shown. The icon for the aircraft is at the position of maximum radiation signal. The points on the flight path are the GPS data points reported every 200 ms.

Figure 6 shows examples of the cross-track offsets for the flights over (a) the ^{137}Cs source and (b) the ^{152}Eu source. The radiation icon marks the location of the source. The airplane icon marks the location of the Sandstorm at the peak of radiation intensity. The dotted line is the flight path; each dot represents a GPS reading. We recorded the source locations with a cellular phone to only four decimal places and that corresponds to about a 30-foot uncertainty for the sources. The GPS receiver in the pod was a MediaTek MT3339, which has a specified precision of 3 m, and a typical horizontal dilution of precision (HDOP) of its readings during the flights was 1.3, so the positional

uncertainty of the Sandstorm was on the order of 15 feet.

Although the Apollo was able to locate both the ^{137}Cs and ^{152}Eu sources, the amount of data it collected was insufficient to identify the sources. Figure 7a shows a close-up of the largest intensity peaks of Figure 5, displaying the altitude above ground and the total radiation signal, as well as energy-windowed signals for ^{137}Cs (662 keV) and ^{152}Eu (344 keV). Figures 7b and 7c show spectra extracted from the peak data for ^{137}Cs and ^{152}Eu , respectively. Neither spectrum is adequate for source identification.

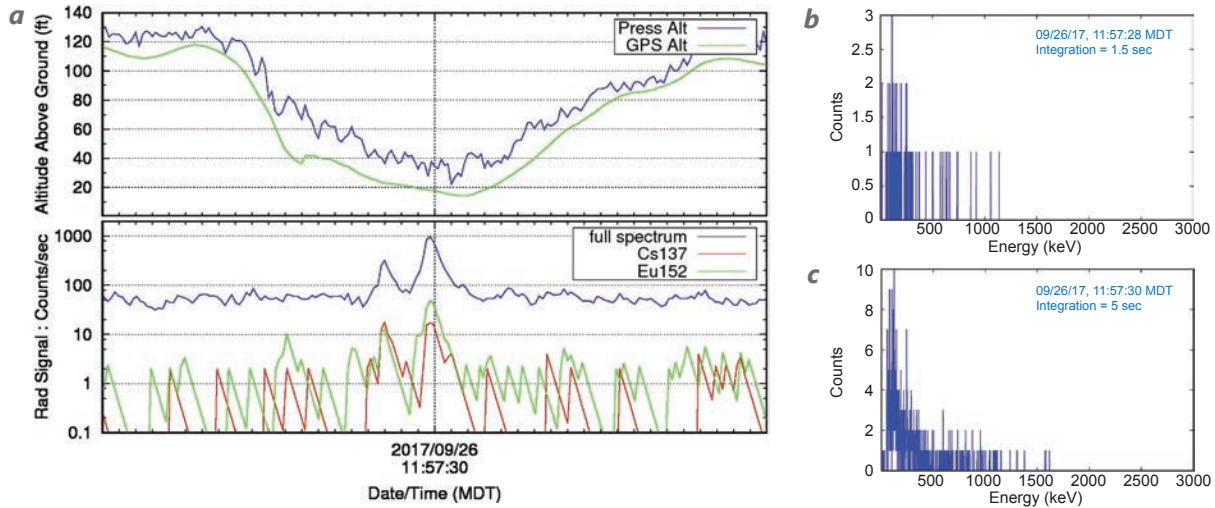


Figure 7. (a) This close-up of the largest radiation peaks seen in Figure 5 shows clearly defined intensity peaks of the integrated full spectrum; however, the energy-windowed peaks for (b) ^{137}Cs and (c) ^{152}Eu barely rise above the noise. The small CZT crystals do not efficiently produce photopeaks, so the bulk of the gamma absorption is spread over the Compton continuum.

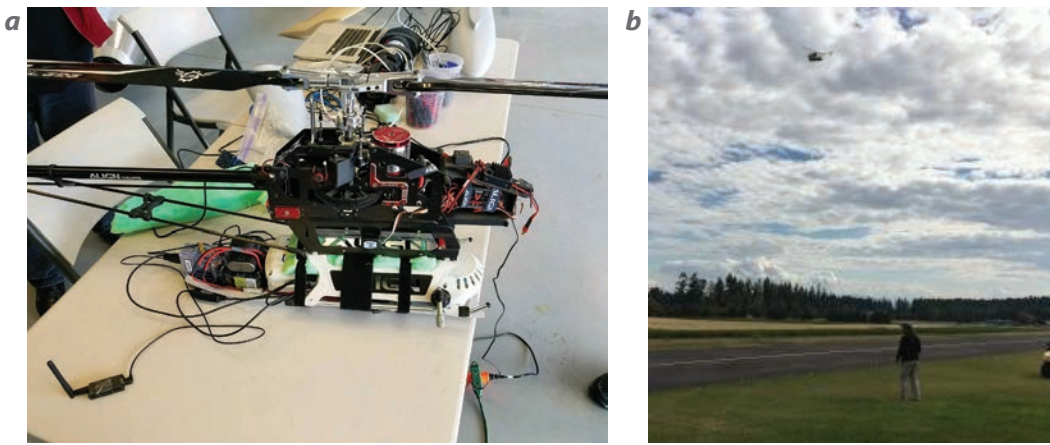


Figure 8. (a) The Apollo detector is strapped to the landing skids of a T-Rex 600 RC helicopter. The CZT crystals are located in the round section in the front. The batteries and the clear plastic case of the Raspberry Pi are located on the tray behind the Apollo. The 915 MHz 3DR radio is sitting on the table in the lower left of the photo. (b) The T-Rex with the Apollo hovering over a radioactive source.

shows the Apollo strapped to the T-Rex 600. The photo does not show a large block of foam placed beneath the tray. Figure 8b is a photograph taken at the Kalispell airfield showing the T-Rex with the Apollo flying over a radioactive source.

We flew the T-Rex and the Apollo slowly over several radioactive

Radiation Sensing with the Apollo Detector on a T-Rex 600 Helicopter

Data from the Apollo collected during the Sandstorm flights confirmed the original concern that a fixed-wing platform moved too fast for useful spectral data to be obtained from the small crystals of the Apollo. Consequently, we improvised and mounted the Apollo onto the landing skids of a T-Rex 600 RC helicopter. Lowering the center of gravity of the loaded helicopter raised some concerns, so we flew a tool box weighing 10 pounds as a dead weight to test flight stability before risking the expensive Apollo detector. Figure 8a

sources, and we attempted to keep the T-Rex hovering in place for a while to collect enough data to construct a gamma image. The T-Rex did not have an autopilot, and manual control was not adequate to keep the helicopter stationary for more than a few seconds. Figure 9 shows results from a slow, continuous-motion flight over four radioactive sources— ^{152}Eu , ^{137}Cs , and ^{133}Ba , as well as a cobalt-60 (^{60}Co) source. The red pin markers on Figure 9a indicate the locations of the sources, and the blue line is the flight path recorded by the Raspberry Pi. The plots (Figure 9b) display GPS

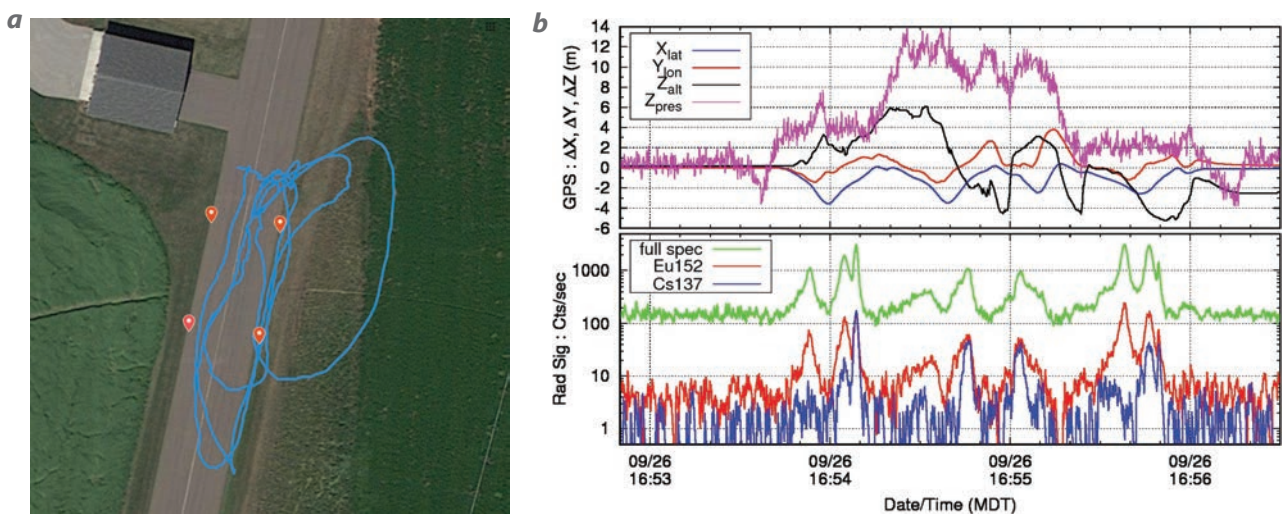


Figure 9. (a) With four radioactive sources placed on the runway (see markers), the T-Rex helicopter was flown manually over them, nominally in a square pattern; the blue line shows the actual flight path measured by the GPS receiver on the Raspberry Pi. (b) Relative GPS location as a function of time is plotted above the radiation. Three of the four sources (^{152}Eu , ^{137}Cs , and ^{133}Ba) were identified from the data.

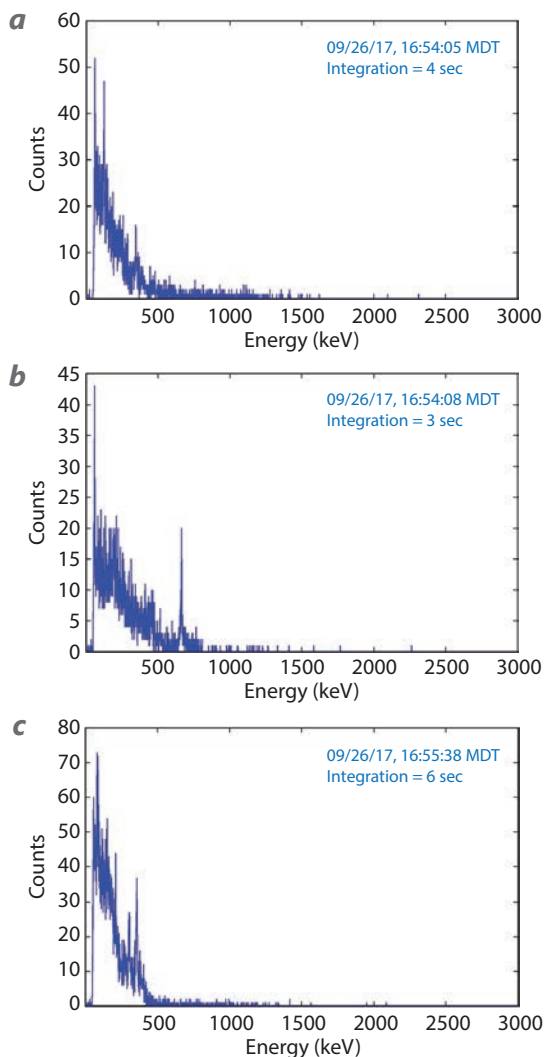


Figure 10. The Apollo collected three identifiable spectra while the T-Rex hovered about 4 m above the radioactive sources (a) ^{152}Eu , (b) ^{137}Cs , and (c) ^{133}Ba . The fourth source, ^{60}Co , was not identified, probably because of the reduced efficiency of the small CZT crystals in capturing the higher-energy gammas.



Figure 11. The 3×6 NaI(Tl) detector with an ORTEC digiBASE is mounted in foam and strapped to the sliding tray of the Sandstorm pod. The Raspberry Pi is attached to the tray with Velcro and a cable tie, and the battery to power the pod is in the upper left of the photo next to the GPS antenna and the wire bundle.

data from the Raspberry Pi and the radiation signals from the Apollo.

The spectra from these data are shown in Figure 10, and three of the sources (^{152}Eu , ^{137}Cs , and ^{133}Ba) were identified. The spectrum of the ^{60}Co source data (not shown) did not distinguish the ^{60}Co source from background. The crystals in the Apollo are too small and the gammas from ^{60}Co (1.17 and 1.33 MeV) are too energetic to produce noticeable photopeaks. Also, the amount of time over the ^{60}Co source was not long enough to reconstruct photopeaks from data in the Compton continuum.

The results obtained from the T-Rex flights in Montana are not ideal, but they do illustrate the potential of flying the Apollo detector on a rotary-wing platform. The results from the Idaho flights presented later in this report illustrate that an autopilot is essential to obtain optimum results from the Apollo detector.

Radiation Sensing with a 3×6 NaI(Tl) Detector on the USI Sandstorm

The 3×6 NaI(Tl) detector is shown in Figure 11. The recommended maximum weight of a payload in the Sandstorm pod is 10 pounds (4.5 kg). Accordingly, we sized the 3×6 NaI(Tl) detector to be within the weight and volume constraints of the pod. The detector, made by Alpha Spectra, has 700 cm³ of NaI crystal, and it weighs 7 pounds. Its photomultiplier tube (PMT) has a standard 14-pin base, and it is plugged into an ORTEC digiBASE for PMT high voltage and data acquisition. The digiBASE connects to the Raspberry Pi by a USB cable, and the software to run it is in the C programming language. The digiBASE is configured to operate in list-mode format, where each gamma event produces an analog-to-digital converter (ADC) reading and a time stamp. The time stamp is read from the free-running clock internal to the digiBASE, and

to synchronize the radiation data with flight telemetry, the C program writes a time fiducial obtained from the Raspberry Pi's GPS-referenced clock into the radiation data stream once per second.

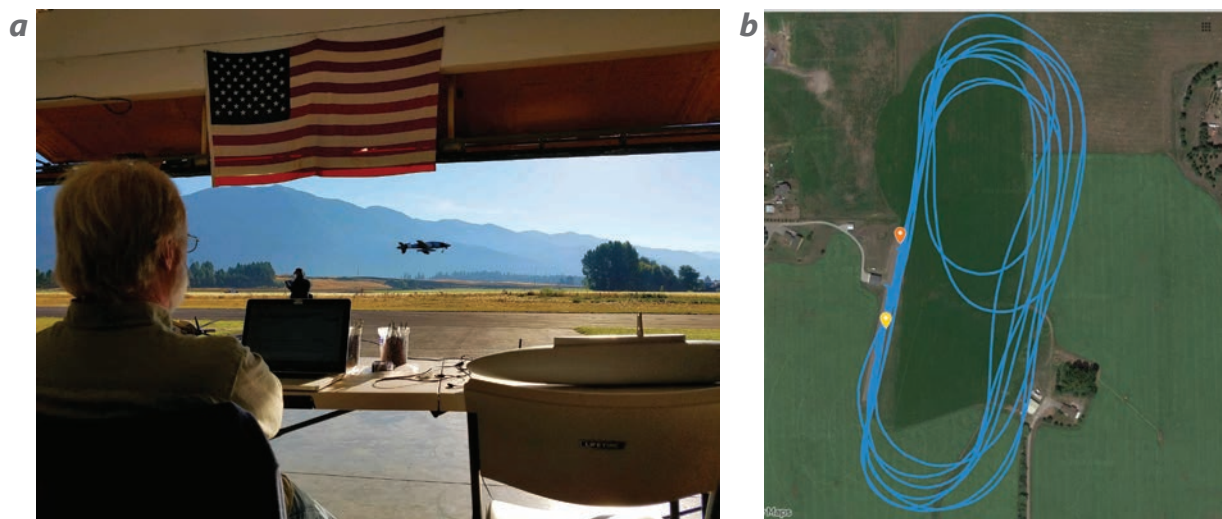


Figure 12. (a) The Sandstorm drone carrying the 3×6 NaI(Tl) detector pod; the Apollo pod sits on the table in the foreground, at right. (b) An aerial photo shows the flight path in blue; the orange pin marks the location of the ^{137}Cs source, and the yellow marks the ^{152}Eu source.

The C program also maintains memory-mapped real-time data of the average gamma spectrum for communications over the radio link to the ground station. On the Raspberry Pi a PHP script accesses the real-time data and transmits the data over the radio to a web browser on the ground station. The HTML page in the web browser is written in HTML5 and JavaScript, and the page is served to the web browser from the Raspberry Pi's Apache server. Once in the browser, the JavaScript in the web page opens a WebSocket connection back to the Raspberry Pi to stream data in real time. The average spectrum is an array of 1024 integers updated 10 times per second, and the PHP script accesses the array only when

requested by JavaScript from the ground station. Nominally, access occurs twice per second. The same PHP script streams telemetry data in the same manner. The data are processed in real time by the web page's JavaScript and plotted in the web browser.

Figure 12a shows the Sandstorm carrying the 3×6 NaI(Tl) detector over the Kalispell airfield and the Apollo pod on the table in the foreground, right. The aerial photo (Figure 12b) shows the flight path for one of the test flights; locations of the ^{137}Cs and ^{152}Eu sources are also shown.

The graphs in Figure 13 show results from the test flight from Figure 12. Strip-chart recordings of the

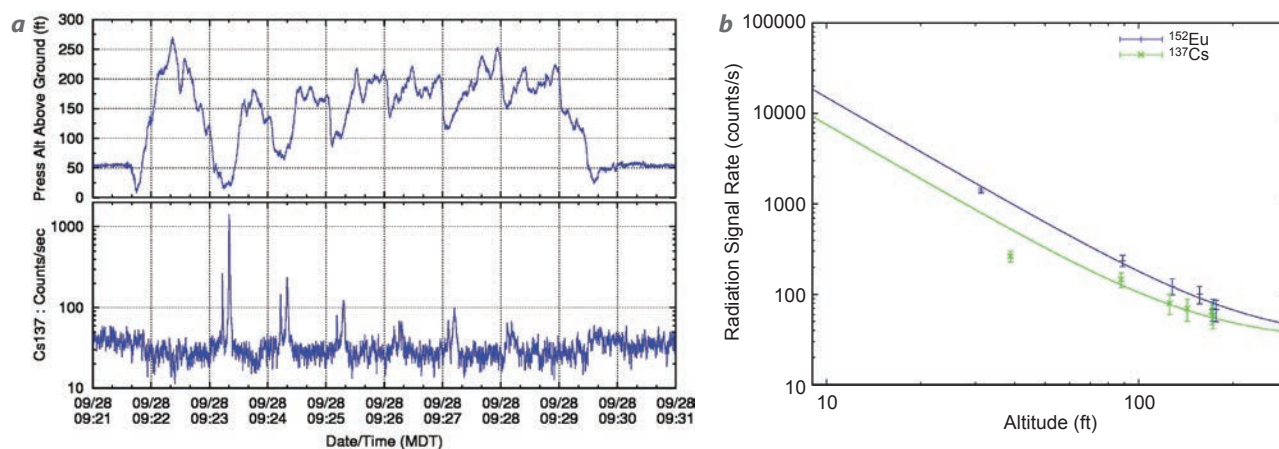


Figure 13. Results from the Sandstorm and 3×6 NaI(Tl) detector flight test showing (a) strip-chart recordings of the pressure altitude and radiation signal as functions of time and (b) the radiation intensity as a function of altitude. The data imply a sensitivity limit of about 200 feet. This limit is very close to that of the Apollo detector, which is surprising, because the sensitive volume of the 3×6 NaI(Tl) detector is about 30 times that of the Apollo detector.

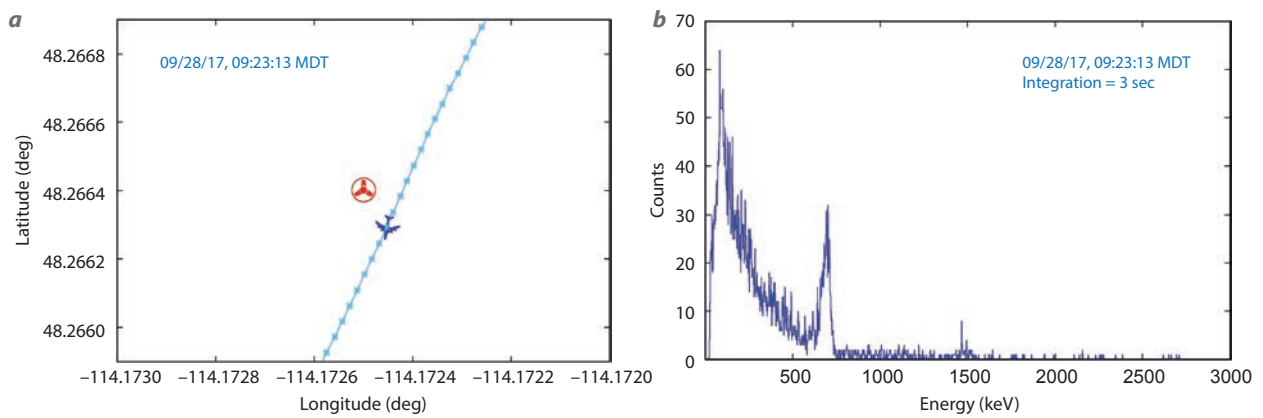


Figure 14. (a) The Sandstorm's flight track and its location at the time of the highest radiation signal. The radiation icon marks the location of the radioactive source. (b) The spectrum clearly identifies ^{137}Cs as the source.

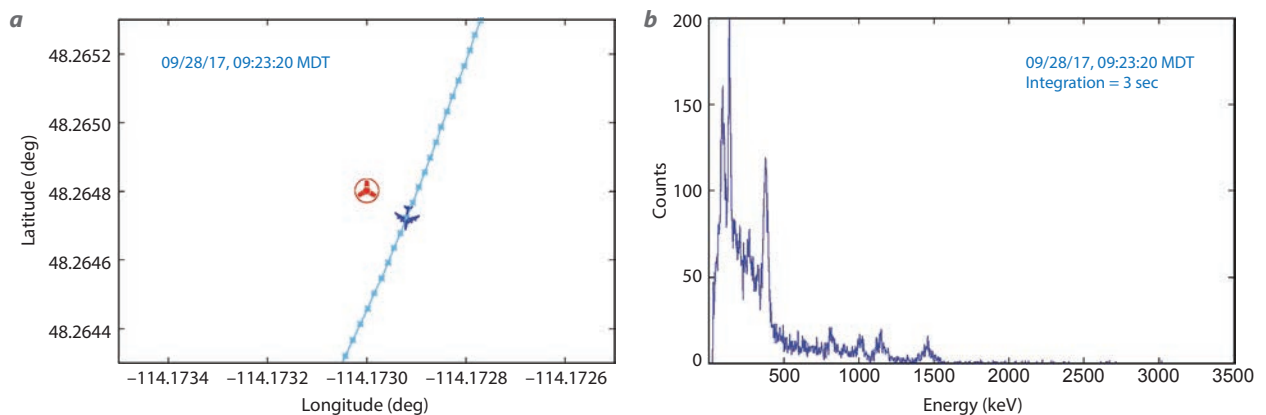


Figure 15. (a) The Sandstorm's flight track and its location at the time of the highest radiation signal. The radiation icon marks the location of the radioactive source. (b) The spectrum indicates the source is ^{152}Eu .

pressure altitude and radiation intensity are plotted as functions of time. We flew the Sandstorm over the ^{137}Cs and ^{152}Eu sources six times at different altitudes to collect data to obtain by extrapolation an estimate of the detector's altitude sensitivity limit. The data imply a detection limit of about 200 feet, which is the same result that we obtained for the Apollo detector. This comes as a surprise, because the 3×6 NaI(Tl) detector volume is about 30 times more than that of the Apollo, and consequently should be at least an order of magnitude more sensitive, which would yield a distance that is at least three times the measured sensitivity limit.

The cross-track offsets for this flight are shown in Figures 14 and 15. Figure 14a shows the flight path over the ^{137}Cs source, and Figure 15a shows the flight path over the ^{152}Eu source. The cross-track offsets for this test are comparable to the cross-track offsets for the test done with the Apollo detector, so the

uncertainties in distance should also be comparable (about the same). The spectra from the 3×6 NaI(Tl) detector, however, are dramatically better than those from the test done with the Apollo detector. The spectrum in Figure 14b shows the unmistakable photopeak of ^{137}Cs , and the spectrum in Figure 15b is clearly from ^{152}Eu .

The spectra in Figures 14b and 15b were generated from the list-mode data file over 3-second segments centered on the time when the radiation levels peaked. An advantage of list-mode data is that we can choose integration times to generate spectra as needed, rather than being constrained by the 1-second intervals traditionally used. As discussed earlier about the Apollo data, there are uncertainties in source location and accuracy of the GPS measurements. Another reason that a location offset occurs is that a systematic error is introduced when we use the exponential averaging routine to smooth the intensity data while searching for the intensity maximum. Exponential



Figure 16. The modified, “stubby” 2×2 NaI(Tl) detector is strapped to the bottom of a 3DR Solo. The detector is controlled by the Solo’s onboard i.MX6 computer.

averaging introduces a systematic delay on the order of the time constant used in the filter. As we can see in the plots, the aircraft has already passed the sources when the radiation signals peak. We used a 0.5-second time constant on these data, and the dots on the flight tracks represent the GPS updates received every 200 ms. The ground speed of the Sandstorm was about 60 miles per hour, so in a half-second it moved about 15 m. This offset is comparable to the uncertainty of the source locations, and it is consistent with the offsets seen in the plots. Considering the uncertainty of the source placements then the radiation data can be used to locate the sources to within 15 to 30 m.

Radiation Sensing with a 2×2 NaI(Tl) Detector on a 3DR Solo Quadcopter

The 3DR Solo quadcopter is capable of lifting a payload of 1 kg (2.2 pounds) for a flight time of about 10 minutes. The expansion port on the chassis bottom provides access to raw battery power, regulated 5 V, and the USB interface of the Solo’s onboard i.MX6 computer. The i.MX6 uses the Arm Cortex-A9 instruction set, and the computer operating system is Yocto Linux. There are no development libraries included in the 3DR Solo as distributed by 3DR, but the necessary libraries can be installed from the Yocto Linux repositories. A C compiler and the USB development library are required to build the program that operates the gamma detector; the program was ported from the Raspberry Pi with minimal changes.

The Solo’s ground controller provides its own 2.4 GHz wireless access point to which a computer can join. A client computer can access the radiation data through

a Python-based web server that we configured on the Solo. The web page for detector access is identical to the Raspberry Pi’s, but there is a difference in the implementation: the Raspberry Pi’s web server is configured to run PHP scripts, whereas the Solo’s web server is configured to run Python scripts.

Initial flights of the 3DR Solo in Montana with a standard, off-the-shelf 2×2 NaI(Tl) detector were successful, but the flight stability was marginal due to the low center of gravity and large moment arm of the standard-sized detector. Consequently, we asked Alpha Spectra to manufacture a modified, “stubby” version of the detector, which is 2 inches shorter and 4 ounces lighter than the standard detector. Figure 16 shows the modified, “stubby” 2×2 NaI(Tl) detector strapped to the bottom of a 3DR Solo. This configuration has better flight stability, and the detector performance is comparable to that of a standard detector.

The modified 2×2 NaI(Tl) detector was strapped to a 3DR Solo and tested in Nevada at the Desert Rock Airstrip on March 27, 2018. Figure 17 shows results from this test. We used two radioactive sources, ^{137}Cs and ^{152}Eu . The strip-chart plot (Figure 17a) shows the radiation signal as a function of time. Spectra were generated from the list-mode data for ^{137}Cs and ^{152}Eu sources. Note that the spectrum collected over the ^{152}Eu source (Figure 17c) also shows the signal from the ^{137}Cs source. The sources were separated by about 50 m, and the Solo hovered at an altitude of 25 m, so the sources were not far enough apart to be completely isolated. The flight plan for the Solo was to fly to the first source and hover for 80 seconds, and then fly to the second source and hover for 2 minutes. With winds blowing at a speed between 10 and 15 knots, the Solo struggled somewhat while flying in this head wind, but otherwise it performed well.

Mapping Radioactive Contamination with the Apollo Detector and Modified 2×2 NaI(Tl) Detector on the Virginia Tech Hexacopter

The Huckleberry Hustle exercise was organized by the Defense Threat Reduction Agency (DTRA) and conducted at the Radiological Response Training Range (RRTR) at the Idaho National Laboratory during the week of April 23, 2018. For this exercise, radioactive bromine-82 (^{82}Br) was explosively dispersed in three craters at the test range. This particular isotope was chosen because of its short 35-hour half-life to ensure that if any items were inadvertently contaminated during the exercise they would be clean again within two weeks. Our

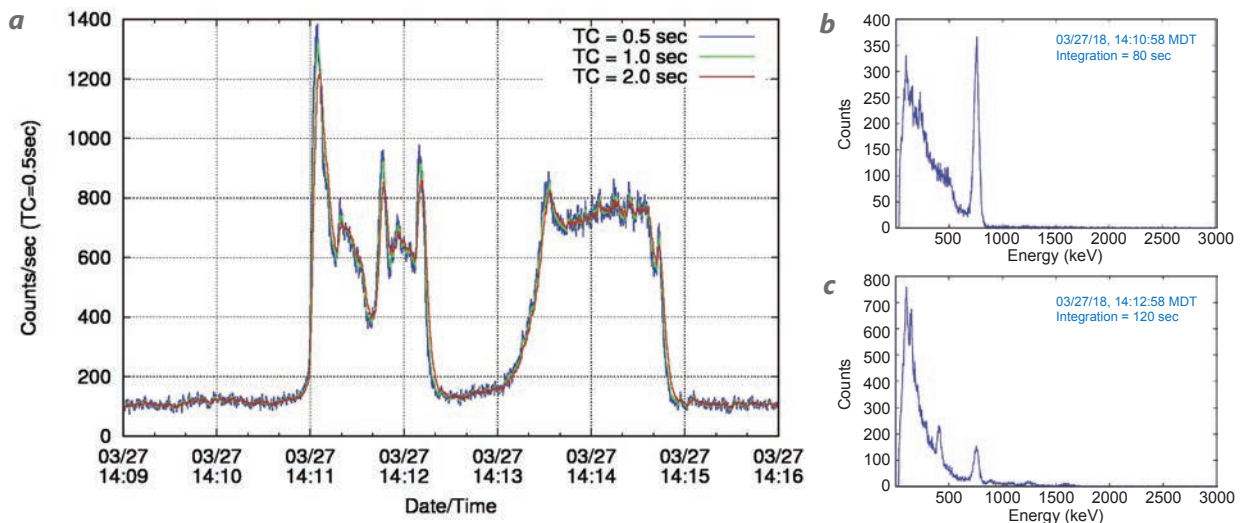


Figure 17. The 3DR Solo with the modified 2×2 NaI(Tl) detector hovered over ^{137}Cs and ^{152}Eu sources. (a) The total radiation signal as a function of time. The spectra extracted from the list-mode data are plotted for (b) the ^{137}Cs source (clearly identified) and (c) the ^{152}Eu source, which also shows the 662 keV peak of ^{137}Cs .

participation was organized through the Remote Sensing Laboratory at Andrews Air Force Base by Jessica Feener and Lance McLean, and we teamed up with the Unmanned Systems Laboratory (USL) at Virginia Tech. During the exercise we flew the Apollo detector and the modified (“stubby”) 2×2 NaI(Tl) detector simultaneously on a hexacopter provided by Virginia Tech. Figure 18 shows the Virginia Tech hexacopter with the two detectors mounted beneath the chassis and the front of the Apollo pod with the

nose cone removed to expose the Raspberry Pi and a cellular phone.

There were occasional communications issues caused by a nearby cellular phone repeater, which consistently jammed communications when the hexacopter was flying over one of the craters. Also, the Apollo began to overheat later in the week when outdoor temperatures exceeded 80°F (that is why there are vent holes in the pod shown in Figure 18). Overall, the test flights conducted at the RRTR during the week

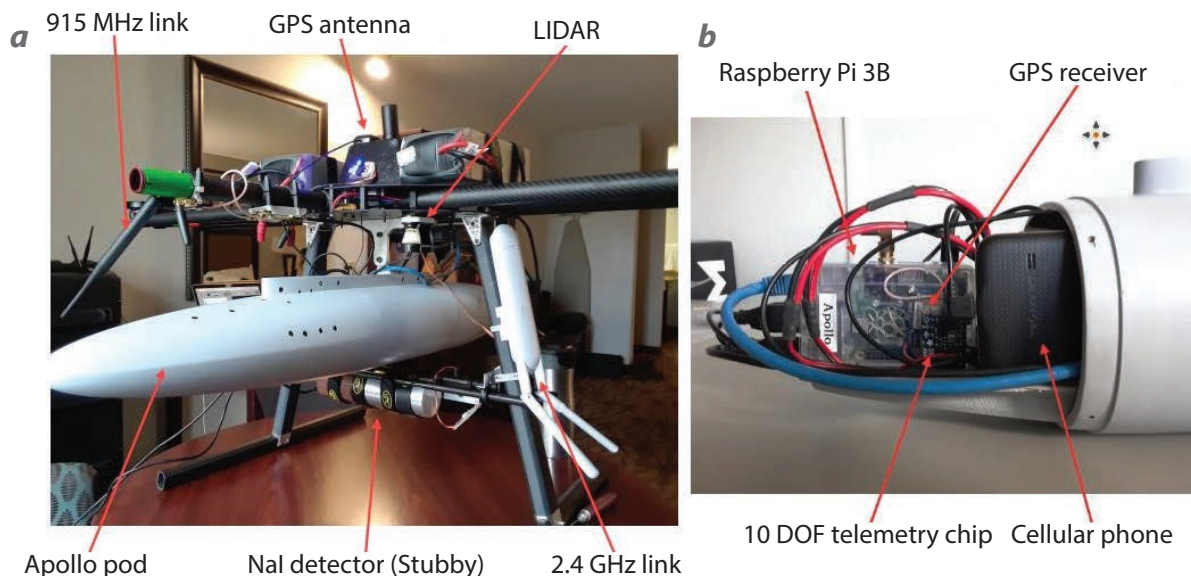


Figure 18. (a) The Apollo pod bolted to the chassis of the Virginia Tech hexacopter. The 2×2 NaI(Tl) “stubby” detector is beneath the Apollo strapped to a pair of carbon fiber rods attached to the landing struts. (b) The Apollo pod with the nose cone removed to reveal the Raspberry Pi and cellular phone. The system was tested at the RRTR in April 2008 and again in July 2018.

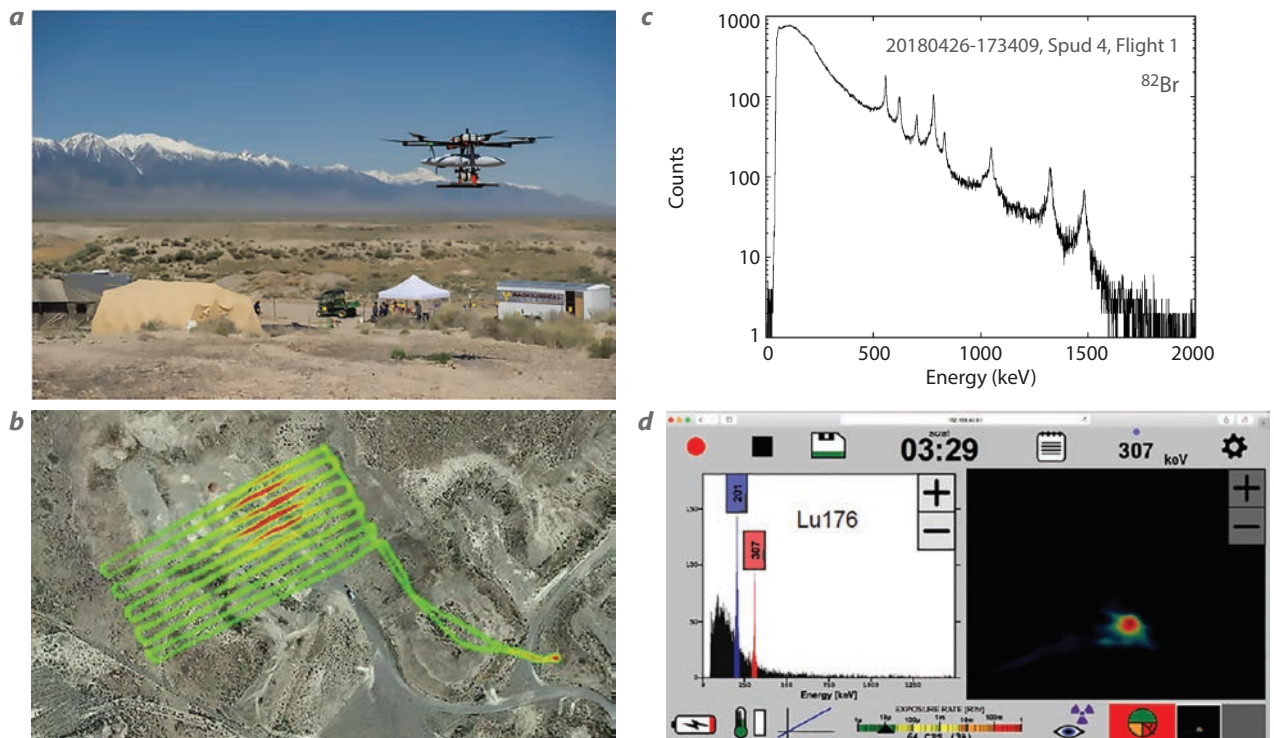


Figure 19. (a) The Virginia Tech hexacopter in flight carrying the Apollo and modified 2×2 NaI(Tl) detectors. (b) An aerial photo with the flight track superimposed shows the distribution of radioactive contamination. (c) Plot of a ⁸²Br spectrum collected by the Apollo. (d) A screen capture of the Apollo’s graphical interface during a calibration run on the ground.

of April 23, 2018, were extraordinarily successful. Spectra from both detectors clearly identified ⁸²Br, and the radioactive contamination distributions around the craters were clearly mapped.

Figure 19 shows (a) the Virginia Tech hexacopter in flight carrying both detectors, (b) a flight track mapping the distribution of radioactive contamination, (c) a spectrum of ⁸²Br, and (d) the graphical console of the Apollo during a calibration run. The Apollo console is accessible over the high-speed data link (either 4G LTE or Ethernet), but not over the low-bandwidth 915 MHz link.

On July 26, 2018, the Virginia Tech hexacopter crashed while participating in a second exercise at the RRTR. The aircraft was on autopilot and was halfway through flying a grid when it suddenly dropped out of the sky into the contamination area. Radiation

control personnel retrieved the aircraft and put it into quarantine for two weeks to allow the ⁸²Br to decay away. When we recovered it in August, it was severely damaged. All of the propellers and half of the carbon fiber booms were broken. Inspection of the wreckage was conducted but shed little light on what caused the crash. The log file from Mission Planner indicated that shortly before the crash the electronic speed controller (ESC) on motor 6 was commanded to full throttle, suggesting that the aircraft had lost lift on propeller 6. The current hypothesis is that either a propeller failure or an overheated ESC shutdown of motor 6 could have caused the crash. Figure 20 shows (a) the flight path of the hexacopter up until the crash and (b) photos of some of the damaged parts. The hexacopter was a total loss, and the pod was severely damaged, but both detectors survived the crash, and both have flown since this incident.



Figure 20. The Virginia Tech hexacopter crashed during a radiation survey flight at the RRTR in Idaho on July 26, 2018. (a) The flight path up until the crash. (b) Although the aircraft was a total loss, both detectors survived.



Figure 21. The chemical sensor pod was mounted to the belly of the Sandstorm, and the air sampling tube and VOC sensor chip were mounted below the left wing

Drone-Borne Chemical Detection

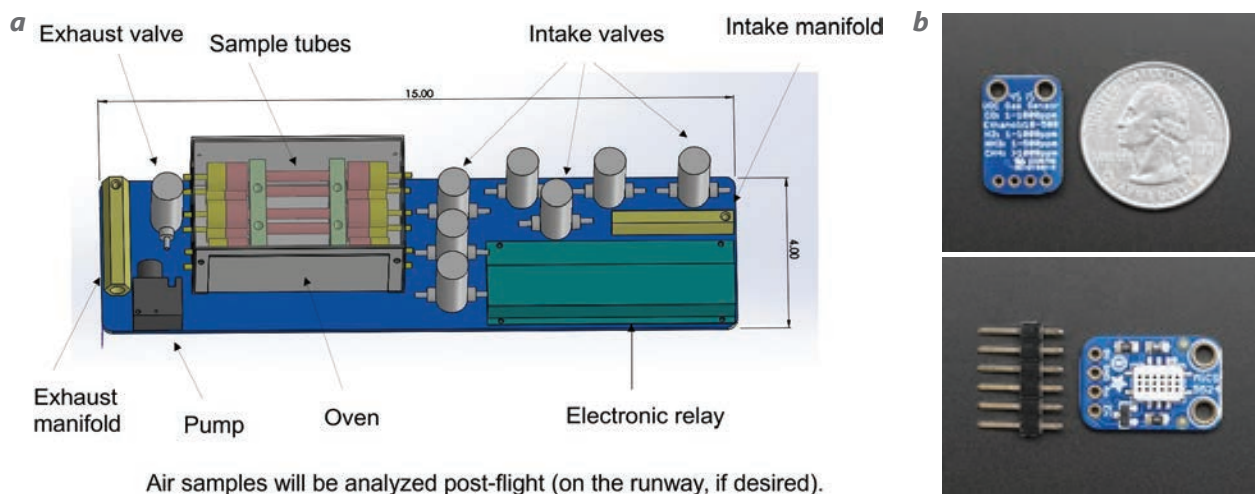
Chemical Detection with a Sensor Chip on the USI Sandstorm

Originally we planned to conduct a chemical test at the Kalispell airfield in Montana using an RC helicopter to lift a liter of a common solvent, such as alcohol or acetone, and release it rapidly into the flight path of the Sandstorm carrying the chemical detector. The logistics of coordinating the two flights and performing the chemical release were not difficult, but, the plume dynamics in any wind condition other than complete calm were prohibitive. Several seconds would be required for the helicopter to get out of the way of the Sandstorm, during which time the chemical would disperse too rapidly to be detectable once the Sandstorm reached the site of the

plume. Also, the minimum speed of the Sandstorm, being 40 knots, meant that time within the plume would be only a fraction of a second. A fall backup option was to build a bonfire at the end of the runway, however because the test would occur in the middle of fire season in Montana, lighting any fires would be unwise. Ultimately, we decided to place a sprayer on the runway and fly the Sandstorm at very low altitudes through the sprayer's small plume.

The chemical detector for the Sandstorm consists of a volatile organic compound (VOC) sensor chip and a vacuum sampler. Figure 21 shows the chemical sampler pod mounted beneath the Sandstorm, and the VOC sensor chip can be seen mounted on a rod extending forward of the wing. The sampler collects air samples for post-flight analysis, but it does not provide real-time data. The VOC sensor chip, however, does provide real-time data, and we can use these data to map the extent of a chemical plume. The VOC sensor chip flown in Montana is an Amphenol SGX Sensortech MiCS-5524 gas sensor mounted on a circuit board by Adafruit. This chip has a tin oxide surface catalytic thermal sensor normally used in alcohol breathalyzers. It is powered by 5 V, and it outputs an analog voltage. The Raspberry Pi does not have an onboard ADC, so a Texas Instruments ADS1015 ADC chip measures the voltage from the VOC sensor chip and communicates it over the I2C bus. The 10 DOF telemetry chip already communicates over the I2C bus, so its program has been modified to include readings of the ADC chip, and it stores the chemical readings in the telemetry data file.

Figure 22 shows the concept of the chemical sampler. It consists of six sampling tubes filled with Carbotrap



Air samples will be analyzed post-flight (on the runway, if desired).

Figure 22. (a) The solid model of the chemical sampler (Teflon tubing not shown) and (b) the VOC sensor chip from Adafruit

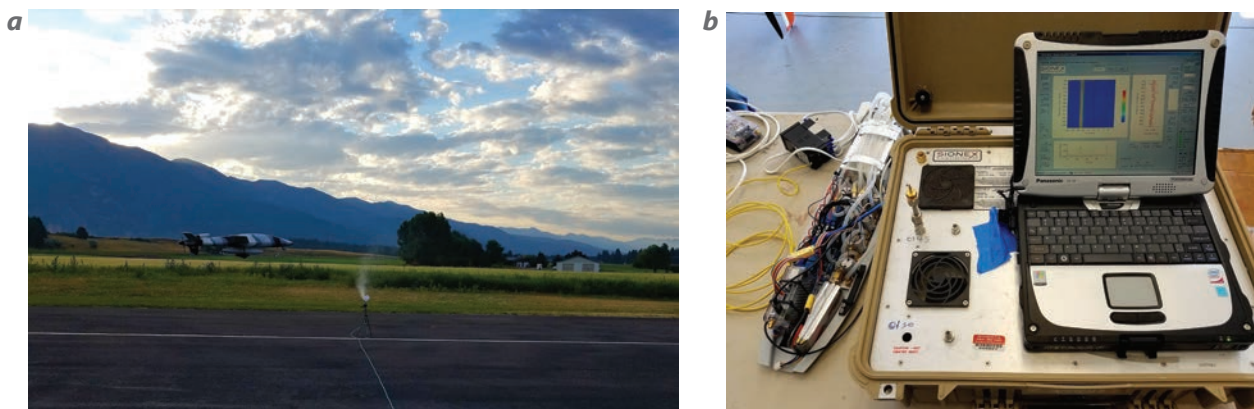


Figure 23. (a) The Sandstorm flying through a small alcohol plume released from a sprayer and (b) the Sionex differential mobility mass spectrometer next to the Sandstorm pod tray containing the chemical sampler and Raspberry Pi

300 activated charcoal that are housed in a small oven mounted on the pod tray. Intake and exhaust manifolds, solenoid valves, vacuum pump, vacuum plumbing, and electronic relays complete the system. It is powered by a 3S LiPo (three-cell lithium polymer) battery and is controlled by the Raspberry Pi via its GPIO port. During flight the pump and valves are controllable from the ground station via a web page. We can configure the system to begin collecting samples automatically once a plume is detected by the VOC sensor.

Figure 23a shows the Sandstorm about to fly through an alcohol plume created by the sprayer on the runway. The chemical sampler sitting on the table next to a Sionex differential ion mobility mass spectrometer reading out the samples collected during the flight is shown in Figure 23b.

Figure 24 shows data from the VOC sensor during flight. Shown are altitude above ground and voltages from the VOC chip for isopropyl alcohol and denatured alcohol.

Chemical Detection with Sensor Chips on a 3DR Solo Quadcopter

The Sandstorm is not an ideal platform for chemical sensing and sampling. Its minimum speed is 40 knots, so it passes through a plume very quickly, and during the tests at the Kalispell airfield in Montana, it was in the plume for only a fraction of a second. The sampler's small pump can move only 100 mL per minute through a sample tube, so the detection sensitivity is severely limited. A rotary-wing platform would be more appropriate

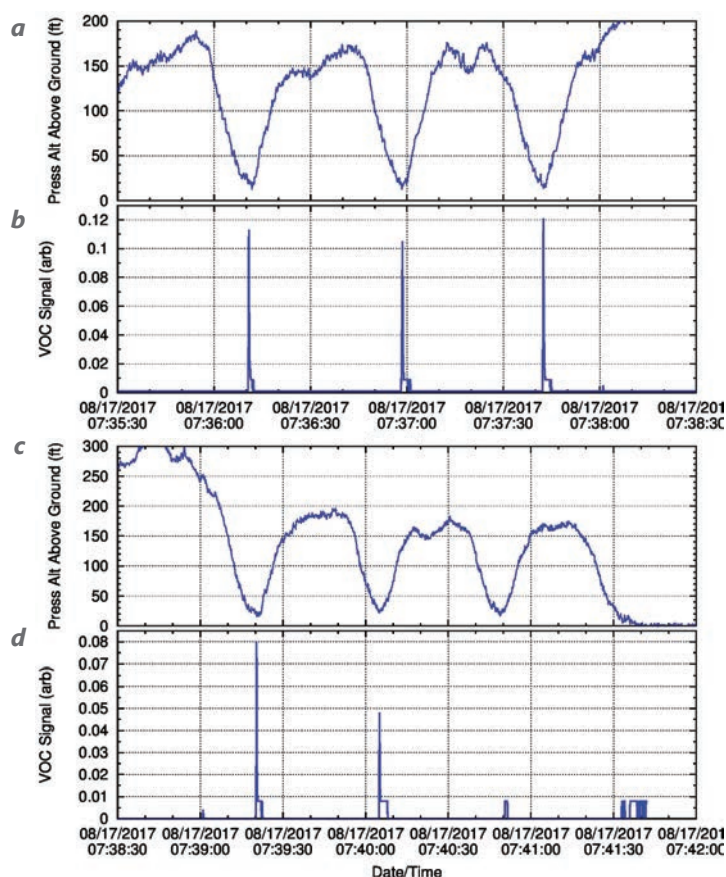


Figure 24. Results from the chemical detection test flight conducted at the Kalispell airfield on August 17, 2017, showing (b, d) real-time output of the VOC sensor as a function of time during the flight and (a, c) the altitude above ground of the Sandstorm. (Note that the troughs in the altitude indicate the location of the chemical sprayer.) The graphs are results from (a, b) isopropyl alcohol and (c, d) denatured alcohol (ethanol tainted with methanol).

because it can hover for arbitrary durations for adequate air sampling. After we completed tests with the Sandstorm in Montana, we decided to develop a chemical detector for the 3DR Solo quadcopter.

Conceptually, there is no difference between a chemical detector for a rotary-wing platform and one for a fixed-wing platform; but it has been downsized to fit the small 3DR Solo. The new sampler consists of the same type of vacuum pump used in the Sandstorm's chemical sampler and a single Carbotrap 300 sample tube. In the original design, we included two solenoid valves to isolate the sample tube; however, after we discovered that the solenoids interfered with the Solo's magnetometer, we bypassed them. The new detector also included an additional sensor chip to supplement the MiCS-5524. We added an MQ-135 gas sensor to detect smoke, ammonia, and benzene, as well as some nitrogen and sulfur compounds. This chip is commonly used in air quality monitors.

The I2C bus on the 3DR Solo is not accessible from the expansion port. Rather than making extensive modifications to the Solo to access its I2C bus we opted to use the Solo's USB interface to read and control the chemical detector. This required an intermediate circuit to provide digital input/output (I/O) and ADC readings. For this circuit we utilized a Teensy 3.2, which is an Arduino-style microcontroller with multiplexed 12-bit ADC and 8-bit digital I/O. Communications to the Teensy are over USB, and the code to control it is in a C-like language written in the Arduino integrated development environment.

The flight test of the Solo's chemical detector occurred during the week of August 27, 2018, at the USI airfield in Antigo, Wisconsin. This location was chosen because it would permit an open bonfire of organic solvents to create a chemical plume. To that end, four garbage cans of kerosene- and/or acetone-soaked rags were placed in an open field and ignited. The 3DR Solo, flying on autopilot, executed a grid pattern over the field, collecting smoke and measuring real-time signals from the VOC sensor chips. The smoke sample was later analyzed with a gas chromatograph–mass spectrometer (GC-MS).

The images in Figure 25 show the quadcopter in flight over the fires and the flight plan displayed on a tablet computer attached to the 3DR Solo's controller. The flight plan was composed in an Android fork of Mission Planner called Tower, and it was uploaded to the quadcopter from the tablet over the 3DR Solo's Wi-Fi.

As we discovered during the previous chemical detection test in Montana, simulating the plume



Figure 25. (a) The 3DR Solo quadcopter flying over garbage cans filled with kerosene-soaked burning rags. (b) The 3DR controller with the tablet computer showing the flight plan uploaded to the 3DR Solo.

conditions from a chemical disaster can be difficult. Although the rags soaked with flammable liquids generated a much larger plume than the sprayer we used in Montana, the plume was still very susceptible to wind. During the first test flight we discovered that propeller wash from the quadcopter can have a profound effect on the plume. In later flights we mounted the VOC sensor chips and collection tube on a carbon fiber rod to keep them away from the propeller wash. This change, however, did not solve the problem; it merely delayed the onset of the propeller wash effect rather than eliminating it.

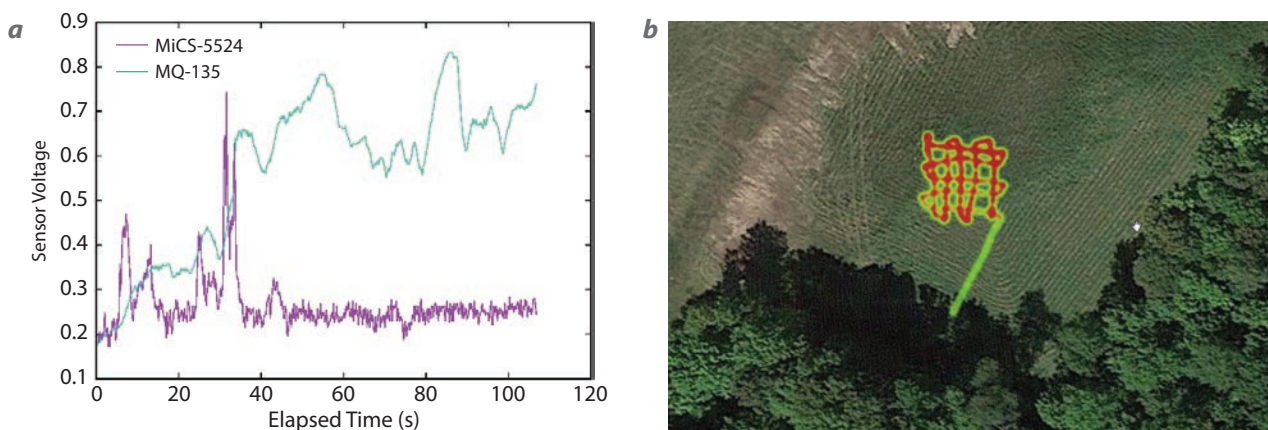


Figure 26. (a) The VOC output voltages as a function of elapsed time and (b) the GPS tracks weighted by the MQ-135 data. The MiCS-5524 exhibited fast signal response and recovery, but the MQ-135 was slow to respond, and it exhibited signal persistence.

As mentioned earlier, we added an MQ-135 gas sensor to the chemical detector for the 3DR Solo to supplement the MiCS-5524. We added this second sensor because we also wanted to test its performance and use the MiCS-5524 sensor data as control. We were also interested in testing the MQ-135's ability to detect some sulfur compounds; our original plan included adding a sulfur-based herbicide to the bonfire after we finished our initial tests with organic solvents. We discovered on the first test flight that the MQ-135 sensor chip's response and recovery to

a smoke exposure was very slow. Figure 26a shows the response of the two VOC sensor chips while the Solo was flying over the kerosene fires, and Figure 26b displays the GPS tracks weighted by the MQ-135 signal. In light of the problematic response of the MQ-135, and because propeller wash from the quadcopter can have a significant effect on the plume, we decided to scrap the idea of burning any sulfur compounds.

Figure 27 shows results from the test flight conducted at the USI airfield in Wisconsin. The figure shows the results of GC-MS analysis of the smoke collected by

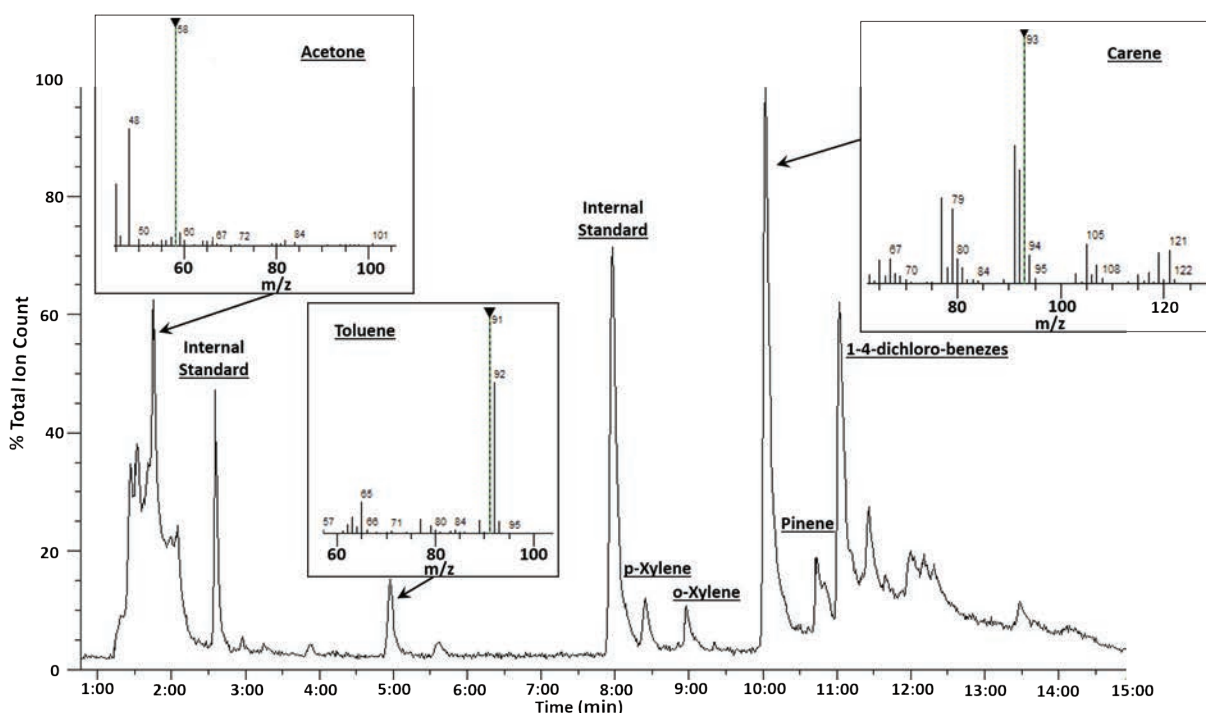


Figure 27. Results from the GC-MS of sampled smoke show toluene, which is a major component of kerosene; acetone, which was also added to the flame; and various combustion products (carene, pinene, etc.) generated from burning polyester (some of the burning rags were polyester clothing)



Figure 28. (a) The 3DR Solo carrying the spectrometer in flight and (b) the 3DR Solo with an Ocean Optics Flame-S spectrometer mounted on the expansion bay directly behind the GoPro camera. Mounted behind the spectrometer are the lidar and the Teensy 3.2. The two VOC sensors are mounted on the front legs. The yellow device in the background of the photograph is the GC-MS we used to analyze the smoke samples.

the sampler. The toluene peak indicates the presence of unburned kerosene. The acetone peak is present because in this test we burned both acetone- and kerosene-soaked rags. Several compounds such as carene and pinene are combustion products from burning polyester; some of the rags we burned were polyester clothing that the good folks of USI had picked up at a thrift store.

Spectroscopy

Optical Spectroscopy from a 3DR Solo Quadcopter

The Wisconsin test also provided an opportunity to fly an optical spectrometer on the 3DR Solo. The spectrometer was an Ocean Optics Flame-S previously fielded in April 2017 during the Helios Pyrois exercise at the NNSS. The spectrometer is sensitive from 200 to 900 nm, and the computer code to run the spectrometer from a Raspberry Pi was already available. The code was ported to the 3DR Solo with minimal changes. Figure 28 shows the 3DR Solo in flight carrying the spectrometer and a close-

up of the 3DR Solo with its peripheral equipment. All of the peripherals connect to the USB of the Solo's expansion port. The laptop computer in Figure 28b displays a spectrum of an LED flashlight we used to align the fiber telescope on the quadcopter. Spectra are displayed in real time by an HTML page served from the Python web server of the Solo. Essentially all of the Raspberry Pi's functionality has been ported to the Solo's onboard i.MX6 computer.

As the Helios project inspired us to fly the Ocean Optics spectrometer on a drone, we sought out a test scenario similar to that of Helios, and we accomplished this by collecting data from a series of small detonations of reactive targets (Tannerite), reputed to be a mixture of aluminum (Al) powder, ammonium nitrate (NH_4NO_3), and ammonium perchlorate (NH_4ClO_4). We expected to see strong bands of aluminum monoxide (AlO) emissions, but no evidence of Al combustion is found in the spectra shown in Figure 29. The spectra do, however, show emissions from sodium (Na) and potassium (K), which are commonly seen in dirty combustion. Surprisingly, a strong and unexpected emission from lithium (Li) is also visible in the spectra.

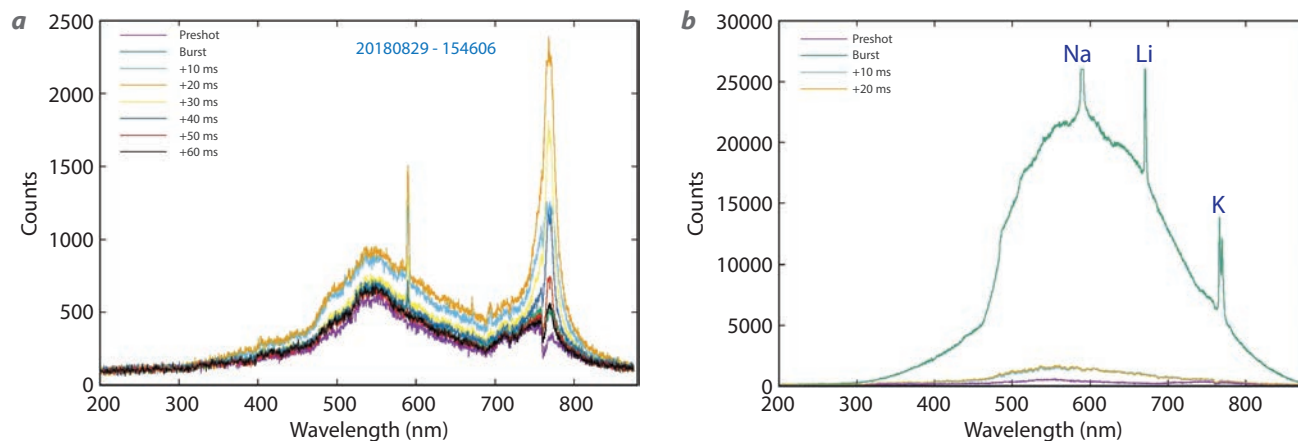


Figure 29. Optical spectra from small Tannerite detonations were collected by an Ocean Optics Flame-S spectrometer mounted on a 3DR Solo. The spectra show commonly found combustion contaminants of Na and K, as well as an unexpected emission from Li, but the spectra show no evidence of Al combustion.

CONCLUSION

We have successfully developed and flight tested a variety of detectors for aerial measurements from fixed-wing and rotary-wing drones. Aerial radiation detection is the most advanced of our capabilities to date, but we are currently capable of detecting only gamma radiation. In the near future, however, we plan to add a neutron detection capability. Chemical detection is currently limited to VOCs, and we would like to extend the capability to include sulfur and phosphorus compounds. Our spectroscopic sensitivity extends from the near ultraviolet through the visible into the near infrared. The ultraviolet sensitivity extends as far as it reasonably can for any atmospheric application, but we would like to extend much further into the infrared. Adding a hyperspectral capability would open up numerous possibilities for remote sensing. In most cases we have used off-the-shelf parts to build the detection systems. This is an important consideration; because the detectors fly in hazardous conditions, they should be considered expendable. If a sensor is considered too expensive to risk losing, then it will never become a useful asset.

ACKNOWLEDGMENTS

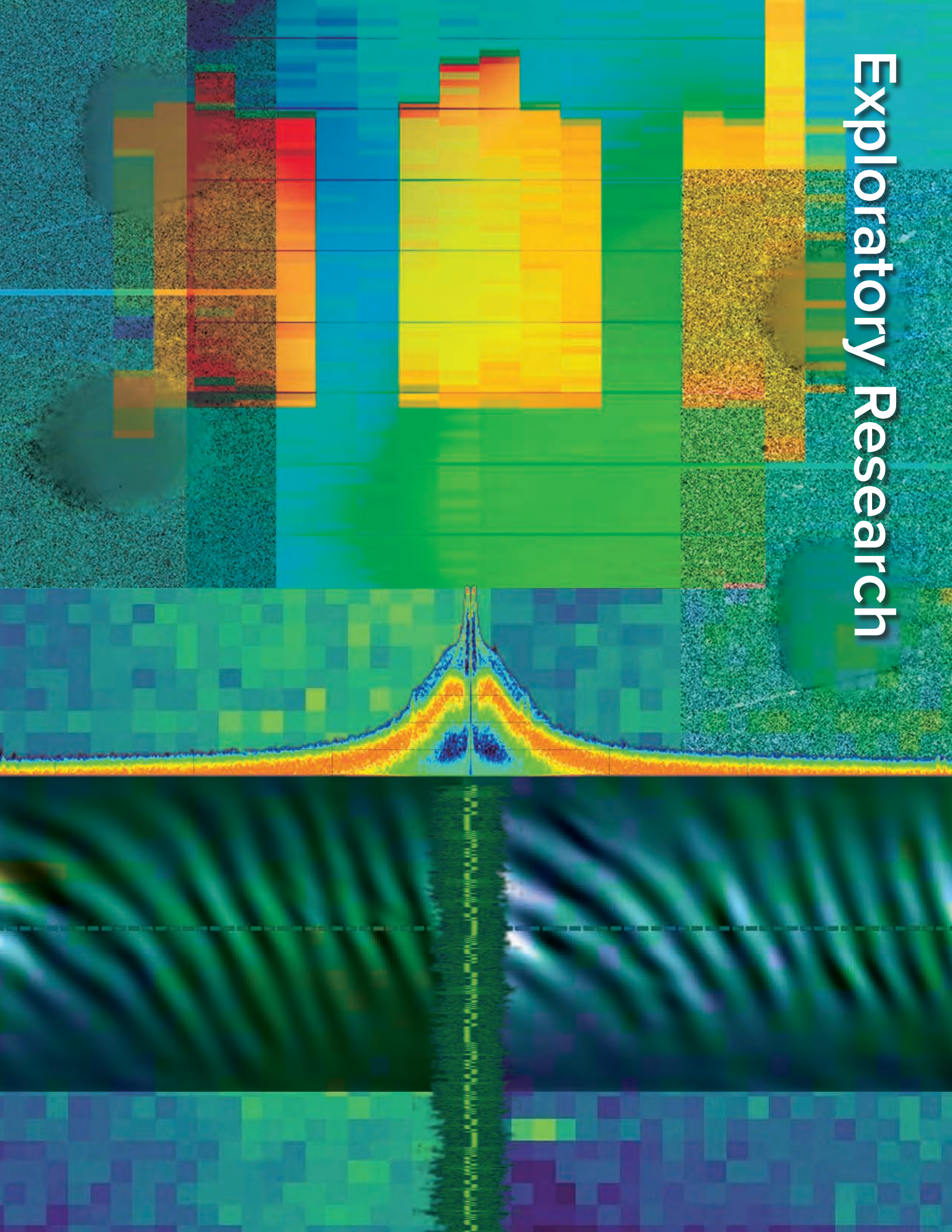
We would like to thank Mark Adan, Howard Bender, Don Bintz, John Bird, Edward Bravo, Keith Chase, Dan Haber, Joann Jackson-Bass, Tom Keenan, Mike Madlener, Rusty Malchow, Karen McCall, Chris Melchor, Drew Morgan, Mark Norsworthy, Justin Sands, Bill Tremblay, and Hovig Yalian for their contributions to this work.

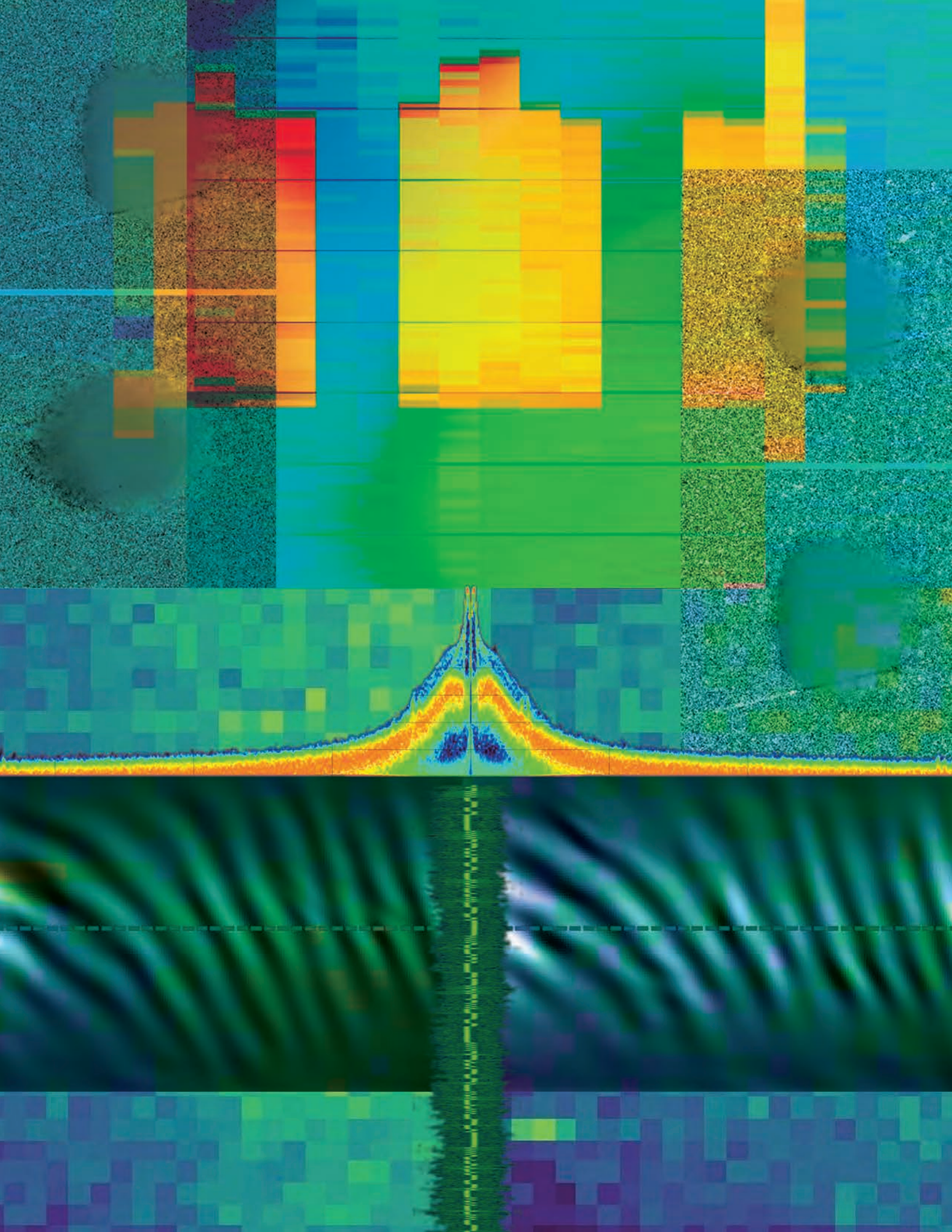
REFERENCES

Frayer, D., M. D. O’Neill, M. Mavroleon, C. Hollabaugh, J. Lawson, R. Trainham, S. Fall, “Drone Video Platform—Collision Avoidance, Situational Awareness, and Communications,” in *Site-Directed Research and Development*, FY 2017, National Security Technologies, LLC, and Mission Support and Test Services, LLC, Las Vegas, Nevada, 2018, 69–77.

This page left blank intentionally

Exploratory Research







Simultaneous Raman and Pyrometric Temperature Measurements in a Shock Wave–Compressed Material

STL-009-17 ■ Year 2 of 2

Gene Capelle,^{1,a} Brandon La Lone,^a and Jason Mance^a

¹capellga@nv.doe.gov, (805) 681-2252

^aSpecial Technologies Laboratory



With the goal of demonstrating a technique different from pyrometry for measuring the temperature of a shock-compressed state, we built a system for measuring temperature using Raman spectroscopy. We then carried out experiments in toluene shocked to pressures up to 9 GPa and compared temperatures measured simultaneously by Raman spectroscopic techniques and pyrometry. A toluene sample was shock compressed between sapphire windows; as the shock reverberated between the windows, the pressure increased stepwise. While the sample was near its peak pressure, we fired a probe laser and measured the ratios of the Raman anti-Stokes scattered lines to the corresponding Stokes lines with a spectrometer. Simultaneously, we measured the sample thermal radiance with a pyrometer. Both the Raman and pyrometry measurements yielded similar temperatures. Comparisons of this type are necessary to validate pyrometry as a temperature diagnostic and to determine whether corrections of pyrometric measurements made at the surface of an opaque sample yield accurate temperatures in the bulk material. In FY 2017 we demonstrated this technique (Capelle 2018), and in FY 2018 changes to the experimental hardware and analysis reduced the uncertainty in the Raman- and pyrometry-measured temperature significantly.

BACKGROUND

Temperature measurements are critical to understanding and modeling the equation of state (EOS) of a shocked material (Zel'dovich 1966). Recently, researchers have made substantial improvements in the ability to determine the temperature of a shocked metal sample using

optical pyrometry with accompanying reflectivity measurements to identify the emissivity at similar shock stresses (Blanco 1999; Partouche-Sebban 2002, 2003, 2005; La Lone 2013). Pyrometry involves measuring the optical emission from a shock-heated sample in one or more visible or IR bands. A best-fit temperature can be calculated by correcting the

measured output using the sample's emissivity and comparing it to the output of an ideal black body.

When an opaque sample is used in a pyrometry experiment, the temperature is determined at its surface (i.e., at its interface with the window needed to maintain shock stress in the sample, not in the bulk sample), but it is the bulk temperature that is required for EOS calculations. Also worrisome are the effects of the adhesive or other means of fastening the window to the sample. Additional problems include temperature differences between the window and sample caused by thermal and shock impedance mismatches and possible nonthermal sources of light emission, such as window fractoluminescence, that can contaminate a pyrometry signal. Consequently, comparisons are needed between pyrometry and some other dynamic temperature diagnostic, such as neutron resonance spectroscopy (Yuan 2005, Swift 2008) or Raman spectroscopy.

Raman spectroscopy has been used as a bulk temperature diagnostic in shocked materials (Wood 1994; Pangilinan 1997a, 1997b), as it uses the temperature dependence of the intensity ratios of anti-Stokes to Stokes Raman emission line pairs for various vibration modes. The intensity ratio (Long 1977) is given in Equation 1 as a function of the temperature, T ,

$$\frac{I_{AS}(f_0)}{I_S(f_0)} = \frac{f_0 + \Delta f^4}{f_0 - \Delta f^4} \exp\left(\frac{-h\Delta f}{kT}\right), \quad (1)$$

where I_{AS} and I_S are the anti-Stokes- and Stokes-shifted line intensities, f_0 and Δf are the probe laser and Raman-shift frequencies, and h and k are the Planck and Boltzmann constants. For low temperatures, the anti-Stokes lines can be relatively weak while the Stokes lines may not change much. Ideally, one value of T should fit all the Raman spectral lines. Therefore, if possible, it is advantageous to use a Raman spectrum with several lines. Confidence in both diagnostics, pyrometry and Raman spectroscopy, would be improved by showing that they agree for some material.

Raman spectroscopy has some advantages over pyrometry. Emissivity need not be measured, and background light from the window or elsewhere should have a smaller effect on the Raman emission than it does on a pyrometry detector where it adds linearly to the radiance from the material of interest. However, because it is not useful for metals, the Raman temperature diagnostic is less developed than pyrometry, and further work is necessary to optimize the Raman technique for shock wave experiments.

The intense laser pulses we use to compensate for small anti-Stokes Raman cross sections can cause light-scattering problems and perhaps heating or even decomposition of components. Raman spectroscopy must use samples that are transparent in the region around the pump laser frequency, and transparent materials typically have very low emissivities. If a pyrometry measurement, which requires significant emissivity, is to be compared to Raman spectroscopy in the same material, then some care must be taken in finding a material that is both Raman active and also emissive in some other waveband region where pyrometry can work. Furthermore, because pyrometry of a metal measures its surface temperature, we must also make a comparison of the surface and bulk temperatures to substantiate the accuracy of the pyrometry corrections that we must apply to derive bulk temperatures for metals. Our goals in this study were to compare Raman and pyrometric temperature measurements on a given shocked sample to increase confidence in pyrometry and to make measurements to help determine the corrections we must make to learn the bulk material temperature.

PROJECT

We selected toluene (Sigma-Aldrich, Burlington, Massachusetts, 99.9% purity) as the experimental test material. It is visibly transparent; Raman active, with at least some Raman lines relatively free from other interferences, such as Raman emission from the window material; not fluorescent when illuminated at 532 nm; readily available; not excessively toxic; and it has strong mid-wave IR (MWIR) absorption (i.e., high emissivity) for simultaneous pyrometry measurements. Figure 1 is a schematic of the experiment. A sapphire-tipped projectile was accelerated to approximately 400 m/s in a single-stage light gas gun. The projectile impacted a thin sapphire window sandwiching a 0.5 mm thick toluene sample between another thick sapphire window and imparted a shock of around 2 GPa pressure in the liquid. The shock reverberated between the sapphire windows, each reflection increasing the toluene pressure until it equilibrated with the sapphire windows near 9 GPa. The toluene sample was limited in thickness because the pressure “ringup” was required to be nearly complete before edge release waves from the circumference of the sapphire could interfere with the measurements at the center. Also, we kept the projectile velocity low enough to avoid the sapphire becoming opaque when its elastic limit was exceeded at ~15 GPa (Barker 1970).

The two main project goals this year were to gain more dynamic data and to reduce the uncertainty in the Raman and radiance temperature measurements. First, we increased the laser energy on the target from 35 to 120 mJ per pulse in the Raman measurement. Although still-higher energy could be used, 120 mJ was chosen because sample damage occurred after multiple pulses at 200 mJ. Also, we used new laser cavity optics to eliminate laser beam hot spots and increase beam uniformity. A new fiber bundle was acquired with tighter packing for more efficient light collection, and data analysis methods were improved. For the pyrometry measurement, we replaced a long pass filter with a bandpass filter centered on MWIR emission of toluene and temporarily mounted a CCD camera in the gas gun barrel for precise pyrometer alignment. Also, we evaporated a thin layer of chromium onto part of the rear (16 mm thick) sapphire window to improve photonic Doppler velocimetry (PDV) reflection from the target surface. In previous dynamic experiments, reflections from multiple test cell window surfaces resulted in a confusing PDV return. Finally, we added a barrel extension to the gas

gun to allow faster bullet speeds (for higher stress/temperature) without reducing the pre-trigger delay for laser triggering. These changes resulted in much-improved data quality and accuracy.

The test cell configuration is shown in Figure 2. We used a Big Sky model CFR400 pulsed laser (532 nm wavelength, 120 mJ per pulse, 12 ns pulse length), focused to a spot about 2 mm in diameter at the toluene sample, to excite Raman Stokes and anti-Stokes emissions from the toluene. The laser was fired near the time the sample reached its peak pressure. The laser beam was reflected off a mirror and into the cell at normal incidence and in the direction opposite to the impactor motion. We designed the sabot behind the impactor to be hollow and blackened inside and to have an opening behind the sapphire impactor to allow the excitation laser beam to pass into the interior of the sabot to be absorbed and thus reduce light scattering. The illuminated area in the toluene was imaged onto a 300 mm long by 1.5 mm core optical fiber. The collection optics, roughly 20° off normal, consisted of two small lenses mounted in a 13 mm diameter tube

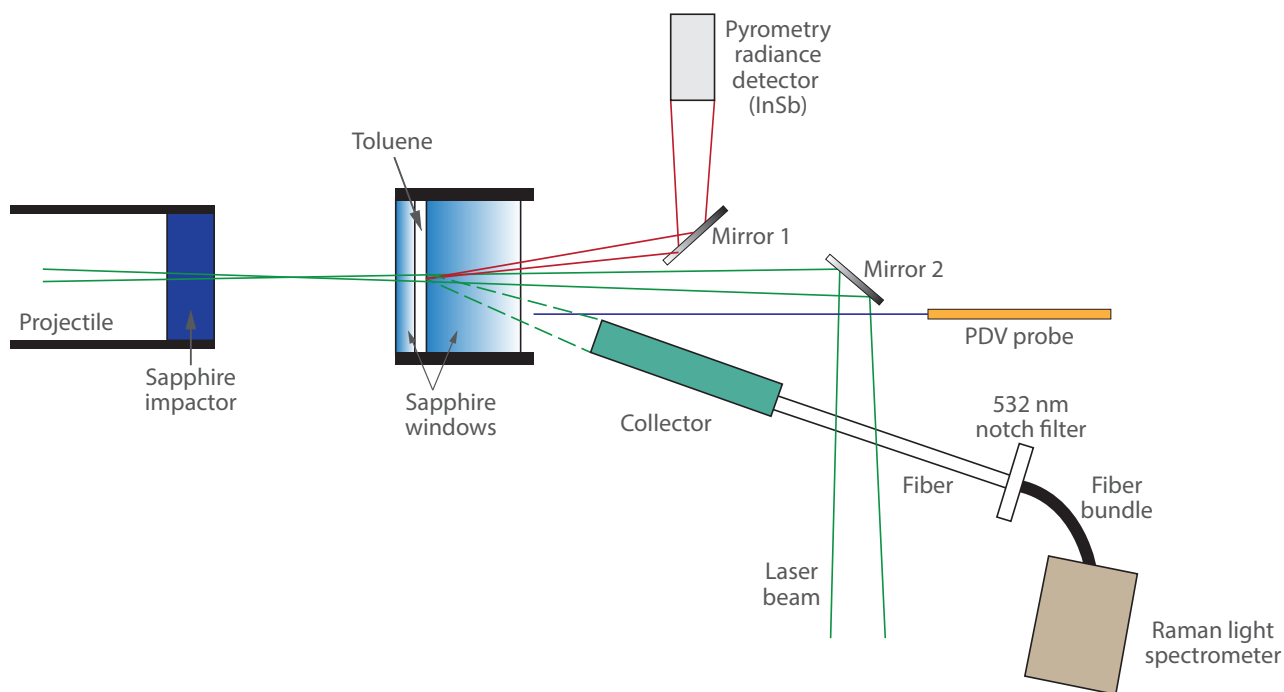


Figure 1. Schematic of the experiment to measure Raman spectroscopy and radiance simultaneously in a thin toluene sample. The impactor is launched by a gas or powder gun. The laser beam, slightly converging, provides an excitation diameter of ~2 mm in the toluene. The sapphire windows contain the toluene and drive up the pressure from the impactor. Mirror 1, which is gold, delivers IR pyrometry light, and Mirror 2 is for the Raman laser. The collector images Raman-scattered light into the 1.5 mm core optical fiber, while the fiber-optic bundle carries light to the Raman spectrometer. The 532 nm notch filter removes reflected and scattered laser light.

that slipped into the mount shown in Figure 2. The lenses collected light from the toluene and filled the full 0.22 numerical aperture of the optical fiber. After passing through a filter assembly (fiber collimator to 532 notch filter to reversed fiber collimator), the light entered a fiber-optic bundle that formed a line on its other end. The fiber bundle output was coupled to the entrance of a Princeton Instruments Isoplan 160 Spectrometer paired with an intensified CCD detector used to provide both gain and gating around the 12 ns laser pulse to reduce background light. This detection system recorded wavelengths from 490 to 580 nm with a spectral resolution of ~ 0.6 nm. A fiber-optic interrupt beam across the projectile path and a delay generator triggered the laser and detector gate at the desired time.

For pyrometry, a gold mirror mounted below the laser optical path collected light for an indium antimonide (InSb) thermal radiance detector (Teledyne Judson model J10D-M204-R250U-60). A small spot near the center of the toluene sample is imaged through a sapphire window in the gas gun test chamber wall onto the detector via a pair of 50 mm diameter off-axis parabolic mirrors. In the collimated space between the mirrors, we placed an optical bandpass filter (3160–3610 nm) centered on the toluene MWIR band. Dynamic emissivity was not measured. Back illumination of the pyrometer assembly, together with a small CCD camera temporarily threaded down the gas gun barrel to the target, allowed for precise

positioning of the InSb view area. Interface velocity was measured with PDV; the PDV probe held the optical fiber that delivered the incident laser light and collected the Doppler-shifted return. Because of the multiple surfaces, we coated a portion of the inner surface of the 16 mm window with 100 nm of chromium to provide an unambiguous PDV return signal from the surface of interest. The velocity measurements were converted to sample pressure using the shock Hugoniot of Z-cut sapphire.

Raman Measurements

Figure 3a shows the scattered Raman spectrum under shocked (red) and ambient (black) conditions using data obtained in FY 2017 (Capelle 2018). Figure 3b, which is background-subtracted shocked data from a May 2018 experiment, shows the increase in signal-to-noise ratio of the data after we improved the experiment this year. The Raman lines shift and widen slightly during the compression. Also, the anti-Stokes lines increase relative to the Stokes lines, as would be expected at the higher temperature. The background increases significantly, which may imply increased optical scattering during the dynamic experiment. Finally, the sapphire Raman signal increases under shock compression, which was useful in estimating the sapphire temperature.

To determine the temperature of the material, we used Equation 1 and compared the ratios of the

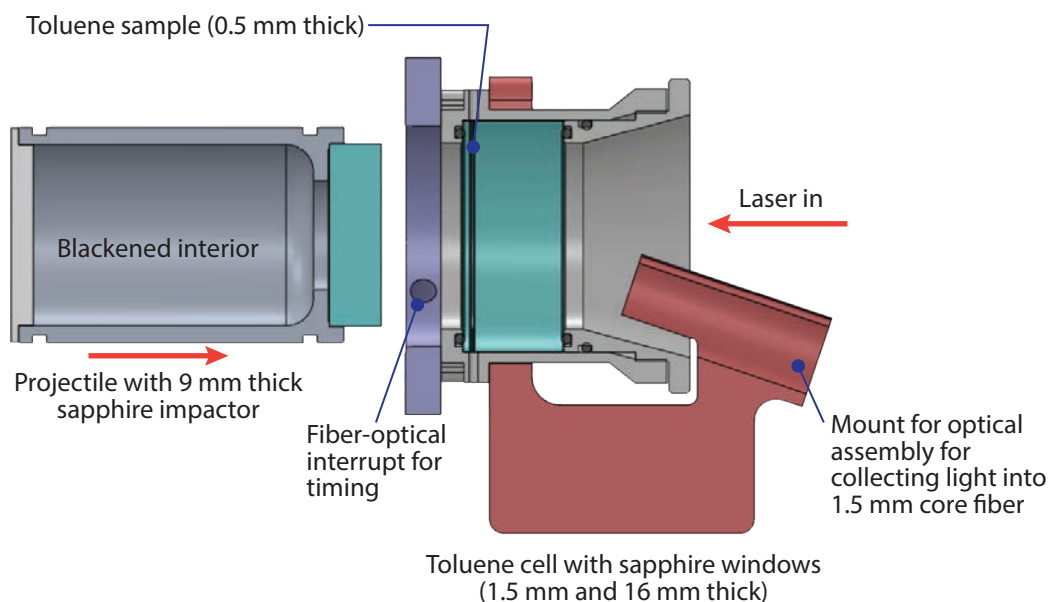


Figure 2. Rendering of the projectile, toluene target region, and Raman experiment diagnostics. The impactor is a 35 mm diameter sapphire cylinder from 9 to 16 mm thick, and the two sapphire windows are 1.5 and 16 mm thick.

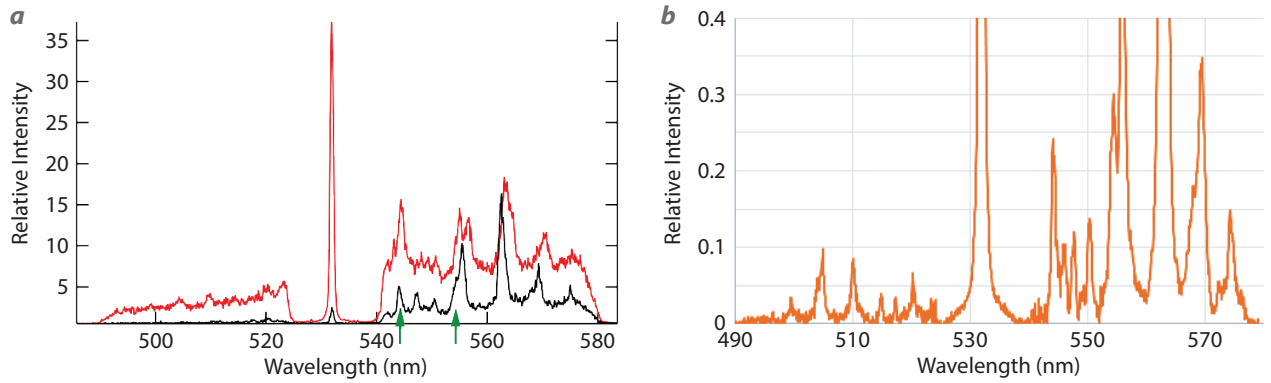


Figure 3. (a) Data from May 2017 show a Raman spectrum from a shocked 0.5 mm thick toluene sample (red). The excitation laser signal line is at 532 nm, with Stokes lines to the right, and anti-Stokes lines to the left. Signals are cut off near 490 and 580 nm at the edge of the camera. The black line is static (unshocked) data at room temperature. The green arrows indicate the two major sapphire Raman lines (of roughly equal intensities) in this region of the spectrum. (b) Background-corrected signal from a May 16, 2018, shock experiment shows improvement in the signal-to-noise ratio.

intensities of the anti-Stokes and Stokes lines in the Raman spectrum. To find the spectral lines, we performed nonlinear least squares fitting (NLSF) using OriginLab software, fitting the known Raman line pairs to the measured spectrum. Before attempting a fit, the background was subtracted from the spectrum. We assumed the background varies slowly, and then we iterated it until the baseline of the fit matched the baseline of the data.

The spectrum of a Raman line was assumed to take the form of a Lorentzian function,

$$I(f) = \frac{A}{2\pi} \cdot \frac{w}{(f - f_1)^2 + (w/2)^2}, \quad (2)$$

for some amplitude A , center line frequency f_1 , and width w , characterizing the line. It is assumed that the line frequencies are known and that all the lines have the same width, which is determined mainly by the resolution of the spectrometer. In the NLSF, the anti-Stokes line amplitudes are scaled to the Stokes amplitudes by the use of Equation 1. We call the unscaled Stokes line amplitudes A_n , the line frequencies f_n , and the Raman shift frequencies $\Delta f_n = |f_n - f_0|$. For each measured spectral channel i with frequency f_i , the value of the fit function is shown in Equation 3, where the sum n is over the number of line pairs N , in the spectrum. The first term

in the large brackets contains the anti-Stokes lines and the second term the Stokes lines. The Rayleigh scattered line at $\Delta f_0 = 0$ is omitted from the equation for simplicity but was included in practice. An important added constraint to the fitting algorithm is that the anti-Stokes-to-Stokes ratios of all lines in the Raman spectrum must yield the same temperature (for lines emanating from the same material). Initial fits were done such that the NLSF would determine all amplitudes independently, and it was apparent that constraining the lines to a shared temperature greatly reduces the uncertainty in the results, especially when the signal-to-noise ratio is low and background subtraction is difficult. Consequently, we let the NLSF find the values of A_n for each of several values of T .

Figure 4 shows this scaling technique applied to data from the May 2018 experiment for various trial temperatures fit to two Raman lines and the average residual error for each temperature, leading to the residual-minimized measured temperature of the toluene of 530 (10) K. The sapphire Raman lines give a temperature of 328 (30) K for the sapphire window material. Figure 5 is a comparison of data and the best fit, using these temperatures. At the toluene interfaces, the stress in the sapphire was the same as the toluene pressure, but away from the toluene, the stress was less. We expect from our many hydrodynamic simulations of shock experiments with windows that

$$F_i(f_i) = \frac{1}{2\pi} \sum_{n=1}^N \underbrace{A_n \left(\frac{f_0 + \Delta f_n}{f_0 - \Delta f_n} \right)^4 \exp\left(\frac{-h\Delta f_n}{kT}\right) \left(\frac{w}{(f_i - [f_0 + \Delta f_n])^2 + (w/2)^2} \right)}_{\text{Anti-Stokes Peaks}} + \underbrace{A_n \left(\frac{w}{(f_i - [f_0 - \Delta f_n])^2 + (w/2)^2} \right)}_{\text{Stokes Peaks}} \quad (3)$$

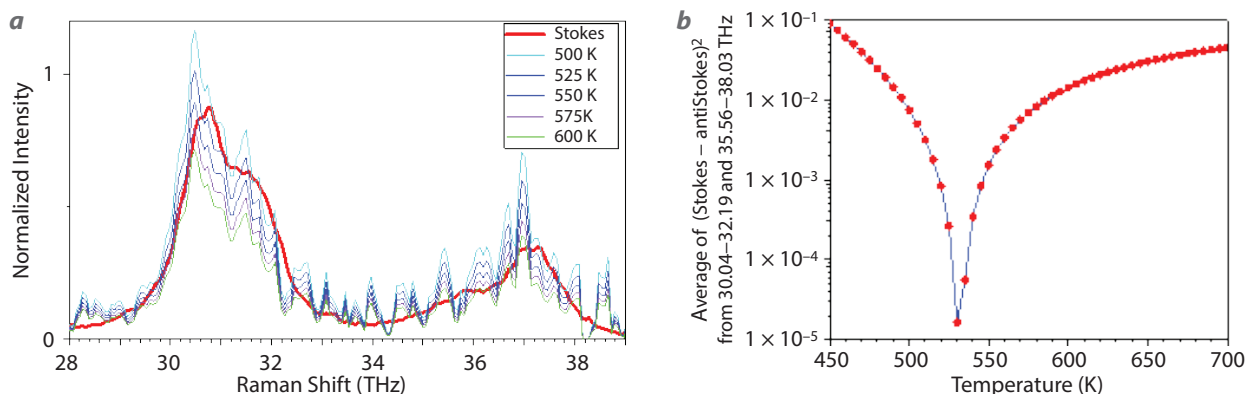


Figure 4. (a) Anti-Stokes lines scaled by various temperatures and overlaid on corresponding Stokes lines. (b) Average of residual squared vs. temperature for the various temperature fits.

they should remain relatively cool, so this result appears valid.

A high-velocity (600 m/s) experiment was unsuccessful due to triggering and impact flash problems; it is possible that toluene decomposition at the high pressure also contributed to a bright flash that obscured the Raman data.

Pyrometry Measurements

We fielded a pyrometer similar to that of La Lone (2013). We calibrated the detector using a black body source having the same geometry as that of the dynamic measurements, with the black body replacing the toluene and impactor. When combined with the newly added bandpass filter, the pyrometer viewed an optical range from 3.16 to 3.61 μm . We assume emissivity (ϵ) = α , where α is the absorptivity for our sample. We feel certain that toluene is strongly emissive in its stretch mode vibration bands from 3.2 to 3.6 μm and that in this region $\epsilon \approx 1$. Most of the toluene emission viewed by the pyrometer comes from the region very close to the window, as is confirmed by this year's calibrated temperature-time profiles, so it is not a volume measurement, but neither is it purely a surface measurement. Small signal levels, a background impact flash, and a ≈ 400 K detector noise floor had an impact on the accuracy of the pyrometry measurements; nevertheless, with the new bandpass filter, the uncertainty was reduced, and the pyrometry-measured value of 490 K compares reasonably closely to the 530 K Raman-derived temperature. Estimated uncertainty of the pyrometry measurement is $+5/-10$ K due to electrical noise, with an additional uncertainty of at least ± 10 K due to experimental issues (the changing background from impact flash, differences

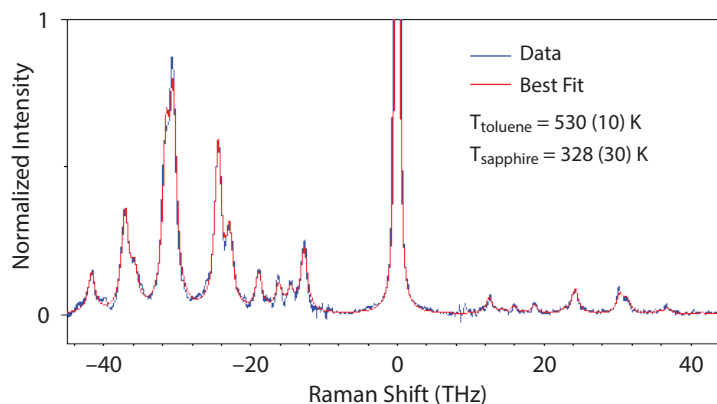


Figure 5. Comparison of data and best fit for experiment shown in Figure 4

in alignment when transferring the detector and optical system detector from the black body calibration configuration to the actual experiment, etc.). Because the pyrometry temperature measurement is from the region of the toluene very close to the cooler (measured by Raman to be 328 K) window, it could be slightly lower than the volume temperature, but due to the small number of experiments and the uncertainty in the pyrometry measurement, we cannot yet make this claim. For future experiments, losing some pyrometer frequency response by increasing detector size and capacitance to gain stronger signal and improve measurement accuracy is worth considering.

CONCLUSION

We designed and fielded experiments at the Special Technologies Laboratory gas gun to demonstrate a Raman temperature measurement of a shock-compressed state; further, we measured simultaneously, by Raman spectroscopy and by pyrometry, the temperature in a thin toluene sample

shocked to near 9 GPa by a reverberating shock wave. A sapphire impactor caused a 0.5 mm thick toluene sample to undergo multiple shock compressions between sapphire windows, raising its pressure stepwise. From the measured Raman spectrum we fit the Stokes and anti-Stokes Raman scattering line pairs with independent amplitudes for every pair and the amplitude ratio for each pair fixed by the assumed temperature. Then we repeated the fit with different temperature values to find the temperature with the best spectrum agreement. Using this method, we were able to reduce the Raman-measured temperature uncertainty to ± 10 K.

We used a high-speed MWIR detector system to make simultaneous toluene pyrometry and Raman measurements. The values obtained, both last year and this, were in reasonable agreement for the two methods. While this agreement is preliminary because of the limited number of experiments, the agreement in temperatures is encouraging. Future efforts—more experiments and improved accuracy of the measurements—will continue to confirm these results. Note that both the Raman and pyrometry measurements represent temperatures in the compressed material (i.e., in the bulk volume of the liquid), though pyrometry measured only a small volume adjacent to the window, whereas Raman measured the entire volume. Because most shock compression experiments of interest to us involve opaque materials such as tin, whereas pyrometry measures only the surface temperature, modifications to the experimental design could provide a way to measure the volume and surface temperatures for comparison purposes.

ACKNOWLEDGMENTS

We would like to thank Mike Grover, Eric Larson, and Ben Valencia for their contributions to this work.

REFERENCES

Barker, L. M., R. E. Hollenbach, “Shock-wave studies of PMMA, fused silica, and sapphire,” *J. Appl. Phys.* **41** (1970) 4208.

Blanco, E., J. M. Mexmain, P. Chapron, “Temperature measurements of shock heated materials using multispectral pyrometry: Application to bismuth,” *Shock Waves* **9**, 3 (1999) 209–214.

Capelle, G., B. La Lone, J. Mance, “Simultaneous Raman and pyrometric temperature measurements of a shock wave-compressed material,” in *Site-Directed Research and Development*, FY 2017, National Security Technologies, LLC, and Mission Support and Test Services, LLC, Las Vegas, Nevada, 2018, 19–25.

La Lone, B. M., G. D. Stevens, W. D. Turley, D. B. Holtkamp, A. J. Iverson, R. S. Hixson, L. R. Veaser, “Release path temperatures of shock-compressed tin from dynamic reflectance and radiance measurements,” *J. Appl. Phys.* **114**, 6 (2013) 063506.

Long, D. A., *Raman Spectroscopy*, McGraw Hill, London, 1977, 84.

Pangilinan, G. I., Y. M. Gupta, “Temperature determination in shocked condensed materials using Raman scattering,” *Appl. Phys. Lett.* **70** (1997a) 967.

Pangilinan, G. I., Y. Gupta, “Use of time-resolved Raman scattering to determine temperatures in shocked carbon tetrachloride,” *J. Appl. Phys.* **81** (1997b) 6662.

Partouche-Sebban, D., D. B. Holtkamp, J. L. Pélissier, J. Taboury, A. Rouyer, “An investigation of shock induced temperature rise and melting of bismuth using high-speed optical pyrometry,” *Shock Waves* **11**, 5 (2002) 385–392.

Partouche-Sebban, D., J. L. Pélissier, “Emissivity and temperature measurements under shock loading, along the melting curve of bismuth,” *Shock Waves* **13**, 1 (2003) 69–81.

Partouche-Sebban, D., et al., “Measurement of the shock-heated melt curve of lead using pyrometry and reflectometry,” *J. Appl. Phys.* **97**, 4 (2005) 043521.

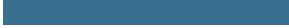
Swift, D. C., A. Seifter, D. B. Holtkamp, V. W. Yuan, D. Bowman, D. A. Clark, “Explanation of anomalous shock temperatures in shock-loaded Mo samples measured using neutron resonance spectroscopy,” *Phys. Rev. B* **77**, 9 (2008) 092102.

Wood, S. M., Y. M. Gupta, G. I. Pangilinan, “Time-resolved Raman measurements in shock z-cut, α -quartz subjected to tension,” *AIP Conf. Proc.* **309**, 1 (1994) 1571–1574.

Yuan, V. W., J. D. Bowman, D. J. Funk, G. L. Morgan, R. L. Rabie, C. E. Ragan, J. P. Quintana, H. L. Stacy, “Shock temperature measurement using neutron resonance spectroscopy,” *Phys. Rev. Lett.* **94**, 12 (2005) 125504.

Zel'dovich, Ya. B., Yu. P. Raizer, *Physics of Shock Waves and High-Temperature Hydrodynamic Phenomena*, Academic Press, New York, 1966.

This page left blank intentionally



Multi-Axial Time-Resolved Spectroscopic Technique for Magnetic Field, Electron Density, and Temperature Measurements in Dense Magnetized Plasmas

LO-001-16 ■ Year 3 of 3

**Eric C. Dutra,^{1,a} Jeffrey A. Koch,^a Radu Presura,^b Piotr Wiemior,^c
Timothy Darling,^c Roberto Mancini,^c and Aaron Covington^c**

¹dutraec@nv.doe.gov, (925) 960-2584

^aLivermore Operations

^bNew Mexico Operations—Sandia

^cUniversity of Nevada, Reno



We are developing a multiaxial time-resolved spectroscopic technique for simultaneous measurement of magnetic field strengths, electron densities, and temperatures of dense magnetized plasmas for Z-pinch and dense plasma focus applications. These plasma properties are determined by analyzing experimental emission spectra with a code that includes Zeeman splitting as well as collisional and Doppler broadening. With increasing electron densities and temperatures, collisional and Doppler broadening dominate the measured line profiles, making it difficult to separate the Zeeman component. There are two approaches we can use to make Zeeman splitting measurements under such conditions: the first uses a polarization technique to separate out the circularly and linearly polarized components, where the circular component is more affected by Zeeman splitting; the second is the technique used in this work, and it is based on the different widths of Zeeman-split fine-structure components. In the second year of the project, we developed the Zeeman-splitting fine-structure code, modeled magnetohydrodynamic Z-pinches, and performed proof-of-principle laser ablation Z-pinch experiments (LAZE). This year, we refined the LAZE technique, improved spectral simulations, collected data at higher plasma temperatures, and measured electron number density and electron temperature. Aluminum oxide plasma was generated using the Ti:sapphire/Nd:glass laser and Z-pinch pulse-power generator at the Nevada Terawatt Facility at the University of Nevada, Reno. To determine the electron temperature, we used the Boltzmann plot method for the transitions $(\text{Al III } 4d \ ^2D_{3/2} \rightarrow$

$4p\ ^2P_{1/2}$) at 451.2564 nm, (Al III $4d\ ^2D_{5/2} \rightarrow 4p\ ^2P_{3/2}$) at 452.9194 nm, (Al III $4p\ ^2P_{3/2} \rightarrow 4s\ ^2S_{1/2}$) at 569.6603 nm, and (Al III $4p\ ^2P_{1/2} \rightarrow 4s\ ^2S_{1/2}$) at 572.2728 nm. Simultaneously, we used Mach-Zehnder laser interferometry to measure the electron number density. We compared simulated spectra from PrismSPECT to our measurements; electron temperature ranged from 1.4 to 2.2 eV, while the electron number density ranged from 2.3×10^{17} to 6.9×10^{17} cm⁻³ early in the pinched plasma formation.

BACKGROUND

Spectroscopic techniques in the visible wavelength range are often used in plasma experiments for measuring Zeeman splitting induced by the magnetic field, electron densities via collisional broadening, and temperatures from Doppler broadening. Pulsed-power research Z-pinch machines, such as the Z machine at Sandia National Laboratories, the dense plasma focus (DPF) machine at the NNSS, and Zebra at the University of Nevada, Reno (UNR), produce dense magnetized plasmas using a Marx bank to drive current through a wire or gas. These machines can have an electric current rise time on the order of hundreds of nanoseconds, with target performance that is magnetically driven and dependent on the current that travels along the outer sheath of the plasma column formation. This current induces a magnetic field that compresses the plasma, thereby increasing plasma electron density and temperature, which can be measured noninvasively with spectroscopy. The characterization of magnetic fields, field symmetries, and electron densities and temperatures provides information about the current distribution and current loss across the anode–cathode gap. We can use these plasma parameters to validate modeling codes used in the design of new pulsed-power Z-pinch machines.

In the first year of this project, we collaborated with UNR to develop a Zeeman-splitting spectroscopic model that allowed us to identify relative broadening or splitting induced by the magnetic field (Dutra 2016); we also used this model to post-process our data. This model shaped our choices of spectroscopic equipment for experiments. We purchased, assembled, and characterized a streaked spectroscopy system and used it to record initial time-resolved emission spectra from dense magnetized plasma. We used these measurements in conjunction with spectral emission modeling to develop an analysis procedure for estimating magnetic field strengths, electron densities, and electron temperatures (Dutra 2017).

In FY 2017 we developed an analysis code for simulating and measuring emission lines. We found that when plasma temperatures and densities are high, collisional and Doppler broadenings dominate line profiles, obfuscating Zeeman component measurements (Dutra 2018). In general, two techniques can measure the collisional and Doppler and Zeeman components. The first method measures both the linearly polarized components of the spectra, which are dominated by collisional and Doppler broadening, and the circularly polarized components, which are affected by Zeeman broadening (Stambulchik 2007, Tessarin 2011, Blesener 2012). Measurement of the circularly polarized emission spectra allows a deconvolution of the collisional and Doppler broadening from the Zeeman broadening, enabling a simultaneous measurement of the magnetic fields, electron densities, and electron temperatures (Rochau 2010, Gomez 2014).

The second approach investigates the fine-structure components of a given multiplet, which are split differently due to the magnetic field. The energy shift due to the L and S coupling and the magnetic field is given by the Hamiltonian (H)

$$H = AL \cdot S = (L + 2\omega)B, \quad (1)$$

where L is the orbital angular momentum, S is the spin-orbital momentum, and A is a constant and multiplies the spin-orbit coupling. The second term is the magnetic field operator; B is the magnetic field and ω is the magnetic moment.

We can then use the Hamiltonian to calculate the energy shifts using either of the following two methods. These techniques were discussed in the FY 2016 SDRD final report (Dutra 2017). The first method uses a perturbative expansion with which, depending on the number of terms in the expansion, either a weak or a strong field case can be approximated. Alternatively, one can solve the Hamiltonian exactly by compiling the Hamiltonian

matrix, diagonalizing the matrix, and calculating the energy eigenvalue of the diagonalized matrix. Using the selection rules, one can then map the emission transitions onto a calculated line profile given by the collisional- and Doppler-broadened terms. Because the doublet components have similar collisional and Doppler broadening in the same plasma, the difference in the line broadening of the two doublets depends on the magnetic field, along with the L and S components of the Landé g factor (Stambulchik 2007, Tessarin 2011, Blesener 2012).

This year we studied visible spectroscopic techniques used to determine electron number densities (N_e) and electron temperatures (T_e). The Boltzmann plot method is frequently used for determining T_e in plasma. If local thermal equilibrium (LTE) is present, we can use this method to compare the relative intensity of a thermometric species to calculate the T_e of a plasma. If LTE conditions are met, the excitation temperature, which governs the distribution of energy level excitation through the Boltzmann equation, and the ionization temperature (T_i), which governs the ionization equilibrium through the Saha equation, should both be equal to T_e , which characterizes the Maxwellian distribution of electron velocities (Naeem 2013). We can use two tests to determine whether we can assume an LTE. The first method is to verify the McWhirter criterion (Griem 1997, Hussain 2016). The second method is to model the plasma emission spectrum using PrismSPECT under both non-LTE and LTE conditions and compare results to the data we observed this year in aluminum oxide (Al_2O_3) laser ablation Z-pinch experiments (LAZE). If LTE conditions are met, we can calculate plasma temperature using two or more atomic lines in the form of integrated line intensity ratios (Harilal 1998, Shaikh 2006, Musadiq 2013).

An LTE condition requires sufficiently high collision frequencies between the ions and electrons. LTE requires that the collisional transition rates between the energy levels of interest, as described by the Boltzmann equation, be significantly larger than the competing radiative rates. A semiclassical argument proposed by McWhirter states that the minimum N_e required for LTE conditions is given by

$$N_e \geq 1.6 \times 10^{12} T_e^{-\frac{1}{2}} (\Delta E)^3, \quad (2)$$

where T_e is the electron temperature in K, ΔE is the energy difference between the states in eV, and N_e is the electron number density in cm^{-3} (Shaikh 2006).

In parallel with new plasma spectroscopic diagnostic development, a new technique for creating Z-pinch plasma is also being explored at the Nevada Terawatt Facility (NTF) at UNR, where researchers are using a Ti:sapphire/Nd:glass laser (Leopard) to ablate a material into the anode–cathode gap region of the Z-pinch pulsed-power generator (Zebra). Effectively, Leopard creates a laser-ablated plume of material as a load or current path for Zebra. The LAZE technique has certain advantages over typical gas or wire array Z-pinch experiments. LAZE provides excellent temporal control compared with gas puff techniques while minimizing phase coexistence of target materials because the plume is pre-ionized and atomized. LAZE also limits the spatial extent of the ablation plume, which leads to very compact and reproducible pinches. These are all important pinch characteristics for obtaining high-quality spectroscopic data. In our experiments, we used the LAZE technique on Al_2O_3 targets while studying the spectroscopic signature of the Z-pinch plasma as it evolves with increasing current. Our approach is to use optical emission spectroscopy to characterize the pinch of the LAZE plasma to determine N_e and T_e .

PROJECT

Experimental Setup

We conducted experiments at the NTF using the 1.5 TW Zebra pulsed-power generator. Zebra's Marx bank stores 150 kJ of energy and, following pulse shaping and compression, delivers ~ 1.0 MA of current to a plasma target with a rise time of ~ 100 ns. Initially, target material was laser-ablated from the surface of a solid target mounted on the cathode using the NTF Leopard laser (1057 nm, 100 μm spot size, 20 J at 0.8 ns Ti:sapphire/Nd:glass laser system). The ablation plume expanded across the anode–cathode gap in ~ 2 μs . After the plume spanned the vacuum gap, it served as the load for the current from the Zebra pulsed-power generator to travel through. As current passed through the ablation plume, it rapidly created a plasma cloud within the anode–cathode gap. As the current rose, the $\mathbf{J} \times \mathbf{B}$ force increased, causing the ionized material within the anode–cathode gap to implode and pinch along the vertical z -axis.

We used an optical spectroscopy probe to collect visible light emitted from the plasma. As seen in Figure 1, the probe was aligned in the plane of the magnetic field direction, 4 mm above the cathode, and

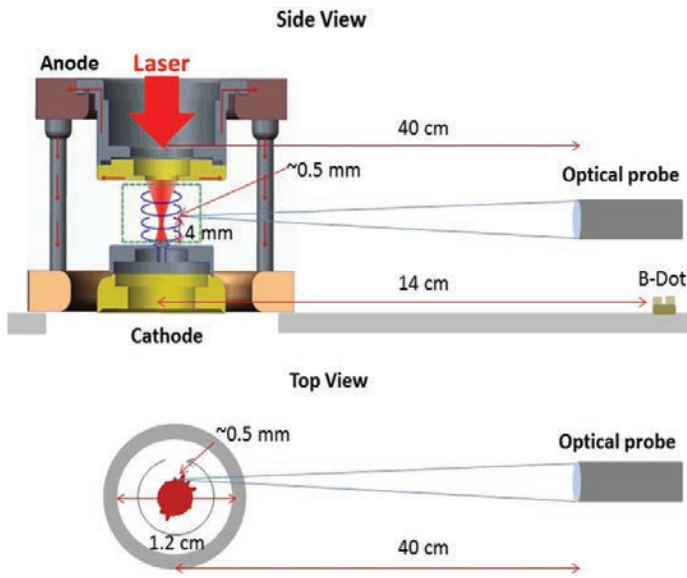


Figure 1. Diagram of the Zebra LAZE load, located at the center of the chamber. The laser enters from the top of anode, the B-dot probe is located 14 cm from the center chamber, and the optical probe is located 40 cm from the center chamber. The field of view of the optical probe is ~ 0.5 mm, shown by both the side and top views. The green, dashed-line rectangle represents the Mach-Zehnder field of view. Not to scale.

radially offset by 1.5 mm from the center axis, with a spot size < 0.5 mm. The optical probe is a lens relay system connected to an off-axis parabolic reflective collimator (Thorlabs RC12FC-P01) and coupled to a fiber-optic cable. The output of the fiber-optic cable is fed to a Princeton Instruments Acton SpectraPro SP-2750 spectrometer coupled to an NNSS medium-speed streak camera (model L-CA-24) that records data on a Spectral Instruments SI-1000 CCD camera. The sweep window of the streak camera was configured for a sweep duration of 480 ns. The slit width on the spectrometer was set by the 50 μm diameter core of the fiber. We set the spectrometer center wavelength to 480 nm, with an approximate spectral window of 235 nm. Data collection started 250 ns before the peak Zebra current. The data acquired by the streak spectrometer system were logged and stored on a PC through the CCD software for subsequent analysis. N_e was measured with a Mach-Zehnder interferometer, while T_e was measured using the Boltzmann method as described by Ohno (2006). We performed

simulations using PrismSPECT and compared them to the experimental spectra collected from the streak spectrometer system.

Results and Analysis

Multiple experiments were fielded and analyzed. Figure 2 depicts a typical time-resolved streaked spectrum from these experiments, where the y -axis is the temporal axis in nanoseconds and the x -axis is the wavelength in nanometers.

Figure 3 is a typical spectral lineout, taken at the 18 ns mark of the record length shown in Figure 2 and averaged over 2 ns. In all datasets, a series of lineouts were taken, ranging from 0 to 22 ns, and each averaged over 2 ns. The spectral lines are noted on Figure 3 and in Table 1. The transitions of interest are (Al III $4d^2D_{3/2} \rightarrow 4p^2P_{1/2}$) at 451.2564 nm, (Al III $4d^2D_{5/2} \rightarrow 4p^2P_{3/2}$) at 452.9194 nm, (Al III $4p^2P_{3/2} \rightarrow 4s^2S_{1/2}$) at 569.6603 nm, and (Al III $4p^2P_{1/2} \rightarrow 4s^2S_{1/2}$) at 572.22 nm. The low electron density and excited upper and lower levels led us to suspect that the emission lines are optically thin. To confirm this, we performed a series of PrismSPECT calculations; these calculations showed that the optical depths are < 0.2 for a representative 5 mm plasma dimension, indicating that the lines are all optically thin. Therefore, we ignore optical depth effects on line intensities and widths. The statistical weight, g_i , and the transition strength, $g_k A_{ki}$, are calculated from PrismSPECT tables as

$$g_i A_{ki} = 2J_i + 1, \quad (3)$$

where J_i is the total angular momentum, and

$$g_k A_{ki} = 6.6703 \times 10^{15} \times \frac{g_i f_{ik}}{\lambda^2}, \quad (4)$$

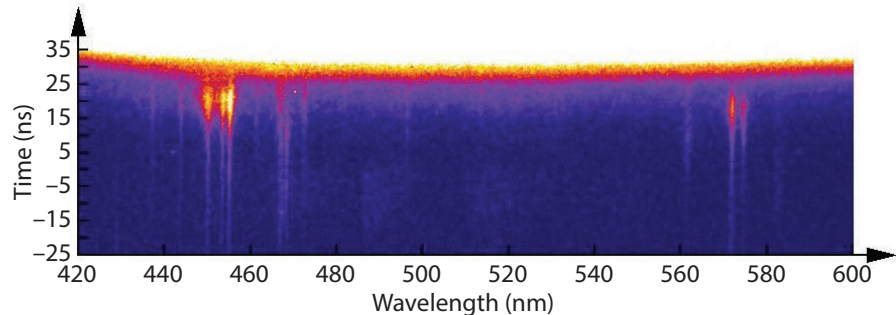


Figure 2. The streaked spectrum from Al_2O_3 LAZE. $t = 0$ is the start on the lineout taken shortly after start of current ramp.

Table 1. Aluminum III (Al III) transitions. Wavelengths (λ_{air} and λ_{vac}) and lower and upper energy levels (E_i and E_k) were found in the National Institute of Standards and Testing (NIST) atomic spectra database (NIST 2018). Oscillator strength (f_{ik}) was found in PrismSPECT tables. Statistical weights (g_i and g_k) and transition strength ($g_k A_{ki}$) were calculated from PrismSPECT tables.

#	λ_{air} (nm)	λ_{vac} (nm)	TRANSITION ($k \geq i$)	g_i	g_k	f_{ik}	$g_k A_{ki}$ (s^{-1})	E_i (eV)	E_k (eV)
1	447.9892	448.1142	5g $^2G_{7/2} \rightarrow 4f \ ^2F_{5/2}$	6	8	1.350	2.69×10^9	20.781332	23.548131
2	447.9968	448.1228	5g $^2G_{9/2} \rightarrow 4f \ ^2F_{7/2}$	8	10	1.310	3.48×10^9	20.781409	23.548155
3	451.2564	451.3831	4d $^2D_{3/2} \rightarrow 4p \ ^2P_{1/2}$	2	4	1.310	8.58×10^8	17.808269	20.555031
4	452.8942	453.0215	4d $^2D_{3/2} \rightarrow 4p \ ^2P_{3/2}$	4	4	0.131	1.70×10^8	17.818203	20.555031
5	452.9194	453.0459	4d $^2D_{5/2} \rightarrow 4p \ ^2P_{3/2}$	4	6	1.170	1.52×10^9	17.818203	20.554884
6	569.6603	569.8183	4p $^2P_{3/2} \rightarrow 4s \ ^2S_{1/2}$	2	4	0.859	3.53×10^8	15.642348	17.818203
7	572.2728	572.4318	4p $^2P_{1/2} \rightarrow 4s \ ^2S_{1/2}$	2	2	0.427	1.74×10^8	15.642348	17.808269

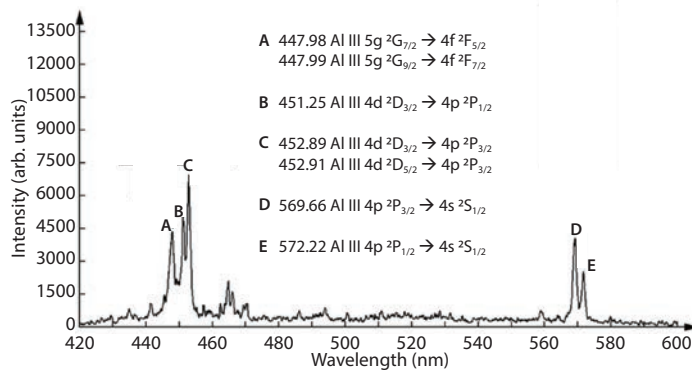


Figure 3. Emission spectrum. Lineout taken from streaked spectrum, Figure 2, at 18 ns from Al_2O_3 LAZE.

where g_i is the statistical weight of the lower energy level, A_{ki} is the transition probability, f_{ik} is the oscillator strength, and λ is the wavelength of the transition from the upper level state k to the lower level state i . Table 1 includes the corresponding transition, wavelength, transition strength, oscillator strength, energy level, and statistical weight needed to calculate the electron temperature.

Electron Temperature

The Boltzmann plot method, widely used to analyze spectroscopic data, uses the relative intensity of two or more spectral lines that have relatively large energy differences to calculate the electron temperature (T_e) of the plasma. However, effective application of the Boltzmann plot method for the measurement of

T_e requires that the excitation level be reached under an LTE condition (Griem 1963, 1997). Using Equation 2, we can show that the required electron number density (N_e) to fulfill the McWhirter criterion needs to be greater than $\sim 5 \times 10^{15} \text{ cm}^{-3}$. Using both interferometric techniques and spectral simulations, N_e was shown to be $\sim 3 \times 10^{17} \text{ cm}^{-3}$. Therefore, the McWhirter criterion is satisfied, and we may assume an LTE plasma.

The derivation of the Boltzmann plot formulae used in the data analysis follows. Let us consider the two energy levels of a spontaneous emission spectral line, E_i and E_j , with atomic densities N_i and N_j for the lower and upper energy levels, respectively. Under LTE conditions, we can use the Boltzmann distribution to relate N_i and N_j as

$$\frac{N_j}{N_i} = \frac{g_j}{g_i} e^{\left(\frac{-E_j - E_i}{kT_e}\right)}, \quad (5)$$

where g_i , g_j are the statistical weights of the respective states, k is the Boltzmann constant, and T_e is the electron temperature. If we define the total population density as N , then the relationship of the total population distribution over the atomic state is given by

$$\frac{N_j}{N_i} = \frac{g_j}{Z(T)} e^{\left(\frac{-E_j}{kT_e}\right)}, \quad (6)$$

where $Z(T)$ is the partition function given by

$$Z(T) = \sum_m g_m e^{\left(\frac{E_m}{kT_e}\right)}, \quad (7)$$

where g_m is the degeneracy factor, or number of quantum states s that have the same energy level defined by E_m .

The intensity of this emission line from upper to lower state can be written as

$$I_{ji} = \frac{hc}{4\pi\lambda_{ji}} A_{ji} N_j, \quad (8)$$

where λ_{ji} is the wavelength of the emitted light, h is Planck's constant, c is the speed of light in vacuum, and A_{ji} is the transition probability. Inserting this result into Equation 6 gives us

$$\frac{I_{ji}\lambda_{ji}}{g_j A_{ji}} = \frac{hcN}{4\pi Z(T)} e^{\left(\frac{E_j}{kT_e}\right)}. \quad (9)$$

Taking the logarithm of both sides gives

$$\ln \frac{\lambda_{ji} I_{ji}}{g_j A_{ji}} = -\frac{E_j}{kT_e} + C, \quad (10)$$

where C is

$$\ln \left(\frac{\lambda_{ji} I_{ji}}{g_j A_{ji}} \right). \quad (11)$$

T_e can be calculated from the slope of the straight line (Ohno 2006).

The various spectroscopic factors such as statistical weight, transition probability, wavelength, and upper energy level are given in Table 1, and they can also be found in the online National Institute of Standards and Testing (NIST) atomic spectra database (NIST 2018). Using the Boltzmann plot method, we can calculate the plasma electron temperature from the observed transitions. Using the data above and the fully compiled transition list (NIST 2018) of these transitions, we can calculate the electron temperature of an LTE plasma based on the fact that the densities of the various excited

states are proportional to the statistical weight and the exponential of negative ratio of the excitation energy and the thermal energy kT_e (Naeem 2013). Inserting these quantities into Equation 10, then plotting the left side of Equation 10 versus E_j (upper energy level of the line emission) and fitting with a straight line, we can calculate the electron temperature, where the slope of the line is $-1/kT_e$.

Electron temperature was studied as a function of current and time. In our experiments, Zebra has a current rise time of approximately 100 ns, with target performance that is magnetically driven and dependent on the current that travels along the outer sheath of the plasma column. This current induces a magnetic field that compresses the plasma, increasing plasma electron number density and temperature. The calculated electron temperatures for four different experiments, shown in Figure 4, ranged from 1.4 to 2.2 eV and increased with time and current. The data shown are within the first 30 ns of the current rise.

PrismSPECT Simulations

We used PrismSPECT collisional-radiative spectral analysis code to simulate the Al_2O_3 emission spectra. The simulations used PrismSPECT's low-temperature model and were performed for both non-LTE and LTE models. A comparison between non-LTE and LTE was performed over a range of suitable experimental parameters for both electron number density and electron temperature. The spectra simulated for non-LTE and LTE were identical, which confirmed the initial assumption that the plasma was in LTE.

We then used the PrismSPECT low-temperature model to simulate spectra for Al_2O_3 LTE plasma and compared them to the experimental data. Figures 5a,

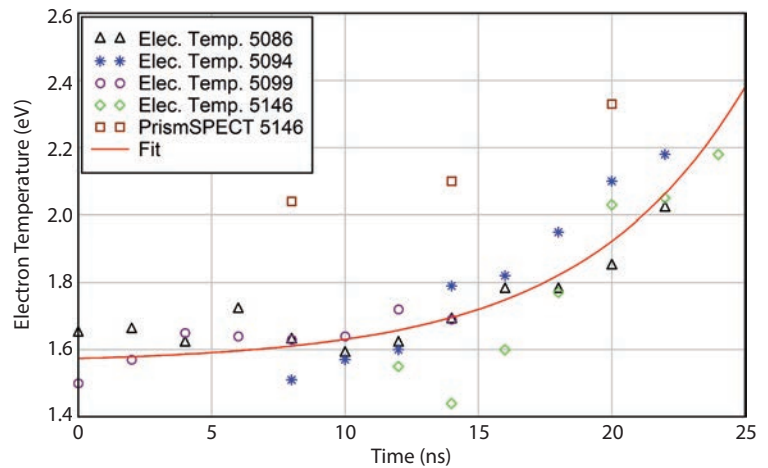


Figure 4. The calculated electron temperature using the Boltzmann plot method

Table 2. Experimentally derived and simulated electron number densities and electron temperatures

#	CALCULATED ELECTRON DENSITY (cm ⁻³)	CALCULATED ELECTRON TEMPERATURE (eV)	SIMULATED ELECTRON DENSITY (cm ⁻³)	SIMULATED ELECTRON TEMPERATURE (eV)
5086	–	1.6–2.0	4.0–4.8 × 10 ¹⁷	2.1–2.2
5094	–	1.5–2.2	3.5–4.7 × 10 ¹⁷	2.0–2.3
5099	–	1.5–1.7	3.1–3.6 × 10 ¹⁷	1.9–2.0
5146	2.0–7.0 × 10 ¹⁷	1.4–2.0	4.2–5.9 × 10 ¹⁷	2.3–2.6
5148	3.0–5.0 × 10 ¹⁷	–	–	–

5b, and 5c are lineouts from Zebra experiment #5094 taken at 8, 14, and 20 ns, respectively. The experimental data have been corrected for the responsivity of the streak camera, spectrometer, and fiber-optic system. Using PrismSPECT software, we set up a parameter sweep for ion temperature and ion density that ranged from transition energies and densities of 1.2 to 3 eV and 1 × 10¹⁷ to 5 × 10¹⁷ cm⁻³, respectively. We used these parameters to iteratively calculate the spectrum. This simulated spectrum was then compared to the experimental data. We compared the simulated N_e and T_e to the N_e and T_e calculated from experimental data using the methods discussed in the previous section (Table 2).

Electron Number Density

We can obtain the electron number density using Mach-Zehnder interferometry to measure the relative phase shifts of the beam after traveling through the plasma. The phase shift of an interferometric fringe in a plasma slab (ϕ) is given by a line integral in Gaussian units (Hutchinson 2002)

$$\phi = \frac{c}{4\pi\lambda n_c} \int N_e \cdot dl = \lambda \cdot 4.46 \cdot 10^{-14} \int N_e \cdot dl, \quad (12)$$

where λ is the laser wavelength, N_e is electron density (per cm⁻³), n_c is the cutoff density, c is the speed of light, and the integration is performed along the probe laser beam path. We used an Ekspla NL315 laser with 1.7 J of energy at a wavelength of 532 nm and a pulse width of 0.6 ns. As plasma density increases, interference fringes become thinner, and the distance between fringes decreases.

The 2-D map in Figure 6 shows the electron linear density along the laser path calculated with the

IDEA [Interferometric Data Evaluation Algorithms] software (Hipp 2003). To determine N_e , we performed an Abel inversion transform in IDEA. We obtained the symmetric data required for the Abel inversion transform by using the “remove linear tilt” and “averaging left and right” functions in IDEA (Hipp 1999, 2003). We performed this calculation on an interferogram of the anode–cathode gap region of our plasma source during the initial stages of the current rise. We used IDEA to calculate the N_e on multiple experiments, two of which are presented in Table 2 (experiments 5146 and 5148). The N_e values reported in Table 2 are calculated from data collected in the region monitored by the streaked spectrometer system. The interferometric data and emission spectra were collected in the same time period. Experiments 5086, 5094, and 5099 used a manual fringe analysis technique described by Anderson (2015), which also yielded $N_e \sim 5 \times 10^{17}$ cm⁻³. Table 2 shows a comparison of the experimental N_e calculated with IDEA and those simulated with PrismSPECT.

Dense Plasma Focus Experiments

We conducted DPF experiments using the Gemini DPF machine at the NNSS North Las Vegas Facility. The DPF capacitor bank stores 1 MJ of energy and delivers ~2 MA of current into the plasma. Low-density gas, typically deuterium, fills the evacuated DPF housing or tube. A large voltage applied between the anode and cathode ionizes that gas such that the conductivity increases rapidly as the current-carrying plasma sheath is formed. As the current increases, the $\mathbf{J} \times \mathbf{B}$ force increases, accelerating the plasma sheath to the end of the anode. As the plasma sheath reaches the end of the anode, it accelerates radially inward. The current

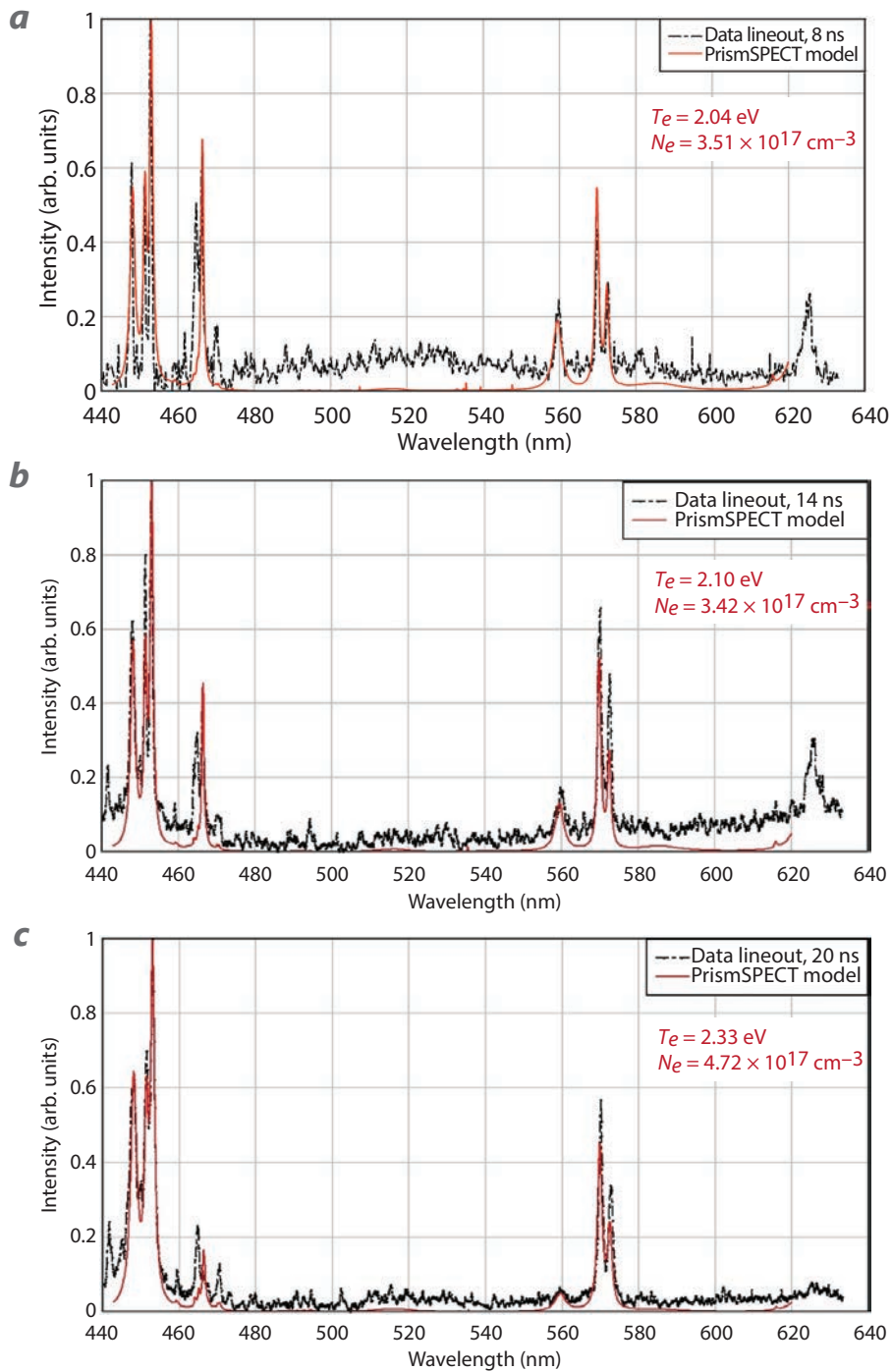


Figure 5. LAZE Al_2O_3 spectra of experiment #5094 from (a) 8 ns, (b) 14 ns, and (c) 20 ns into the record length of the emission spectrum

continues to rise and the $\mathbf{J} \times \mathbf{B}$ force increases, causing the ionized material within the anode–cathode gap to implode and pinch along the vertical z -axis.

As we did with the experiments on Zebra, we used an optical spectroscopy probe to collect visible light emitted from the plasma (Figure 7). The probe was aligned in the plane of the magnetic field direction, ~ 5 mm above the anode, directly through the center

axis, with a spot size < 0.5 mm. (For a description of the optical probe, fiber, spectrometer, and streak camera system, see *Experimental Setup*.) The spectrometer center wavelength was set to 480 nm with an approximate spectral window of 235 nm. Data collection started 250 ns before the approximate time of pinch. Preliminary data acquired by the streak spectrometer system were logged and stored on a PC through the CCD software for subsequent analysis.

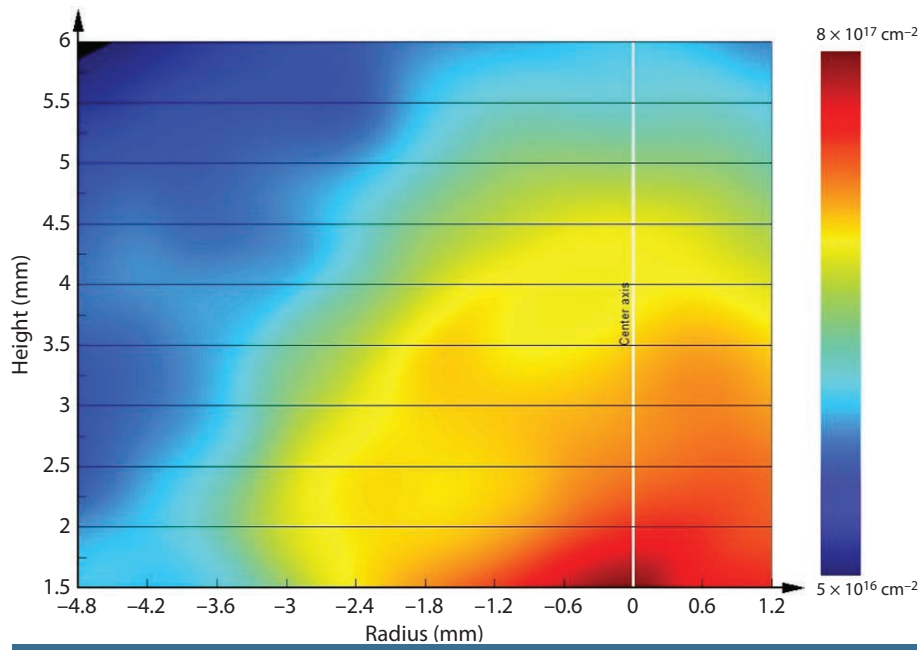


Figure 6. A 2-D map of the electron linear density calculated with IDEA (see text for details) of experiment #5146

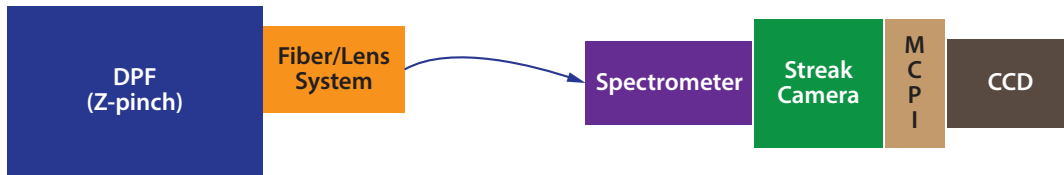


Figure 7. Diagram of the setup used to collect data on the Gemini DPF. The optical probe is located radially 40 cm from the pinch, and the field of view of the optical probe is ~ 0.5 mm.

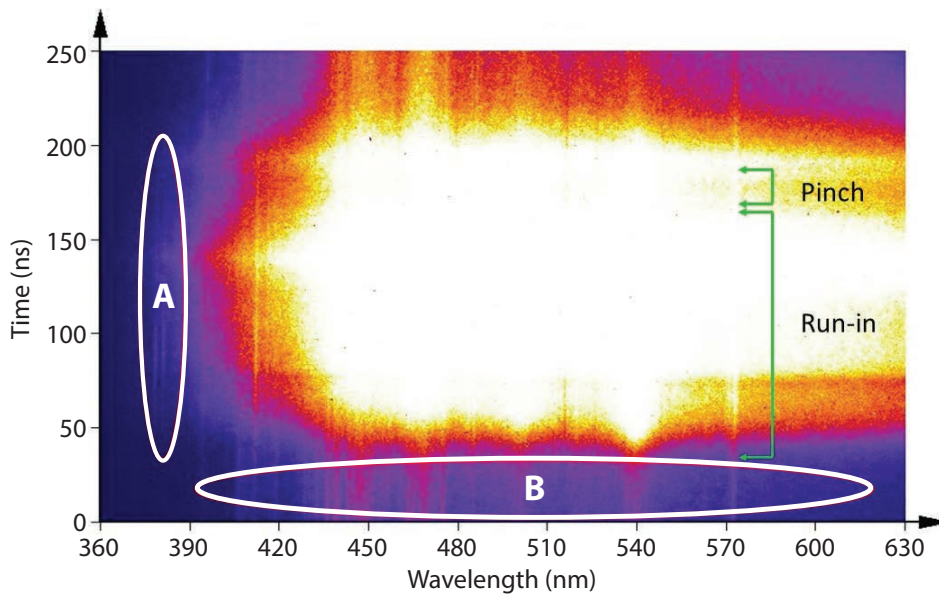


Figure 8. Streaked spectrometer image from Gemini DPF filled with oxygen. Multiple emission lines from before into the beginning of the run-in appear (B), and the O VI doublet is visible through the run-in into the pinch region (A).

Figure 8 depicts a time-resolved streaked spectrum from the DPF experiments. Preliminary analysis has shown a series of oxygen emission lines and the O VI doublet. We could use both of these emission lines to measure the magnetic fields, electron densities, and electron temperatures.

CONCLUSION

We have developed a spectroscopic model that incorporates collisional and Doppler broadening along with Zeeman splitting. The model was benchmarked against the PrismSPECT code across a range of experiment parameters. We made spectroscopic measurements of laser-ablated Z-pinch using the Al III, C IV, Ti IV, and O VI doublets and the $4P\ ^2P_{3/2}$ to $4S\ ^2S_{1/2}$ and $4P\ ^2P_{1/2}$ to $4S\ ^2S_{1/2}$ transitions. In our final year of the project, we explored visible spectroscopic techniques used to determine N_e and T_e . We used the Boltzmann plot method and PrismSPECT spectroscopic simulations to determine N_e and T_e for Al_2O_3 LAZE plasmas. These data allow us to more carefully constrain early plasma evolution, which in turn should lead to more accurate plasma models. Using temporally resolved spectroscopic data captured from the LAZE technique enables us to analyze trends in both N_e and T_e as a function of current, which is a function of time. Early in the current rise, we found that after 20 ns, N_e increased from 3.5×10^{17} to 4.7×10^{17} cm^{-3} and T_e increased from 1.4 to 2.2 eV. Discrepancies between the N_e and T_e determined from experimental data and the simulated spectra range from 7% to 32%, depending on how well resolved the transitions were in the experimental spectra. The simulated spectra assumed a single N_e and T_e ; however, the spectroscopic data were integrated over the diagnostic line of sight and may include an N_e and T_e distribution not accounted for in the present analysis.

Planned future improvements include a magneto-hydrodynamic simulation of the plasma and a radiation transport model to determine the spectral emission along the line of sight of the diagnostic, which should help to more accurately interpret the experimental conditions and provide even more precise time-resolved data. Finally, we were able to field our diagnostic on the Gemini DPF and collect very useful data. Future work would include follow-on experiments and analysis of the subsequent data.

This work was presented at the 60th Annual Meeting of the American Physical Society Division of Plasma Physics. A manuscript, “Electron Temperature and

Electron Number Density Measurements in Laser Ablation Z-pinch Experiments of Al_2O_3 ” (Dutra 2019) has been submitted to the journal *Physics of Plasmas*, and two more manuscripts are in preparation for the same journal.

ACKNOWLEDGMENTS

The authors would like to thank the support staff and graduate research assistants at the UNR NTF for help in fielding diagnostics, running the Zebra machine, and providing facilities for our experiments. We would like to gratefully acknowledge support from the State of Nevada Governor’s Office for Economic Development (GOED) via the Knowledge Fund and the Nevada Center for Applied Research (NCAR). These matching funds help to share the costs of staffing, equipping, and conducting experiments at the NTF.

REFERENCES

- Anderson, A., “Investigation of the ablation and implosion phases in 1 MA wire array Z-pinch with UV and X-ray diagnostics,” doctoral dissertation, University of Nevada, Reno, 2015, https://scholarworks.unr.edu/bitstream/handle/11714/2506/Anderson_unr_0139D_11793.pdf?sequence=1&isAllowed=y, accessed on May 1, 2018.
- Blesener, K. S., S. A. Pikuz, T. A. Shelkovenko, I. C. Blesener, D. A. Hammer, Y. Maron, V. Bernshtam, R. Doron, L. Weingarten, Y. Zarnitsky, “Measuring magnetic fields in single aluminum wire plasmas with time-resolved optical spectroscopy,” *High Energy Density Physics* **8**, 3 (2012) 224–226.
- Dutra, E. C., J. A. Koch, R. Presura, W. A. Angermeier, T. Darling, S. Haque, R. C. Mancini, A. M. Covington, “Development of a spectroscopic technique for simultaneous magnetic field, electron density, and temperature measurements in ICF-relevant plasmas,” *Rev. Sci. Instrum.* **87**, 11 (2016) 11E558.
- Dutra, E. C., J. A. Koch, R. Presura, W. Angermeier, T. Darling, R. Mancini, A. Covington, “A multi-axial time-resolved spectroscopic technique for magnetic field, electron density, and temperature measurements in dense magnetized plasmas,” in *Site-Directed Research and Development*, FY 2016, National Security Technologies, LLC, Las Vegas, Nevada, 2017, 23–32.
- Dutra, E. C., J. A. Koch, R. Presura, W. Angermeier, T. Darling, R. Mancini, A. Covington, “A multi-axial time-resolved spectroscopic technique for magnetic field, electron density, and temperature measurements in dense magnetized plasmas,” in *Site-Directed Research and*

- Development, FY 2017, National Security Technologies, LLC, and Mission Support and Test Services, LLC, Las Vegas, Nevada, 2018, 27–34.
- Dutra, E. C., J. A. Koch, R. Presura, P. Wiewior, A. M. Covington, “Electron Temperature and Electron Number Density Measurements in Laser Ablation Z-pinch Experiments of Al_2O_3 ,” to be published, 2019.
- Gomez, M. R., S. B. Hansen, K. J. Peterson, D. E. Bliss, A. L. Carlson, D. C. Lamppa, D. G. Schroen, G. A. Rochau, “Magnetic field measurements via visible spectroscopy on the Z machine,” *Rev. Sci. Instrum.* **85**, 11 (2014) 11E609.
- Griem, H. R., “Validity of local thermal equilibrium in plasma spectroscopy,” *Phys. Rev.* **131**, 3, (1963) 1170.
- Griem, H. R., *Principles of Plasma Spectroscopy*, Cambridge University Press, 1997.
- Harilal, S. S., C. V. Bindhu, V. P. N. Nampoori, C. P. G. Vallabhan, “Time evolution of the electron density and temperature in laser-produced plasma from $\text{YBa}_2\text{Cu}_3\text{O}_7$,” *Appl. Phys. B: Laser and Optics* **66** (1998) 633–638, <https://link.springer.com/article/10.1007/s003400050448>, accessed on May 1, 2018.
- Hipp, M., P. Reiterer, J. Woisetschlaeger, H. Philipp, G. Pretzler, W. Fliesser, T. Neger, “Application of interferometric fringe evaluation software at Technical University Graz,” *Proc. SPIE* **3745**, Interferometry ’99: Applications (1999).
- Hipp, M., P. Reiterer, “User Manual for IDEA 1.7, Software for Interferometrical Data Evaluation,” 2003, http://optics.tu-graz.ac.at/idea/Manual_IDEA17.pdf, accessed on October 2, 2017.
- Hussain, T., M. A. Gondal, M. Shamraiz, “Determination of plasma temperature and electron density of iron in iron slag samples using laser breakdown spectroscopy,” in *IOP Conf. Series: Materials Science and Engineering* **146** (2016) 012017, <http://iopscience.iop.org/article/10.1088/1757-899X/146/1/012017/pdf>, accessed on March 1, 2017.
- Hutchinson, I. H., *Principles of Plasma Diagnostics*, 2nd edition, Cambridge University Press, 2002, http://staff.ustc.edu.cn/~jlxie/PD_Hutchinson_Diagnostic.pdf, accessed on March 1, 2017.
- Musadiq, M., N. Amin, Y. Jamil, M. Iqbal, M. A. Naeem, H. A. Shahzad, “Measurement of electron number density and electron temperature of laser-induced silver plasma,” *Int. J. Engin. Technol.* **2**, 1 (2013) 32–43.
- Naeem, M. A., M. Iqbal, N. Amin, M. Musadiq, Y. Jamil, F. Cecil, “Measurement of electron density and temperature of laser-induced copper plasma,” *Asian J. Chem.* **25**, 4 (2013) 2192–2198, http://www.asianjournalofchemistry.co.in/User/ViewFreeArticle.aspx?ArticleID=25_4_98, accessed on March 1, 2017.
- NIST Atomic Spectra Database (version 5.5.6, April 6, 2018; accessed June 2018), <https://www.nist.gov/pml/atomic-spectra-database>.
- Ohno, N., M. A. Razzak, H. Ukai, S. Takamura, Y. Uesugi, “Validity of electron temperature measurement by using Boltzmann plot method in radio frequency inductive discharge in the atmospheric pressure range,” *Plasma and Fusion* **1**, 028 (2006) 028-1–028-9, https://www.researchgate.net/publication/239610388_Validity_of_Electron_Temperature_Measurement_by_Using_Boltzmann_Plot_Method_in_Radio_Frequency_Inductive_Discharge_in_the_Atmospheric_Pressure_Range, accessed on March 1, 2017.
- Rochau, G. A., J. E. Bailey, Y. Maron, “Applied spectroscopy in pulsed power plasmas,” *Phys. Plasmas* **17**, 5 (2010) 055501.
- Shaikh, N. M., B. Rashid, S. Hafeez, Y. Jamil, M. A. Baig, “Measurement of electron density and temperature of a laser-induced zinc plasma,” *J. Phys. D: Appl. Phys.* **39** (2006) 1384–1391.
- Stambulchik, E., K. Tsigutkin, Y. Maron, “Spectroscopic method for measuring plasma magnetic fields having arbitrary distributions of direction and amplitude,” *Phys. Rev. Lett.* **98**, 22 (2007) 225001.
- Tessarini, S., et al. “Beyond Zeeman spectroscopy: Magnetic-field diagnostics with Stark-dominated line shapes,” *Phys. Plasmas* **18**, 9 (2011) 093301-1–093301-9, https://www.researchgate.net/publication/234016439_Beyond_Zeeman_spectroscopy_Magnetic-field_diagnostics_with_Stark-dominated_line_shapes, accessed January 18, 2017.

This page left blank intentionally



Correlation between Hot Spots and 3-D Defect Structure in Single and Polycrystalline High-Explosive Materials

NLV-035-16 ■ Year 3 of 3

Cameron Hawkins,^{1,a} Oliver Tschauner,^b Zachary Fussell,^b
Jason McClure,^c Daniel Hooks,^d and Jesse Smith^e

¹hawkinmc@nv.doe.gov, (702) 295-9807

^aNorth Las Vegas

^bUniversity of Nevada, Las Vegas

^cBlock Engineering

^dLos Alamos National Laboratory

^eAdvanced Photon Source



A novel approach that spatially identifies inhomogeneities from microscale (defects, conformational disorder) to mesoscale (voids, inclusions) is developed by the use of synchrotron x-ray methods: radiography, Lang topography, micro-diffraction mapping, and bandpass Laue diffraction. The former three techniques provide a nondestructive method for statically characterizing millimeter-sized samples prior to shock experiments. The Laue diffraction technique can be applied during shock experiments. We can use these characterization maps to correlate continuum-level measurements in shock-compression experiments to mesoscale and microscale structures. In FY 2016, we began analyzing high-explosive analogous materials and developing software that can be used as a diagnostic tool on samples before shock-compression experiments and after on recoverable samples (Hawkins 2017). We continued in FY 2017 by examining high-explosive material samples of C-4 as well as pentaerythritol tetranitrate (PETN) and also expanded the capabilities of the software (Hawkins 2018). In FY 2018, we began exploring Laue diffraction in an effort to prove the capabilities of the software and to develop a diffraction method for dynamic shock.

BACKGROUND

Knowing how hot spots form in high-explosive (HE) materials during the initial stages of detonation is

one of the keys to understanding the detonation process. HE materials are usually not refined single crystals, but compounds of crystallites of one to a few HE compounds and binders. Impedance mismatch

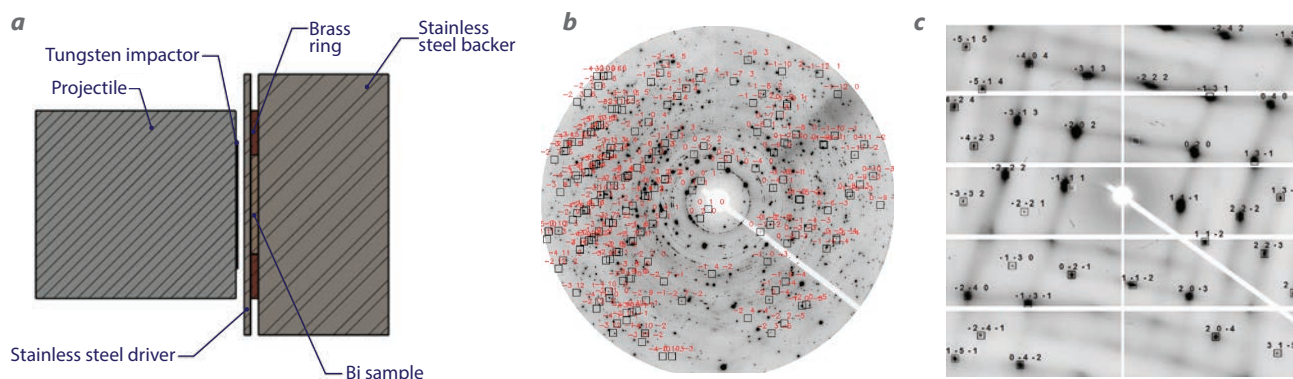


Figure 1. (a) Bismuth sample setup for the gas gun experiments; (b) x-ray diffraction pattern of sample (various bismuth crystallites) recovered from shock, with modeled Bi-II Miller indices overlaid (red); and (c) Bi-II' 20 μm shock-recovered single-crystal diffraction pattern with modeled Miller indices overlaid (black)

between binder and crystallites can influence the response of material to shock. In addition, accidental but unavoidable inhomogeneities such as cracks, voids, grain boundaries, inclusions of fluid or solid phases in the crystallites, and crystal lattice defects, can affect the initial response of the material to shock and can operate as locations for hot spot formation. Thus, correlating the given, initial inhomogeneities to hot spot formations is key to understanding the initial stages of detonation (Cawkwell 2008, Kuklja 2014). Such correlation, quantitatively established, helps provide an understanding of the performance of HEs, therefore allowing them to become more reproducible, more reliable, and safer.

During dynamic compression, localized stress and temperature in aggregate samples are affected by defects, voids, impurities, and other inhomogeneities that exist prior to shock. These crystal lattice defects produce weak points by inducing lattice strain. In a solid without internal structural degrees of freedom, such as a face-centered cubic metal, such local strain would induce small-scale reverberations. In molecular solids, such as most HE materials, the local strain around the defects can be relaxed by changes in the conformational state of the molecules. In other words, the excess free energy from induced strain will be converted in part into an increase in internal energy. In HE materials, different conformational states of molecules have different sensitivities to shock (Tsyshevsky 2016). Thus, defects induce local strain, which then induces changes in sensitivities. We examine the extent of such changes of conformation around defects in HE materials, as well as the nature of these conformational changes in terms of sensitivity.

Local changes in the molecule structure that have higher sensitivity to shock can therefore lend

themselves to detonation. Researchers have examined the surface of β -HMX crystallites and concluded that the presence of a layer of δ -HMX, which is highly sensitive, as well as the thickness of this layer, control the bulk sensitivity of HMX (Surber 2007, Chen 2014, You 2015). Current techniques of spatially resolved defect characterization (transmission electron microscopy [TEM] dark field, Leeds Electron Microscopy and Spectroscopy Centre [LEMAS]) are destructive and cannot be applied to samples prior to shock experiments. Furthermore, these methods are restricted to very small (nanometer) length scale, whereas characterization of samples prior to shock needs to extend to millimeter scale or beyond. Characterization of voids and impurities in HE samples is presently restricted to submillimeter length scale and lacks correlation of impurity location with impurity phase identification. There is a need for nondestructive characterization techniques that cover the mesoscale (millimeter to micron) and microscale (micron to nanometer) to provide a way to understand the stress and temporal evolution upon shock loading.

PROJECT

We conducted multiple campaigns at the Advanced Photon Source (APS) at Argonne National Laboratory to continue static characterization and to develop dynamic methods. The radiography and Lang topography diffraction techniques were performed at APS Sector 16 (High Pressure Collaborative Access Team [HPCAT]). The radiography focuses on mesoscale defects, whereas the Lang topography is used for a fully 3-D quantitative assessment. Both are used during static applications of a sample at the pre-shock stage. The bandpass Laue white-light

diffraction technique was performed at APS Sector 32. We can use this technique to show structure and defect evolution during dynamic compression.

Radiography and Lang Topography Diffraction Techniques

We conducted several campaigns throughout the year at APS Sector 16 (HPCAT) to perform radiography and Lang topography diffraction techniques on several samples. Our goal this year was to provide a way to integrate the developed software directly to the beam line. Ultimately, this was not possible due to concerns from APS that the software would interfere with the beam line. Nonetheless, the software can be used as a stand-alone post-processing tool for analyzing recorded data. The samples of interest this year included bismuth (Bi) and ammonium nitrate (NH_4NO_3) for shock experiments and additional work as well as several samples of C-4.

Bismuth has been studied throughout the project because of the multiple phase changes it undergoes during shock (Hawkins 2017, 2018). Several samples were analyzed at the APS beam line and then reanalyzed after being shocked with a single-stage gas gun. Bismuth polycrystals were pressed in a brass ring having an inner diameter of ~ 4 mm and a height of 0.3 mm loaded into the recovery chamber. The tungsten impactor was launched at 540 m/s, driving a shock wave through the stainless-steel driver and into the sample with a peak stress of 11 GPa. Recovered crystal diffraction patterns and the recovery chamber configuration are given in Figure 1a. Analysis indicates melting at grain boundaries and recrystallization with a high-pressure phase of bismuth being recovered to ambient conditions. Additional work was performed at the Los Alamos

National Laboratory (LANL) Center for Integrated Nanotechnologies (CINT), allowing us to further characterize the shocked bismuth samples. At CINT, we used a scanned probe microscope and an atomic force microscope to quantify phase proportions. Samples are currently awaiting calorimetry at LANL to measure specific heat of Bi-II' versus Bi-I.

Several samples of C-4 were analyzed this year at the APS Sector 16 beam line. One of the samples seemed to have recrystallized; it was too fine-grained (powder-like), which rendered it incompatible with this technique, and the analysis was not performed. The crystals are required to be approximately two times the size of the beam ($3 \times 5 \mu\text{m}^2$), so the minimum crystal size is $6 \times 10 \mu\text{m}^2$. The major takeaway from the experiment was that because the RDX crystals “healed” between the time the sample was first analyzed last year and the time the sample was reanalyzed this year, the recrystallization may have changed the C-4 detonation properties. We postulate that it would take more to detonate this sample now than if it had been in the highly deformed state.

Figure 2 shows the diffraction pattern, and Figure 3 shows the associated Lang topograms of one of the C-4 samples, constructed with the software developed during the previous years of the project. This distribution can be used as an input parameter for forward modeling the crystal structure and shock-induced deformation during in situ bandpass Laue diffraction experiments. We imaged C-4 samples in hopes of shocking them at a facility such as APS Sector 35 with bandpass Laue diffraction or at the Special Technologies Laboratory with alternative diagnostics equipment. This, however, proved to be logistically difficult, and an alternative was to study non-HE samples at APS Sector 32.

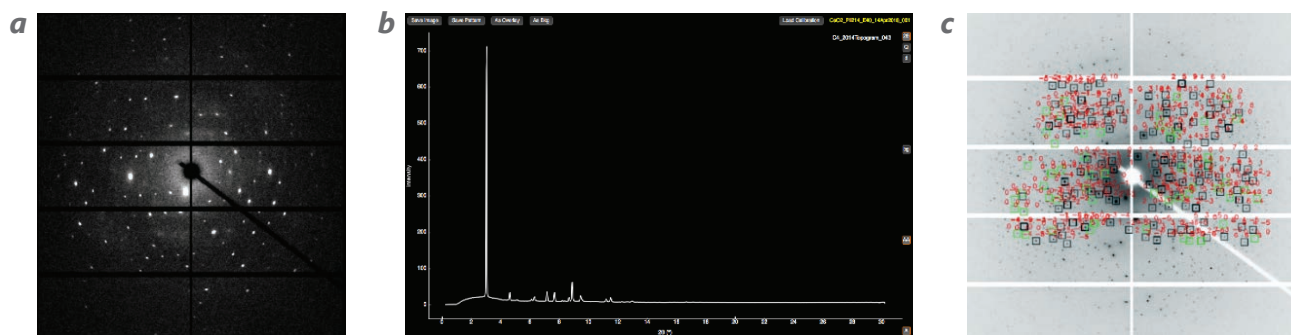


Figure 2. HE C-4 sample (a) diffraction pattern, (b) integrated pattern, and (c) pattern with indexed reflections produced by GSE_ADA/RSV software (Przemyslaw 2013)

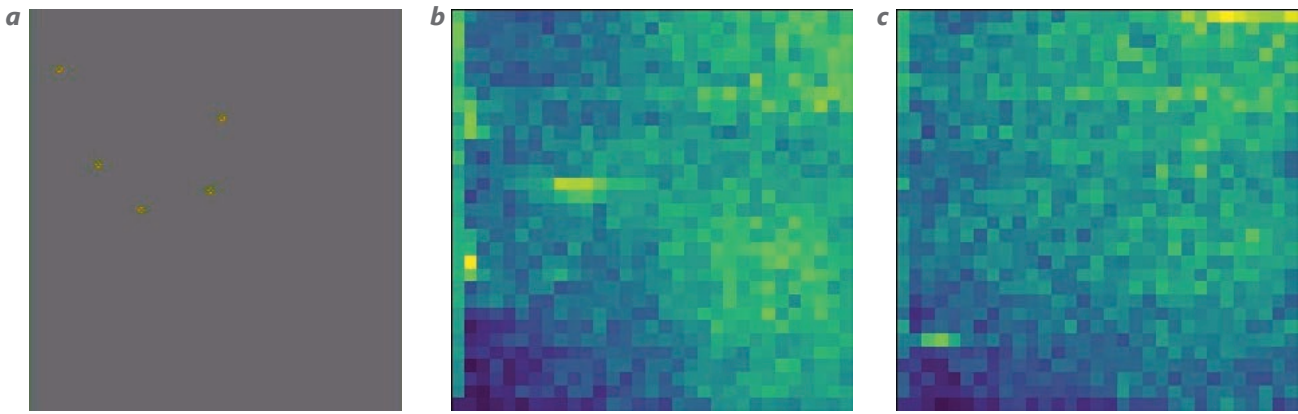


Figure 3. Lang topography of C-4 sample showing (a) locations of peak intensity reflections and (b, c) topographic reconstructions created using software we developed that reveal dislocation kernels

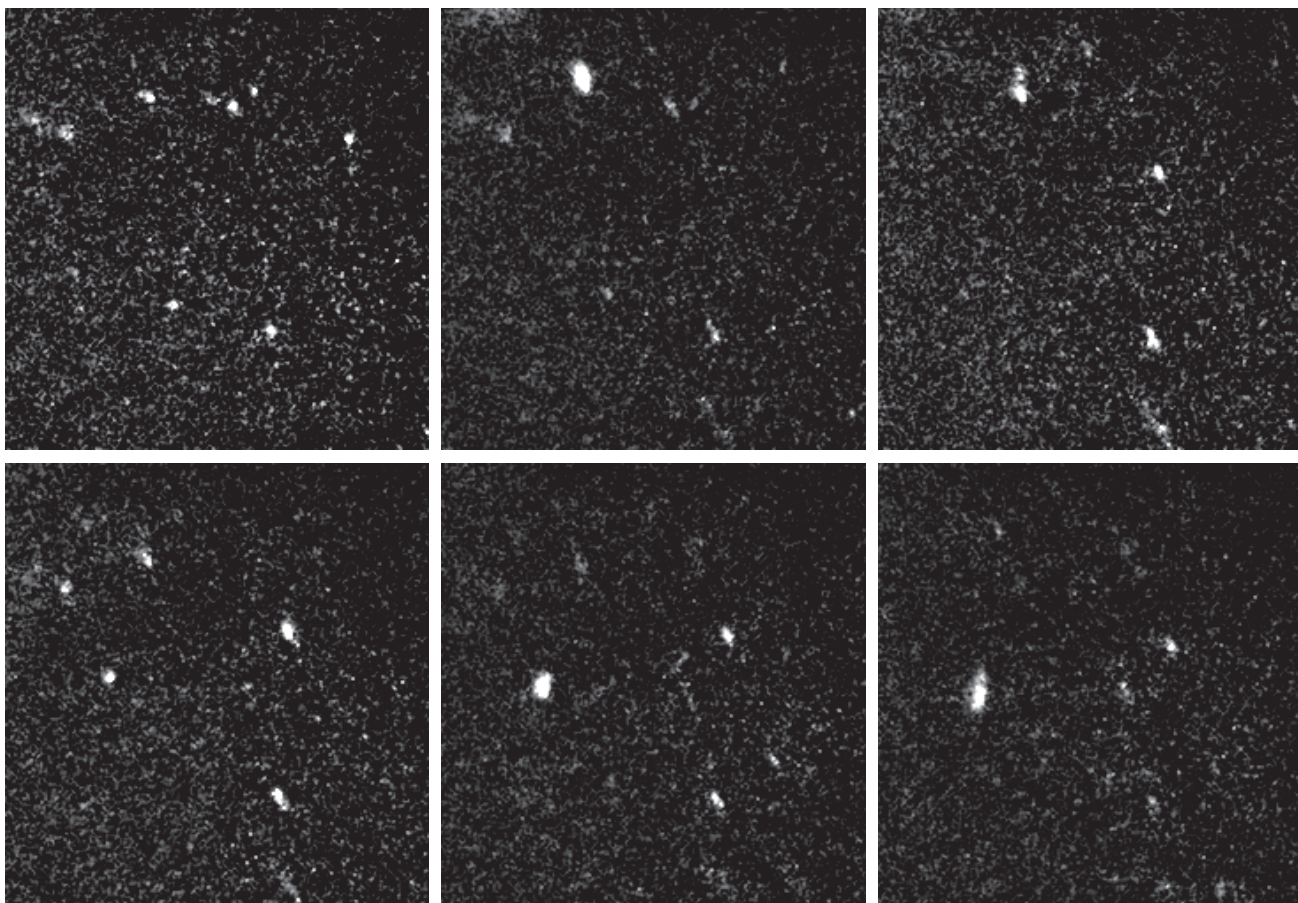


Figure 4. Dynamic impact of tin images (at 10 μ s intervals) show shifting peak intensities, confirming that Laue diffraction will capture dynamic impact data

Bandpass Laue Diffraction Technique

Because hot spots and detonation waves emit considerable light, HE hot spot characteristics may be captured during dynamic compression using specialized optical imaging, phase contrast imaging, radiometry and IR imaging. Several concerns have been raised over these techniques regarding spacial and temporal resolution in addition to the limitation of only observing the surface of an opaque sample. The bandpass Laue diffraction technique is an alternative method that can provide diffraction patterns during high dynamic rates, which may allow us to see structural changes or defects in situ throughout the sample volume.

In these experiments, samples were limited to non-HE materials because of restrictions at the APS sector. We used a split Hopkinson bar to dynamically compress five samples at approximately 100 m/s: bismuth, Nd:YAG (neodymium-doped yttrium aluminum garnet), tin, zirconium, and titanium. Although we planned to image the samples statically first using Lang tomography at APS Sector 16 and then image them again dynamically using Laue diffraction at APS Sector 32 for comparison and verification, logistics prevented this. However, our experiments confirmed that the bandpass Laue diffraction technique is viable for capturing the dynamic diffraction of a sample during dynamic compression. Each experiment captured 246 images over a 180 μ s timeframe. Shown in Figure 4 are images taken from the dynamic compression experiment on tin. As can be seen, the peak intensities shift from one frame to another, which provides a way to see the evolution of the diffraction pattern during dynamic impact.

CONCLUSION

At the conclusion of this multi-year project, we have a well-established static technique in place and a good path forward for developing a dynamic diffraction method. In addition, we created and fully matured an analysis software tool for nondestructive 3-D characterization of defects and crystal orientation using static diffraction techniques.

The radiography and Lang topography diffraction techniques at APS Sector 16 provide a nondestructive static method of mapping defects in samples. This method is portable to any beam line, and the software developed for analysis can be used after data collection. Several samples, including HEs, were analyzed during the project, providing insight into how well the method works with varying factors. The

minimum grain size is specific to the beam line, so for the APS beam line, which is $3 \times 5 \mu\text{m}^2$, the smallest grain size is $6 \times 10 \mu\text{m}^2$ for this static method. Other beam lines with different beam sizes would have different grain size minimum limitations.

The bandpass Laue diffraction technique performed at APS Sector 32 is a promising dynamic method. The peak shape of reflections obtained by this technique can be correlated with Lang topograms as a measure of defect type and orientation. This allows us to move forward from pre-shock diagnostics (Lang) to in situ probing (defect evolution during compression). LANL will continue these dynamic diffractions studies at APS Sector 32.

ACKNOWLEDGMENTS

We would like to thank Robert Hixson, Darrin Valentine, and Mark Knickerbocker of NNSS for their contributions to this work. Portions of this work were performed at HPCAT (Sector 16), APS, Argonne National Laboratory. Operations support of HPCAT was provided from DOE-NNSA under award No. DE-NA0001974 and DOE-BES under award No. DE-FG02-99ER45775, with partial instrumentation funding by the National Science Foundation. The APS is operated for the DOE Office of Science by Argonne National Laboratory under contract No. DE-AC02-06CH11357. High Pressure Science and Engineering Center (HiPSEC) support for the project was provided from the Department of Energy through Cooperative Agreement DE-NA-0001982.

REFERENCES

- Cawkwell, M. J., T. D. Sewell, L. Zheng, D. L. Thompson, "Shock-induced shear bands in an energetic molecular crystal: Application of shock-front absorbing boundary conditions to molecular dynamics simulations," *Phys. Rev. B* **78** (2008) 014107.
- Chen, M.-W., S. You, K. S. Suslick, D. D. Dlott, "Hot spots in energetic materials generated by infrared and ultrasound, detected by thermal imaging microscopy," *Rev. Sci. Instrum.* **85**, 2 (2014) 023705.
- Hawkins, C., O. Tschauner, Z. Fussell, J. McClure, S. Root, E. Machorro, E. Daykin, "Correlation between hot spots and 3-D defect structure in single and polycrystalline high-explosive materials," in *Site-Directed Research and Development*, FY 2016, National Security Technologies, LLC, and Mission Support and Test Services, LLC, Las Vegas, Nevada, 2017, 33–41.

Hawkins, C., O. Tschauner, Z. Fussell, J. McClure, S. Root, “Correlation between hot spots and 3-D defect structure in single and polycrystalline high-explosive materials,” in *Site-Directed Research and Development*, FY 2017, National Security Technologies, LLC, Las Vegas, Nevada, 2018, 35–41.

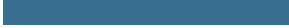
Kuklja, M. M., “Quantum-chemical modeling of energetic materials: Chemical reactions triggered by defects, deformations, and electronic excitations,” chap. 3 in *Advances in Quantum Chemistry* **69**, J. R. Sabin, ed., Academic Press, Cambridge, Massachusetts, 2014, 71–145.

Przemyslaw, D., K. Zhuravlev, V. Prakapenka, M. L. Rivers, G. J. Finkelstein, O. Grubor-Urosevic, O. Tschauner, S. M. Clark, R. T. Downs, “High pressure single-crystal micro X-ray diffraction analysis with GSE ADA/RSV software,” *High Pres. Res.* **33**, 3 (2013) 466–484.

Surber, E., A. Lozano, A. Lagutchev, H. Kim, D. D. Dlott, “Surface nonlinear vibrational spectroscopy of energetic materials: HMX,” *J. Phys. Chem. C* **111**, 5 (2007) 2235–2241.

Tsyshevsky, R. V., O. Sharia, M. M. Kuklja, “Molecular theory of detonation initiation: Insight from first principles modeling of the decomposition mechanisms of organic nitro energetic materials,” *Molecules* **21**, 2 (2016) 236.

You, S., M.-W. Chen, D. D. Dlott, K. S. Suslick, “Ultrasonic hammer produces hot spots in solids,” *Nat. Commun.* **6** (2015) 6581.



Quasielastic Plastic Flow in Dynamically Compressed Metals

LAO-002-18 ■ Year 1 of 1

**Jason Scharff,^{1,a} Mike Grover,^b Brandon La Lone,^b Matt Staska,^b
Gerald D. Stevens,^b Dale Turley,^b and Ruben J. Valencia^b**

¹scharfrj@nv.doe.gov, (505) 663-2139

^aNew Mexico Operations—Los Alamos

^bSpecial Technologies Laboratory



We are investigating inelastic deformation occurring in shock-compressed single crystals of tin. The project addresses an ongoing need for a time-dependent inelastic deformation response model that could be implemented into NNSA hydrodynamic codes (e.g., FLAG). High-fidelity strength and damage model development and implementation is a high priority of the nuclear weapons programs. Prior work has focused primarily on controlling the internal microstructure (grain size, texture, anisotropy) of polycrystalline metal through processes such as annealing and hot/cold rolling. However, very little experimental effort has been devoted to clarifying inelastic deformation mechanisms and understanding plastic flow in dynamically compressed single-crystalline metals. Our results this year show anisotropy in the elastic wave speeds, Hugoniot elastic limit, the time evolution of the plastic shock front, and release for three different orientations of single-crystal tin.

BACKGROUND

Stockpile certification is critically tied to the NNSA's predictive capability framework. Thus, it is paramount that the NNSA laboratories develop high-fidelity physics models to accurately predict dynamic plastic deformation of weapon-relevant metals subjected to high strain rate compression. Decades of research have established that metals exhibit rate-dependent stress-strain behavior due to the irreversible motion of crystal lattice defects called dislocations. Ideally for polycrystalline metals, this means the microstructural

origins of strength and plastic deformation should be determined as a function of crystallographic orientation under shock compression.

Plasticity and damage models being developed at Los Alamos National Laboratory (LANL) for use in next-generation production hydrodynamic codes on exascale computing platforms, such as in their Advanced Simulation and Computing (ASC) program, must contain the best available data on metal microstructure. Mesoscale simulations of the dynamic response of polycrystalline metals to shock-

loading events can provide unprecedented insight into the competition of several operative mechanisms within the microstructure, but only if the necessary constituents are individually based on sound physics. LANL's approach represents a marked departure from more traditional elastic-plastic model development and calibration (e.g., Preston-Tonks-Wallace [PTW], Johnson-Cook, Steinberg-Guinan-Lund [SGL], Mechanical Threshold Stress [MTS]) and requires a constitutive description for individual grains, including defects such as dislocations, within an explicit representation of the microstructure geometry and evolving deformation fields.

the loading process, which creates a back-stress condition. As the material unloads, the dislocations reverse motion, giving rise to the observed quasielastic unloading response (Figure 1b).

The use of single crystals removes any complexities associated with polycrystalline heterogeneities. For example, experiments performed on single crystals eliminate grain boundary problems. Additionally, since glide planes and glide directions are well defined, the theoretical and computational analyses become more tractable, and a unifying basis for calculating nonlinear elastic response and rate-dependent plastic flow can be achieved (Johnson 1970). Under development

within the LANL ASC program is a physically consistent theoretical framework for combining an equation of state (EOS) with crystal plasticity for the purpose of modeling the shock response of single and polycrystalline metals (Luscher 2013). LANL's response model

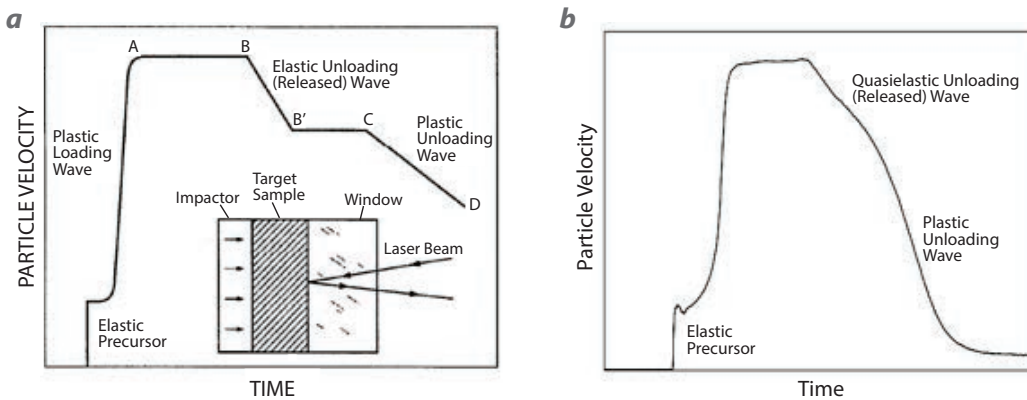


Figure 1. (a) Hypothetical (ideal) particle velocity record (Johnson 1992) and (b) an actual polycrystalline tantalum shock and release wave profile demonstrating non-ideal elastic-plastic response in the unloading wave (Rigg 2007)

We are collaborating with LANL scientists to investigate inelastic deformation mechanisms occurring in unloading and reloading kinematics from the shocked-compressed state in tetragonal tin single crystals; part of this effort is to provide data to the LANL ASC program. The measured loading and unloading particle velocity time histories in shocked metals exhibit well-known (but not well-understood) deviations from typical elastic-plastic response models that are often used to describe shock wave behavior in metals. For example, shock and release wave measurements in polycrystalline metals such as aluminum, tantalum, beryllium, uranium, and plutonium demonstrate significant departure from the ideal elastic-plastic response (Figure 1a) upon release in particular. In the case of polycrystalline tantalum (Figure 1b), the measured release wave shows a gradual transition from elastic behavior to fully plastic behavior, an indication that some amount of plastic deformation is occurring along the entire release path as the material unloads. It has been hypothesized that dislocations pile up at grain boundaries during

for single-crystal copper has been successfully implemented into a 3-D Lagrangian finite element code. While the LANL ASC program was successful in matching simulations with current experimental data, the program has prioritized a need for additional experimental data on other metals of cubic and lower crystal symmetries.

Tin (Sn) is used extensively as a model material because of its relatively simple phase diagram and low melting temperature. We have conducted a number of experiments using tin because these characteristics of tin make it particularly suitable for use in experiments with the gas guns at the NNSS and the Special Technologies Laboratory. For example, in our previous collaborative project with LANL, we conducted reverse ballistic plate impact shock/release and shock/reshock experiments to assess quasielastic behavior in polycrystalline β -Sn and compressive strength on second shock in β -Sn and body-centered-tetragonal [bct]-Sn. Figure 2 is a plot of shock/release and shock/reshock data for β -Sn. SESAME 2161 and PTW fit the shock/reshock plastic wave data quite well for

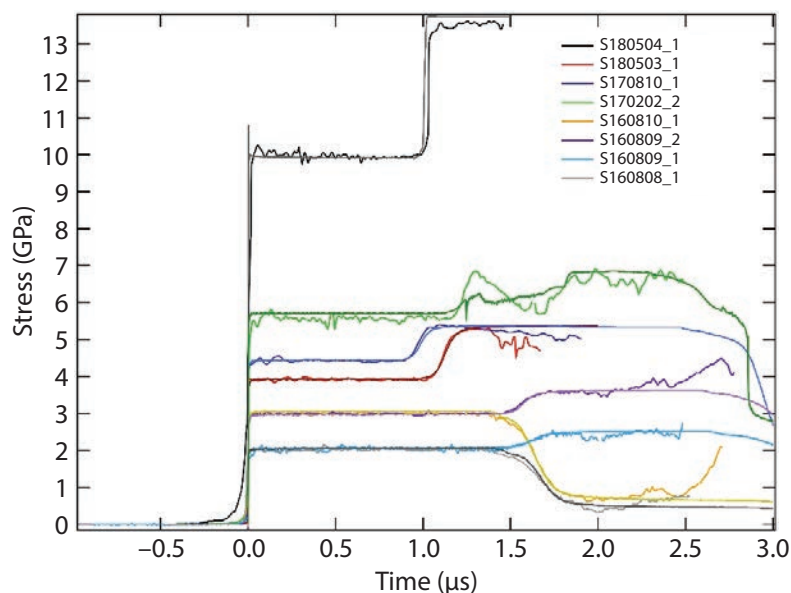


Figure 2. Shock/release and shock/reshock experiment and simulation of β -Sn in the front surface impact configuration. For the reshock experiments, tin was backed by copper, whereas for the release experiments, tin was backed with syntactic foam and impacted into either a lithium fluoride or sapphire anvil. We used the Mie-Grüneisen form of the EOS in conjunction with PTW strength parameters provided by LANL to calculate all wave profiles in CTH with the exception of shot S170202_2. In S170202_2, we applied the PTRAN option for the EOS to obtain better agreement with the data, which indicates the onset of the phase transition from beta to body-centered tetragonal (bct).

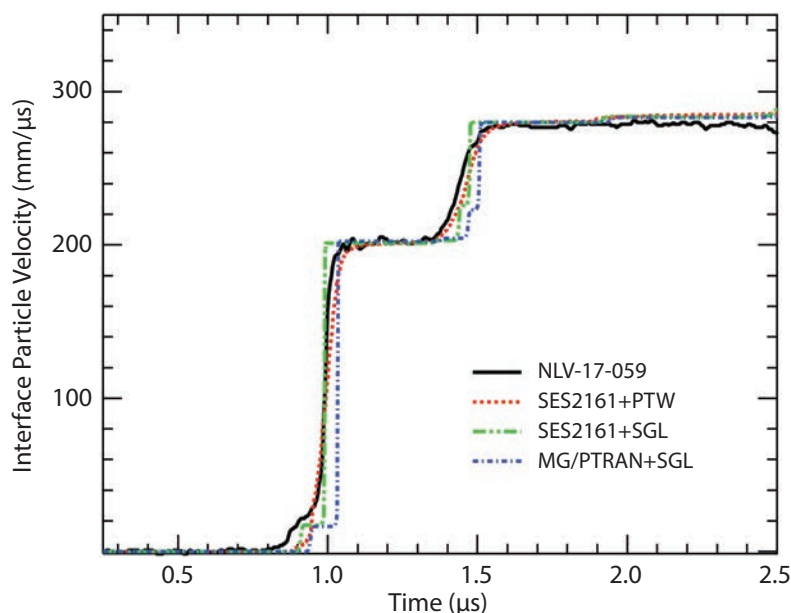


Figure 3. Shock/re-shock experiment and simulation of β -Sn in the traditional transmission impact configuration. A layered impactor composed of quartz and copper was used against tin backed by a quartz window. We performed the CTH simulations using the SESAME EOS Table 2161 with either PTW or SGL strength models. The PTRAN model was also paired with SGL strength.

both β -Sn and bct-Sn. Moreover, the quasielastic release wave seems to be calculated adequately for the shock/release experiments. However, the elastic precursor wave amplitude is calculated incorrectly for tin shocked in the standard transmission impact geometry, shown in Figure 3. Based on these results, LANL has started to re-parameterize PTW for tin and test whether or not “tuning” the shear modulus can prevent the plastic wave from overrunning the precursor wave.

LANL has begun an effort in FY 2019 to develop a multiphase strength model that accurately describes the high strain rate plastic deformation in polycrystalline tin based on single-crystal dynamic strength data. However, single-crystal material models cannot be unambiguously constrained by traditional measurements of the shock or stress-strain response of polycrystalline metals. Instead, these models require comprehensive measurements of the anisotropic shock response of single crystals for their calibration and validation. Our experimental results contribute to this LANL effort by providing a unique dataset for benchmarking and calibration of a dislocation-mediated plasticity model derived for tin.

PROJECT

Figure 4 is a model view of the target assembly used to measure the particle velocity time histories of a tin single-crystal sample backed by a lithium fluoride (LiF) window. A 3 mm thick Z-cut quartz impactor launched from the gas gun creates a shock in a 3 mm thick single crystal of [100], [110], or [001] orientation tin targets backed by a 5 mm thick LiF [100] window attached with a very thin layer of adhesive. The gun has a 40 mm diameter launch tube and uses pressurized helium as the propellant, which is capable of generating impact velocities up to about 800 m/s. An optical beam interrupt (OBI) near the

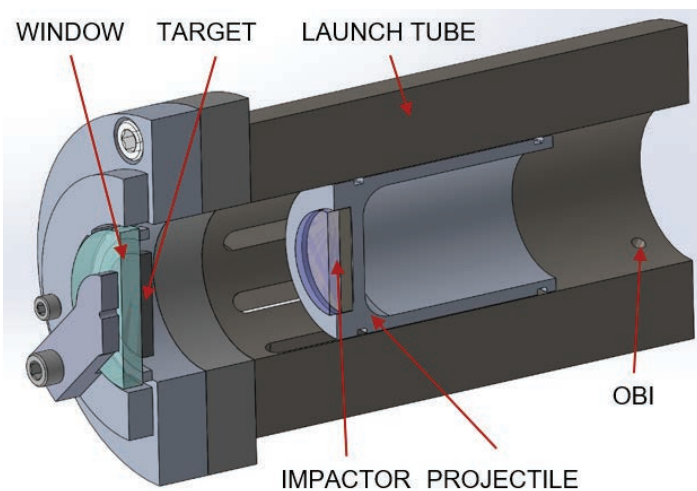


Figure 4. Model view of the target assembly

end of the launch tube provides a trigger signal for the photonic Doppler velocimetry (PDV) diagnostics. For these experiments, impactor velocities ranged from 241 to 248 m/s. The diameters of the impactors, targets, and windows were 25 mm. We obtained the single-crystal tin targets, having a purity of 99.999%, from Princeton Scientific Corporation. Both sides of the target were polished to a roughness of less than $0.01 \mu\text{m}$ with an orientation accuracy of less than 0.1° . We measured particle velocity time histories of the shock and release wave profiles with a two-fiber, heterodyned PDV probe at the interface between the tin target and LiF window, and we used a homodyne collimating PDV probe to measure the projectile velocity at impact.

We chose the impact configuration carefully to maintain the tin samples in the beta phase and

Table 1. Experiment parameters

PART	MATERIAL	IMPACTOR VELOCITY, U_D	THICKNESS (mm)	DIA. (mm)	DENSITY, ρ_0 (g/cm ³)	LONGITUDINAL WAVE SPEED, C_L (mm/ μs)	SHEAR WAVE SPEED, C_{S1} (mm/ μs)	SHEAR WAVE SPEED, C_{S2} (mm/ μs)
Experiment 180731-1								
Impactor	Z-cut quartz	0.2407 ± 0.0002	3.058 ± 0.001	25	2.65	6.40	4.70	–
Target	Sn [100]	–	3.370 ± 0.004	25	7.30	3.15	1.79	1.72
Window	LiF	–	4.998 ± 0.001	38	2.64	6.56 ± 0.03	4.93 ± 0.08	–
Experiment 180801-1								
Impactor	Z-cut quartz	0.2454 ± 0.0002	3.059 ± 0.002	25	2.65	6.40	4.70	–
Target	Sn [110]	–	3.257 ± 0.014	25	7.30	3.54	1.04	1.73
Window	LiF	–	4.981 ± 0.002	38	2.64	6.56 ± 0.03	4.93 ± 0.08	–
Experiment 180802-1								
Impactor	Z-cut quartz	0.2485 ± 0.0003	3.058 ± 0.001	25	2.65	6.40	4.70	–
Target	Sn [001]	–	3.316 ± 0.045	25	7.30	3.53	1.74	1.74
Window	LiF	–	5.022 ± 0.001	38	2.64	6.56 ± 0.03	4.93 ± 0.08	–

Table 2. HEL data for Sn [100], [110], and [001]

TARGET	PARTICLE VELOCITY, U_p (m/s)	HUGONIOT ELASTIC LIMIT, σ_{HEL} (GPa)	HUGONIOT STRESS, P_H (GPa)
Sn [100]	16 ±2	0.29 ±0.04	2.28 ±0.01
Sn [110]	19 ±2	0.38 ±0.04	2.37 ±0.06
Sn [001]	58 ±6	1.14 ±0.12	2.41 ±0.04

well below the 6 to 8 GPa phase boundary. Thus, the maximum stress achieved in the target was designed to not exceed 2.5 GPa. Table 1 summarizes the impact conditions and experimental dimensions pertinent to each experiment executed this year. Interface particle velocity time histories are displayed in Figure 5. The wave profiles will be discussed in detail later; however, even a first-glance comparison reveals very diverse behavior for these three orientations of β -Sn. The arrival times of the wave profiles have been corrected such that impact occurs at $t = 0$. The transit time of the shock wave through the target after impact was calculated from the target thickness and the assumption that the elastic wave travels at the ultrasonic longitudinal wave speed, C_L , indicated in Table 1.

The wave profiles shown in Figure 5 illustrate the evolution of the compression and release wave resulting from impact and unloading due to the reflection of the rarefaction wave from the back surface of the impactor. The profiles clearly show multiple waves running through the targets due to differences in the elastic and plastic wave speeds. We used impedance matching conditions to extract the Hugoniot states from each experiment and estimate the Hugoniot elastic limit (HEL).

Hugoniot Elastic Limit

The HEL is the point on the shock Hugoniot at which the material transitions from a pure elastic state to an elastic-plastic state. Above the HEL, the material is unable to resist shear stresses and begins behaving more as a liquid. We determined the HEL for each of the three different orientations of β -Sn directly from the measured particle velocity wave profiles (Figure 5)

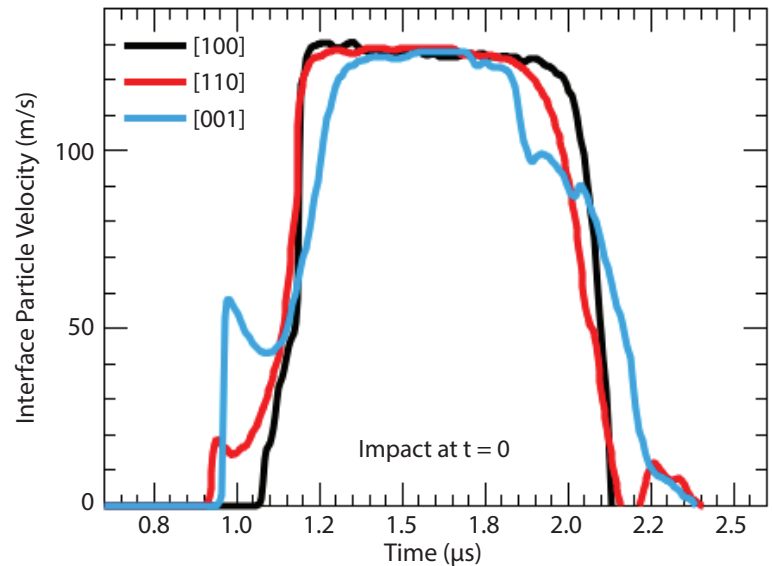


Figure 5. Interface particle velocity time histories of single-crystal β -Sn targets shock loaded and released from a Z-cut quartz impactor

using the impedance matching condition at the interface between the tin target and LiF window and solving the equation

$$\sigma_{HEL} = \frac{Z_T + Z_W}{2} u_p, \quad (1)$$

where Z_T and Z_W are the shock impedances for the target and window, respectively, and u_p is the observed interface particle velocity at the peak of the transition from elastic to plastic behavior. For the target, $Z_T = \rho_0 C_L$ with $\rho_0 = 7.3 \text{ g/cm}^3$ and $C_L = 3.15, 3.54,$ and $3.53 \text{ mm}/\mu\text{s}$ for Sn [100], [110], and [001], respectively (Table 1). For the window, $Z_W = \rho_0(C_0 + s u_p)$ with $\rho_0 = 2.64 \text{ g/cm}^3$, the extrapolated bulk velocity $C_0 = 5.15 \text{ km/s}$, and the slope $s = 1.35$.

The HEL data are listed in Table 2 along with the Hugoniot stress, P_H , determined from the peak

amplitude of the plastic wave using the impedance matching conditions for multiple shock waves.

CONCLUSION

During this project, we observed anisotropy in the elastic wave speeds, Hugoniot elastic limits, plastic compression, and release wave profiles for single-crystal β -Sn [100], [110], and [001] shocked to a Hugoniot stress not exceeding 2.5 GPa. In FY 2019, under programmatic funding for science campaigns, we will continue to focus on the orientation dependence of the compressive and tensile strengths during shock wave loading and unloading in single-crystal tin. We are also planning experiments to determine the anisotropies in longitudinal wave speeds on the shock Hugoniot. Finally, we plan to utilize the technique developed at the Sandia National Laboratories Z accelerator to perform off-the-principal Hugoniot/isentropic dynamic compression experiments at the Thor pulsed-power accelerator to measure the orientation-dependent flow strength in both the β -Sn and β c-Sn.

ACKNOWLEDGMENTS

We would like to thank Darby J. Luscher, Saryu Fensin, and Justin Brown for their insightful discussions pertaining to this work.

REFERENCES

- Johnson, J. N., O. E. Jones, T. E. Michaels, “Dislocation dynamics and single-crystal constitutive relations: Shock-wave propagation and precursor decay,” *J. Appl. Phys.* **41** (1970) 2330.
- Johnson, J. N., R. S. Hixson, G. T. Gray III, C. E. Morris, “Quasielastic release in shock-compressed solids,” *J. Appl. Phys.* **72** (1992) 429.
- Luscher, D. J., C. A. Bronkhorst, C. N. Allenman, F. L. Addessio, “A model for finite-deformation nonlinear thermomechanical response of single crystal copper under shock conditions,” *J. Mech. Phys. Solids* **61** (2013) 1877–1894.
- Rigg, P. A., unpublished manuscript, 2007.



Dynamic Measurement of Chemical Composition and Chemical Reaction with Surrounding Gas of Shock Wave–Generated Ejecta Particles

STL-011-17 ■ Year 2 of 2

Dale Turley,^{1,a} Jason Mance,^a Brandon La Lone,^a Gene Capelle,^a
Mike Grover,^a and Ruben J. Valencia^a

¹turleywd@nv.doe.gov, (805) 681-2239

^aSpecial Technologies Laboratory



The goal of this work is to dynamically observe chemical reactions of ejecta with a surrounding gas and to measure the content of a shock wave–generated ejecta cloud. In the first year of this work, we demonstrated the use of laser-induced breakdown spectroscopy as a diagnostic for measuring the atomic content of an ejecta cloud (Turley 2018). This year we demonstrated the use of coherent anti-Stokes Raman spectroscopy (CARS) to measure the temperature of shock-compressed deuterium gas, the first time this has been accomplished. Ultimately, the goal is to use CARS to measure the temperature of shock-compressed deuterium entrained with ejecta and to observe heating of the ejecta caused by viscous drag and exothermic chemical reaction with gas.

BACKGROUND

The study of metal surfaces subjected to high-pressure shock waves has been an important area of research within the weapons community for many years. When a metal surface is produced by standard machining techniques, the resulting surface will possess some surface roughness, often with a characteristic periodicity. A shock wave propagating through the material will interact with these surface features and eject material (ejecta) from the surface.

A number of diagnostic tools have been developed in an effort to learn about the evolution and transport

properties of ejecta; however, questions concerning how ejecta material interact with pressurized gas are still unresolved. In particular, we are studying, in collaboration with Los Alamos National Laboratory, how ejecta particles break up and travel in a gas. Ejecta fragments in gases can split into smaller fragments due to hydrodynamic processes such as viscous drag. It is also possible that particles break up when chemical conversion or reactions with the surrounding gas occur. To explore this possibility, we recently performed a number of experiments with cerium and tin ejecta (neither are Raman active) in reactive and nonreactive gases (to be published). In that work we

measured the ejecta radiance and converted the data to radiance temperatures via Planck relationships. The results strongly suggest that cerium ejecta immersed in deuterium gas react exothermically and cause a temperature increase beyond that predicted by viscous drag alone. However, because the ejecta emissivity is unknown, the accuracy of the radiance temperature method is uncertain, and an alternative technique for measuring ejecta temperature is desired.

This year we explored coherent anti-Stokes Raman spectroscopy (CARS) as an alternative method for determining the dynamic temperature of ejecta entrained within a compressed gas. Because the cerium ejecta are not Raman active, we designed and executed experiments to measure the temperature of the surrounding Raman-active gas. If the ejecta and the gas were in thermal equilibrium during our measurement, then we could infer the dynamic temperature of the ejecta. If an exothermic reaction occurred between the gas and ejecta, then it would be evidenced by an increase in the gas temperature.

We targeted the Q-branch in D_2 , which includes transitions between adjacent vibrational levels ($\Delta v = 1$) with the same rotational J number ($\Delta J = 0$). The difference frequency ($\omega_{\text{pump}} - \omega_{\text{Stokes}}$) is chosen to match the vibrational energy ω_{vib} , which occurs around 2900–3000 cm^{-1} in D_2 .

We designed a CARS system after Roy (2005). We used a 532 nm doubled Nd:YAG (neodymium-doped

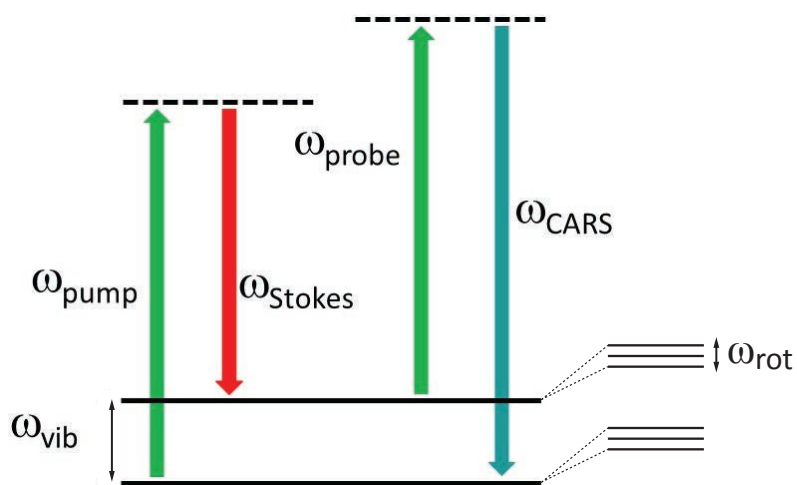


Figure 1. Schematic energy level showing the various CARS laser beam frequencies

PROJECT

CARS

CARS is a laser-based method used for measuring the rotational spectra in a material. CARS requires three input beams (called pump, Stokes, and probe) to create an output beam (called the CARS beam), which contains information about the Boltzmann-distributed population of rotational energy levels within the target material, which in this case is deuterium gas (D_2). A schematic energy-level diagram is shown in Figure 1. The pump beam excites molecules to an upper level, and the difference frequency of the pump and Stokes beams, ($\omega_{\text{pump}} - \omega_{\text{Stokes}}$), is chosen to overlap a vibrational transition in the gas. Raman-scattered light from a probe beam with frequency ($\omega_{\text{probe}} + \omega_{\text{pump}} - \omega_{\text{Stokes}}$) will be coherent and cause a CARS beam to emerge. In our approach, the Stokes laser spectrum is broad so it can cover multiple transitions, and the pump spectrum is narrow so that the rotational lines are resolved in the CARS spectrum. The spectrum of the CARS beam is then measured with a spectrometer, and the relative intensities of the transitions are directly related to their Boltzmann-distributed populations.

yttrium aluminum garnet) laser to serve as the pump and probe beams. The pulse width was 150 ps in duration with an energy of 35 mJ per pulse. We split a portion of this beam to pump a dye cell mixed with DCM (dichloromethane) and ethanol to create a Stokes beam with spectral width of 30 nm FWHM centered near 630 nm. This was sufficient to cover the Q-branch transitions that occur at 630–633 nm shifted from the 532 nm narrowband pump laser. The 532 nm probe beam scatters to create a CARS signal at 458–461 nm. Most of this energy is used for converting the Stokes beam in the dye cell. Typical pulse energies in the gas are on the order of 1 mJ for the pump and probe pulses and 100 μJ for the Stokes pulse. We could increase the system performance by improving the Stokes beam spatial profile and spectral match; however, we found the signal in this configuration adequate for our experiments.

The pump, probe, and Stokes beams were spatially co-focused in a BOXCARS geometry (Thomas 2017), and the CARS beam was separated by the use of dichroic mirrors. The CARS beam was coupled into a 200 μm optical fiber, and the fiber output was coupled to the input slit of a 1-meter spectrometer with a grating

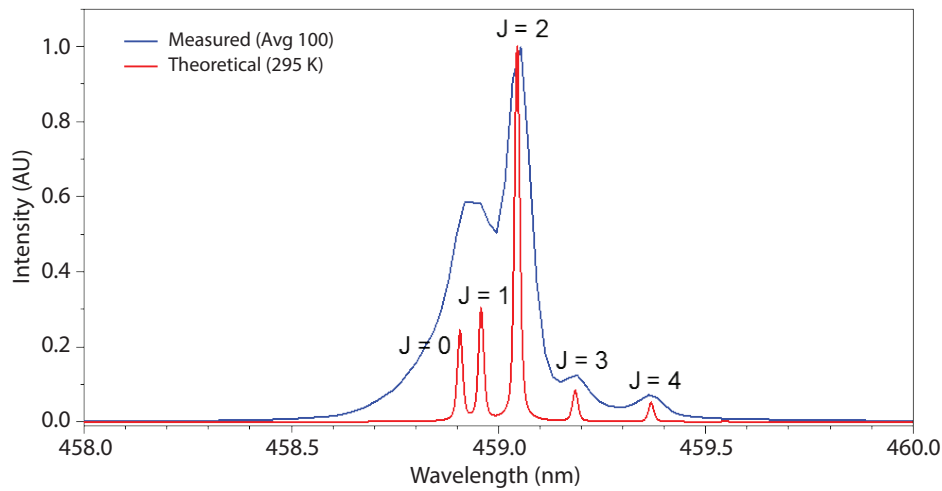


Figure 2. Measured CARS spectrum in D_2 at room temperature overlaid with a theoretical spectrum. Line resolution in the measured spectrum is limited by the spectrometer.

of 2400 grooves per millimeter. The spectrum was measured with an intensified CCD camera (Andor iCCD) synchronized to the laser pulse.

Static measurements of the CARS spectrum were taken at room temperature and pressure. Figure 2 shows an averaged signal overlaid with a theoretical spectrum. The spectrometer does not have enough spectral resolution to distinguish individual lines, but it is still possible to accurately extract the peak amplitudes. We measured the spectrometer response to a narrow input spectrum and found the shape fits well to the sum of a Gaussian and Lorentzian profile. Using this function, we performed a nonlinear least squares fit to obtain the amplitude of each peak. The relative amplitudes of the peaks were then related to the temperature through a Boltzmann distribution

$$\frac{I_{J_A}}{I_{J_B}} = \frac{\left[\frac{1}{2}(2J_A + 1)(3 + (-1)^{J_A}) \exp\left(\frac{-B_e J_A (J_A + 1)}{k_B T}\right) \right]^2}{\left[\frac{1}{2}(2J_B + 1)(3 + (-1)^{J_B}) \exp\left(\frac{-B_e J_B (J_B + 1)}{k_B T}\right) \right]^2}, \quad (1)$$

where the rotational constant $B_e = 30.4 \text{ cm}^{-1}$ for D_2 (Brannon 1968, Majstorović 2015), k_B is Boltzmann's constant, I_{J_A} and I_{J_B} are the intensity of any pair of spectral lines with rotational quantum numbers J_A and J_B , and T is the temperature.

Dynamic Experiments

We create ejecta by detonating a high explosive placed behind a metal target with a pattern of surface defects on the side opposite the explosive charge.

The explosive sends a shock wave through the metal sample; when the shock wave reaches the surface, it begins to move, and ejecta are produced from the surface defects. For the dynamic experiments reported in our work, the metal target surface was purposefully polished so that no ejecta were produced by the shock wave. We chose this geometry to allow study of the compressed gas independent of interactions with ejecta. We are planning to study the gas/ejecta system in a follow-on study.

In our study, a shock wave is created at the interface between the shocked metal and the gas. The shock wave in the gas travels slightly faster than the free surface of the metal. After $10 \mu\text{s}$, the shock wave has moved $\sim 2 \text{ mm}$ in front of the metal surface, creating a separation such that the laser beams can pass through the compressed gas. With the appropriate timing and alignment, the compressed gas can be probed without interference from the metal free surface. We used photonic Doppler velocimetry to measure the start of motion of the metal and the free surface velocity. We verified laser timing in the dynamic experiment using a fast framing camera that simultaneously images the shocked metal, shocked gas, and the light flash from the CARS signal.

In order to observe the shock wave propagating in the gas, we coupled a Schlieren imaging system to the framing camera. Because there was no room to image off-axis from the CARS lasers, we devised a coaxial scheme that shared the optical path between the Schlieren and CARS systems. A diagram of the optical setup and an image showing the shock wave propagating in the gas are shown in Figure 3.

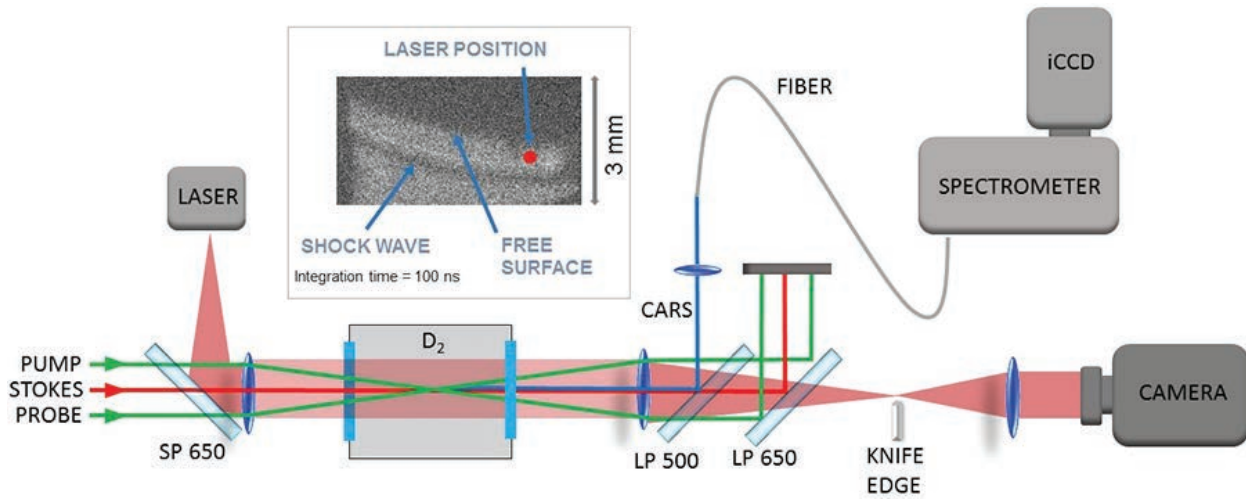


Figure 3. Diagram of the optical setup. Schlieren imaging at the time of the CARS spectrometry confirms laser positioning within shock-compressed D_2 . SP 650 is a short pass filter, passing wavelengths shorter than 650 nm. LP 500 and LP 650 are long pass filters passing wavelengths longer than 500 nm and 650 nm, respectively.

Prior to the dynamic experiment, the CARS lasers were aligned using a beam profiler so that they were spatially overlapped at their beam waist. We used a 20 GHz photodiode and detector to check the temporal overlap of the pump and Stokes laser pulses. We adjusted the probe laser to arrive 150 ps later than the pump and Stokes pulses to reduce non-resonant background signals. This configuration produced a CARS spectrum with excellent signal-to-noise ratio. The data from our dynamic experiment are shown in Figure 4 along with the results of a nonlinear fit used to determine temperature. The nonlinear fit finds the best-fit theoretical spectrum by floating parameters for the temperature and an overall scaling factor. The best-fit temperature of 1080 K is hotter than expected from theoretical models that predict temperatures of shock-compressed gas from velocity.

As shown in NACA (1953), for a 1-D shock wave in an ideal gas, the ratio of the shock wave temperature T_1 to the initial temperature T_0 is given by

$$\frac{T_1}{T_0} = \frac{[2\gamma M^2 - (\gamma - 1)][(\gamma - 1)M^2 + 2]}{(\gamma + 1)^2 M^2}, \quad (2)$$

where γ is the ratio of the specific heat at constant pressure (c_p) to the specific heat at constant volume (c_v) (1.4 for D_2). M is the Mach number

$$M = \frac{U_s}{C_0}, \quad (3)$$

where U_s is the shock velocity in the gas, and C_0 is the ambient sound speed (910 m/s for D_2). Finally, the change in density, ρ , is given by

$$\frac{\rho_1}{\rho_0} = \frac{(\gamma + 1)M^2}{(\gamma - 1)M^2 + 2}. \quad (4)$$

These relationships were determined using thermodynamics. We can further constrain the problem by using the Hugoniot conservation of mass relationships to obtain the ratio of the metal free surface velocity u (which is also the gas particle velocity) to the gas shock velocity U_s :

$$\frac{u}{U_s} = \frac{\rho_1 - 1}{\frac{\rho_1}{\rho_0}}. \quad (5)$$

Using these equations, we calculate an expected shock wave temperature of 700 K—well below the measured temperature of 1080 K.

Error Analysis

Determining the accuracy of the temperature measurement is not trivial because the dominant error source is not typical noise. The ratio of the RMS fluctuations in the noise floor to the peak signal intensity of the data shown in Figure 4 is ~ 0.01 ; however, the difference between the theoretical and

experimental data is much larger. We found that the CARS signal itself has large fluctuations in the peak intensities on single laser shot basis. Similar problems have been reported in the literature (Greenhalgh 1985; Snelling 1987, 1994) where the fluctuations are blamed on interference effects that occur as a result of phase noise generated in the dye conversion process used to create the Stokes beam. We quantified these fluctuations for our system by making 20 single CARS measurements on D_2 at room temperature; we found that the peaks fluctuated around their average value with a standard deviation of 40%. Using Gaussian statistics, we then calculated the probability, as a function of temperature T , that a measured peak (J) fluctuated to the value $I_{measured}$ when the expected value was I_{theory} ,

$$P_J(T) = \frac{1}{\sqrt{2\pi\sigma^2}} \exp\left(-\frac{(I_{measured} - I_{theory}(T))^2}{2\sigma^2}\right), \quad (6)$$

for $\sigma = 0.4$. The probability of observing the measured spectrum as a function of temperature is the product of the probabilities of all observed peaks. The resulting probability distribution is plotted in Figure 5. In order to calculate the probability that the temperature lies within a certain range, we integrate the curve over that range. Integration from 950 to 1300 K gives a 93% probability that the temperature is within this range, with the peak occurring near 1080 K, in agreement with the nonlinear fit. The probability that the actual temperature was below 950 K is less than 0.1%, which is well outside the expected 700 K.

$$P(T) = \prod_{J=0}^{J-8} P_J. \quad (7)$$

We postulate four possible causes for this discrepancy. First, the deuterium gas may have been contaminated. If oxygen were present, combustion could occur and add heat to the system. We are planning more dynamic experiments with equipment installed to check the purity of the deuterium gas prior to the experiment.

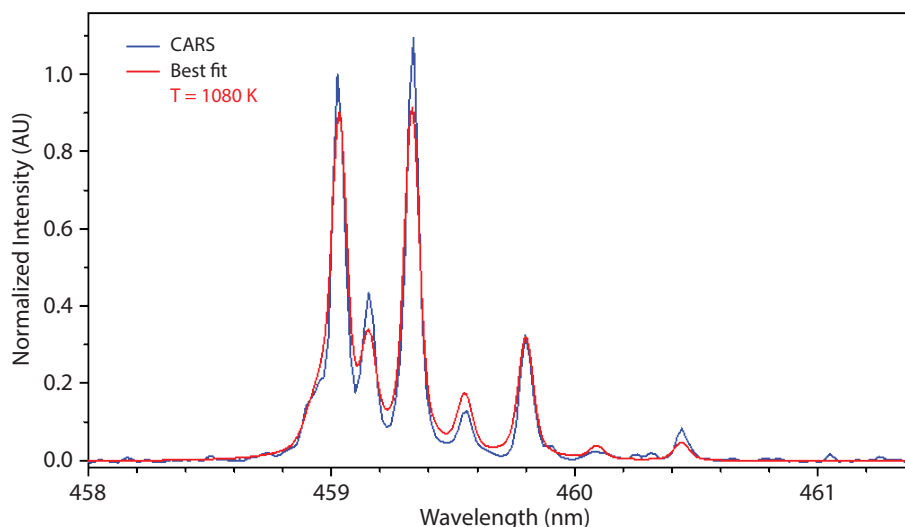


Figure 4. Dynamic CARS spectrum measured in shocked D_2

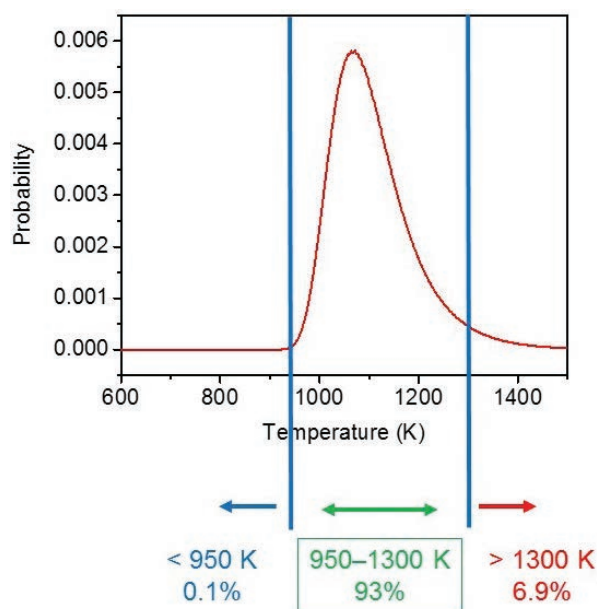


Figure 5. Probability distribution analysis for dynamic data in Figure 4. 93% of the area under the probability curve exists from 950–1300 K, indicating the temperature is likely in this range.

Second, our method for extracting temperature from the data may be inaccurate. We plan to make static measurements at elevated temperatures in a heated cell to check our method. Third, our error analysis may be incorrect, and the CARS spectral fluctuations may be larger than we expect. We plan to repeat the dynamic experiment several times to establish reproducibility of our results. Fourth, theoretical calculations we used to determine the expected temperature may be incorrect.

CONCLUSION

We believe that for the first time we have demonstrated the use of CARS to measure temperature in shock-compressed deuterium gas. We measured a temperature of 1100 K with a lower bound of 950 K. This measurement disagrees with theoretical estimates that predict temperatures near 700 K. We attribute the dominant source of error in our measurement to laser phase noise in the Stokes beam. However, our error analysis suggests the Stokes noise is not sufficient to cause the discrepancy between the measured and expected results. We plan to make more dynamic and static measurements to find the source of this discrepancy. After we have established reliable results in shock-compressed deuterium, we plan to make measurements in shock-compressed gas entrained with reactive and nonreactive ejecta under an FY 2019 SDRD project.

REFERENCES

- Brannon, P. J., C. H. Church, C. W. Peters, “Electric field induced spectra of molecular hydrogen, deuterium and deuterium hydride,” *J. Mol. Spectrosc.* **27**, 1–4 (1968) 44–54.
- Greenhalgh, D. A., S. T. Whittley, “Mode noise in broadband CARS spectroscopy,” *Appl. Opt.* **24**, 6 (1985) 907–913.
- Majstorović, G. Lj., N. M. Šišović, “Rotational and gas temperatures of molecular deuterium in a hollow cathode glow discharge,” *J. Res. Phys.* **38-39**, 1 (2015) 11–22.
- National Advisory Committee for Aeronautics (NACA), Report 1135, Equations, Tables, and Charts for Compressible Flow, 1953, <https://ntrs.nasa.gov/archive/nasa/casi.ntrs.nasa.gov/19930091059.pdf>, accessed on September 1, 2018.
- Roy, S., T. R. Meyer, J. R. Gord, “Broadband coherent anti-Stokes Raman scattering spectroscopy of nitrogen using a picosecond modeless dye laser,” *Opt. Lett.* **30**, 23 (2005) 3222–3224.
- Snelling, D. R., T. Parameswaran, G. J. Smallwood, “Noise characteristics of single-shot broadband CARS signals,” *Appl. Opt.* **26**, 19 (1987) 4298–4302.
- Snelling, D. R., R. A. Sawchuk, T. Parameswaran, “Noise in single-shot broadband coherent anti-Stokes Raman spectroscopy that employs a modeless dye laser,” *Appl. Opt.* **33**, 36 (1994) 8295–8301.
- Thomas, L. M., A. Satija, R. P. Lucht, “Technique developments and performance analysis of chirped-probe-pulse femtosecond coherent anti-Stokes Raman scattering combustion thermometry,” *Appl. Opt.* **56**, 31 (2017) 8797–8810.

Turley, D., J. Mance, G. Capelle, B. La Lone, M. Grover, R. J. Valencia, “Dynamic measurement of chemical composition and chemical reaction with surrounding gas of shock wave-generated ejecta particles,” in *Site-Directed Research and Development*, FY 2017, National Security Technologies, LLC, and Mission Support and Test Services, LLC, Las Vegas, Nevada, 2018, 49–54.



Next-Generation Photomultiplier Detectors Using Transmissive III-Nitride Semiconductor Electrodes

NLV-049-16 ■ Year 3 of 3

Robert Buckles,^{1,a} Alexander Sudderth,^a and Ke-Xun Sun^{a,b}

¹bucklera@nv.doe.gov, (702) 295-0323

^aNevada Operations

^bUniversity of Nevada, Las Vegas



In the third year of the project, we produced a novel, ultrafast, aluminum-gallium-nitride-based photoelectron multiplier as well as the cesium chemical vapor deposition chamber and wafer fixturing for bonding and sealing with the photocathode developed in the project's first two years (Buckles 2017, 2018a). The advanced photomultiplier as a whole will find use in high-energy gamma/neutron prompt diagnostics. The project addresses an ongoing need for solid-state photomultiplier devices to replace high-quality vacuum tube technology, and it also addresses the greater need for detectors with high linearity, faster and cleaner impulse response, and ease of manufacturability. Programmatic detector development projects in FY 2019 will complete the full assembly and operational test of the prototype detector.

BACKGROUND

The NNSA has provided prompt gamma/neutron diagnostics for Stockpile Stewardship, high energy density physics applications, and defense programs throughout the NNSA complex, the Defense Threat Reduction Agency, and other agencies for decades. While we have endeavored to improve our techniques, methods, and instruments since legacy days, the photomultiplier tube (PMT) industry has stagnated, vastly dwindling to a point of collapse, and solid-state technologies have almost completely supplanted vacuum tube technology. Recently, the lighting, power, and broadcast industries have embraced the advent of high-performance Nobel-winning Group III-nitride semiconductors. Leveraging these

advanced technologies, we seek to produce a novel device to surpass the aging vacuum tube detector, while surmounting the limitations of intermediate technologies such as glass microchannel plates. The high-mobility semiconductor “mesh” multiplier we are developing is our response to the PMT quandary. Prompt neutron/gamma signatures are high-speed analog signals, too fast for counting electronics but too low in light yield for typical amplifiers, and are typically converted to near-UV light through the use of a fast scintillator material. The PMT can apply greater than 1 million gain with good linearity and temporal response. Our semiconductor mesh photomultiplier should exceed the typical characteristics of a vacuum PMT (Buckles 2018b).

PROJECT

Photodetector Design

The conceptual and fabrication work done in FY 2016–FY 2017 culminated in a preliminary photomultiplier design that would mate with the photocathode wafer (Buckles 2017). Figure 1 illustrates multiplier wafers stacked on the photocathode and capped by an anode wafer. Epilayer thicknesses, interfaces, vacuum bonding and contacts with illustrated operational bias, field lines, and electronic flow are indicated to convey the operation of a PMT. The anode represents another silicon wafer with the exact shape as a multiplier but with just a simple metal electrode. The grid electrodes are intended to promote hot electron transport, increasing the local field within the activated surfaces, possibly exceeding the free-space field, with ready emission through the vacuum barrier.

The heterojunction interfaces provide 2-D electron gas (2DEG) or 2-D hole gas (2DHG) layers with high mobility for transport and field uniformity. Because of a quantum-mechanical eigenstate cusp that exceeds the Fermi level energy, these layers provide essentially free carriers and therefore behave unimpeded, much as would flow in an actual conductor.

High electron mobility transistors are constructed in this fashion such that they produce extremely fast or wideband switches for power millimeter-wave components. It is our expectation that these layers will provide high current-mode charge replenishment to forestall charge saturation. The negative electron affinity (NEA) layer is achieved principally through cesium activation, and some samples will also utilize a thin, 2 nm layer (~4 atoms) of aluminum nitride (AlN) to promote the electron gas state for greater surface conductivity and resist oxidation. In future developments we hope to use silicon delta doping

(but performance efficacy is not yet proven), which may obviate the need for cesiation.

The gain mechanism is provided by the collisional impact within the aluminum-gallium-nitride (AlGa_{0.3}N) material due to the free-space bias field between devices (vacuum), through the etched holes in the silicon substrate. This is unlike a microchannel plate, which would produce scattered secondaries off its fine glass capillary walls. The holes are relatively large here, with an aspect ratio of 2, and although some secondaries might be produced from the silicon wall, the bulk are accelerated directly into the epilayer. We use silicon because it is easy to etch free-space passages, whereas harder substrates—sapphire or gallium nitride (GaN)—are too difficult to etch completely. Although this is a radical departure from all-solid-state devices such as avalanche photodiodes, the vacuum barrier provides the isolation to limit dark current with relatively low internal field, while providing high-field region. This is the best property of the classical PMT.

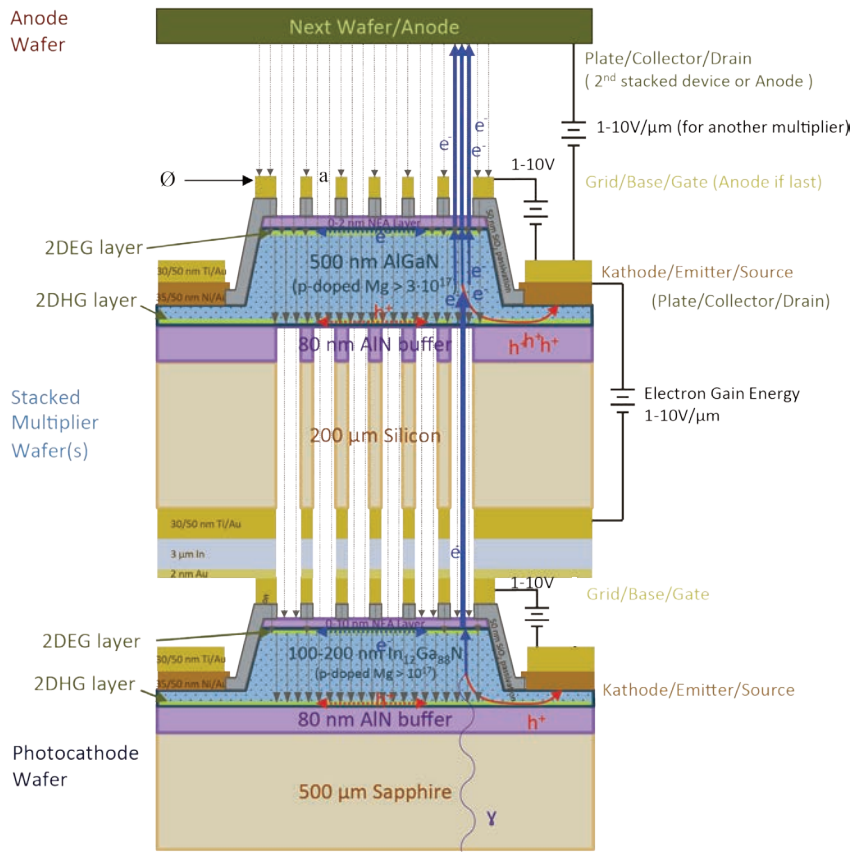


Figure 1. A cross-sectional view of the stacked photomultiplier device with illustrated operational bias, field lines, and photoelectronic flow (not to scale). Passivation and acceleration openings (a) are 100 μm circles (low aspect ratio of just 2) with exactly the same hexagonal array pattern as the photocathode. Overall diameter Ø is 1 to 20 mm. The configuration of each wafer device is that of a planar triode or vertical field effect transistor.

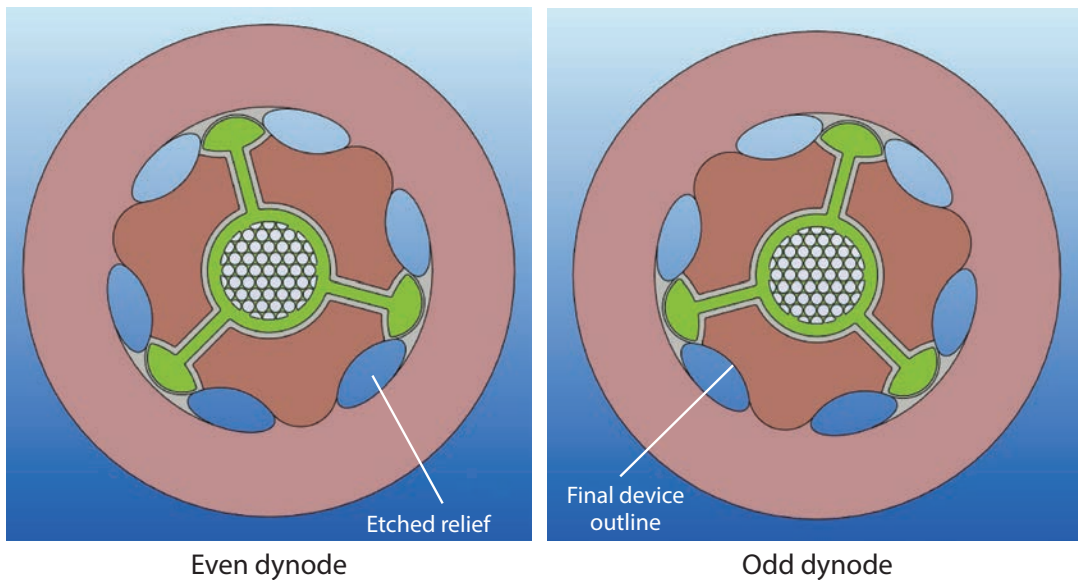


Figure 2. A stackable multiplier geometry with left and right (even and odd) symmetrical hexalobular electrodes for a 1 mm device viewed from the backsides of the wafers. Three redundant lobes are used on each, for bonding (green) to a mating mesa top grid electrode and mesa bottom cathode (brown). Devices are diced from a wafer following the indicated outline, parting the light tan section of the wafer. The etched reliefs (vias) leave the tips of the lobes unbonded, allowing circuitry connection after the device is diced from the wafer. Larger devices follow this same convention.

We chose AlGaIn as the multiplier material for its greater mechanical strength and immunity to all but deep UV light that might result from residual interaction from the high-speed electrons, knowing that this choice will require more kinetic energy due to the higher band gap. AlN may also be a good choice, but at the sacrifice of less gain. We expect the collisional impact energy to be dispersed within 250 to 500 nm by collisional ionization estimates (Tut 2006, Özbek 2012), and the dispersed energy will then be transported as hot electrons to the top surface for release back into a vacuum and reaccelerated. Silicon also plays an important role as a mechanical substrate having half the thermal expansion of AlGaIn. Upon cooling from deposition, the AlGaIn epilayer remains under tension, and if it does not rupture after the substrate is etched through, it remains under tension as a freestanding film. The material must be protected from gross puncture contact and handled with more care than a typical wafer.

Multiplier Construction

Before fabrication could begin, we required more specific electrode design for bonding and sealing as well as for making electrical contact after assembly to

operate the PMT. Because the PMT is a stack of three to seven wafers bonded together to seal the vacuum within, we paid great attention to the arrangement of contacts, insulation, and sealing mechanisms, particularly to the backsides of the multiplier wafers. For each wafer, there must be two conductors, one on either side of the epilayer (but both on the top surface). They must remain distinct when the wafers are bonded together, so the backside of the adjacent wafer must hold the electrodes that bond to the mating epilayer. Because the electrodes are vertically attached, however, there is no space for typical wire bonding; the electrodes must extend to the edge of the assembly without being vertically obstructed. Therefore, each wafer includes large etched “vias,” in addition to the vacuum passages, that reveal the underlying stacked electrodes. These will be edge contacted after the device is segmented from the wafer. Figure 2 illustrates electrodes on the backsides of wafers and etched vias; note that the electrode geometry must be offset when they are stacked. We designate this left and right offset symmetry as “even” and “odd,” respectively, referring to the dynode number. Following the bonding step, the device is separated by dicing. The lighter region bounding the device indicates a dicing perimeter.

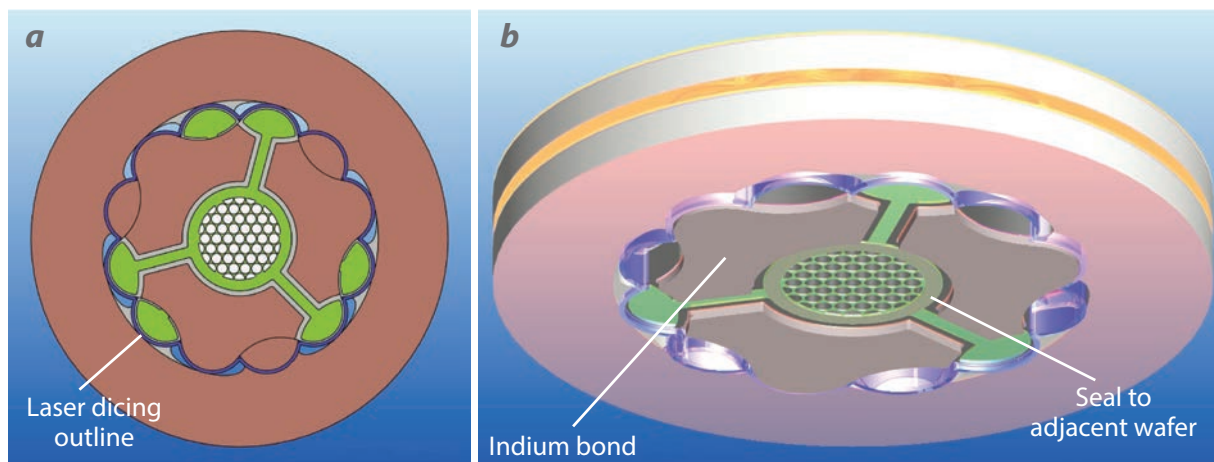


Figure 3. (a) “Even” and “odd” stacked dynodes showing the tip of each lobe that will remain unbonded and accessible to external circuitry. The purple outlines indicate the cutting path for laser dicing. (b) A 3-D view of the stacked dynodes showing the thick indium sealing metal that will electrically bond to an adjoining grid and cathode. The heavy outer indium provides a strong mechanical support while the inner indium ring provides the vacuum seal to the emission epilayer. A silicon nitride insulator (not shown) covers and surrounds the green electrode separating the two indium regions.

Figure 3 shows the resulting stack of two such wafers and four distinct electrodes. The stacking can be repeated alternately with even and odd symmetry. The 3-D view illustrates the indium sealing metal that is deposited on the electrodes on the backsides of the wafers and forms an electrical and mechanical bond. In this way, many highly precise PMTs can be fabricated as one unit and then segmented with a laser dicing process (Figure 4). One downside to the even and odd symmetry is a need for duplicate mask sets, as we cannot simply flip them over. To save some cost, we limited our anode to be of the even symmetry only, and as a result, we always have an odd total number of dynodes, one, three, or five. In total, about

19 masks were designed and fabricated for all steps of the lithography. If the design process is repeated for a different geometry, this nonrecurring engineering reoccurs, but otherwise, the cost of running more wafers of the same geometry is quite inexpensive. The fabrication cost of repeated runs becomes much less expensive than a typical high-end PMT today.

In all, we set out to fabricate nine multiplier wafers (Figure 5) with some variation in epilayer thickness: five at 500 nm thickness and four at 250 nm. We initially considered three epilayer thicknesses, 250, 500, and 1000 nm, and wanted three of each, not knowing whether thin material would be mechanically strong enough to be suspended over the etched hole,

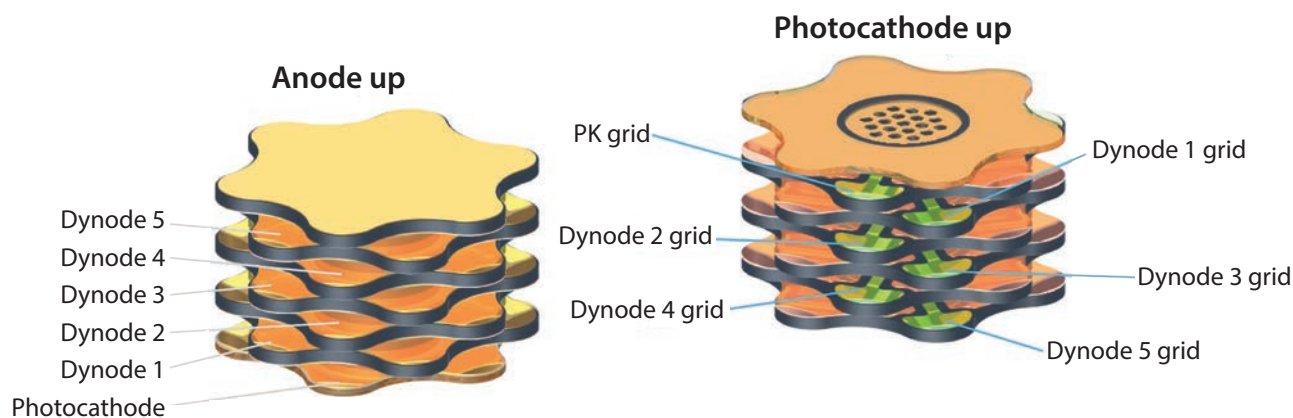


Figure 4. Vertically scaled view of a 5-dynode stacked wafer PMT device, with views from the anode and photocathode. Actual thickness is just 2 mm, and device diameters range from 3 to 24 mm. The largest is about the size and shape of a quarter-dollar coin. Electrode attachment can be single-sided or dual-sided multilayer flex circuitry.

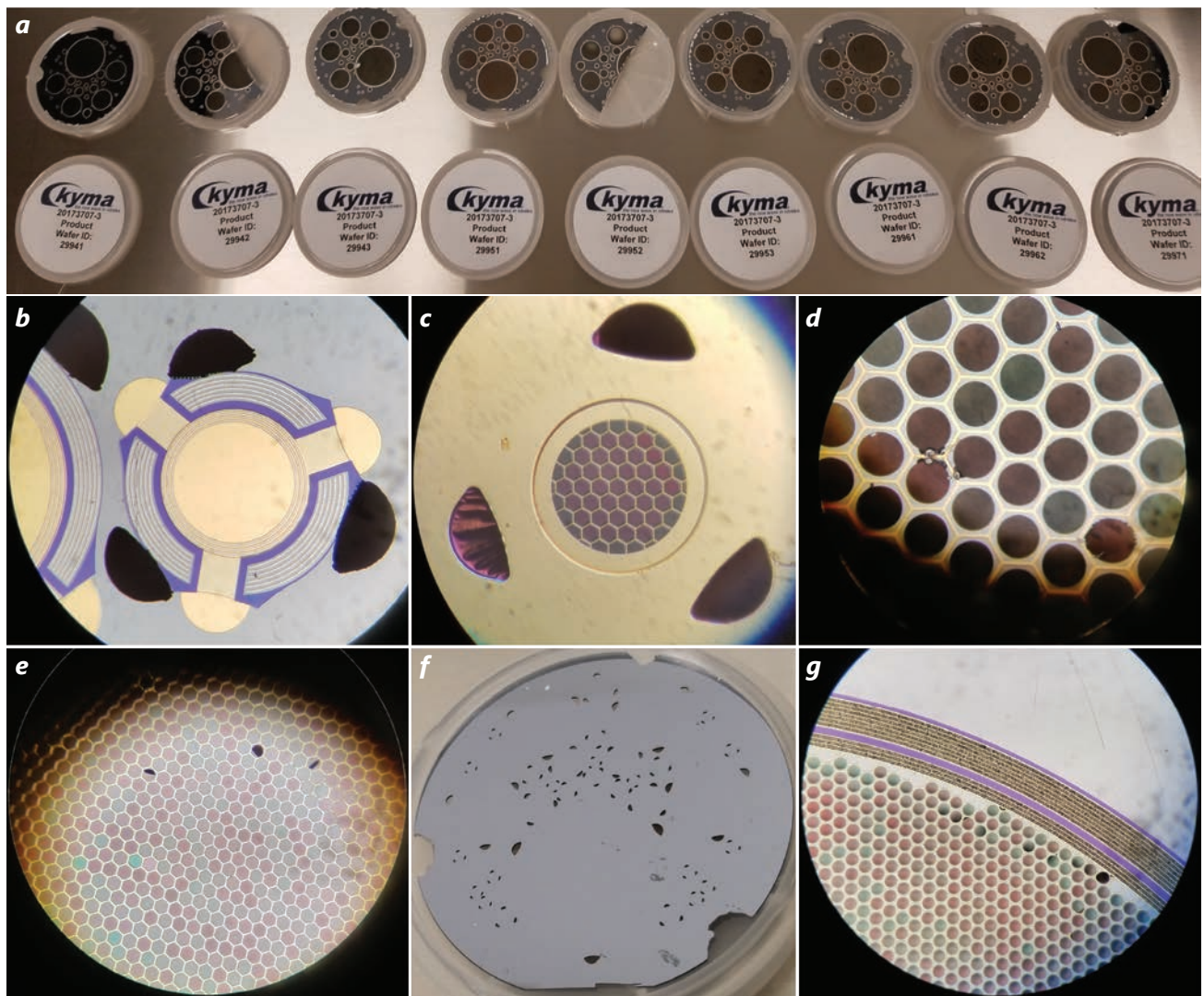


Figure 5. (a) Nine photomultiplier wafers were fabricated, each revealing the 20, 10, 4, 2, and 1 mm devices with representative close-up views through a microscope of (b) 1 mm anode device showing electrodes, silicon nitride insulators (purple), indium rings, and vias; (c) mating multiplier to (b); (d) backside view of a large device illustrating circular etched holes in the silicon with the suspended epilayer beyond (color variation indicates optical interference and slight thickness variation in the suspended material); (e) topside view of the same large device showing very few punctures (worst case); (f) mechanical engineering sample showing all of the vias across the whole wafer and three precision alignment notches along the perimeter; and (g) bottom view of a large device along the mesa edge showing the upper indium vacuum seal and lower indium electro/mechanical joint. Overall, the backside etching of the vacuum free-space paths was highly successful, and the slight defects should not prohibit assembly and operation.

but we also worried about the growth stability of AlGa_N on the non-native silicon substrate. Indeed, initial trials showed that an epilayer with a thickness of 1000 nm developed too much stress and cracked. But surprisingly, both 250 and 500 nm epilayers remained intact after etching. In fact, there are very few punctures noted in the many thousands of suspended epilayers fabricated, and we expect that they will still be functional devices.

Some other defects included slight burning of the photoresist, which damaged some areas of the bottom metal mesh around the etched holes and the indium lines that are used for bonding. The advantage of having several devices means that some yield loss can be tolerated, and we expect some of these defects will have no effect on assembly, yet successful operation remains to be seen. Two wafers were fully cracked in half (the first two) due to excessive heat rate in

one of the process steps, but this error was not repeated on the subsequent wafers. Unfortunately, we had no extra materials, so we lost two of the more-needed odd multipliers, but devices on them are still useful for wafer-level studies. Therefore, we have but four odd and three even multipliers, which will allow us to make two 3-dynode assemblies and have one even multiplier left over.

We also considered the dependence of the NEA surface chemistry (aside from cesiation) in three of the samples (two 500 nm and one 250 nm) by depositing a 2 nm layer of AlN (~4 atoms) over the AlGaN. It is energetically unfavorable having an abruptly higher band gap, but it is intended to be a thin barrier to favor the hot electrons, while perhaps exhibiting greater extinction of the dark current and reduced surface oxidation in the weeks or months leading up to sealing. We expect the NEA layer formation may possibly supply a small reservoir of free electrons near the surface; if successful, this method could be an alternative to delta doping. We need more odd wafers to explore this aspect of the multiplier, independent of thickness.

In addition to these multiplier wafers, we obtained four anode wafers that are geometrically identical to an even multiplier, but they have no epilayer or vacuum passage etchings, just the base metal electrode. Several mechanical test articles were also acquired for alignment trials and commissioning of the cesiation chamber. We obtained six even multiplier replicas showing just the vias and notches, four bare silicon wafers with notches

only, and two sapphire photocathode replicas. We will explore operation and test the deposition and wafer alignment before proceeding with a real PMT assembly.

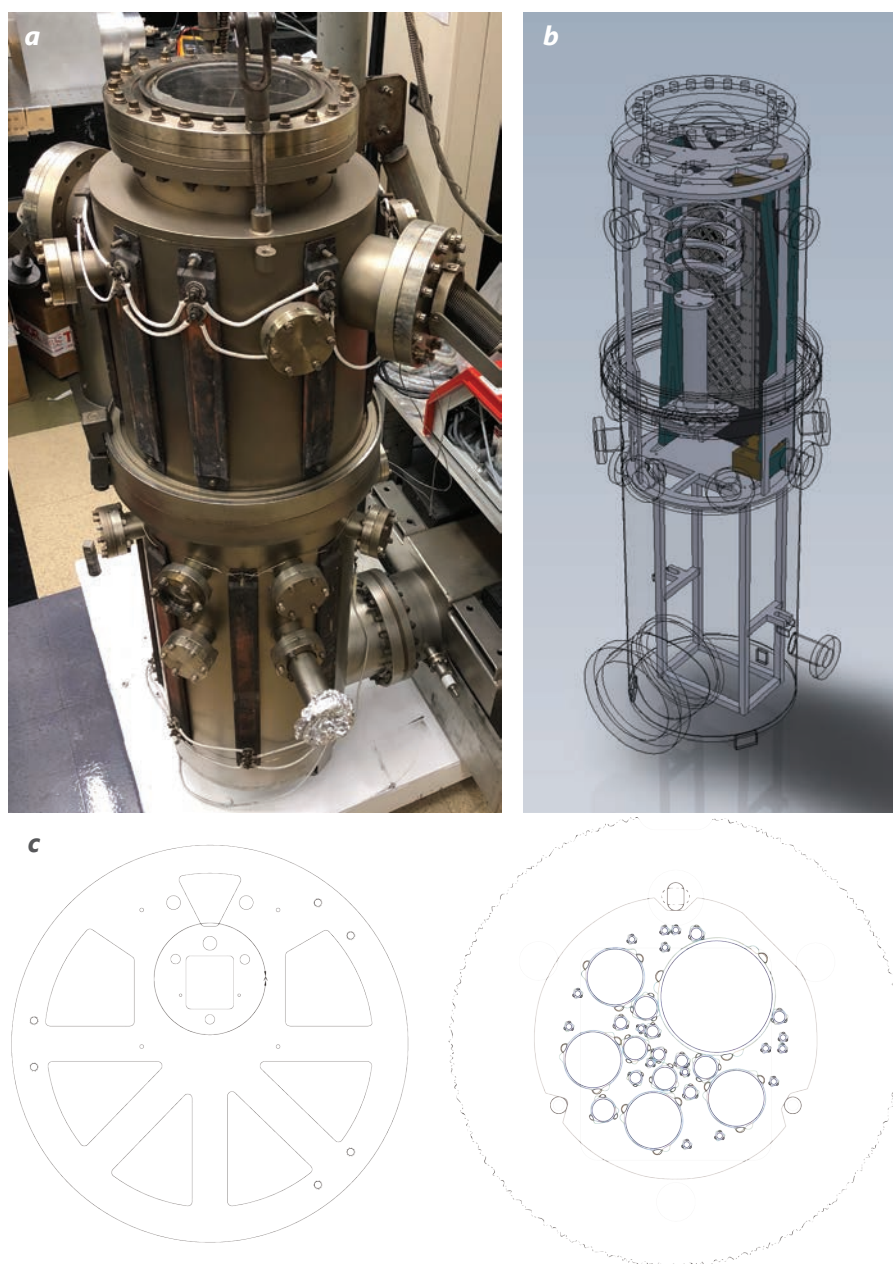


Figure 6. (a) The Varian bell jar cesium vapor deposition chamber, approximately 4' tall. (b) A transparent CAD model of the chamber showing the wafer cassette elevator and alignment plate at the top. (c) A top perspective view of the wafer alignment plate, with a zoomed-in auxiliary view of the alignment pins and a 2" diameter wafer stack. The bullet-nosed pins allow up to 2 mm gross misalignment, and when rotated into position they will align the wafers to within 2 μ m tolerance set by the notches in the wafers. The drive ball screw, gearbox, and ultrahigh vacuum rotary coupling are not shown in the lower section.

PMT Assembly

Much of the latter half of the project was spent producing the assembly fixtures for stacking and aligning the wafers within the cesium chamber. The operation is much like a typical “wafer cassette” robotic handler that manipulates wafers within a vacuum system. However, we could not afford the sophistication of such a device, nor would it be appropriate for the high-temperature process of cesium vapor deposition at 300°C. Instead, we designed a simpler platform and carriage for mounting the wafers with 1” spatial separation for vapor deposition, and an “elevator” for bringing the wafers together. Details of the deposition process are beyond the scope of this report, and the deposition process has yet to be performed; however, we have assembled a precision cesium dispenser drawing on the work of Dr. Ursel Fantz of the Max Planck Institute (Fantz 2012). Following deposition, the system is pumped back down to ultrahigh vacuum, and a linear stage rises up through the wafer stack in an elevator-like manner, stopping at each platform to captivate the wafer before moving up to the next “floor,” thereby entraining each wafer in a coarsely aligned stack. When it reaches the ceiling, which contains the alignment pins, we manipulate the stack into alignment.

Figure 6 shows the Varian bell jar vacuum system used at Livermore Operations for more than 30 years of prototype bialkali photocathode production. We have retrofitted it with the wafer cassette elevator and updated its thermal controls with modern process controllers, heaters, and the precision cesium dispenser. In preparation for precision alignment, we have etched into the silicon wafers three alignment features: one notch as a pivot and two flats, which will mate to precision registration pins in the fixture. Two of the pins are static and slide into the notch and a flat in the wafer, while a rotating elliptical pin contacts the second flat and presses the whole stack into alignment against the other two. The actuation forces are magnetic, small, and persistent, with the only moving part being the rotating pin.

We manipulate the stacks manually using linear/rotary “wobble sticks” that can be configured for a variety of tasks such as pulling, pushing, and twisting. The moving stage parts and wobble sticks are special in that no wet lubricants can be used, and dry tungsten disulfide coatings are used for reducing friction. Nothing is outgassed, especially at high temperature, and no vacuum penetrations are made with O-rings or fluid bearings; only hard metal seals and magnetic coupling on the rotary/linear actuators are used. This

rigor is necessary to achieve the ultrahigh vacuum level below 10^{-10} Torr. The linear stage is thus a custom commercial product with all-metal high-temperature parts. After we worked with a vendor to establish design specifications and order the needed parts, the vendor informed us that it would be unable to fabricate the stage due to shortages of labor and parts. But ultimately the expertise we gained through this process encouraged us to make our own stage, mostly composed of COTS materials. We have procured most of the parts (bearings, slides, and gears), fabricated most of the fixtures, and obtained two ultrahigh vacuum linear/rotary wobble sticks from the Kurt J. Lesker Company. We examined the potential of adapting another commercial vacuum stage, but the plastic parts and bearings in it would need re-engineering, so it was simpler to start from other commercial components and design the custom platform.

At the time of this publication, the stage is fully designed and final custom parts are nearing fabrication. Under programmatic funding, the Detector Engineering group will support commissioning the wafer alignment elevator and cesium deposition chamber. Our goal is to assemble the first prototype crystalline mesh PMT in FY 2019. Much of the assembly, already underway, is occurring via an executed subcontract with the University of Nevada, Las Vegas (UNLV) and the Nevada Nanotechnology Center. Other details of photoemission and multiplier gain measurements also continue at UNLV, but in lieu of cesium activation, which must remain at ultrahigh vacuum, the inactivated samples are difficult to measure; we await the fully sealed PMT as the most expedient proof of concept.

CONCLUSION

In the third year of this project, we completed the fabrication of the prototype AlGaIn multiplier wafers and demonstrated that a suspended 250 nm thick epilayer can indeed be fabricated. This is the critical element of the crystalline mesh PMT, a necessary component for a high-gain photomultiplier, and crucial to supplant high-quality vacuum tube technology. Several mechanical engineering challenges were overcome in the design of wafer-inclusive electrodes, electrical insulation, cesium activation, precision stacking alignment, and indium ultrahigh vacuum sealing. These efforts will allow very high-bandwidth attachment in a waveguide structure without bond wires. Such direct wafer-level

device engineering has only been implemented for MEMS [microelectromechanical systems] devices at partial vacuum, and ours will be one of the first all-semiconductor vacuum electron devices. The SDRD project has been transferred to programmatic funding through detector engineering work for the complete proof-of-concept device. A provisional patent for this work has been secured.

ACKNOWLEDGMENTS

We would like to thank Dr. Jacob Leach and Kyma Technologies, Inc., in Raleigh, North Carolina, for their expertise in III-nitride growth and custom device fabrication. They were instrumental in helping us resolve the electromechanical challenges of wafer stacking.

REFERENCES

- Buckles, R., K. Crawford, K.-X. Sun, P. O’Gara, “Next-generation photomultiplier detectors using transmissive III-nitride semiconductor electrodes,” in *Site-Directed Research and Development*, FY 2016, National Security Technologies, LLC, Las Vegas, Nevada, 2017, 59–68.
- Buckles, R., K.-X. Sun, “Next-generation photomultiplier detectors using transmissive III-nitride semiconductor electrodes,” in *Site-Directed Research and Development*, FY 2017, National Security Technologies, LLC, and Mission Support and Test Services, LLC, Las Vegas, Nevada, 2018a, 61–67.
- Buckles, R. A., I. Garza, J. N. Bellow, K. J. Moy, G. A. Chandler, C. L. Ruiz, B. M. Jones, “Superlinearity, saturation, and the PMT–Tailoring and calibration methodology for prompt radiation detectors,” *Rev. Sci. Instrum.* **89** (2018b) 10K122.
- Fantz, U., R. Friedl, M. Fröschle, “Controllable evaporation of cesium from a dispenser oven,” *Rev. Sci. Instrum.* **83** (2012) 123305.
- Özbek, A. M., “Measurement of impact ionization coefficients in GaN,” PhD dissertation, North Carolina State University, 2012.
- Tut, T., M. Gokkavas, B. Butun, S. Butun, E. Ulker, E. Ozbay, “Experimental evaluation of impact ionization coefficients in Al_xGa_{1-x}N based avalanche photodiodes,” *Appl. Phys. Lett.* **89** (2006) 183524.



Adaptive Source Localization Using Augmented Reality

RSLN-024-18 ■ Year 1 of 1

**James Essex,^{1,a} Colin Okada,^a Aaron Podovich,^a Michael Reed,^a
Avery Guild-Bingham,^a and Dan Haber^a**

¹essexjj@nv.doe.gov, (702) 295-8714

^aRemote Sensing Laboratory–Nellis



We have developed a proof-of-principle platform that demonstrates radiation measurement mapping in a GPS-denied environment. We integrated 30 Hz position and orientation information from a Microsoft HoloLens augmented reality (AR) headset with 1 Hz radiation measurements from four detectors, leveraging the spatial awareness capabilities of AR to develop a new anomaly detection, filtering, and adaptive source localization software pipeline that allows several algorithms to simultaneously compute the predicted location of a radiation source at 1 Hz and render a holographic representation of the source in real-world coordinates.

BACKGROUND

The ability to quickly and accurately locate a radioactive source is a desired capability for multiple missions. Existing backpack-based radiation systems can be improved through refinement that allows for faster delivery of analysis and visualizations to a sensor operator. Current systems have several shortfalls. They (1) use 1-D anomaly detection algorithms and a temporal data stream to determine a threat by evaluating data from the past against the most current measurement, (2) do not collect location-based data in GPS-denied environments, (3) are not orientation aware and do not remove signal attenuation by the operator from analysis, (4) do not provide the operator an estimate of the source location, and (5) are not dynamic and do not autonomously adapt

the algorithmic approach based on the constraints of data collection.

Methods of performing localization of radiation sources by using multiple measurements or multiple sensors are documented in the literature. However, localization implementations are not widespread because they require permanent installation of the sensors (Liu 2010), current spatial mapping technologies used within transient operations have fidelity limitations (Baidoo-Williams 2013), the sensor location must be manually registered (Vilim 2011), or processing capabilities and computing latency are operational constraints. Additionally, all localization algorithms are affected by not only the number or geometrical distribution of measurements and detector event averaging, but also background noise, which has not been accounted for by past researchers.

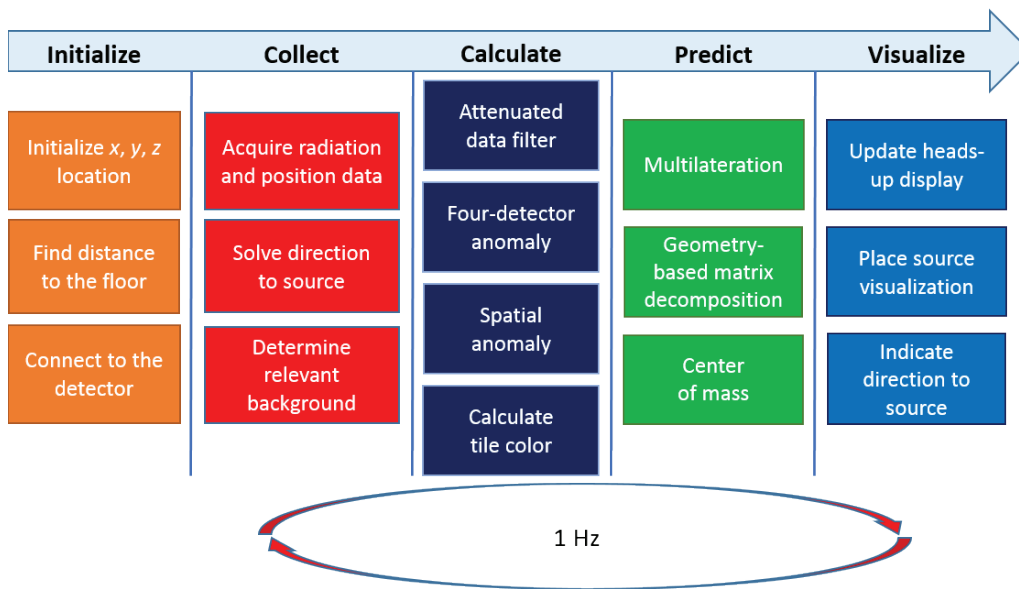


Figure 1. Overview of the software architecture running on the HoloLens CPU

PROJECT

We integrated the positional awareness and visualization capabilities of an augmented reality (AR) platform with a radiation sensor, thereby allowing field operators to visualize radiation. The AR platform acquires data from a multi-detector backpack system and uses positional data to compute the location and intensity of a radiation source. The software performs multiple other novel functions including spatially aware anomaly detection and filtering to remove operator-attenuated data from the localization calculation. Individual software elements, broken into five subcomponents, are initialize, collect, calculate, predict, and visualize (Figure 1).

We initially evaluated three different detection systems, each having either one, two, or four sodium iodide (NaI) crystal detectors. We chose the four-crystal design because it allows for a 1 Hz calculation that indicates the direction to highest count rate relative to the direction the operator is heading (i.e., operator’s heading). The detection system is composed of four 2" × 2.5" × 8" NaI crystals with individual multichannel analyzers capable of 3 MeV resolution in 1024 channels. The controller was modified in such a way that it allows a custom data package to be output via USB at 1 Hz. We developed a separate microcontroller that ingests the data from the USB and outputs the data over wireless with only a few milliseconds of lag. The HoloLens, connected to the microcontroller, ingests and decodes the binary data package once per second.

When the HoloLens is first turned on, it uses built-in infrared emitters and scanners and a depth camera to locate the distance to the floor. The data from these sensors provide the ability to precisely track movement of the headset/operator. Once the floor is found and the coordinate system is initialized, the software tracks the movement of the operator and renders a holographic tile on the floor each time the operator changes position by 0.25 m.

The software tracks all measurements in either a background buffer or an anomaly buffer. Measurements that do not trip either of the two anomaly algorithms are placed in the background buffer. If the current measurement is determined an anomaly, it is placed into the anomaly buffer but only if it passes the attenuation filter (Figure 2). The

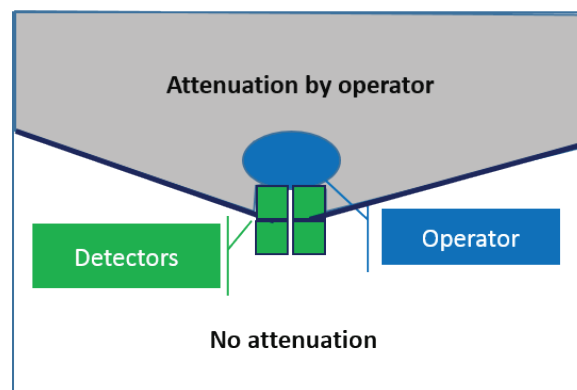


Figure 2. A graphic representation of the attenuation filter. If the direction of highest count rate is in the gray area, the data are not included in the localization calculation.

filter ensures that the measured values are clean measurements of the source and do not include attenuation by the operator.

Anomaly Detection

Two separate anomaly detection routines are running simultaneously. The spatial anomaly routine retrieves any previously collected background data in a ring around the current measurement. Relevant background data are considered to be at least 5 m from the current location and not greater than 10 m. We use these data to calculate the average and standard deviation of background and to compare to the current measurement. Leveraging previously collected background data for anomaly detection improves the background estimate and decreases the probability of a false positive.

An instantaneous anomaly detection algorithm leverages the self-occluding geometry of the detectors and uses the gross count differences in the four detectors as a metric of when a source is present. The sensitivity of this algorithm is more pronounced for low-energy gamma photons where attenuation by the detectors is higher, and it is also valuable when the operator is stationary or insufficient background has been collected.

Source Localization Predictions

All prediction algorithms implemented and tested use multiple measurements to perform source localization. Multilateration solves a system of equations based on radiation transport models and uses position and summed gamma gross count values. To achieve accurate solutions to multilateration localization, we have to filter out data where the operator was between the source and the detectors. The second method is a geometric least-squares decomposition that uses position and calculated angle. The third method uses a center-of-mass algorithm to localize but requires measurements on multiple sides of the source.

We performed initial verification of prediction calculations by outputting a log of all data collected and comparing predictions to the actual source location. With additional work, we can select and reject measurements more intelligently and implement a best-fit metric in the real-time system.

Multilateration

Given multiple measurements with detectors of similar response, but at different known locations, we want

to determine the location and strength of an unknown source.

$N = 5$ Measurements to Locate One Source

For an individual detector at location (x_i, y_i, z_i) , the counts in the detector from the source will be

$$N_i = \frac{A\varepsilon\rho}{(x_i - x)^2 + (y_i - y)^2 + (z_i - z)^2}, \quad (1)$$

where A is the unknown activity in becquerels, ε is the detector efficiency at 1 m, ρ is the gamma ray production per decay, and the unknown location of the source is (x, y, z) . This can be rewritten as

$$x_i^2 + x^2 - 2xx_i + y_i^2 + y^2 - 2yy_i + z_i^2 + z^2 - 2zz_i - \frac{A\varepsilon\rho}{N_i} = 0. \quad (2)$$

If there are two locations, we can subtract these expressions to remove the quadratic dependence on the unknown location.

$$\begin{aligned} 2(x_i - x_j)x + 2(y_i - y_j)y + 2(z_i - z_j)z - (x_i^2 - x_j^2) \\ - (y_i^2 - y_j^2) - 2(z_i^2 + z_j^2) + A\varepsilon\rho\left(\frac{1}{N_i} - \frac{1}{N_j}\right) = 0 \\ 2(x_i - x_j)x + 2(y_i - y_j)y + 2(z_i - z_j)z \\ - (R_i^2 - R_j^2) + A\varepsilon\rho\left(\frac{1}{N_i} - \frac{1}{N_j}\right) = 0 \\ a_{ij}x + b_{ij}y + c_{ij}z + d_{ij}A + e_{ij} = 0, \end{aligned} \quad (3)$$

with

$$\begin{aligned} a_{ij} &= 2(x_i - x_j), \\ b_{ij} &= 2(y_i - y_j), \\ c_{ij} &= 2(z_i - z_j), \\ d_{ij} &= \varepsilon\rho\left(\frac{1}{N_i} - \frac{1}{N_j}\right), \\ e_{ij} &= -(R_i^2 - R_j^2), \text{ and} \\ R_i^2 &= x_i^2 + y_i^2 + z_i^2. \end{aligned} \quad (4)$$

We now have a linear equation with four unknown variables (x, y, z, A) . If there are three more

measurements at three more locations, using the same process as shown above, we can obtain four linear equations with four unknown quantities. We can determine the unknown quantities by solving the system of four equations with elimination.

***N* > 5 Measurements to Locate One Source**

If there are more measurements than unknown variables, the system is over-constrained, and the solution is determined by least-squares minimization. First, compute the square

$$\sum_{i \neq j} (a_{ij}x + b_{ij}y + c_{ij}z + d_{ij}A + e_{ij})^2 = 0. \quad (5)$$

Next, take the derivative with respect to the unknown variables (x, y, z, A) to arrive at the coupled linear equations

$$\begin{aligned} \langle a_{ij}a_{ij} \rangle x + \langle a_{ij}b_{ij} \rangle y + \langle a_{ij}c_{ij} \rangle z + \langle a_{ij}d_{ij} \rangle A \\ + \langle a_{ij}e_{ij} \rangle &= 0, \\ \langle b_{ij}a_{ij} \rangle x + \langle b_{ij}b_{ij} \rangle y + \langle b_{ij}c_{ij} \rangle z + \langle b_{ij}d_{ij} \rangle A \\ + \langle b_{ij}e_{ij} \rangle &= 0, \\ \langle c_{ij}a_{ij} \rangle x + \langle c_{ij}b_{ij} \rangle y + \langle c_{ij}c_{ij} \rangle z + \langle c_{ij}d_{ij} \rangle A \\ + \langle c_{ij}e_{ij} \rangle &= 0, \text{ and} \\ \langle d_{ij}a_{ij} \rangle x + \langle d_{ij}b_{ij} \rangle y + \langle d_{ij}c_{ij} \rangle z + \langle d_{ij}d_{ij} \rangle A \\ + \langle d_{ij}e_{ij} \rangle &= 0; \end{aligned} \quad (6)$$

the equations are solved using elimination to get the unknown quantities.

Geometric Decomposition

A technique similar to the multilateration routine would incorporate three or more source direction projections to determine the source location. After the important relevant source projection vectors have been identified, the source is localized in XY space by means of a generalized least-squares fit function. First, determine the equation of line associated with each vector in the form of

$$y = m_i x + b_i \text{ for } i \in (1, n). \quad (7)$$

After these series of equations are determined, we can determine the convergence point by solving the system of equations where $AX = b$ and

$$A = \begin{bmatrix} 1 & -m_1 \\ \vdots & \vdots \\ 1 & -m_n \end{bmatrix}, b = \begin{bmatrix} b_1 \\ \vdots \\ b_n \end{bmatrix}, \text{ and } X = \begin{bmatrix} y_0 \\ x_0 \end{bmatrix}. \quad (8)$$

We can rearrange this equation to have a unique solution in the following form

$$\begin{bmatrix} y_0 \\ x_0 \end{bmatrix} = (A^T A)^{-1} A^T b, \quad (9)$$

and it can be weighted by an arbitrary scalar (W) by

$$\begin{bmatrix} y_0 \\ x_0 \end{bmatrix} = (A^T W A)^{-1} A^T W b. \quad (10)$$

The initial weighting is based on gross gamma counts but can also be weighted according to a spectral-based alarm in real time.

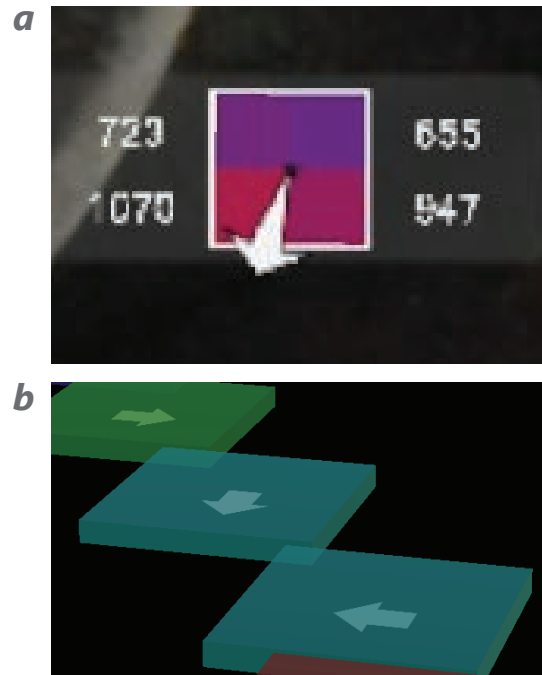


Figure 3. (a) A snippet from the heads-up display, which renders a directional indicator pointing in toward the highest radiation (down = behind the operator). (b) An example of holographic tiles with arrows in real-world coordinates, pointing toward the source.

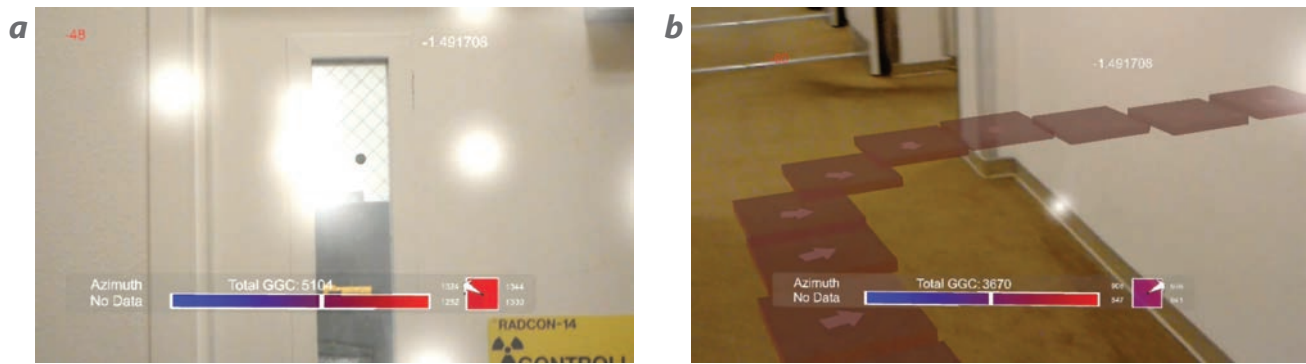


Figure 4. (a) A view through the HoloLens that shows the predicted source location as a holographic orb with white holographic photons streaming off the object. (b) The tile placement as the operator walked around a corner and then turned back around to observe the path. Note that the arrows are pointing in the direction of elevated counts.

Center of Mass

Using spatial clustering of data points, one can estimate a source location with a center-of-mass estimation approach on that cluster set. An estimated source location can be determined by the weighted sum of net counts multiplied by the relative position recorded by the HoloLens. Dividing that result by the net counts over the spatial data cluster would yield the source location estimate or center of mass as demonstrated in Equation 11,

$$x_s = \frac{\int w_i x_i dA}{\int w_i dA}, y_s = \frac{\int w_i y_i dA}{\int w_i dA}, \quad (11)$$

where (x_s, y_s) are the estimated relative source coordinates, and w_i is the weight function based on either net counts or an alarm algorithm. This method has the advantage of numerical simplicity, and can be used in conjunction with a spectral alarm algorithm that would have a low weight function for counts due to elevated background or naturally occurring radioactive materials (NORM). Source estimates resulting from a low total weight function can be rejected, thereby preventing false source location indications. The method is robust and has high accuracy for isotropic sources that are within the detectable distance of the detector, assuming that the detector path bounds the source on at least two sides. A drawback of this implementation is that the source location can only be estimated within a region bounded by the source path. Because of this limitation, the source location will be estimated on the edge of a bounded region. We need to use other methods to project the source location outside a bounded spatial cluster.

Visualization

Each time a tile is rendered, the direction to the source is determined by the use of the most recent radiation data from the four detectors. We can determine this direction via trigonometry using the gamma gross count values of each detector to return an angle θ such that $-\pi < \theta \leq \pi$. With this information and the operator's heading, the angle to the highest count rate can be calculated. We use the angle to render an arrow in the heads-up display and to place a directional indicator on the tile (Figure 3). The tile color is assigned based on a continuously updated Jenks optimization method designed to minimize each class's average deviation from the class mean.

With the source location calculated, the software renders a holographic object representing the source at the predicted location; as new data are collected and the estimate is refined, the predicted location is updated. A holographic representation of photons also streams from the source location and is a visual cue for the operator that a source has been found (Figure 4).

CONCLUSION

Even the most robust laptop, tablet, or mobile visualization software frequently falls short of triggering appropriate responses in a sensor operator. AR will solve many of the existing shortfalls by enabling persistent and dynamic visualization of sensor response as an overlay in real-world dimensions. It will also allow completely new ways to efficiently fuse multiple data streams and consume complex analysis in real time.

We have demonstrated radiation measurement mapping and source localization by integrating detector responses, analysis, and meaningful visualization in GPS-denied settings. We have integrated 30 Hz position and orientation information from an AR headset with 1 Hz radiation measurements from four detectors. We leveraged the spatial awareness capabilities of AR to develop a new anomaly detection, filtering, and adaptive source localization technique that allows several algorithms to simultaneously compute the predicted 2-D location of a radiation source at 1 Hz and render a holographic representation of the source in real-world coordinates.

Advancing this capability has the potential to equip overt radiological/nuclear search teams with a hands-free, intuitive visualization capability, enabling localization in rooms or buildings without access, such as apartment complexes, office spaces, or high-rise buildings, and reducing the time to find a potential threat in large venues, such as warehouses, parking garages, or maritime container ships.

ACKNOWLEDGMENTS

We would like to thank Terry Smith, Mark Norsworthy, Krikor Hovasapian, and Steve Carragher for their contributions to this work.

REFERENCES

- Baidoo-Williams, H., S. Dasgupta, R. Mudumbai, E. Bai, "On the gradient descent localization of radioactive sources," *IEEE Signal Process. Lett.* **20**, 11 (2013) 1046–1049.
- Liu, A. H., J. J. Bunn, K. M. Chandy, "An analysis of data fusion for radiation detection and localization," *2010 13th International Conference on Information Fusion*, Edinburgh, 2010, 1–8.
- Vilim, R., R. Klann, J. Thomas, "Integrated treatment of detector arrays for source tracking," *Nucl. Technol.* **175**, 1 (2011) 314–325.



Man-Portable Dense Plasma Focus for Neutron Interrogation Applications

NLV-009-17 ■ Year 2 of 3

**Brady Gall,^{1,a} Michael Heika,^a Michael Blasco,^a Joseph Bellow,^a
Bernard T. Meehan,^a Vincent DiPuccio,^a Adam Wolverton,^a
James Tinsley,^b and Nichelle Bennett^c**

¹gallbb@nv.doe.gov, (702) 295-3117

^aNevada Operations

^bSpecial Technologies Laboratory

^cSandia National Laboratories



A small dense plasma focus (DPF) neutron generator was designed and tested in support of Threat Reduction Science and Technology's active interrogation applications. These applications require a portable, high-output neutron-generating device to enable the reliable detection of clandestine special nuclear materials in remote or emergency response settings. The system developed thus far in this three-year research endeavor successfully demonstrated that DPF technology is a viable path toward this capability. It produces an average of 2.5×10^7 neutrons per pulse using pure deuterium fuel and can be operated with a 5-second repetition rate. The DPF weighs approximately 50 lb and is compatible with standard utility hookups and battery power. This report details the design and optimization of the DPF plasma source geometry and the construction and test results of a tabletop pulsed-power test stand to drive the DPF neutron source. A third year of this project will continue to improve the portable DPF source and make the device ready for further testing. We are particularly interested in how well we can detect highly enriched uranium using the portable DPF as an interrogating neutron source and the Sandia National Laboratories' mobile imager of neutrons for emergency responders as the sensing instrument.

BACKGROUND

The dense plasma focus (DPF) device has long been considered an inexpensive, compact source for pulsed

neutrons (Mather 1964, 1965; Bernard 1977), and it is currently being explored for a range of applications from activation analysis and plasma nanotechnology to radiography and material detection (Gribkov 2006,

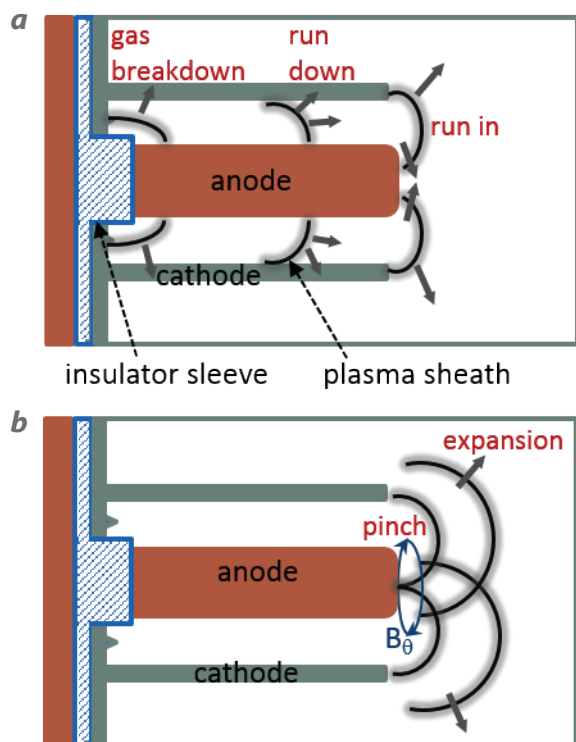


Figure 1. The DPF operation phases. During the gas-breakdown phase, the voltage pulse is injected through the insulator sleeve (blue), and a plasma sheath (black) is formed between the anode tube (brown) and the cylindrical cathode (gray). This sheath is accelerated axially during the run-down phase and radially during the run-in phase. After the pinch phase, the plasma expands radially and axially to the outer cathode.

Zhang 2007, Hussain 2010, Krishnan 2012, Rawat 2013). Recent development of the DPF has focused on increasing the device's portability and pulse repetition rates (Lee 1998, Rapezzi 2004, Shukla 2015, Niranjana 2016). The goal of this project is to leverage these advances in portable pulsed-power technology, along with existing expertise in large-scale DPF systems at the NNSS, to build a new, compact device capable of meeting the needs of Threat Reduction Science and Technology's neutron-based programs, including nuclear search, warhead confirmation and monitoring, and render safe (Office of Defense Nuclear Nonproliferation 2018). These programs involve inspecting an object suspected to contain special nuclear material (SNM) using gamma or neutron radiation fields. By examining the response products emitted from the object, we may ascertain its internal composition and configuration. For many reasons, it is not practical for test objects to be shipped from multiple locations to a central location for inspection.

Instead, we need a reliable, high-flux neutron source that can be brought to the object's location. The source must produce at least 10^6 neutrons per second, be reasonably portable and rugged, and be simple to operate (NNSS 2016). Such a source would enable us to accomplish these mobile applications.

Compact neutron source technology is a mature field of research, and many options are available as COTS devices. Some systems, such as the Adelphi DT108API, operate in continuous mode, while others, such as the Thermo Scientific MP 320, produce microsecond-scale bursts of neutrons at a high repetition rate. Both continuous and pulsed modalities can be used for SNM detection, but pulsed sources offer additional functionality; of special interest to us is their ability to measure target-generated gamma die-away from fission multiplication, which augments the capability of an SNM-sensing platform. Short pulses increase the fidelity of this measurement and are therefore preferable for this application. The DPF can produce pulses up to 10,000 times shorter than the MP 320 neutron generator and maintain a comparable time-average neutron flux. Furthermore, DPF systems can be made quite compact, enabling mobile operation. With the ability to generate high-amplitude, short-pulse-width neutron fields in a readily transportable form factor, DPF technology is an ideal candidate for portable active interrogation applications.

PROJECT

This project is a three-year investigation to design and build a portable DPF for defense nuclear nonproliferation applications. Last year we designed a new DPF plasma source geometry, procured compact high-voltage hardware, developed control system software, and assembled and tested a tabletop pulsed power driver (Gall 2018). This year we fabricated the new DPF plasma source, shrunk the tabletop pulsed-power driver, coupled the DPF to the pulsed-power driver, and tested the integrated system for neutron production. The result was a successful and repeatable demonstration of neutron output with an average yield of 2.5×10^7 neutrons per pulse and a pulse width of approximately 30 ns FWHM.

This report describes the work we completed in FY 2018. An overview of the basic principles of the DPF is presented, followed by a description of the mechanical design of the pulsed-power driver and plasma source. We next detail experimental configuration and diagnostics used to measure the

electrical and radiological output of the DPF and the experimental results. Future scope and goals for FY 2019 also are presented.

Dense Plasma Focus Operational Principle

The DPF device is a coaxial accelerator with a blunt anode termination that is filled with a low-density gas, typically pure deuterium or a deuterium-tritium mixture. As the accelerator is pulsed, the gas is ionized and accelerated through the $\mathbf{J} \times \mathbf{B}$ force to the end of the anode. The plasma pinches at the anode tip with sufficient velocity to create neutrons by fusion processes.

DPF operation occurs in four phases, as shown in Figure 1. The gas ionizes in the first phase with the arrival of a high-voltage pulse. This phase is called the gas-breakdown phase. The conductivity increases rapidly as the current-carrying plasma sheath is formed. As the current rises and the $\mathbf{J} \times \mathbf{B}$ force increases, the plasma sheath is accelerated to the end of the anode. This second phase is referred to as the run-down phase. The third phase, or the run-in phase, occurs after the plasma sheath reaches the end of the anode and is accelerated radially inward. The fourth phase is the pinch phase, where the plasma densities and temperatures (energies) have increased sufficiently to enable fusion reactions.

Design of the Portable Dense Plasma Focus

The dimensions and geometry of the DPF anode and cathode geometry were designed and optimized in FY 2017. The details of this design process are documented in the previous year's report (Gall 2018) but also summarized here. The simulations of the DPF were performed by the use of the fully relativistic electromagnetic particle-in-cell code, Chicago, created by the developers of LSP (Welch 2001); nine different geometries were tested. A non-comprehensive matrix of various metrics was explored, including anode length (4, 5, and 7 cm), anode terminal shape (flat, hemispherical, toroidal, and with/without a hole), gas pressure (2, 6, and 6.5 Torr), and insulator thickness (2 and 4 mm). Of these parameters, the top performer in terms of total neutron output was the 5 cm anode, hemispherical terminal with a hole, 6 Torr fill pressure, and 2 mm insulator, producing 1.1×10^8 neutrons per pulse.

Figure 2 shows a cross-sectional view of the coaxial anode and cathode configuration used for this experiment. This system used the dimensions determined from modeling for the top-performing design. The main challenge in implementing the plasma process chamber was negotiating the high-voltage penetration into the vacuum envelope. The high-voltage anode must protrude into the vacuum chamber without touching or approaching the metal walls of the chamber itself. Failure in this will lead to high-voltage breakdown in air or surface flashover, which will prevent the desired plasma process from occurring. For our experiment the anode was inserted into a hollow cylinder (insulator) made from a material with high dielectric strength, such as ceramic or glass, which then was inserted into an aperture in the vacuum chamber wall. Two to three thousandths of an inch (mil) of clearance between diameters of nested components was found to be sufficient to allow for assembly and provide O-ring compression for vacuum competence. We applied high-vacuum grease to the O-rings prior to assembly for added vacuum standoff. In addition, to reduce electrical losses, we inserted indium, a soft, conductive metal, between all metallic interfaces.

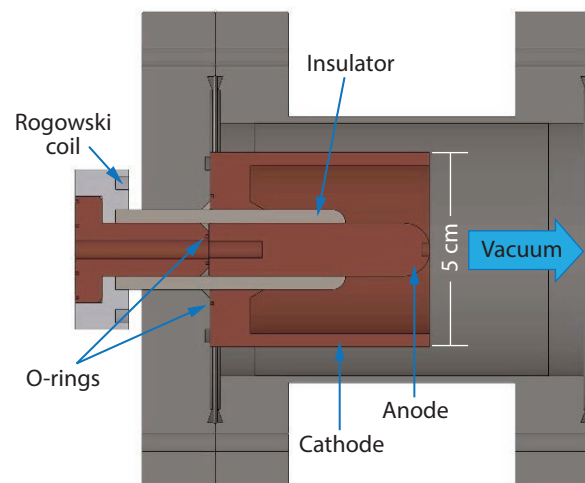


Figure 2. Diagram of DPF plasma process chamber

The vacuum chamber was a 4.5" ConFlat flange nipple custom ordered from vacuum component vendor Kurt J. Lesker Company. A ConFlat connection on one port (right side, as shown in Figure 2) provided vacuum and deuterium, and the other port held the DPF structure (left side). The anode and cathode were made of oxygen-free copper and were held in place with 6-32 bolts. We tested several insulator materials, including borosilicate glass (Pyrex), glass mica (Macor), and

boron nitride; further testing will determine the best insulator material. In general, Pyrex is inexpensive but cannot be easily machined, so each specimen can vary in radius. Macor and boron nitride can be precisely machined but are expensive. Macor is also significantly more rugged than either Pyrex or boron nitride, which is a noteworthy benefit for portable applications. The copper, glass, and ceramic materials were COTS purchases from McMaster-Carr. The Rogowski coil was held in place by a custom-designed acrylic cup we fabricated using the Formlabs Form 2 stereolithography rapid prototyping platform. Figures 3 and 4 show photographs of the assembled DPF.

Figure 5 shows the assembly of the DPF chamber coupled to the pulsed-power driver. We used a radial arrangement of six General Atomics 31150 0.5 μ F, 30 kV capacitors to drive the high-current pinch. A Pulsed Power Solutions TDI4-100k/45H cold cathode thyatron, centrally located in the capacitor bank, controlled plasma switching. To couple the DPF chamber to the thyatron, we used 1/8" aluminum plates cut to specification with a water jet cutter. A combination of Mylar sheets, Kapton tape, and Konform acrylic resin conformal coating spray was used for electrical insulation. The specifics of the control system were detailed in last year's report (Gall 2018). The control system consisted of a LabVIEW-based input/output (I/O) platform and an UltraVolt 250 W, 30 kV DC power supply.

Experimental Configuration

Figure 6 shows the experimental configuration we used to measure neutron output of the portable DPF system. A Windows PC running National Instruments (NI) LabVIEW software communicated with analog and

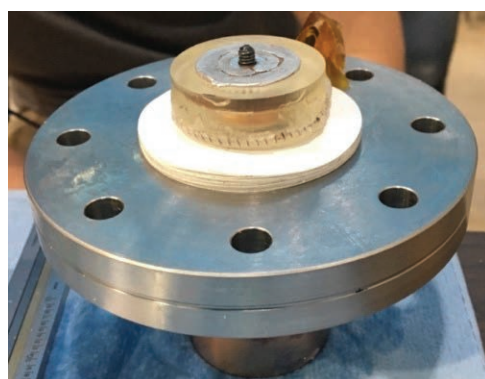


Figure 3. Power injection feedthrough for the DPF tube, showing the Rogowski coil and Mylar insulator (white disks at the chamber wall surface)

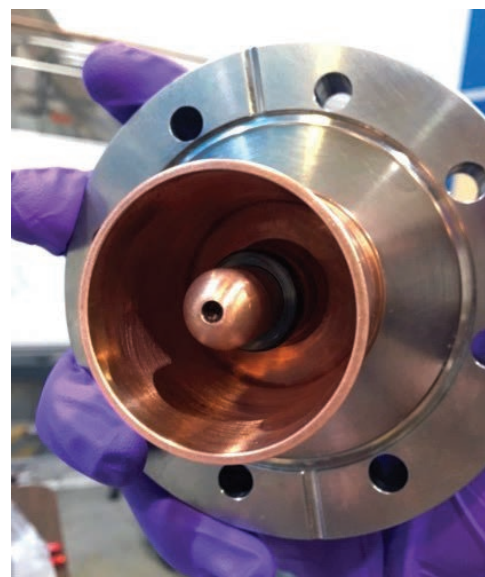


Figure 4. The assembled DPF, showing the anode, insulator, cathode, and back wall of the vacuum chamber

digital I/O channels via a fiber-optic cable with an NI digital-to-analog converter (DAC). The high-voltage charging system was operated with the NI DAC, which supplied low-level logic and relay closures. LabVIEW also controlled a Stanford Instruments DG 535 trigger generator for firing the DPF and triggering the digitizer. We installed a pair of photomultiplier tubes (PMTs) to measure the time-domain profile of the DPF radiation output. A detector consisting of a 1" diameter, 1" long Eljen EJ-232 plastic scintillator was placed 30 cm from the DPF. A second detector was placed 3 m from the source and used a paddle-shaped EJ-232 scintillator measuring approximately 15" long, 3" wide, and 1" deep. The DPF current was measured with a Rogowski coil installed at the anode of the DPF. A Teledyne LeCroy HDO6104 12-bit, 2.5 GS/s digitizer captured the PMT and Rogowski coil data, which were then transferred to the PC for analysis.

We used a silver activation detector developed at the Los Alamos Scientific Laboratory to quantify the neutron output of the DPF (Lanter 1966). The detector comprised four type 1B85 Geiger tubes wrapped with

0.01" thick natural silver foil, surrounded by a block of polyethylene moderator measuring 12" \times 12" \times 6" and encased with galvanized steel. We calibrated the detector using the 1 MJ Gemini DPF located in North Las Vegas. The detector was positioned over a range of distances from the Gemini source from 60 cm to 25 m. We determined an F-factor for each position by dividing the yield of the Gemini DPF source by the cumulative counts measured by the silver detector over a 46-second interval.

Figure 7 shows the measured F-factor over the tested positions along with two overlaid fitted curves. The first fit uses a quadratic function to approximate the calibration curve, and it has an R^2 of 0.992. While

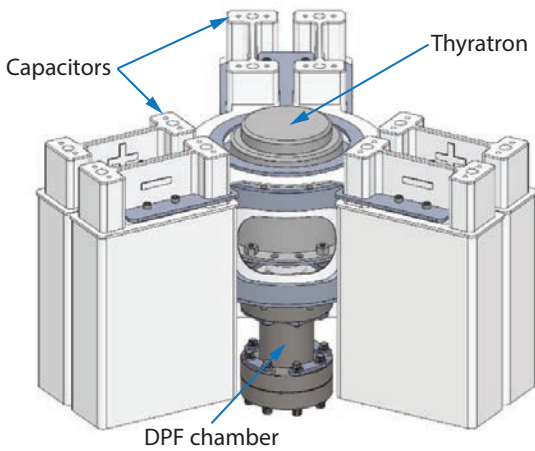


Figure 5. Capacitor bank and DPF

the fit is quite good for far positions, closer positions clearly diverge from the quadratic (Knoll 2000). To obtain a more accurate approximation, we used a power law curve fit, which maintained agreement with the measured data, even at the 60 cm position. A relation of $y = 4.8 \times 10^5 x^{1.6}$ was determined, where x is the source-to-detector distance in meters and y is the F-factor for that position. Figure 8 shows photographs of the silver detector in place at the Gemini DPF and portable DPF laboratories.

Figure 9 shows an example measurement from the multichannel scalar (MCS) connected to the silver activation detector after exposure to neutron radiation

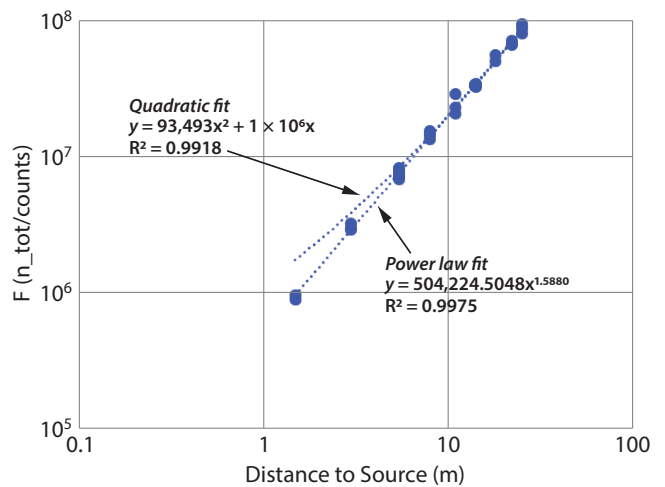


Figure 7. Calibration curve for the silver activation detector

from the portable DPF. The MCS was set such that it used a 2.3-second bin width and had a background count rate of approximately 2.5 counts per bin. The DPF radiation pulse arrived at the detector at approximately the 760-second time mark, as indicated by the 600-count-tall bin. Incident prompt gamma flux saturated the detector and abruptly died away, and the neutron flux caused the formation of ^{110}Ag via the capture reaction with ^{109}Ag . This ^{110}Ag then beta decayed to ^{110}Cd with a half-life of 24.6 seconds. The beta products caused scintillation in the Geiger tube,

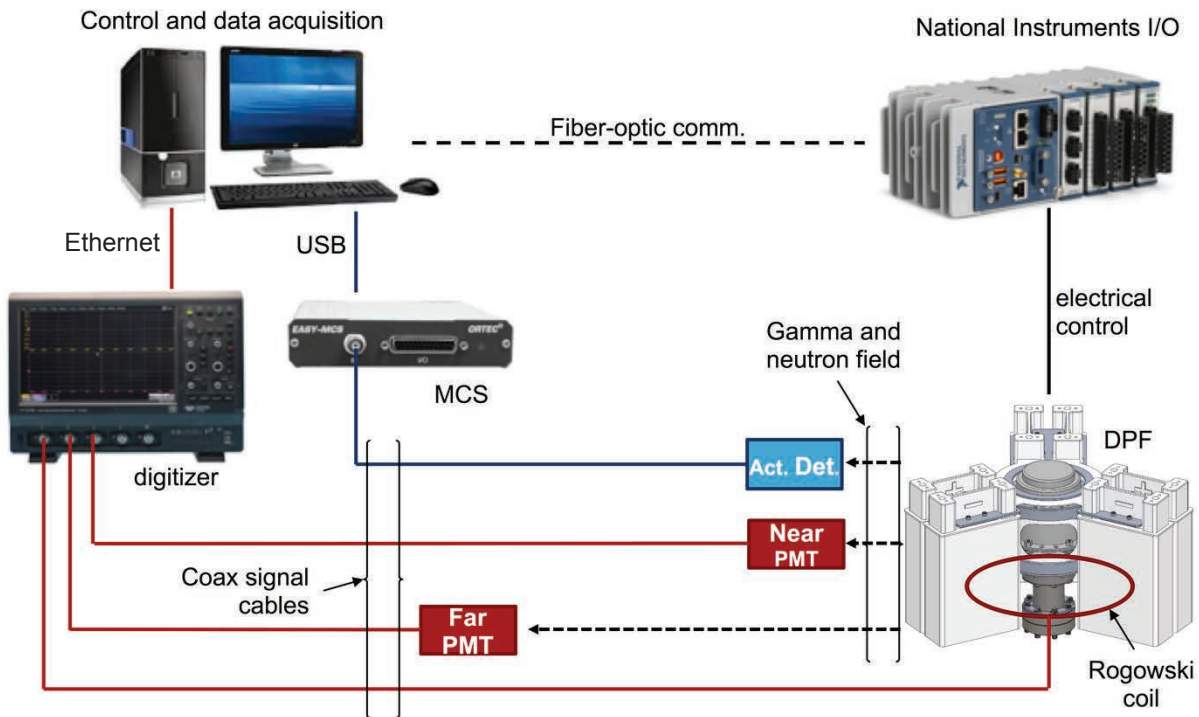


Figure 6. Experimental configuration for DPF testing for neutron production

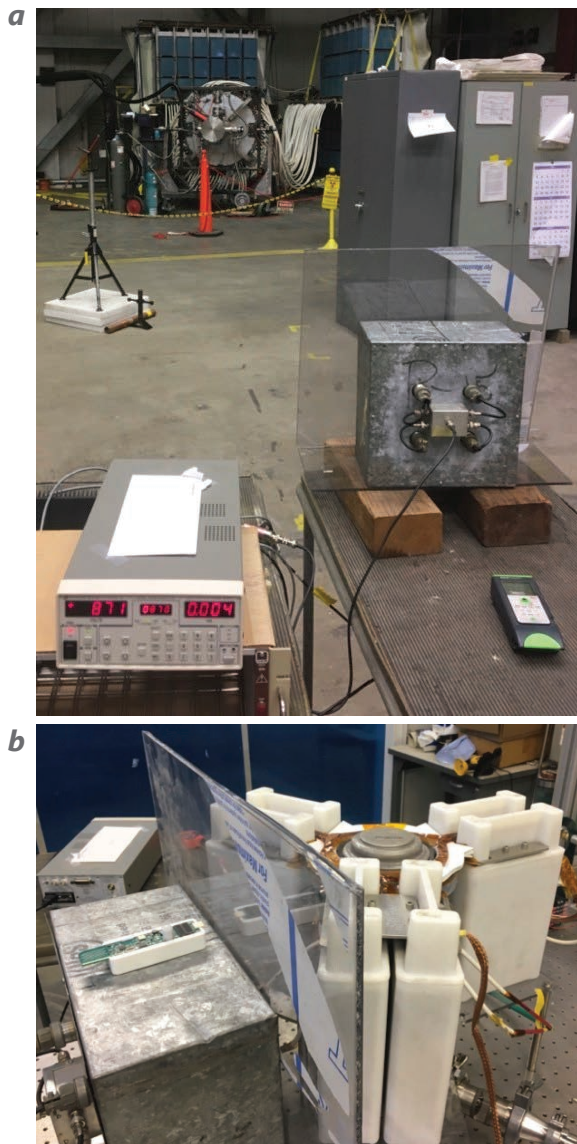


Figure 8. Silver activation detector (a) being calibrated at the Gemini DPF 15 m from the source and (b) in use at the portable DPF 30 cm from the source

creating the post-experiment decay spectrum. The first two bins after the pulse were discarded due to gamma saturation, and the next 20 bins were then summed. The data shown in Figure 9a amount to a total of 668 counts over this interval, or 616 net counts after subtracting background. Multiplied by the extrapolated F-factor for the 30 cm position (7.27×10^4 neutrons per count) corresponds to a total yield of 4.48×10^7 neutrons. Figure 9b shows that the activity decays with a constant λ of 0.02715 s^{-1} , which corresponds to a half-life $t_{1/2} = \ln(2) / \lambda$ of 25.53 s. This agrees closely with the theoretical half-life for the decay of ^{110}Ag (24.6 s) and confirms that neutron radiation was produced by the DPF source.

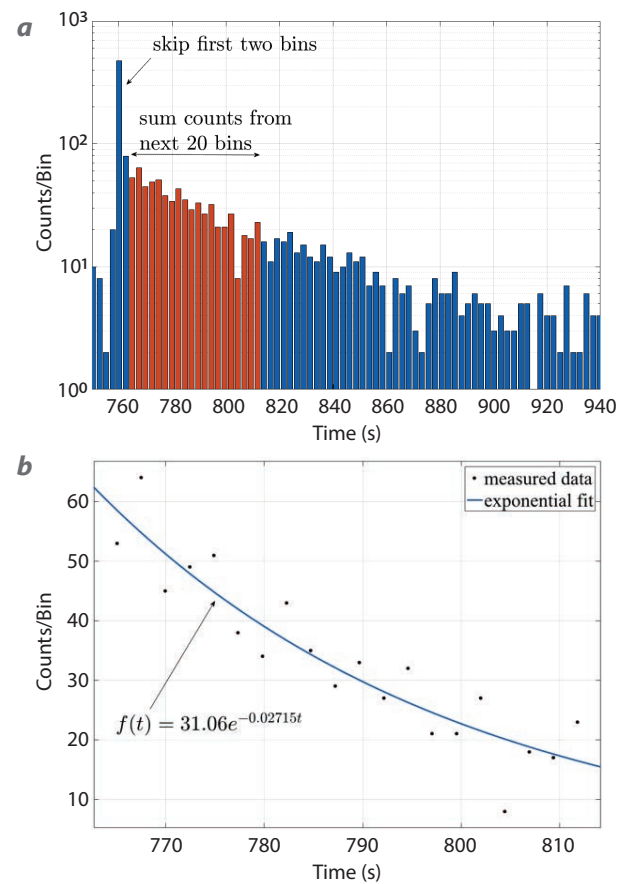


Figure 9. (a) Measured activation signal from the portable DPF at 30 cm and (b) exponential curve fit of the same measurement, characteristic of the decay of ^{110}Ag

Results

Figure 10 shows the measured neutron yield for a sequence of 38 shots we executed using the portable DPF system. This configuration used a charge voltage of 25 kV, fill pressure of 5.25 Torr deuterium, and a Pyrex insulator sleeve. The chamber was evacuated to a base pressure of 1×10^{-5} Torr and refilled with deuterium gas after every 10 shots. A maximum yield of 6.56×10^7 was measured early in the sequence, and the average yield of the shots that successfully produced neutron yield was 2.50×10^7 .

A trend of decreasing neutron output as the sequence progressed is apparent in the data. Furthermore, approximately half of the shots did not result in measurable neutron production. These effects may be related to each other, due to a variety of factors. Inspecting the DPF after the shots, we found charring at the interface between the two pieces of the anode cylinder, which we suspect was caused by the high current density at that point, which limited the flow

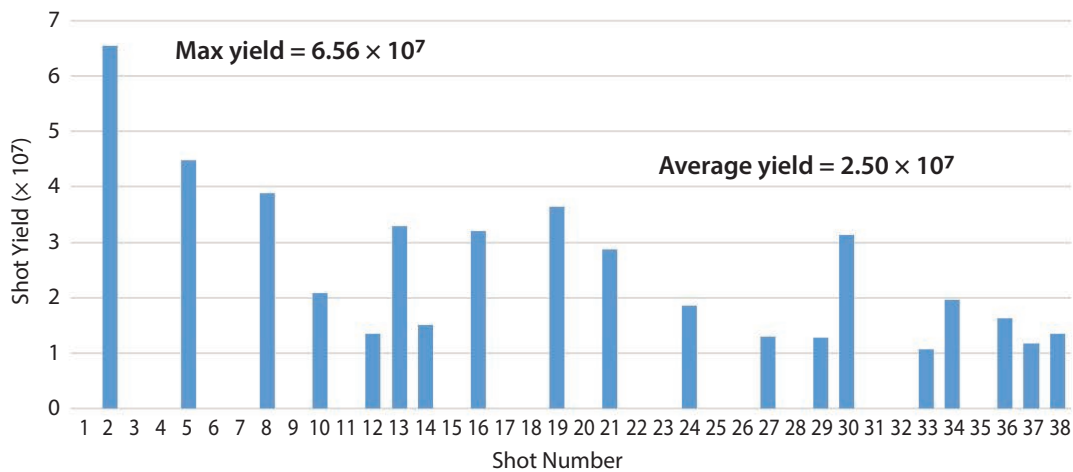


Figure 10. Measured neutron yield on the portable DPF for a series of 38 shots

of current to the vacuum system and inhibited pinch formation. A second explanation is that the ion beam generated in the pinch caused ablation of the stainless-steel wall of the vacuum chamber; particulates ablated from the wall, including iron and carbon, formed monatomic layers throughout the surfaces of the plasma source and restricted the flow of current in the device. The next generation of this system will address both of these problems. We can avoid the charring in the anode by moving to a single anode cylinder such that no interface will be present. Placing a copper or molybdenum beam stop in the ion path will prevent the formation of monolayer contaminants; this technique has been successfully used for repeated pinch formation in other NNSS DPF systems.

Figure 11 shows the gamma and neutron time-of-flight measurements for one shot on the portable DPF system. The waveform from the near detector (30 cm, blue) shows a pulse envelope with two distinct peaks

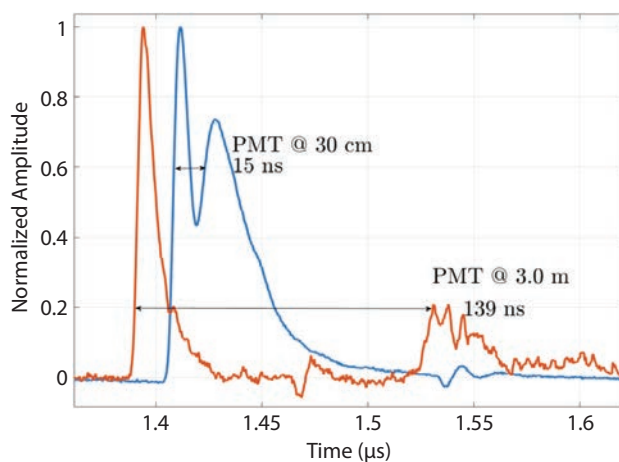


Figure 11. Time-of-flight measurements of gamma and neutron pulses from the portable DPF

separated by 15 ns. The first, sharper peak is from the gamma pulse generated from the DPF, and the second, wider pulse is due to the neutron field. The far detector (3 m, orange) shows these same two pulses, but they are separated by 139 ns. The theoretical separations between the gamma and 2.45 MeV neutron species are 12.6 and 126 ns for the near and far detectors, respectively, which closely match the measured results. The two detectors also show that the neutron pulse broadens in time, increasing from an FWHM of 30 ns at the near detector to greater than 50 ns at the far detector. The gamma pulse remains relatively unchanged at approximately 7 ns FWHM at both detectors.

The final diagnostic used in this experiment was the Rogowski coil, which measured the input current to the DPF plasma source. We fabricated the coil using a length of LMR-100 coaxial cable. This cable was selected because it has excellent loss and dispersion properties and can mechanically bend enough to tightly couple to the small radius of the DPF anode. The Rogowski coil is a standard current diagnostic tool in DPF systems found at the NNSS and in the broader community due to its ruggedness, ease of implementation, and quality of measurement. The coil uses Faraday’s law of electromagnetic induction to convert the azimuthal magnetic field generated by the DPF into a voltage differential at the two conductors of the coaxial cable. The amplitude of the voltage signal measured on the cable corresponds to the first derivative of the DPF current $dI(t)/dt$, so it must be integrated in post-processing to return current as a function of time.

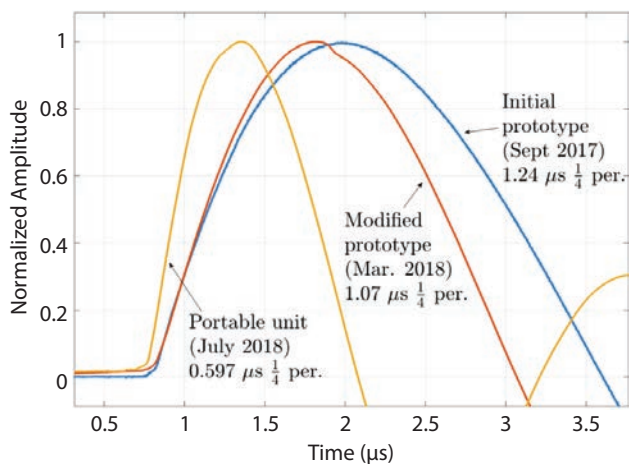


Figure 12. Measured current from the initial prototype, modified prototype, and portable unit DPF systems

Figure 12 shows Rogowski coil current waveforms for the portable DPF system compared to the initial prototype (September 2017) and modified prototype (March 2018) DPF systems we developed in this SDRD project. Each waveform is normalized and shows the first half-period of the underdamped RLC (resistor-inductor-capacitor) circuit response that is characteristic of DPF pulsed-power systems. Most notably, each successive iteration had a decreased time to maximum current compared to its predecessor. The initial prototype, modified prototype, and portable unit DPF systems took 1.24, 1.07, and 0.597 μs to reach maximum current, respectively. This trend is important and indicative of improved DPF performance. In general, a faster rise time results in higher power density in the pinch, increasing the neutron production of the device. Parasitic inductance is the primary cause of increased rise time, and consequentially, reduced neutron output. We can

reduce inductance by minimizing the physical size of the current-carrying components (Lehr 2017).

Figure 13 shows the progressively smaller systems we have developed. We determined the inductance of each of these systems from their respective current waveforms using DPF modeling software RADPF (Lee 2014), and a steady decrease in this metric was observed. The initial prototype (Figure 13a), modified prototype (Figure 13b), and portable unit DPF (Figure 13c) systems measured 112, 79, and 41 cm in length and had calculated inductances of 200, 160, and 55 nH, respectively. This shows a direct correlation between size and inductance of the device, and demonstrates that by minimizing the footprint of the DPF, we significantly reduced parasitic effects. For reference, a value of 40 nH is typically considered an excellent inductance for a DPF system (Lee 2010).

Future Work

The ability to determine the presence and location of materials such as highly enriched uranium (HEU) is a fundamental capability of nonproliferation applications. We developed the portable DPF to enable this capability, and while it may theoretically be able to accomplish this mission, it has not been tested in a real-world experiment. To address this, we extended the initial two-year scope of this project to a third year, specifically to test how well the newly developed portable DPF can detect HEU.

The proposed experiment will take place in late FY 2019 at the Device Assembly Facility at the NNSS, which can support the use of large quantities of HEU. The test is modeled after a similar experiment that a team of investigators from the Department of Nuclear Engineering and Radiological Sciences at the University of Michigan conducted using a commercial

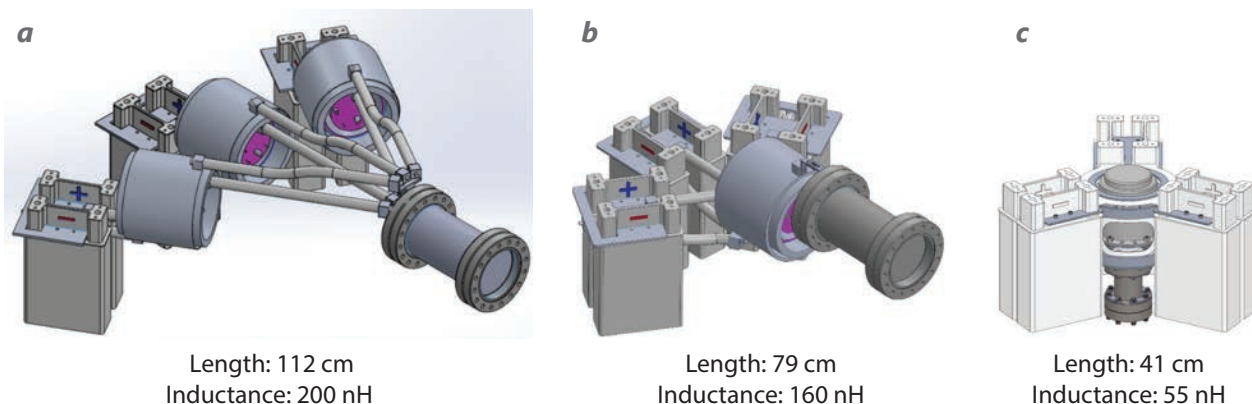


Figure 13. DPF systems developed in this SDRD project include the (a) initial prototype, (b) modified prototype, and (c) portable unit



Figure 14. The SNL MINER detector array system will be used in our FY 2019 tests to detect HEU

CONCLUSION

A portable DPF neutron source was developed in support of mobile nuclear nonproliferation applications within the Threat Reduction Science and Technology mission. This project began as a two-year endeavor to study DPF phenomenology, use these findings to develop a suitable plasma source, design the auxiliary hardware and software to power the plasma source, and fabricate and test the source for neutron production. We used an iterative process to arrive at a final configuration that weighs approximately 50 lb, is powered by standard utility hookups and is battery-compatible, and produces an average of 2.5×10^7 neutrons per pulse. The system is readily convertible to an automated control system with a 5-second repetition rate, which satisfies the neutron yield requirement

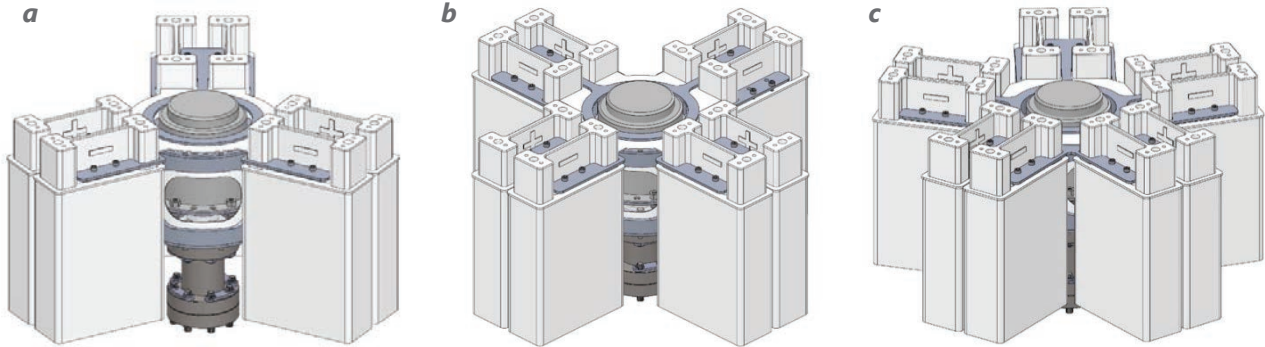


Figure 15. Designs for DPF capacitor bank optimization are (a) 3 μF , 125 kA; (b) 4 μF , 166 kA; and (c) 5 μF , 208 kA

radiation-generating device (RGD) (Hamel 2017). In the planned test, we will use the portable DPF and pure deuterium fuel to produce 2.45 MeV neutrons. The inspection object will be placed near the DPF and will comprise a 13.7 kg sphere of HEU (93% ^{235}U). We will then use the Sandia National Laboratories (SNL) mobile imager of neutrons for emergency responders (MINER) detector array (Figure 14) to sense and localize the HEU sample (Goldsmith 2014).

In preparation for this test, we will further upgrade the DPF to increase repetition rate, reliability, and output. In particular, larger capacitor banks will be investigated. Figure 15 shows three versions, the current 3 μF model, and 4 and 5 μF designs. Additional capacitors were added with no increase in footprint and marginal increase in weight. This will allow the DPF to drive higher-current pinches, increasing the total neutron output of the device.

for a viable render safe tool as laid out in the 2016 SDRD *NNSS Technology Needs Assessment* (NNSS 2016). A third year of this project will continue to improve the portable DPF source and make the device ready for further testing. We are particularly interested in how well we can detect HEU using the portable DPF as an interrogating neutron source and the SNL MINER detector as the sensing instrument.

This work has demonstrated that a small-scale DPF is a promising approach and a viable candidate for mobile SNM detection needs. With relatively modest investment, we made steady advances and succeeded in developing a realistic proof-of-principle device. Continued support of this project and its goals will certainly see further improvement in portable DPF technology and increase our nation's nuclear nonproliferation capability.

ACKNOWLEDGMENTS

The team would like to thank Stephen Molnar for greatly assisting with design and construction, E. Chris Hagen for project planning guidance, Al Mitlyng for diligently working to procure components, Gladys Arias-Tapar for designing an RGD registration plan and work package for this project, Nathan Sipe for accommodating and de-conflicting team member scheduling, and Aaron Luttmann and Alex Plionis for guidance and direction in nonproliferation applications.

REFERENCES

- Bernard, A., P. Cloth, H. Conrads, A. Coudeville, G. Gourlan, A. Jolas, Ch. Maisonnier, J. P. Rager, “The dense plasma focus—A high intensity neutron source,” *Nucl. Instrum. Methods* **145**, 1 (1977) 191–218.
- Gall, B., N. Bennett, T. Meehan, M. Heika, M. Blasco, V. DiPuccio, J. Bellow, A. Wolverton, J. Tinsley, R. O’Brien, “Man-portable dense plasma focus for neutron interrogation applications,” in *Site-Directed Research and Development*, FY 2017, National Security Technologies, LLC, and Mission Support and Test Services, LLC, Las Vegas, Nevada, 2018, 79–90.
- Goldsmith, J., J. Brennan, M. Gerling, S. Kiff, N. Mascarenhas, J. Van de Vreugde, “MINER—A mobile imager of neutrons for emergency responders,” SAND2014-19365R, Sandia National Laboratories, Albuquerque, New Mexico, 2014, <https://www.osti.gov/servlets/purl/1172910>, accessed on October 1, 2018.
- Gribkov, V., A. Dubrovsky, L. Karpiński, R. Miklaszewski, M. Paduch, M. Scholz, P. Strzyżewski, K. Tomaszewski, “The dense plasma focus opportunities in detection of hidden objects by using nanosecond impulse neutron inspection system (NINIS),” *AIP Conf. Proc.* **875** (2006) 415.
- Hamel, M. C., J. K. Polack, M. L. Ruch, M. J. Marcath, S. D. Clarke, S. A. Pozzi, “Active neutron and gamma-ray imaging of highly enriched uranium for treaty verification,” *Sci. Rep.* **7** (2017) article no. 7997, <https://www.nature.com/articles/s41598-017-08253-x>, accessed on October 1, 2018.
- Hussain, S., S. Ahmad, M. Z. Khan, M. Zakaullah, A. Waheed, “Plasma focus as a high intensity flash X-ray source for biological radiography,” *J. Fusion Energy* **22**, 3 (2010) 195–200.
- Knoll, G. F., *Radiation Detection and Measurement*, 3rd edition, John Wiley & Sons, Inc., New York, 2000, <https://phyusdb.files.wordpress.com/2013/03/radiationdetectionandmeasurementbyknoll.pdf>, accessed on October 1, 2018.
- Krishnan, M., “The dense plasma focus: A versatile dense pinch for diverse applications,” *IEEE Trans. Plasma Sci.* **40**, 12 (2012) 3189–3221.
- Lanter, R. J., D. E. Bannerman, “The silver counter: A detector for bursts of neutrons,” LA-3498-MS, Los Alamos Scientific Laboratory, Los Alamos, New Mexico, 1966.
- Lee, S., P. Lee, G. Zhang, X. Feng, V. A. Gribkov, M. Liu, A. Serban, T. K. S. Wong, “High rep rate high performance plasma focus as a powerful radiation source,” *IEEE Trans. Plasma Sci.* **26**, 4 (1998) 1119–1126, <https://www.plasmafocus.net/IPFS/otherpapers/High%20rep%20rate%20high%20performance%20plasma%20focus%20as%20a%20powerful%20radiation%20source.pdf>, accessed on October 1, 2018.
- Lee, S., S. H. Saw, “Numerical experiments providing new insights into plasma focus fusion devices,” *Energies* **3**, 4 (2010) 711–737.
- Lee, S., “Plasma focus radiative model: Review of the Lee model code,” *J. Fusion Energy* **33**, 4 (2014) 319–335.
- Lehr, J., P. Ron, *Foundations of Pulsed Power Technology*, Wiley-IEEE Press, Hoboken, New Jersey, 2017.
- Mather, J. W., “Investigation of the high-energy acceleration mode in the coaxial gun,” *Phys. Fluids* **7**, 11 (1964) S28.
- Mather, J. W., “Formation of a high-density deuterium plasma focus,” *Phys. Fluids* **8**, 2 (1965) 366.
- Nevada National Security Site, “SDRD Technology Needs Assessment R&D,” National Security Technologies, LLC, Los Alamos, New Mexico, 2016.
- Niranjan, R., R. K. Rout, R. Srivastava, T. C. Kaushik, S. C. Gupta, “A 10⁹ neutrons/pulse transportable pulsed D-D neutron source based on flexible head plasma focus unit,” *Rev. Sci. Instrum.* **87** (2016) 033504.
- Office of Defense Nuclear Nonproliferation (NA-22), “DNN R&D Call for Proposals,” 2018.
- Rapezzi, L., M. Angelone, M. Pillon, M. Rapisarda, E. Rossi, M. Samuelli, F. Mezzetti, “Development of a mobile and repetitive plasma focus,” *Plasma Sources Sci. Technol.* **13** (2004) 272.
- Rawat, R. S., “High-energy-density pinch plasma: A unique nonconventional tool for plasma nanotechnology,” *IEEE Trans. Plasma Sci.* **41**, 4 (2013) 701–715.
- Shukla, R., A. Shyam, R. Verma, E. Mishra, M. Meena, K. Sagar, P. Dhang, “Results of ultracompact plasma focus operating in repetitive burst-mode,” *IEEE Trans. Plasma Sci.* **43**, 8 (2015) 2354–2358.
- Welch, D. R., D. V. Rose, B. V. Oliver, R. E. Clark, “Simulation techniques for heavy ion fusion chamber transport,” *Nucl. Instrum. Methods Phys. Res. A* **464**, 1–3 (2001) 134–139.
- Zhang, T., et al., “Optimization of a plasma focus device as an electron beam source for thin film deposition,” *Plasma Sources Sci. Technol.* **16** (2007) 250.

Silicon Strip Cosmic Muon Detectors for Homeland Security

RSLN-018-16 ■ Year 3 of 3

**J. Andrew Green,^{1,a} David D. Schwellenbach,^b Ron Lipton,^c Paul M. Rubinov,^c
Cristinel V. Gingu,^c Michael J. Utes,^c William E. Cooper,^c Johnny B. Green,^c
Humberto Gonzalez,^c Miguelangel Marchan,^c and Vale Glasser^c**

¹greenja@nv.doe.gov, (702) 295-8614

^aRemote Sensing Laboratory–Nellis

^bNew Mexico Operations–Los Alamos

^cFermilab

Muon tomography and radiography are important detection technologies used to locate special nuclear materials in shielded containers for homeland security applications (Morris 2008). The current technology uses gas-filled drift tubes for position-sensitive charged particle detection and tracking. Drift-tube systems are prohibitively large in size and mass as well as having high development and maintenance costs. Due to the ambiguity of hit location and hit time, the tracking and calibration software needed for industrial-scale drift-tube systems is complex, labor-intensive, and costly. The purpose of this project is to build, test, and evaluate a muon tracking system based on silicon microstrip detectors similar to those used in the particle and nuclear physics communities for high-resolution tracking. To date we have built detector planes, and we have successfully read and analyzed LED and laser data from microstrip sensors. We have built a partial 1 ft² demonstration tracker capable of collecting cosmic-ray data to include the data acquisition design and analysis codes. Work based on this project received an R&D 100 award in 2018.

BACKGROUND

High-energy protons and nuclei constantly bombard Earth's atmosphere from many different sources. Much of the sun's low-energy flux is captured by Earth's magnetic field, but higher-energy flux enters from outside the solar system. This flux of high-energy

particles interacts with the upper atmosphere to create short-lived mesons that then decay into many different particles, principally muons/anti-muons, photons, and electrons/positrons. At sea level the muon flux, which dominates, is approximately 10,000/min/m² (Figure 1). The spectrum falls exponentially with energy (Grieder 2001).

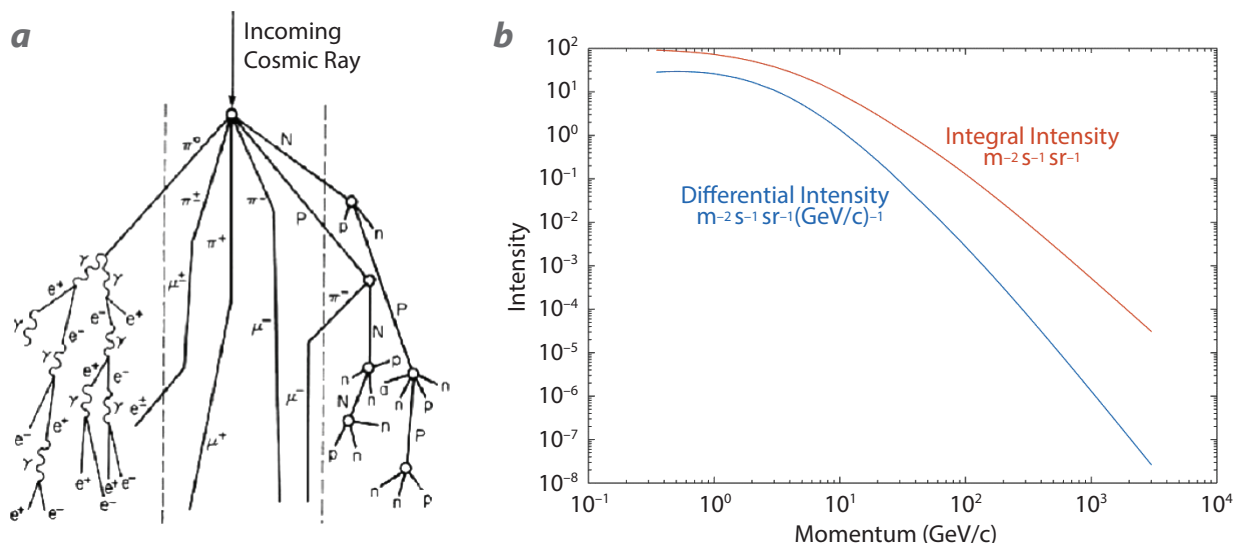


Figure 1. (a) A diagram illustrates how a high-energy cosmic hadron from outer space impacts Earth's atmosphere to create a flux of muons at sea level; (b) fitted differential and integral spectra of vertical muon data at sea level (data from Grieder 2001)

Muons are similar to electrons but have about 200 times the mass ($m_{\mu} = 106 \text{ MeV}/c^2$). Unlike protons and neutrons, muons are subject only to weak and electromagnetic forces. The decay of a muon is described as $\mu^+ \rightarrow e^+ + \nu_e + \bar{\nu}_{\mu}$, with a lifetime of $\tau = 2.2 \mu\text{s}$ at rest. The mean cosmic ray muon energy is about 4 GeV (Patrignani 2016). Relativistic time dilation increases the effective lifetime by the Lorentz factor ($\gamma = E/m_0c^2 \doteq 38$), which means the muons have an effective lifetime of $\gamma\tau = (38) \times (2.2 \mu\text{s}) = 83 \mu\text{s}$. The properties of the high-energy muon make it a great candidate for passive imaging. At GeV and higher energies, the muon is highly penetrating through matter because of its high mass and low relative energy loss. A 4 GeV muon has a range of about 3 meters in iron or 18 meters in water (Groom 2001). Muon multiple scattering through matter depends on density and atomic number. Hence, tracking the muons above and below a scene allows us to see locations in space where most scattering occurs. The zenith-angle distribution of these particles is roughly $\cos^2(\theta)$, where θ is from the zenith (Grieder 2001, Patrignani 2016). This angular variation allows 3-D imaging with muons since the object is being illuminated from multiple directions. Furthermore, about 55% of the muons are positively charged (μ^+), and 45% are negatively charged (μ^-). The negative muons can interact with atomic electron shells and nuclei, and in the target they can create secondary coincident x-rays, gammas, and neutrons that may also be used for special nuclear material detection (Nagamine 2007).

Multiple modes of tracking and detecting secondaries may be employed, and these are discussed in numerous papers (Morris 2008, Schwellenbach 2013, Livingstone 2016). Regardless of the method to reconstruct via secondaries and/or multiple-scattering methods, an excellent tracking capability is required. The focus of this work is to develop a much more compact and efficient tracking technology for detecting muon positions and trajectories when they enter or exit a scene of interest. Though significant resources have been spent on drift-tube systems for cargo scanning, drift-tube detectors continue to present significant hardware, software, and physical stability/quality issues. While silicon detectors of the same scale will have a higher initial production cost, we expect that over time the long-term costs should decrease in some cases. High channel density (factor of ~ 400 compared to drift tubes) allows silicon detectors to be used very compactly. Additionally, silicon-based tracking opens up the field for the use of smaller trackers. For demonstration purposes, one of our goals is to construct a tabletop (or small rack-mount) system that may be used to demonstrate the capability.

Using lithography methods, silicon sensors (Figure 2) are typically created from 0.3 or 0.5 mm thick silicon wafers that are several inches on a side (depending on crystal growth and fabrication technology). The sensors for this project were designed, mounted, assembled, and tested at Fermilab. They are fabricated with many closely spaced aluminum microstrips on top to locate charged particles passing through the silicon below. The detection medium is the depletion

layer (about 0.3 mm for 0.5 mm wafer), which is created by reverse-biasing the sensor (as one would reverse-bias a diode) with a nominal voltage of 200 V. The solid-state medium is advantageous over gas-filled drift tubes due to the larger particle energy deposition, which is an order of magnitude higher than 2" of argon at 1 atmosphere (Groom 2001). The hit location of the particle is determined by taking a weighted-mean position of the hit, where the weights come from the pedestal-subtracted analog-to-digital converter (ADC) readout of each microstrip by a front-end chip called an ASIC (application-specific integrated circuit). ASICs are critical components in the design of high-density detection systems, and their properties must be tuned to the problem at hand. For instance, the microstrip capacitance, the expected event rate, and whether self-triggering and other logic will be required, all affect how the chip is designed.

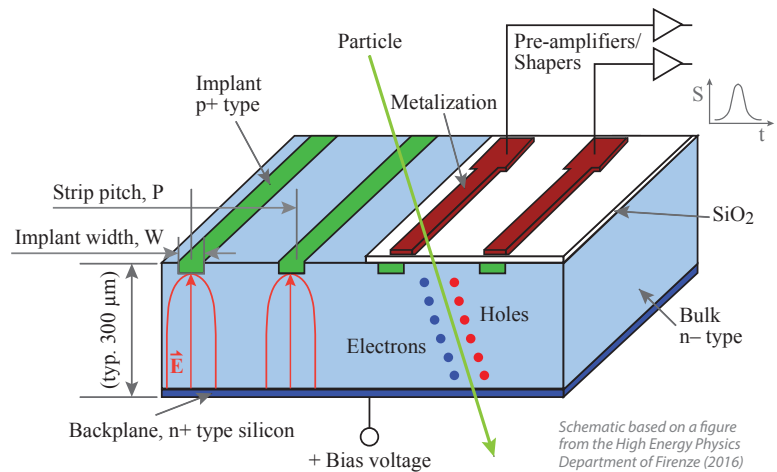


Figure 2. Cross section of a silicon strip sensor (image from High Energy Physics Department of Firenze [2016]). The bias voltage is delivered at the bottom, and the electrodes are at the strip locations on top. Each silicon strip channel has a metallic pickup, giving an image-charge response to a minimum-ionizing particle in the bulk silicon. This yields position in one dimension via center-of-charge of channel numbers hit. Another sensor layer with orthogonal strips will yield the other needed hit coordinate. Multiple X–Y layers allow measurement of position and direction.

PROJECT

Conceptual Design

We have designed a small-scale system of nominal tracking area, $\sim 1 \text{ ft}^2$ (0.1 m^2), with an emphasis on developing lower-cost scaling and maintaining the desirable aspects of silicon-strip detectors: high spatial resolution, ease of use, and compactness. We are investigating performance, feasibility, tracking capabilities, applications, cost-scaling, and reliability. To do this, we have teamed with detector experts in the Particle Physics Division at Fermilab. This project sought to develop variations that would reduce cost per unit and area for cosmic muon tracking as opposed to the expense related to particle detection in the high-rate/radiation beam experiments on which they are typically used.

Our sensors, which are 0.5 mm thick with $122 \mu\text{m}$ pitch (Figure 2) between microstrips, work by immediate charge response ($< 1 \text{ ns}$); therefore, they do not depend on gas-drift timing resolution or gas-drift calibration to obtain good position-resolution tracking (as is the case for drift tubes). The small pitch is needed to allow the silicon layers to be a few centimeters apart vertically and achieve the same

or better angular resolution as the current drift-tube detectors. Hence, detector thickness (with all X and Y layers incorporated) decreases from about 2 feet (for the case of drift tubes) to a few inches (for the case of silicon microstrips). The 1 ft^2 detector is composed of multiple 3×3 arrays of 10 cm square silicon microstrip sensors arranged for 3-D tracking. The sensors we are using were originally fabricated for the Compact Muon Solenoid (CMS, Figure 3) detector at the Large Hadron Collider at CERN. The sensors used for this project came from dry storage. The tracking detector conceptual design is composed of multiple perpendicular layers of silicon strips to compute the cosmic-ray trajectories. To reduce risk, smaller sub-units are being prototyped to better understand how multiple silicon sensors are wire bonded in series to each other and to the ASICs to produce the data acquisition readout and to check performance and noise pedestals.

The NNSS and Fermilab team has selected a path forward to complete the first detector string, which is based on an ASIC called the SKIROC (Silicon Kalorimeter Integrated Read-Out Chip) and shown in Callier (2011). This component was originally developed for current and future high-energy physics (HEP) experiments. The SKIROC is a 64-channel front-end interface that amplifies and digitizes the

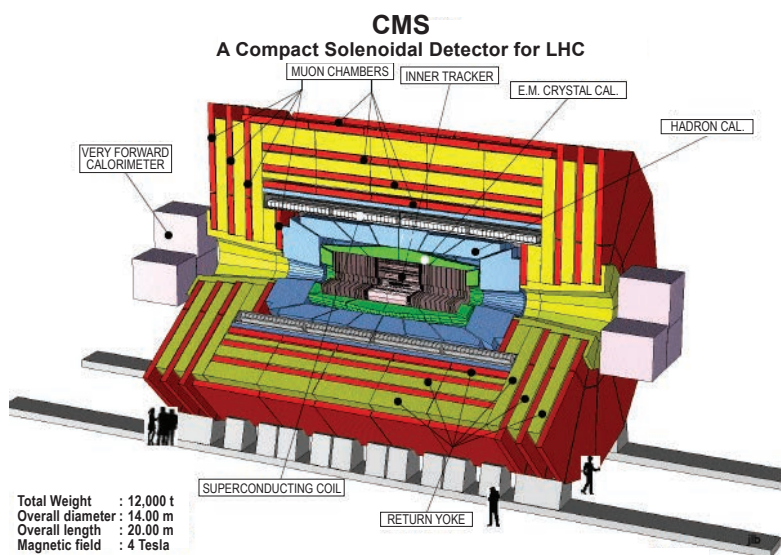


Figure 3. The sensors for this project were originally developed for the Compact Muon Solenoid (CMS) collider-detector at CERN (Krammer 2011), partly funded by the DOE Office of Science. Many tens of square meters of silicon sensors have been built to instrument the CMS central tracking system. This SDRD project leverages the same U.S.-based expertise and test equipment.

microstrip signals. Each channel on the chip reads out one microstrip. To provide greater dynamic range, it provides high-gain and low-gain analog-to-digital conversions. Internal or external triggering (triggers cause an event to be digitized and stored) is possible. Each chip is about 1 cm² in size. The SKIROC was designed for the CMS and International Linear Collider (ILC) programs to read out a fine-grained silicon-based calorimeter (OMEGA 2016).

For initial development work, sensor data in this project were read by a hybrid of custom and off-the-shelf data acquisition architecture developed for particle test-beam work. In the final year, we completed the full readout architecture, which includes all of the boards needed to funnel the thousands of channels of microstrip data to a single-board computer (SBC).

The current silicon-strip sensors in use in HEP and associated ASICs are designed to function in high particle occupancy, event rate, and radiation damage environments.

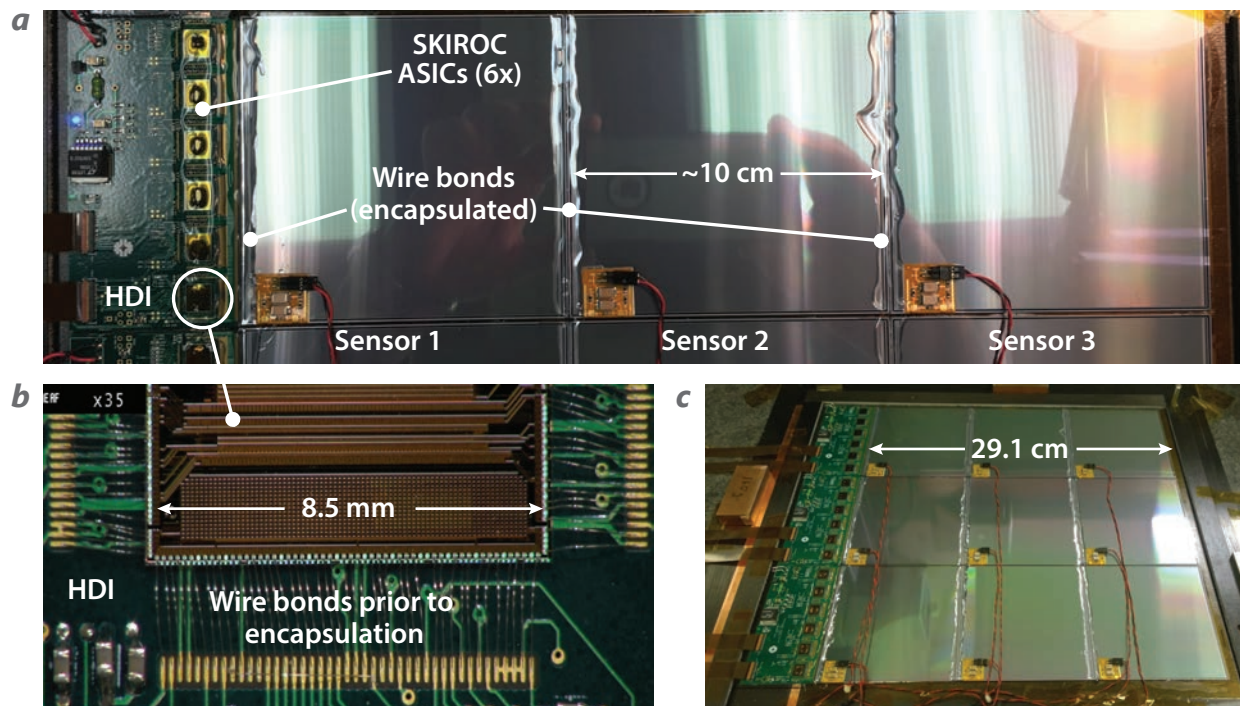


Figure 4. (a) One of the first fully assembled and tested detector strings with readout chips on the left with three sensors wire bonded in series. The microstrips run left to right, and are 122 μm pitch. (b) Magnified view of part of a SKIROC chip and wire bonds that interface the chip to the high-density interface (HDI) board. The same wire bonding is also used to connect the sensor microstrips across the 1 mm gap between sensor squares. (c) Fully assembled 1 ft² sensor plane all mounted on a carbon-fiber board.

Typical sensors in a high-radiation environment need to be cooled to low ambient temperatures, such as -10°C . While our type of sensor does need a relatively high channel density and robustness, it will not operate in such a challenging environment. To reduce cost and area, we pursued efficiencies that optimized our detectors for operation with cosmic-ray rates/occupancies and for room-temperature operation.

Electronics and Readout

Basic Architecture

The overall architecture for the 1 ft^2 detector is as follows: a scintillator “paddle” is used to trigger the tracker externally; self-triggering is certainly possible, but scintillator triggering was used in the prototype. A 3×3 array of sensors measures one of the X or Y components of the particle tracks. The sensors are mounted on carbon-fiber boards, which have a favorable coefficient of expansion and low mass. Each of the 3×3 arrays is composed of three columns of three sensors wire bonded in series. Each column is read out by six SKIROC chips mounted on one high-density interface (HDI) board (Figures 4 and 6). A similar pair of X – Y sensor planes is placed about 2 cm below the first plane pair to create a tracking module. A separate tracking module for the region below the object being scanned (target) allows cosmic-ray tracking above and below the target object.

Adaption of Previously Designed Electronics

This project adapted previously developed technology to build our tracker. The silicon microstrip sensors, “CMS ST” sensors, have been in dry storage for over 10 years. Testing has shown them to be in good condition for this project, and they are in sufficient supply (Green 2017). The SKIROC ASIC chip for front-end readout of the microstrips was originally designed not for tracking, but for silicon-based calorimetry upgrades for the HEP program. However, the properties of the SKIROC are expected to be sufficient for readout of our microstrips. For initial readout tests in the first two years of the project, we used currently existing input/output boards to read data from the HDI and then push the data to an off-the-shelf Zedboard (an SBC). This readout architecture is for the purpose of reading out test-beam setups that are used to develop detectors for the previously

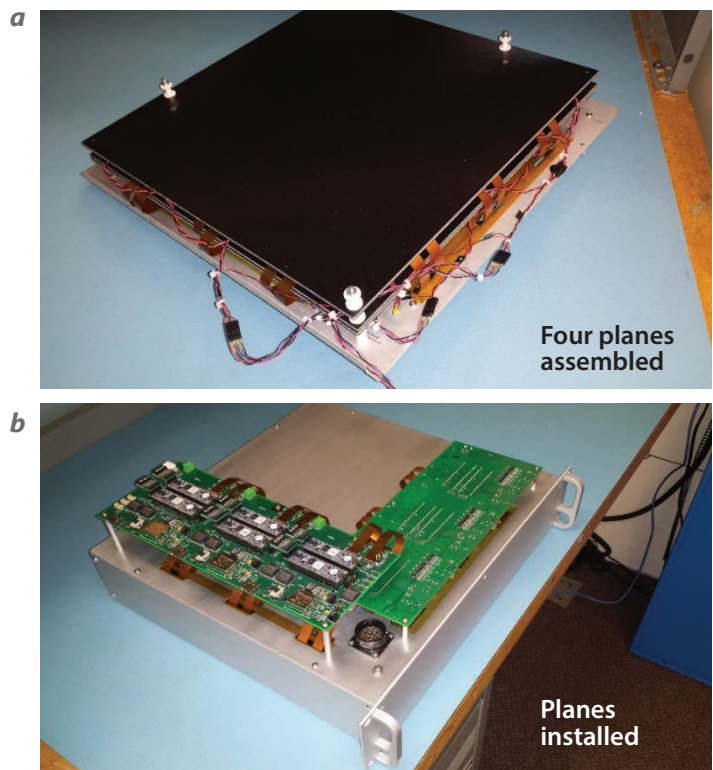


Figure 5. (a) Assembled orthogonal planes. The sensors on the top layer are face downward. (b) The planes in their enclosure with lid boards for reading out the digitized HDI data. The output data from the lid boards are transmitted via HDMI cables to the Zedboard (not shown).

mentioned HEP efforts. However, these boards do not work with our mechanical layout and need for reduction in cabling. We later designed HDI readout boards (lid boards) tailored to our detector geometry. The Zedboard at the end of the readout chain has a high-definition multimedia interface (HDMI) that can accept 12 HDMI data cables.

Because the SKIROC was not originally developed for reading out our microstrips, the pitch between the SKIROC signal pads is such that we can only read out every other microstrip. This will end up giving us effectively a $244\text{ }\mu\text{m}$ pitch instead of the more ideal $122\text{ }\mu\text{m}$. The resulting tracking angular resolution is conservatively 5 mrad , which is sufficient for proof of concept, as typical high- Z material scattering is in tens of milliradians. This is just one of many adaptations required to make forward progress. However, typical hit resolution with charge sharing is likely to be below $100\text{ }\mu\text{m}$ (competitive with the best drift tubes). While several ASICs were considered for our project, the SKIROC was the best combination of price and capability. The alternative would have been to purchase chips that are ~ 10 times the cost of the

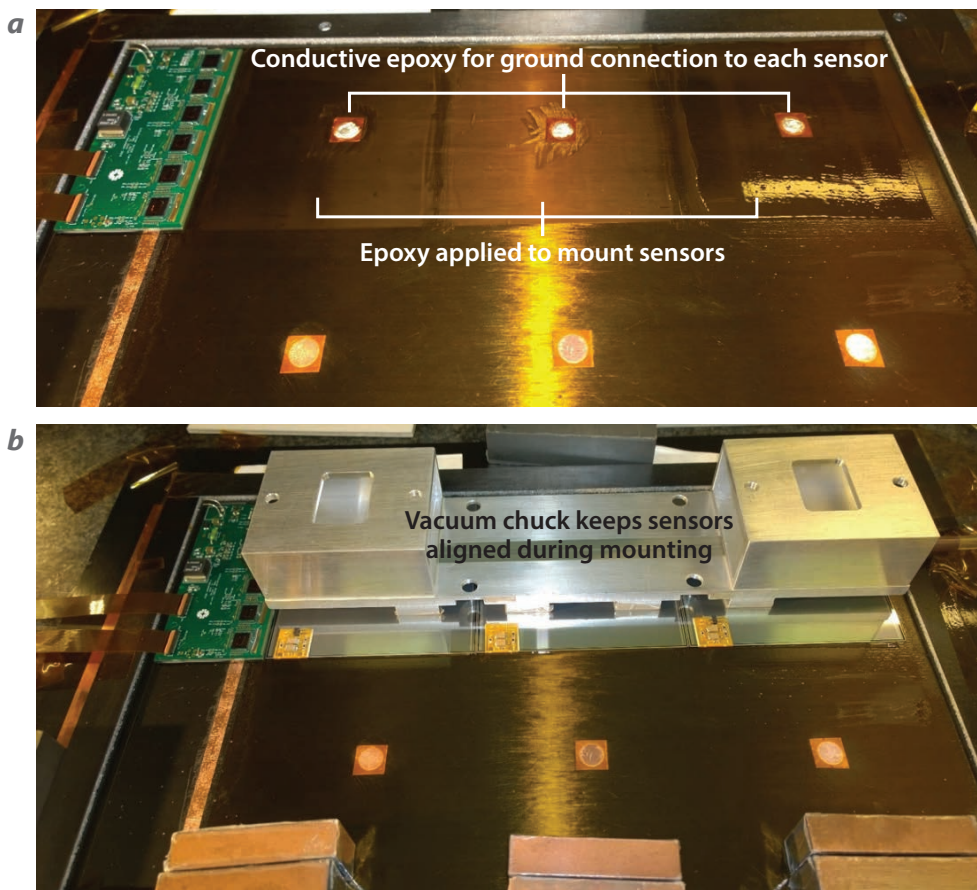


Figure 6. (a) Preparing a set of three sensors for gluing onto the carbon-fiber base. (b) The three sensors are pre-aligned and then placed together with a vacuum chuck, a device that uses a vacuum to preserve the alignment of the sensors while being glued and moved into position.

preparation are required to fabricate the detectors. The coordinate measurement machine aligns components before they may be glued or mounted. Automated wire-bonding machines make the hundreds of ultrasonic soldering connections possible between the ASIC, HDI, and sensor microstrips. An encapsulation machine correctly applies the encapsulant silicone, Sylgard 186, to protect wire bonds and chips. Numerous diagnostic equipment is used for repair and characterization. A “vacuum chuck” is used to maintain alignment of three sensors in a column prior to gluing (Figure 6). Masks are used to control where glue is applied, and conductive epoxy is used to maintain certain connections to each sensor.

SKIROC, or worse, to design and fabricate our own ASIC, which is outside the scope of this SDRD.

Similarly, the data acquisition system consists of field-programmable gate array (FPGA) firmware and embedded Linux software, much of which was also derived from the codes used in prior HEP projects.

In initial development, we used another adapted board, the FPGA Mezzanine Card Input/Output (FMCIO) board, to pull data from the HDI and push those data to the Zedboard via HDMI. As mentioned earlier, geometry requirements dictated that we design a lid board, which replaces the FMCIO board and is capable of reading out more HDIs. This made possible the current geometric layout (Figure 5).

Detector Fabrication

Techniques in detector fabrication were developed to ensure mechanical alignment, electrical contact, and protection from the environment. Significant capital machinery, materials, technical experience, and

Mechanical Design

Figure 7 presents a side view of one of the two tracking modules. The enclosure includes light shielding as well as ventilation. Unlike photomultiplier systems, rigorous light shielding is not needed. An X - Y plane was made from two 1 ft² planes mechanically mounted back to back and with the microstrips running perpendicularly. The distance between two X - Y planes per tracking module is set to about 2 cm. This distance is set so that for a conservative 100 μ m hit resolution, the angular resolution will be approximately $0.1 \text{ mm}/20 \text{ mm} = 5 \text{ mrad}$. Due to this spacing, the solid angle acceptance of this system is a few to several times the solid angle of our prior drift-tube detectors, depending on configuration. This results in more valid tracks per unit time from cosmic rays, greater ratio of tomographic coverage area to detector area, and reduced Z-smearing of target images.

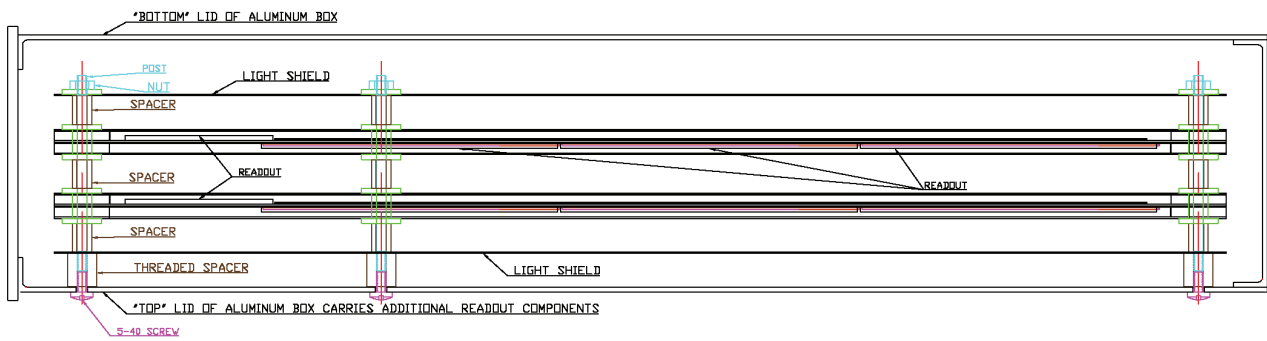


Figure 7. Side-view mechanical drawing of one full detector assembly. Shown are the outer enclosure and two stacked X–Y planes edge-on. Their vertical spacing will be about 20 mm. Two such assemblies were produced.

Software and Analysis

A C++ set of classes has been written to allow convenient exploration and plotting of the data. These tools were used to determine signal-to-noise ratios as a function of high voltage, measure pedestals and response to laser and LED light pulses, and test proper detector function. Additionally, these codes are used to make plots and perform diagnostics on the data stream that results from each trigger event. Each event contains each microstrip’s ADC values, headers that provide coarse- and fine-time, board address, and health information. All data are used to ensure event integrity. The plots can also show systematic problems, such as when certain channels are not present in the readout, do not respond correctly to LED or laser light, or have unusually high noise. These result in repairs to the affected hardware and firmware.

CONCLUSION

We have designed a tabletop silicon microstrip muon-tracking system that uses adapted HEP detectors previously developed at Fermilab. We have built many of the major components. This experience will lead to larger-scale cosmic muon tracking and associated applications. We have established the detector fabrication, board electronics, firmware, and subsequent software needed to take data from many sensors. Our work was awarded an R&D 100 award in 2018.

In addition to our cosmic-ray application, this technology is being adapted by a Pacific Northwest National Laboratory (PNNL) project to track the decay of radioactive gases in a spectrometer. The PNNL tracker uses one sensor and one HDI in addition to the same readout boards developed for this project.

We have also enriched the experience of engineering students at Fermilab through internship and cooperative programs and at the University of Nevada, Las Vegas, in a senior design project.

Due to the overlap that this project has with others, some work on problem-solving into FY 2019 continues. One outstanding issue is that during a readout of LED-illuminated microstrips, many channels show no response. This is currently thought to be a possible problem with wire-bond continuity or with timing synchronization. The team continues to troubleshoot this problem. For much the same reason, the cosmic efficiency is unexpectedly low (a few percent). The PNNL detector—which uses only one sensor but is based on the same technology—shows ideal results both for cosmic readout and for LED readout. This is currently being actively pursued.

REFERENCES

- Callier, S., F. Dulucq, C. de La Taille, G. Martin-Chassard, N. Seguin-Moreau, “SKIROC2, front end chip designed to readout the Electromagnetic CALorimeter at the ILC,” *J. Instrum.* **6** (2011) C12040, <https://iopscience.iop.org/article/10.1088/1748-0221/6/12/C12040/pdf>, accessed November 10, 2016.
- Green, J. A., D. D. Schwellenbach, R. Lipton, P. M. Rubinov, C. V. Gingu, M. J. Utes, W. E. Cooper, J. B. Green, “Silicon strip cosmic muon detectors for homeland security,” in *Site-Directed Research and Development*, FY 2016, National Security Technologies, LLC, Las Vegas, Nevada, 2017, 73–80.
- Grieder, P. K. F., *Cosmic Rays at Earth: Researcher’s Reference Manual and Databook*, Elsevier Science, Amsterdam, The Netherlands, 2001, 363–364.
- Groom, D. E., N. V. Mokhov, S. I. Striganov, “Muon stopping power and range tables 10 MeV–100 TeV,” *Atomic Data and Nuclear Data Tables* **78**, 2 (2001) 183–356.

High Energy Physics Department of Firenze, “Silicon Detector.gif,” http://hep.fi.infn.it/CMS/sensors/Silicon_Detector.gif, accessed December 5, 2016.

Krammer, M., “Silicon detectors,” Institute of High Energy Physics, Vienna, Austria, 2011, http://www.hephy.at/fileadmin/user_upload/Lehre/Unterlagen/Praktikum/Halbleiterdetektoren.pdf, accessed November 10, 2016.

Livingstone, S., V. Anghel, A. Erlandson, C. Jewett, O. Kamaev, M. Thompson, “Recent results using the cosmic ray inspection and passive tomography (CRIP) system for SNM imaging and detection,” poster 2B-7 presented at SORMA West 2016, University of California, Berkeley, May 22–26, 2016.

Morris, C. L., et al., “Tomographic imaging with cosmic ray muons,” *Science and Global Security* **16** (2008) 37–53.

Nagamine, K., *Introductory Muon Science*, Cambridge University Press, New York, 2007, 40–68.

OMEGA, “SKIROC,” <https://portail.polytechnique.edu/omega/en/products/products-presentation/skiroc>, accessed November 10, 2016.

Patrignani, C., et al. (Particle Data Group), “Review of particle physics,” *Chin. Phys. C* **40** (2016) 100001.

Schwellenbach, D., et al., “Passive imaging of warhead-like configurations with cosmic-ray muon tracking scanners,” in *Site-Directed Research and Development*, FY 2012, National Security Technologies, LLC, Las Vegas, Nevada, 2013, 129–134.



Transient RF and Optical Plasma Signatures

STL-024-17 ■ Year 2 of 2

**Clare Kimblin,^{1,a} Ian McKenna,^a Brandon La Lone,^a Manuel J. Manard,^a
Jason Mance,^a Jonathan Madajian,^a Mary D. O'Neill,^a Matthew Staska,^a
Gerald D. Stevens,^a and Ruben J. Valencia^a**

¹kimbliew@nv.doe.gov, (805) 681-2257

^aSpecial Technologies Laboratory



The goal of this two-year project was to bring laboratory control to RF and optical measurements to better understand the conditions under which transient RF signatures are produced in large-scale high-explosive field experiments. To this end we have developed critical test capabilities to support statistically repeatable laboratory experiments and have collected and analyzed time-resolved RF and optical data that directly support RF modelers. In FY 2017, time-resolved RF emissions, optical emission spectra, and plasma images were collected following laser ablation of graphite. RF emissions were strongest in the first ~20 ns and coincided with the fastest growth of the plasma plume. The source of the RF emissions produced following laser ablation could not be tied directly to turbulent interactions between particles, a mechanism that is a key factor in some RF models. In FY 2018, we performed rapid decompression experiments that limit RF production to triboelectric- and fracto-emission charging mechanisms, broaden the time regime over which RF and optical signals are recorded (to tens of milliseconds), and enable better spatial and time resolution of discharge events. Coincident RF emissions and lightning discharges were observed with turbulently mixed silica-based samples. Many discharges were observed with dry pumice and volcanic ash, while only one was recorded with dry, spherical glass beads. No indications of macroscopic lightning were observed in RF and optical data collected from rapid decompression experiments performed with conductive graphite flakes.

BACKGROUND

The ability to distinguish high explosive (HE) package designs based on RF observables remains a major objective of HE test programs, but RF emissions resulting from a detonation are still not well understood. Current methods to study RF from large-scale HE experiments are not readily repeatable and do not allow for the separation of RF emissions originating from fundamentally different sources such as air shock, detonation, combustion, and ground impact. Solid carbon is a major constituent of product mixtures following detonation of carbon-rich HE (Watkins 2017), and it is thought that significant RF emissions are produced by charging and subsequent discharging of carbon particulates. Lawrence Livermore National Laboratory (LLNL) modeling efforts are focused on contributions to RF by carbon particles, but discharges have not been observed optically in chemical HE field experiments, and modelers lack empirical data such as cluster size and shape to support their simulations.

To address significant knowledge gaps in the correlation between optical and RF signals in HE test events and the species that produce the signatures, we have explored a number of repeatable laboratory methods to create small-scale, repeatable sources of RF and optical signatures.

In the first year of this project, we used laser ablation of graphite as a laboratory method to generate carbon clusters and explore their role in RF generation (Kimblin 2018). Our goal was to measure RF and optical signatures associated with laser-ablated graphite and to separately characterize the clusters produced under the same conditions in a custom high-pressure cluster source that feeds to an ion mobility mass spectrometer (IM-MS). Following laser ablation of graphite in air, we collected time-resolved RF, optical emission spectra, and plasma images. The measured RF signal lasted ~ 150 ns, and the strongest RF was observable in the first ~ 20 ns when the plasma size changed most dramatically. During the first 20 ns, only continuum emission was observable spectroscopically, with ionic species such as C^+ and N^+ appearing at ~ 50 ns. Our results suggested that the strong early-time RF emission may be caused by the rapid expansion of the plasma, implying that the strong RF comes from the fast-moving charge and/or a rapid drop in charge density. A number of processes are likely to generate electric fields that lead to subsequent discharge and RF emissions following laser ablation of graphite, including (1) differential

ejection of electrons or ions during the ablation process and creation of an electric field at the graphite surface, (2) charging of delaminated layers of graphite as they separate from the substrate, (3) collective behavior in plasma ionized by shock-heated air, (4) triboelectric contact charging between carbon clusters and separation based on Stokes number, and (5) charging of carbon atoms and clusters while immersed in the plasma (J. Sears, pers. comm., June 9, 2017). The short duration of the RF signature, obscuration of optical signatures by continuum emission, and the multitude

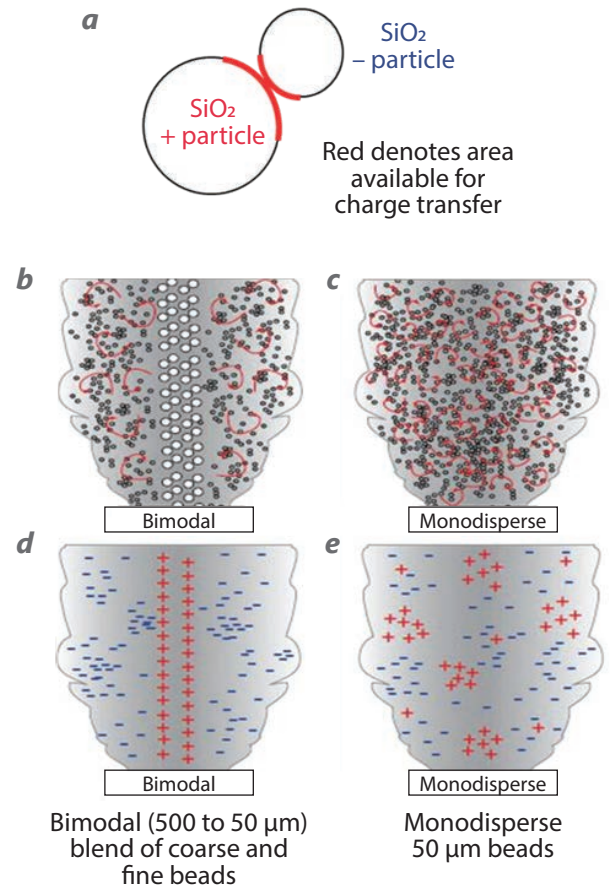


Figure 1. Mechanisms associated with particle charging and notional charge separation. (a) Triboelectric contact charging between insulating particles in turbulent regions (figure adapted from Kok [2009]). Turbulence-promoted triboelectric contact charging for (b) a bimodal mixture of coarse beads and fine particles and (c) a monodisperse mixture of fine particles, followed by charge separation based on Stokes number with (d) coarse beads tending to have relative positive charge at the core of the flow and fine particles tending to have relative negative charge beyond the core, and (e) fine particles forming transient clusters with differing relative charge densities (figures 1b–1e adapted from Cimarelli [2014]).

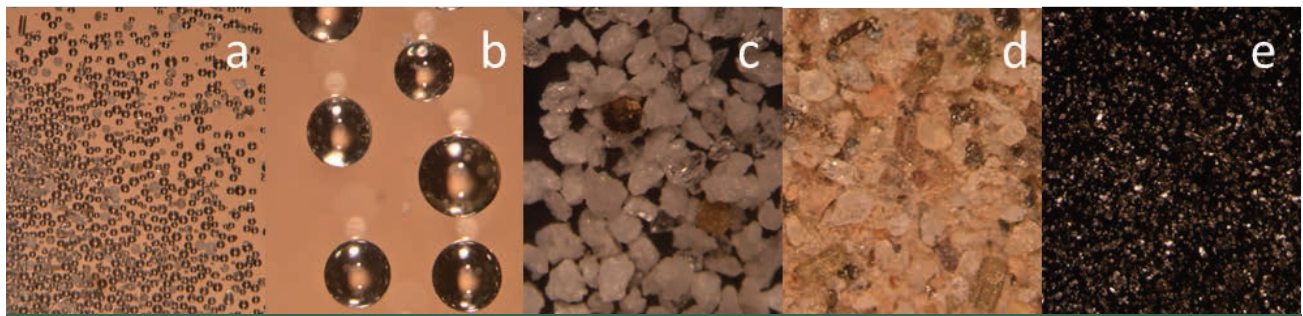


Figure 2. Samples used for experiments (at 64x magnification): (a) glass beads (50 μm), (b) glass beads (500 μm), (c) pumice (<250 μm), (d) volcanic ash (<250 μm), and (e) graphite flakes (44 μm)

of possible mechanisms that could produce the RF signal prohibited us from correlating RF emissions with physical and chemical processes. In mid-FY 2018, we used a new, far more direct approach to generate and measure RF emissions. The novel technique, first reported by Alatorre-Ibargüengoitia (2011), allowed us to generate laboratory-scale lightning as a result of triboelectric, and likely fracto-emission, charging due to turbulent flow of well-defined particulate samples.

This work is pertinent to informing and testing predictive RF models. Our research has contributed to current nonproliferation and treaty verification programs by providing empirical data from controlled tests to RF modelers. In addition to RF, we expect that future work using the laboratory-scale rapid decompression platform, discussed in this report, will help advance optical diagnostics research and support the development of optical models of explosions.

PROJECT

Rapid Decompression Experiments

Overview and Theory

To produce measurable discharges from particles in the laboratory, we designed, modeled, built, and instrumented a rapid decompression apparatus, drawing on the research done by Alatorre-Ibargüengoitia (2011) and Cimarelli (2014). Cimarelli (2014) demonstrated that lightning could be generated when loose, electrically insulating particles in a shock tube are subjected to instantaneous decompression (from ~ 10 MPa argon to atmospheric pressure ~ 0.1 MPa). Following decompression, loose particles are vertically accelerated and ejected through a nozzle (~ 3 cm in diameter) into a large air-filled tank. Cimarelli (2014) performed experiments with volcanic ash and micron-size glass beads and used a high-speed

camera and two inductive antennas to record changes observed as a function of sample type. Their results indicate that lightning generation is controlled by turbulence and an abundance of fine particles.

The mechanistic components thought to provide the charging and charge separation between electrically insulating particles are turbulence, which promotes electron transfer between colliding particles with low conductivity (triboelectric contact charging) (Figure 1a) and separation of similarly sized particles into like-charged clusters by their relative Stokes numbers (Figures 1b–1e). The transient clustering of like-charged particles generates electric fields that can lead to the charge gradients needed for discharges.

Samples and Diagnostics

Using the system described in the next section, we performed rapid decompression experiments (from ~ 7.5 MPa to atmospheric pressure $P_a = 0.1$ MPa) at room temperature with argon. The particulate samples we selected for our experiments varied in homogeneity, shape, size, and electrical conductivity. As shown in Figure 2, they consisted of four silica-based samples (a–d) and one graphite sample (e). The graphite sample consisted of electrically conductive graphite flakes (44 μm in diameter) from Alfa Aesar. The silica-based samples consisted of a bimodal distribution of spherical glass beads, (a) fine beads (50 μm in diameter) mixed with between 5% and 20% by weight of (b) coarse beads (500 μm in diameter), from USA Scientific, Inc.; (c) pumice (predominantly ~ 177 μm in particle size, with a maximum of 250 μm ; samples were 99% "1/2" and 1% "0–3/4" by weight) from CR Minerals Corporation; and (d) Mount Saint Helens volcanic ash (sieved to a maximum particle size of 250 μm) from American Educational Products, LLC. Pumice and volcanic ash are inhomogeneous mixtures, typically 75% and 65% silica by weight, respectively, with various metal oxides (e.g., Al_2O_3 , Fe_2O_3 , CaO) (Taylor 1980). We used these samples in

the condition they were received, or we baked them in an oven to remove excess water that can alter the conductivity of a material. Dry volcanic ash is nonconducting ($\rho > 1.56 \times 10^7 \Omega\text{m}$), but the conductivity of volcanic ash increases abruptly with the adsorption of water (Wardman 2012). Sample weights ranged from 16 g (graphite flakes) to ~70 g (volcanic ash). Photographs of materials at 64x magnification are shown in Figure 2.

We used a Photron SA4 monochrome high-speed imaging camera (20 kfps, 50 ms integration time, ~100–200 ms record length) to observe turbulence under ambient light conditions and to measure the durations, spatial lengths, and locations of macroscopic optical discharges in a darkened lab. We also used a ThorLabs DET36A silicon photodiode when conducting experiments in a dark room to record broadband light emission levels (350–1100 nm) from the lightning discharges. Time resolution was limited by the 14 ns rise time of the detector. The optical signal was recorded on a 50k Ω input impedance to optimize the signal-to-noise ratio.

The RF diagnostics for the experiments consisted of nine antennas described in Table 1. Six antennas were custom-built at the Special Technologies Laboratory (STL).

In order to obtain quantitative numerical values from antenna measurements, it is important to use calibrated antennas. While we attempted to calibrate our custom-built antennas using a frequency sweeper and high-speed oscilloscope, we were unable to obtain conclusive results. In future work, we will utilize an anechoic chamber to calibrate custom diagnostic equipment. For the COTS active antenna, an antenna

factor (AF) provided by the manufacturer was applied to the results. The FFT of an AF-corrected pulse corresponding to a discharge observed between 26.385 and 26.3875 ms in experiment 180823-3 has broadband spectral content that compares well to the broadband spectral content observed in FFTs of pulses recorded by the inductive antennas. A more detailed discussion of power spectral density analysis for silica-based materials is presented under *Results and Analysis*. Additional details are provided in Appendix A of this report.

Platform

In lieu of building a stand-alone system, we modified the existing STL gas gun to conduct the rapid decompression experiments. Parametric models of the modified gas gun are shown in Figure 3, with labels indicating relevant components. Prior to fabrication and purchasing of parts, we performed computational fluid dynamics (CFD) simulations for safety and verification purposes. By taking into account the goal exit pressure at the nozzle, and assuming that the final in-use pressure was 50% of typical maximum gas gun operations, the maximum pressure buildup in the breech of the gas gun was determined. We then used this maximum breech pressure and the known volume and properties of the gas to determine the event duration. We also used these CFD models to estimate gas and particle velocities as well as the mechanical structure's influence on turbulence and particle interactions. These simulations accurately predicted system behavior. Figure 4 shows a frame of a turbulent flow simulation for a simplified system. Models predicted what was observed experimentally. In the model shown in Figure 4, the burst disc ruptures

Table 1. Antennas characteristics

ANTENNA TYPE	QUANTITY	MANUFACTURER	PART NUMBER	LOWER RANGE	UPPER RANGE	LOCATION
Inductive	3	STL	Custom	–	–	Internal, surrounding vent
Dipole	2	STL	Custom	1 MHz	500 MHz	Internal
Rogowski	1	STL	Custom	–	–	Internal, surrounding vent
Discone Active	1	Antenna Research Associates, Inc.	SAS-2/A	100 Hz	1 GHz	External
Hoop	1	Electro-Metrics Corporation	EM-6772	100 kHz	30 MHz	External
Biconical	1	Eaton	3109	20 MHz	300 MHz	External

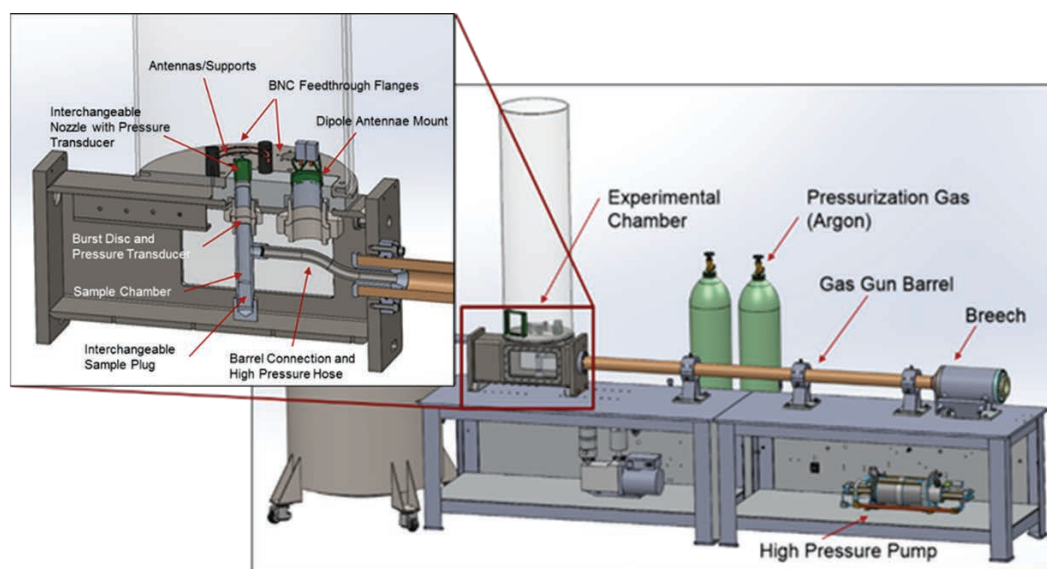


Figure 3. Parametric model image of the STL gas gun as modified for rapid decompression experiments, with an expanded cut-out view of the sample chamber and the base of the experimental test chamber. The burst disc and RF antennas around and adjacent to the vent nozzle are shown. Lightning was observed above the vent and within the perimeter of the ring antennas and antenna supports.

at ~1000 psi, and approximately 2 ms later, the sample is lofted up through the vent. This corresponds to the time when sample ejection was observed experimentally.

Argon gas was pressurized with a Haskel pump into the barrel up to a 1000 psi burst disc located just below the vent nozzle (inset in Figure 3). An RF and optically

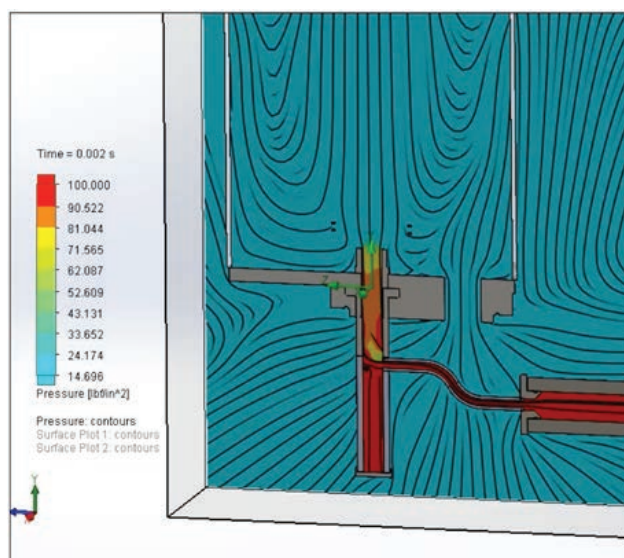


Figure 4. Still image from turbulent flow simulation showing the time (2 ms) when the pressure above the sample is reduced. This corresponds to the time when sample ejection through the vent occurred experimentally.

transparent acrylic cylinder housed the vent nozzle and was used as the experimental test chamber. Interchangeable vent nozzles included a straight aluminum nozzle, and acrylonitrile butadiene styrene (ABS)-printed plastic nozzles (one straight and one with internal helical fluting) were available to provide vent materials with differing electrical conductivity and to impart alternative flow patterns.

Sample volumes (34 and ~44 mL) and positions (below the gas outlet) were also varied through the use of two sample plugs of different lengths. Diagnostics were triggered by a pressure transducer located just below the burst disc.

Between August 14 and 23, 2018, we performed 17 rapid decompression experiments at room temperature (ranging from 65°F to 70°F), with relative humidity ranging from ~58% to 75%. Particles were typically ejected over a ~100 ms time period at an initial speed of approximately 200 m/s. Lightning was observed out to ~100–200 ms with pumice and volcanic ash. After ~100 ms the experimental chamber opacity made lightning observation more difficult due to suspended particulates. Table 2 provides an overview of experimental parameters by sample type and indicates whether or not lightning was observed optically.

Results and Analysis

Silica-Based Materials

With pumice and volcanic ash samples (both dried in an oven at ~600°F), significant discharges ranging in size from a few millimeters to over 20 cm long were consistently observed. Figure 5 shows representative enhanced high-speed camera frames with lightning generated by pumice and volcanic ash samples.

Table 2. Rapid decompression experiments performed August 14–23, 2018

SAMPLE TYPE	EXPER. NO. (YYMMDD-#)	OBSERVED BURST PRESSURE	PLUG LENGTH	MASS (g)	NOZZLE TYPE	ROOM ILLUMINATION	DISCHARGES OBSERVED OPTICALLY
No sample	180814-1	220 [†]	Short	–	Original AI	Ambient	No
No sample	180817-1	1155	Short	–	Original AI	Ambient	No
Residual VA	180822-2	1160	Short	–	t-ABS	Ambient	<i>Lightning</i>
GB 5% coarse	180815-1	512 [†]	Short	~45	Original AI	Ambient	No
GB 5% coarse	180815-2	1123	Short	~45	Original AI	Ambient	No
GB 20% coarse	180815-3	1060	Short	50	Original AI	Ambient	No
GB 20% coarse	180816-1	1070	Medium	50	Original AI	Ambient	No
Dry GB 5% coarse	180821-1	1120	Short	~64	t-ABS	Ambient	No
Dry GB 5% coarse	180821-2	1120	Short	67	t-ABS	Dark	1 discharge
GF	180816-3	~1100	Medium	16	Original AI	Ambient	No
GF and GB 7% coarse	180816-4	1132	Short	21	Original AI	Ambient	No
Dry VA	180821-3	1170	Short	65	t-ABS	Dark	Numerous
Dry VA	180822-1	1130	Short	65.88	t-ABS	Dim	Numerous
Dry VA	180822-3	~1100	Short	69.84	Original AI	Ambient	Numerous
Dry VA	180823-1	1110	Short	65	s-ABS	Dark*	Numerous
Dry pumice	180823-2	1100	Short	24	s-ABS	Dim	Numerous
Dry pumice	180823-3	1167	Short	23	Original AI	Dark*	Numerous

[†]Lower pressure burst disc used; *With photodiode
 GB = glass beads; GF = graphite flakes; VA = volcanic ash
 s-ABS = straight ABS; t-ABS = toroidal ABS (% shorter than AI)

(Videos are available; see Appendix A of this report.) The antennas closest to the vent demonstrated a strong correlation with optical observation of discharges in high-speed imagery; there also was a strong correlation with photodiode pulses when experiments were performed in the dark.

Results from a pumice experiment (180823-3) are shown in Figure 6a, where photodiode counts are plotted above the traces from three representative antennas that were inside the experimental chamber. Spikes in the RF data for two of the antennas that surrounded the vent, the Rogowski antenna and the upper inductive antenna, correspond to photodiode peaks. In the trace from the lower dipole antenna, which was slightly further away from the vent, some additional spikes that do not correspond to photodiode

peaks or to signals in the other internal antennas are apparent. For the COTS antennas, which were located several feet from the vent and external to the experimental chamber, Figure 6b shows a high degree of correlation among the antenna signals and also between the antenna and photodiode signals, although some discrepancies are observed (e.g., at roughly 24 ms). Similar correlation between photodiode and antenna signals was observed in experiments with volcanic ash. In Figure 7, external antenna signals from a volcanic ash experiment (180823-1) are overlaid on the photodiode trace.

We performed preliminary analysis of peaks recorded by the upper inductive antenna during experiment 180823-3 to investigate pulse shapes and frequency content. It is believed that pulse fingerprints may ultimately be able to help constrain particle types.

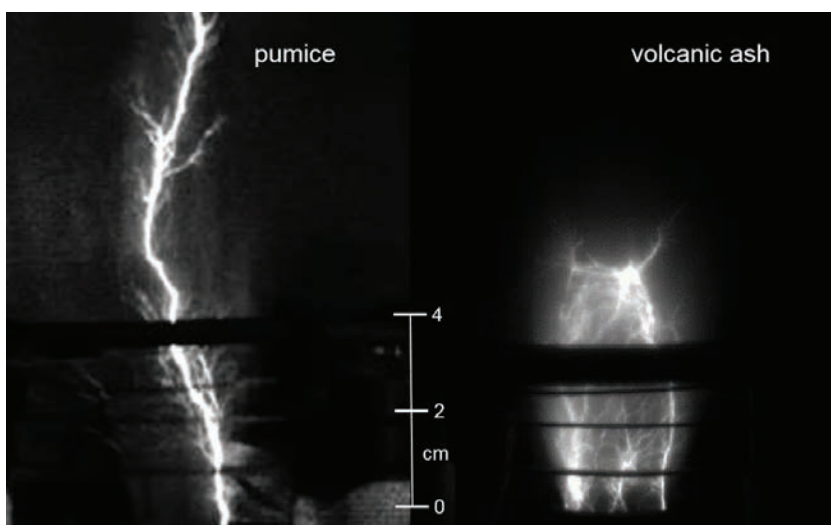


Figure 5. Enhanced high-speed camera imagery frames showing one frame each when lightning was observed with pumice (experiment 180823-3) and volcanic ash (experiment 180823-1)

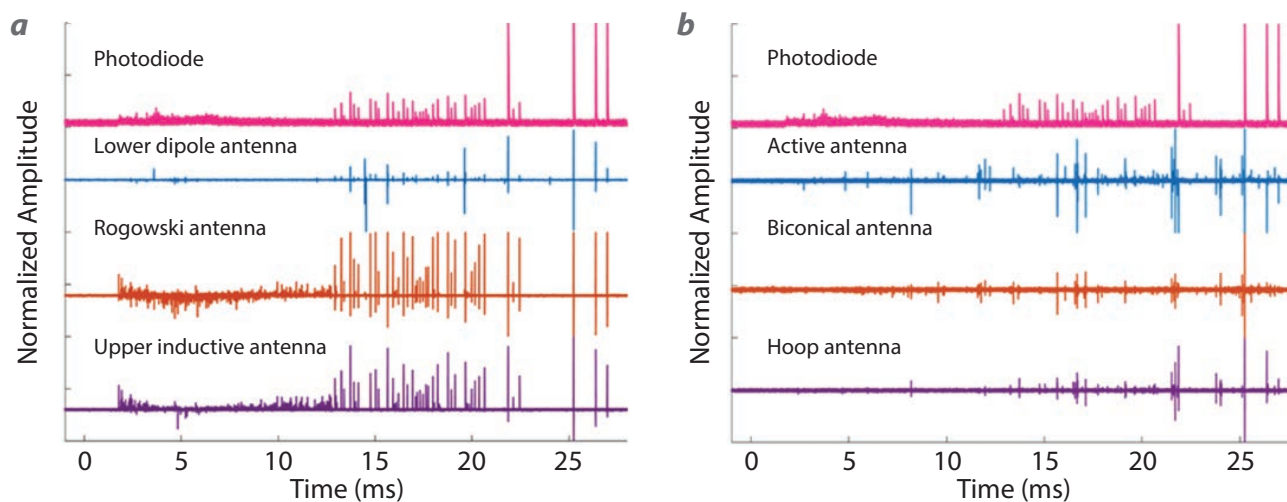


Figure 6. Pumice experimental results (experiment 180823-3) showing photodiode counts with (a) RF signals from three antennas that were inside the experimental chamber and (b) RF signals from three COTS antennas that were outside the experimental chamber

In our preliminary analysis of peak families, we observed what appeared to be several different pulse shapes showing up repeatedly over the record length (~33.5 ms). The results are shown in Figure 8a. The color-coded circles in Figure 8a correspond to the close-up views of signals at 13.73 and 26.38 ms in Figure 8b. Also displayed in Figure 8b are the corresponding camera frames showing time-correlated discharges. The close-up view $t \sim 26.38$ ms shows two antenna spikes that are 1.3 μ s apart; these spikes correspond to two photodiode signals (black trace) that are also 1.3 μ s apart. With a framing camera we may be able to observe distinct lightning signatures associated with the RF and photodiode signals.

For all of the RF peaks recorded by the upper inductive antenna over the 33.5 ms collection period that corresponded to photodiode counts, and thus to observable lightning, we calculated the power spectral density of each peak and averaged the results. As shown in Figure 9a, the peaks have broadband content from ~100 kHz to 20 MHz. The RF background signal recorded 6.5 ms prior to the rupture of the burst disc was used as a control and showed no spectral content. The broadband spectral content shown in Figure 9a matches what was observed with the AF-corrected COTS active antenna for the peak at 26.385 ms (see Appendix A of this report), and both correspond to

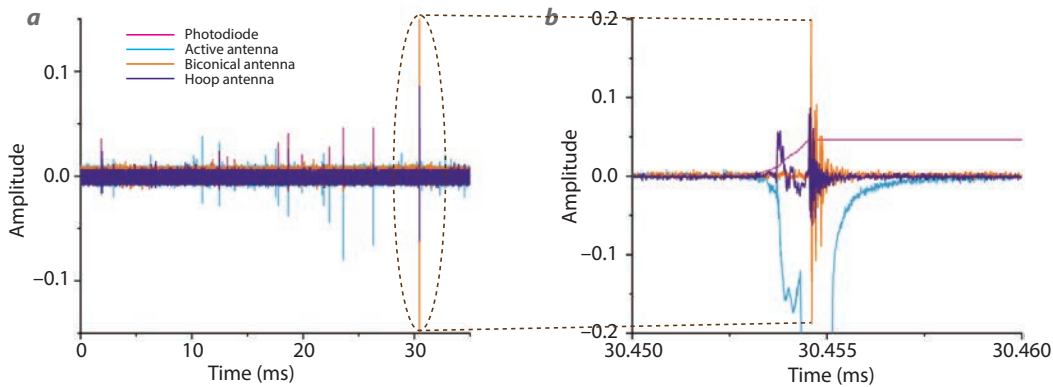


Figure 7. (a) Volcanic ash experimental results (experiment 180823-1) showing correlation between the photodiode counts and signals from the three external COTS antennas. (b) A close-up view at 30 ms showing that the rising edge of the photodiode trace corresponds closely to changes in the active and hoop antenna traces.

the broadband spectral content of natural lightning reported by Willett (1990) (shown in Figure 9b).

With volcanic ash, the power spectral density curve derived from the upper inductive antenna RF signals recorded between 0 and 33.5 ms (not shown here) is also similar to that observed with pumice and to what is reported for natural lightning.

With glass beads (experiment 180821-2), only one indication of lightning was observed in the imagery, and only one significant non-bimodal peak appears in the upper inductive antenna data (Figure 10a). The source of the bimodal peaks seen in the upper inductive antenna data is not known; they correspond

to peaks recorded by the external antennas, but no corresponding peaks are seen in photodiode signals. The bimodal peaks appear at early times and, to a lesser extent, between ~25 and 30 ms. Figure 10b shows the power spectral density spectrum derived from the peak at 31.77 ms

when lightning was observed with glass beads. This spectrum is similar to that observed with pumice and volcanic ash, and therefore also corresponds to what is reported for natural lightning by Willett (1990).

Graphite Flakes

We performed two rapid decompression experiments with uniformly sized, 44 μm diameter graphite flakes in ambient room lighting conditions. Bright spots were observed in high-speed camera imagery from experiment 180816-3 (Figure 11), and we think they resulted from ambient light reflecting off the

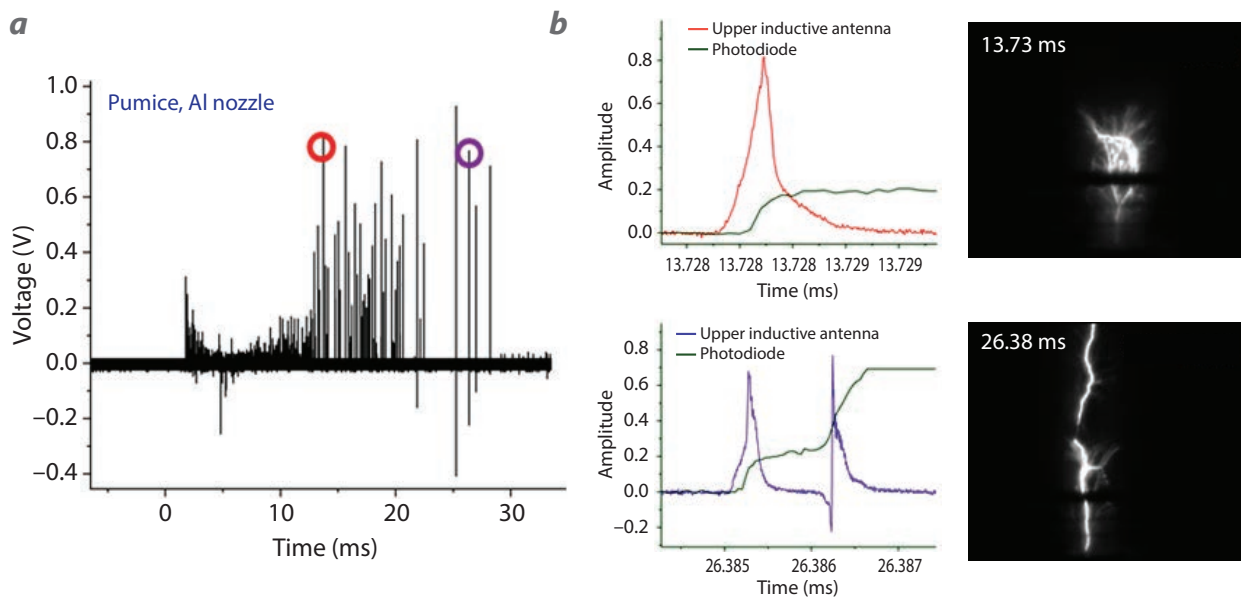


Figure 8. (a) Pumice experimental results (experiment 180823-3) showing upper inductive antenna pulses observed for the duration of scope record. (b) Close-up views at 13.73 and 26.38 ms, with corresponding camera frames.

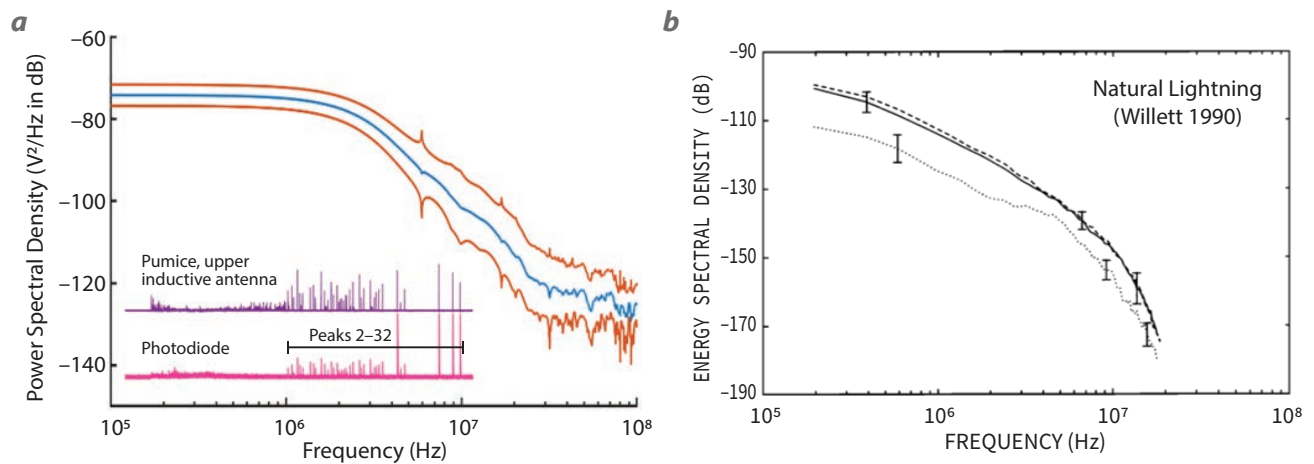


Figure 9. (a) Pumice experimental results (experiment 180823-3) showing power spectral density (blue trace) for RF emission corresponding to peaks 2–32 on the photodiode, with upper and lower standard deviations (orange traces); the inset (from Figure 6a) shows RF emissions recorded by the upper inductive antenna (purple trace) corresponding to photodiode peaks 2–32 (pink trace). (b) Comparison to natural lightning spectral content (figure taken from Willett [1990]).

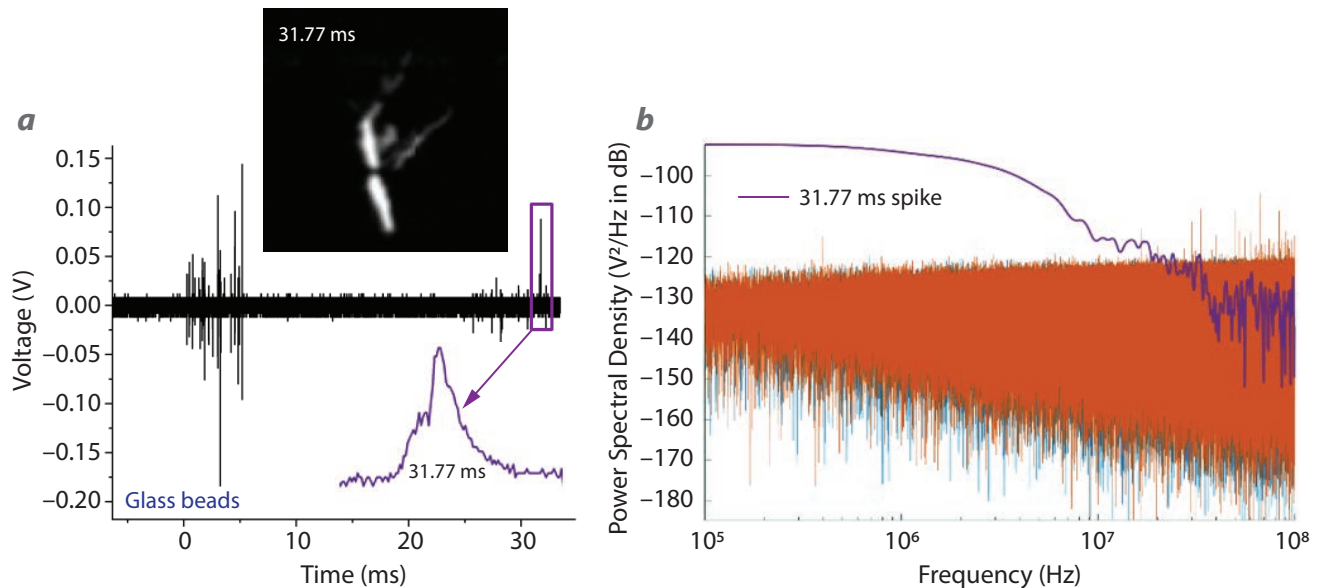


Figure 10. Glass beads experimental results (experiment 180821-2) showing (a) upper inductive antenna pulses observed for the duration of the scope record, with a close-up view of the peak at 31.77 ms when lightning was observed; and (b) power spectral density spectrum derived from the isolated peak when lightning was observed at 31.77 ms (purple trace), with corresponding camera frame, compared to power spectral density spectra of all RF emissions between 0 and 33.5 ms (orange trace) and 6.5 ms before burst disc rupture (blue trace).

faces of the graphite flakes. Camera imagery does not show indications of discharges on a scale larger than the flake size, and RF data do not indicate that macroscopic lightning was produced. We expect that if we perform experiments with graphite flakes in the dark, the bright spots will not appear. In the upper inductive antenna data, only intense bimodal peaks were observed (Figure 12a), and these appear at early times (~1 ms) when the graphite sample was ejected

from the vent and fanned out. Similar peaks are seen in the lower inductive antenna data, but no corresponding peaks are observed in the data from the external antennas. Video imagery from the experiment suggests that the graphite particles may have physically impacted the upper inductive antenna that surrounded the vent. The power spectral density spectrum from the first 10 ms does not have a broadband signal that corresponds to natural lightning, and the power

spectral density spectrum taken from 10 to 35 ms also does not have broadband spectral content (Figure 12b).

The absence of coincident RF and optical signals agrees with simulations that charge transfer is dependent upon electrical properties and particle geometry. Unlike the dry silica-based samples, graphite is electrically conductive. It is expected that with flakes, exchange of electrons via surface contact may also be impeded relative to surface contact between more spherical geometries. We would like to perform this experiment with non-flake graphite powder, and with microdiamonds, which are nonconductive and are also produced as a result of the detonation of certain explosives.

High-Pressure Cluster Source

A high-pressure cluster source was assembled and tested in the second year of the project (Figure 13a). This cluster source was designed to operate in a pressure regime ranging from 10 to 1000 Torr. These pressures are approximately 100 to 10,000 times higher than the operating pressure of typical cluster sources. Cluster ions are generated by pulsed laser vaporization of a translating/rotating sample (typically a rod that is ¼" in diameter) that is housed in the body of the cluster source. The body of the source is pressurized with

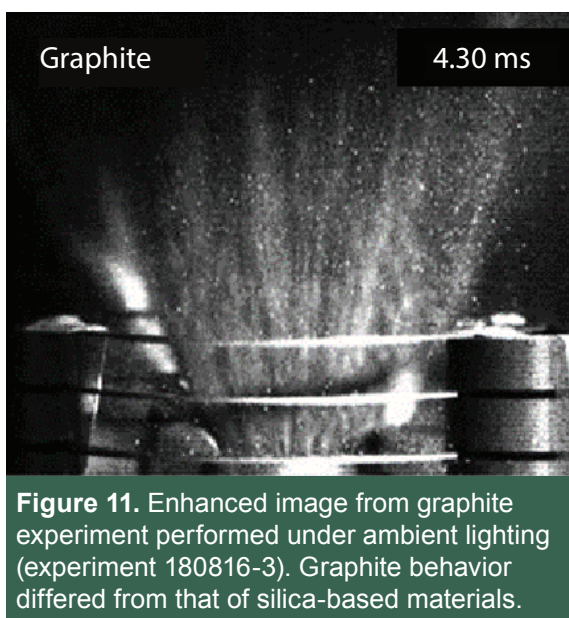


Figure 11. Enhanced image from graphite experiment performed under ambient lighting (experiment 180816-3). Graphite behavior differed from that of silica-based materials.

helium, neon, or argon. Ions exiting the source are guided and focused by an ion funnel for injection into the IM-MS for analysis. Carbon clusters produced by laser ablation of graphite under vacuum using a traditional cluster source, at conventionally low pressure ($\sim 10^{-2}$ Torr, $t = \sim 1 \mu\text{s}$) are shown in Figure 13b. While clusters up to C_{166}^+ were also observed, higher molecular weight clusters are expected to be produced when conditions are optimized using the high-pressure source.

Testing of the high-pressure source demonstrated that it was capable of operating at pressures of approximately 1000 Torr while simultaneously maintaining the desired pressure in the vacuum chamber housing the source. Once the operating pressure range of the source was verified, cluster formation testing was initiated. We used copper and graphite sample rods to test for cluster formation. We varied several experimental parameters in order to determine the optimal conditions for generating cluster ions with the system. These tests found that the source was capable of generating excellent total ion counts, but the majority of these ions were atomic ions, with only a small population of clusters being formed. Testing and development of the source is expected to continue in FY 2019 as part of another SDRD project.

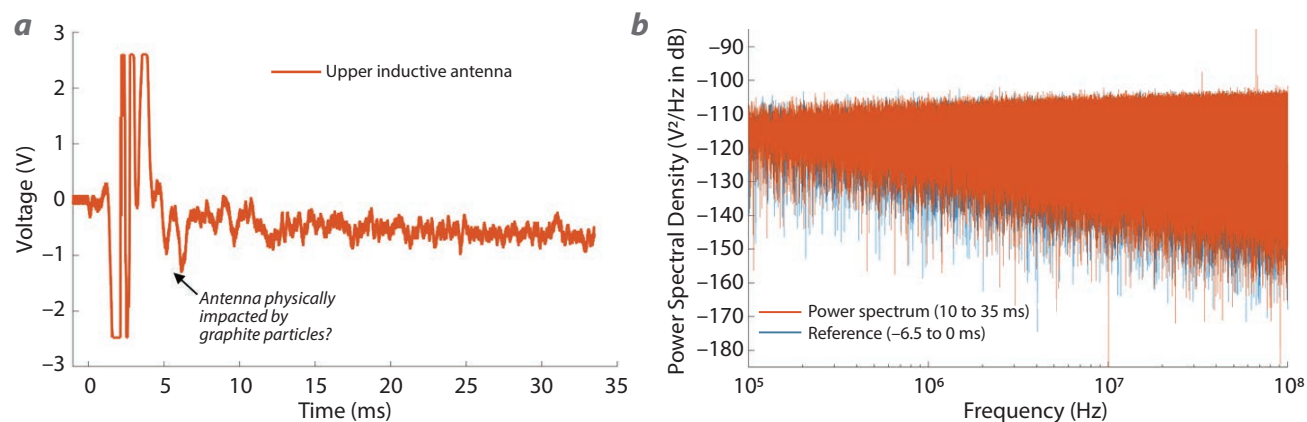


Figure 12. (a) Graphite experimental results (experiment 180816-3) showing the upper inductive antenna trace. (b) Lack of a 100 kHz to 20 MHz broadband signal corresponds to camera data that also indicate the absence of lightning.

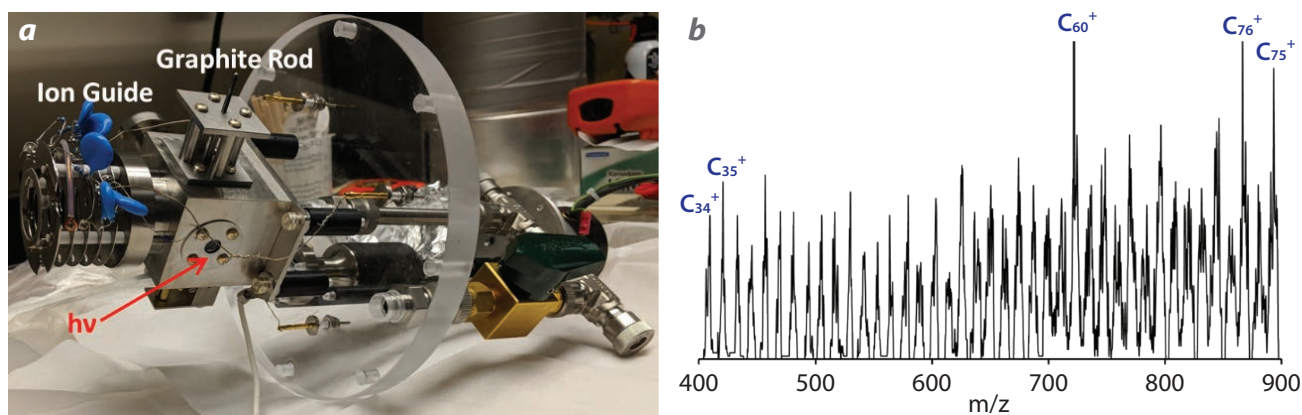


Figure 13. (a) High-pressure pulsed-valve cluster source designed to operate at pressures up to 5 orders of magnitude higher than a conventional cluster source. The ion guide mates to the ion funnel of the IM-MS. (b) Carbon clusters produced by laser ablation of graphite under vacuum using a different cluster source operating at conventionally low pressure ($\sim 10^{-2}$ Torr, $t = \sim 1$ μ s).

CONCLUSION

We have demonstrated that we can create and measure emissions from discharges resulting from triboelectric- and fracto-emission charging mechanisms associated with particles under turbulent conditions. These experiments provide experimental evidence that corresponds to LLNL simulations that correlate internal hydrodynamic and electrostatic behavior. Experimental results indicate that particle shape, size, and electrical properties are fundamental to the detected output. This capability will be an asset to the Defense Nuclear Nonproliferation community and may also impact stockpile stewardship work.

We foresee significant future work in this area. Initially, we would like to perform additional analysis of the data already collected and further characterize the antennas we used in the experiments. At this point, it is not clear whether charged clusters are discharging to ground rather than to clusters of particles with opposite charge. In future experiments of this type, we will examine the termination/propagation point of the discharges and implement mitigating measures as needed. Prior to executing additional experiments, we will consult with modelers to ensure that the samples and diagnostics selected inform their models and are best tailored to their needs. We expect that experiments with microdiamonds, a nonconductive allotrope of carbon that is produced by detonation of certain HEs, and with metals/metal oxides will generate new insights. Models will be further informed by additional diagnostics that we can use to derive experimental conditions. For instance, to derive charge-to-mass ratios for particles, we could

use measurements of the charge on particles that fall into a Faraday cup connected to an electrometer. To derive temperature following a discharge, we could use spectroscopic techniques such as coherent anti-Stokes Raman scattering or a high-speed hyperspectral camera to examine ionic, atomic, and molecular emissions. To feed optical models, we could apply absorption spectroscopy, millimeter-wave spectroscopy, and particle-sizing techniques to characterize the controlled particle plumes produced by the rapid decompression apparatus.

For future rapid decompression measurements, a stand-alone rapid decompression system that is not reliant on the gas gun is needed. The design and building of such a system will be investigated in a follow-on study to this SDRD project that is scheduled to take place in FY 2019. A stand-alone rapid decompression platform would provide a new test facility that will allow us to work directly with laboratories on parametric experiments performed at STL. Such a platform would also allow us to test new diagnostics before they are taken to the field.

Another important part of this project has been the design, fabrication, and testing of a high-pressure cluster source that mates to an IM-MS. In FY 2018 the cluster source was placed in the IM-MS source chamber and used in preliminary tests. In future work its operation will be optimized for the production of clusters that are high in molecular weight. The system will enable us to perform thermodynamic studies of large clusters, which are also very relevant to understanding characteristics of HE experiments and may provide diagnostic handles on species involved.

ACKNOWLEDGMENTS

We would like to thank Rick Allison and Tom Keenan for design and fabrication support, Eric Larson and Kevin Lee for electrical engineering support, Dale Turley for logistical support, Paul Kemper (University of California, Santa Barbara) for technical support with the cluster source, and Jason Sears (LLNL) for his contributions as an RF modeler. We also thank Gary Walker (Remote Sensing Laboratory–Nellis) for lending us the COTS antennas and for advice on setting them up.

REFERENCES

- Alatorre-Ibargüengoitia, M. A., B. Scheu, D. B. Dingwell, “Influence of the fragmentation process on the dynamics of Vulcanian eruptions: An experimental approach,” *Earth Planet. Sci. Lett.* **302**, 1–2 (2011) 51–59.
- Cimarelli, C., M. A. Alatorre-Ibargüengoitia, U. Kueppers, B. Scheu, D. B. Dingwell, “Experimental generation of volcanic lightning,” *Geology* **42**, 1 (2014) 79–82.
- Kimblin, C., I. McKenna, M. J. Manard, D. Gardner, X. L. Mao, G. Walker, “Transient RF and optical plasma signatures,” in *Site-Directed Research and Development*, FY 2017, National Security Technologies, LLC, and Mission Support and Test Services, LLC, Las Vegas, Nevada, 2018, 105–112.
- Kok, J. F., N. O. Renno, “A comprehensive numerical model of steady state saltation (COMSALT),” *J. Geophys. Res. Atmos.* **114** (2009) D17204.
- Taylor, H. E., F. E. Lichte, “Chemical composition of Mount St. Helens volcanic ash,” *Geophys. Res. Lett.* **7**, 11 (1980) 949–952.
- Wardman, J. B., T. M. Wilson, P. S. Bodger, J. W. Cole, D. M. Johnston, “Investigating the electrical conductivity of volcanic ash and its effect on HV power systems,” *Phys. Chem. Earth* **45–46** (2012) 128–145.
- Watkins, E. B., et al., “Evolution of carbon clusters in the detonation products of the triaminotrinitrobenzene (TATB)-based explosive PBX 9502,” *J. Phys. Chem. C* **121**, 41 (2017) 23129–23140.
- Willett, J. C., J. C. Bailey, C. Leteinturier, E. P. Krider, “Lightning electromagnetic radiation field spectra in the interval from 0.2 to 20 MHz,” *J. Geophys. Res. Atmos.* **95**, D12 (1990) 20367–20387.

Appendix A

Rapid Decompression Experiments— Samples and Diagnostics

One of the COTS antennas used in the rapid decompression experiments was a discone active antenna manufactured by Antenna Research Associates, Inc. Summarized below is our initial attempt at applying the antenna factor (AF) obtained from the manufacturer's datasheet (Figure A1) to 180823-3 dry pumice experimental results (Figure A2). We note that for peaks that correspond to lightning, similar results to those obtained with the custom STL upper inductive antenna are obtained with the corrected active antenna.

The active antenna was ~ 1 m away from the experiment, so the unit of measure in the y -axis, dB m^{-1} , can be approximated as dB.

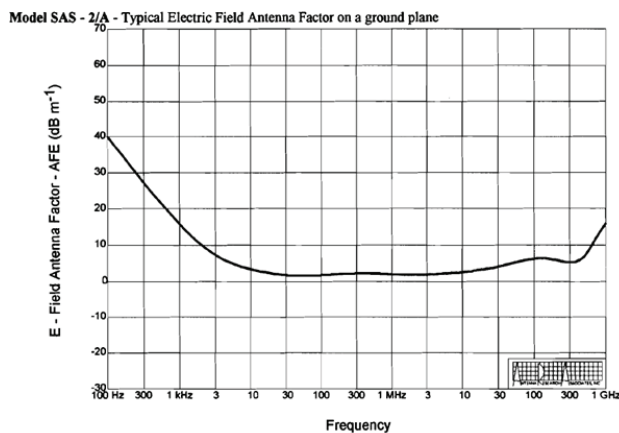


Figure A1. Manufacturer-supplied antenna factor for the active antenna

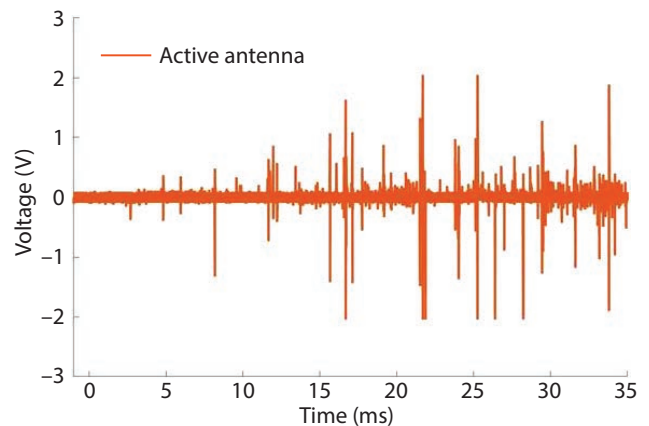


Figure A2. Signals measured on the active antenna in volts (pumice, experiment 180823-3)

The difference between the raw and antenna factor–corrected data is fairly subtle but is easier to see in a periodogram of just one RF peak. The FFT of an AF-corrected pulse corresponding to a discharge observed between 26.385 and 26.3875 ms (Figure A4, experiment 180823-3) has broadband spectral content that compares well to the broadband spectral content observed in periodograms derived from the custom inductive antenna. The power spectral density also matches nicely with that from lightning shown in Figure 9b (Willett [1990]).

Video from this project is available at https://nlv-ddsprd1-ws.nts.ops/NNSS_SDRD/ProjectOutcomePageViewEdit.aspx?Action=ViewDetails&PK_ProjectOutcome=562&View=562 and from the principal investigator.

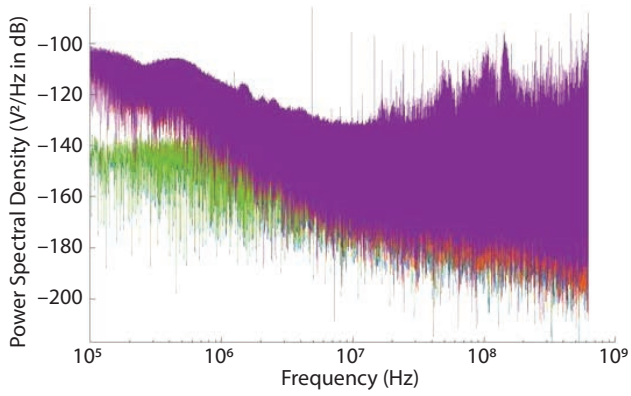


Figure A3. AF-corrected periodogram, where the blue trace is the FFT from time -2 to 0 ms (reference), the green trace is the reference plus antenna factor, the orange trace is the FFT from time 0 to 35 ms (signal), and the purple trace is the signal plus antenna factor.

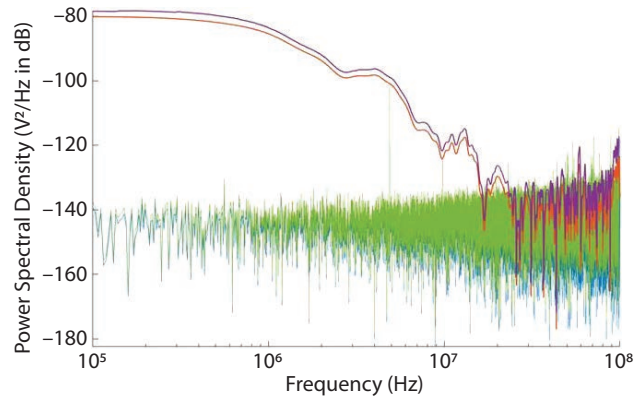
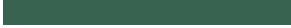


Figure A4. The blue trace is the FFT from time -2 to 0 ms (reference), the green trace is the reference plus antenna factor, the orange trace is the FFT of just one peak (from time 26.385 to 26.3875 ms), and the purple trace is the FFT of the same peak plus antenna factor.



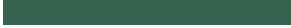
Triggerable Mode-Locked Laser for Synchronization with Dynamic Compression Experiments

STL-044-18 ■ Year 1 of 1

Brandon La Lone^{1,a} and Jason Mance^a

¹lalonebm@nv.doe.gov, (805) 681-2046

^aSpecial Technologies Laboratory



Mode-locked lasers are immensely useful in many areas of physics, and we are beginning to see more uses for them in dynamic compression science. However, one limitation is that we cannot trigger a mode-locked laser to create a pulse on demand, which creates a synchronization problem with single-event experiments. The purpose of this project was to create a triggerable mode-locked laser by injecting an optical pulse into the laser cavity that seeds the mode-locking process. The mode-locked laser pulses would then be an integer number of round-trip times from the seed and be precisely known in time. We acquired a mode-locked fiber laser with a connectorized cavity so that we could attempt various pulse injection schemes. While we were able to have some influence on the mode-locking dynamics, we were unable to create a triggered pulse with any reliability. Potential paths forward are discussed.

BACKGROUND

Mode-locked lasers (MLLs) emit a train of very short optical pulses, normally less than one picosecond in duration, at a constant repetition rate that is the inverse of the cavity round-trip time. The term “mode-locked” refers to the fact that all of the longitudinal modes in the laser cavity are in phase, and these lasers are so spectrally broad that they propagate many such modes (our fiber lasers have 10,000 to 100,000 longitudinal modes). Because of their properties of being short in time, high in peak power, spectrally broad, and with stable repetition rates, these lasers have found

many uses. Notable uses are in nonlinear optics and spectroscopy. In dynamic compression science, MLLs are used in broadband laser ranging, time-stretched photonic Doppler velocimetry, and temporal imaging. However, one major drawback of MLLs is that the phase of the pulse train cannot be precisely controlled. This characteristic makes it a challenge to synchronize any one pulse. Current solutions involve complicated feedback systems that actively modulate the laser cavity length or loss to control the timing; however, these systems are highly complex, and obtaining precise timing control is still a challenge (Miura 2002). For dynamic experiments such as gas-gun, high-

explosive, pulsed-power, or laser-driven shock wave experiments, we often achieve this synchronization by creating a clock signal from the laser itself and using it to trigger the dynamic event. However, in many experiments, this solution is not possible. For example, on a gas-gun experiment, the arrival time of the shock wave cannot be triggered with certainty by an external clock.

The goal of this project was to create a triggerable MLL for use on single-event dynamic compression experiments that are asynchronous with any clock. When an MLL is first switched on, the mode-locking process normally happens spontaneously. Our concept was to seed the laser cavity with optical pulses that would evolve into the mode-locked pulses, effectively facilitating precise control over the phase of the MLL pulse train. Furthermore, the plan was to observe MLL dynamics using recently developed spectrum-to-time mapping techniques.

PROJECT

Observing the Mode-Locking Process

The first step in this project was to develop a method to observe the mode-locking dynamics of our femtosecond fiber laser. We used recently developed methods of converting the optical spectrum into the time domain (Herink 2016). Initial tests were performed with a laser from Kphotonics at a repetition rate of 12.5 MHz. The output of the laser was sent through a dispersion compensation module equivalent to the dispersion in 30 km of SMF-28 fiber and then detected with a high-bandwidth photodiode and digitizing oscilloscope. The dispersion compensation module temporally stretches each laser pulse such that the long wavelengths arrive on the detector before the short wavelengths, which enables us to determine the spectral content on a pulse-by-pulse basis. By

recording many pulses, we generate a spectrum versus time record. We set up the oscilloscope to record the moment when the laser spontaneously mode-locks, which happens soon after the laser is turned on. The result of one of these records is shown in Figure 1. The figure shows that early in the record when the number of cavity round trips is less than 1000, there is some optical noise at all wavelengths. As the system evolves, a short (~150 ps) pulse forms with a pronounced wavelength of about 1562 nm. At around 900 cavity round trips, the laser transitions from the relatively long (picosecond), spectrally narrow pulse

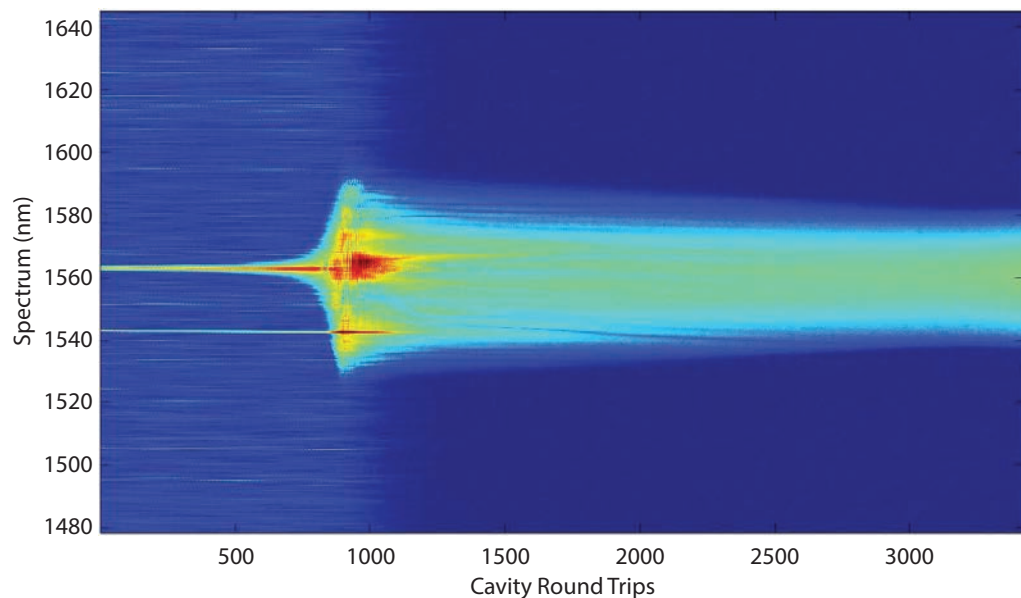


Figure 1. Spectrum versus cavity round-trip number of a mode-locked fiber laser about the moment that mode-locking occurs spontaneously. For this laser, each cavity round trip is equal to 80 ns.

to a short (femtosecond), spectrally wide pulse. The system is essentially a noise-free, stable MLL pulse after about 3000 cavity round trips. With this method, we could directly observe the mode-locking dynamics. Our plan was to inject a 150 ps duration, 1562 nm wavelength pulse at a specific time, rather than allowing mode-locking to occur spontaneously.

Connectorized Mode-Locked Laser

In order to try our pulse injection method, we needed to have access to the laser cavity (typically, lasers are sealed, and all fiber connections are fusion spliced). Kphotonics built us a custom laser that had part of the cavity broken out with fixed connection (FC)/angled physical contact (APC) fiber connectors. Figure 2 shows a schematic and picture of the laser. The laser

is built entirely of polarization-maintaining (PM) fiber, and has an erbium-doped fiber gain medium pumped with 976 nm light from a laser diode and a carbon nanotube-based saturable absorber (SA) component. The SA has reduced optical loss at high intensities, which makes the cavity prefer to lase in the pulsed “mode-locked” state. The carbon nanotube technology is a proprietary Kphotonics technology. The connections marked OC (output coupler) and SA are external to the laser such that the laser cavity is complete only when a fiber jumper is connected from OC to SA. In addition to building the custom

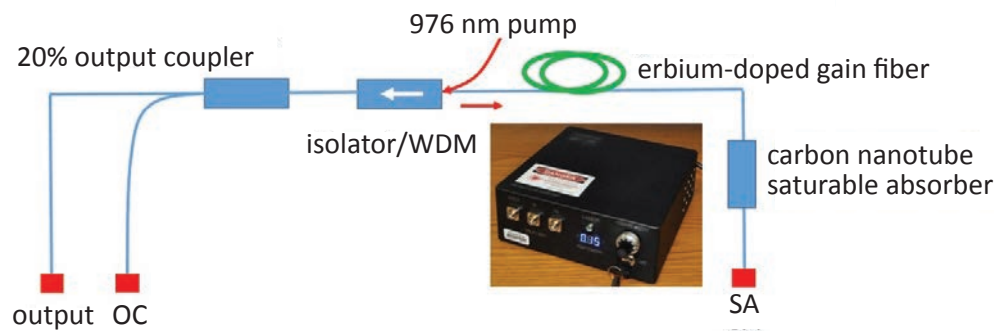


Figure 2. Schematic diagram and picture of a custom mode-locked fiber laser made by Kphotonics specifically for this project. OC and SA are fiber connections on the outside of the laser such that the cavity is complete only when a fiber jumper is connected from OC to SA. The carbon nanotube saturable absorber is the element that enables mode-locking to occur.

fiber connections to the cavity, Kphotonics added an adjustable pump current control to our laser, something that is not available on standard units. This allowed us to place our own components into the cavity and adjust the pump power to compensate for the added loss.

Pulse Injection Tests on Mode-Locked Fiber Laser

In order to perform pulse injection tests, we connected a 50/50 PM fiber splitter with one side connected to the OC port and the other connected to the SA port to complete the cavity. By fine-tuning the pump current, we were able to cause the laser to spontaneously mode-lock with the splitter in place, so the splitter did not prevent lasing. External pulses were injected into the unused port of the 50/50 splitter such that light would propagate toward the SA port in the counterclockwise direction, which is the direction of normal lasing of the cavity. Next, we constructed a system in order to replicate the 150 ps/1562 nm pulse that occurs prior

to spontaneous mode-locking. To obtain the desired wavelength, we passed a continuous-wave (CW) amplified spontaneous emission (ASE) source through a tunable bandpass filter. We then modulated the CW source with a Mach-Zehnder modulator to create 150 ps optical pulses. In order to drive the Mach-Zehnder modulator, we used a function generator to trigger a picosecond pulse generator (AVTECH). The generated pulse was then electrically amplified with an RF amplifier (Tektronix PSPL5865) designed to amplify picosecond electrical pulses on a DC background. Finally, we sent the laser output through

a fiber dispersion module and recorded the dynamics with a fast photodetector and digitizer. A schematic of the system is shown in Figure 3.

We conducted pulse injection tests using a variety of approaches. One of the approaches we used was to inject a single pulse into the laser cavity and monitor how the cavity responds.

We also injected a continuous train of pulses into the cavity with the pump turned off (or powered down to a low output level), and then turned on (or up) the pump and monitored the dynamics. We also experimented with an approach in which a sinusoidal optical signal was injected into the cavity with a frequency that matches the natural MLL pulse train frequency.

In all cases where multiple pulses or cavity modulations were used, the repetition rate was set to an integer division of the natural mode-locked repetition rate of the laser. Because the picosecond pulse generator was only capable of running at repetition rates up to approximately 4 MHz, it was not possible to seed at the natural 40 MHz rate of the laser. In order to match the 40 MHz laser rate, we replaced the TTL and picosecond pulse generators in Figure 3 with a function generator that outputs a sine wave. We were able to match the laser repetition rate, or integer divisions, to better than 10 kHz.

Surprisingly, in all cases we found it very difficult to have a strong effect on the mode-locking process.

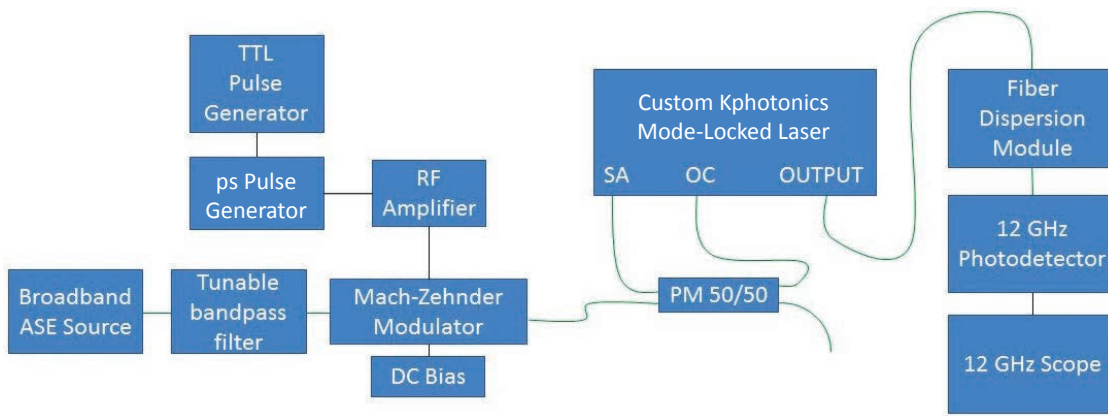


Figure 3. Schematic diagram of the system used to inject seed pulses into the laser cavity and monitor the mode-locking process

When we injected short pulses, the laser often responded either by amplifying the short pulses and prohibiting mode-locking, or by ignoring them and mode-locking from random noise as if the seeded pulses were not present. In the case where the injected

pulses were amplified, they neither broadened spectrally nor became temporally shorter; the system was essentially acting as a simple fiber amplifier. We sent the output of the 150 ps pulses from the Mach-Zehnder modulator through a fiber amplifier to

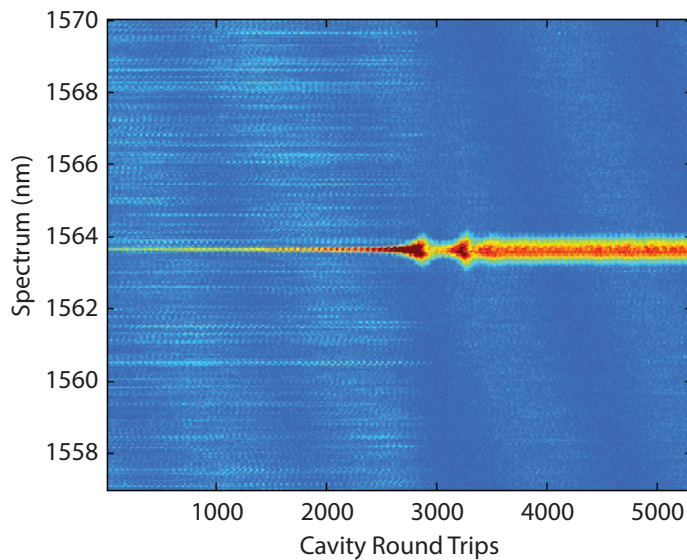


Figure 4. Mode-locking of the laser with an external sinusoidal modulation from an ASE source. The spectrum on the y-axis only refers to the laser spectrum. The ASE source is seen as somewhat faint and broad diagonal lines in the image, and the laser spectrum is seen as the horizontal red/green line that broadens at around 3000 cavity round trips when mode-locking begins. The laser repetition rate and the external modulation frequency are slightly out of phase, which is why the ASE source appears as diagonal lines (the data analysis that created this image was in phase with the laser frequency). Mode-locking always started at the null (darker blue bands) of the ASE source modulation.

increase the energy of the injected pulses. The laser did not appear to respond differently as the seeded pulse energy was increased. Eventually the higher-energy pulses extracted too much stored energy from the gain medium, and mode-locking was inhibited. We had limited success when we seeded the cavity with a sinusoidal pulse train, and the result of one such test is shown in Figure 4. The modulation rate was slightly higher than the natural repetition rate, and this modulation is seen as broad diagonal lines in Figure 4. We found that the mode-locking of the laser always started in one of the minimums of the pulse modulation, and this is seen in Figure 4 at around 3000 cavity round-trip times. However, the pulse train did not form with a phase precise enough to accurately control the pulse timing, and thus this would not work as a triggerable MLL source.

We initially planned to place a Mach-Zehnder modulator in the cavity and use it to prevent the cavity from lasing or mode-locking until just before the seed pulses were injected. This would also allow us to modulate the cavity losses and potentially offer better control over the preferred phase of the mode-locked pulse train. However, because of a mismatch between the polarization state of the Mach-Zehnder modulator and the preferred polarization state of the laser, we could not obtain mode-locking with the Mach-Zehnder modulator in the cavity.

CONCLUSION

The inability to accurately synchronize MLL pulses with short-lived transient events, such as dynamic compression experiments, or with other mode-locked lasers limits the applications for which MLLs can be used. The goal of this project was to inject a triggered seed pulse into a mode-locked fiber laser such that the laser would spontaneously lock to the seed pulse time and make a triggerable MLL. A secondary goal was to observe the mode-locking dynamics by stretching the pulses in dispersive fiber, which converts the spectrum into the time domain and gives us a spectrum versus time view of the mode-locking process. We constructed a prototype laser system, in collaboration with Kphotonics, that allowed us to control laser pump power and inject pulses into the laser cavity, and we were able to observe mode-locking dynamics on a single-shot timescale. However, we were unable to reliably initiate the mode-locking process. In general, it was surprisingly difficult to influence the laser's natural mode-locking dynamics beyond turning it off when the energy of the pulses pulled enough gain out of the laser cavity to prevent lasing.

For this work, we used an incoherent ASE source to create the seed pulses and a bandpass filter with a broad bandwidth compared to the spectrum of the picosecond pulses that naturally occur as the laser mode-locks from noise. For future work, it may be advantageous to use a coherent CW laser diode tuned precisely to this natural wavelength instead of an ASE source and bandpass filter.

We were also unable to modulate the cavity loss due to polarization discrimination issues in the Mach-Zehnder modulator. Obtaining a Mach-Zehnder modulator that does not inhibit mode-locking and placing it in the cavity would provide more control over when the laser is permitted to mode-lock. The development and application of predictive models for mode-locking would also be valuable.

REFERENCES

Herink, G., B. Jalali, C. Ropers, D. R. Solli, "Resolving the build-up of femtosecond mode-locking with single-shot spectroscopy at 90 MHz frame rate," *Nat. Photonics* **10** (2016) 321–326.

Miura, T., H. Nagaoka, K. Takasago, K. Kobayashi, A. Endo, K. Torizuka, M. Washio, F. Kannari, "Active synchronization of two mode-locked lasers with optical cross correlation," *Appl. Phys. B* **75**, 1 (2002) 19–23.

This page left blank intentionally

Gas-Phase Ion-Neutral Interactions of Cerium Ions with Deuterium

STL-002-18 ■ Year 2 of 3

Manuel J. Manard,^{1,a} Paul R. Kemper,^b and Rusty Trainham^a

¹manardmj@nv.doe.gov, (805) 681-2121

^aSpecial Technologies Laboratory

^bUniversity of California, Santa Barbara

The gas-phase interactions of cerium clusters and deuterium neutrals were investigated using a temperature-dependent reaction cell that is embedded between two quadrupole mass analyzers. Cerium clusters (Ce_m^+ , $m = 2, 3$) have been generated with our instrumentation, and rate constants have been acquired for the dissociation of deuterium gas (D_2) to form Ce_2D_4^+ and Ce_3D_6^+ , respectively, as a function of temperatures ranging from approximately 235 to 515 K. The rate constants vary from approximately $3.0 \times 10^{-14} \text{ cm}^3/\text{s}$ to $2.9 \times 10^{-13} \text{ cm}^3/\text{s}$ for Ce_2^+ reacting to form Ce_2D_4^+ and from $2.0 \times 10^{-12} \text{ cm}^3/\text{s}$ to $7.0 \times 10^{-12} \text{ cm}^3/\text{s}$ for Ce_3^+ reacting to form Ce_3D_6^+ . For both systems, the rate constants increase with temperature. Arrhenius analysis of the data indicates an activation energy barrier of 0.13 eV exists along the potential energy surface for the reaction of Ce_2^+ with D_2 , and the barrier is 0.04 eV for the reaction of Ce_3^+ with D_2 . A combination of experimental and theoretical analysis suggests that the reactions of both the cerium dimer and trimer are exothermic. Electronic structure calculations were performed using density functional theory at the B3LYP level to characterize all reactant and product species. In FY 2019, we will seek to extend these methods to Ce_m^+ clusters ranging from $m = 4$ to 25.

BACKGROUND

In recent years, there has been increased interest in characterizing the fundamental properties of cerium interacting with deuterium (Buttler 2017). These experiments seek to increase the understanding of the physics leading to ejecta breakup, transport,

and reactivity. Ejecta are fragments formed from shocked surfaces where sheets of material are removed as a shock wave propagates through the surface. Validation and verification of nuclear weapon simulations, specifically transport models, can be limited if uncertainty in the composition of the ejecta cloud exists. Ejecta density and size distributions are

measured using dynamic holography, Mie scattering, x-ray radiography, and piezo electric pins. None of these techniques can be used to determine the time evolution of the chemical composition of an ejecta field. Instrumentation developed at the Special Technologies Laboratory (STL) has been used to investigate these chemical phenomena. Detailed studies of the gas-phase thermodynamic and kinetic properties of these species have been carried out to provide insight into the fundamental processes governing reactivity of ejecta at the molecular level in support of ongoing stockpile longevity research efforts. Specifically, by probing the reactions that occur when shocked material interacts with other chemical species in their surroundings, the results acquired here could provide information leading to improved diagnostic capabilities for the stockpile stewardship community as well as provide experimental data for use as simulation benchmarks.

PROJECT

Experimental Method

The experimental details of the instrument have been previously provided (Manard 2014, 2015). Briefly, cerium (Ce) clusters (Ce_m^+) are generated by pulsed laser vaporization of a translating/rotating cerium rod in a high-pressure neon (Ne) bath gas. The Ne is flowed through a copper (Cu) coil that is immersed in liquid nitrogen to remove impurities in the bath gas that lead to the formation of cerium oxide ions. The desorbed cerium plasma is entrained in a high-pressure pulse of the inert bath gas that collisionally cools the plasma and drives cluster formation. The timing of the Ne pulse is synchronized with a laser using a Stanford Research Systems delay generator (DG535). The typical Ne pulse width is approximately 200 μs , with a backing pressure of approximately 30 psi. Cerium cations exiting the source are then mass selected by the first quadrupole mass filter and injected into the reaction cell.

The reaction cell is a Cu block that is 4 cm in length with entrance and exit orifices measuring 0.5 mm in diameter. The cell can be filled with either inert (helium, He) and/or reactive (deuterium, D_2) gases. These gases are flowed through the cell so a constant pressure is maintained. The typical pressure of gases in the cell ranges from 1.5 to 4 Torr. Pressure in the cell is measured using a capacitance manometer. The experimental temperature range of the cell can vary

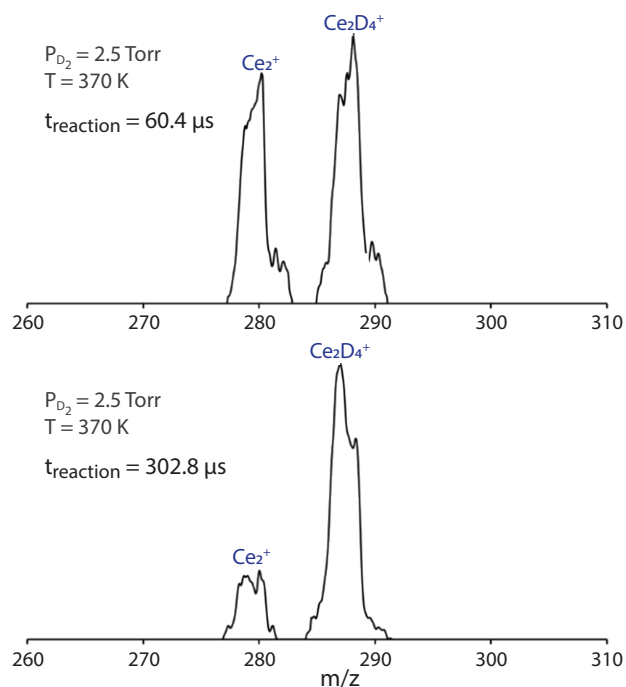


Figure 1. Mass spectra illustrating the time-dependent relative concentrations of Ce_2^+ to Ce_2D_4^+ , showing reaction products at times of 60.4 and 302.8 μs

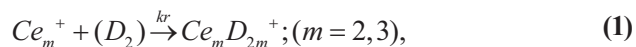
from 80 to 800 K. Temperatures greater than 300 K are achieved by resistive heating of tantalum resistors embedded in the cell body, while temperatures below 300 K are reached by flowing liquid-nitrogen-cooled nitrogen gas through channels that are also present in the cell body. The temperature is monitored by three thermocouples placed at various locations on the cell. Multiple thermocouples are used to verify no significant temperature gradients exist across the cell. Ions are drawn through the cell under the influence of a weak electric field (drift voltage). The field is weak enough so that the thermal energy of the ions is not significantly perturbed. Ions exiting the cell are mass selected by a second quadrupole mass filter and detected using a conversion dynode and Channeltron electron multiplier. The amount of time ions spend in the cell is controlled by adjusting the drift voltage and/or the pressure in the cell. Typically, the pressure is left constant and the drift voltage is varied to alter reaction times. If the relative ratio of the product to reactant peaks does not change with time, then temperature-dependent equilibrium methods can be used to obtain thermodynamic properties of the system. If the relative ratio does change with time, then reaction rate constants can be acquired, and we can determine how the rate constants vary with temperature.

Experimental Results

Mass spectra of Ce_2^+ , acquired with 2.5 Torr of D_2 filling the reaction cell at a temperature of 370 K, are shown in Figure 1, and mass spectra of Ce_3^+ , acquired with a mixture of 0.2 Torr of D_2 and 2 Torr of He filling the reaction cell at a temperature of 310 K, are shown in Figure 2. In both cases, the mass resolution of quadrupole mass analyzers was reduced to increase ion signal intensity. The most abundant, naturally occurring isotope for Ce is 140. Accordingly, the spectra were obtained by mass selecting either $m/z = 280$ (Ce_2^+) or $m/z = 420$ (Ce_3^+) with the first quadrupole and scanning the second quadrupole over the mass range shown in the figures. It is clear from these spectra that two D_2 ($m/z = 4$) ligands are bound to Ce_2^+ , which corresponds to the peak shown at $m/z = 288$. Alternatively, three D_2 ligands are bound to Ce_3^+ , corresponding to the peak at $m/z = 432$.

The upper and lower spectra in Figure 1 were acquired at reaction times of about 60.4 μs and 302.8 μs , respectively. The upper and lower spectra in Figure 2 were acquired at reaction times of approximately 39.7 μs and 78.8 μs , respectively. It is apparent from these data that the relative ratios of the Ce_2^+ and Ce_3^+ reactants to the respective products peaks are changing significantly with time, suggesting that the system has not reached equilibrium. Thus, time-dependent rate constants were acquired for these systems.

Rate constants for the pseudo-first order reaction in Equation 1 were acquired from the expression given in Equation 2,



$$\ln \left[\frac{Ce_m^+}{Ce_m^+ + Ce_m^+ D_{2m}^+} \right] t = k_r \rho_L t; (m = 2, 3), \quad (2)$$

where $[Ce_m^+]$ is the concentration of unreacted Ce_m^+ , $[Ce_m^+ + Ce_m^+ D_{2m}^+]$ is the sum of the concentration of unreacted Ce_m^+ and the $Ce_m D_{2m}^+$ concentration (representing the concentration of reactant cluster ions at time $t = 0$), ρ_L is the number density of D_2 in the reaction cell at a given pressure and temperature, t is time in seconds, and k_r is the rate constant for the reaction. The concentrations used in Equation 2 are directly proportional to the peak intensities in the mass spectra acquired after the ions exit the cell. Rate constants for the overall reaction of Ce clusters with D_2 were acquired by varying the amount of time the Ce_m^+ ions spend in the cell and plotting the left-hand

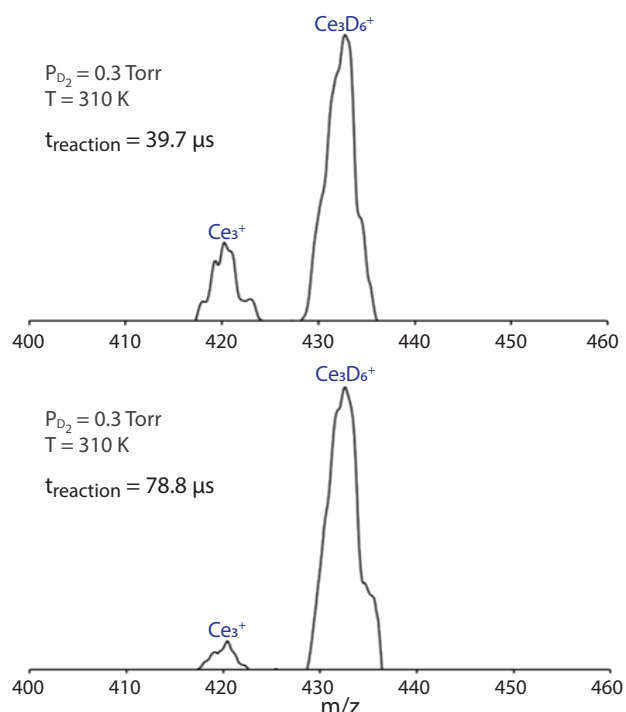


Figure 2. Mass spectra illustrating the time-dependent relative concentrations of Ce_3^+ to $Ce_3D_6^+$, showing reaction products at times of 39.7 and 78.8 μs

side of Equation 2 as a function of time. The resulting plots are approximately linear, with slopes that are proportional to the rate constants as a function of temperature, T , $k_r(T)$. The temperature of the cell was varied over a wide range to determine the effect of temperature on the experimental rate constants for both systems. These data are shown in Figures 3 and 4.

It is clear from the data shown in Figures 3 and 4 that the measured rate constants increase with temperature for the reaction of both the Ce dimer and trimer with D_2 . This implies that the reaction becomes more efficient as the temperature is increased. Phenomena such as these are generally observed for reactions where an activation energy barrier lies along the potential energy surface (PES) leading from reactants to products. Accordingly, Arrhenius analysis of the rate data was performed to determine the height of the activation energy barriers of the two systems. The Arrhenius expression is shown in Equation 3,

$$\ln k_r(T) = \ln A - \frac{E_a}{RT}, \quad (3)$$

where R is the gas constant, E_a is the activation energy of the reaction, and A is the pre-exponential factor. A

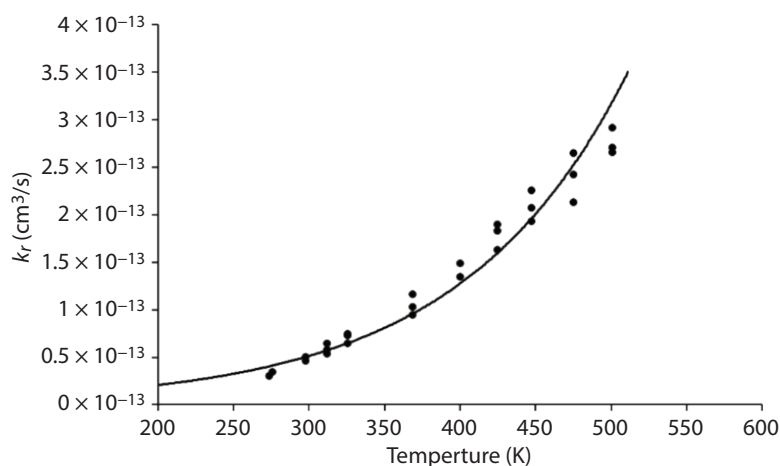


Figure 3. Experimentally measured rate constants for Ce_2^+ reacting with D_2 to form Ce_2D_4^+ as a function of temperature. The curve through the data points is provided to guide the eye; details of the analysis are given in the text.

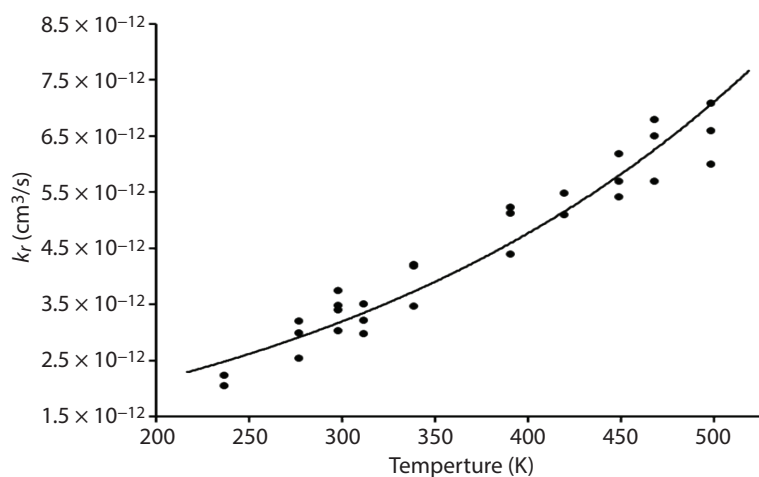


Figure 4. Experimentally measured rate constants for Ce_3^+ reacting with D_2 to form Ce_3D_6^+ as a function of temperature. The curve through the data points is provided to guide the eye; details of the analysis are given in the text.

plot of the natural log of the rate constants versus $1/T$ is linear with a slope proportional to the activation energy of the reaction. These plots are shown in Figure 5 for Ce_2^+ reacting with D_2 and Figure 6 for Ce_3^+ reacting with D_2 . The activation energies obtained from these plots are 0.13 eV for the Ce_2^+/D_2 system and 0.04 eV for the Ce_3^+/D_2 system.

Theoretical Method

All reactant and product species were characterized theoretically to determine atomic and molecular parameters needed to analyze the experimental data and to identify factors important in the bonding of

Ce clusters with D_2 . Density functional theory (DFT) calculations were carried out using the B3LYP hybrid functional and the NWChem software package. For all calculations reported here, deuterium was described using the standard 6-311++G** basis set. The basis set and effective core potential (ECP) used to treat Ce was developed by the Stuttgart-Dresden group and is referred to as “Stuttgart RSC 1997 ECP.” For heavier elements, atomic basis sets make use of ECPs to replace a certain number of core electrons with an effective potential to reduce the complexity of the calculation. Here, 28 of cerium’s 58 core electrons are replaced by the ECP, while all remaining electrons are explicitly treated by the basis set.

Geometry optimizations of all ions examined here were performed using multiple candidate structures to determine a true global minimum. To confirm that the geometry obtained from calculation was a global minimum, vibrational frequencies and rotational constants were also calculated to ensure the geometry did not actually correspond to a saddle point. This would manifest itself as a negative vibration frequency in the calculation.

Discussion

A previous investigation of the reaction of Ce^+ with D_2 found Ce^+ inserts into the deuterium sigma bond, forming two equivalent Ce^+-D covalent bonds, and that the overall reaction is exothermic (Manard 2018). A similar reaction motif was explored for the Ce_2^+ and Ce_3^+ interaction with D_2 . Specifically, when cluster ions interact with a neutral diatomic molecule, two types of bonds can form. The first is primarily electrostatic in nature, where a largely unperturbed D_2 ligand is relatively weakly bound to the cluster ion. The second is a covalent bond between the cluster and one or both of the deuterium atoms in D_2 . Here, a significant amount of electron density is shared between the Ce cation and one or both of the D_2 atoms. To form these new covalent bonds, the existing sigma bond in D_2 may be significantly altered or completely broken. It should be noted that

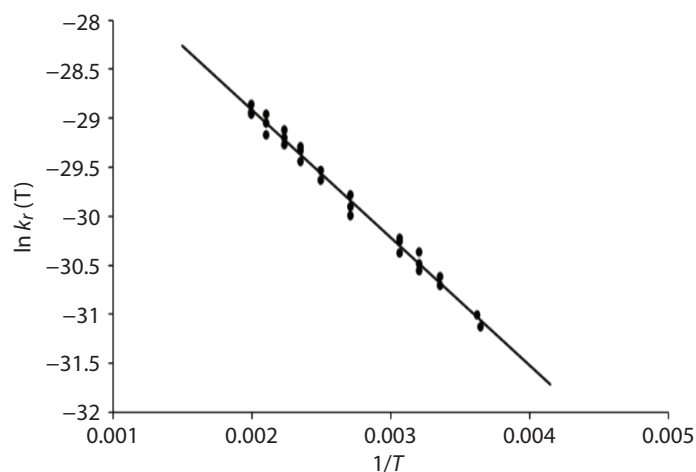


Figure 5. Plot of $\ln k_r(T)$ vs. $1/T$ for the reaction of $\text{Ce}_2^+ + 2(\text{D}_2) \rightarrow \text{Ce}_2\text{D}_4^+$. The line is a least-squares fit of the data that has a slope proportional to the activation energy of the reaction. The temperature range is from 265 to 515 K.

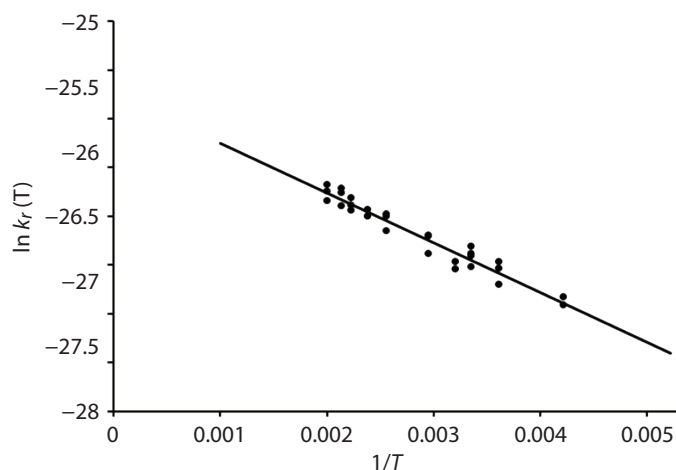


Figure 6. Plot of $\ln k_r(T)$ vs. $1/T$ for the reaction of $\text{Ce}_3^+ + 3(\text{D}_2) \rightarrow \text{Ce}_3\text{D}_6^+$. The line is a least-squares fit of the data that has a slope proportional to the activation energy of the reaction. The temperature range is from 235 to 500 K.

the electrostatic interactions described above reach equilibrium extremely quickly, on timescales that are much faster than those achievable with the current design of the reaction cell ($\ll 10 \mu\text{s}$). Thus, the fact that rate constants can be measured on the timescale of the experiment strongly suggests the bonding interaction is not of an electrostatic nature.

Figure 7 shows the minimum energy geometries of the Ce_2D_4^+ and Ce_3D_6^+ complexes calculated from DFT as well as the minimum energy geometries of the Ce_2^+ and Ce_3^+ cluster ions. Pertinent bond lengths

are provided. For both the dimer and the trimer systems, the minimum energy Ce_2D_4^+ and Ce_3D_6^+ complexes involve dissociation of the D_2 sigma bonds and formation of Ce-D bonds. For reference, the calculated unbound D_2 bond length is 0.766 Å. Using the reaction formula given in Equation 1, the energy for forming the Ce_2D_4^+ ion shown in Figure 7 is -3.69 eV , and the energy for forming the Ce_3D_6^+ ion shown in Figure 7 is -6.17 eV . It is clear that the formation of these inserted species are exothermic according to DFT. However, the thermochemistry associated with the insertion process was examined, using DFT energies, to ensure this mechanism is physically plausible.

First, for the reaction, DFT suggests that the energy required to dissociate the D_2 , as shown in Equation 4,



is approximately 4.56 eV. Thus, to break the D_2 bond, an energy in excess of this amount must be available in the Ce_m^+ ($m = 2, 3$) insertion mechanisms. Now, consider the dissociation reaction shown in Equation 5,



where $m = 2$ and the Ce_2D_4^+ ion is the conformation shown in Figure 7. DFT suggests that the energy required to break this bond is approximately 3.20 eV. Because all Ce⁺-D bonds are equivalent (D_{4h} symmetry), the energy released by forming these four bonds is approximately -12.76 eV . When the cost of breaking the two deuterium bonds (9.12 eV) is removed from this value, DFT suggests the overall insertion reaction is exothermic by approximately -3.68 eV for the dimer system.

A similar analysis for the trimer ($m = 3$) indicates that loss of a D atom from the Ce_3D_6^+ ion shown in Figure 7 requires 3.30 eV, suggesting the overall $m = 3$ insertion reaction is exothermic by approximately -6.12 eV . This strongly supports the hypothesis that the mechanism giving rise to the experimental rate constants is insertion of cerium clusters into the D_2 bonds.

The combined experimental and theoretical analysis of the Ce dimer and trimer reacting with D_2 clearly suggests that both PESs have activation energy

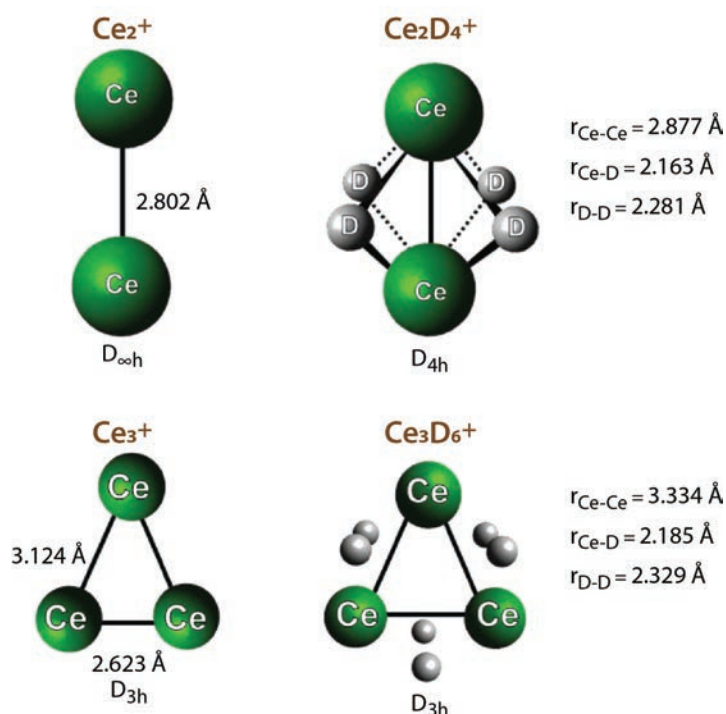


Figure 7. Theoretical geometries of Ce_2^+ , Ce_2D_4^+ , Ce_3^+ , and Ce_3D_6^+ complexes calculated at the DFT B3LYP level. Bond lengths, r , are in angstroms.

barriers that are higher in energy than the respective reactant energy asymptotes while simultaneously culminating in products that are exothermic relative to the reactants. The difference in the magnitude of the two energy barriers (0.13 eV for the dimer vs. 0.04 eV for the trimer) can be observed by comparing the rate constants measured for the two systems. Specifically, the rate constants measured for the Ce_2^+/D_2 reaction are approximately a factor of 10 less than those measured for the Ce_3^+/D_2 reaction. A barrier height of 0.04 eV is nearly at the thermal energy available to the trimer system for the temperature range used in the experiment. Thus, the reaction occurs significantly faster than for the dimer system, where the activation energy is significantly larger than the available thermal energy. Here, the Boltzmann distribution of available states allows the reaction to proceed to products. However, the energy barrier reduces the efficiency of the reaction for the Ce_2^+/D_2 system by a factor of 10. The underlying cause for what gives rise to the respective barriers is currently under investigation.

CONCLUSION

Ce_m^+ clusters ($m = 2, 3$) have been generated, and rate constants have been acquired for the dissociation of D_2 to form Ce_2D_4^+ and Ce_3D_6^+ as a function of temperatures ranging from about 235 to 515 K. The rate constants vary from approximately $3.0 \times 10^{-14} \text{ cm}^3/\text{s}$ to $2.9 \times 10^{-13} \text{ cm}^3/\text{s}$ for Ce_2^+ reacting to form Ce_2D_4^+ and from $2.0 \times 10^{-12} \text{ cm}^3/\text{s}$ to $7.0 \times 10^{-12} \text{ cm}^3/\text{s}$ for Ce_3^+ reacting to form Ce_3D_6^+ . Arrhenius analysis of the data indicate an activation energy barrier of 0.13 eV exists along the PES for the reaction of Ce_2^+ with D_2 and an activation energy barrier of 0.04 eV exists along the PES for the reaction of Ce_3^+ with D_2 . The fact that the rate constants measured for the Ce_3^+/D_2 system are approximately a factor of 10 faster than the Ce_2^+/D_2 system is attributed to this difference in the heights of the respective energy barriers. A combination of experimental and theoretical analyses (DFT/B3LYP level) suggests that the overall reaction with D_2 is exothermic for both the Ce dimer and trimer. The underlying cause for what gives rise to the respective barriers is currently under investigation. In FY 2019, we will extend this combined experimental and theoretical effort to Ce_m^+ clusters ($m = 4-25$) to determine the nature of their bonding interactions with D_2 . Finally, a manuscript detailing the results obtained in FY 2017 on the reaction of Ce^+ with D_2 has been submitted for publication to the *International Journal of Mass Spectrometry* and is currently undergoing peer review.

REFERENCES

- Buttler, W. T., S. K. Lamoreaux, R. K. Schulze, J. D. Schwarzkopf, J. C. Cooley, M. Grover, J. E. Hammerberg, B. M. La Lone, A. Llobet, R. Manzanares, "Ejecta transport, breakup and conversion," *J. Dynam. Behav. Mat.* **3** (2017) 334–345.
- Manard, M. J., "An experimental and theoretical investigation into the chemical properties of uranium and thorium ions in the gas-phase and on surfaces," in *Site-Directed Research and Development*, FY 2013, National Security Technologies, LLC, Las Vegas, Nevada, 2014, 103–107.

Manard, M. J., “An experimental and theoretical investigation into the chemical properties of uranium and thorium ions in the gas-phase and on surfaces,” in *Site-Directed Research and Development*, FY 2014, National Security Technologies, LLC, Las Vegas, Nevada, 2015, 139–147.

Manard, M. J., P. R. Kemper, R. Trainham, “Gas-phase ion-neutral interactions of cerium ions with deuterium,” in *Site-Directed Research and Development*, FY 2017, National Security Technologies, LLC, and Mission Support and Test Services, LLC, Las Vegas, Nevada, 2018, 113–119.

This page left blank intentionally



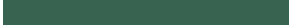
Dark-Fringe Velocimeter for Measuring Fast Transient Features in Shock Wave Profiles with 1 m/s Precision and 50 ps Time Resolution

STL-013-18 ■ Year 1 of 1

**E. Kirk Miller,^{1,a} Brandon La Lone,^a Eric D. Larson,^a
and John W. Wesolowski^a**

¹millerek@nv.doe.gov, (805) 681-2237

^aSpecial Technologies Laboratory



We have developed a velocimetry system that is capable of recording ~1 m/s velocity changes on the 50 ps timescale for shock wave compression experiments. This is an order-of-magnitude improvement in the velocity-time resolution product over existing techniques. Doppler-shifted laser light from a moving target is directed into a Michelson interferometer with an unbalanced path length of 50 ps. We actively balance the initial phase of the interferometer to be destructively interfering in order to achieve excellent velocity sensitivity while also retaining high time resolution. In this manner, small changes in velocity result in relatively large changes in the interferometer output levels. We achieve destructive interfering of the cavity by using a custom feedback circuit to tune the laser current and temperature. We tested the system on a shock experiment at the Special Technologies Laboratory gas gun. Although the system did not fully demonstrate the capabilities of the dark-fringe velocimeter, its velocity record did match a reference photonic Doppler velocimeter signal, indicating it is capable of obtaining accurate velocities even with a cavity delay of only 50 ps. A path forward for improving the diagnostic is in place.

BACKGROUND

Wave profiles (velocity vs. time histories) in shock wave experiments provide a wealth of information. Along with quantitative values of density compression and stress, they provide insight into material strength,

dislocation dynamics, phase transitions, and phase transition kinetics. To observe structure in the wave profiles generally requires nanosecond time-resolution measurements; however, some features, such as elastic precursor relaxations and phase transformations, can require sub-100 ps time resolution (Jensen 2009). This

is especially needed if thin samples are used, which is common practice for laser shock experiments, or if the samples are expensive and/or hazardous.

The two most commonly used techniques for velocity measurements are velocity interferometer system for any reflector (VISAR) and photonic Doppler velocimetry (PDV). Both systems trade off lower velocity accuracy for better time resolution. For a VISAR, the minimum time resolution is the cavity delay time (if it is not limited by detector bandwidth); however, decreasing the cavity delay time lessens velocity precision. For example, a VISAR operating at 532 nm and having a 50 ps delay time has a velocity per fringe constant of 5.32 km/s. If each detector channel had perfect contrast with 6-effective-bit recording, the signal level on that channel would be

$$S = 2^6 \cdot \frac{1}{2} \left[1 - \cos \left(2\pi \cdot \frac{u}{5.32 \text{ km/s}} + \varphi_0 \right) \right], \quad (1)$$

where S is the signal level in resolved elements, u is the target velocity, and φ_0 is the initial interferometer phase. The maximum value of the derivative of S is

$$\frac{dS_{\max}}{du} = 38 \frac{\text{resolved elements}}{\text{km/s}} = 1 \frac{\text{resolved elements}}{26 \text{ m/s}}. \quad (2)$$

Each resolved element is a velocity step of 26 m/s or greater. With two detectors 90° out of phase, this velocity precision could be theoretically realized at all locations in phase space. While such velocity accuracy with 50 ps time resolution is never achieved in practice with a VISAR, it does nonetheless set a theoretical bound. (Note that this is better than the anecdotal VISAR resolution of “1% of a fringe,” which would be 53 m/s of velocity uncertainty in this case.)

In theory, a PDV system has worse velocity precision than VISAR. Dolan (2010) showed that the best possible frequency uncertainty in PDV analysis is

$$\Delta f = \sqrt{\frac{6}{f_s}} \frac{\sigma}{\pi} \tau^{-1.5}, \quad (3)$$

where f_s is the sample rate, σ is the noise fraction, and τ is the analysis duration. Assuming essentially noise-free data with 6 effective bits means that the noise fraction is $\sigma = 1/26$. Furthermore, assuming a

sample rate of 50 GS/s, and an analysis time of $\tau = 50$ ps, then the frequency uncertainty is $\Delta f = 154$ MHz. With the typically used wavelength for PDV being at 1550 nm, this translates to a velocity uncertainty of 120 m/s to achieve 50 ps time resolution.

PROJECT

The goal of this project was to develop a velocimetry system capable of 1 m/s velocity precision with 50 ps time resolution, reducing the velocity uncertainty to a level that is more than an order of magnitude lower than that of a VISAR or PDV. The concept, which we termed “dark-fringe velocimetry,” is related to the extremely sensitive phase detection achieved by the Laser Interferometer Gravitational-Wave Observatory

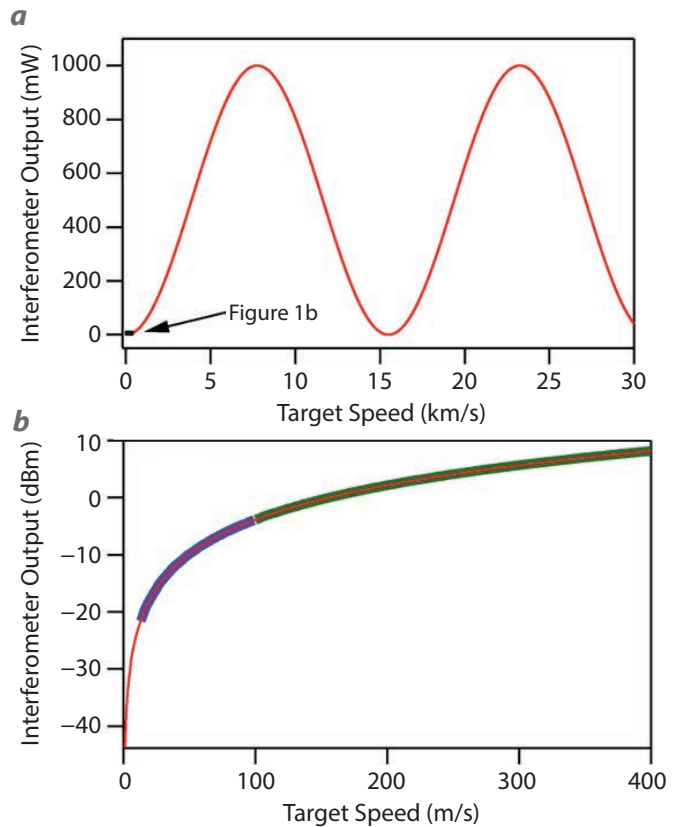


Figure 1. (a) The optical output power as a function of speed for a 50 ps unbalanced interferometer cavity with a maximum output of 1000 mW. The tiny green box indicated by the arrow shows the range of powers and velocities of Figure 1b. (b) The change in output power (in dBm) as a function of speed for this cavity. The blue and green curves represent 6 effective bits of dynamic range for detectors with sensitivities of 100 and 400 m/s, respectively.

(LIGO) gravity wave detectors and fiber-optic gyroscopes. Both use interferometric techniques where the interferometer is forced to be destructively interfering. With destructive interference and a large amount of optical power in the cavity, small changes in the interferometer phase result in large fractional changes in the optical output; essentially all of the detector effective bits are used over a narrow range of interferometer phases. The LIGO detectors take this concept to the extreme by operating with 100 kW of optical power in the cavity, near-perfect destructive interference, and sensitive optical detectors. They are able to detect changes in the interferometer phase to better than 10–13 radians, or 0.1 prad (Blackburn 1996). Fiber-optic gyroscopes use the same technique to achieve microradian accuracy (Lefevre 2012). For our purpose, we require milliradian phase accuracy, as described in detail below.

Dark-Fringe Velocimetry Theory

The dark-fringe velocimeter is similar to a VISAR—Doppler-shifted laser light reflected from a target is directed into an unbalanced Michelson interferometer. However, unlike a VISAR, which is initially at quadrature, the interferometer phase of the dark-fringe velocimeter is actively balanced so that destructive interference is achieved before the start of motion. We chose to build the system with an operating wavelength near 1550 nm because lasers and high-bandwidth detectors are readily available at this wavelength. The interferometer, with its unbalanced path length, acts as an optical filter to Doppler-shifted light. For a 50 ps cavity delay and 1550 nm light, the output of the cavity can be written in terms of the target velocity as

$$I = I_0 \cdot \frac{1}{2} \left[1 - (1 - \delta) \cos \left(2\pi \cdot \frac{u}{15.5 \text{ km/s}} + \varphi_0 \right) \right], \quad (4)$$

where δ represents the fractional loss of extinction due to a small relative power or polarization imbalance in the cavity.

Figure 1a shows the interferometer output vs. target speed for an optical input power of 30 dBm (1000 mW), $\delta = 0$, and $\varphi_0 = 0$. Figure 1b, a zoomed-in view near $\varphi_0 = 0$, is plotted in dBm and illustrates how the dark-fringe system is more sensitive to small velocity changes. The blue and green portions of the curve represent 6 effective bits of dynamic range for detectors with different sensitivities with maximum velocities of 100 and 400 m/s, respectively.

For 6-effective-bit detection ($S = 2^6 = 64$ resolved elements) with a maximum detectable signal of $u = 100$ m/s (blue curve in Figure 1b), the signal vs. velocity for this portion of the curve is given approximately by

$$S \cong 6400 \cdot u^2 \left[\frac{\text{km}}{\text{s}} \right]^{-2}, \quad (5)$$

where we used the approximation $\cos(\theta) \cong (1 - \theta^2/2)$ for small θ and forced $S = 64$ at $u = 0.1$ km/s. The peak velocity sensitivity for the blue curve occurs at the top of the dynamic range, or at $u = 100$ m/s. At this location the slope of the curve is

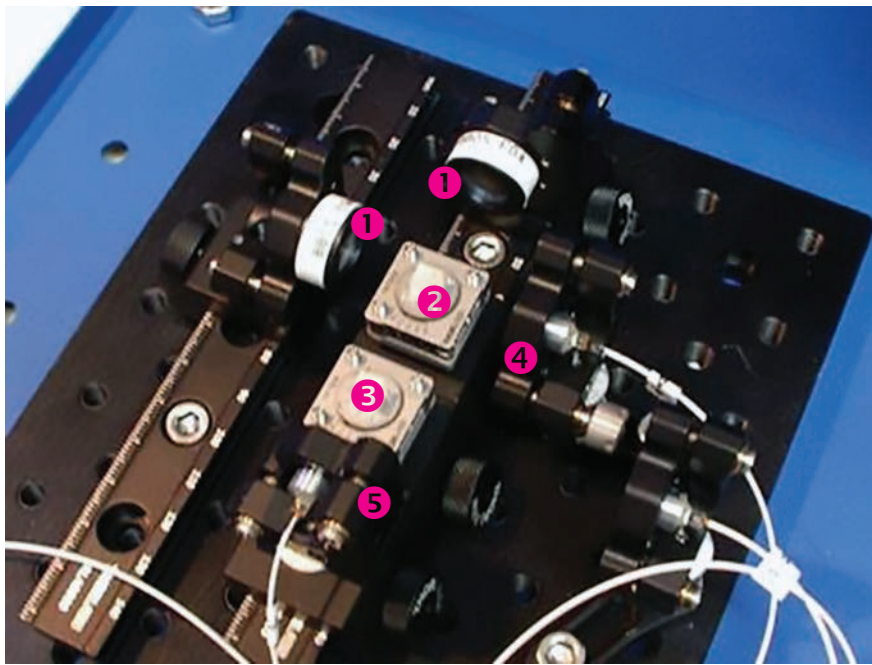
$$\frac{dS_{\text{max}}}{du} = \frac{1280}{\left(\frac{\text{km}}{\text{s}} \right)}. \quad (6)$$

So the theoretical velocity precision (one resolved velocity step) is $\Delta u = 1/1280$ km/s or 0.8 m/s. This is a 30x improvement over the theoretical VISAR velocity precision and 150x improvement over PDV's precision. The trade-off with our technique is that one detector can cover only a relatively narrow range of velocities. However, in principle, we could use multiple detectors, each with a different coverage, to increase the measureable velocity range while retaining excellent velocity precision and time resolution. This stacking of detector coverages is what is illustrated by the different colored segments of the curve in Figure 1b.

Active Balancing of the Dark-Fringe Velocimeter

The previous section showed that the theoretical velocity precision is more than an order of magnitude better with a dark-fringe velocimeter compared with existing methods. For the system to operate, the cavity must be set to nearly complete destructive interference prior to the start of motion. This requires minimizing both δ and φ_0 in Equation 4.

To minimize δ we built the interferometer cavity using bulk, free-space optics. The interferometer cavity is shown in Figure 2. Using spectral interferometry, we measured the cavity delay time to be 51.94 ps. Single-mode fiber optics send and collect the light via fused fiber collimators. Single-mode fiber ensures that the mode field is always perfectly overlapped for the two legs of the cavity. Therefore, we accomplished power



❶ Mirrors, ❷ beam splitter, ❸ polarizer, ❹ output collimator, and ❺ input collimator

Figure 2. The interferometer cavity, showing the input and output fiber collimators, the cleanup polarizer, the beam splitter, and the cavity mirrors

balancing between the two legs by simply tilting one of the cavity mirrors to tune the coupling ratio. Use of a free-space cavity also ensures that the polarization between the two legs overlapped. However, the beam splitter has a slight polarization dependence (all beam splitters do), so it was necessary to use a cleanup polarizer at the entrance to the interferometer to maintain equal optical power in the two legs. In short, we minimized the δ term in Equation 4 without active feedback.

Minimizing the interference phase, φ_0 , required active control to compensate for vibrations, air currents, and laser frequency drifts. To adjust the interferometer phase, we chose to actively tune the laser wavelength rather than the interferometer path length. In the future this will allow multiple lasers, each going to a different target location, to use the same interferometer cavity rather than requiring a separate cavity for each target location. (However, in hindsight, tuning the cavity would have given us more options for laser sources, which may have been more advantageous.) We made rapid changes in the laser wavelength by controlling the laser current, and larger, slower changes by changing the temperature in a feedback circuit. We

added a small-amplitude 20 kHz current to the main laser current to determine the phase of the interferometer transmission curve. The laser wavelength increases with current. When the main laser current is near the null, the total interferometer output power (including the dither) passes through the null twice during each dither period. The green curve in Figure 3 shows a small amplitude that has twice the frequency of the dither. When the laser is operating on the long wavelength side of the null (assuming the dither amplitude is too small to reach the null), the dither current and interferometer output are in phase (increasing the current increases the output), as shown by the black curve in Figure 3. When the laser is on the short wavelength side of the null, the dither current and interferometer output are out of phase (increasing the current decreases the output), which is

illustrated by the blue curve in the figure. The feedback circuit must compare the relative phases of the dither current and interferometer output, and increase the main current when the phases are opposite, or decrease when the phases are in sync.

An electrical block diagram of the custom-built laser controller circuit, which contains two programmable CPUs, is shown in Figure 4. The nominal base current and temperature are set by the user and controlled by one CPU. The other CPU puts the 20 kHz current dither on top of the base current to dither the laser wavelength. A portion of the interferometer output is sent to a photodetector so that this CPU can sense the optical dither. The fine current adjust then tunes the laser toward the null, depending on the relative phase between the current dither and the optical dither, and it essentially “locks” on the null. This system can compensate for small vibrations at frequencies less than 1 kHz. If the range of the fine current adjust is exceeded, the CPU that controls the base current and temperature will slowly adjust the temperature set point until the system finds a cavity null and locks.

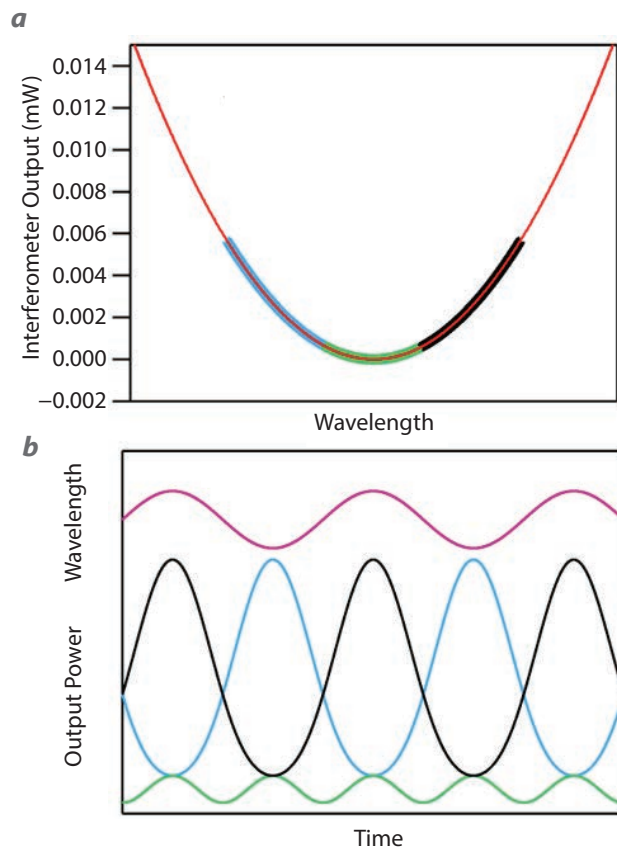


Figure 3. Illustration of how the feedback control system detects the phase of the interferometer output to null it. Figure 3a shows the interferometer transmission curve as a function of input optical wavelength in red. The blue, green, and black curves represent different locations for the laser wavelength (left, center, and right of the zero phase location), and the wavelength dither magnitude is represented by the length of the colored segment. Figure 3b shows the time dependence. The wavelength vs. time is shown as the magenta curve, which dithers at 20 kHz. The blue, green, and black curves represent the interferometer output for three different locations on the transmission curve (left, center, and right of the zero phase location). When the wavelength is too short (blue curves), the output is out of phase with the wavelength dither; when it is nearly right (green curves) the output frequency is double the dither frequency; and when it is too long (black curves), the output is in phase with the wavelength dither. By comparing the phase of the wavelength dither with the output of the cavity, the feedback circuit can adjust the main current in the proper direction to tune the laser to seek the desired center location (at zero interferometer phase).

Dynamic Test of Dark-Fringe Velocimeter

We performed one experiment on the Special Technologies Laboratory (STL) gas gun to test the dark-fringe velocimeter dynamically. A schematic diagram of the experiment setup is shown in Figure 5. The objective was to measure the free surface velocity of a shocked 0.5 mm thick 1018 steel target mounted to a quartz buffer plate. We chose 1018 steel as we believed that the elastic precursor would have a fast transient feature that would be difficult to resolve with PDV. The dark-fringe laser light (1541.4 nm at 4°C and 200 mA) outputting 36 mW was sent to and from the target via a three-port circulator and a collimating probe. We adjusted the probe position to maximize the return light, and about 10 mW of return light exited port 3 of the circulator. After the circulator, a portion of the return light was sent directly to a high-speed detector, and we used it as a beam intensity monitor (BIM) to account for changes in signal level due to changes in the return intensity from tilt, roughening of the surface, and other conditions during the experiment. We used an erbium-doped fiber amplifier (EDFA) to increase the optical power of the remainder of the light to 200 mW before sending it to the dark-fringe interferometer cavity. The output of the cavity was then split, with half of the light going to a high-speed photodetector and half to the control electronics used for nulling the interference phase. We estimated that if the interferometer phase were maximized, there would be about 23 mW of optical power on the high-speed receiver. With the active nulling of the cavity, the power level was kept to about 16 μ W, about 32 dB down from the peak. We used a standard two-fiber PDV system to view the target, which allowed us to compare velocities.

It became clear as we set up the experiment that the feedback circuit was not actually holding the interferometer phase at the null, but instead was oscillating back and forth across the null at a frequency of \sim 500 Hz, and that the amplitude of this unwanted oscillation far exceeded the 20 kHz dither amplitude. Therefore, we knew that when the shock wave arrived, the starting phase would be on either the low or high optical frequency side of the null with about a 50/50 probability. Unfortunately, in this case it started on the low optical frequency (long wavelength) side. The experimental results are shown in Figure 6. Because the starting phase was on the low frequency side and the Doppler shift increases the optical

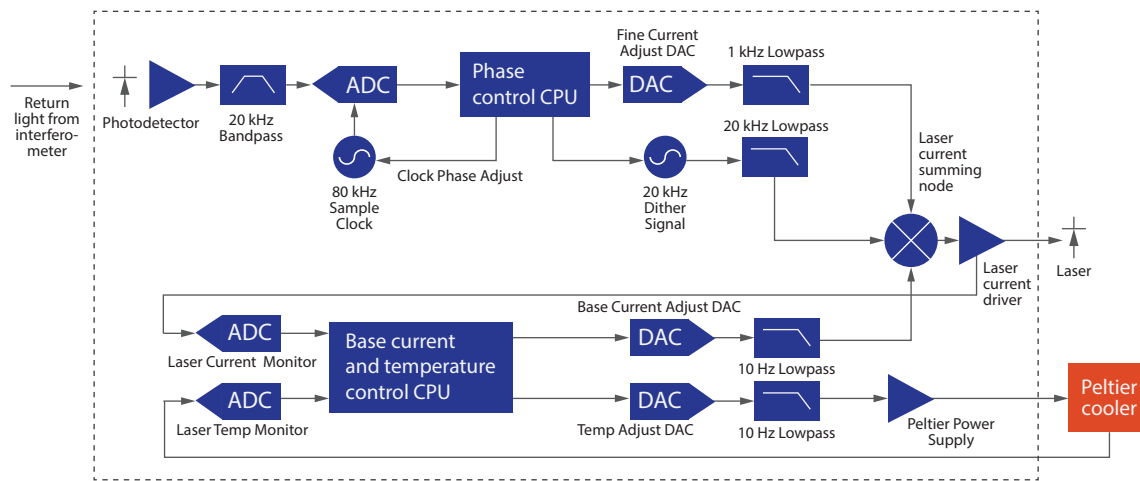


Figure 4. The feedback control circuit for tuning the laser wavelength is such that the interferometer starts at zero phase when the experiment begins

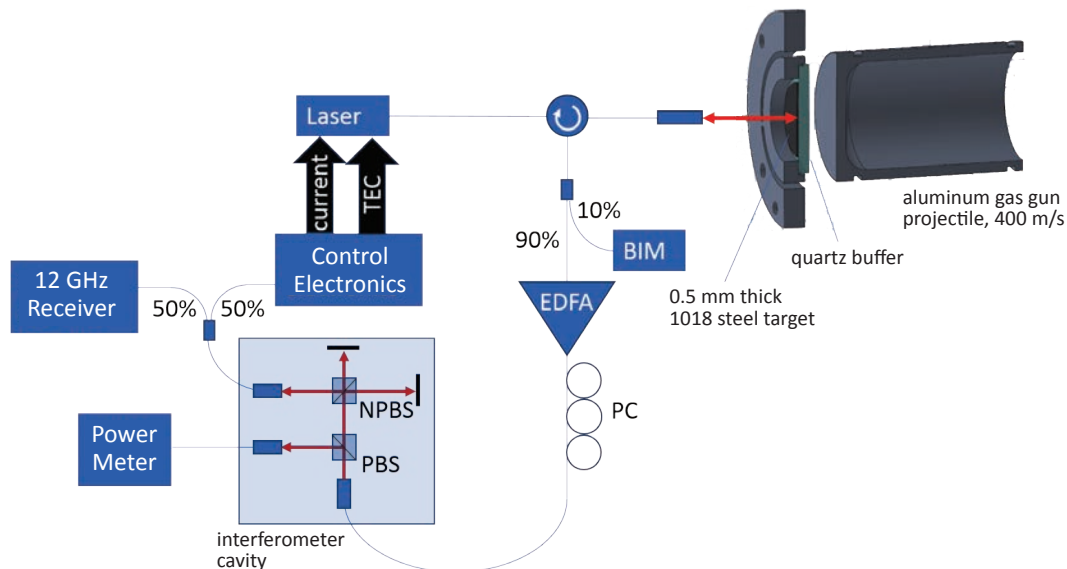


Figure 5. Block diagram of the experimental setup for testing the dark-fringe velocimeter at the STL gas gun, including the polarization controller (PC)

frequency, the velocity increase initially decreased the signal level and then increased it. Therefore, the overall signal stayed fairly low throughout the experiment, and the signal-to-noise ratio was poor. Prior to converting signal levels to velocity, we first applied a 50-point (1 ns) Savitzky-Golay filter to smooth the data and then divided out the BIM; the smoothed and normalized data are also shown in Figure 6 for comparison. The smoothing somewhat negates the inherent time-resolution benefit but should not be necessary on a future experiment with healthier signal levels. Normalizing by the BIM had the effect of flattening out some of the steps and removing some of the lower-frequency oscillations in the signals.

We converted the signals to velocity by taking the square root of the normalized voltages, unwrapping the phase where it crossed zero, and applying a scalar factor such that the peak velocity matched the PDV data. The resulting signals are shown in Figure 7 along with the PDV data. We analyzed the PDV data using a 1 ns FFT window to match the time resolution of the smoothed dark-fringe signal. The feature that we were hoping to observe is the elastic precursor in the 1018 steel, which can be seen just after shock breakout in the PDV data at a velocity of just under 100 m/s. However, because the dark-fringe signal passed through zero phase, where there is no signal, there is a range of velocities between about 20 and 120 m/s for

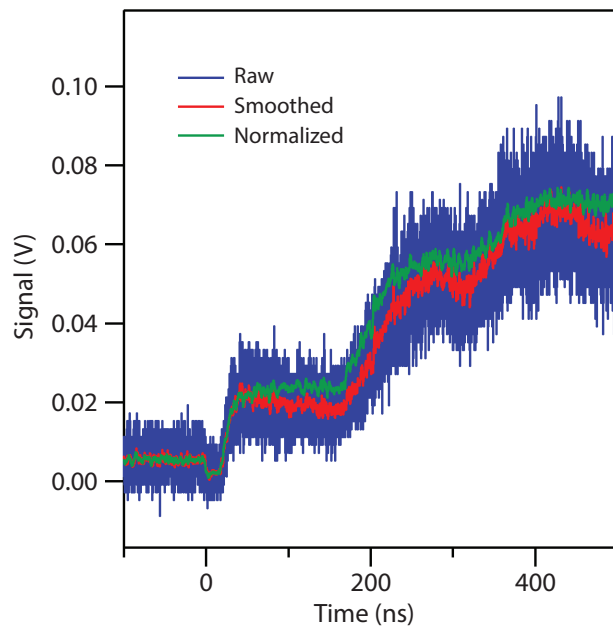


Figure 6. Raw signal vs. time record for the gas gun experiment

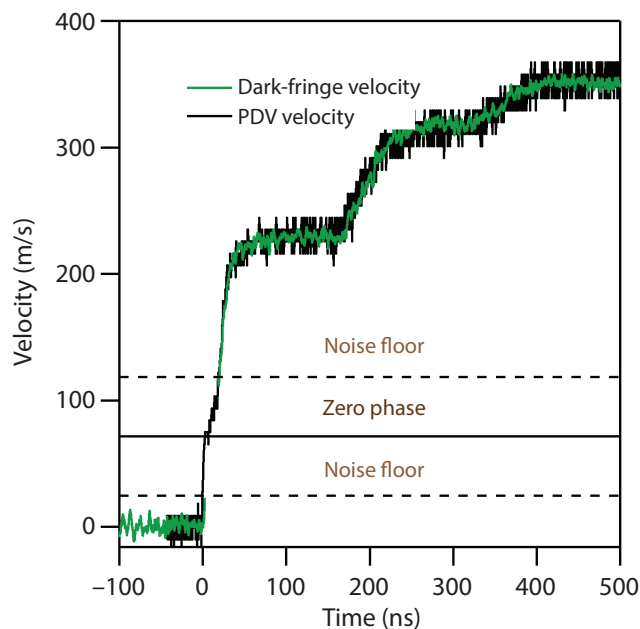


Figure 7. Free surface velocity record of the 1018 steel target. Because the initial phase of the dark-fringe interferometer was on the low-frequency side of the transfer curve, there is a range of signal missing where it went through zero phase. The horizontal dashed lines bracket the region where there is no measurable signal, and the horizontal black line shows where the zero interferometer phase is located in velocity space.

which there is no data; this range is indicated by the horizontal dashed lines in the figure. Therefore, neither the precursor nor any pullback was seen in the dark-fringe data. The subsequent steps in the velocity record are a result of the shock wave reverberating between the free surface of the steel target and the quartz buffer plate. The agreement between the dark-fringe velocity record and the PDV data in the steps region is quite good, which demonstrates that the technique does work to produce an accurate velocity-time profile. However, there is not really a fast transient velocity feature in this dataset that demonstrates the full capabilities of our diagnostic.

After the experiment, we were able to fix the issues with the oscillatory behavior, and the system now locks at zero phase (or a preset non-zero phase if desired). However, we have not yet had an opportunity to perform another dynamic experiment.

CONCLUSION

We have developed a new type of velocity measurement diagnostic that is capable of an order-of-magnitude improvement in velocity precision compared with existing techniques at 50 ps time resolution. Termed dark-fringe velocimetry, the system works in a similar manner to a traditional VISAR, but the interferometer phase is actively balanced to zero such that small Doppler shifts result in large signal amplitude changes. We tested the system on a gas gun experiment. The experiment did not fully demonstrate the capabilities of the dark-fringe velocimeter, but the velocity record did match a reference PDV signal, indicating that the system is capable of obtaining accurate velocities even with a cavity delay of only 50 ps.

We will continue to refine this instrument in FY 2019 under different auspices. Some small issues with the instrument have already been addressed, and we plan to conduct more experiments to demonstrate the velocity-time resolution capabilities of dark-fringe velocity. Pending completion of successful experiments, we expect to publish our results.

ACKNOWLEDGMENTS

We thank Ben Valencia, Mike Grover, and Matt Staska for their experimental assistance with this project.

REFERENCES

Blackburn, J. K., “The Laser Interferometer Gravitational Wave Observatory Project: LIGO,” 1996, <https://dcc.ligo.org/public/0073/P960031/000/P960031-00.pdf>, accessed April 9, 2019.

Dolan, D. H., “Accuracy and precision in photonic Doppler velocimetry,” *Rev. Sci. Instrum.* **81** (2010) 053905.

Jensen, B. J., G. T. Gray III, R. S. Hixson, “Direct measurements of the α - ϵ transition stress and kinetics for shocked iron,” *J. Appl. Phys.* **105** (2009) 103502.

Lefevre, H., “The fiber-optic gyroscope: Achievement and perspective,” *Gyroscopy and Navigation* **3**, 4 (2012) 223–226.



A Semiconductor-Based High-Yield X-Ray Photocathode

LO-007-17 ■ Year 2 of 3

**Kathy Opachich,^{1,a} Andrew MacPhee,^b Otto Landen,^b Ning Chen,^c
Ashwini Gopal,^c Salah Udin,^c Terry Hilsabeck,^d Eric Huffman,^d
Jeffrey A. Koch,^a Jun Feng,^e Dave Bradley,^b and Sabrina Nagel^b**

¹opachiyp@nv.doe.gov, (925) 960-2520

^aLivermore Operations

^bLawrence Livermore National Laboratory

^cNanoShift, LLC

^dGeneral Atomics

^eLawrence Berkeley National Laboratory



In this three-year project, we are developing a silicon-based, high-yield x-ray photocathode for use in the spectral energy range from 1 to 30 keV. In our previous work (Opachich 2016a, 2017a), we fabricated and tested a structured photocathode that showed an improvement of 3x in measured secondary electron yield. We can extend this concept to increase the yield up to an order of magnitude higher than what was previously demonstrated. The design necessitates the use of structures with wall angles from 1° to 3°. Unlike the previous 10° wall angle design, when coated with gold this geometry introduces a loss of electric field and thus loss of signal from the photocathode. We can circumvent this problem by using insulating materials or a solid-state approach to generate a charge depletion region within a doped silicon substrate. Several cathode designs were modeled in FY 2017 (Opachich 2018). In FY 2018, we fabricated a set of test devices. In FY 2019, we will develop a method to coat the cathodes with cesium iodide using atomic layer deposition and characterize the cathode performance. Here we discuss the device design, modeling, and fabrication results, along with the next steps toward the completion of the project in FY 2019.

BACKGROUND

Time-resolved x-ray diagnostics are widely used at the National Ignition Facility (NIF) (Miller 2004).

Currently, the facility uses streak camera detectors such as the Diagnostic Insertion Manipulator Imaging Streak Camera (Opachich 2012), Streaked Polar Instrumentation for Diagnosing Energetic Radiation

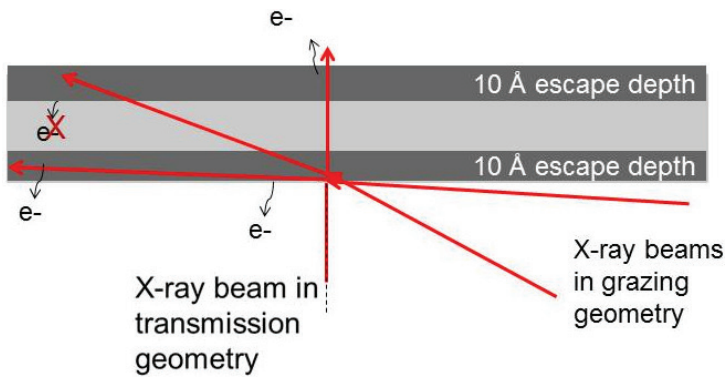


Figure 1. Example of the grazing incidence and transmission geometry. The electron escape depth (not to scale) is shown on both sides of the photocathode. Electrons that are generated within the bulk do not contribute to the measured yield.

(SPIDER) (Khan 2012), and time dilation imaging tubes (Hilsabeck 2010, Nagel 2012) for imaging in the 5 to 10 keV range. The introduction of the Advanced Radiographic Capability on NIF will provide imaging sources that extend well above 10 keV. However, current detectors rely on photocathode materials to convert photon signals to electrons, which are then dispersed temporally with the use of voltage ramps and magnetic fields. The imager detector efficiency and operational range drop significantly above 10 keV

due to a sharp reduction in quantum efficiency (QE) of most photocathode materials (i.e., gold and cesium iodide [CsI]) (Hara 2000, Khan 2013, Opachich 2014). Geometrically enhanced photocathodes provide a potential solution, and they can be easily integrated into existing detectors without compromising performance.

We can improve the electron yield by better matching the x-ray path length to the very thin top-most emission layer of the photocathode, defined as the electron escape depth. We accomplish this by changing the incidence angle of x-ray photons to a very shallow, near-grazing geometry, as shown in Figure 1. The secondary electron escape depth is typically very thin; for example, in gold, it is limited to the top 10 Å of the photocathode surface (Henke 1981, Fraser 1992). We need

incidence angles below $\sim 20^\circ$ to provide significant enhancement. Grazing incidence detectors have utilized this geometry and demonstrated improvement in photocathode QE by a factor of 15 to 20 times in the soft x-ray range (Feng 2010). This effect can also be extended to the 10–30 keV range, as predicted by the semiempirical model by Fraser (1983a, 1983b).

Changing the incidence angle of current NIF detectors is costly and may not be possible due to engineering

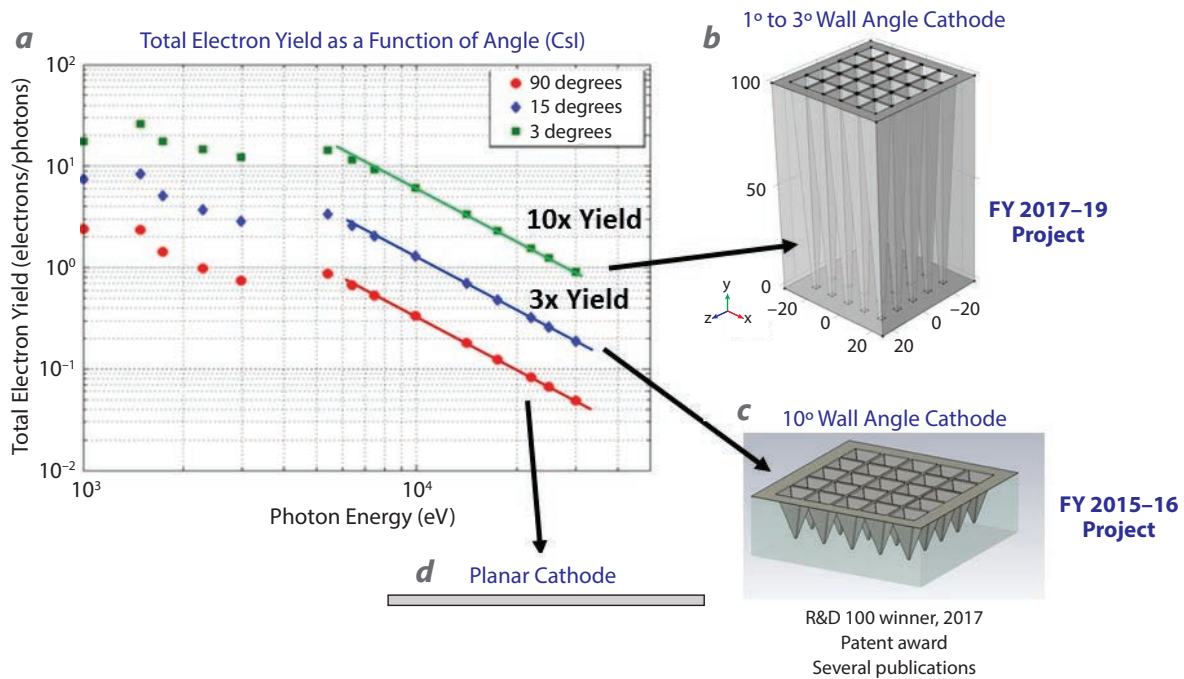


Figure 2. Predicted yield for planar, 10°, and shallow-angle cathode designs. (a) Calculated expected secondary electron yield as a function of energy. Three incidence angles are shown. (b) A structure with a 1°–3° wall angle. (c) A structure with a 10° wall angle has improved yield by 3x. (d) An example of a planar photocathode.

design constraints; however, it is fairly simple to change the design of the photocathodes by introducing geometrically enhanced surfaces such as pillars, cones, or recessed cavities. In our previous SDRD effort, we modeled, fabricated, and tested a recessed pyramid photocathode (Opachich 2014, 2015, 2016b). The photocathode used a 10° structure wall angle and showed a yield increase of 3x. The predicted yield and recessed pyramid photocathode design are shown in Figures 2a and 2c. For comparison, the yield from a standard planar photocathode is shown in Figures 2a and 2d. An increase of an order of magnitude is predicted with the use of a 3° wall angle in the same recessed structure, as seen in Figures 2a and 2b. Such shallow angles require the recessed pyramids to be much longer than those previously fabricated and necessitates a new design. The longer structure depth and use of a metal cathode coating would introduce a loss of electric field within the recessed cavities. This would negate any yield improvements from the structure, because the field is needed to extract and accelerate photoelectrons out of the cavities. One solution is to use a dielectric material as a substrate and an alkali metal photocathode. Metal/oxide/silicon layers can be used to generate a depletion region. Here electron carrier densities can be manipulated with the selection of an appropriate device design and voltage (Velasquez-Garcia 2011a, 2011b). The feasibility of such an approach was validated with COMSOL modeling software, and the results of this modeling exercise showed that although this approach works for small (submicron) structures, the electric fields within the substrate are not adequate for structures that are $20\ \mu\text{m}$ or greater in depth. As a solution, we developed a second design that uses a glass substrate, with a CsI coating over the entire surface of the high-density, etched, shallow-angle structures.

PROJECT

Semiconductor and High-Density Shallow-Angle Photocathode Concepts

The details of the proposed solid-state photocathode design are described in our previous SDRD report (Opachich 2017a). The design did not hold for structures that were larger than a few microns. In addition, several unknowns were identified for the semiconductor-based design. The behavior of electron and hole carriers in a large external electric field introduced by the detector in the acceleration gap

region needs investigation. The design requires pulsed operation and timing that take into account carrier transport through the bulk of the material. Finally, the full-scale design will be costly to fabricate due to cathode size and pattern density. For these reasons, we chose to pursue a high-density, shallow-angle cathode design as an alternative solution.

In the alternative high-density, shallow-angle cathode design, a glass substrate is used with structures etched along the top of the device. The top and bottom of the device are coated with metal so that when voltage is applied, it will generate an electric field within the recessed pyramids. The entire cathode surface, along with the recessed pyramid walls, is then coated with a CsI emission layer. The design is shown in Figure 3.

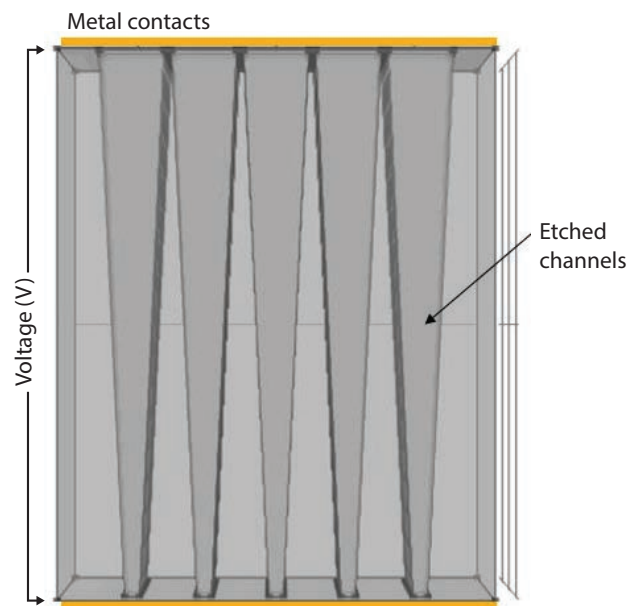


Figure 3. Alternative high-density, shallow-angle cathode design. High-density channels are etched into a glass substrate. The top and bottom of the device are coated with a conductive layer, and then the entire emission surface, including the walls of the recessed pyramids, is coated with CsI.

High-Density, Shallow-Angle Structured Cathode Simulation Results

The simulation results for the high-density, shallow-angle device are shown in Figure 4. Because the device's substrate is made from an insulating material, silicon dioxide (SiO_2), the electric potential shown in Figure 4a is uniform within the channels and the substrate. When photons are incident onto the photocathode, the resulting photoelectrons are generated at the wall surface of the channels and

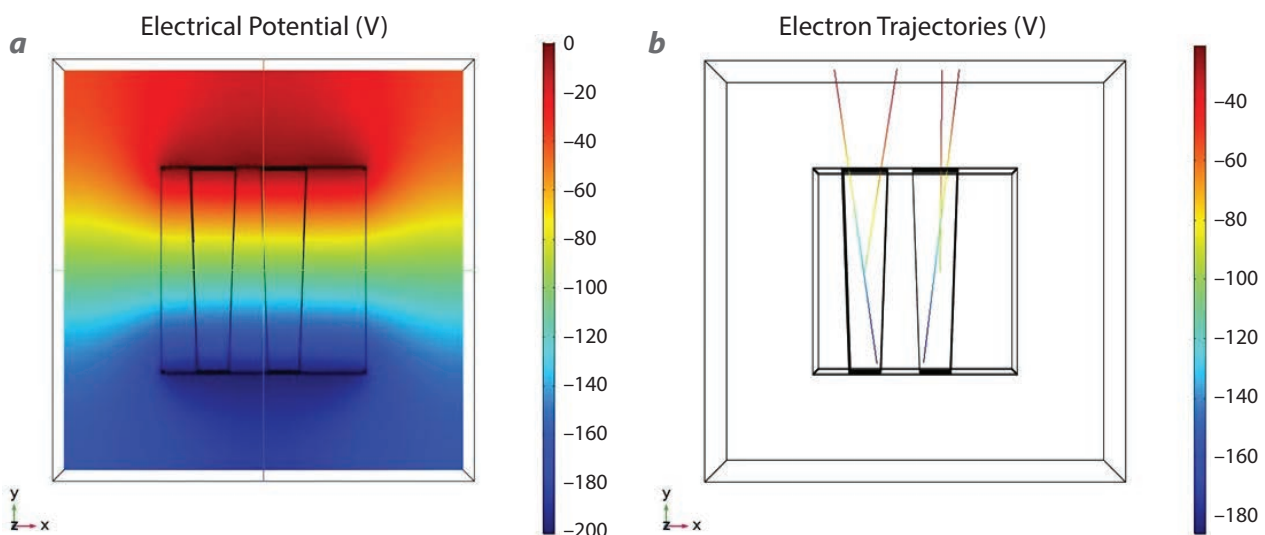


Figure 4. High-density, shallow-angle cathode modeling in COMSOL showing (a) electrical potential within the channel and substrate and (b) electron trajectories

must escape the photocathode without secondary interactions. Electron trajectories are influenced by the applied voltage and the depth of the channels. The resulting electron trajectories for a 40 μm deep structure held at -200 V are shown in Figure 4b. Here we see that, for our given cathode thickness and voltage, electrons that are generated at the bottom of the structure are able to clear the outer aperture of the channel. We used the modeling results to finalize the high-density, shallow-angle cathode prototype fabrication requirements.

Fabrication Results

The high-density, shallow-angle structures were fabricated by NanoShift, LLC. The high-density pattern was plasma etched into SiO_2 substrates. The etching process had two major challenges: masking material selectivity and slow etch rate. To make a well-defined recessed structure, we need a masking material with high selectivity that can overcome the slow etch rate. Several masking materials of various thicknesses were tested. These included Microchem KMPR resist masks on which silicon was deposited by low-pressure chemical vapor deposition and plasma-etched chemical

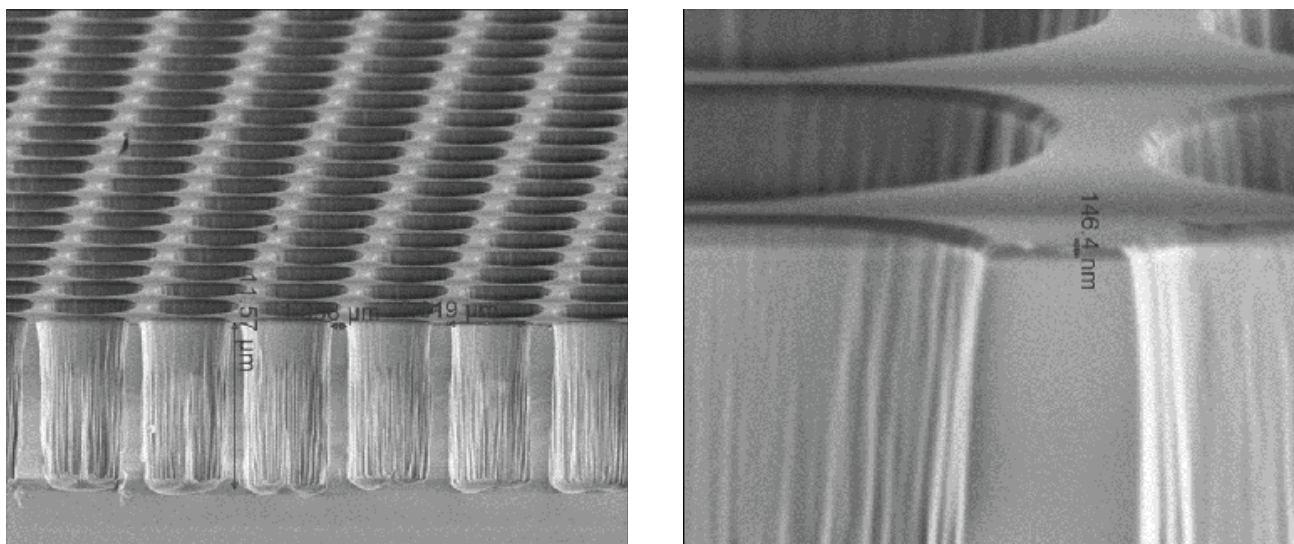


Figure 5. High-density shallow-angle cathode fabrication images. A uniform pattern is seen, with structures that are 20 μm deep.

vapor deposition. The plasma-etched chemical vapor deposition process proved to be the most successful; however, because the etch rate around the square edges was faster, the separation sidewalls were etched away. We created a new mask to mitigate this effect. The resulting structures are shown in Figure 5.

CONCLUSION

We have identified a new photocathode concept to improve photoelectron yield by an order of magnitude in the 1 to 30 keV range. We used the COMSOL modeling software to investigate the feasibility of semiconductor-based photocathode and high-density, shallow-angle designs. The modeling results show that for structures that are 20–60 μm deep, the high-density, shallow-angle cathode design is feasible. We developed a fabrication process and built a set of prototype photocathodes this year. These cathodes will be coated via atomic layer deposition at Argonne National Laboratory in FY 2019, which is the focus of the third year of this SDRD, and then tested at the Advanced Light Source.

To date, related work (spanning several years) resulted in a patent application (Opachich 2017b), several presentations at the High Temperature Plasma Diagnostics Conference (Opachich 2014, 2016b), a talk at the SPIE Optics and Photonics Conference (Opachich 2015), and two talks at the National Inertial Confinement Fusion Diagnostics Meeting (Opachich 2014, 2015). The project on which this research is based won an R&D 100 award in 2017. The modeling work discussed in this report and subsequent device fabrication will help improve this technology even further.

REFERENCES

- Feng, J., K. Engelhorn, B. I. Cho, H. J. Lee, M. Greaves, C. P. Weber, R. W. Falcone, H. A. Padmore, P. A. Heimann, “A grazing incidence x-ray streak camera for ultrafast, single-shot measurements,” *Appl. Phys. Lett.* **96**, 13 (2010) 134102.
- Fraser, G. W., “The characterisation of soft x-ray photocathodes in the wavelength band 1–300 Å: I. Lead glass, lithium fluoride and magnesium fluoride,” *Nucl. Instrum. Methods Phys. Res.* **206**, 1–2 (1983a) 251–263.
- Fraser, G. W., “The characterisation of soft x-ray photocathodes in the wavelength band 1–300 Å: II. Caesium iodide and other insulators of high photoelectric yield,” *Nucl. Instrum. Methods Phys. Res.* **206**, 1–2 (1983b) 265–279.
- Fraser, G. W., M. T. Pain, J. E. Lees, C. R. Binns, J. F. Pearson, P. R. Houghton, “The characterisation of gold x-ray photocathodes,” *Nucl. Instrum. Methods Phys. Res. A* **321**, 1–2, (1992) 385–391.
- Hara, T., Y. Tanaka, H. Kitamura, T. Ishikawa, “Performance of a CsI photocathode in a hard x-ray streak camera,” *Rev. Sci. Instrum.* **71**, 10 (2000) 3624–3626.
- Henke, B. L., J. P. Knauer, K. Premaratne, “The characterization of x-ray photocathodes in the 0.1–10-keV photon energy region,” *J. Appl. Phys.* **52**, 3 (1981) 1509–1520.
- Hilsabeck, T. J., et al., “Pulse-dilation enhanced gated optical imager with 5 ps resolution,” *Rev. Sci. Instrum.* **81** (2010) 10E317.
- Khan, S. F., et al., “Measuring x-ray burn history with the Streaked Polar Instrumentation for Diagnosing Energetic Radiation (SPIDER) at the National Ignition Facility (NIF),” *Proc. SPIE* **8505** (2012) 850505.
- Khan, S. F., et al., “Characterization of the x-ray sensitivity of a streak camera used at the National Ignition Facility (NIF),” *Proc. SPIE* **8850** (2013) 88500D.
- Miller, G. H., E. I. Moses, C. R. Wuest, “The National Ignition Facility: Enabling fusion ignition for the 21st century,” *Nuclear Fusion* **44**, 12 (2004) S228.
- Nagel, S. R., et al., “Dilation x-ray imager a new/faster gated x-ray imager for the NIF,” *Rev. Sci. Instrum.* **83**, 10 (2012) 10E116.
- Opachich, K., et al., “High-yield x-ray photocathodes for next-generation imaging detectors,” in *Site-Directed Research and Development*, FY 2015, National Security Technologies, LLC, Las Vegas, Nevada, 2016a, 147–152.
- Opachich, K., et al., “High-yield x-ray photocathodes for next-generation imaging detectors,” in *Site-Directed Research and Development*, FY 2016, National Security Technologies, LLC, Las Vegas, Nevada, 2017a, 119–126.
- Opachich, K., et al., “A semiconductor-based high-yield x-ray photocathode,” in *Site-Directed Research and Development*, FY 2017, National Security Technologies, LLC, and Mission Support and Test Services, LLC, Las Vegas, Nevada, 2018, 155–160.
- Opachich, Y., A. MacPhee, “Photocathode,” U.S. Patent Application No. 15/249,197, Publication No. US 2017/0062169 A1, filed August 26, 2016, and published March 2, 2017 (2017b).
- Opachich, Y. P., et al., “High performance imaging streak camera for the National Ignition Facility,” *Rev. Sci. Instrum.* **83**, 12 (2012) 125105.
- Opachich, Y. P., P. W. Ross, A. G. MacPhee, T. J. Hilsabeck, S. R. Nagel, E. Huffman, P. M. Bell, D. K. Bradley, J. A. Koch, O. L. Landen, “High quantum efficiency photocathode simulation for the investigation of novel structured designs,” *Rev. Sci. Instrum.* **85**, 11 (2014) 11D625.

Opachich, Y. P., et al., “Precision fabrication of large area silicon-based geometrically enhanced x-ray photocathodes using plasma etching,” *Proc. SPIE* **9591** (2015) 95910O.

Opachich, Y. P., et al., “Structured photocathodes for improved high-energy x-ray efficiency in streak cameras,” *Rev. Sci. Instrum.* **87**, 11 (2016b) 11E331.

Velasquez-Garcia, L. F., S. A. Guerrero, Y. Niu, A. I. Akinwande, “Uniform high-current cathodes using massive arrays of Si field emitters individually controlled by vertical Si ungated FETs—Part 1: Device design and simulation,” *IEEE Trans. Elect. Dev.* **58**, 6 (2011a) 1775–1782.

Velasquez-Garcia, L. F., S. A. Guerrero, Y. Niu, A. I. Akinwande, “Uniform high-current cathodes using massive arrays of Si field emitters individually controlled by vertical Si ungated FETs—Part 2: Device fabrication and characterization,” *IEEE Trans. Elect. Dev.* **58**, 6 (2011b) 1783–1791.



Single-Crystal X-Ray Spectropolarimeter

SO-003-18 ■ Year 1 of 2

**Radu Presura,^{1,a} Matthew S. Wallace,^a Isiah Pohl,^a Paul Flores,^a
Craig Kruschwitz,^b and Ken Moy^c**

¹presurr@nv.doe.gov, (505) 844-8069

^aNew Mexico Operations–Sandia

^bNew Mexico Operations–Los Alamos

^cSpecial Technologies Laboratory



Magnetic fields and electron beams are ubiquitous in high energy density (HED) laboratory plasmas. In their presence, the x-ray plasma emission may become polarized. Measuring the polarization degree of the spectral lines can provide insight into the magnetic field strength or the electron acceleration mechanisms. We are addressing this need by developing a polarizing x-ray spectrometer (spectropolarimeter) that uses a single crystal as an x-ray polarization beam splitter. This solution avoids the uncertainties introduced in earlier measurements by using a different crystal or a different experiment to measure each linear polarization direction. This year we identified suitable crystals and planes that can be used for polarization splitting of spectral lines from ions of interest in HED plasmas. We also traced x-ray paths through the polarization-splitting crystals to assess the contribution of the non-polarizing internal crystal planes and performed ray tracing of the spectropolarimeter in experimentally relevant configurations. In addition to developing a fairly mature conceptual instrument design, we designed and built a simplified fixture for crystal characterization and alignment on Manson and synchrotron x-ray sources. In FY 2019 we will characterize several polarization-splitting crystals, will improve the numerical tools developed to evaluate the crystal performance, and will design spectropolarimetric diagnostics for HED experiments.

BACKGROUND

Polarized x-rays are emitted by hot, anisotropic plasmas and synchrotrons. In the case of high

energy density (HED) plasmas, measuring the x-ray polarization provides information about the mechanism causing the anisotropy. The MagLIF concept uses a strong axial magnetic field to confine

fuel ions and to reduce plasma thermal conductivity (Slutz 2010, Gomez 2015); however, there is no direct measurement of the magnetic field strength and space distribution at stagnation. Beams of energetic electrons are responsible for hard x-ray inner-shell emission in Z-pinch, with fluences significantly above those expected for thermal emission (Ampleford 2014). The fact that the acceleration mechanisms and locations of these energetic electrons are uncertain limits the ability to control them. Properties of magnetic fields and electron beams are accessible through polarization measurements of the radiation emitted by plasmas. Analyzers for the x-ray spectral range rely on 90° scattering (Barkla 1905); high reflectivity is ensured by diffraction at a 45° Bragg angle on appropriate crystals (Wagner 1928). This particular type of scattering only occurs at certain photon energies; therefore, the technique is called x-ray spectropolarimetry.

broadening. The latter method works if the emission is highly reproducible from experiment to experiment, which is rarely the case for HED sources such as Z-pinch.

We could significantly reduce these difficulties using an x-ray polarizing beam splitter to enable simultaneous measurements of both mutually orthogonal linear polarizations along the same line of sight. Such an x-ray optic would extend the reliable use of the non-perturbing, sensitive spectropolarimetric techniques to the measurement of electron beams and magnetic fields in HED plasmas. A spectropolarimeter would also simplify and decrease the duration of polarization measurements at synchrotron x-ray sources.

PROJECT

Certain crystals are natural x-ray polarizing beam splitters, as noted by Baronova (2003) and Pereira (2009). When an x-ray beam is incident on a crystal plane at a 45° Bragg angle, the reflected beam is linearly polarized in a direction perpendicular to the dispersion plane (Figure 1a). This occurs for wavelengths λ that satisfy

$$n\lambda = \sqrt{2d}, \quad (1)$$

where n is the diffraction order and d is the interplanar distance. A second beam with linear polarization orthogonal to that of the first beam can be obtained in a direction perpendicular to both the incident beam and the first linearly polarized beam by reflection on a plane intersecting the first crystal plane at 120° (Figure 1b). These planes are oriented as two diagonal planes in a cube. In fact any crystal with three-fold symmetry

(i.e., with cubic or hexagonal lattices) contains internal planes that can be used for polarization splitting. To create similar reflection conditions for the two linear polarizations, we define the crystal surface (green plane) as the bisecting plane of the polarizing planes as depicted in Figure 1c. The polarizing planes intersect the surface at $\pm 30^\circ$, along the cube diagonal shown as a white dashed line. In this case, the surface Bragg angle is 54.7° (Pereira 2009). Correct operation requires that the incident beam be maintained in the bisector

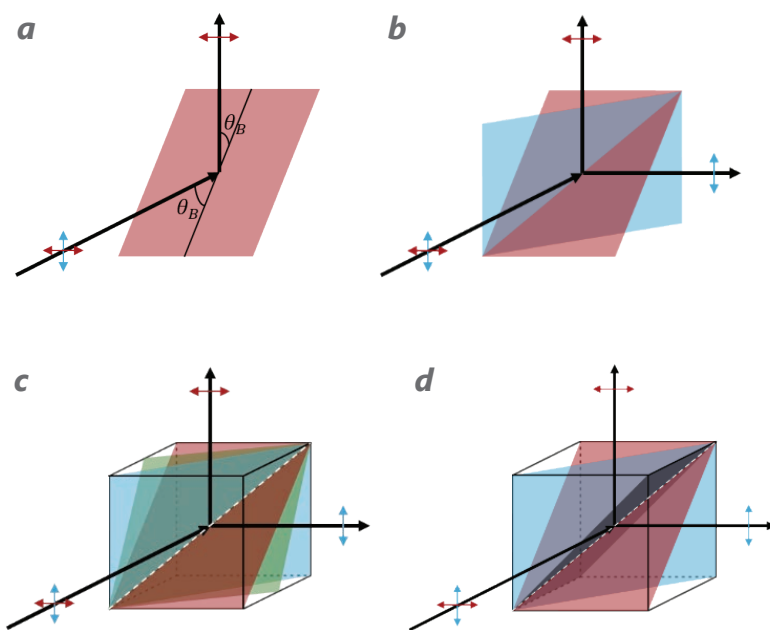


Figure 1. Polarization-splitting geometry. Red and blue are the polarization-splitting planes, green is the optimum surface plane, and gray is the optimum incidence plane.

Plasma polarization measurements have been performed both in the laboratory and on stellar objects using either a pair of crystals oriented for mutually perpendicular reflections or the same crystal in different orientations for successive experiments. But both methods are problematic for spatially extended, short-lived sources. In the first case, it is difficult to ensure that the radiation measured with the two crystals is emitted from the same plasma region; furthermore, the spectral lines are distorted by source

plane of the two polarization-splitting planes, which is determined by the cube diagonal and the normal to the crystal surface (the third cube diagonal plane, shown in gray in Figure 1d). This geometry ensures that the two polarized reflections occur for the same point in the source in the same crystal region, and therefore they suffer similar absorption.

Crystal Selection for Polarization Splitting

To enable a given application, one has to select a hexagonal or cubic crystal containing polarization-splitting planes with spacing d that satisfies Equation 1 for the wavelength of an emission line of interest. For hexagonal crystals, the condition for the polarization-splitting planes $\{h k i l\}$ to contain the c -axis implies the corresponding Miller index $l = 0$ and the interplanar distance

$$d = \frac{\sqrt{3}}{2} \frac{a}{\sqrt{h^2 + hk + k^2}}, \quad (2)$$

where a is the lattice constant. Note that due to the symmetry $h + k + i \equiv 0$. Once a polarizing plane with independent Miller indices h_{p1} and k_{p1} is selected, the surface plane is determined by a 30° rotation and the second polarizing plane by further 30° rotation, as shown in Figure 2. For the clockwise case, the Miller indices of the surface are

$$h_s = 2h_{p1} + k_{p1}, \quad k_s = -h_{p1} + k_{p1}, \quad (3a)$$

and those of the second polarizing plane are

$$h_{p2} = h_{p1} + k_{p1}, \quad k_{p2} = -h_{p1}. \quad (3b)$$

Similarly, given the surface plane, the polarization-splitting planes are determined by rotations with $\pm 30^\circ$,

$$h_{p1} = 2h_s + k_s, \quad k_{p1} = -h_s + k_s, \quad (4a)$$

and

$$h_{p2} = h_s - k_s, \quad k_{p2} = h_s + 2k_s. \quad (4b)$$

Equivalent equations were derived for crystals with cubic symmetry.

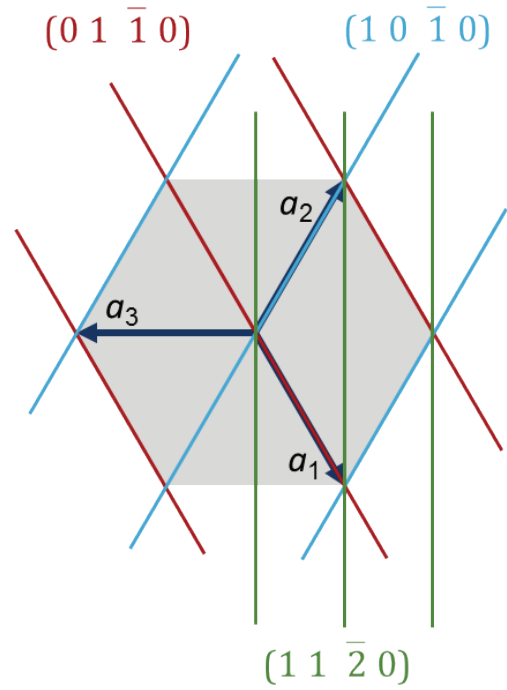


Figure 2. Example of surface and polarization-splitting planes geometry for crystals with hexagonal symmetry. The figure shows the case with surface plane $(1\ 1\ \bar{2}\ 0)$ and the polarization-splitting planes $(0\ 1\ \bar{1}\ 0)$ and $(1\ 0\ \bar{1}\ 0)$.

Considering a number of crystals commercially available and the most common ions in the HED plasmas of interest, we performed a systematic search of crystal plane-spectral line matches that satisfy Equation 1 for Bragg angles within $\pm 5^\circ$ of the 45° polarizing value. We used an algorithm similar to one created by Loisel (Schollmeier 2016) to run XOP (Sanchez del Rio 2004) iteratively, over a selection of crystal planes and spectral lines. Our algorithm used the `diff_pat.exe` program, specific to flat crystals, rather than `cryst_ml.exe` (Presura 2019). The best matches for crystals and cuts procured for this project are shown in Table 1.

The search included ten crystals and planes with $h, k \leq 10$, as well as twelve thermal lines and two characteristic lines for ten ions. Out of the 140,000 possible combinations, 50,000 were found to be allowed and distinct. For 2343 of these, the Bragg angle was $40^\circ < \theta_b < 50^\circ$, and they were passed to XOP so that the integrated reflectivity and rocking curve width were calculated for each polarization. By further requiring that the perpendicular integrated reflectivity $R_s \geq 0.1\ \mu\text{rad}$ and the polarization contrast $R_s/R_p < 1\%$, the number of satisfactory matches was reduced to 347.

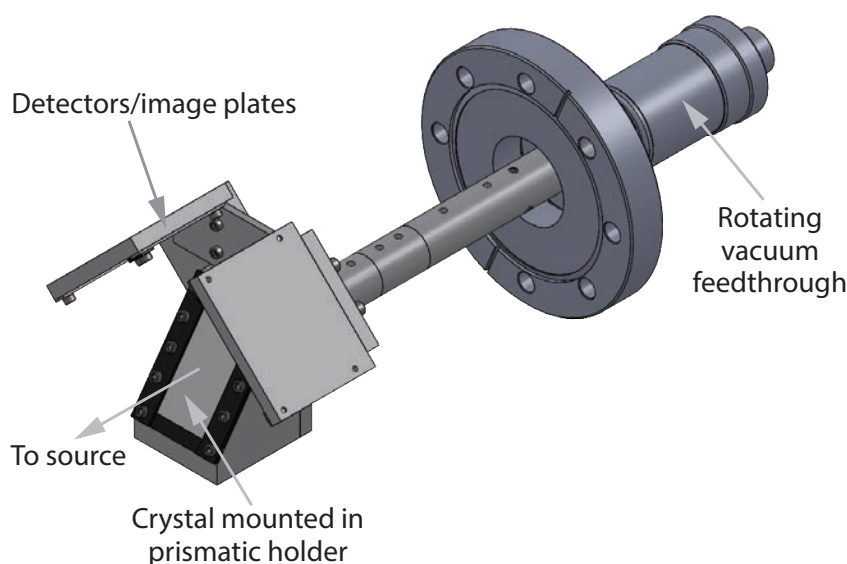


Figure 3. Setup for crystal characterization on a Manson x-ray source

Crystal Characterization Setup

Before being used in a spectropolarimeter, each crystal has to be characterized and aligned using a known x-ray source. Ideally, this process is performed on a synchrotron, which is a bright source of polarized x-rays with tunable photon energy (Pereira 2014). However, basic characterization and alignment can be performed on a laboratory point x-ray source, such as a Manson source.

The polarization-splitting geometry is shown in Figure 1c. Any spectropolarimeter configuration and crystal characterization setup has to fulfill those geometric requirements. Figure 3 shows an arrangement for crystal characterization on a Manson x-ray source. The crystal is installed on a prismatic holder with a 35.3° angle, which ensures 45° angles on the polarizing planes. The linearly polarized reflections are directed perpendicularly to each other and to the incident x-rays. Each of them is incident at 90° on a detector. Figure 3 shows image plate holders, but silicon diodes are an alternative option.

This part of the setup can be installed on a goniometer and used at a synchrotron. For Manson source characterization, the crystal holder is attached to a rotating vacuum feedthrough, with the rotation axis pointing to the x-ray source.

We used ray tracing to locate and identify the reflections recorded onto the detectors. Figure 4 shows examples of results on one detector for a Manson source with copper anode, considering

Table 1. Best matches for six crystal cuts and ion lines observed in pinch plasmas or characteristic lines available for crystal characterization and alignment. The table shows reflections for polarization-splitting planes symmetric to the surface in up to five diffraction orders (n). The search did not include transitions with photon energies over 30 keV. For each splitting plane, the photon energy that satisfies Equation 1 in the first order is given in the column E_{45} .

SURFACE PLANE	SPLITTING PLANE	$2d$ (Å)	E_{45} (keV)	$n = 1$	$n = 2$	$n = 3$	$n = 4$	$n = 5$
Quartz 1 1 $\bar{2}$ 0	1 0 $\bar{1}$ 0	8.510	2.060	Al 1s - 3p	Ar 1s - 4p	Mn 1s ² - 1s2p	Fe 1s ² - 1s3p	Cu 1s - 3p
Quartz 1 0 $\bar{1}$ 0	1 1 $\bar{2}$ 0	4.913	3.569	Al 1s ² - 1s3p	Co 1s ² - 1s2p	Zn 1s ² - 1s3p	Y K α	Mo 1s ² - 1s2p
Ge 4 2 2	2 2 0	4.000	4.384	Ar 1s - 4p	Cu 1s - 2p	Kr 1s ² - 1s2p	Mo K α	Mo 1s - 3p
InSb 2 2 0	4 2 2	2.645	6.629	Fe 1s ² - 1s2p	Kr 1s ² - 1s2p	Ru K α	Sn K α	33.145
Ge 2 2 0	4 2 2	2.310	7.591	Co 1s ² - 1s2p	Kr 1s ² - 1s3p	Mo 1s - 4p	30.362	37.952
LiF 2 2 0	4 2 2	1.644	10.665	Zn 1s ² - 1s3p	Mo 1s ² - 1s3p	31.996	42.662	53.327

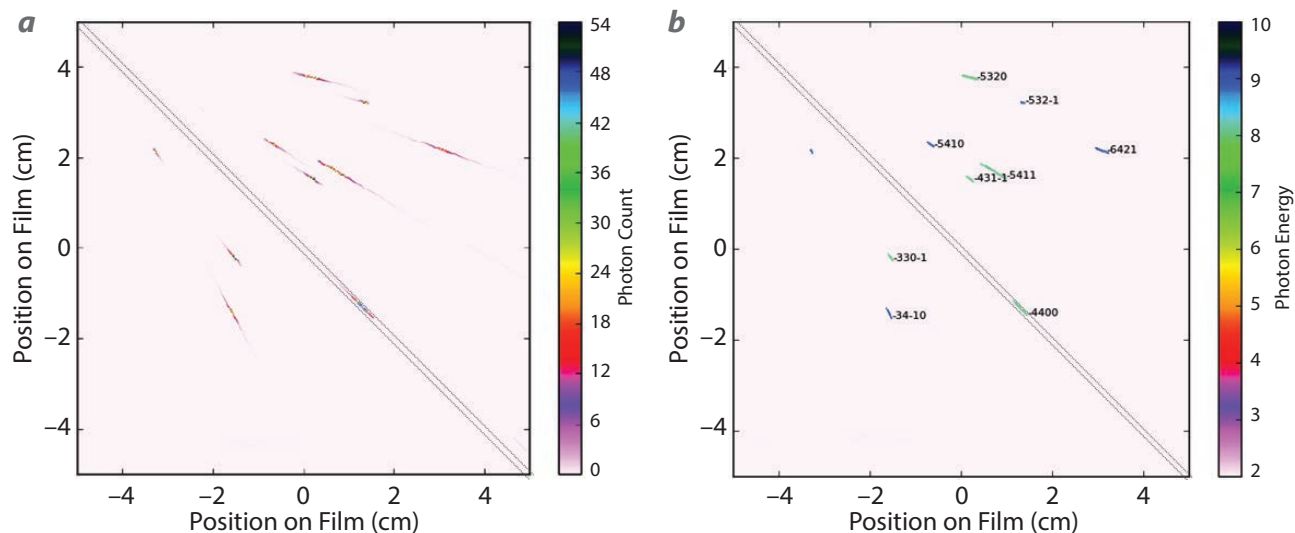


Figure 4. Ray tracing for X-cut quartz with $\{1\ 0\ \bar{1}\ 0\}$ splitting planes, when using a copper anode Manson source. Only results for one detector are shown. The image plate origin corresponds to the location of photons with energy $E_{45} = 2.06$ keV (or integer multiples of E_{45}) incident on the crystal center at $\theta_B = 54.7^\circ$ Bragg angle. Each reflection is labeled in the photon energy plot with the Miller indices of the reflecting plane. The dotted lines indicate the reflections from the polarizing plane.

the $K_{\alpha 1}$ (8.048 keV), $K_{\alpha 2}$ (8.028 keV), and K_{β} (8.905 keV) characteristic lines and neglecting the bremsstrahlung radiation. We selected an X-cut quartz crystal to analyze the polarization of the K_{α} lines by reflection in the $n = 4$ order on the $\{1\ 0\ \bar{1}\ 0\}$ planes ($\theta_B \approx 46.5^\circ$). The crystal height along the symmetry axis was 5 cm. Its center was situated at 45 cm from the source, and the detectors were placed at 5 cm from the crystal. A slit parallel to the c -axis was located at 40 cm from the source. In Figure 4, the polarized reflections fall between the dotted lines. The other reflections observed in neighboring regions of the detector in Figure 4 are produced by internal planes other than the polarizing planes. This effect becomes stronger for higher-energy photons. Knowing the locations of

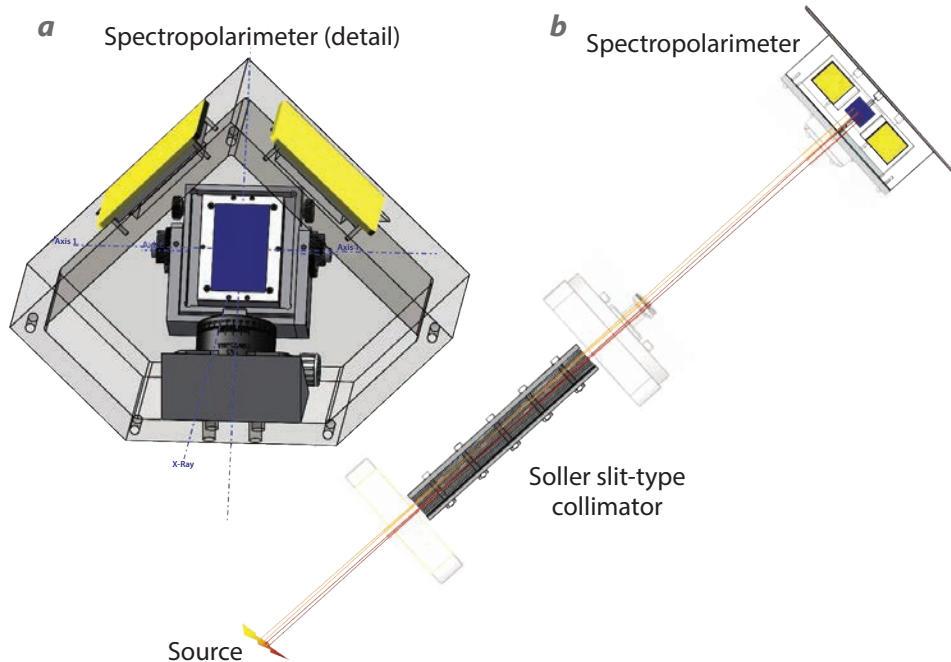


Figure 5. The main components of the instrument are the spectropolarimeter and the collimator. (a) In this rendering, the front plate of the spectropolarimeter is transparent to show the crystal (blue) attached to its holder (dark gray) via a rotation stage. The crystal mount also allows pitch and yaw adjustments. In the instrument version presented, the detectors (yellow) are image plate cassettes. (b) The multi-plate collimator and ray paths to the crystal from two adjacent source regions.

these unintended reflections is important when using space-integrating detectors, such as the silicon diodes. These features are also helpful for determining orientation and aligning the crystals.

Spectropolarimeter Design Concept

A generic instrument design that can be adapted to various applications is underway. Figure 5 shows the main components of a working instrument: the spectropolarimeter proper and a Soller slit-type collimator.

The spectropolarimeter configuration, based on Figure 1c, is a version of the setup used for crystal characterization installed in a hard x-ray shielding enclosure. The crystal is mounted on an angled prismatic holder that has roll (around the symmetry axis), pitch, and yaw (in the surface plane) adjustments to compensate for errors in the crystal cutting, as determined during characterization. The stage used to correct the roll can be used to rotate the crystal to positions where polarizing planes nonsymmetric to the surface are brought into the polarization-splitting position with respect to the incident beam (Pereira 2014).

The collimator is necessary to restrict the x-rays incident on the crystal to planes containing the symmetry axis. This feature is important for extended x-ray sources because only in this case do the two mutually orthogonally polarized reflections occur for the same incident beam (Wallace 2018). Fortuitously, this provides space resolution to the spectropolarimetric measurement. For practical collimator lengths, if one avoids x-rays originating in neighboring regions of the source from overlapping on the detector, the use of the collimator limits the number of resolution elements.

CONCLUSION

En route to developing a single-crystal x-ray spectropolarimeter, we systematically evaluated combinations of crystal planes and x-ray emission lines to find matches with acceptable integrated reflectivity and high polarization contrast. This search identified desirable crystal cuts, which were subsequently procured. A simplified spectropolarimetric setup was designed and built for characterizing and aligning the crystals on Manson and synchrotron sources. A conceptual instrument design for the x-ray spectropolarimetry of HED plasmas is in an advanced

stage. A possible high-impact application is the measurement of the compressed axial magnetic field at stagnation in MagLIF targets on the Sandia National Laboratories Z machine by Zeeman spectroscopy. Currently no other direct technique is available for this measurement. As a consequence, the physical design of the instrument and the crystal selection have been optimized for this application. The spectropolarimeter will also be useful for measuring the electron distribution anisotropy in HED plasmas, primarily in Z-pinch plasmas, with the goal of better understanding and optimizing, for example, the parameters of the electron beams responsible for nonthermal emission and the electric fields that accelerate ions in dense plasma focus machines. In FY 2019, we will characterize several polarization-splitting crystals suitable for HED settings and will design spectropolarimetric diagnostic instruments for HED experiments. We will also extend the capability of the numerical tools we developed for crystal performance modeling by accounting for the crystal reflection properties.

ACKNOWLEDGMENTS

We would like to thank our Sandia National Laboratories colleagues Guillaume Loisel, Dave Ampleford, Matt Gomez, and Ming Wu for their contributions to this work.

REFERENCES

- Ampleford, D. J., et al., “Contrasting physics in wire array z pinch sources of 1–20 keV emission on the Z facility,” *Phys. Plasmas* **21** (2014) 056708.
- Barkla, C. G., “Polarised Röntgen radiation,” *Philos. Trans. R. Soc. Lond. A* **204** (1905) 467–479.
- Baronova, E. O., M. M. Stepanenko, “A novel x-ray polarimeter based on hexagonal crystal, for application to thermonuclear fusion experiments,” *Plasma Physics and Controlled Fusion* **45**, 7 (2003) 1113–1120.
- Gomez, M. R., et al., “Demonstration of thermonuclear conditions in magnetized liner inertial fusion experiments,” *Phys. Plasmas* **22** (2015) 056306.
- Pereira, N. R., “X-ray polarization splitting with the Baronova–Stepanenko spectropolarimeter,” *High Energy Density Physics* **5**, 1–2 (2009) 89–92.
- Pereira, N. R., R. Presura, M. Wallace, A. Kastengren, “X-ray polarization splitting by a single crystal evaluated with synchrotron x-rays,” *Rev. Sci. Instrum.* **85**, 7 (2014) 073503.

Presura, R., et al., “Polarization-splitting crystals for 2–25 keV spectral lines,” submitted to *Rev. Sci. Instrum.* (2019).

Sanchez del Rio, M., R. J. Dejus, “Status of XOP: An x-ray optics software toolkit,” *Proc. SPIE* **5536** (2004) 171–174.

Schollmeier, M. S., G. P. Loisel, “Systematic search for spherical crystal X-ray microscopes matching 1–25 keV spectral line sources,” *Rev. Sci. Instrum.* **87**, 12 (2016) 123511.

Slutz, S. A., M. C. Herrmann, R. A. Vesey, A. B. Sefkow, D. B. Sinars, D. C. Rovang, K. J. Peterson, M. E. Cuneo, “Pulsed-power-driven cylindrical liner implosions of laser preheated fuel magnetized with an axial field,” *Phys. Plasmas* **17**, 5 (2010) 056303.

Wagner, E., P. Ott, “Versuche über die Polarisation spektralzerlegter Röntgenstrahlen,” *Ann. Phys.* **390**, 4 (1928) 425–469.

Wallace, M. S., S. Haque, P. Neill, N. R. Pereira, R. Presura, “Spatially resolved single crystal x-ray spectropolarimetry of wire array z-pinch plasmas,” *Rev. Sci. Instrum.* **89**, 1 (2018) 015106.

This page left blank intentionally



A Spectral Evaluation of the Application of Super-Resolution to Commercial Satellite Imagery

STL-010-18 ■ Year 1 of 2

Chris Burt,^{1,a} Janice Lawson,^a Bill Ford,^b Mary D. O’Neill,^a and Eric Moore^b

¹burtcb@nv.doe.gov, (805) 681-2022

^aSpecial Technologies Laboratory

^bRemote Sensing Laboratory--Andrews



We evaluated the spatial and spectral impact that super-resolution algorithms have on commercial satellite multispectral imagery, and we developed important capabilities for the NNSA. Panchromatic (pan) sharpening, a conventional super-resolution algorithm, was examined, and a novel machine learning approach was explored. We applied these techniques to an established remote sensing evaluation dataset and evaluated their impacts using peak signal-to-noise ratio and a comparison of image classification results. Our analysis showed that pan sharpening was able to improve spatial resolution by more than 6x without impacting the spectral fidelity of the data. The machine learning approach allowed us to use a single image to improve resolution by 2x, with minor spectral fidelity loss. In FY 2019 of this SDRD, we will examine machine learning approaches to improve image classification using a novel spectral training dataset.

BACKGROUND

Commercial satellite multispectral imagery (MSI) is inexpensive and extensively used by many DOE and intelligence community programs, especially in access-denied locations. Although the number and availability of these satellites continue to increase, the industry focus has shifted from improving spatial resolution (or decreasing ground sample distance [GSD]) to creating small, cheap sensors with short revisit times. As image detector resolutions seemingly plateau, more focus has been placed on post-processing techniques that can improve spatial resolution. These

techniques are collectively referred to as super-resolution (SR).

SR is well documented in the literature; however, it is not clear whether the process of spatial image sharpening distorts spectral profiles such that traditional material identification techniques are compromised. When SR is applied to multiband data, the spectral information is typically synthesized by interpolation of nearby pixels, and noise is reduced by frequency filtering. While many studies have evaluated the spatial impact of SR techniques, few have attempted to quantify the spectral impact. Our

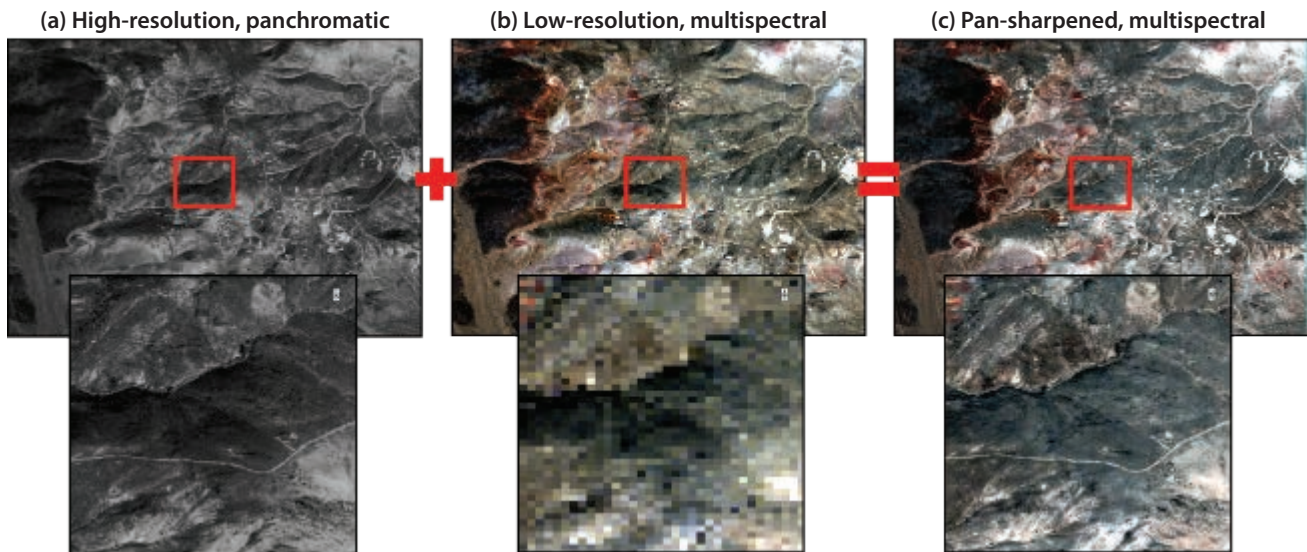


Figure 1. WV3 data of Cuprite, Nevada. (a) High-resolution panchromatic band, (b) true-color composite of low-resolution multispectral bands, and (c) pan-sharpened true-color composite.

research evaluates the impact SR has on both when applied to commercial satellite MSI.

We evaluated conventional and novel SR techniques, including panchromatic (pan) sharpening and a machine learning (ML) approach. In order to quantify the spatial and spectral impact of SR, we used a dataset from a canonical remote sensing test site (Cuprite, Nevada). This location has been well surveyed, and the hydrothermal alteration minerals have been well mapped. Kruse (2015) created a pseudo-ground truth image using a mixture-tuned matched filtering classification of high-spatial and high-spectral resolution Airborne Visible/Infrared Imaging Spectrometer (AVIRIS) hyperspectral imagery. This dataset, while not perfect, is the most accurate pixel-based ground truth of Cuprite available.

PROJECT

Pan Sharpening

Although other conventional SR techniques were examined during this research, for brevity, we discuss only pan sharpening, which achieved the best results. Pan sharpening is a popular method for enhancing the spatial resolution of an image, but it requires a co-collected, high-resolution panchromatic image. Pan sharpening enhances resolution by up-sampling the low-resolution bands to the same resolution as the high-resolution panchromatic band. As such, image-to-image registration is vital for pan sharpening

and a source of error. The Gram-Schmidt pan-sharpening algorithm, introduced by Laben (1998), was designed for MSI and uses the spectral response function of a specific sensor to simulate the high-resolution panchromatic band from the low-resolution multispectral data.

To ensure proper spatial alignment, we ortho-corrected the Cuprite WV3 multispectral and panchromatic data using the 30 m Advanced Spaceborne Thermal Emission and Reflection Radiometer (ASTER) Global Digital Elevation Model. The Gram-Schmidt algorithm was then applied to the datasets through a workflow in ENVI, a standard image-processing package (Harris Geospatial Solutions 2018). Figure 1 highlights the enhanced spatial resolution of the pan-sharpened data.

Machine Learning (CosmiQNet)

ML is a powerful computer processing technique that has recently become widely used in a variety of fields due to the development of convolutional neural networks (CNNs) and parallel processing. ML has been proven effective in spatial image analyses, such as feature extraction, object detection, road tracking, and car counting. Many powerful open-source ML networks have been published, including AlexNet (Krizhevsky 2012), GoogLeNet (Szegedy 2015), and ResNet (He 2016). Deshpande (2016) offers a great overview of the most important, recent CNNs. Due to the potential positive impact of ML on the nonproliferation mission, much of our efforts during this project focused on applying ML to the SR problem.

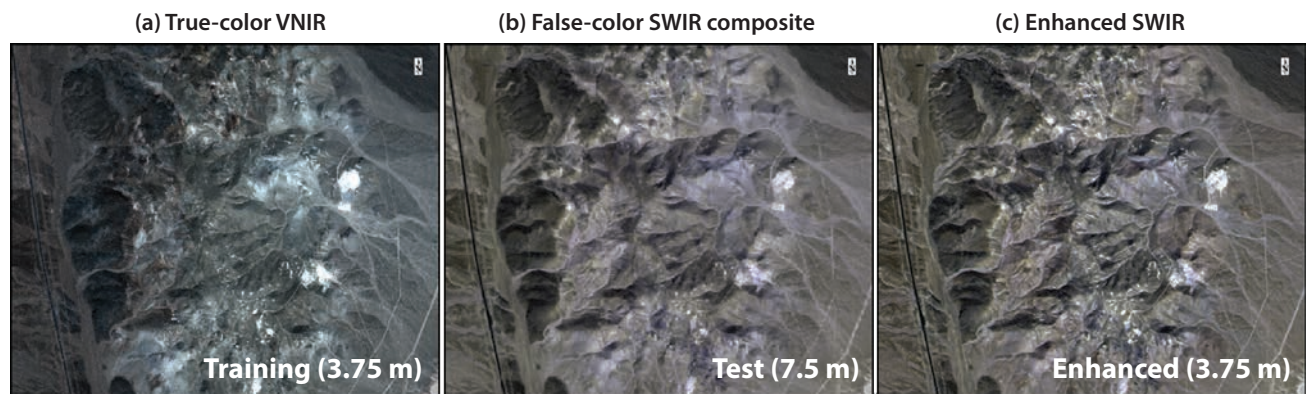


Figure 2. Spatial subsets of WV3 Cuprite data. (a) The true-color VNIR composite used to train the network, (b) the 7.5 m false-color SWIR composite that the trained network was applied to, and (c) the false-color 3.75 m CosmiQNet-enhanced SWIR bands.

Using a deep neural network (DNN) called CosmiQNet to enhance resolution of commercial MSI was proposed by Patrick Hagerty at CosmiQWorks through a three-part series of blog posts published in November 2016, December 2016, and March 2017. Using perturbative layers, Hagerty created an architecture for a DNN to train the network a layer at a time, and then applied CosmiQNet to the original, low-resolution image to increase its spatial resolution. As standard DNNs are incapable of handling the extremely large output space of SR images, Hagerty developed a new DNN using perturbations of the identity map. Each new perturbation was given a trainable weight, and its contributions to the final output were estimated.

It is beneficial that CosmiQNet does not require supervised training (e.g., no labeled data) and can be used with a single dataset. The network down-samples the original low-resolution image (a factor of 2, in our case) and then attempts to sharpen the image. This is done in iterations of subsampled regions so that each image is treated as multiple data points. Each iteration is evaluated by a peak signal-to-noise ratio (PSNR). When the PSNR of the iteration compared to the original image is 1 dB, the network is trained.

The weights “learned” by the trained network are then applied to the low-resolution image (by simple matrix multiplication), and spatial features are sharpened for a pseudo-decrease in GSD. This technique does not add pixels (unlike pan sharpening) but rather increases the sharpness of the spatial features in the scene, and to the viewer it looks as if spatial resolution has been increased. To compensate for this, we up-sampled our test images by a factor of 2 (i.e., from 7.5 to 3.75 m) prior to applying the trained network. This added the pixel space required to hold the newly created spatial information (i.e., the created pseudo-GSD).

We initially trained the network with the eight high-resolution (3.75 m) visible-near infrared (VNIR) bands from Cuprite. We chose to resample the 1.24 m GSD VNIR bands to 3.75 m prior to training the network. In Hagerty (2017), the network was proven most effective when the GSD was decreased by a factor of 2. Thus, we sought to decrease the 7.5 m short-wave infrared (SWIR) bands to 3.75 m. We wrote custom code to apply the trained network to the eight low-resolution (7.5 m) SWIR bands from the same WV3 collection. Our code then created the enhanced image shown in Figure 2.

Next, we examined the utility of CosmiQNet when applied to MSI that contains areas of interest to nonproliferation. We used the Cuprite-trained network to enhance WV3 eight-band SWIR data of an NNSS underground nuclear explosion testbed (these data were from Defense Nuclear Nonproliferation’s Underground Nuclear Explosion Signatures Experiment Venture). The spatial enhancements were similar to the Cuprite results shown in Figure 2.

These analyses show that CosmiQNet effectively increases the sharpness of an image. However, small changes in the parameters of the network have large impacts on the quality of the enhanced image. These parameters seem to vary, depending on image size, the amount of in-scene spatial structure, and other factors. Additionally, fine-scale visual artifacts were observed when the new, enhanced image was being constructed. We believe these visual artifacts are produced by the way we re-create the enhanced image and are not inherent to the ML technique. We are investigating ways to optimize parameters and testing new methods to use the CNN more effectively. These efforts will continue next year.

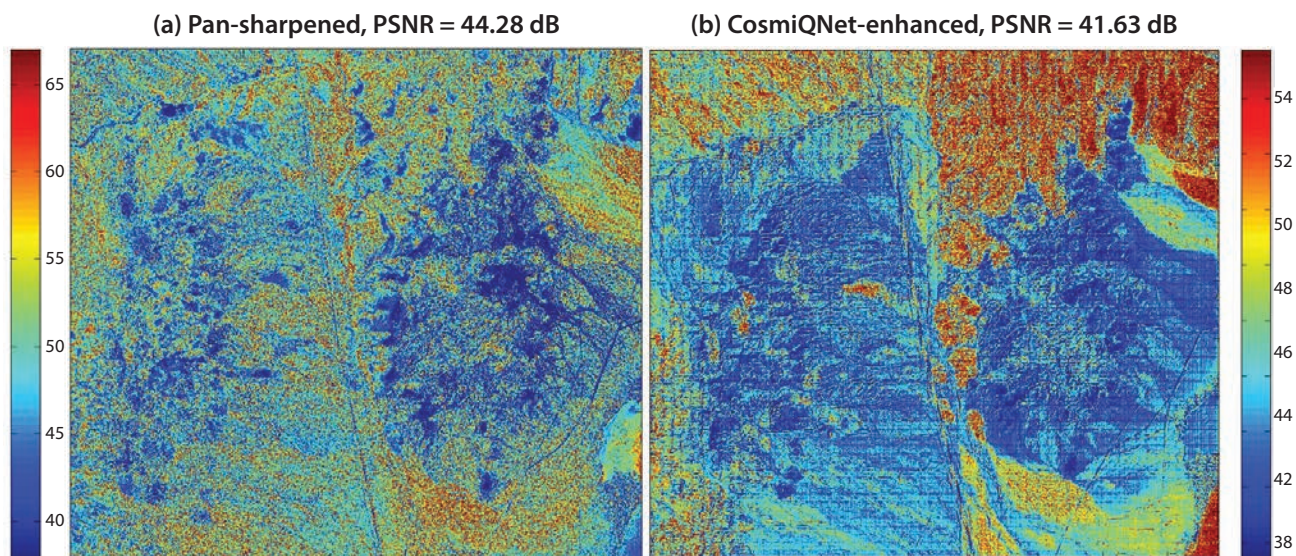


Figure 3. PSNR pixel distribution for the Cuprite data. (a) Pan-sharpened data and (b) CosmiQNet-enhanced data. Note the different color bar scale for each image.

Evaluations

To evaluate SR techniques, researchers have traditionally used city scenes, which contain a large number of spatial features and tend to be easier to spatially enhance than rural scenes. It is important to note that for our quantitative SR evaluations, we specifically chose a scene with low spatial structure (Cuprite), as locations of this type are often of interest to the nonproliferation community.

Spatial (Peak Signal-to-Noise Ratio)

As shown by Hagerty and many others (e.g., Elbakary 2008), PSNR is the metric that researchers typically use to quantify the spatial improvement of an SR algorithm. PSNR uses the mean squared error of the original image compared to an enhanced image to estimate the human perception of image quality improvement. The larger the PSNR, the better quality an image will be perceived to have. We calculated this metric for the WV3 Cuprite data enhanced by pan sharpening (44.28 dB) and CosmiQNet (41.63 dB). We also calculated the PSNR pixel distribution across the images to further analyze the type of spatial data the algorithm most improves. Figure 3 shows that in areas of high spatial structure, CosmiQNet performs better (larger PSNR, red pixels). In areas of lower spatial structure, the algorithm performs worse (lower PSNR, blue pixels). This result is similar to that reported by Hagerty in part 3 of his blog series (2017).

Image Classification Accuracy (Spectral)

To explore the spectral impact of SR, we initially examined the average spectra for regions identified as specific minerals in Kruse (2015). We selected these regions of interest (ROIs) for the original WV3 data, the pan-sharpened data, and the CosmiQNet-enhanced data, and calculated the average spectrum of each ROI. The plots in Figure 4 illustrate the similarities between the pan-sharpened and original spectra (blue and orange, respectively). The CosmiQNet-enhanced spectra (gray) are also very similar to the original spectra with somewhat larger differences in shape.

To approximate the spectral fidelity of an image, one can use an image classifier such as adaptive coherence estimator (ACE) (Kraut 2005) to assign each pixel an identification, and then compare that result (or rule image) to a labeled ground truth image. This comparison is a standard ML and remote sensing tool for statistically evaluating the results of an image classification.

As a baseline, we applied ACE to the original, low-resolution WV3 SWIR Cuprite data. The same analysis was performed on the pan-sharpened and CosmiQNet-enhanced imagery. The resulting rule images were compared to the ground truth rule image, and the accuracies of their classifications were calculated. The rule images and the accuracy percentages are shown in Figure 5 and Table 1, respectively.

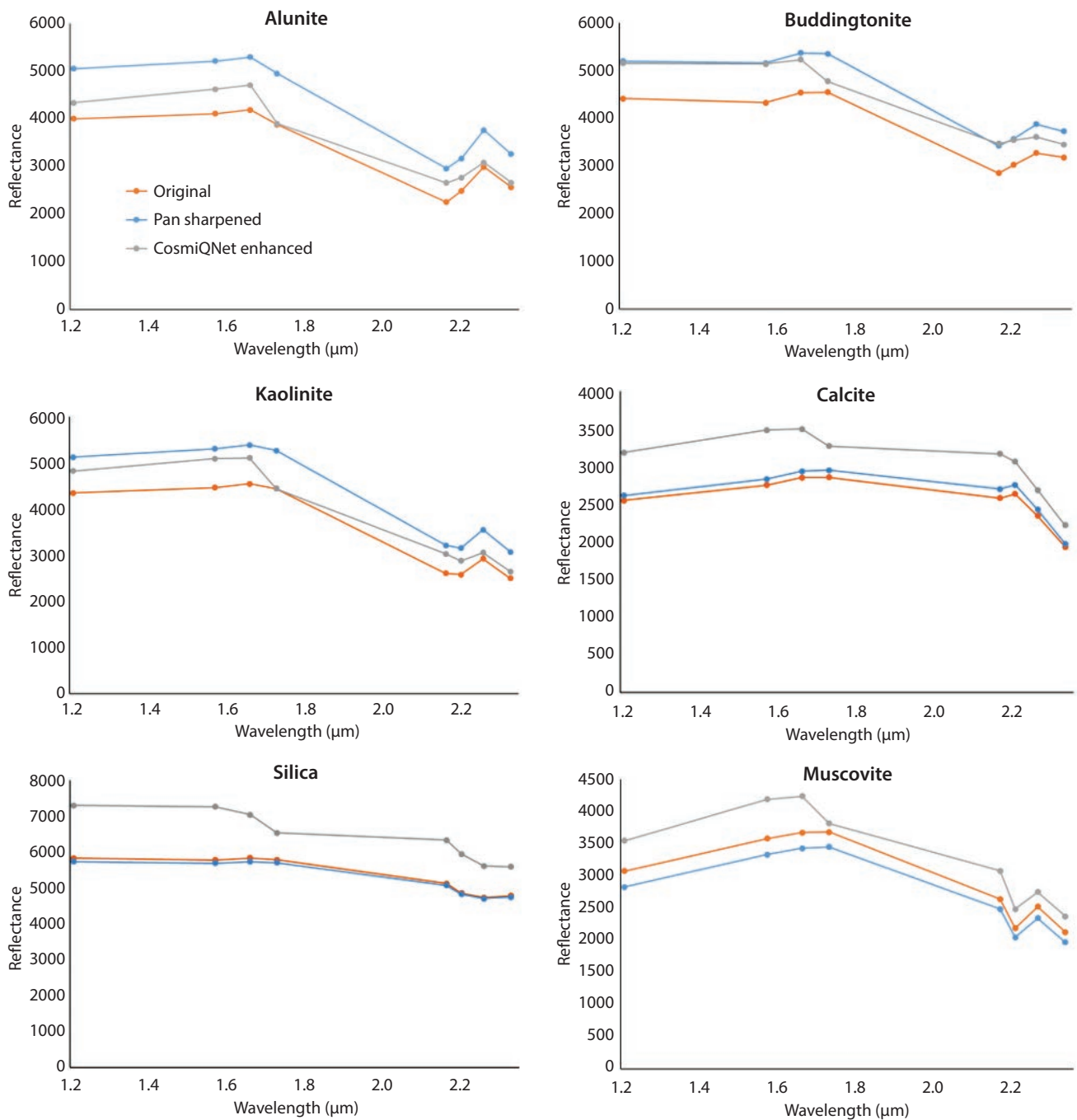


Figure 4. Spectral plots of average spectra for mineral ROIs. Note the similarity in spectral shape and the location of spectral features. The legend on the first plot applies to all plots.

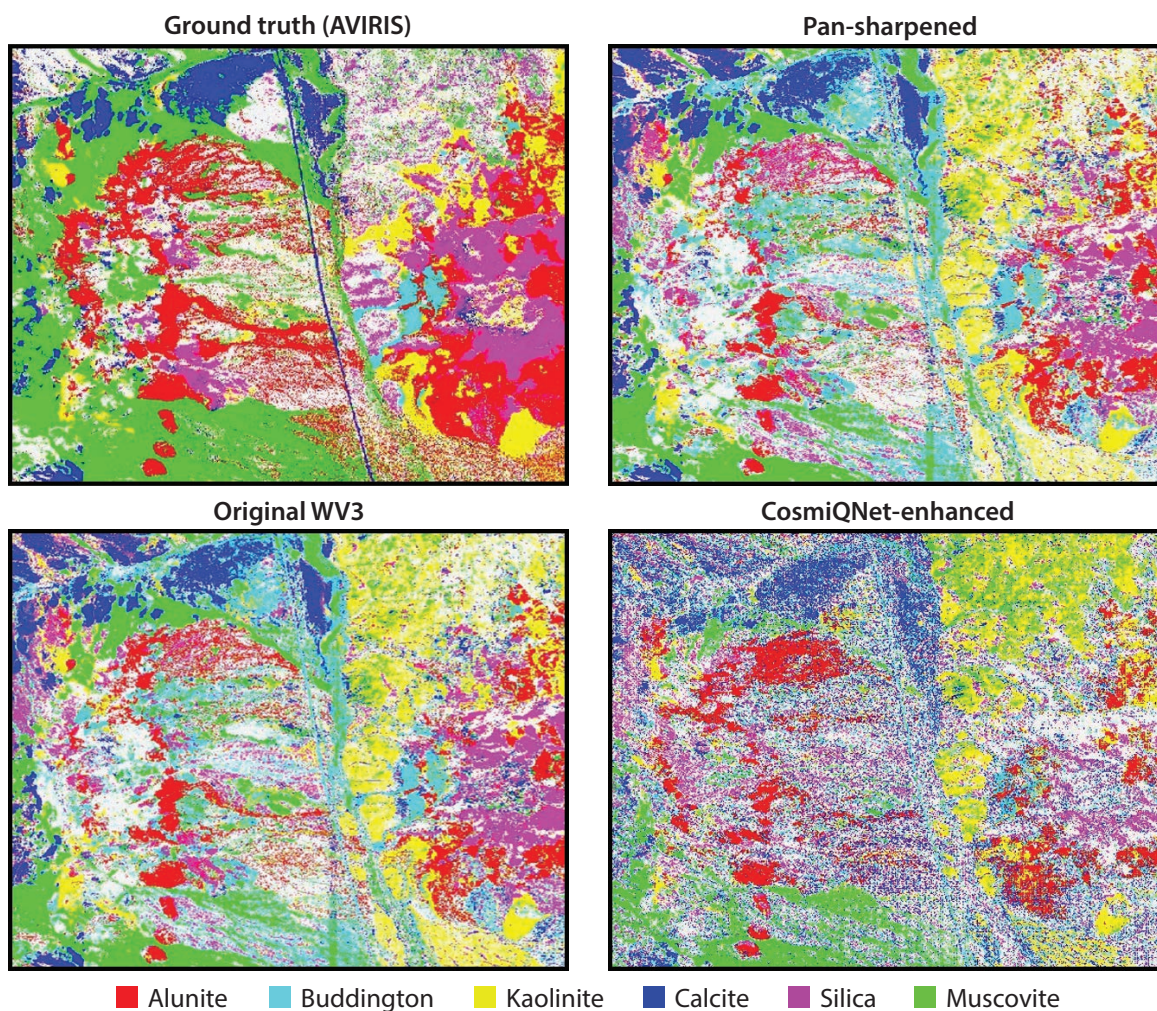


Figure 5. Classification rule images of the Cuprite dataset. The ground truth image of Cuprite is based on that of Kruse (2015). Accuracy percentages are shown in Table 1; white represents unclassified material.

Table 1. Classification accuracies for WV3 Cuprite dataset

MATERIAL	ORIGINAL	PAN-SHARPENED	CosmiQNET-ENHANCED
 Alunite	33%	29%	27%
 Buddingtonite	59%	57%	29%
 Kaolinite	36%	31%	21%
 Calcite	53%	56%	40%
 Silica	33%	29%	18%
 Muscovite	34%	35%	31%
 Unclassified	48%	50%	38%
Overall	39%	39%	31%

This analysis shows that the pan-sharpened data perform similarly to the original, low-resolution data. This result is positive, as it shows that the critical spectral profiles have not been drastically altered. The CosmiQNet-enhanced data do show a decrease in classification accuracy; however, these data contain visual artifacts that negatively impact the classification performance. As noted previously, we believe it will be possible to optimize the parameters of our image enhancement algorithm, which will remove the visual artifacts.

CONCLUSION

This research has shown the effectiveness of the Gram-Schmidt pan-sharpening technique and the CosmiQNet DNN. Pan sharpening was able to greatly increase spatial resolution (more than 6x) without affecting the spectral fidelity of the data. Although the ML approach has limitations, including a large up-front time outlay, this technique has proven to be effective when using a single image without the requirement of a co-collected panchromatic band or additional collections. These may be significant benefits for some implementations where multiple sensors and repeated collections are unavailable or undesirable. The presence of visual artifacts in the DNN-enhanced images negatively affected our spatial and spectral evaluations. We believe these artifacts are not inherent to the technique, but rather are caused by the way we rebuilt the enhanced image. With additional analysis, we are confident these artifacts can be mitigated.

Due to the potential negative impact on spectral fidelity, SR techniques are traditionally not used with spectral target detection and identification analyses. However, this research has shown the impact to be minimal.

In FY 2019, we will expand our ML research in an effort to improve target detection in spectral imagery. We will use a novel process with the Cuprite dataset to train a custom spectral neural network with approximately a million labeled data points. With transfer learning techniques, we believe we can use the trained network to do the “heavy lifting” for future target detection and image classification of ML applications. This will allow us to apply the network to targets of interest to sponsors. By combining our custom spectral classification network with standard spatial networks, we intend to create a robust tool for target detection.

ACKNOWLEDGMENTS

We would like to thank Dr. Fred Kruse of Horizon GeoImaging, LLC, for his Cuprite dataset (Kruse 2015) and Patrick Hagerty, formerly of CosmiQWorks, whose white papers on the ML SR algorithm motivated this work.

REFERENCES

- Deshpande, A., “The 9 deep learning papers you need to know about (understanding CNNs part 3),” Github (blog), August 24, 2016, <https://adeshpande3.github.io/The-9-Deep-Learning-Papers-You-Need-To-Know-About.html>, accessed September 8, 2018.
- Elbakary, M., M. Alam, “Superresolution construction of multispectral imagery based on local enhancement,” *IEEE Geosci. Remote Sens. Lett.* **5**, 2 (2008) 276–279.
- Hagerty, P., “Super-resolution on satellite imagery using deep learning, part 1,” *The DownLinQ* (blog), November 18, 2016, <https://medium.com/the-downlinq/super-resolution-on-satellite-imagery-using-deep-learning-part-1-ec5c5cd3cd2>, accessed December 1, 2016.
- Hagerty, P., “Super-resolution on satellite imagery using deep learning, part 2,” *The DownLinQ* (blog), December 6, 2016, <https://medium.com/the-downlinq/super-resolution-on-satellite-imagery-using-deep-learning-part-2-c9ce41dc0ee0>, accessed December 12, 2016.
- Hagerty, P., “Super-resolution on satellite imagery using deep learning, part 3,” *The DownLinQ* (blog), March 8, 2017, <https://medium.com/the-downlinq/super-resolution-on-satellite-imagery-using-deep-learning-part-3-2e2f61eeed1d3>, accessed March 12, 2017.
- Harris Geospatial Solutions, “ENVI,” <https://www.harrisgeospatial.com/docs/GramSchmidtSpectralSharpening.html>, accessed December 1, 2017.
- He, K., X. Zhang, S. Ren, J. Sun, “Deep residual learning for image recognition,” *2016 IEEE Conference on Computer Vision and Pattern Recognition (CVPR)*, Las Vegas, Nevada, 2016, 770–778.
- Kraut, S., L. L. Scharf, R. W. Butler, “The adaptive coherence estimator: A uniformly most-powerful-invariant adaptive detection statistic,” *IEEE Trans. Signal Processing* **53**, 2 (2005) 427–438.
- Krizhevsky, A., I. Sutskever, G. E. Hinton, “ImageNet classification with deep convolutional neural networks,” in *Advances in Neural Information Processing Systems 25: 26th Annual Conference on Neural Information Processing Systems 2012*, Lake Tahoe, Nevada, December 3–6, 2012, 1097–1105.

Kruse, F. A., W. M. Baugh, S. L. Perry, “Validation of DigitalGlobe WorldView-3 Earth imaging satellite shortwave infrared bands for mineral mapping,” *J. Appl. Remote Sens.* **9**, 1 (2015) 096044.

Laben, C. A., B. V. Brower, “Process for enhancing the spatial resolution of multispectral imagery using pan-sharpening,” U.S. Patent 6,011,875, filed April 29, 1998, and issued January 4, 2000.

Szegedy, C., W. Liu, Y. Jia, P. Sermanet, S. Reed, D. Anguelov, D. Erhan, V. Vanhoucke, A. Rabinovich, “Going deeper with convolutions,” *2015 IEEE Conference on Computer Vision and Pattern Recognition (CVPR)*, Boston, Massachusetts, 2015, 1–9.



Dynamic Test Prediction and Characterization through Modeling-Informed, Multisource Data Fusion

NLV-006-17 ■ Year 2 of 3

**Aaron Luttmann,^{1,a} Derek Constantino,^a Jared Catenacci,^a
Margaret Hoeller,^{a,b} Tori Hoff,^c Doug L. Trone,^a Alexander Delgado,^a
Emily Jackson,^d Margaret Hock,^{a,e} and Jesse Adams^{a,f}**

¹luttmab@nv.doe.gov, (702) 295-0303

^aNevada Operations

^bIllinois Institute of Technology

^cEmbry-Riddle Aeronautical University

^dRemote Sensing Laboratory—Andrews

^eUniversity of Alabama in Huntsville

^fUniversity of Arizona



A comprehensive approach to detecting nuclear proliferation activities includes direct and indirect physical sensing as well as informational sensing. Whereas proliferation detection has focused on the direct physical sensing of radiation or explosives signatures, there has been a recent shift toward improving our capabilities for detecting patterns of life and tying them to illicit behaviors by adding informational data sources—such as open source media, power grid, and cyber information—and indirect physical sensing—such as seismic, acoustic, or magnetic signatures for traffic patterns and material movement. The focus of this project is to advance the science of fusing informational and multimodal physical signatures to characterize weaponization experiments at the NNSS. During the first year of the project, we used informational data sources to develop a profile of experimental activities at several NNSS facilities. This year, we augmented informational sensing with multimodal physical sensing, using a low-fidelity, low-power, low-cost wireless sensor array, on targeted experimental campaigns to demonstrate the existence of emergent features in multisource data that are capable of characterizing experimental facility operations. In FY 2019 we will advance classification algorithms and other analytics approaches to characterize experiments at NNSS facilities, collect further multimodal data on high-value campaigns, and lay out a framework for persistent monitoring of experimental facilities at the NNSS.

BACKGROUND

Weaponization of special nuclear material (SNM) requires a robust experimental program that most adversaries attempt to develop in secret. This usually involves hiding and shielding SNM, making direct sensing of the radiological signatures difficult. It is commonly believed that measuring human behaviors—so-called patterns of life—can augment the radiation sensing by providing additional information that helps identify illicit activities. This often involves “informational sensing,” which includes the analysis of open media, such as internet sources (Gastelum 2018) and public reports and analyses (Kornell 2016), and nonphysical data, for example, power grid or internet activity (Luttman 2018).

Another approach to characterizing patterns of life is by collecting data on compact, low-power arrays; the Canary multi-sensor platform (Kornell 2017, Miller 2018), shown in Figure 1, was developed for this purpose. Canaries were designed to operate with portable batteries and to automatically network to one another when energized. Each Canary has a suite of 10 to 14 sensors. We used several of the Canary’s sensors to test two key hypotheses of multimodal sensing: (1) that patterns of life can be tied directly to experimental signatures (i.e., that people’s behaviors can be tied to the physics of weaponization experiments) and (2) that analyzing multiple sensing modalities simultaneously can provide more information than any mode individually or even than all the modes when analyzed in series. Furthermore, we considered that making this approach useful to proliferation detection scientists would require well-established field operations and software tools for processing and analyzing the resulting data. In FY 2018 we focused on data collection and analysis demonstrations of these principles.

PROJECT

Our primary goal in testing the Canary sensors this year was to collect libraries of data measuring physics signatures of weaponization-oriented experiments and patterns of life describing personnel behaviors around the experiments. We collected data at the North Las Vegas (NLV) gas launcher, intermittently gathered data at the dense plasma focus (DPF) pulsed neutron source in NLV, and also collected data during a highly enriched uranium (HEU) neutron interrogation

campaign at the Area 11 DPF. In order to field at these three campaigns, we did significant work to make the Canary sensor systems field ready. Additionally, we developed analysis techniques for interpreting data and extracting the signatures of interest.

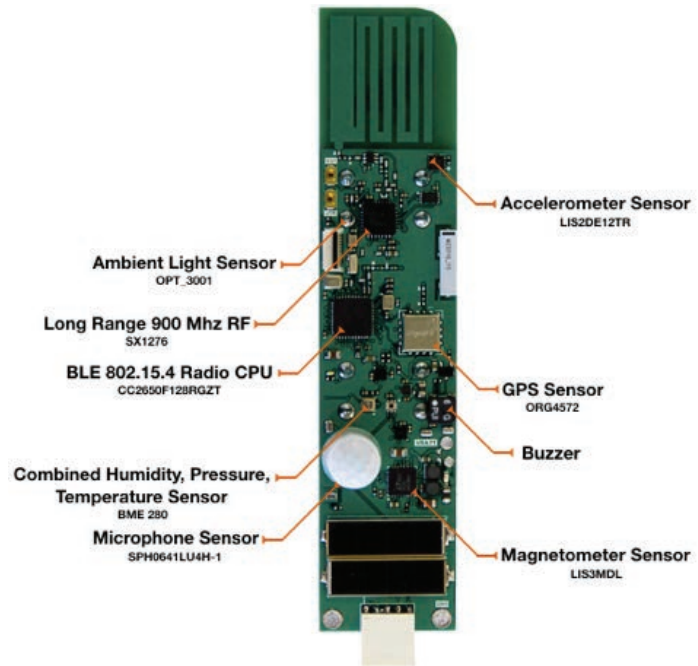


Figure 1. Canary multi-sensor. This small, low-cost, low-power sensor board is designed to automatically network with other Canaries in its communications range through a central laptop.

Wireless Sensor Array—Canaries

The Canary is a multi-sensor platform designed for fielding as a wireless, distributed array. The primary software runs from a laptop, and the collection of Canaries that are within communications range will automatically network to one another and to the laptop (Kornell 2017, Miller 2018).

For the experimental campaigns described in this report, each Canary was outfitted with the following sensors: accelerometer (x,y,z), magnetometer (x,y,z), ambient light, humidity, temperature, pressure, passive infrared (PIR), battery temperature, and battery voltage. Each Canary records 13 measurements at one-second intervals, so every second we collected a 13-dimensional measurement vector that can be used to analyze and classify activities.

Before fielding the Canary multi-sensor platforms on high-value experiments, we first tested and characterized the operational paradigm for their use. Canaries automatically and wirelessly construct a mesh network whereby each Canary can communicate

with the others as well as with the master computer. The computer's USB receiver collects the data being "pitched" by each sensor system at 1 Hz during optimal operations. In order to determine where to position the Canaries, we needed to know the distances over which the Canaries could pitch to the master computer, so we devised tests to determine the maximum range over which the Canary network would operate.

During the first range test, we varied the height of the USB receiver on the master computer and also the distance from a single Canary sensor to the computer. Table 1 shows that when the USB receiver is next to the computer at a height of 0 m, the maximum distance over which the Canary could communicate with the computer was about 3 m. When the USB receiver was raised to 3 m above ground, however, the Canary could successfully pitch at a distance of 14 m from the computer. This became a dominant factor in fielding the Canary arrays during our experiments.

We can also increase the distance between the Canaries and the master computer by daisy-chaining the Canaries so that one Canary pitches to another

Table 1. Basic Canary range test, where the height of the USB receiver on the master computer and the distance from the Canary to the computer were varied. "Yes" indicates the master computer was able to recognize the Canary at the specified distance and receive data from it.

RECEIVER HEIGHT (m)	DISTANCE FROM CANARY TO COMPUTER (m)	COLLECTION
0	3	Yes
0	5	No
1	5	Yes
1	10	Yes
1	15	No
2	10	Yes
2	15	No
3	10	Yes
3	12.5	Yes
3	14	Yes
3	15	No

Canary, which then pitches the data to the computer. As shown in Table 2, even with the Canaries 20 m apart and 8 m from the master computer to the closest Canary, they were able to connect and pitch data but not consistently. In fact, network dropout was the primary failure mode during experimentation; therefore, we did not daisy-chain the sensors during high-value experiments.

Multimodal Data Collection—NLV Field Tests

To establish a library of experimental signatures and to demonstrate the viability of fielding the Canaries on experiments, we collected multimodal sensing of physics phenomena at the NLV DPF and gas launcher facilities. We did not intend to connect patterns of life to experimental signatures, but rather sought to provide a database of measurements that could be used to develop algorithms for identifying emergent features in multimodal data. Our premise is that while many behaviors or events are directly measurable by a single sensor or inferable from a sequential analysis of multiple modalities, there are important signatures that can be characterized only through the simultaneous analysis of data streams that do not share the same systematic errors.

Dense Plasma Focus Experiments

The NLV DPF, operated in the A1 facility, is a nuclear fusion device used as a short-pulse neutron source (~200 ns). We collected data at the facility on May 29, July 19 and 24, and August 1, 2018. The Canaries were fielded on the DPF tube, near the two capacitor banks, on the DPF frame, and on the vacuum pump. Notes

Table 2. Range test results with daisy-chained Canaries, where the distances between the Canaries and between the closest Canary and the master computer were varied

DISTANCE FROM COMPUTER TO CANARY (m)	DISTANCE BETWEEN CANARIES (m)	CONNECTION
8	15	Yes
10	15	No
8	20	No
8	20	Yes
8	20	No

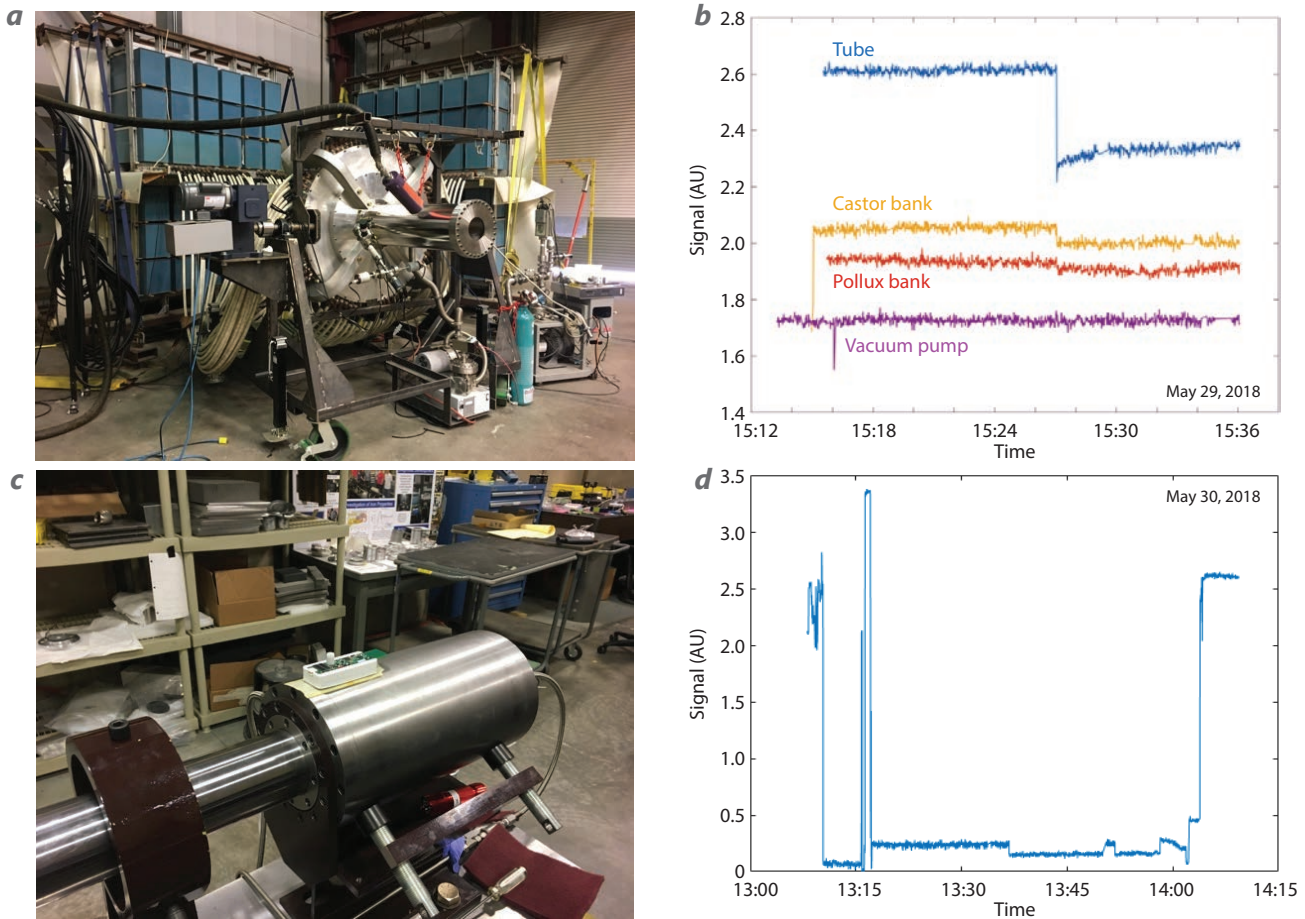


Figure 2. (a) The DPF and (b) a plot of the z-direction magnetometers from four Canaries fielded on the DPF. (c) The Canary sensor on the breach of the gas launcher and (d) a plot of its z-direction magnetometer signal.

were taken at one-second intervals for every charge, charge completion, and experiment time.

Figure 2a is a photo of the A1 DPF, and Figure 2b is a plot of the z-direction magnetometer signals from the four Canaries fielded at 15:27 on May 29. The experiment is clearly indicated by the sharp decrease in the magnetometer signal on the DPF tube (blue), is discernible on the Canaries on the two capacitor banks (yellow and orange), but was not recorded by the Canary magnetometer on the vacuum pump (purple).

Gas Launcher Experiments

The Canary multi-sensor platforms were also fielded on the gas launcher, a single-stage gas gun at the NLV C3 facility. Canaries (one at each location) were fielded on the catch tank, on the breach, near the vent, and on the shock absorber. Figure 2c shows the Canary sensor sitting on the gas launcher breach, and Figure 2d the z-direction magnetometer for the single experiment we performed. The experiment was executed at 13:58, which is somewhat noticeable as a blip in the signal,

but only given the ground truth. The large spikes in the signal around 13:15 are the result of the Canary being moved around by the people installing it; none of the significant features correspond to the firing of the machine.

The tests conducted at these NLV facilities established a baseline fielding paradigm for the Canaries and provided data that could be used to develop analysis techniques. The data could also be provided to other researchers for other characterizations (because the data are not sensitive).

Multimodal Data Collection—*SNM Campaign at the NNSS*

One of the most important classes of experiments for nuclear weapons development is measuring the reactivity of SNM, so such experiments make a natural use case for measuring patterns of life, determining signatures that identify the experimental behaviors, and tying those behaviors to physical signatures of the

Table 3. Modes of DPF operation

CATEGORY	PATTERN OF LIFE
Warm standby	No operations are in progress, and no personnel are present.
Nonscientific operations	Personnel are present for nonscientific operations (e.g., machine maintenance), and the DPF is not active.
Low-security experimentation	Technical personnel are present, and the DPF is operational, but neither security personnel nor SNM is present.
High-security experimentation	Technical and security personnel are present, and the DPF is operational for SNM experiments.

experiments. In June 2018, NNSA Defense Programs sponsored an active neutron interrogation experiment with HEU at the NNSS in Area 11; we were allowed to measure both physical signatures from the DPF pulses and pattern-of-life signatures from personnel and vehicle movement during this experiment. Three Canary multi-sensors were networked inside the DPF building, and three more were networked to each other along the road. This was the first time physics and pattern-of-life data were collected simultaneously at an HEU interrogation experiment.

The DPF facility at the NNSS has four operation categories, as described in Table 3. A complete lack of signatures indicates the facility is in warm standby; pattern-of-life signatures without physics signatures indicate nonscientific operations; but only both the pattern-of-life and physics signatures can detect and distinguish the two kinds of experimentation. Whereas the facility at Area 11 is often on warm standby—and nonscientific operations and low-security experimentation campaigns occur reasonably frequently—high-security experiments are quite rare, but an HEU active interrogation campaign took place from June 18 through 29, 2018. By collecting Canary measurements, we sought to link human patterns of life to the experiment physics signatures to fully detect and identify the high-security experiment.

A set of four Canaries, labeled NW, SW, NE, and SE, was to be fielded along Plasma Drive, the main road leading to the facility's point of access, but we reduced the sensor count to three to improve network connectivity. Three more Canaries were placed inside the DPF building, one on the DPF tent frame, another on the capacitor frame, and a third on the vent tube. During the campaign, nearly 50 individuals were working in an otherwise deserted site, and the DPF team conducted approximately 10 to 15 fusion events (neutron pulses) per day. The Canaries recorded data prior to morning planning meetings until after the last vehicle left the site at end of day.

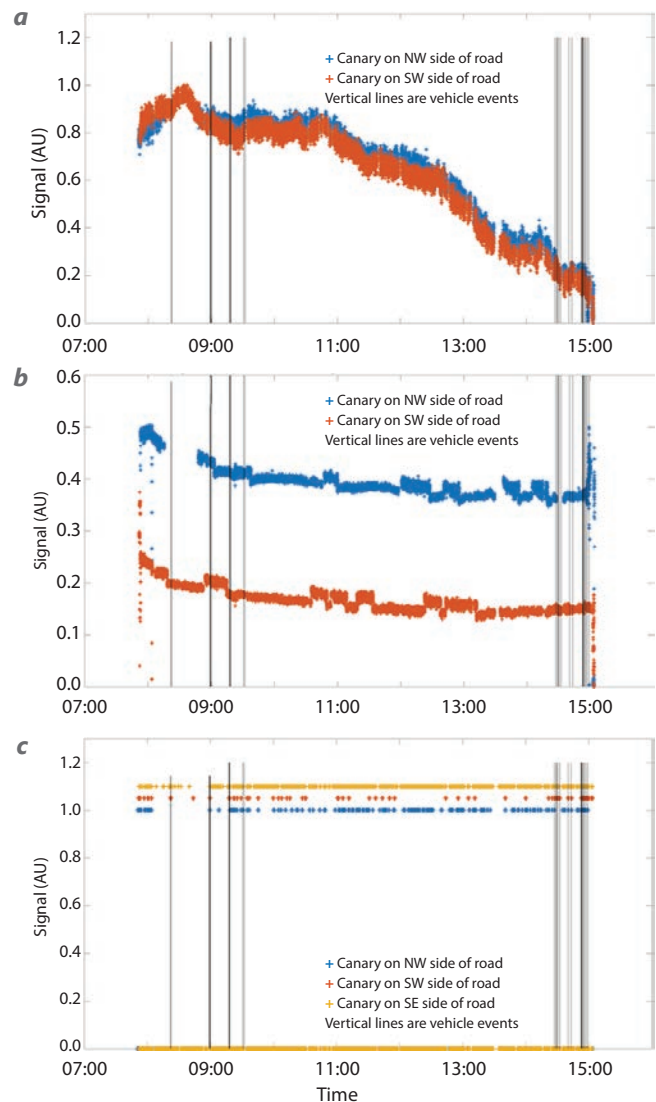


Figure 3. (a) Pressure, (b) magnetometer, and (c) PIR measurements, made June 29, 2018, from multiple Canaries along the road leading to the DPF facility. Note that there are no clear signatures from the vehicle events.

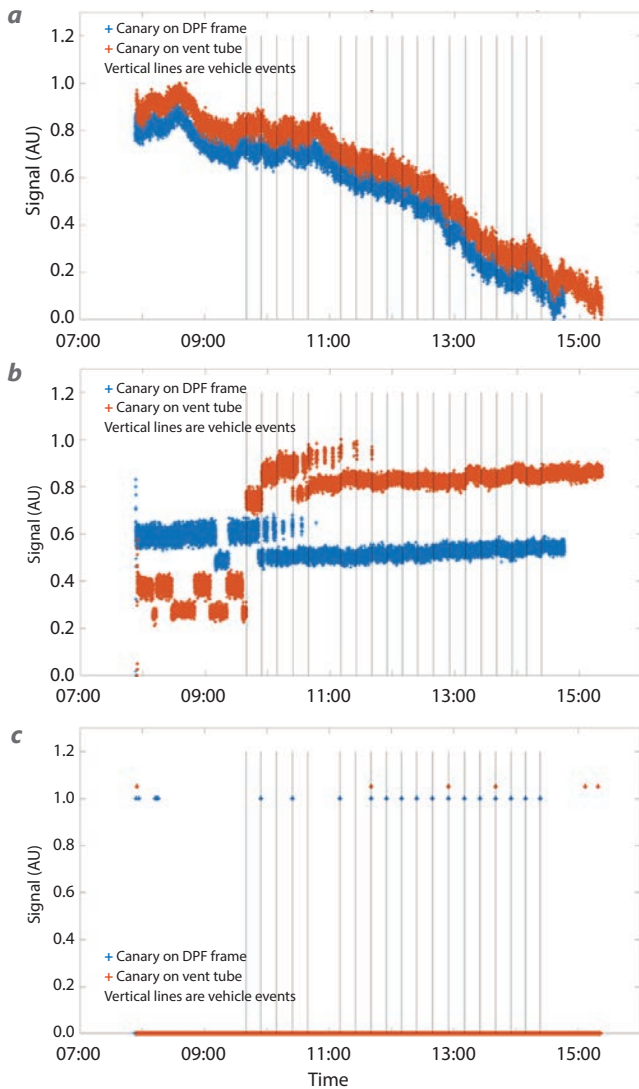


Figure 4. (a) Pressure, (b) magnetometer, and (c) PIR measurements made on June 29, 2018, from multiple Canaries inside the DPF facility

Figure 3 shows the pressure, magnetometer, and PIR measurements for Canary sensors placed on the west side of Plasma Drive near the data collection trailers. The data were collected on June 29, 2018. We also collected ground truth data, noting when personnel walked by the sensors and when vehicles drove by. As can be seen from Figure 3, none of the features on the sensor signals shown has any clear correlation with vehicle events, which are indicated by vertical lines. Thus, a more sophisticated analysis of the data was required (detailed below).

Figure 4 shows pressure, magnetometer, and PIR measurements from the same day, taken inside the DPF building. These measurements are from the Canaries we placed on the DPF frame and the vent tube to detect when the DPF is fired (i.e., when a

nuclear fusion event [neutron pulse] occurs). The physics signatures of the fusion events would be linked to vehicle patterns. Vertical lines in Figure 4 indicate the times of the fusion events. Neither the pressure sensor nor the magnetometer shows any discernible correlations to the DPF firing times. The PIR sensor for the Canary on the DPF frame (blue) does identify quite a few of the events—but not all of them—and there are spurious PIR signals from both Canaries.

Analysis Methods for Multivariate Data

As noted above, each Canary pitches a 13-dimensional data vector each second, and the first step in analyzing the data is to compare it to the ground truth data. To expedite this process, we developed an analysis software tool that allows the user to upload Canary data files and corresponding ground truth files. Each Canary and each modality can be selected, plotted, and compared to ground truth events of interest. Figure 5 shows the output of the analysis tool. In this example, the *z*-direction magnetometer (blue plot) from a Canary on the DPF frame is overlaid with vertical lines representing the DPF firing times.

While each modality on each Canary shows some indication of the ground truth events of interest, none of them clearly classifies the vehicle patterns on the road or the DPF firing in the building.

We placed three Canaries inside the DPF building, one on the DPF tent frame, one on the capacitor frame, and one on the vent tube. Every second a 39-dimensional vector was constructed as we concatenated data from the 13 sensors on each of the three Canaries over approximately 5.5 hours. This resulted in a $39 \times 20,266$ data matrix on which classical principal component analysis (Jolliffe 2002) was performed. Whereas the data vectors themselves did not cluster in their native 39-dimensional space in a way that separated the DPF firing times from other times, they did, in fact, cluster in principal component space. Figure 6a shows the time evolution of the projection of the data vectors onto the fourth principal component. Nearly all the time points are blue and have values around 0, but there are outliers, shown in orange, with significantly larger weights. Figure 6b shows the orange points on a time plot with vertical lines showing the ground truth data of DPF firing times. Note that all of the outliers from principal component four are on the blue vertical lines, which is to say that the outliers in principal component four correspond exactly to the DPF firing events.

The time evolution of all the principal components is detailed in Constantino (2018), but none of the

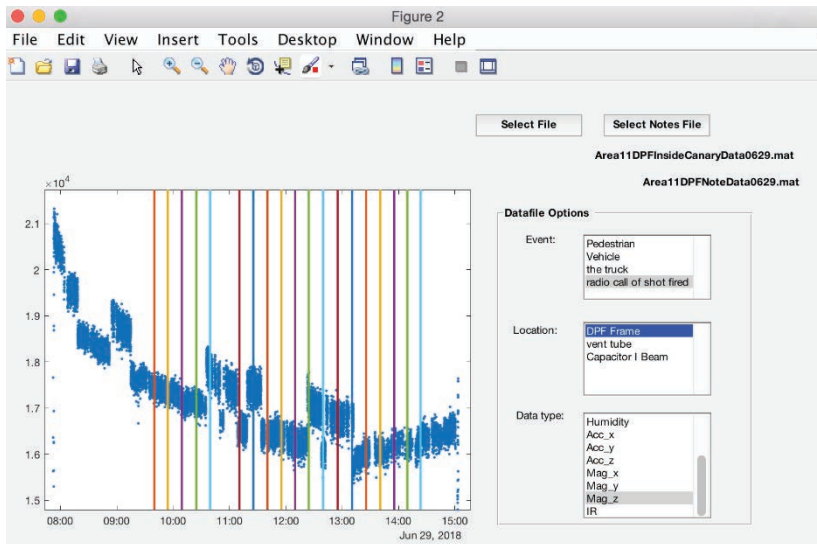


Figure 5. Software program developed for the analysis of Canary data. The user interface integrates the Canary data with user-provided ground truth data detailing the actual events of interest.

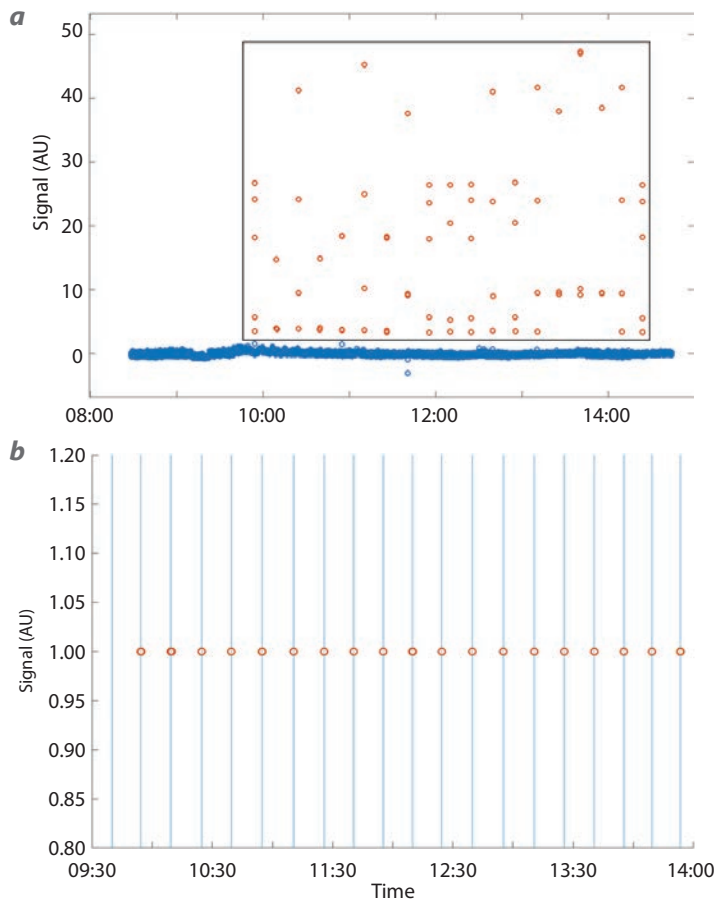


Figure 6. (a) The magnitude of the projection of each second's data vector onto the fourth principal component of the data matrix. (b) Outliers with respect to the fourth principal component, plotted in time with the ground truth data of DPF firing events (vertical lines). Data were obtained June 29, 2018.

other principal components shows significant clustering of any kind.

Informational Sensing— Power and Cyber

Like last year (Luttman 2018), this year we monitored the NNSS U1a facility to illustrate how informational data sources could uncover pattern-of-life information, which could then be used to infer experimental activities. Two subcritical experiments (SCEs) were executed in FY 2018, Vega in December 2017 and Lamarck in August 2018. As with the Eurydice SCE, the dates of major experimental activities, namely insertion and experiment, could be determined from the power consumption alone. Figures 7a and 7b show the daily power

consumption for the weeks leading up to Vega and Lamarck, respectively. The figures clearly document the daily and weekly patterns of the facility, with the power consumption being higher during the times personnel were present. Insertion is indicated by an unusually early start time of approximately 6 a.m. Notice that for Vega, the week of insertion and the week after were five-day work weeks instead of the usual four-day work weeks. For Lamarck, two weeks prior to insertion, there was a five-day work week. The need for Friday work is driven by experiment needs and is inconsistent across experiments; thus, it cannot be tied directly to specific activities. However, the occurrence of Friday work is more likely as an SCE approaches.

Another outstanding feature in the power consumption is usage when the facility is not active. There is a very clear static baseline of 80 to 90 kilowatt hours that the facility typically draws when the facility is not in use, overnight and on weekends and holidays. For the Eurydice SCE, we observed an increase in this baseline the night before the experiment. This trend was also observed for Lamarck; however, there was no increase in the overnight power consumption prior to the Vega SCE. For each of the SCEs, experiment day can be easily inferred from the start time being between 4 and 5 a.m., significantly earlier than any other day.

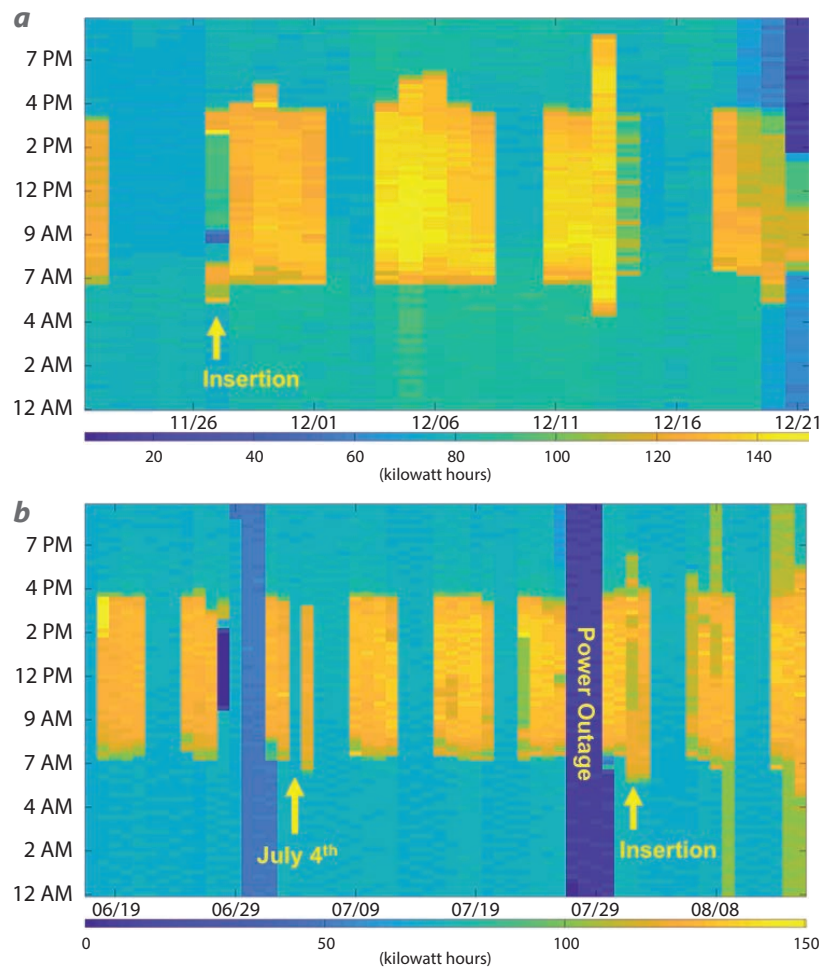


Figure 7. The power consumption for the U1a facility around the time periods of the (a) Vega and (b) Lamarck SCEs

Another important experiment to monitor is the Dry Alluvium Geology (DAG) series, which is a follow-on to the source physics experiments (SPEs), and whose first shallow, subsurface, conventional explosive test was conducted in July 2018. The locations and relative yields of the SPEs were estimated in FY 2017 (Luttman 2018) by the use of a far-field seismic model, and this same approach was applied to the initial DAG experiment, DAG-1.

DAG-1 was relatively small, having a yield of ~2000 lb of TNT, which is roughly equivalent to the energy released during a 3.2 magnitude earthquake. Thus, the seismic signature from the event was only prevalent on ten of the seismic sensors we could access (one-third of the sensors used for our assessment of the SPEs). Because of this, we have not been able to estimate the experiment yield. However, using the methodology previously developed, we were able to determine the experiment time to within 65 ms and the location to within 1.18 km. From each seismic sensor,

one can compute the arrival time of the signal and a circle around the sensor in which the explosion is most likely to have taken place. Figure 8 shows those circles computed for each of the ten seismic sensors that measured DAG-1, and the optimal intersection point of those circles (red dot) is computed as the location of the experiment. The yellow star is the true location of the experiment, and the distance between the true location and the computed location is ~1.18 km.

CONCLUSION

During the second year of this project, our three highest priorities were to advance the Canary multi-sensors to a high enough technological readiness level to be used on high-value experiments, to develop analysis techniques that demonstrate physics and pattern-of-life features can be extracted from multimodal data, and to continue the FY 2017 work using power grid and seismic information to

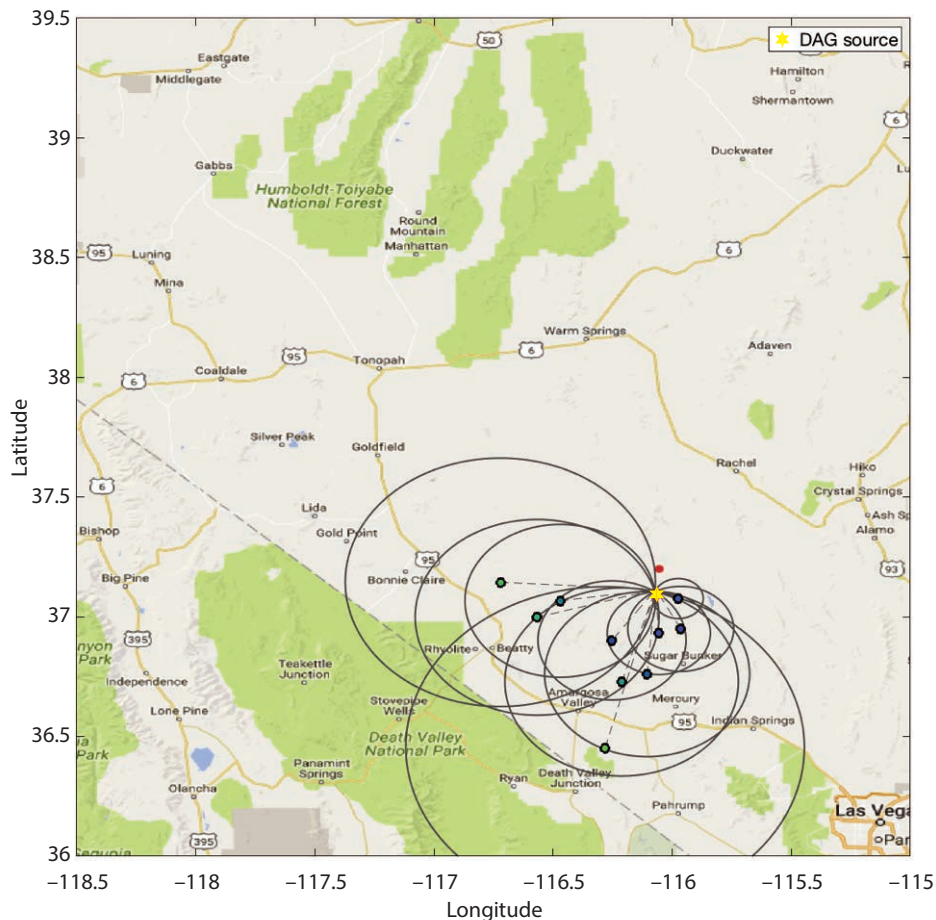


Figure 8. Back projection of the DAG experiment location using data captured by seismic sensors available on the University of Nevada, Reno, seismic repository. The red dot is the computed location of the experiment, and the yellow star is the true location of the experiment.

characterize experiments at U1a and at the DAG experimental facility. All three objectives were met. Moving into the third year of the project, we will focus on more advanced analysis techniques of multimodal data, which will be applied to new datasets collected at experimental campaigns around the NNSS with new multi-sensor platforms.

ACKNOWLEDGMENTS

The team would like to thank Bethany Goldblum and Christopher Stewart from the University of California, Berkeley, for their support and assistance with getting the Canary sensors up and running and fielded. We would also like to thank Professor Dongsheng Wu of the University of Alabama in Huntsville and Professor Matthias Morzfeld of the University of Arizona for their scientific and technical support.

REFERENCES

Constantino, D., M. Hoeller, T. Hoff, A. Luttmann, E. Jackson, B. Goldblum, C. Stewart, “Multi-sensor fielding and analysis for interdependent networks,” Nevada National Security Site, DOE/NV/03624--0267, 2018.

Gastelum, Z. N., T. M. Shead, “Preliminary application of neural networks to support assessment of ground-based imagery for international safeguards analysis,” *Proceedings of the Institute of Nuclear Materials Management Annual Meeting*, Indian Wells, California, July 16–20, 2017.

Gastelum, Z. N., T. M. Shead, “Inferring operational status of nuclear facilities with convolutional neural networks to support international safeguards verification,” *J. Nucl. Mater. Management*, 2018, in press.

Jolliffe, I. T., *Principal Component Analysis*, 2nd edition, Springer, 2002.

Kornell, J., Z. N. Gastelum, B. L. Goldblum, “Informational sensing for nonproliferation,” in *Proceedings of the Advances in Nuclear Nonproliferation Technology and*

Policy Conference, Santa Fe, New Mexico, September 25–30, 2016.

Kornell, J., P. Rangel, S. Ono, “Canary: Low-power, self-organizing reporting devices: Situational awareness using distributed sensor arrays,” in *Site-Directed Research and Development*, FY 2016, National Security Technologies, LLC, Las Vegas, Nevada, 2017, 97–101.

Luttman, A., J. Catenacci, K. Joyce, J. Paulson, C. Montenegro, D. L. Trone, “Dynamic test prediction and characterization through modeling-informed, multi-source data fusion,” in *Site-Directed Research and Development*, FY 2017, National Security Technologies, LLC, and Mission Support and Test Services, LLC, Las Vegas, Nevada, 2018, 175–183.

Miller, E. K., H. Kornell, “Low-power, self-organizing reporting devices: Situational awareness using distributed arrays,” in *Site-Directed Research and Development*, FY 2017, National Security Technologies, LLC, and Mission Support and Test Services, LLC, Las Vegas, Nevada, 2018, 129–133.

Real-Time Modification of a Modulated Wireless Digital Bit Stream

RSLN-015-18 ■ Year 1 of 1

Ryan Martin^{1,a}

¹martinrp@nv.doe.gov, (702) 295-8758

^aRemote Sensing Laboratory–Nellis

We have demonstrated that the monitoring and modification of a digital command and control signal can be performed on a wired communication bus. With ease of installation and affordability, many systems of interest are being updated to include an implementation over a wireless interface. Novel techniques require development in order to maintain the digital symbols in a known state.

BACKGROUND

As the technical competence of our adversaries increases, so does their ability to develop unique methods to protect high-value assets and facilities as well as provide sophisticated wireless triggers to improvised explosive devices. The current skills used by explosive ordnance disposal technicians are based in legacy technologies, and they cannot effectively identify and respond to new, sophisticated wireless protocols in the continuously evolving threat space. This project sought to develop methods to more accurately identify, discriminate, and provide a solution to those protective devices that emit unique RF and/or microwave frequency signatures in an environment that is already heavily saturated with extraneous signals through normal emissions or intentional congestion.

The only technique currently capable of providing a solution to these devices involves jamming the frequency region in question so that the master and slave devices cannot communicate. To defend against this, newer systems have some form of jam detection. Therefore, as jamming is becoming ineffective, an intelligent method of maintaining a desired digital bit stream without triggering trouble conditions in the master or slave devices is needed. To address this issue, we explored implementing software-defined radio (SDR) systems and a method to insert information into the digital symbol stream of interest. The use of SDR systems coupled with the appropriate user interface reduces the requirements for custom hardware that has limited configuration flexibility across multiple frequencies or signatures. This approach ensures the possibility of a technical refresh without the limitations imposed by hardware- or firmware-only solutions.

PROJECT

As a proof-of-principle experiment, a radio developed by the Remote Sensing Laboratory (RSL) was used to demonstrate the technique of arbitrarily inserting symbols into a command-and-control signal. This was adequate to demonstrate the method and to modify the message being sent. However, this method depended on specific hardware—the RSL radio itself, which would not be easily adaptable to other modulation techniques. Modulation is the modification of some signal parameter (e.g., amplitude, phase, or frequency) in order to transmit information. While numerous modulation formats are available, we chose to study amplitude shift keying (ASK), frequency shift keying (FSK), and frequency hopping spread spectrum (FHSS) in conjunction with FSK.



Figure 1. While the size of a benchtop instrument is not ideal, the plug-and-play capabilities offered by the reconfigurable chassis is excellent for general-purpose testing

The information-containing symbols transmitted over the communication channel are limited in this study to correspond to binary digits (i.e., bits) or a symbol possessing a distinct value of zero or one. This fundamental representation of a symbol state as a bit over the physical layer (layer 1 of the Open Systems Interconnection architecture) can be referred to as the protocol data unit (PDU). Higher-order symbol states in other modulation techniques increase the data rate of the communication signal. For example, 4-PSK (phase shift keying) implements symbol states that include two bits per symbol or 00, 01, 10, and 11. It is important to not confuse the baud rate or symbol rate with the bit rate because multiple bits may be transmitted per symbol.

The first modulation type studied was ASK, also commonly referred to as on-off-keying. The latter may be more understandable, as a one bit (1) is represented when there is a signal present (i.e., on) and a zero bit (0) is represented in the absence of a signal (i.e., off).

We evaluated the ASK technique using the National Instruments PXI chassis (Figure 1). This system is connected to a host PC running the LabVIEW software package for control of the transmitter and receiver. Two limitations of this benchtop instrument are its size and lack of portability. We initially thought the PXI would be suitable for demonstration purposes, even in lieu of the form factor, but we immediately noted that there was a large delay between the receive/transmit cycle.

To keep things simple, assume that a message is composed of a preamble, a first code word, the data payload, and potentially some number of tail bits. The actual implementation may include convolutional coding, Manchester encoding, data whitening, bit interleaving, or others as available in the specific system. The preamble enables the receiver of the intended information to lock onto the clock of the transmitter and synchronize to the burst of data being transmitted. This process in the receiver is typically referred to as clock recovery and will be discussed further in a later section.

Once the preamble has been detected and the receive system's clock is synchronized with that of the transmitter, it can begin sampling the bits in the appropriate locations to reconstruct the transmitted message. This is the earliest point at which one may begin to decide if the bits should be modified. The frequency spectrum is very crowded, and altering messages that are not of interest potentially could result in the intended message being missed. Suppose that the first code word is a sequence of 0,1,0,1,0,1,0,1,0,1. Based on the preamble, code word, and frequency transmitted, a correlation can be made that this is indeed the signal of interest, assuming the properties of the protocol are unique. Because the correct parameters are met, inserting the sequence of 1,0,1,0... could be transmitted at a later time with the PXI chassis. Herein lies the problem. Due to communication over the peripheral component interconnect backplane, placing streamed data on the stack overhead from the Windows operating system, the minimum response time from a received burst or packet to a transmit cycle is far too slow. Essentially, by the time the chassis is ready to respond to the message, the event has already transpired and the information makes it through unmodified.

Next, SDRs were examined for suitability. We selected the Universal Software Radio Peripheral (USRP) from Ettus Research as the experimental platform (Figure 2). Two benefits of these radios are their small size and extensive frequency range.

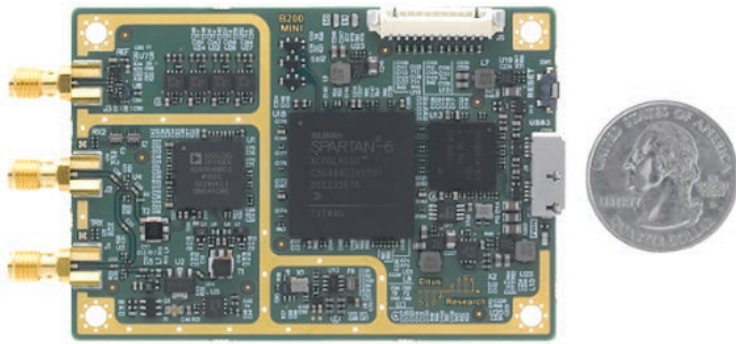


Figure 2. The Ettus B205 is small in size but delivers a broad range of coverage from 70 MHz to 6 GHz

With an SDR, arbitrary signals can be demodulated, processed, and modulated onto a carrier frequency through the development of software algorithms. This resolves the issues previously mentioned regarding reconfigurability. However, it was discovered that the hardware still has a long delay between the receive/transmit cycle. SDR devices continuously stream sampled in-phase and quadrature (I/Q) complex data to and from a host PC. This streaming technique and the issues outlined in the following discussion will explain this delay and a resolution to the problem.

The general architecture of an SDR is represented in Figure 3. The discussion will proceed from the top right antenna and move to the left in the signal chain representing the Rx or receive section. The Tx or transmit signal chain is represented by the bottom row and is simply a reversal of the process. The antenna, mixers, oscillators, phase-locked loops, amplifiers, and filters translate a received RF/microwave analog signal to an intermediate frequency or complex baseband signal (represented by the section labeled

“RF” in the diagram). Now, as seen in the figure, there are two paths for data, in-phase (I) and quadrature (Q), jointly defined as I/Q. The quadrature data (sine) are merely shifted in phase by 90° relative to the I data stream (cosine). Modifying the phase of a high-frequency signal is difficult to achieve in hardware, costly to build, and not very flexible, but using the I/Q method circumvents these issues.

Next, the baseband I/Q data are sampled by two separate analog-to-digital converters (ADCs) at the rate of the ADC. To satisfy the Nyquist criterion, the samples need to be taken at a rate that is twice the desired frequency of interest at a minimum (e.g., if a bandwidth of 26 MHz is required, then the sampling rate must be at least 52 MHz). It is important to note that this is not the I/Q rate. While the I/Q rate is related to bandwidth and sample rate, it is neither parameter. It is the rate of sampling of the I and Q components of the signal after the signal has been processed digitally by digital signal processing (DSP). An I/Q rate of 26 MS/s (one million samples per second or one sample every 1 μs) actually means the system is sampling at 52 MS/s to account for both the I and Q samples. The ADCs run at a fixed rate of 100 MS/s in the instance of the Ettus N210, for example. These samples are clocked into the field-programmable gate array (FPGA). The samples are down-converted digitally and decimated (DSP occurs here). Following this, the digital samples are streamed to the host computer via the interface of choice (i.e., USB, Ethernet, or MXI [multisystem extension interface] bus). The rate of I/Q would be measured at this point. As an example, this is

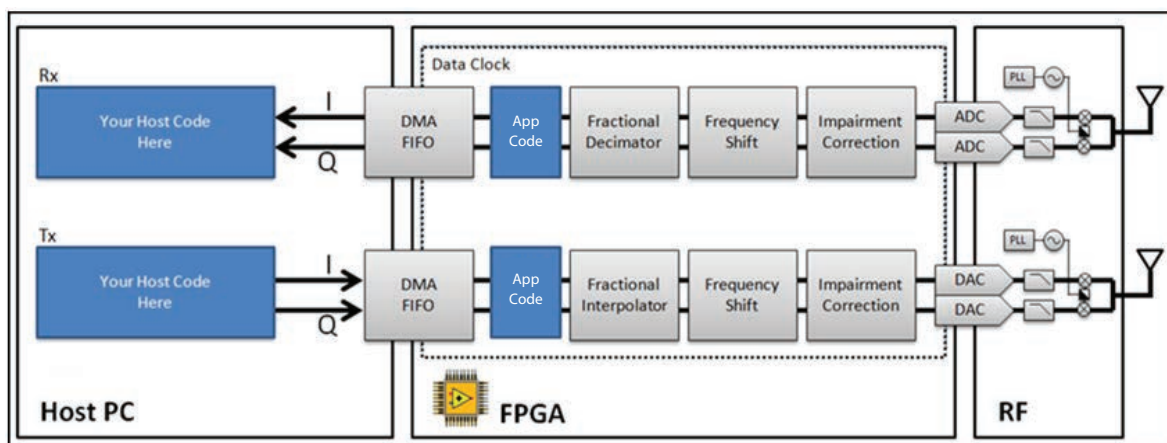


Figure 3. The general structure of an SDR is composed of an RF front end and an FPGA streaming data to and from a host general purpose computer for transmission and reception

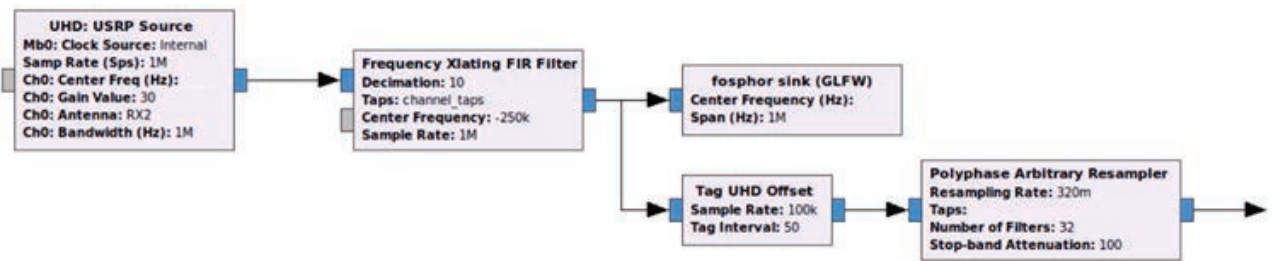


Figure 4. This workflow retrieves signals from the USRP source and performs frequency conversion, decimation, filtering, sample tagging, and resampling all in four subsequent blocks. Blue terminals represent complex data input or output.

25 MS/s for 16-bit sampling widths and 50 MS/s for 8-bit sampling widths at a maximum due to the constraints of the FPGA for the Ettus N210.

Let us now discuss the block labeled “Your Code Here” in the FPGA portion of Figure 3. If the FPGA code/firmware were to be modified, real-time performance could be achieved and the host PC could be removed from the process. However, once again the reconfigurability issue arises. The time it takes

expecting samples or if the buffers are full (i.e., the PC has not processed the samples yet) and additional samples cannot be loaded into the buffer, respectively. The host PC requires time to receive the data from the bus, process the data, decide whether or not to react, packetize the samples for transmission over the desired medium, and then initiate a transmission over the bus (e.g., Ethernet). This is where the delay is introduced. Similar to the PXI chassis, reaction times were observed that are far too long.

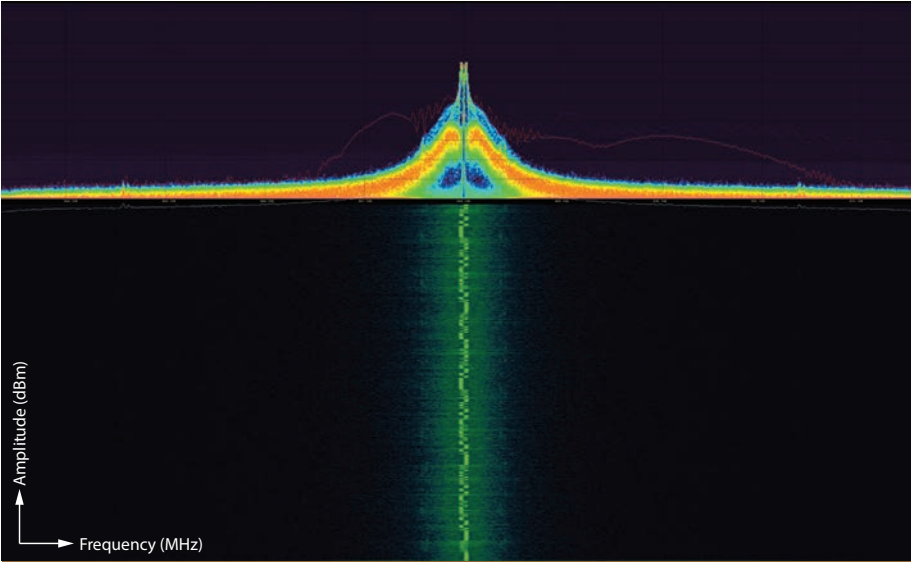


Figure 5. The mark and space frequencies of the FSK signal can be clearly seen

to write the code for a firmware process in hardware description language is time intensive, so the program is costly to produce and not easy to modify.

Going back to the issue of reaction time from transmit to receive in the host PC, it can be seen that the SDR section of the diagram (i.e., the FPGA and RF front end) is not really concerned with the state of the PC. The SDR will continuously stream samples at the requested I/Q rate and will generate underflow or overflow conditions if the PC data buffer is empty and

Fortunately, there is a resolution to this issue that makes the SDR platform a feasible method going forward. The solution lies in stream tagging. The GNU Radio (2018) PDU Utilities and Timing Utilities out-of-tree modules developed by Sandia National Laboratories (2018) enable fast reaction times. Tags (i.e., received sample timing information) are periodically attached to data samples at a user-selectable rate. The start of a burst (SOB) can be determined with methods such as energy threshold detection or the correlation of a known access code (e.g., preamble plus first code word) with the data. Other ways to identify the SOB event exist but are not outlined here. Because it is much easier to process information at the PDU level, the system should convert the oversampled information to a PDU as quickly as possible. If an SDR is sampling at 1 MS/s, and if the symbol rate of the protocol is 200 μ s, there are 200 samples per symbol. Consequently, it is more efficient to process one sample every 200 μ s instead of 200 samples every 200 μ s to decrease the processor load on the host PC.

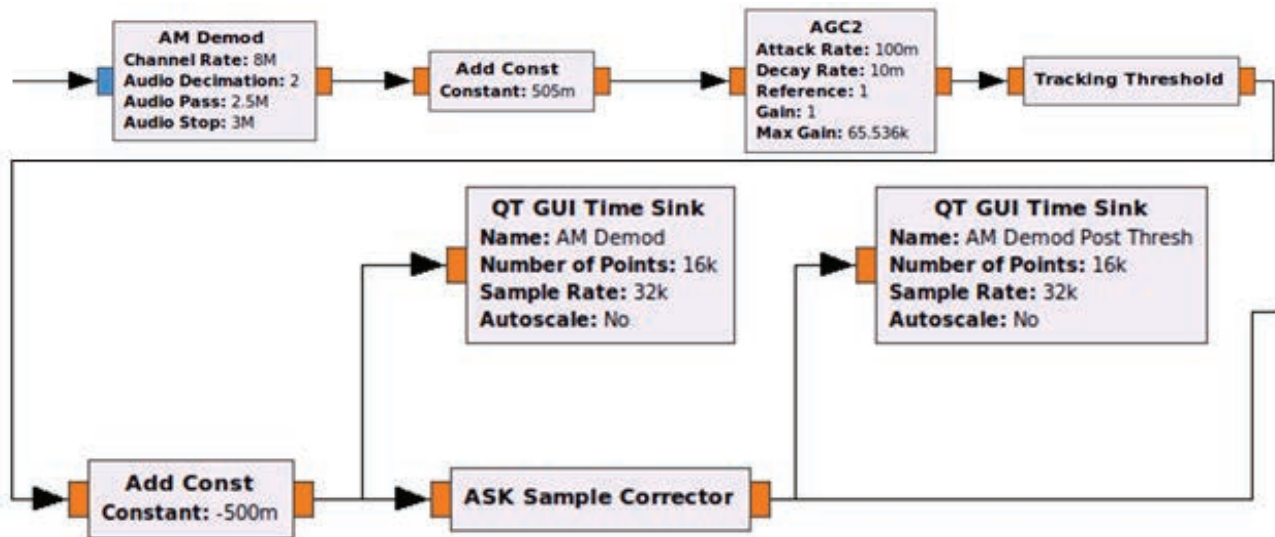


Figure 6. The demodulated samples are adjusted for amplitude and timing correction

After the samples are converted into a PDU, the data can be processed and/or modified if desired. The data are then converted from a PDU back into streaming data with associated SOB and end of burst tags for transmission via the Universal Hardware Driver (UHD).

Implementation of the System in a GNU Radio Flow Graph

As seen in Figure 4, DSP functions are implemented in blocks and are easily visualized in the flow graph of the GNU Radio Companion diagramming function. The GUI is not required to execute the flow graphs, as this function can be accomplished via the command line. The UHD USRP Source block is a user interface between the users and the USRP for setting center frequency, sample rate, and bandwidth, among other parameters. For the example system, the bandwidth and sample rate were made equal and set to a value of 1 MS/s.

First, the algorithm should attempt to translate the signal to baseband or the original frequency range prior to transmission. For example, the audio baseband frequency range is from 20 Hz to 20 kHz. This is accomplished via the Frequency Xlating Finite Impulse Response (FIR) Filter. This is a very useful block, as it accomplishes three functions simultaneously: the block translates the input signal to a new center frequency, applies a FIR filter, and decimates the sample rate. The filter response is configured via the Taps variable. In this instance, the Low-pass Filter Taps variable block is used with an ID of “channel_taps.” Important parameters include

gain (1), cutoff frequency (50 kHz), transition width (100 kHz), and windowing function (Hamming). It may be noted that the center frequency used is a negative number in this example. Due to an offset between the center frequency of the USRP and the actual signal of interest, the center frequency of the filter was adjusted to relocate the signal. Correspondingly, the center frequency of the USRP source could have been adjusted to locate the signal near 0 Hz.

The FIR filter block has two outputs, the phosphor sink and the Tag UHD offset block. The fosphor sink is a real-time spectrum analyzer visualization tool with signal persistence (Figure 5). The Tag UHD offset block applies timing tags to the received samples. In this case the sample rate is 100,000 samples per second because the previous block decimated the samples by a factor of 10 from 1 MS/s. The tagging interval is set at 50. Therefore, a timing tag will be applied to every fiftieth sample. Next, the sample is re-sampled to a much lower rate. This can be calculated as the product of the symbol rate and the number of samples per second divided by the quotient of the sample rate and the decimation factor. For this example, the symbol rate is 4000 symbols per second and the desired number of samples is 8. Therefore, the resampling rate may be calculated as

$$\begin{aligned}
 \text{resampling}_{gate} &= \frac{\text{symbol}_{rate} * \text{samples_per_symbol}}{\frac{\text{original_sample_rate}}{\text{decimation}}} \\
 &= \frac{4000 * 8}{\frac{1,000,000}{10}} = \frac{32,000}{100,000} = 0.320.
 \end{aligned} \tag{1}$$

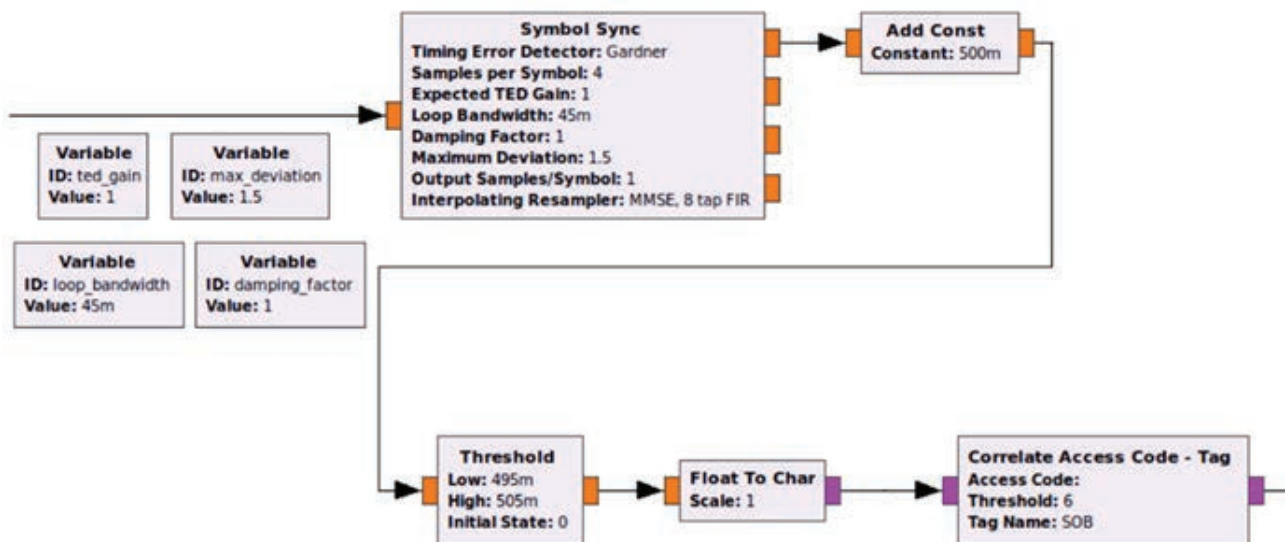


Figure 7. Timing recovery is performed and binary information is sliced to produce PDUs. Magenta terminals represent streams of character type data.

The output of the resampled signal is input to the AM demodulation block (Figure 6). This block produces a float stream in the range of $[-1.0, +1.0]$. The terminals of the blocks indicate what type of sample data are being passed. Complex data (blue) are input and, as mentioned, the output is a float stream (orange). If the intent was to demodulate FSK, the Quadrature Demod block would be used instead (not shown in the figures). The logic for ASK and FSK flow graphs is similar, and the FSK case will not be discussed further. An implementation to accommodate for the FSK should follow from the ASK case.

Next, the samples are shifted in amplitude to the range $[0, 1.0]$ in order to apply an automatic gain control (AGC). An out-of-tree module was developed to automatically adjust the output of the AGC. This provides additional reliability in the amplitude of the

signal. Because this protocol is based on an amplitude technique, the system needs to accommodate for both strong and extremely weak signals. This is accomplished by the tracking threshold block. Once the amplification and threshold adjustments are applied, the shift in amplitude is removed.

With prior knowledge of the protocol of interest (only an example in this case), we know that the sample rate now must be a factor of four because our resampling rate of 0.320 dropped our sampling rate down to 32,000 samples per second ($100,000 \times 0.320$). Additionally, the AM Demod block decimated the sample rate by a factor of two, and now the sample rate is 16 kS/s. Because the symbol rate is 4000 symbols per second in this example and so it can be determined that there are four samples per symbol. If the sampling

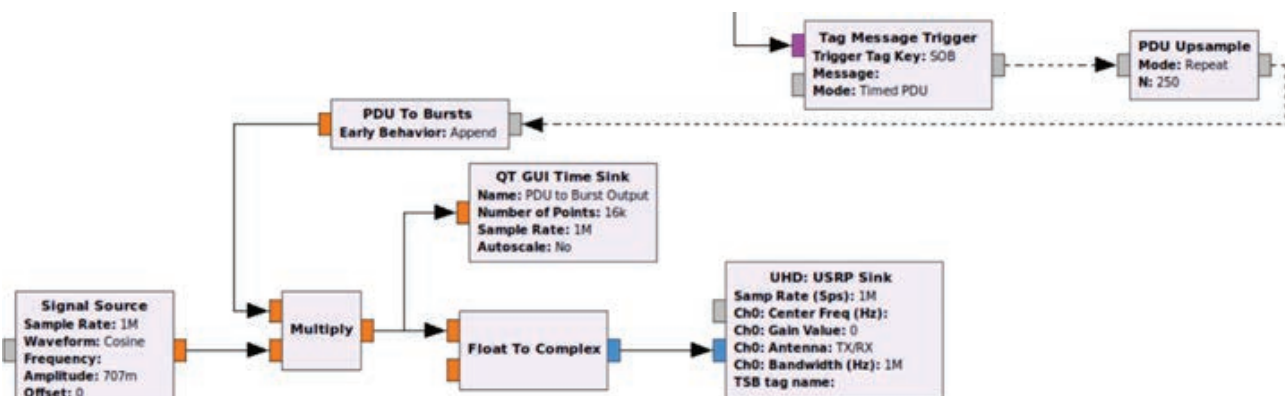


Figure 8. Upon the arrival of a sample with an associated start of burst tag, the PDU is converted back to a stream of data and transmitted back over the channel via the USRP

instant is off slightly and produces three or five identical sample states in a row, the incorrect edge sample is adjusted by the ASK Sample Corrector out-of-tree module to correspond to the correct state. The Time Sink blocks (Figure 6) are present in the flow graph for visualization/verification.

Symbol synchronization is performed by the Symbol Sync block (Figure 7). As mentioned, the input is now at four samples per symbol. This block outputs one sample per symbol. The parameters for the timing error detector can be optimized by continuously iterating on the parameters of the detector gain, maximum deviation, loop bandwidth, and damping factor. The Gardner timing error detector was selected because it does not require prior knowledge of the transmitted signal. It is not a data-aided feedback detector and is independent of phase recovery. The next three blocks of Figure 7 (add const, threshold, and float to char) output a zero or one depending on whether the samples break the threshold. The signal is finally at the required PDU and may be correlated with a known access code for the example protocol. If the access code corresponds to the known value, an SOB tag is attached to the sample.

The correlated access code-tag block looks for this SOB tag and will emit a timed PDU message upon receiving the trigger. The message is defined by a polymorphic type or a generic container of data that may be passed transparently between GNU Radio blocks. In this instance, the polymorphic type is a dictionary and a 32-bit floating-point vector. The PDU is then up-sampled by a factor of 250 in the PDU Upsample block of Figure 8. This gives 250 samples per symbol. Because the original example sample rate was at 1 MS/s or 1 μ s per sample, this makes sense, as the example protocol has a 250 μ s symbol period for this arbitrary example. The PDU is then converted back to streaming data and multiplied with a carrier wave. Finally, the stream is converted to a complex number and transmitted by the UHD USRP sink. It is not shown in this flow graph, but the imaginary component of the float to complex block should have the sine or quadrature component of the signal as an input. It is also important to note that the data stream defined by the polymorphic type is only transmitted when the SOB tag is received by the tag message trigger block.

CONCLUSION

We have demonstrated that it is possible to modify digitally modulated bits in real time over a radio frequency interface. Because the waveform is identical to the signal expected by the radio, jam detection is not triggered. This technique was implemented for ten distinct systems employing ASK, FSK, and FHSS modulations. All selected systems had some implementation of a jam detection method. When the core blocks from GNU radio did not provide the required functionality, custom out-of-tree blocks were developed in the C++ programming language.

ACKNOWLEDGMENTS

We would like to thank Jacob Gilbert and Sandia National Laboratories for their contributions to this work. Without the timing and protocol data unit utilities, this work would not have been possible.

REFERENCES

- GNU Radio, GNU Radio Manual and C++ API Reference, 2018, <https://www.gnuradio.org/doc/doxygen/index.html>, accessed September 23, 2018.
- Sandia National Laboratories GitHub, 2018, <https://github.com/sandialabs>, accessed June 5, 2018.
- Stearns, S. D., *Digital Signal Processing with Examples in MATLAB®*, 2nd edition, CRC Press 2002, Boca Raton, Florida.

This page left blank intentionally

Algorithm Development for Targeted Isotopics

RSLA-002-17 ■ Year 2 of 3

Eric Moore,^{1,a} Bill Ford,^a Emma Hague,^a and Johanna Turk^b

¹mooreet@nv.doe.gov, (703) 853-7994

^aRemote Sensing Laboratory–Andrews

^bBarnstorm Research

We have used a convolutional neural network (CNN) architecture to classify various isotopes of time-sequenced gamma ray spectra, as a typical output of a radiation detection system of a type commonly fielded for security or environmental measurement purposes. A 2-D surface (waterfall plot) in time-energy space is interpreted as a monochromatic image, and standard image-based CNN techniques are applied. This allows for the time-sequenced aspect of the data to be incorporated naturally as a run as opposed to standard algorithms that arbitrarily time bin the data to satisfy the intuition of a human spectroscopist. The results of this novel application of a CNN algorithm will be presented along with a comparison to conventional techniques. In FY 2017 we demonstrated that we can use adaptive algorithms to not only accurately identify isotopes, but also provide information about other aspects of the spectra (Moore 2018a). In FY 2019 we will utilize trained machines, and apply transfer learning to knowledge already gained in a *source* domain to new *target* domains related to specific threat isotopes where we would have limited access to training datasets.

BACKGROUND

This research addresses the lack of robust automated identification algorithms for gamma ray spectroscopy, specifically in the realm of low statistics, potentially low signal-to-noise data. Source encounters during radiological searches are typically brief, usually spanning from 0.5 to 2.5 seconds, and most detection tools, whether automated or manually employed by a human spectroscopist, are designed to handle spectral data of much longer duration. Traditionally, search

processes have focused on “detect,” “localize,” and “identify” as separate steps in an overall process.

Today, however, many more detection instruments have multichannel analyzers embedded; this has resulted in an exponential growth in the need to process spectral information. Source encounters can be operationally difficult or dangerous to duplicate, so analysis based on available data is critical; this approach represents a significant change from the reach-back method we have relied on. In the current search environment, it is critical—from a technical,

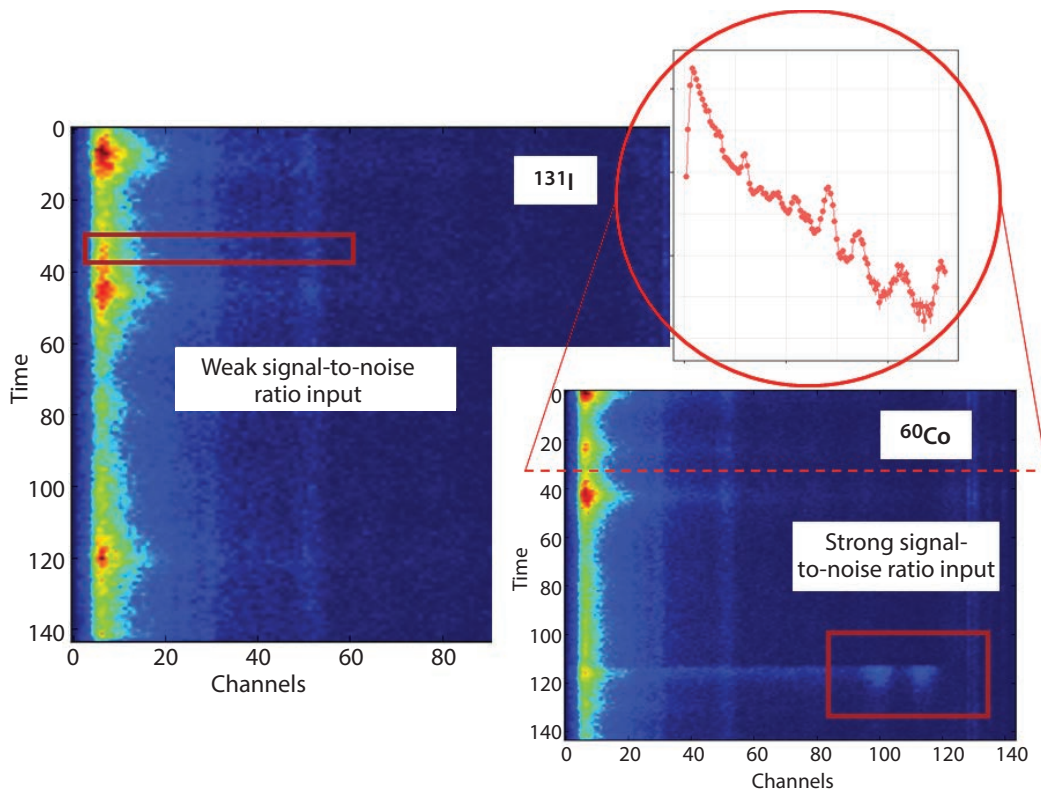


Figure 1. Waterfall plots (false color of monochromatic images, 144×144 pixels) illustrate the nature of the input used for training and testing the network. The signal-to-noise ratio may be strong or weak (the red boxes are meant to illustrate this, and do not correspond to an object detection box). The 3-second time slice from the run (inset red circle) illustrates how the data are formatted.

operational, and political perspective—that short source encounter data be adjudicated with as much confidence as is reasonably achievable. And it is quite clear that current methodologies do not begin to approach the true precision limits possible with the collected data.

PROJECT

Convolutional neural networks (CNNs) are most frequently used for processing 2- or 3-D image data (Lecun 1998, Torrey 2010). CNNs, ideally suited for this type of data due in large part to their tendency to reduce the dimensionality of the data in a natural way, lead to a more computationally realistic problem (Krizhevsky 2012). CNNs have spawned explosive growth in the application of ever deeper neural architectures (Simonyan 2015, Urban Radiological Search Data Competition 2018) and in propagating trained architectures and libraries for training new architectures (Kuhn 2008, Pedregosa 2011, Abadi 2015). The availability of CNN tools has

motivated us to exploit these techniques in our (1-D plus time) domain space, allowing us to transform non-time-series but time-sequenced 1-D data into 2-D monochromatic image data (Figure 1). Each input image is 144×144 pixels (time and channel energy), and the time axis is “stretched” to fit this number of bins; thus, some runs may have one-quarter-second binning and some multiple-second binning depending on the varying lengths of individual runs. A max-one normalization is the only other preprocessing performed on the images.

Clearly, we can examine these data as 1-D data by training an algorithm on the individual spectra without considering the time-sequenced aspect of the data (Ford 2018a). A comparison of these two approaches is found later in this report. We were motivated to recast the data to a 2-D dataset for several reasons, but our greatest motivation for pursuing this technique was to use the body of work on transfer learning (TL) in 2-D image processing (Torrey 2010, Ruder 2017), although TL is not the object of this work (Moore 2018b). In the area of radiation detection, and in countering weapons

of mass destruction, the radioactive sources of greatest concern are also the ones with the least available datasets. Due to the lack of large datasets related to threat objects, it would seem natural to train on a source domain of medical and industrial sources and transfer the knowledge of spectroscopy thus acquired to target domains like special nuclear material.

Visualizing data as false-color waterfall images has been relatively common in security operations. The y -axis is time and the x -axis is energy of incoming photons. A cross section along x at a fixed time y yields a gamma ray energy spectrum (histogram) as shown in the inset in Figure 1. The color on the waterfall image represents height or intensity (counts) at a given time and energy coordinate.

Data

The data we used came from a data competition (Urban Radiological Search Data Competition 2018) run by Lawrence Berkeley National Laboratory (LBNL) for the DOE Office of Defense Nuclear Nonproliferation Research and Development. The simulated spectral data were supplied in list mode format (i.e., individual photon energy and arrival time). The data were then binned into time and energy spectra (Figure 1 inset) as described above. The variation in background radiation in the dataset is substantial, although not necessarily more so than typical, and the source locations do not necessarily result in greater total gamma ray flux read (Figure 2).

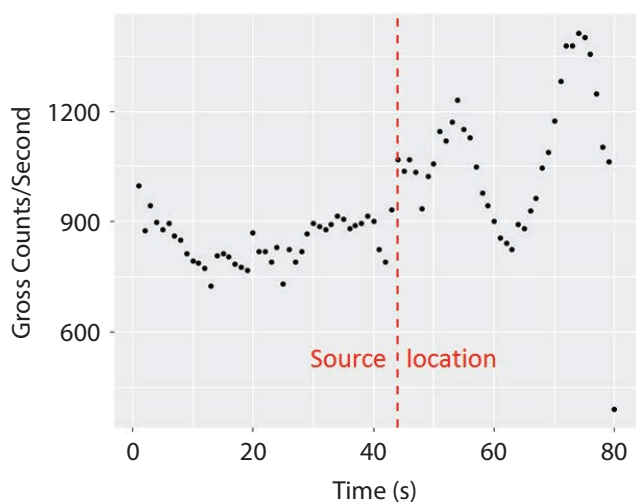


Figure 2. The number of photons detected in the measured energy range per second for one run. It can be seen that the anomaly detection must be isotopically based.

The spectra used were modeled in a simulated city (background) with sources placed at random locations throughout (gamma ray readings only). There are six source classes each including subclasses having varying activity and shielding located within the simulated city, and one class representing background only, for a total of seven classes. The six simulated source classes are highly enriched uranium (HEU), weapons-grade plutonium (WGPu), ^{131}I , ^{60}Co , $^{99\text{m}}\text{Tc}$, and HEU combined with $^{99\text{m}}\text{Tc}$. The training set contains 9800 samples (“runs”): 5000 background and 800 of each of the source classes. Only one example of the seven classes is present in any given run, and runs vary substantially in duration. The background varies throughout the city, but is not altered from one run to the next; the duration of the run varies, and the speed also varies.

There was a concern that the similarity of the background from one run to the next might introduce a bias; therefore, two completely separate input image sets were fed through two differently constructed networks, essentially giving separate analyses on the two datasets formatted slightly differently. The time binning in the first dataset (the y -axis in Figure 1) is of varying bin width, simply the total time of the run divided into 144 bins. To compensate for the potential bias of identical background for different runs, we separated out 30-second time intervals from each run to construct the second dataset; the selected time interval includes the source, but it falls into a randomly selected time within the newly defined run, and this new waterfall is then used as the input image. Excluding the 2 seconds at the start and end of each 30-second sampling, the location is selected via a unitary sampling along the y -axis (time), so there would be no preferred location; the competition designers did not assign a source to the first 30 seconds of their run. Because both the aforementioned data constructions yielded similar results, we show only one result; however, it is worth noting that the network is robust against varying time binning or stretching/contracting of the image along the *temporal* axis.

Architecture

A number of adaptive algorithms have been employed over a period of several years for gamma identification, but these have been focused primarily on 1-D spectra and classifying these spectra one-dimensionally, just as any human spectroscopist would. In this work, we refocus on the data as they come into the instrument, in a time sequence, moving away from the

inherently human-centric bias of prior data formatting approaches.

We used multiple machine learning algorithms to classify the dataset from LBNL (Urban Radiological Search Data Competition 2018). Although two of the methods used are discussed in this report, our emphasis is on the CNN architecture approach. Converting the data from a 1-D form into a 2-D form and utilizing a CNN approach allowed us to take advantage of the robust body of work already done in the image classification community. The architecture begins with 10 convolutional layers, and every other convolutional layer is followed by a max pooling layer. The output of the convolutional and pooling layers is then flattened to create a dense layer that feeds into three fully connected layers. A rectified linear unit (ReLU) nonlinearity is applied to both the convolutional and dense layers, and it still needs to be demonstrated that “dying” nodes are not a problem. The output of the three dense (fully connected) layers is fed into a seven-class output layer with *softmax* (σ), which is a typical normalization method for categorical distributions,

$$\sigma(z)_j = \frac{e^{z_j}}{\sum_{k=0}^K e^{z_k}} \text{ for } j = 1, \dots, K, \quad (1)$$

where σ is given by the standard exponential function at each coordinate divided by the sum of the exponential function applied to each coordinate, so the output coordinates sum to unity. This arrangement gives a total of 14 layers, and by normal convention, only layers with trainable weights count, so the total number of trainable parameters (weights) in the network is approximately 8.2 million.

The architecture employed was heavily influenced by the AlexNet and VGGnet architectures (Krizhevsky 2012, Simonyan 2015). A number of similar architectures were tried, loosely based on other successful image classification architectures, and further architectures are being tested (Abadi 2015, He 2016). The final selection of an architecture is very much driven by the size and representativeness of the dataset.

The architectures we investigated were chosen because of their proven success with other image classification problems. In addition, we hope in FY 2019 to apply TL techniques to radiological data, but this work is addressed elsewhere (Moore 2018b).

Training

The network converges relatively quickly, in approximately 25 to 50 epochs, using a batch size of 75 on a training set of 5400 waterfalls. Figure 3a shows the convergence within 50 training epochs. Convergence is considered to occur as the cost function is minimized; the cost is given by the cross entropy E as

$$E = -\frac{1}{N} \sum_{n=0}^N y_n \log(p_n) + (1 - y_n) \log(1 - p_n), \quad (2)$$

where p refers to the predicted value for an event and y to the label (true) class for each event. Half the training runs contain no source (background), and the other half are equally divided over the remaining six classes.

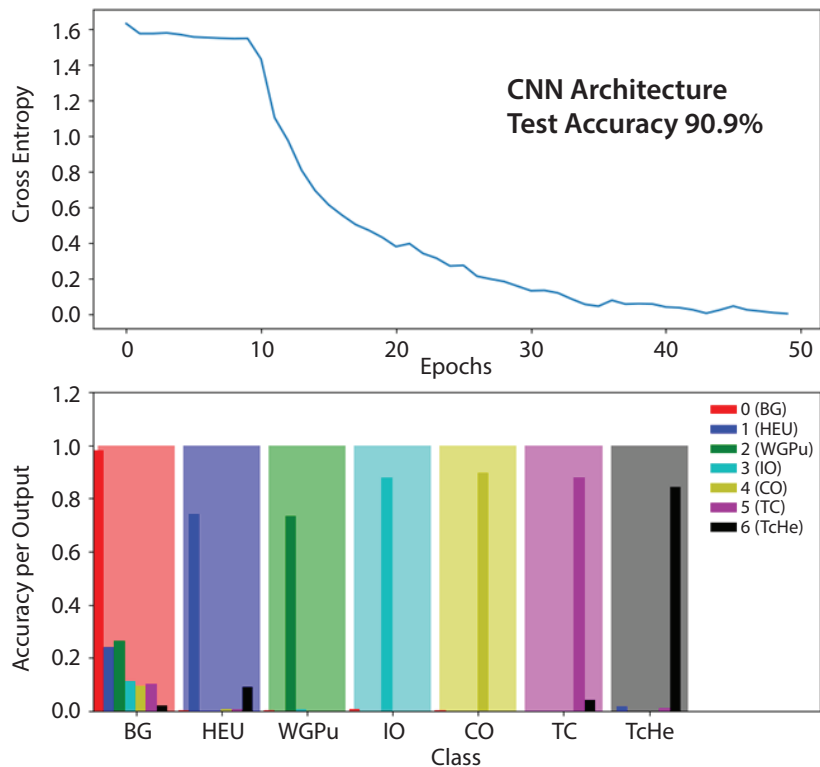


Figure 3. The colored bands are the CNN-predicted classes, and the colored bars represent the true classes; if bar and block colors match, the classification is correct. The main area of failure is source events being classified as background (false negatives). The classes are background, HEU, WGPu, ^{131}I , ^{60}Co , $^{99\text{m}}\text{Tc}$, and HEU combined with $^{99\text{m}}\text{Tc}$.

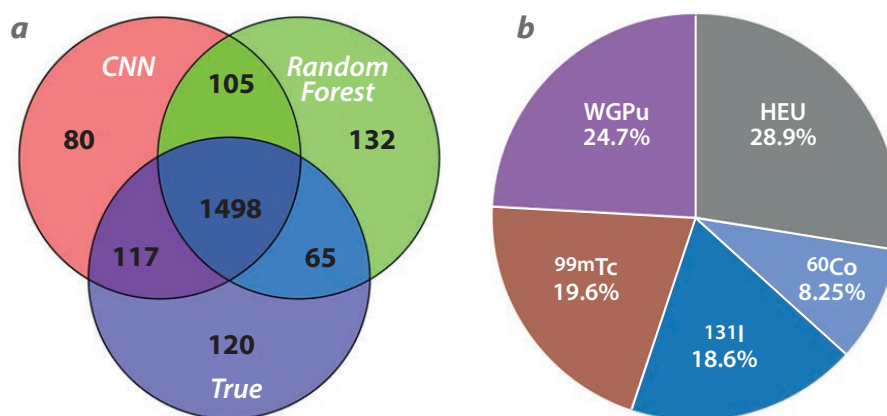


Figure 4. (a) The Venn diagram shows all event overlaps. (b) A pie chart of the 87 events that both the CNN and random forest incorrectly classified as background (double false negatives).

Due to the abundance of background events, too few training events or too complex an architecture can lead to “trapping” all the events in the background class; however, it should be remembered that in real data, there are a number of background types, so one cannot fix this situation easily by reducing the proportion of background. Alternatively, we could try to use a separate detection algorithm to pick out “hits” first; this approach will be examined in future work, but it was not the approach taken here.

The training algorithm, as implemented, can be run in a reasonable time on a single graphics processing unit (GPU); running without a GPU, even on multiple cores, has been too slow for the tuning of the hyperparameters, which has not yet been completed but will be necessary.

Interpretation of a set of feature maps is inherently difficult, and some are always more difficult than others (Zeiler 2014); trying to remove features that are not readily interpretable is not generally a productive activity, because networks are, at least partially, used to do things with the data that a person may not be able to do.

Results

The focus of this paper is on the technique of utilizing an image where the x -axis of the image represents energy and the y -axis represents time. The primary results are focused on the CNN performance and classification techniques on gamma-ray spectrum formatted as monochromatic images; however, we also present one of the 1-D analyses that have been done for comparison.

Metric Importance—Accuracy vs. Recall

Although we primarily report accuracy in this paper, it should be noted that we would, in an operational setting, have a very low tolerance for false negatives in the target domain; therefore, it might be more appropriate to maximize recall. Although false negatives are a significant concern for the problem domain, this paper is not focused on the end solution but on the initial application of the methodology; that being said, we have begun to investigate the false negative rates in particular, and the current state of those conclusions is shown below.

2-D Accuracy—CNN

The overall accuracy of the network described above was 91%, and the algorithm performed worst on the threat classes (Figure 3). The network’s ability to distinguish one source from another is good; however, the greatest shortfall is that source spectra are too often classified as background. For examples of feature maps, see Ford (2018b).

The output layer of the network yields a *softmax* that can be characterized as a kind of confidence level. The default is to choose as the prediction the class that has the highest associated *softmax* value. Approximately a third of the false negatives choose the true source as their second choice, and this may indicate that more training on a larger dataset might allow for improvement on a signal-to-noise ratio limit (Ford 2018b).

1-D Comparison—Random Forest

In addition to the CNN algorithm, we applied multiple 1-D algorithms to our dataset (Urban Radiological

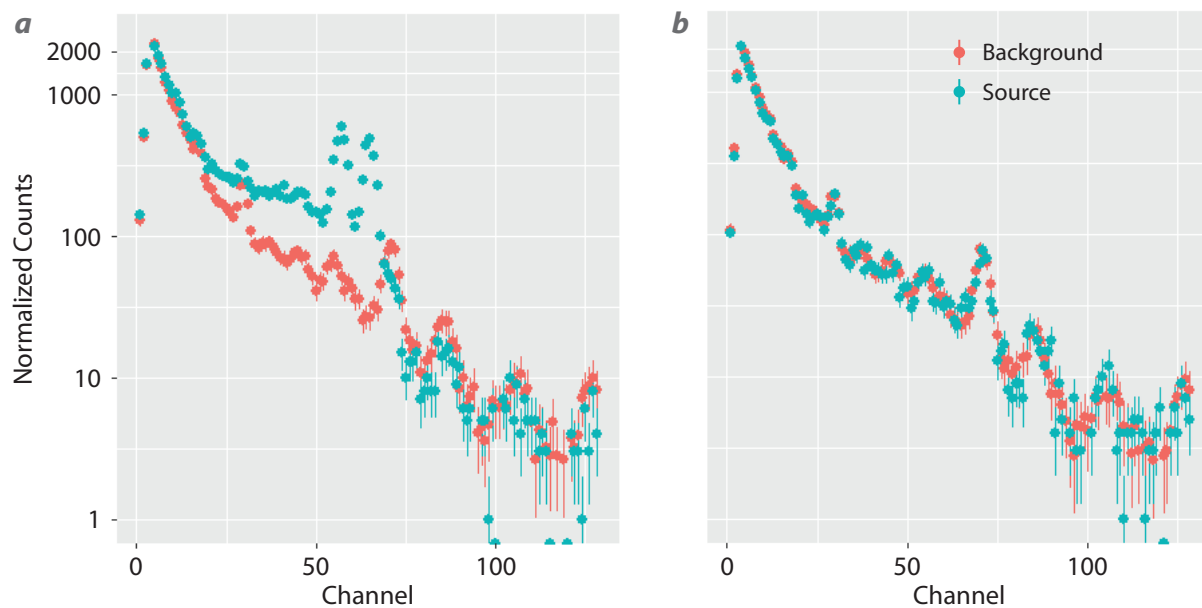


Figure 5. (a) A spectrum that both the CNN and random forest could classify, and (b) a spectrum that both the CNN and random forest misclassified as background instead of ^{60}Co (as it was labeled). At some signal-to-noise ratio, the labeling is of questionable validity. The background, shown for reference, is normalized to the maximum of the signal spectrum.

Search Data Competition 2018). We ran a random forest algorithm on the 1-D dataset and then clustered it by like classifications in semi-sequential events. This and other 1-D methods are more fully described by Ford (2018c). The dataset was binned in energy and time, but the input (x_i) is a 1-D energy vector, individual spectra (inset Figure 1), so a single waterfall will be many individual spectra where each must individually be classified. If there is enough of one class within a prescribed time window, the run as a whole is assigned into that particular class. Only one class per run is allowed, but the clustering requirement prevents multiple assignments in almost all cases. The Venn diagram (Figure 4a) shows all event overlaps; the red circle, for example, shows the CNN properly classified 1615 (1498 + 117) events and misclassified 185 (105 + 80) events. Both the CNN and random forest algorithms misclassified 120 events. The random forest correctly classified 65 events that the CNN misclassified, and the CNN correctly classified 117 events that the random forest misclassified. The results suggest that combining the two methods might improve overall performance.

The total number of events misclassified by the CNN was 185 of 1800 in the testing set. The total number of events misclassified by the random forest was 237 of 1800 on the same testing set. As shown in the Venn diagram (Figure 4a), the number of events properly classified by both methods was 1498. The total number

of events properly classified by either the CNN or the random forest or both was 1680 (1498 + 117 + 65). The total misclassifications by both the CNN and random forest, the intersection of error, was 120 events, and of these 105 were misclassified in the same way by both the CNN and random forest. Of the 105 events misclassified in the same way by both algorithms, 87 of them were false negatives by both algorithms (predicted background when a source was present). It is worth examining these double false negatives in detail to see if classification is realistically possible by any method. The signal-to-noise ratio of the dataset is not known a priori; many of the double false negatives may be the result of an absence of actual signal. Although this question is still being studied, of the cases that have so far been examined, this is the case (Figure 5b). In the example shown in this figure, no deviation from background can be seen by a human spectroscopist despite being labeled as ^{60}Co .

CONCLUSION

In FY 2017 we demonstrated that we can use predictive models to not only accurately identify isotopes, but also provide additional information about the radiation background (Moore 2018a). This year we used image classification techniques on gamma ray spectrum formatted as monochromatic images where the

x-axis of the image represents energy and the y-axis represents time. The primary results are focused on the CNN performance; however, we also presented one of the 1-D analyses, a random forest algorithm, for comparison. We have demonstrated the utility of implementing image recognition methods into an entirely new domain of radiological identification.

In FY 2019 we will continue the error analysis, and will examine all the relevant subsets of data already mentioned. We will also test some additional architectures (Szegedy 2015, He 2016), and do some additional tuning of parameters and hyper-parameters. We will also consider attempting to take advantage of the strengths of both algorithms by ensembling them. The most important effort of FY 2019, however, will be to demonstrate if TL is reasonable for radiological identification; it is still possible that features inherent in spectroscopy will resist this TL approach (Yosinski 2014). The TL will be presented in a separate publication (Moore 2018b).

ACKNOWLEDGMENTS

We would like to acknowledge the Office of Defense Nuclear Nonproliferation Research and Development NA-22 and the contributors to the Urban Radiological Search Data Competition, 2018.

REFERENCES

- Abadi, M., et al., “TensorFlow: Large-scale machine learning on heterogeneous distributed systems,” preliminary white paper, November 9, 2015, <https://www.tensorflow.org/about/bib>, 2015, accessed March 2016.
- Ford, W. P., E. Hague, T. McCullough, E. Moore, J. Turk, “Threat determination for radiation detection from the Remote Sensing Laboratory,” *Proc. SPIE* **10644** (2018a) 106440G.
- Ford, W. P., E. Hague, E. T. Moore, J. Turk, “Application of CNNs to time-sequenced one-dimensional data in radiation detection,” in draft, 2018b.
- Ford, W. P., E. J. Hague, T. McCullough, E. T. Moore, J. Turk, “Machine learning for gamma spectra,” Symposium on Radiation Measurements and Applications, Ann Arbor, Michigan, June 13, 2018c.
- He, K., X. Zhang, S. Ren, J. Sun, “Deep residual learning for image recognition,” *2016 IEEE Conference on Computer Vision and Pattern Recognition (CVPR)*, Las Vegas, Nevada, 2016, 770–778.
- Krizhevsky, A., I. Sutskever, G. Hinton, “ImageNet classification with deep convolutional neural networks,” in *Advances in Neural Information Processing Systems 25: 26th Annual Conference on Neural Information Processing Systems 2012*, Lake Tahoe, Nevada, December 3–6, 2012, 1:1106–1114.
- Kuhn, M., “Building predictive models in R using the caret package,” *J. Stat. Softw.* **28**, 5 (2008).
- Lecun, Y., L. Bottou, Y. Bengio, P. Haffner, “Gradient-based learning applied to document recognition,” *IEEE Proc.* **86**, 11 (1998) 2278–2324.
- Moore, E., B. Ford, E. Hague, J. Turk, “Algorithm development for targeted isotopics,” in *Site-Directed Research and Development*, FY 2017, National Security Technologies, LLC, and Mission Support and Test Services, LLC, Las Vegas, Nevada, 2018a, 185–192.
- Moore, E. T., et al., “Analysis of gamma-ray spectrum using transfer learning,” in draft, 2018b.
- Pedregosa, F., et al., “Scikit-learn: Machine learning in Python,” *J. Mach. Learn. Res.* **12** (2011) 2825–2830.
- Ruder, S., “Transfer learning—Machine learning’s next frontier,” March 21, 2017, <http://ruder.io/transfer-learning/>, accessed April 2017.
- Simonyan, K., A. Zisserman, “Very deep convolutional networks for large-scale image recognition,” International Conference on Learning Representations 2015, San Diego, California, May 7–9, 2015.
- Szegedy, C., W. Liu, Y. Jia, P. Sermanet, S. Reed, D. Anguelov, D. Erhan, V. Vanhoucke, A. Rabinovich, “Going deeper with convolutions,” *2015 IEEE Conference on Computer Vision and Pattern Recognition (CVPR)*, Boston, Massachusetts, 2015, 1–9.
- Torrey, L., J. Shavlik, “Transfer learning,” chap. 11 in *Handbook of Research on Machine Learning Applications and Trends: Algorithms, Methods and Techniques*, E. S. Olivas, J. D. M. Guerrero, M. Martinez-Sober, J. R. Magdalena-Benedito, A. J. S. López, eds., IGI Global, Hershey, Pennsylvania, 2010, 1:242–264.
- “Urban Radiological Search Data Competition,” <https://datacompetitions.lbl.gov/competition/1/>, LA-UR-17-26899, accessed 2018.
- Yosinski, J., J. Clune, Y. Bengio, H. Lipson, “How transferable are features in deep neural networks?” in *Advances in Neural Information Processing Systems 27: 28th Annual Conference on Neural Information Processing Systems 2014*, Montreal, Canada, December 8–13, 2014, 1:3320–3328.
- Zeiler, M. D., R. Fergus, “Visualizing and Understanding Convolutional Networks,” in *Computer Vision—ECCV 2014*, D. Fleet, T. Pajdla, B. Schiele, T. Tuytelaars, eds., *Lecture Notes in Computer Science* **8689** (2014) 818–833.

This page left blank intentionally



Dynamic Algorithms for Aerial Measurements

STL-018-18 ■ Year 1 of 1

**Rusty Trainham,^{1,a} Paul Guss,^b Manuel J. Manard,^a Lance McLean,^c
Willy Kaye,^d and Kevin Kochersberger^e**

¹trainhcp@nv.doe.gov, (805) 681-2248

^aSpecial Technologies Laboratory

^bRemote Sensing Laboratory–Nellis

^cRemote Sensing Laboratory–Andrews

^dH3D Corporation

^eVirginia Polytechnic Institute and State University



Detectors for radiation, chemical, and spectroscopic sensing have been developed for fixed-wing and rotary-wing unmanned aerial vehicles, and several techniques and algorithms have been flight tested for handling data in real time. Several filtering algorithms have been tested on noisy data, and computer code has been written for visualizing drone-borne detector data in real time from a web browser. On-the-fly heat mapping of aerial surveys is also discussed.

BACKGROUND

Small unmanned aerial vehicles, or drones, can collect data in environments that are too risky or even lethal for humans, particularly areas of high radiation or radioactive contamination. They can collect chemical and biological samples for remote analysis or on-the-spot real-time analysis. Drones can be valuable assets in responding to wildfires, floods, earthquakes, oil spills, factory explosions, or other disasters. They can also be used in hostile areas where military operations or paramilitary activities are taking place, or where dangerous wildlife lives. In most cases, emergency responders desire to assess the nature of a hazard and establish a zone of quantifiable risk in order to protect personnel or assets. Among the questions they ask are “What is it?”, “Where is it?”, and “How far does

it extend?” Often the amount of time permitted to collect data with a drone is limited, whether it be due to battery lifetime, overflight duration due to airspeed, or the nature of the phenomenon being measured. Rapid and efficient data collection, and some degree of real-time analysis, can be important in assuring the success of a drone mission. To that end, this project has investigated several techniques and algorithms for handling, analyzing, and communicating data in real time or in pseudo real time. The desire is to provide the ground crew with adequate information about the state of the drone and the nature of the environment in which it is flying.

Flying detectors on small drones is challenging. Invariably, the detector payload is limited by volume, weight, and power restrictions. They are subject

to unusual accelerations, vibrations, and rotations. Onboard computing power is often limited, and communications to the ground are frequently over low-bandwidth links. In addition to collecting primary data, such as radiation readings, the detector package also has to collect telemetry and location data. Often, an operator wants actionable data in real time, so there is the added burden of performing real-time analysis on a dynamic data stream. What works on the benchtop often fails in the air because of power interruptions, electrical noise, radio interference or loss of radio link, vibrations and shocks, limited dwell time for measurements, and synchronization issues.

Over the past two years we have flown a variety of radiation detectors, chemical sensors and samplers, and an optical spectrometer on a variety of aerial platforms, both fixed wing and rotary wing. These detectors and aerial platforms are described in detail in our companion report, “Drone Video Platform—Collision Avoidance, Situational Awareness, and Communications” (Trainham 2019); in this report we discuss a few techniques for collecting, storing, transmitting, analyzing, and visualizing data in real time.

PROJECT

To date, at the NNS, aerial radiation detection is our most advanced capability, but we are currently capable of detecting only gamma radiation. Our chemical detection is currently limited to volatile organic compounds, and our spectroscopic sensitivity is from 200 nm (near ultraviolet) to 1000 nm (near infrared). We have flown cameras, but so far they have been limited to GoPro cameras in 1080p video mode. Although the drones have onboard GPS and telemetry for their autopilots, we have opted to collect telemetry independently of the autopilot in order to minimize possible interference with flight operations. Data are stored locally on the drone, and a subset of the data is radioed back to the ground station for real-time monitoring.

A typical dataset consists of detector readings (e.g., radiation, chemical, or spectroscopy), GPS data, and telemetry data (i.e., acceleration, rotation, magnetometer, pressure, temperature, and lidar altitude). The GPS and telemetry readings are updated every 200 ms. Radiation detector readings are collected in list mode, so each recorded gamma hit has an amplitude and time stamp, and those readings are buffered and written to a data file every 100 ms.

Chemical readings are updated every 200 ms, and they are currently stored in the telemetry file. The spectrometer runs asynchronously with an update rate depending on the integration time of a spectral collection. Spectral updates normally occur every few milliseconds. The fastest update interval is 1 ms, which is the instrumental limit, and the slowest is arbitrary, but rarely more than 1 second. All data are time stamped by a real-time clock referenced to GPS time. The time stamps are in Unix time (i.e., the number of seconds elapsed since the midnight of January 1, 1970, UTC, not counting leap seconds) and formatted to microsecond precision, and they are accurate to better than 100 μ s absolute time of day. The time stamps allow data across all three data files (detector, GPS, and telemetry) to be correlated and merged.

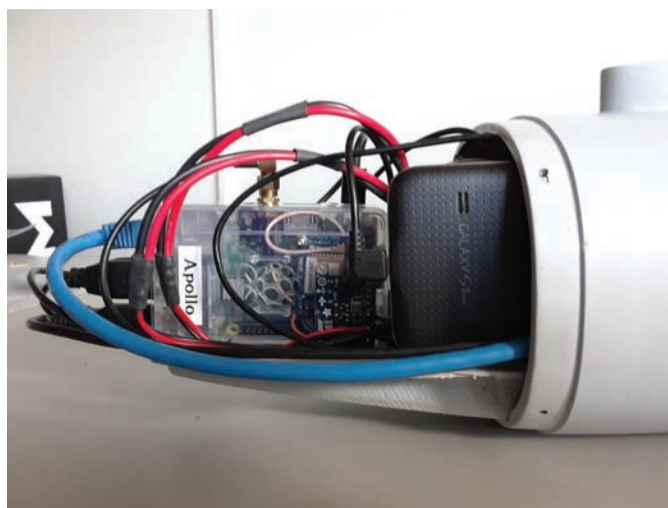


Figure 1. A Raspberry Pi 3B collects data from a radiation detector or chemical sensor, along with GPS and telemetry data. The mobile phone provides internet connectivity for streaming data in real time to external clients.

Except for the 3DR Solo implementation, data collection is performed by a Raspberry Pi 3B single-card computer equipped with a GPS receiver and a ten-degree-of-freedom (10 DOF) telemetry chip. Figure 1 shows a Raspberry Pi (labeled Apollo) in a plastic case to which a GPS receiver and a 10 DOF telemetry chip are attached. Next to it is a mobile phone that provides 4G LTE internet connectivity for streaming data to external clients. Three separate programs are currently required for reading and writing data from detectors, GPS, and telemetry. The program for reading the radiation detectors spools list-mode data to a log file, where each data entry consists of elapsed time in microseconds since the start of data acquisition and an



Figure 2. The detector pod for chemical or radiation detection is attached to the belly of the Sandstorm.

analog-to-digital converter reading for each gamma hit. At the top of each second a Unix time stamp is written to the radiation log file; the time stamp serves as a fiducial to mark absolute time of day. This program also maintains a memory-mapped array of the average gamma spectrum, updated every 100 ms, and makes the array available to other programs running on the Raspberry Pi. In particular,

the real-time gamma spectrum is queried by another program that streams the spectral data to external clients on the ground. The data streaming to external clients is through a web server on the Raspberry Pi with the backend code written in PHP for streaming data in real time via the WebSocket protocol. The end user views both the average spectra and radiation intensity data in real time from a web browser. The web browser page is written in HTML5 and JavaScript, and it is served by an Apache web server running on the Raspberry Pi.

Figure 2 shows the Sandstorm drone with the detector pod attached to the belly for an exercise in Columbia Falls, Montana. Pictured is the chemical detector pod flown in August 2017, but we used an identical pod to fly a radiation detector in an exercise conducted in September 2017 at the same airfield. Several milliCurie-level sources of cesium-137 (^{137}Cs), europium-152 (^{152}Eu), barium-133 (^{133}Ba), and cobalt-60 (^{60}Co) were shipped from the Remote Sensing Laboratory (Nellis) to the Unmanned Systems, Inc., airfield in Montana for the exercise. The Apollo, the 3×6 NaI detector, and the 2×2 NaI detector were flown

on a variety of fixed-wing and rotary-wing drones. Our companion report provides more details about the exercise (Trainham 2019).

Figure 3 shows a strip-chart recording of radiation intensity and pressure altitude data from one of the exercises conducted at the airfield in Montana in September 2017. We placed two sources, ^{137}Cs and ^{152}Eu , separated by about 300 m along the runway. The data shown here are filtered by an exponential moving average algorithm with a half-second time constant. For in-flight monitoring the filter

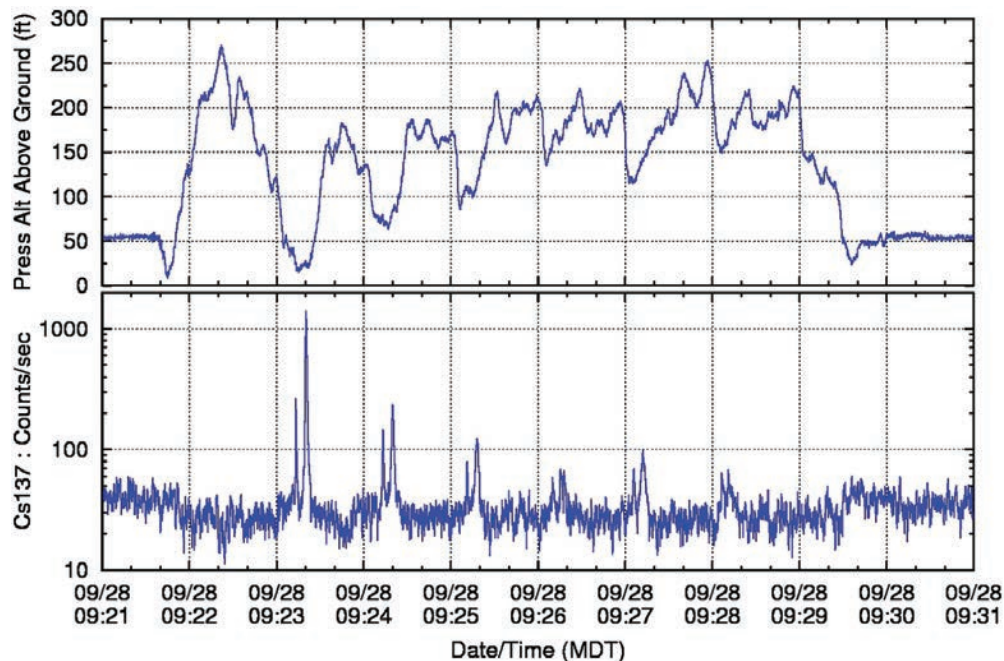


Figure 3. Radiation data within an energy window for the 662 keV ^{137}Cs gamma are filtered by an exponential moving average with a 1-second time constant and plotted beneath the pressure altitude data. The flight was over two sources placed approximately 300 m apart and detected by a 3×6 NaI detector on the Sandstorm.

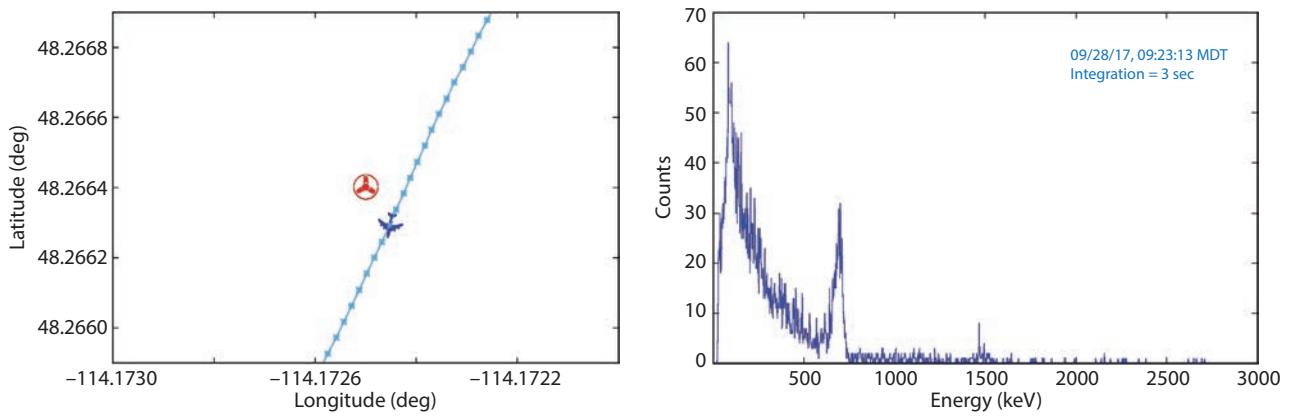


Figure 4. The aircraft location and integrated gamma spectrum are shown here for the first hit at 09:23:13 of the data from Figure 3. The gamma source is ^{137}Cs .

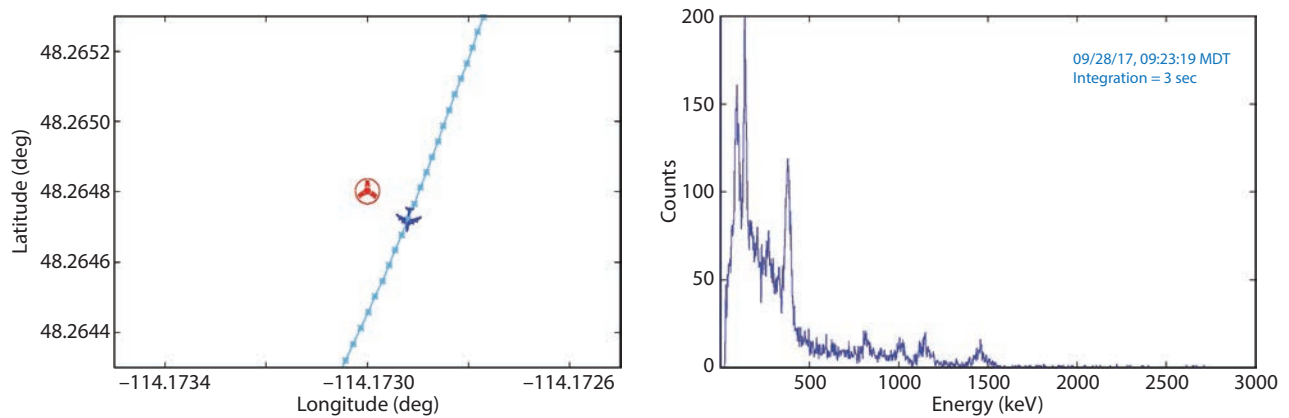


Figure 5. The aircraft location and integrated gamma spectrum are shown here for the second hit at 09:23:19 of the data from Figure 3. The gamma source is ^{152}Eu .

algorithm is implemented by a JavaScript routine that plots the data in real time within a web browser. A similar filter is implemented in a C program used for the post-flight data analysis that generated the plot in the figure. The exponential moving average filter is efficient and simple to implement in code, and it smooths noise that would otherwise obscure the signal. It is not an ideal filter, however, because it introduces a time lag in the signal proportional to the time constant of the filter. In Figure 3, the time lag is not noticeable. In Figures 4 and 5, however, the effect is noticeable. Those figures each show the location of the aircraft with respect to the radiation source at the instant of time when the radiation signal peaks. This location should be the point of closest approach to the source, yet the plots show that the Sandstorm had already passed the source by a couple of data samples (400 to 800 ms). The sample interval here is 200 ms, so the time lag is approximately the same duration as the half-second time constant of the filter. The ground speed provided by GPS was 25.5 m/s, so the distance error in the point of closest approach is about 13 m

due to the lag of the exponential moving average filter. Larger time constants yield greater time lag errors, which we illustrate next with some data from the 3DR Solo implementation.

The 3DR Solo radiation detector implementation utilizes the Solo's onboard iMX6 computer for data collection, rather than a Raspberry Pi. Figure 6 shows a 3DR Solo with a custom 2×2 NaI gamma detector strapped beneath it. The detector was manufactured by Alpha Spectra, and it has a standard 2" cylindrical NaI crystal; however, the unit is 2" shorter and 4 ounces lighter than a standard 2×2 NaI detector. The detector is plugged into an ORTEC digiBASE, which in turn connects to the Solo via a USB cable. The same C program for the Raspberry Pi implementation was ported to the iMX6 processor and Yocto Linux of the 3DR Solo. Readings of GPS and telemetry are logged by a Python program, which queries the Solo's onboard GPS and telemetry chips. The web interface is nearly identical to that of the Raspberry Pi, except that the backend server code for real-time data streaming is written in Python instead of PHP.



Figure 6. The 3DR Solo quadcopter with a 2×2 NaI gamma detector strapped to it has been flown in tests in Nevada and Montana. Similar 3DR Solos with a chemical detector and an optical spectrometer have been flown in Wisconsin.

Figure 7 shows the Solo with the 2×2 NaI detector hovering over a radioactive source at the edge of the runway during a flight test at the Desert Rock Airstrip of the NNSS in March 2018. In the foreground is the Oak Ridge National Laboratory (ORNL) Strelka and another 3DR Solo. For this test two radioactive sources, ^{137}Cs and ^{152}Eu , were placed about 100 m apart along the runway, and the Solo hovered for about 90 seconds over each source at an altitude of 25 m.

Figure 8 is a screen capture of the web page plotting the radiation intensity measured in real time during the test flight at the Desert Rock Airstrip in March 2018. Three curves show the results of the exponential moving average filter for three different time constants. It is clear from the plot that a longer time constant in the filter produces a significantly delayed onset of increasing intensity and generates tails in the curves when the detector moves away from the source. The first bump in the intensity curve is from the ^{137}Cs source, and the

second is from the ^{152}Eu source. Figure 9 shows the gamma spectra collected during the flight while the Solo was hovering over the sources. The figure shows that the ^{152}Eu plot still has a prominent line from the ^{137}Cs source, indicating that the distance between the sources (~100 m) was not large enough to isolate their spectra.

Another noise source seen in rotary-wing aircraft operations is barometer air buffeting by the propeller wash. Figure 10 shows the Virginia Tech hexacopter carrying the Apollo detector pod during an exercise in Idaho in April 2018. The Raspberry Pi with the telemetry chip is inside the nose of the pod, so it is nominally protected from the propeller wash, but the percussive pressure wave from the propeller still affects the pressure readings. The noise on the pressure altitude signal seen here is much higher than that seen on the Sandstorm pressure altitude signal.

The barometer data provide pressure altitude, and Figure 11 shows the altitude data plotted with results from several algorithms that filter the noise. Figure 11a plots altitude data from the full flight, and Figure 11b provides a close-up view of the data at the end of the flight. The filter results shown are from Savitzky-Golay (1964), Kolmogorov-Zurbenko (Yang 2010), Kalman (1960), and exponential moving average (Smith 1997) routines. All of these filters can operate in real time on the Raspberry Pi, but during flights



Figure 7. The 3DR Solo carrying the 2×2 NaI detector is hovering over a ^{152}Eu source at the edge of the runway at the Desert Rock Airstrip. In the left foreground is the ORNL Strelka heavy-lift copter; another 3DR Solo sits to its right.

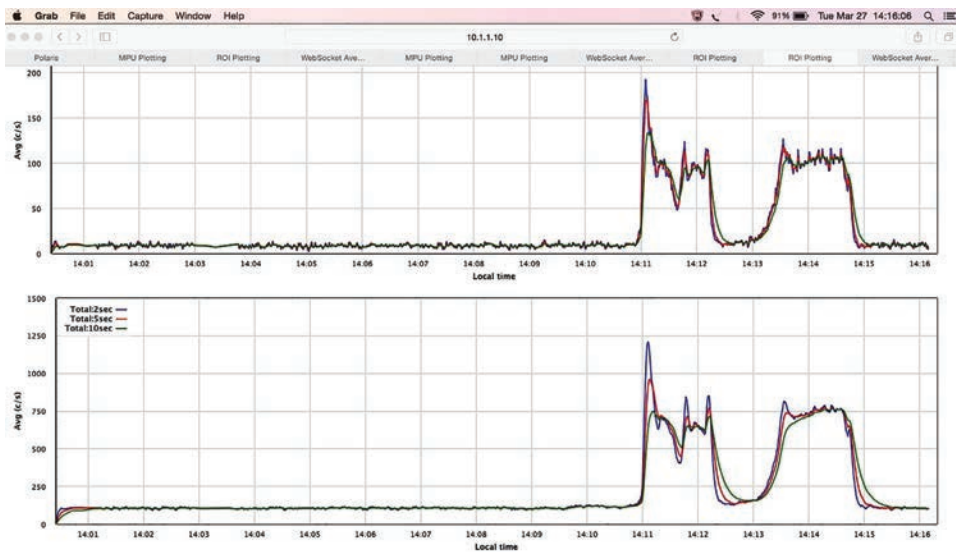


Figure 8. A screen capture of the web page displaying the real-time radiation signal measured by the 3DR Solo carrying a 2x2 NaI detector during the flight test at the Desert Rock Airstrip in March 2018. The corresponding spectra are shown in Figure 9.

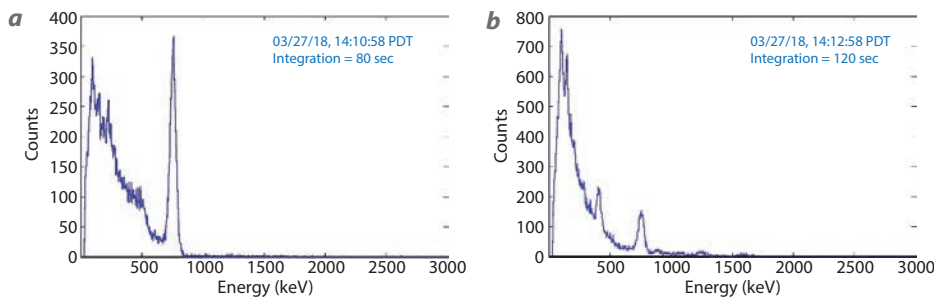


Figure 9. Gamma spectra corresponding to the radiation hits shown in Figure 8 for the (a) ^{137}Cs and (b) ^{152}Eu sources. These spectra show prominent signal from the ^{137}Cs source.



Figure 10. The Virginia Tech hexacopter carries the Apollo detector and the Raspberry Pi in the pod mounted beneath it, and the 2x2 NaI detector is mounted beneath the pod. This photo was taken in April 2018 at an exercise in Idaho.

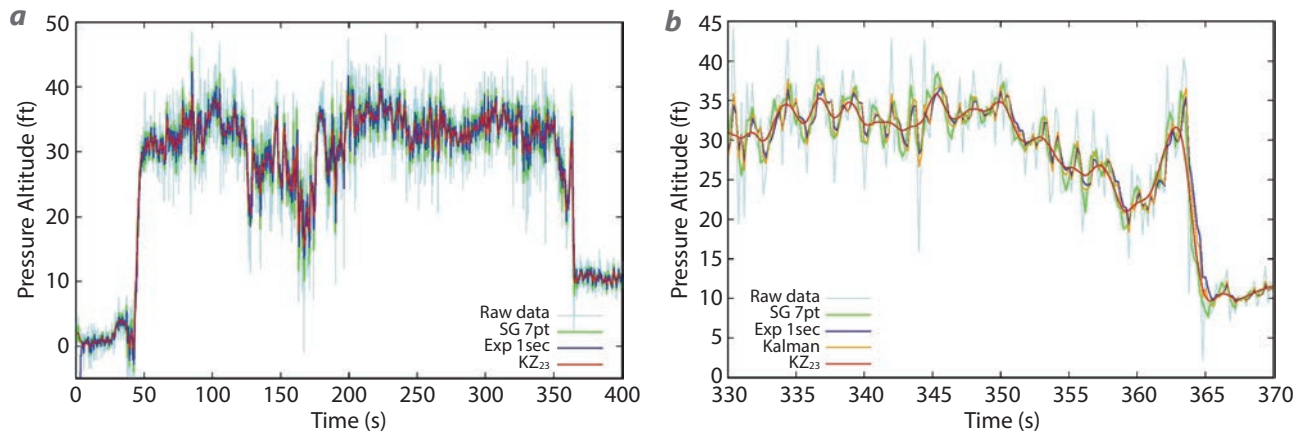


Figure 11. Pressure altitude data are heavily polluted by air buffeting from the hexacopter’s propeller wash, showing (a) the full flight and a (b) close-up of the data. Results of several filter algorithms are plotted together here for comparison. The filters are SG = Savitzky-Golay, Exp = exponential moving average, KZ = Kolmogorov-Zurbenko, and Kalman.

we normally use an exponential moving average, which is an effective filter that is simple to implement. This filter does, however, introduce a time lag, so we tested the other algorithms for suitability. In this particular example the smoothest curve is produced by the Kolmogorov-Zurbenko filter, but the curve has lost some real features in the data. This multiple order moving average filter is complicated to implement and is more CPU intensive than the other filters. The Savitzky-Golay filter is a simple moving polynomial fit whose order can be chosen at will. It is fairly simple to implement, and it has minimal artifacts. The Kalman filter is also rather simple to implement, and it produces reasonable results. All of these filters have tunable parameters, so the results shown here are not

necessarily optimal. Our assessment is that there is no clear winner among these filters.

Finally, we recognize a need for dynamic data mapping visualization that we are currently doing statically. Results of aerial radiation surveys are best interpreted when presented as heat maps. A color-coded breadcrumb trail, such as the one shown in Figure 12a, is relatively simple to implement, but it does not have the visual impact of a true heat map, such as the one shown in Figure 12b. We can create a breadcrumb trail by plotting a color-coded dot at a specific GPS location where a measurement has been made. This offers reasonable visual interpretation, but it can leave large gaps in the survey space, confusing

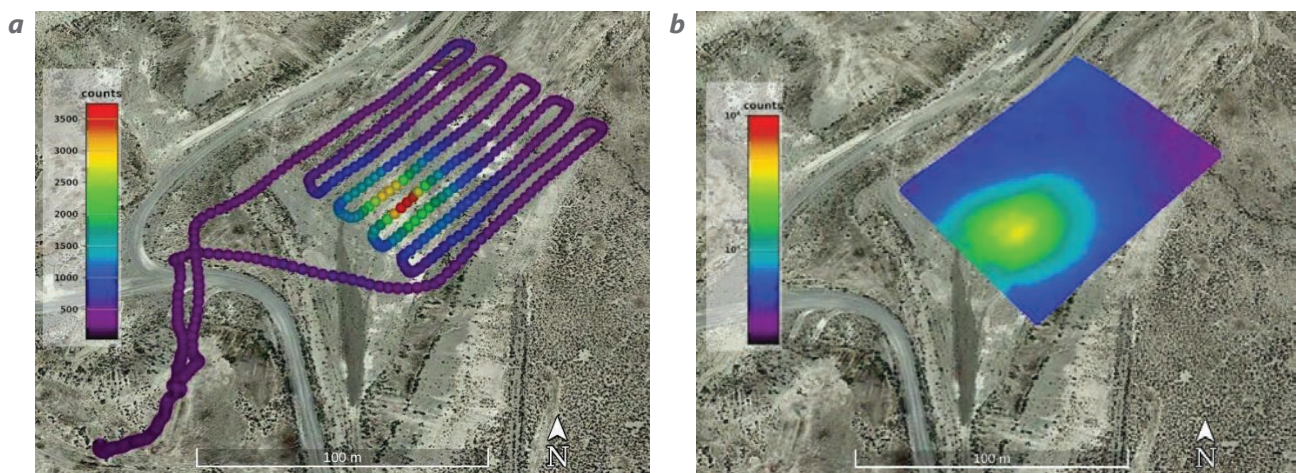


Figure 12. Two radioactive contamination maps from an exercise in Idaho where the Apollo and 2×2 NaI detector flew on the Virginia Tech hexacopter, showing (a) a color-coded breadcrumb trail of 1 second full-scale spectral integrations of the list-mode data and (b) a contamination distribution heat map generated from the same data by Gaussian kriging interpolation

the eye. A true heat map, on the other hand, shows information even in the gaps where data have not been collected, interpolating data from neighboring measurement points. A variety of interpolation techniques exist, and the example shown in Figure 12b is the result of a kriging interpolation (Press 2007). The challenge in producing a real-time heat map is to be able to update interstitial values of the map and continually replot as new data arrive. Doing this in real time would permit the survey pattern to be modified mid-flight to better sample a region of concern. As we see in Figure 12b, the survey pattern has over-sampled the northeast corner of the radioactive contamination region, and it has under-sampled the southwest corner. The resulting heat map cuts off the wing of the distribution of radioactive contamination in a location where we needed data. Real time heat mapping is a feature that we intend to implement in the near future.

CONCLUSION

Because flight durations of drones are usually limited by battery lifetimes to 20 minutes or less, the handling and interpretation of aerial sensor data in real time can be important to maximize the quality and utility of the information being sought. Measurements made in the air are invariably noisier than benchtop measurements, and additional data for location and flight characteristics are also required to put sensor data in context. In this project we explored techniques for collecting and transmitting data as well as using a few real-time filtering algorithms to clean up noisy data. The ability to generate heat maps on the fly will help ensure that the aerial sampling of data is optimally centered and encompasses an adequate region of measurement. This is a feature we will add in the coming year. A proceedings paper describing this work will be submitted to the Military Sensing Symposium in 2019.

ACKNOWLEDGMENTS

We would like to thank Mark Adan, Howard Bender, Don Bintz, John Bird, Edward Bravo, Keith Chase, Dan Haber, Joann Jackson-Bass, Jason Jaworski, Tom Keenan, Mike Madlener, Rusty Malchow, Karen McCall, Chris Melchor, Drew Morgan, Mark Norsworthy, Justin Sands, Bill Tremblay, and Hovig Yaralian for their contributions to this work. Part of this effort was performed under Cooperative Research and Development Agreement # CR005.

REFERENCES

- Kalman, R. E., "A new approach to linear filtering and prediction problems," *J. Basic Eng.* **82**, 1 (1960) 35–45.
- Press, W. H., S. A. Teukolsky, W. T. Vetterling, B. P. Flannery, *Numerical Recipes: The Art of Scientific Computing*, 3rd edition, Cambridge University Press, Cambridge, 2007, 144.
- Savitzky, A., M. J. E. Golay, "Smoothing and differentiation of data by simplified least squares procedures," *Anal. Chem.* **36**, 8 (1964) 1627–1639.
- Smith, S. W., *The Scientist and Engineer's Guide to Digital Signal Processing*, 1st edition, California Technical Publishing, San Diego, California, 1997.
- Trainham, R., P. Guss, M. J. Manard, L. McLean, W. Kaye, K. Kochersberger, "Drone video platform—Collision avoidance, situational awareness, and communications," in *Site-Directed Research and Development*, FY 2018, Mission Support and Test Services, LLC, Las Vegas, Nevada, 2019, 17–37.
- Yang, W., I. Zurbenko, "Kolmogorov–Zurbenko filters," *Wiley Interdiscip. Rev. Comput. Stat.* **2**, 3 (2010) 340–351.



X-Ray Phase Contrast Imaging for Dynamic Material Mix Experiments

LAO-003-17 ■ Year 2 of 3

**Daniel J. Clayton,^{1,a} Daniel Guerrero,^a Craig Kruschwitz,^a
Dave D. Schwellenbach,^a Dan Stutman,^b and Kevin Tritz^b**

¹claytodj@nv.doe.gov, (505) 663-2153

^aNew Mexico Operations—Los Alamos

^bDepartment of Physics and Astronomy, Johns Hopkins University



X-ray phase contrast imaging with transmission gratings for density profile measurements has been developed and tested for dynamic experimental applications. Talbot-Lau x-ray deflectometry is a new method of measuring x-ray refraction in addition to attenuation and ultrasmall-angle scattering that has recently been developed for static imaging, primarily for medical and industrial applications. To obtain density profiles from fast-evolving systems, we must use a flash x-ray source with a spot size much larger than the continuous microfocus sources of static imaging systems, and we can obtain only a single exposure. The challenges to measuring electron density profiles of two mixed elements from a single-image, low spatial resolution system are addressed, and initial results from the first dynamic experiments with one such system, conducted on a gas launcher at the end of FY 2018, are presented. In FY 2019, we will test new techniques to improve the sensitivity and reliability of the diagnostic during new detonator experiments and additional dynamic experiments.

BACKGROUND

In experiments with dynamically evolving solids, liquids, or high-density plasmas, densities are typically probed with x-ray radiation. This usually takes the form of x-ray radiography, in which x-ray attenuation by a sample is measured and used to infer material density. Alternatively, x-ray phase contrast

imaging (PCI), in which the phase shift of x-rays passing through a sample is analyzed, may also be used to infer density, as the index of refraction of x-rays through a sample depends on the density of the material. X-ray PCI has several advantages over traditional radiography; for example, it has a linear rather than an exponential dependence on density, which increases the range of densities over which the

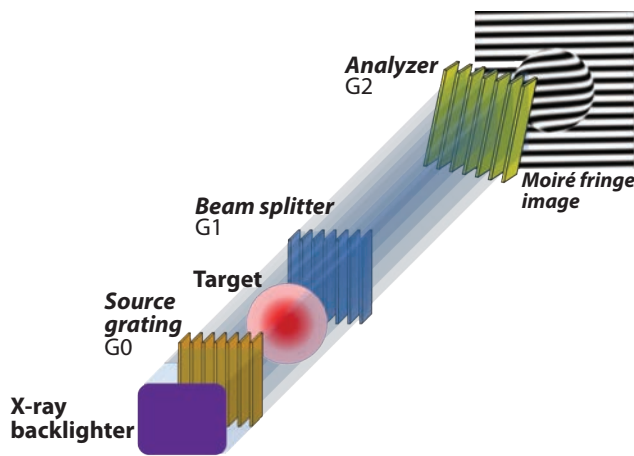


Figure 1. A Talbot-Lau x-ray deflectometer with three transmission gratings. G0 and G2 are x-ray amplitude gratings, and G1 is an x-ray phase grating.

technique is applicable for a given x-ray source with a particular spectrum. Also, because x-ray attenuation scales more strongly with atomic number Z than PCI, PCI is a more sensitive density diagnostic for low- Z materials. We can thus use x-ray PCI to image low- Z samples using high-energy x-rays that can penetrate high- Z material surrounding the samples.

One potential disadvantage of x-ray PCI is its requirement for a coherent, monochromatic light source, historically only available at facilities such as x-ray synchrotrons. Recent advances in the manufacture of x-ray transmission gratings led to the development of Talbot-Lau x-ray deflectometry (TXD) PCI diagnostics, which use compact, incoherent x-ray sources. A Talbot-Lau deflectometer consists of three transmission gratings with equal, micron-scale slit spacing (Figure 1) (Pfeiffer 2006). The basic principle of the instrument is that spatially coherent, monochromatic light passing through a diffraction grating forms images of the grating at periodic distances. This is referred to as the Talbot effect, and the images are formed at multiples of the Talbot length $z_0 = 2g^2/\lambda$, where g is the slit spacing and λ is the x-ray wavelength. When a sample is placed in front of (or behind) the grating, x-rays deflected by the changing index of refraction create fringe shifts in the image. We refer to this phase grating as the beam splitter, or simply G1.

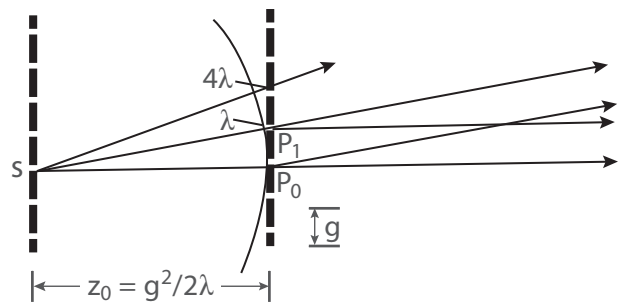


Figure 2. A depiction of the Lau effect, where for a given wavelength λ , coherent light from slits along G0 interfere constructively at the slits along G1, which is placed a Talbot length z_0 away. Image from Jahns (1979).

In the absence of a monochromatic, spatially coherent light source, we can use the Lau effect to simulate such a source while using a polychromatic incoherent source (Jahns 1979). In the Lau method, an amplitude grating with the same slit spacing as G1, referred to as the source grating or G0, is placed in front of the x-ray source. Each slit of G0 can be thought of as an individual coherent light source. When placed a Talbot length $z_0(\lambda)$ in front of G1, each slit of G1 sees

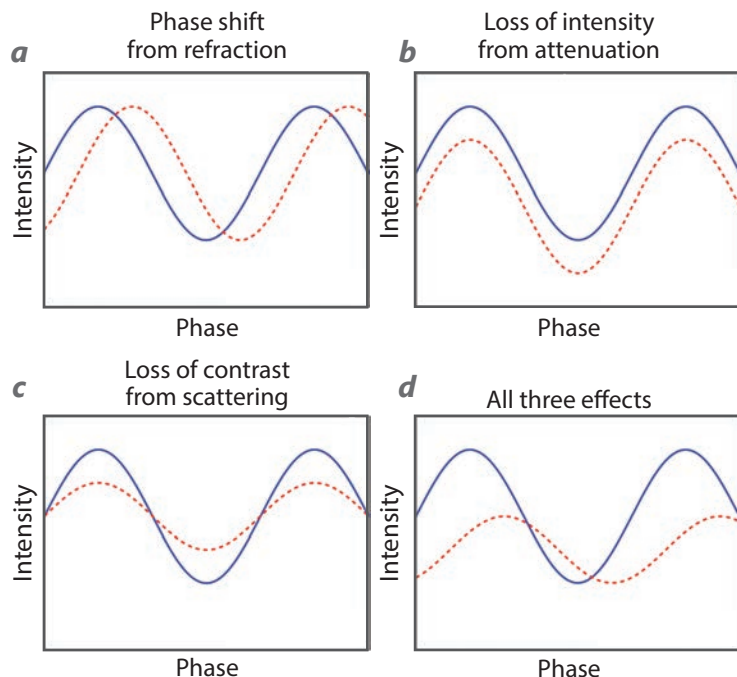


Figure 3. The effects on the background fringe pattern from (a) refraction due to a differential phase shift, (b) attenuation, (c) USAXS, and (d) some combination of the three. The solid blue lines represent the unperturbed background fringe pattern, and the dashed red lines represent changes due to the sample being measured.

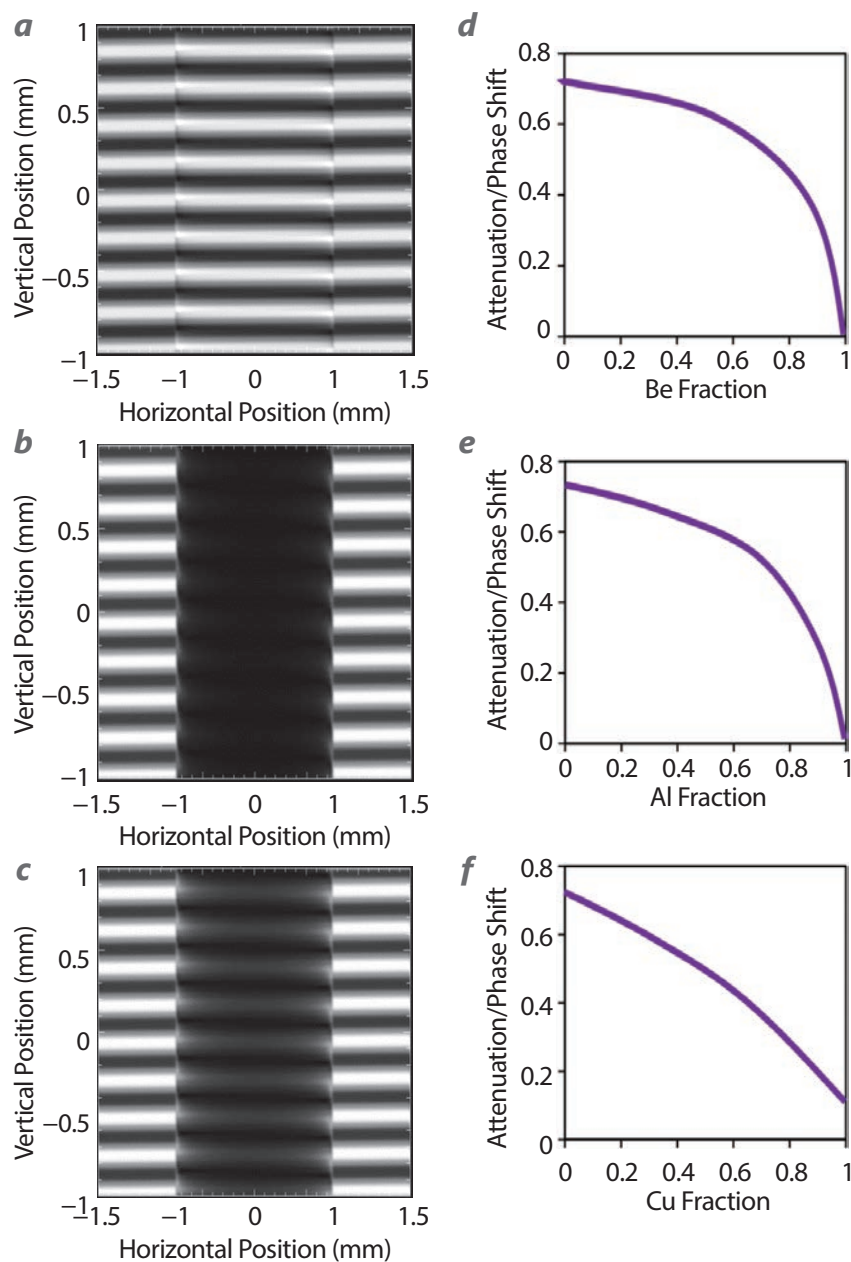


Figure 4. Simulated deflectometry images of (a) pure beryllium (Be), (b) pure uranium (U), and (c) a mix of 60% Be and 40% U; ratio curves (attenuation / phase shift in radians) for (d) Be+U, (e) aluminum (Al)+U, and (f) copper (Cu)+U.

a coherent source of wavelength λ due to constructive interference (Figure 2). With the source grating, it is thus possible to do dynamic x-ray PCI in a small lab setting using a compact flash x-ray tube.

Finally, another amplitude grating, referred to as the analyzer or G2 grating, allows micron-scale fringes to be imaged with a standard camera system. The G2 grating also has the same slit spacing as the G0 and G1 gratings and is placed a Talbot length after G1. The

grating is rotated about the optical axis by a small angle θ , creating a moiré pattern on the detector. These moiré fringes have a period $p_M \sim g/\theta \gg g$. We can thus choose the angle θ to optimize spatial resolution on the detector.

One major advantage of TXD is that it provides three separate measurements in a single image: x-ray attenuation and ultrasmall-angle x-ray scattering (USAXS) are measured in addition to refraction (Pfeiffer 2008). Refraction and attenuation both depend on the line-integrated density of the sample, but with different Z dependencies. The two measurements together can deconvolve the density profiles of a mix of elements. USAXS, caused by micron-scale variations in density, results in a loss of fringe contrast. The effects of all three phenomena on a background fringe pattern are shown in Figure 3.

Simulations with the X-ray WaveFront Propagation (XWFP) code (Weitkamp 2004) show how the densities of two elements can be deconvolved. For this simulation, the x-ray source was a 150 kV tungsten tube filtered with 0.25 mm of uranium for optimal imaging at 100 keV. The sample was a 1.5 mm diameter cylinder of mixed material. The resulting TXD images were simulated, and the ratios of the average attenuation to phase shift over the inner half of the cylinders were computed and plotted as a function of elemental fractions. Both the simulated

images and resulting ratio curves are shown in Figure 4. We can then use these ratio curves, or those obtained from measurements of known samples, to determine the densities of two elements in an unknown mix independently.

While TXD has only been considered for static imaging, except in a few unique cases (Valdivia 2016),

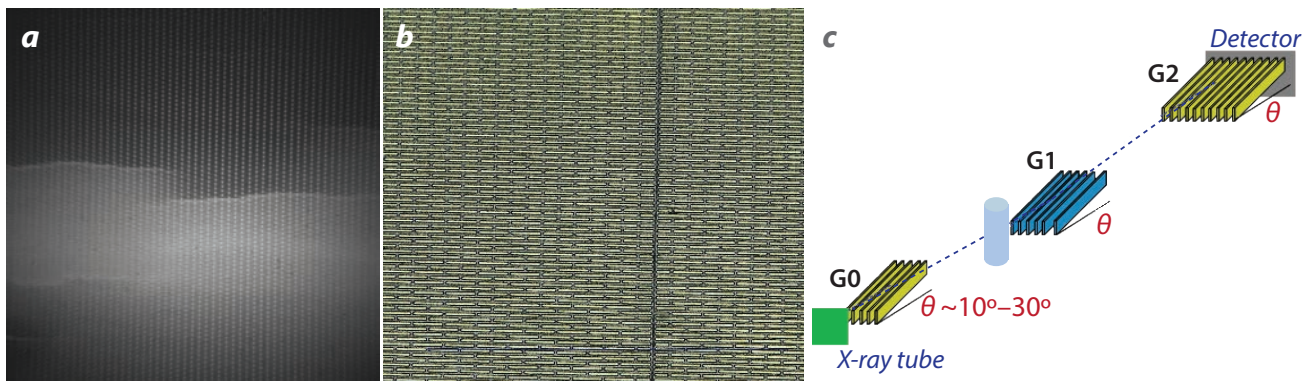


Figure 5. (a) X-ray radiograph, (b) microscope picture of G2 grating, and (c) glancing angle configuration, with gratings rotated to increase their effective thickness

dynamic PCI is only performed at synchrotrons. Dynamic experiments introduce new challenges to TXD. Typically, systems achieve high spatial resolution by using continuous, microfocus x-ray sources with spot sizes less than 10 μm . By comparison, commercially available flash x-ray sources typically have a spot size greater than 1 mm. Previous TXD systems have used phase scanning (Pfeiffer 2008) or fringe scanning (Momose 2006) to obtain separate images of refraction, attenuation, and USAXS. These methods require at least three exposures of the same static object, precluding their use for dynamic experiments. A single exposure also limits photon statistics, reducing the usefulness of single-image fringe-fitting routines. Additionally, flash x-ray sources typically have larger shot-to-shot variability in dose and spectra, and require labor-intensive anode replacements between shots.

In addition to the challenges all dynamic experiments face, many experiments of interest beget additional challenges. Many of these experiments have high densities, and the sources used for flash x-ray radiography have endpoint energies higher than those typically used in TXD. The absorption gratings can become transparent to the high-energy tail of the source spectra, reducing the contrast of the diagnostic. Additionally, many experiments of interest generate their own x-rays that produce a background on the measured signal. TXD systems deployed on these experiments will require shielded, gated cameras to reduce background. Another possible solution to reducing x-ray background is to use spectral filtering with multilayer x-ray mirrors, which will be tested if backgrounds indeed prove bright enough to prohibit accurate density measurements in future experiments. The purpose of this project is to address all of these challenges.

PROJECT

In the first year of the project, a new TXD system was assembled and successfully tested on the bench (Clayton 2018). To address the challenge of using sources with higher endpoint energies than are typical, we obtained new G0 and G2 absorption gratings from Microworks GmbH. These gratings, with a thickness of 240 μm and slit spacing of 4.8 μm , have an aspect ratio $240/4.8 = 50$, greater than any that have previously been produced. These absorption gratings were more difficult to manufacture than the more common lower aspect ratio gratings, and microscopy and x-ray radiography revealed a few irregularities (Figure 5). These new gratings were paired with a previously used G1 phase grating with the same 4.8 μm slit spacing and tested; the test results demonstrated that these irregularities were not severe enough to inhibit the formation of fringes on resulting images. To further increase the effective thickness of the gratings, and thus the fringe contrast of the resulting image, we placed the gratings in a glancing angle configuration, an idea previously patented by Johns Hopkins University (Figure 5) (Stutman 2012). The following results were obtained with a glancing angle of $\alpha = 23.5^\circ$ and gratings with an effective thickness of 600 μm . The gratings were spaced 62.5 cm apart, a Talbot length corresponding to an optimal x-ray energy of about 45 keV.

In FY 2018, we made a significant effort to improve the TXD system on the bench before shipping it to the launcher facility where the first dynamic measurements would be made. The final, installed system consisted of three sections: the source section outside the launcher catch tank, the target system inside the tank, and the imaging section located outside the tank opposite the source section (Figure 6).

The flash x-ray source is based on a Platts design (Platts 1995) with a tungsten anode; it produces 20 ns pulses with a 25 mrad dose at 1 m and an endpoint energy of 250–300 keV. We placed a dosimeter near the x-ray head to normalize the total dose between shots. The x-rays pass through the G0 grating, then through a Lexan vacuum window into the launcher catch tank. Inside, the experimental target is aligned in the line of sight of the diagnostic, and G1 is placed behind the target as close as possible. Lexan surrounds the G1 grating to protect it from pressure

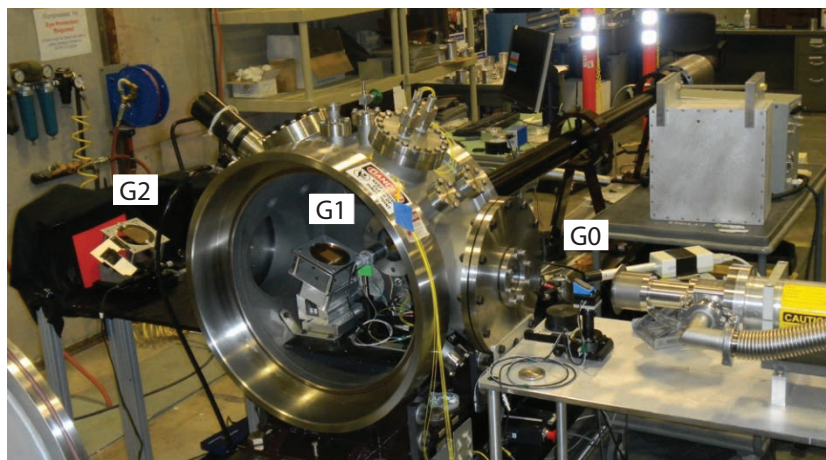


Figure 6. The setup of the Talbot-Lau x-ray deflectometer on the gas launcher catch tank, showing its three sections

waves and shrapnel following a shot. The x-rays then pass through a second Lexan vacuum window toward the imaging system. We placed a P43 scintillator just behind the G2 grating to convert the x-rays to green light and a turning mirror to send the scintillator image to a PI-MAX2 intensified CCD camera. The stainless steel catch tank shields the camera from direct x-ray radiation.

We must carefully align the gratings to obtain a fringe pattern on the images. Testing has shown that the rotation of G1 must be the same as G0 within about 2 arcminutes of angle, and for G2 to produce a measurable moiré pattern, it must be within a range of a few tens of arcminutes. Additionally, the distance between G0 and G1 must be within about 2 mm of the distance between G1 and G2. Aligning a new system properly may require thousands of images, while the flash x-ray source can only produce about 30 images before the anode must be replaced. To field a TXD system within the time constraints of a large experimental facility, we developed new techniques for setting up and aligning the diagnostic. We made inserts for each grating

mount with notches locating the center of the grating, and we used the same metal rod to match the spacing between the centers of G0 and G1 and the centers of G1 and G2. The sensitive G1 grating was then mounted on a new, vacuum-compatible, computer-controlled rotation stage with an encoder that can be operated from the control room. A second, continuous x-ray source (Spellman XRB101 Monoblock, 150 kV, 160 W) is used in place of the flash x-ray source for alignment. The G1 alignment process was then automated, with the camera taking an image every 5 seconds

with the rotation stage moving the grating 1 arcminute between images. Combining these new techniques, we were able to align the TXD diagnostic on the launcher within minutes.

The first dynamic measurements of a TXD diagnostic were performed on shock experiments at the North Las Vegas C3 Gas Launcher Facility, in which a 40 mm bore gas launcher fired a 0.125-inch-thick aluminum projectile at 625 m/s end-on at two types of targets: cylindrical 20 by 20 mm Lexan targets and smaller 6.25 mm diameter Lexan targets surrounded by a 9.5 mm diameter aluminum shell, both with a length of 20 mm.

The target, mounted in the line of sight of the TXD diagnostic, included a piezo pin used to trigger the flash x-ray source and a photonic Doppler velocimetry (PDV) probe to verify the speed of the projectile (Figure 7). The flash x-ray source was triggered at the time when the shock front was expected to reach the middle of the field of view.

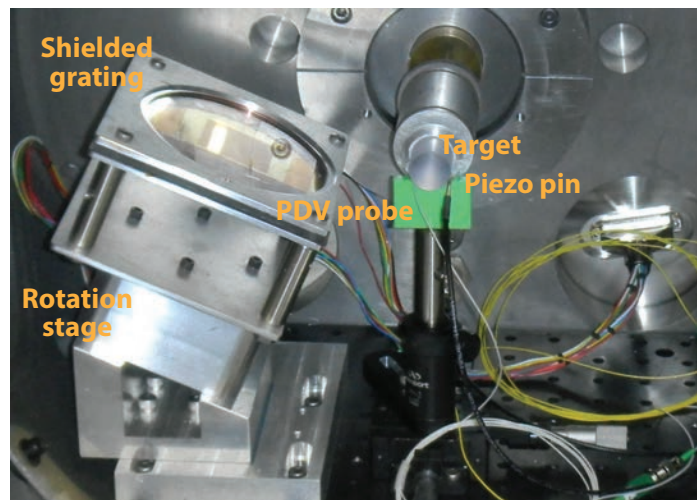


Figure 7. The experimental setup for the Lexan-only target

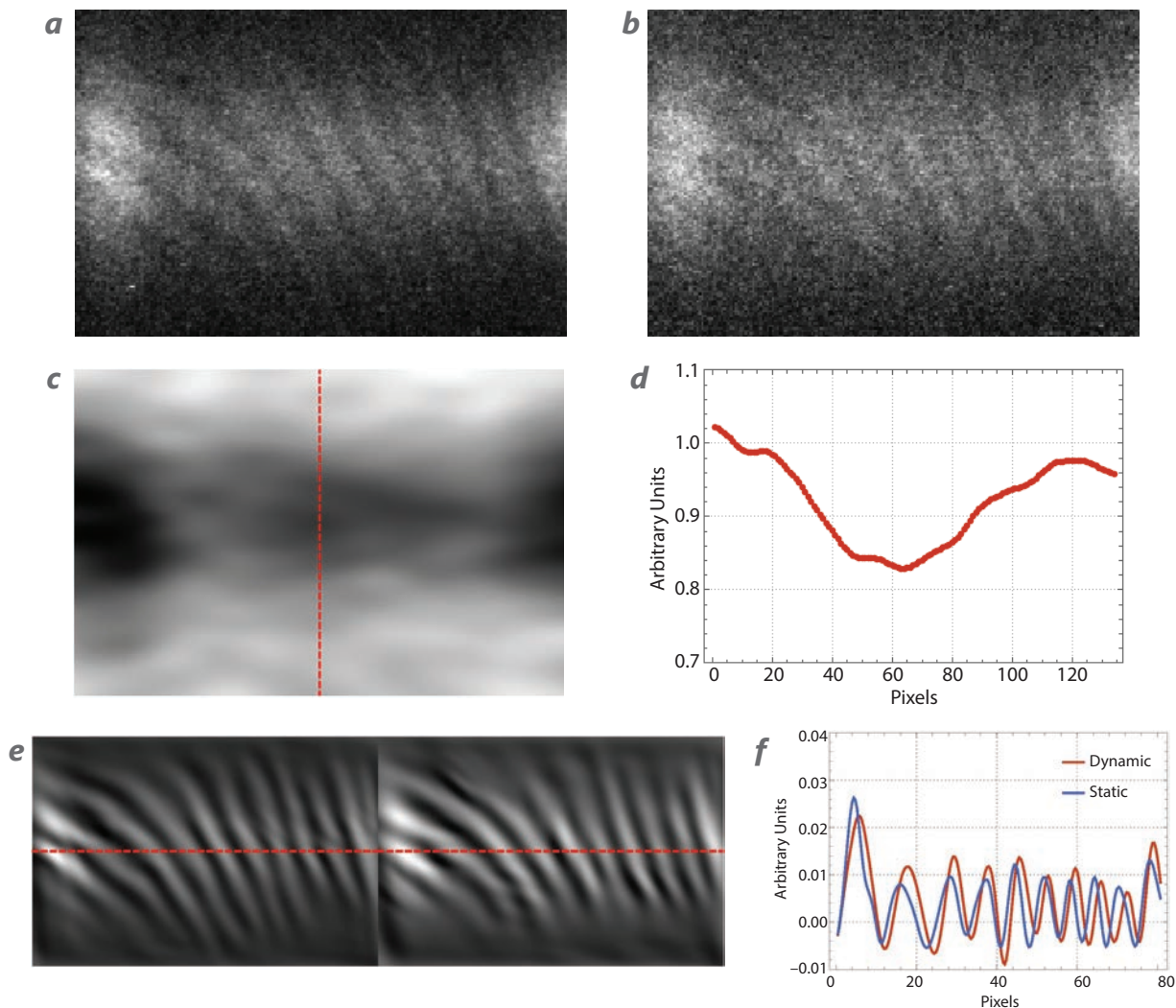


Figure 8. Unprocessed images of the (a) static and (b) dynamic Lexan+Al target, (c) the ratio of attenuation from Fourier decompositions of (a) and (b), (d) a lineout of (c) along the indicated line, (e) the fringes from Fourier decompositions of (a) and (b), and (f) lineouts of (e) highlighting the fringe shift

Preliminary analysis of the data has shown a clear density compression in the shot with the aluminum shell (Figure 8). Additionally, large fringe shifts are seen in both targets. The magnitudes of these fringe shifts do not agree with x-ray images generated by the XWFP code and based on expected density changes from a model of the targets generated with the CTH shock physics code. We will soon perform further experiments on the launcher using a new technique to verify the fringe shifts. Before each shot, a scan will be performed in which the G1 grating is rotated slightly. This will produce a series of static images with different fringe locations. When the dynamic image is collected, the fringes in a region without a density perturbation will be matched to an interpolation along the series of static shots for a “perfect” fringe match. The remaining differential phase shift will thus only

depend on density perturbations rather than any movement in the gratings.

Tests with static imaging have shown that forward modeling, in which deflectometer images are computed from given density profiles and then fit to the raw data, produces more reliable results than the fringe-fitting routines used on high-dose, high-resolution static images. Furthermore, forward modeling has proven to be more robust when experimental images are first deconvolved into separate refraction, attenuation, and USAXS images using Fourier transforms. Both the refraction and attenuation images can then be fit. To deconvolve the experimental data, we first apply a 2-D Fourier transform to the image. The attenuation image is simply taken from the absolute value of the Fourier transform over the interval $\pm 1/2p_M$, where p_M is the moiré period. The refraction image is obtained

by taking the argument, or phase shift, of the Fourier transform over the interval of $\pm 1/2p_M$ about the frequency p_M . While not used in density profile calculations, a USAXS image may be obtained by taking the ratio of the absolute values of the Fourier transforms over these two intervals. Results from a Fourier transform of an experimental image of a static object are shown in Figure 9.

CONCLUSION

TXD was deployed on a dynamic experiment for the first time, and while results were promising, we must conduct further experiments to confirm the capabilities of the diagnostic. We plan to repeat shock physics experiments on the gas launcher using a fringe scanning method. Additional launcher experiments will be conducted in which spall is generated to create large density gradients within the image. A new diagnostic will also be built for detonator experiments, where we use lower-energy x-ray sources to produce larger fringe shifts. The ultimate goal of this project is to map out the parameter space in which TXD has the sensitivity and resolution to accurately measure density profiles of one or more materials.

ACKNOWLEDGMENTS

We would like to thank the C3 Launcher team for all of their contributions to the successful experiments at their facility: Jeff Cates, Tom Graves, Cameron Hawkins, Russ Howe, Drew Martinson, Melissa Matthes, Jason Scharff, and Sarah Thomas.

REFERENCES

- Clayton, D. J., D. D. Schwellenbach, C. Kruschwitz, D. Stutman, K. Tritz, P. Valdivia, "X-ray phase contrast imaging for dynamic material mix experiments," in *Site-Directed Research and Development*, FY 2017, National Security Technologies, LLC, and Mission Support and Test Services, LLC, Las Vegas, Nevada, 2018, 193–199.
- Jahns, J., A. W. Lohmann, "The Lau effect (a diffraction experiment with incoherent illumination)," *Opt. Commun.* **28**, 3 (1979) 263–267.

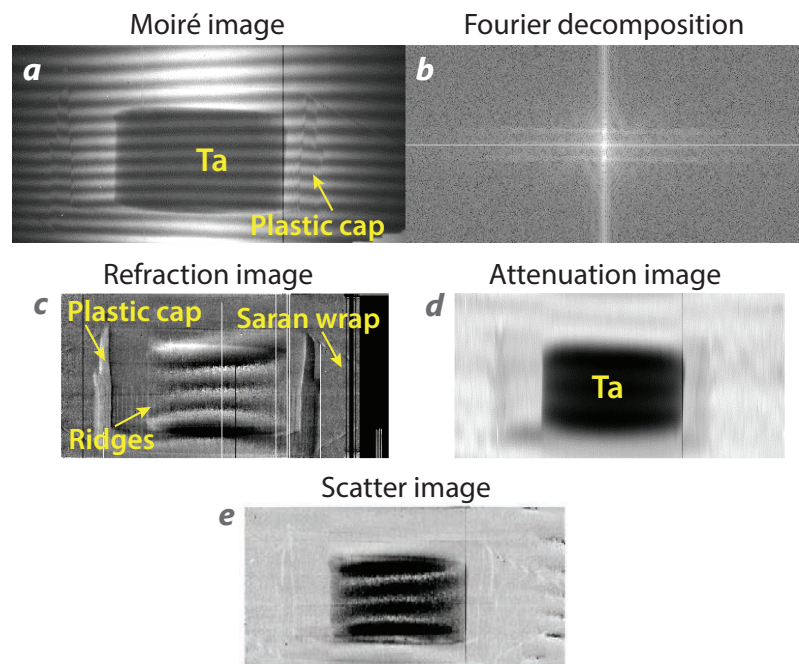


Figure 9. Images of a tantalum (Ta) aerogel sample, showing (a) raw data with moiré fringes, (b) Fourier decomposition of the raw image, (c) refraction, (d) attenuation, and (e) USAXS

- Momose, A., W. Yashiro, Y. Takeda, Y. Suzuki, T. Hattori, "Phase tomography by x-ray Talbot interferometry for biological imaging," *Jpn. J. Appl. Phys.* **45**, 6A (2006) 5254–5262.
- Pfeiffer, F., T. Weitkamp, O. Bunk, C. David, "Phase retrieval and differential phase-contrast imaging with low-brilliance X-ray sources," *Nat. Phys.* **2**, 4 (2006) 258–261.
- Pfeiffer, F., M. Bech, O. Bunk, P. Kraft, E. F. Eikenberry, Ch. Brönnimann, C. Grünzweig, C. David, "Hard-x-ray dark-field imaging using a grating interferometer," *Nat. Mater.* **7**, 2 (2008) 134–137.
- Platts, D., M. P. Hockaday, D. Beck, W. Coulter, C. R. Smith, "Compact flash x-ray units," *Tenth IEEE International Pulsed Power Conference*, Albuquerque, New Mexico, July 3–6, 1995, 892–896.
- Stutman, D., M. Finkenthal, "Glancing angle Talbot-Lau grating interferometers for phase contrast imaging at high x-ray energy," *Appl. Phys. Lett.* **101**, 9 (2012) 091108.
- Valdivia, M. P., D. Stutman, C. Stoeckl, W. Theobald, C. Mileham, I. A. Begishev, J. Bromage, S. P. Regan, "An x-ray backlit Talbot-Lau deflectometer for high-energy-density electron density diagnostics," *Rev. Sci. Instrum.* **87**, 2 (2016) 023505.
- Weitkamp, T., "XWFP: An x-ray wavefront propagation software package for the IDL computer language," *Proc. SPIE* **5536** (2004) 181–189.

This page left blank intentionally

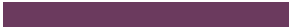


X-Ray Doppler Velocimetry

LO-004-16 ■ Year 3 of 3

**Jeffrey A. Koch,^{1,a} James A. King,^a Richard R. Freeman,^a
Eric C. Dutra,^a and Eric Huffman^a**

¹kochja@nv.doe.gov, (925) 960-2525
^aLivermore Operations



We are developing a novel technique for measurement of bulk fluid motion in materials that is particularly applicable to very hot, x-ray emitting plasmas in the high energy density physics (HEDP) regime. This x-ray Doppler velocimetry technique relies on monochromatic imaging in multiple x-ray energy bands near the center of an x-ray emission line in a plasma, and utilizes bent imaging crystals. Higher energy bands are preferentially sensitive to plasma moving towards the viewer, while lower energy bands are preferentially sensitive to plasma moving away from the viewer. Combining multiple images in different energy bands allows for a reconstruction of the fluid velocity field integrated along the line of sight. We review the technique, and we discuss progress made in the final year of the project towards benchmarking the technique with proof-of-principle HEDP experiments.

BACKGROUND

After several years of focused effort, the National Ignition Campaign at the National Ignition Facility (Miller 2004) ended in 2012 without achieving the goal of ignition and thermonuclear burn in the laboratory (Lindl 2014). The reasons for this failure are not understood, and a variety of possible explanations have been proposed, but it is likely that at least part of the explanation is bulk fluid motion in the compressed hot spot (Spears 2014). This bulk motion serves as an energy sink, trapping implosion kinetic energy that could otherwise transfer to thermal heating and neutron production. Currently, there are no diagnostics

that quantify bulk fluid motion in the hot spot, and this gap between needs and capabilities motivated the x-ray Doppler velocimetry (XDV) project (Koch 2017a, 2017b, 2018a).

Astronomers have long utilized multi-spectral imaging at radio frequencies to measure bulk motion of gas clouds, for example, in distant galaxies (Shu 1982), by measuring Doppler-shifted frequencies of emission lines. An analogous instrument that can measure Doppler energy shifts of x-rays emitted by plasmas, locally in imaging mode, would allow bulk motion in the plasma to be diagnosed. We accomplish this using near-normal-incidence spherical bent crystals that are already widely used for quasi-monochromatic x-ray

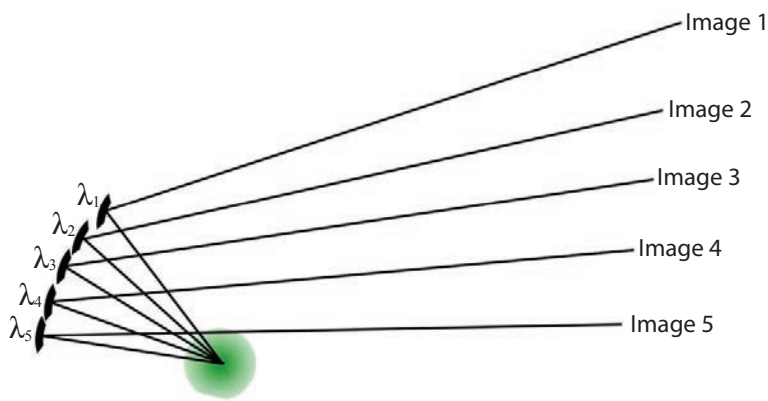


Figure 1. Sketch of one possible implementation of XDV. Five identical imaging crystals project five separate images of the source onto a detector. Each crystal is sensitive to different x-ray energies, in closely spaced bands near the center of an emission line from the source.

imaging applications (Pikuz 1995, Aglitskiy 1998, Uschmann 2000, Koch 2003, Akli 2011, Stoeckl 2012). These systems can provide very large collection solid angles when the angle of incidence is close to normal and the crystal quality is high, and they can be very efficient when used with narrow-band emission line

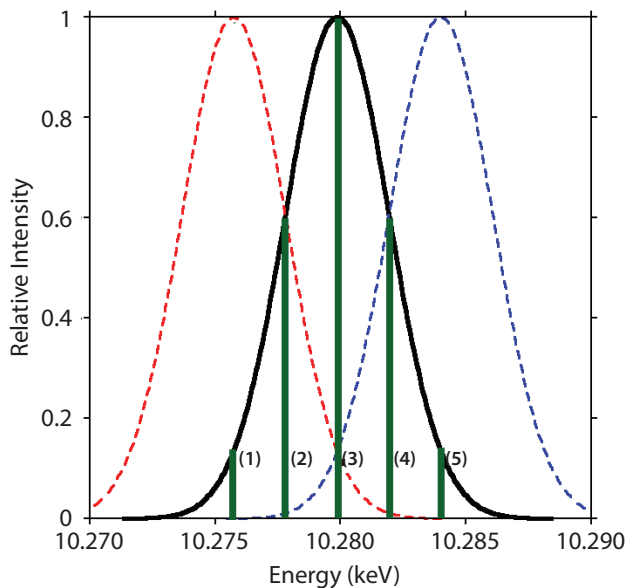


Figure 2. Sketch of the center energy distribution of the crystals shown in Figure 1. An unshifted line would appear brightest in the middle crystal (3). If the source was moving toward the crystal, the line would shift to the right and the source would appear brightest in the blue-tuned crystal (1), while if the source was moving away from the crystal, the source would appear brightest in the red-tuned crystal (5).

sources (Koch 1998). Use of multiple crystals, each tuned to a slightly different energy band, allows a map of fluid velocity (averaged along the line of sight) to be generated, and this is the essential concept behind XDV.

The basic geometry of XDV is shown in Figure 1. Several identical bent imaging crystals, with the same interplanar spacing d , are arranged to view a plasma along a near-common line of sight, and each is configured with a slightly different Bragg angle θ_B . The Bragg equation $\lambda = 2d\sin\theta_B$ implies that the center bandpass of each crystal falls at a slightly different wavelength λ , and therefore a different energy E . If we configure the range of energies to run from the red wing to the blue wing

of the unshifted center of an x-ray emission line from the plasma, then five quasi-monochromatic images will be generated that emphasize velocities corresponding to the Doppler shifts of the centers of the passbands of the five crystals. This is shown schematically in Figure 2. Here, the number of crystals is arbitrarily chosen to be five. A lower bound is two crystals, the minimum necessary to show differences between images, while an upper bound will be limited by the complexity of the instrument and ultimately by view differences between lines of sight, necessary due to the non-zero dimensions of the crystals and mounting fixtures. More details on the XDV technique, as well as simulation results, have been published elsewhere (Koch 2017a, 2017c).

PROJECT

In the third and final year of the XDV project, we focused on two main issues: proof-of-principle experiments at the Sandia National Laboratories (SNL) Z-Beamlet Laser Facility (ZBL) and data analysis procedures to generate an object velocity map from multiple XDV images.

In 2016, SNL constructed a two-crystal x-ray imaging system (Harding 2018) with two wide and widely separated bands intended to provide images of a cobalt-doped Z-produced plasma in the light of Co He- α line emission (7242 eV center, with a 13 eV bandwidth including the entire emission line width) and in the light of continuum emission in a band centered far from the He- α emission line (7265 eV, also with a 13 eV bandwidth). The goal was to map the 2-D

location of Co line emission by subtracting the continuum image from the line emission image. The system mounts two spherically bent Ge (3,5,5) crystals, and two Rowland circle (RC) apertures next to alignment lasers, on a ring surrounding the target plasma at the center. Each crystal casts an image of the plasma onto a common image plate detector approximately 1 meter away from the target.

This configuration is very nearly a two-crystal version of XDV, so we decided to redesign the SNL two-crystal system to yield sensitivity to fluid motion while maintaining the same basic geometry. We did this by (1) moving the band center energies much closer together so that they are both within the Co He- α line width, (2) narrowing the bandwidths of the images produced by the crystals, and (3) redesigning the alignment system so that we can reliably select two very closely spaced center energies.

A drawing of our new XDV imaging system is shown in Figure 3. We reproduced the ring configuration of the current SNL system, mounting it to a flat base for use in ZBL, but made a number of modifications. First, each crystal mount is broadly adjustable in azimuth, over a range sufficient to cover all realistic Bragg angle choices consistent with imaging x-rays in the Co He- α spectral region with spherical Ge (3,5,5) crystals, by means of a rotation axis passing through the center of the surface of the crystal. Second, we restrict the bandpass of the crystals by means of apertures placed at the crystal surfaces, instead of reflecting off the entire crystal surface and restricting bandpass by aperturing on the RC. Finally, we redesigned the alignment system and use a point-like fiber-coupled diode laser placed at the target location to illuminate the crystals and cast shadows of the apertures onto a reflective reticle (Figure 4). The reticle is placed at a predetermined location where the shadows of the aperture edges coincide at a crossover point. Changing center energies requires only repositioning the reticle to a new crossover point and adjusting the azimuth angles of the crystals until the aperture shadows superimpose at the new predetermined location.

In October 2017, we fielded the XDV prototype in experiments at the ZBL facility, using a 2 kJ, 2 ns main laser pulse combined with a 0.2 kJ, 0.5 ns pre-pulse, and best beam focus without a phase plate. We performed three shots on solid

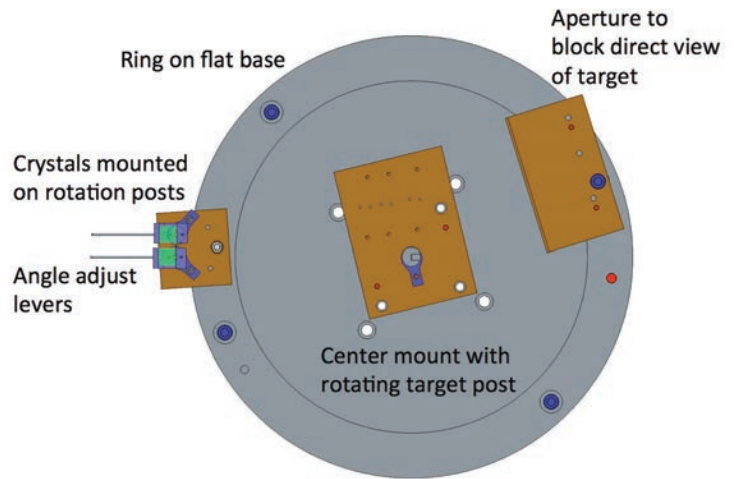


Figure 3. Top view of the ZBL XDV instrument. ZBL irradiates the target post from the top of the drawing, and x-rays from the target reflect off each of the two Ge (3,5,5) crystals to form images through the aperture block onto a distant image plate detector that is not shown. The crystal azimuth angles are adjusted using removable lever posts shown at the left.

(50 μm thick) Co targets, and obtained useful data from all three shots on an image plate detector. The target and diagnostic geometries for the shots are shown in Figure 5. XDV was fielded on all three shots, and we fielded a spherical crystal spectrometer

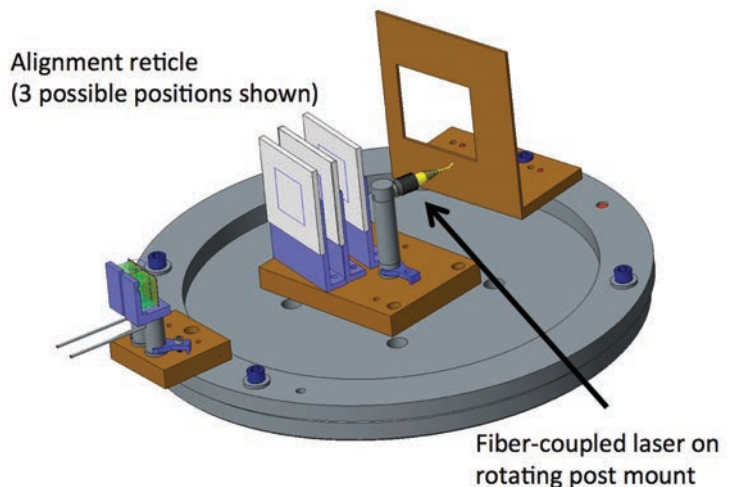


Figure 4. Side view of the ZBL XDV instrument, as configured for alignment. A single-mode fiber-coupled diode laser emits a beam from a point at the target location, and the shadows of the apertures in front of the crystals superimpose on a reticle that can be placed in several predetermined locations (three are shown). Once the crystals are aligned, the reticle and laser are removed, and the laser post is replaced by the target post.

XRS3 on the second and third shots to provide a measurement of the space- and time-averaged spectral line width of the Co He- α line, necessary for quantitative reduction of the XDV images (Koch 2017c). The XDV and XRS3 lines of sight were nearly the same, minimizing parallax errors. For shot 3, the line width was found to be 8.4 eV FWHM.

The XDV images are shown in Figure 6. The left and right crystal images are essentially identical on

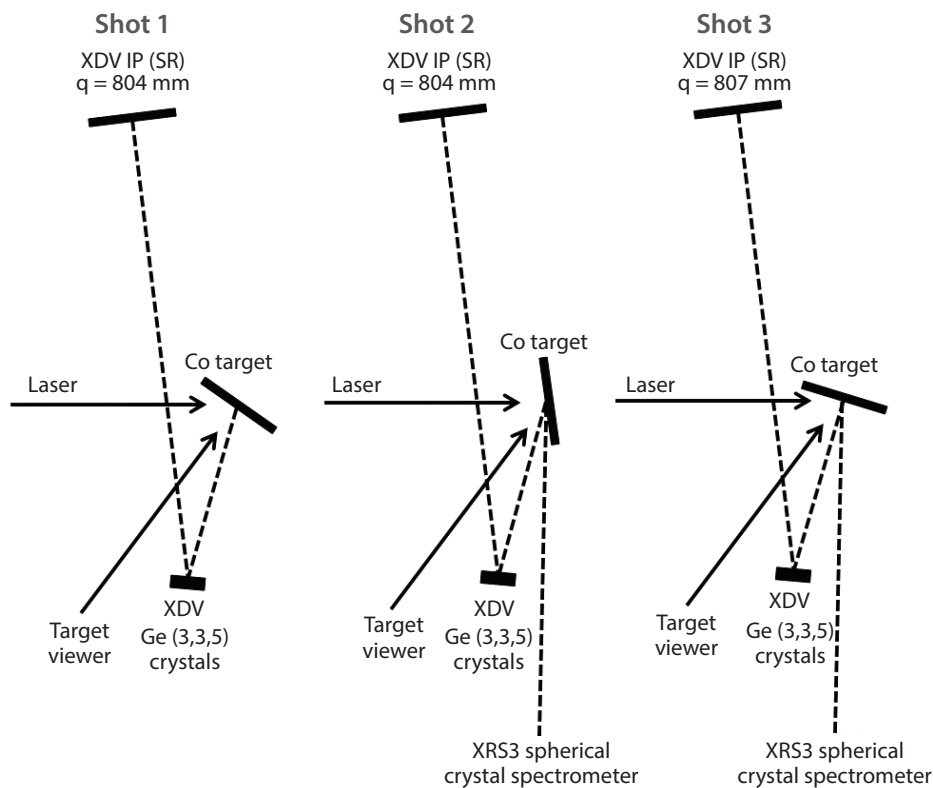


Figure 5. ZBL shot configurations, viewed from the top of the target chamber. Shots 1 and 2 used the same Bragg angle on both crystals (both tuned to line center), while shot 3 kept the right crystal tuned to line center but shifted the left crystal 6.2 eV to the blue side of line center. The main difference between shots 1 and 2 was the rotation angle of the target.

shots 1 and 2, as expected because the center energies were the same (all at line center). However, the plasma images differ between shots 1 and 2, in part because the target angles were different (see Figure 5). This is confirmed by mapping the ratio of the left and right image intensities, showing a broad flat region of constant ratio for both shots. Shot 3, however, shows distinct differences between the left (+6.2 eV shift) and right (line center) images. In particular, the line-center right image shows a halo feature on the lower left that is absent in the blue-shifted left image. This indicates

material that is moving at a lower speed towards the crystals, compared with the rest of the plasma.

We can use a simple analytical unfold to calculate a fluid velocity map from the two XDV images, provided we know the spectral line width (Koch 2017c). This approach is complicated by the fact that the source size is relatively large ($\sim 400 \mu\text{m}$) for imaging without RC apertures. This results in a walking of the apparent center of the image that varies with Bragg angle, and this must be accounted for in analysis. In particular, the centroids of the images are no longer at the same object location, and shifting the images to correct introduces a gradient in the ratio map that must be removed.

The details of these corrections will be published elsewhere, but a preliminary velocity map for shot 3, including the corrections, is shown in Figure 7. We see that a large region of the object space is moving away from the target surface, towards the crystals, at approximately 100 km/s, comparable to what we would expect from a high-energy laser-irradiated Co target ionized to He-like and H-like. In the halo region of the target, the velocity decreases to near zero, and is possibly slightly negative (receding). Given the time-integrated

data and the presence of a strong pre-pulse in the laser, this is not necessarily surprising but does warrant further study with additional target shots.

We are currently building a modified XDV instrument that uses apertures on the RC rather than on the crystals. This will eliminate the need for post-shot corrections to the image data and will allow a cleaner unfold of velocity maps from image data. This instrument will be ready in late 2018, and will be fielded when future opportunities for target shots arise at ZBL.

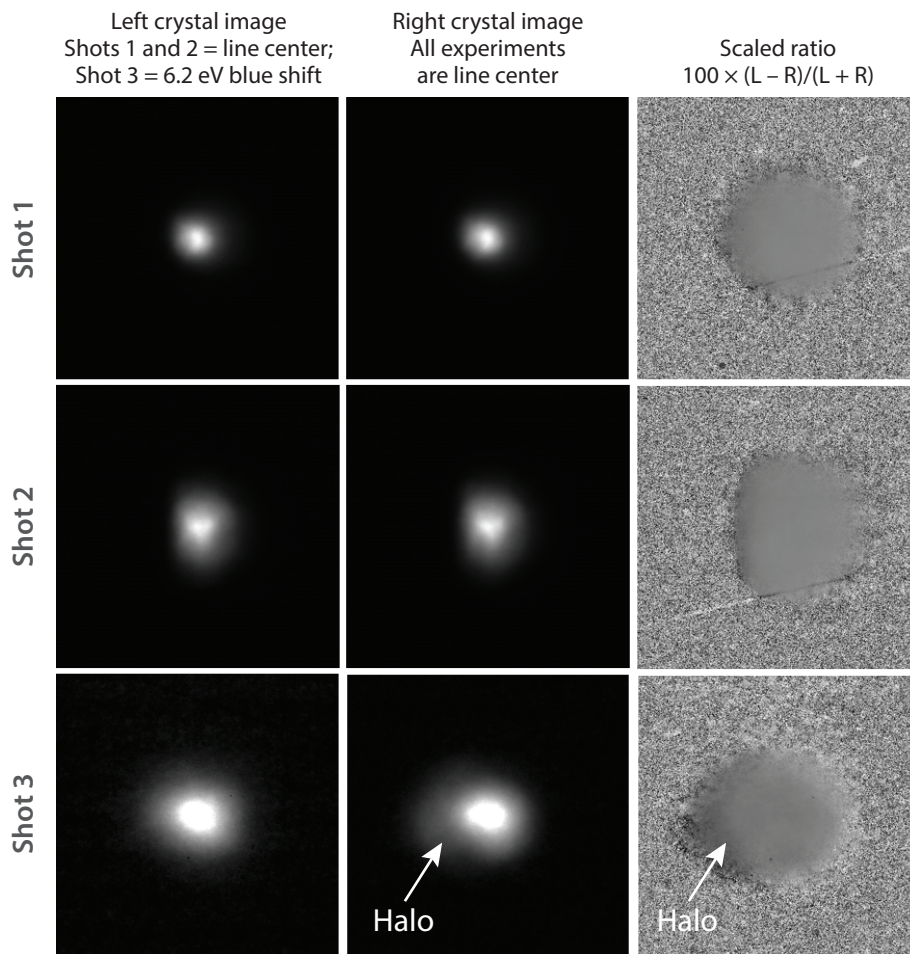


Figure 6. XDV image data from the three ZBL experiments. Clearly evident in the right crystal image of shot 3 is a halo feature that is not seen in the left crystal image, and this corresponds to a region of relatively low velocity along the line of sight.

CONCLUSION

We have described and demonstrated a novel technique for measurement of bulk fluid motion in materials that is particularly applicable to very hot, x-ray emitting plasmas in the HEDP regime. This XDV technique relies on monochromatic imaging in multiple x-ray energy bands near the center of an x-ray emission line in a plasma, and it uses bent imaging crystals. Combining multiple images in different energy bands allows for a reconstruction of the fluid velocity field integrated along the line of sight.

In FY 2018, we designed and built a new dual-crystal imaging instrument as an XDV prototype, and we successfully fielded the instrument at the Sandia ZBL facility. The data demonstrate sensitivity to ablation velocity across a 2-D imaging field of view, and show clear variations in these ablation velocities. We also developed a new technique for velocity map reconstruction from data

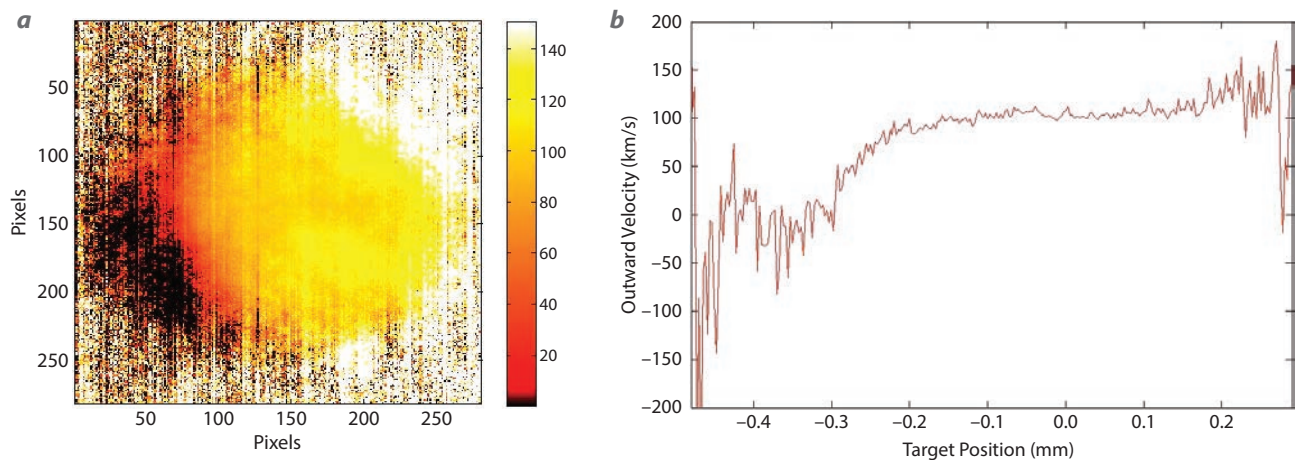


Figure 7. Line-of-sight velocity map for shot 3 (left), with color bar indicating velocities in km/s towards the viewer, along with horizontal profile through the map (right). Ablation velocities are a fairly uniform 100 km/s, except in a region along the left side where velocities drop to near 0 km/s.

obtained without RC apertures. Finally, we have begun design modifications to the instrument to allow RC apertures to be used in future experiments, and we hope to field this instrument in the coming year on shots of opportunity at ZBL.

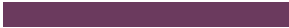
In FY 2018, the XDV concept was awarded a U.S. patent (Koch 2018b). Project progress was reported in a technical seminar at the University of Nevada, Las Vegas, in an HEDP seminar at Sandia National Laboratories in Albuquerque, and in an invited talk at the SPIE Optics+Photonics conference in San Diego. A second refereed journal article, and a proceedings article for SPIE, are in preparation.

ACKNOWLEDGMENTS

We thank our collaborators J. Field, G. Hall, and J. Kilkenny at the Lawrence Livermore National Laboratory; E. Harding, G. Rochau, M. Schollmeier, and J. Porter at Sandia National Laboratories; A. Covington at the University of Nevada, Reno; F. Beg at the University of California, San Diego; and D. Kunkel at the George Washington University, Washington, for their contributions and support.

REFERENCES

- Aglitskiy, Y., et al., “High-resolution monochromatic x-ray imaging system based on spherically bent crystals,” *Appl. Opt.* **37** (1998) 5253–5261.
- Akli, K. U., et al., “A novel zirconium $K\alpha$ imager for high energy density physics research,” *Rev. Sci. Instrum.* **82** (2011) 123503.
- Harding, E., Sandia National Laboratories, to be published (2018).
- Koch, J. A., et al., “High-energy x-ray microscopy techniques for laser-fusion plasma research at the National Ignition Facility,” *Appl. Opt.* **37** (1998) 1784–1795.
- Koch, J. A., et al., “4.5- and 8-keV emission and absorption x-ray imaging using spherically bent quartz 203 and 211 crystals,” *Rev. Sci. Instrum.* **74** (2003) 2130.
- Koch, J. A., et al., “X-ray Doppler velocimetry: An imaging diagnostic of 3D fluid flow in turbulent plasma,” *High Energy Density Physics* **23** (2017a) 184–187.
- Koch, J. A., et al., “X-ray Doppler velocimetry,” in *Site-Directed Research and Development*, FY 2016, National Security Technologies, LLC, Las Vegas, Nevada, 2017b, 173–178.
- Koch, J. A., et al., “X-ray Doppler velocimetry for diagnosis of fluid motion in ICF implosions,” *Proc. SPIE* **10390** (2017c).
- Koch, J. A., et al., “X-ray Doppler velocimetry,” in *Site-Directed Research and Development*, FY 2017, National Security Technologies, LLC, and Mission Support and Test Services, LLC, Las Vegas, Nevada, 2018a, 201–206.
- Koch, J. A., “Methods and systems for imaging bulk motional velocities in plasmas,” U.S. Patent 10,017,577 B2, filed April 4, 2016, and issued July 10, 2018 (2018b).
- Lindl, J., O. Landen, J. Edwards, E. Moses, NIC Team, “Review of the National Ignition Campaign, 2009–2012,” *Phys. Plasmas* **21** (2014) 020501.
- Miller, G. H., E. I. Moses, C. R. Wuest, “The National Ignition Facility,” *Opt. Engin.* **43** (2004) 2841.
- Pikuz, S. A., V. M. Romanova, T. A. Shelkovenko, T. Pikuz, A. Ya. Faenov, E. Förster, “Use of higher-order reflection from mica crystals in x-ray spectroscopic investigations at 0.1–0.3 nm,” *Quantum Elec.* **25** (1995) 16.
- Shu, F. H., *The Physical Universe: An Introduction to Astronomy*, University Science Books, Mill Valley, California, 1982.
- Spears, B. K., et al., “Mode 1 drive asymmetry in inertial confinement fusion implosions on the National Ignition Facility,” *Phys. Plasmas* **21** (2014) 042702.
- Stoeckl, C., G. Fiksel, D. Guy, C. Mileham, P. Nilson, T. C. Sangster, M. J. Shoup, W. Theobald, “A spherical crystal imager for OMEGA EP,” *Rev. Sci. Instrum.* **83** (2012) 033107.
- Uschmann, I., K. Fujita, I. Niki, R. Butzback, H. Nishimura, J. Funakura, M. Nakai, E. Förster, K. Mima, “Time-resolved ten-channel monochromatic imaging of inertial confinement fusion plasmas,” *Appl. Opt.* **39** (2000) 5865.



Fast Spectroscopic Temperature and Pressure Measurements Using a Time Stretch–Dispersive Fourier Transformation

STL-031-18 ■ Year 1 of 1

Jason Mance,^{1,a} Brandon La Lone,^a Jonathan Madajian,^a Eric Larson,^a Mike Grover,^a and Ruben J. Valencia^a

¹mancegj@nv.doe.gov, (805) 681-2366

^aSpecial Technologies Laboratory



This work explores the potential use of time-domain spectroscopy to make megahertz-rate pressure, temperature, and concentration measurements in gases. The diagnostic capability to measure pressure and temperature are essential in high-pressure shock wave science. However, the dynamics evolve on a microsecond timescale, and many conventional methods can only provide a single measurement during this time frame. We developed a time-stretch Fourier transform approach to measure IR absorption spectra in gases that provides pressure, temperature, and concentration measurements at MHz rates. We demonstrate high-resolution (0.01 nm), time-resolved (6.25 million spectra per second) measurements in an acetylene-oxygen gas mixture undergoing combustion. We observe the appearance of rotational spectra consistent with the hydroxyl (OH) radical, which is a common byproduct in the combustion, deflagration, and detonation of fuels and explosives. The ability to measure OH spectra with this technique offers the potential to make these measurements in other combustible gases. In FY 2019, a related SDRD project will leverage our work to examine the possible use of this technique to measure Raman spectra, which would open possibilities to make pressure and temperature measurements in pure gases.

BACKGROUND

Laser-based spectroscopic techniques have been used extensively in high-pressure physics for studying chemical reactions or decompositions and phase transitions and for recording temperatures, pressures,

and material composition. For many of these studies, a method that records high-resolution spectra under dynamic loading on a sub-microsecond timescale is required. Current camera technologies for recording spectra trade time resolution for shorter recording times or lower spectral resolution. A new laser-based

recording technique is needed that can sample quickly, with high spectral resolution and good dynamic range, without sacrificing recording time.

PROJECT

Time-domain spectroscopy based on mode-locked infrared fiber lasers and telecommunications technology has led to recent advancements in optical ranging, high-speed velocimetry, laser science, and spectroscopy, to name a few (Chou 2004, 2007; Dorrer 2004; Solli 2007, 2008; Xia 2010; Godin 2013; Werblinski 2013; La Lone 2015; Herink 2016; Saltarelli 2016; Mahjoubfar 2011, 2017). This research examines time-domain spectroscopy as a potential method for measuring temperature, pressure, and concentration of gases in high-energy shock waves where transient events occur on a microsecond timescale. Conventional methods for measuring spectra map the spectrum into the spatial domain by using a slit or prism to disperse the various wavelengths. Time-domain spectroscopy disperses spectra into the time domain by using materials or geometries that create different temporal path lengths for the different wavelengths. This project maps the spectrum into the time domain using dispersive optical fibers and measures the spectrum using single-point photodetectors. With state-of-the-art digitizers and detectors, it is possible to record at >20 GHz sampling rates continuously with record times on the order of 100 ms. This ability greatly increases spectral resolution, recording speed, and storage capability over that afforded by standard spatial mapping methods. We are developing a diagnostic system for measuring the rotational IR absorption spectra in gases. This year we demonstrate the system's capability to make dynamic 6.25 MHz rate temperature, pressure, and concentration measurements during the combustion of acetylene (C_2H_2) in oxygen (O_2).

Experimental Setup

Figure 1 shows a simplified schematic of the system we designed to measure spectra in the time domain. A fiber-based mode-locked laser with a center wavelength of 1550 nm, bandwidth of 100 nm, pulse length of 100 fs, and repetition rate of 100 MHz, is pulse picked (a method in which an optical switch extracts single pulses from a fast pulse train) with a Mach-Zehnder (MZ) interferometer before the pulse is stretched and amplified in a spool of highly dispersive optical fiber. A fraction of the pulse is diverted and recorded as a reference spectrum. The signal pulse is coupled into free space, double passed through a gas cell, and coupled back into the fiber. A circulator then reroutes the return pulse, which is detected on a 20 GHz bandwidth photodiode/digitizer.

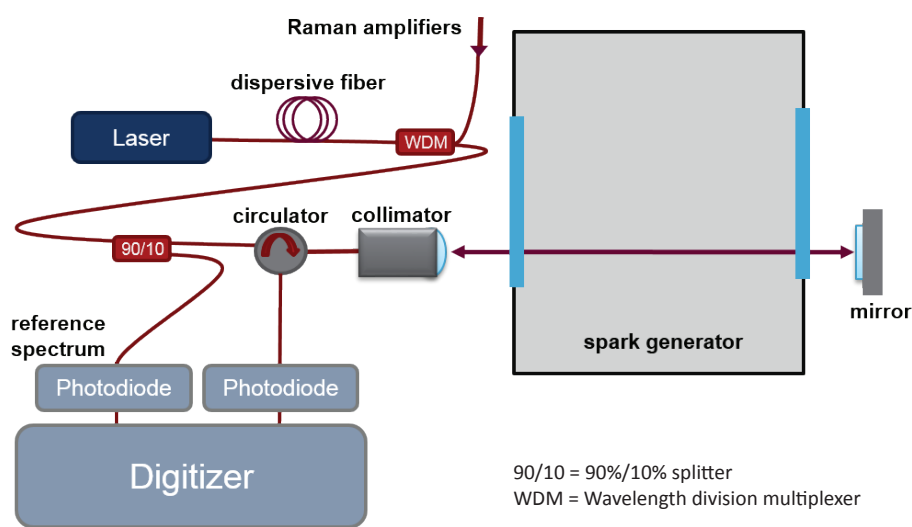


Figure 1. Experimental setup for time-domain spectroscopic measurements of temperature, pressure, and concentration during the combustion of acetylene in oxygen. A mode-locked 1550 nm laser is chirped and Raman amplified in highly dispersive fiber before double passing the combustion cell and being recorded on a photodiode.

We can use long lengths of dispersive fiber to stretch the pulse out to hundreds of nanoseconds in time to acquire spectral resolutions on the order of 0.001 nm, if desired. However, as spectral resolution is increased, the pulse width also increases, and we must decrease the repetition rate to keep pulses from overlapping in time. If high frame rates are wanted, shorter dispersive fiber lengths can be used for smaller stretches, and recording rates from 50 to 100 MHz can be realized. We can also obtain high resolution and fast recording speeds simultaneously by configuring the system to record with high resolution over a narrow spectral range.

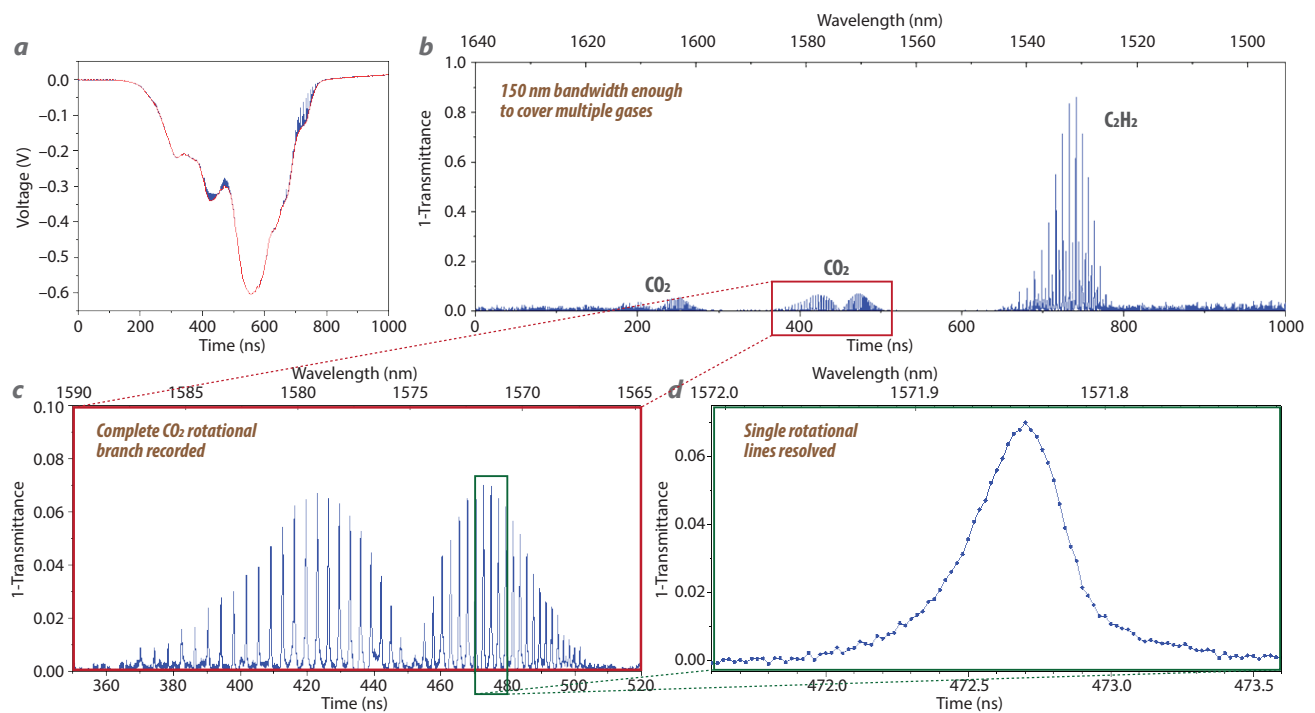


Figure 2. Static time-domain spectral measurements in a $\text{CO}_2/\text{C}_2\text{H}_2$ gas mixture. (a) Absorption lines recorded on top of the spectrum, (b) the absorption spectrum after subtraction of the pulse envelope, (c) a magnified view of one of the rotational R and S branches in CO_2 , and (d) a further magnified view of a single rotational line.

Experiment and Results

We conducted initial measurements to test the system in a 2 m long cell filled with carbon dioxide (CO_2) and trace amounts of C_2H_2 . The results are shown in Figure 2.

For these measurements, the laser pulse was stretched to 200 ns, and the repetition rate was pulse picked down to 2 MHz. We used four Raman pump lasers to amplify the full bandwidth of the laser pulse at wavelengths of 1445, 1465, 1485, and 1500 nm. Figure 2a shows the signal (blue) with the reference spectrum (red); the photodetector response is negative. Figure 2b shows the absorption spectrum (1-transmittance), obtained by dividing out the reference pulse. The measurement demonstrates how this approach can provide simultaneous high spectral resolution over a broad range of wavelengths at MHz rates. The digitizer and photodetector used for these measurements had a 10 GHz recording bandwidth, and the time stretch maps the spectrum into the time domain with a nearly linear chirp resulting in a wavelength-to-time ratio of 0.15 nm/ns. This provides 100 nm wide spectra with 0.015 nm resolution recorded every 500 ns. Figure 2c shows a magnified section of the spectrum, demonstrating the full P and R rotational branches in CO_2 . The

intensity distribution of these lines follows a Boltzmann distribution, from which temperature can be determined. Further magnification (Figure 2d) illustrates that the spectral resolution is more than sufficient to resolve a single rotational line. This makes it possible to measure spectral line broadening effects, which contain information about pressure, temperature, and concentration.

The strong absorption depth of C_2H_2 (near 90% at the peak of the data shown in Figure 2) at the wavelengths available with our current laser system makes it a convenient candidate gas for tests under dynamic conditions, so we adjusted the laser system to target C_2H_2 . In order to observe more rotational lines, we turned off three of the four Raman pumps so that we could increase the power of the remaining one having the shortest wavelength (1465 nm) to obtain more signal near the C_2H_2 lines around 1520 nm. This adjustment also made the temporal length of the pulse shorter so that we could record at a higher repetition rate (6.25 MHz) for the dynamic experiments. Next, we filled the cell with a mixture of 29% C_2H_2 and 71% O_2 (equivalence ratio = 1) and installed a spark generator inside the gas cell. We triggered the scope to begin recording when the spark was initiated and recorded for 2 ms. This experiment provided a time

record of the combustion process. A summary of the observed dynamics follows.

The spark generated a weak shock wave, which took 60 μs to propagate to the probe. As the shock wave passed the probe, there was a reduction in the returned laser intensity caused by beam steering in the shock wave. However, data analysis revealed that the temperature, pressure, and concentration did not change significantly in or immediately after the shock wave passed. The system remained stable for another 50 μs , at which point we began to see fluctuations in the intensity of the return signal as turbulence began to occur in the cell. The temperature, pressure, and concentration, however, remained stable for another 27 μs . At 137 μs after the spark, the C_2H_2 concentration started to decrease as combustion began to occur. Over the next 2 μs , the C_2H_2 spectra rapidly decreased, and OH lines appeared. Figure 3 shows four plots from the 2 ms record that illustrate the process. Figure 3a shows the room-temperature, room-pressure, 29% C_2H_2 lines that are visible and largely unchanged for

the first 137 μs after the spark. Figure 3b shows the C_2H_2 lines decreasing, and Figure 3c, at 138 μs , shows further reduction in C_2H_2 and the emergence of OH lines. By 139 μs (Figure 3d), all of the C_2H_2 rotational spectra have disappeared, and only the OH lines are present. The OH lines remain present and stable, with very little change in the spectra, for the remaining 2 ms record time.

In the 2 μs during which the C_2H_2 lines disappear and the OH lines appear, the temperature and pressure appear to have substantially increased. Figure 4 shows a theoretical OH spectra calculated with the open source online spectrum generator SpectraPlot (Goldenstein 2017). An overlay of the generated spectra onto the data shows an obvious match between features in the theoretical OH and measured data. Note that the two large peaks that appear to exceed the plot limits are from notch filters placed in the system to help with the wavelength-time calibration, so data in these regions (1542–1544 nm and 1550–1552 nm) should be ignored. In Figure 4b theoretical plots of

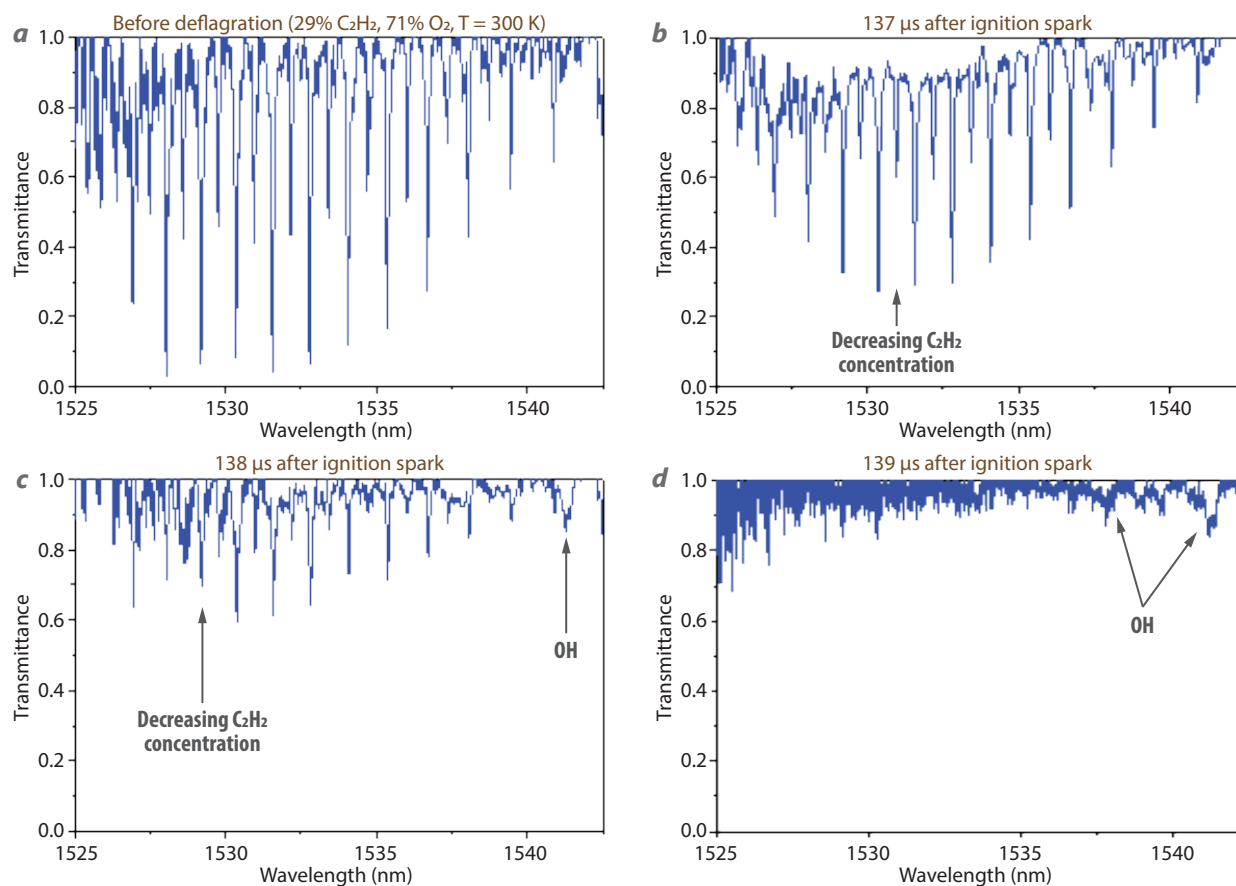


Figure 3. Dynamic combustion of C_2H_2 in O_2 . Complete reduction of C_2H_2 at near room temperature occurs over a 2 μs time frame, and hot/high-pressure hydroxyl (OH) radical lines appear. OH remains present and stable for the remaining 2 ms record time.

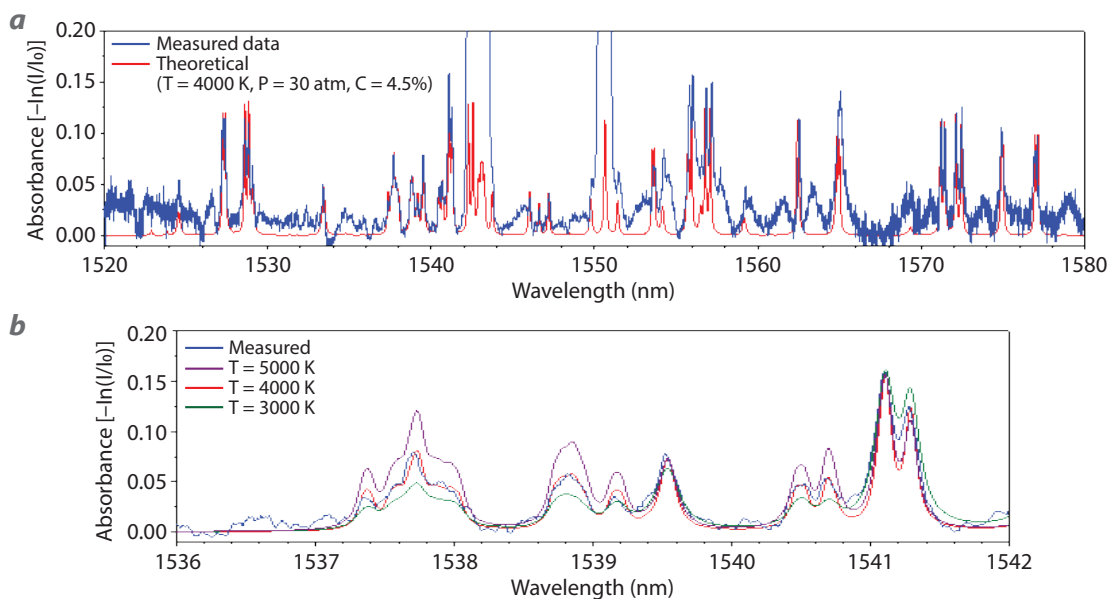


Figure 4. (a) Full recorded spectrum of OH (blue) and theoretical spectrum (red) at temperature 4000 K, pressure 30 atm, and concentration 4.5%. (b) Theoretical spectra at 3000, 4000, and 5000 K overlaid on the recorded data (and zoomed in to the part of the spectrum with the highest signal-to-noise ratio), clearly showing the temperature is near 4000 K, well within ± 1000 K.

spectra at temperatures of 3000, 4000, and 5000 K are overlaid on the section of the data with the highest signal-to-noise ratio. It is clear that the temperature is well within the 3000–5000 K range, with excellent agreement at 4000 K. We used a similar, best-fit-by-eye approach to determine the indicated pressure (30 atm) and concentration (4.5%). We continue to more thoroughly analyze the data. Because of the large datasets (24,000 spectra per experiment, 8000 data points per spectrum) computer programming is required to automate tasks such as background subtraction and frame averaging and to find the best-fit theoretical spectra by floating the pressure, temperature, and concentration parameters.

CONCLUSION

We have demonstrated the use of fiber-based time-domain spectroscopy using IR lasers to make dynamic pressure, temperature, and concentration measurements in a gas by observing the combustion of C_2H_2 in O_2 . We observed the formation of OH radicals as the acetylene underwent deflagration and detonation, which allowed us to time-resolve the change in temperature and pressure throughout the process. The appearance of OH lines, a common intermediate byproduct in the detonation and deflagration of combustible materials, means this

technology offers the potential to measure pressure and temperature in other combustible gases (e.g., hydrogen, toluene, ethanol, propane) when oxygen is present at high pressures and temperatures. Other commonly applied approaches for making pressure, temperature, and concentration measurements (e.g., coherent Raman scattering techniques) often use expensive, high-energy, free-space lasers and fast framing cameras and can be limited to sub-megahertz-rate measurements. The method reported here uses relatively inexpensive low-power fiber-based laser equipment and offers greater speed and resolution without the need for complex, expensive optical systems. Under the FY 2019 SDRD project, “Fast temperature measurements using dispersive time-domain spectroscopy,” the investigator will use our work to determine if this technique can be used to measure Raman spectra, which would allow for measurements to be made in pure gases.

REFERENCES

- Chou, J., Y. Han, B. Jalali, “Time-wavelength spectroscopy for chemical sensing,” *IEEE Photonics Technol. Lett.* **16**, 4 (2004) 1140–1142.
- Chou, J., O. Boyraz, D. Solli, B. Jalali, “Femtosecond real-time single-shot digitizer,” *Appl. Phys. Lett.* **91** (2007) 161105.

Dorrer, C., “Chromatic dispersion characterization by direct instantaneous frequency measurement,” *Opt. Lett.* **29**, 2 (2004) 204–206.

Godin, T., et al., “Real time noise and wavelength correlations in octave-spanning supercontinuum generation,” *Opt. Express* **21**, 15 (2013) 18452–18460.

Goldenstein, C. S., V. A. Miller, R. M. Spearrin, C. L. Strand, “SpectraPlot.com: Integrated spectroscopic modeling of atomic and molecular gases,” *J. Quant. Spectrosc. Radiat. Transf.* **200** (2017) 249–257.

Herink, G., B. Jalali, C. Ropers, D. R. Solli, “Resolving the build-up of femtosecond mode-locking with single-shot spectroscopy at 90 MHz frame rate,” *Nat. Photonics* **10** (2016) 321–326.

La Lone, B. M., B. R. Marshall, E. K. Miller, G. D. Stevens, W. D. Turley, L. R. Veerer, “Simultaneous broadband laser ranging and photonic Doppler velocimetry for dynamic compression experiments,” *Rev. Sci. Instrum.* **86** (2015) 023112.

Mahjoubfar, A., K. Goda, A. Ayazi, A. Fard, S. H. Kim, B. Jalali, “High-speed nanometer-resolved imaging vibrometer and velocimeter,” *Appl. Phys. Lett.* **98**, 10 (2011) 101107.

Mahjoubfar, A., D. V. Churkin, S. Barland, N. Broderick, S. K. Turitsyn, B. Jalali, “Time stretch and its applications,” *Nat. Photonics* **11**, 6 (2017) 341–351.

Saltarelli, F., V. Kumar, D. Viola, F. Crisafi, F. Preda, G. Cerullo, D. Polli, “Broadband stimulated Raman scattering spectroscopy by a photonic time stretcher,” *Opt. Express* **24**, 19 (2016) 21264–21275.

Solli, D. R., C. Ropers, P. Koonath, B. Jalali, “Optical rogue waves,” *Nature* **450** (2007) 1054–1057.

Solli, D. R., J. Chou, B. Jalali, “Amplified wavelength–time transformation for real-time spectroscopy,” *Nat. Photonics* **2** (2008) 48–51.

Werblinski, T., S. R. Engel, R. Engelbrecht, L. Zigan, S. Will, “Temperature and multi-species measurements by supercontinuum absorption spectroscopy for IC engine applications,” *Opt. Express* **21**, 11 (2013) 13656–13667.

Xia, H., C. Zhang, “Ultrafast and Doppler-free femtosecond optical ranging based on dispersive frequency-modulated interferometry,” *Opt. Express* **18**, 5 (2010) 4118–4129.

Multi-Frame X-Ray Imaging Using a Streak Camera with a Patterned Photocathode

LAO-008-16 ■ Year 3 of 3

Daniel Marks,^{1,a} Eric Dutra,^b Catalin Filip,^b and Jeffrey A. Koch^b

¹marksdg@nv.doe.gov, (505) 663-2093

^aNew Mexico Operations—Los Alamos

^bLivermore Operations

We continued development of two time-resolved x-ray imaging systems based on LiSens image compression (Wang 2015) and compressed ultrafast photography (Gao 2014). The modified patterned gold photocathode developed in our second year (Marks 2018) was tested with dynamic plasma imaging at the Janus laser at the Lawrence Livermore National Laboratory Jupiter facility. The new photocathode demonstrated greatly improved contrast from the experiments done in our first year (Marks 2017), and we added a flange to angle the camera to eliminate direct x-ray transmission through the system. We also designed a new system, conceived in the first year of our research, which uses image compression first developed for LiSens with a regular streak camera with 1-D input. This year we used this system to collect dynamic images at the University of Nevada, Reno, and at the facility for Cordin Scientific Imaging. At the Cordin Scientific Imaging facility, we used a rotating mirror in a benchtop configuration rather than a regular camera. We demonstrated effective 2-D imaging and made further refinements of the system based on the acquired data.

BACKGROUND

The fastest existing multi-frame x-ray imager is the dilation x-ray imager (DIXI) camera (Gao 2014), which uses a time-dilating chamber and variable-voltage photocathode strips to achieve <10 ps images. Because a separate pinhole is used for each image, the DIXI has parallax issues. DIXI is constrained to five frames in the configuration used at the National Ignition Facility,

which limits the useful continuous time window. The DIXI camera is also an expensive, complicated, heavy instrument, and incorporates large magnets. There are many applications where using such a camera would be impractical or impossible. A multi-frame imaging system that uses compressed ultrafast photography (CUP), such as we developed, is simpler, faster, less costly, and easier to field, and likely to find wider use and application.

CUP is a recently developed compressed sensing technique that compresses a time sequence of images onto a single streak camera image. Gao (2014) demonstrated CUP's compression of very sparse images onto a single streak camera sweep using a patterned mask to impose fixed high-frequency content onto an image. CUP uses a wide-open streak camera slit to streak the full image. We internally developed and demonstrated an improved version of CUP in simulations during an earlier SDRD project (Frayer 2016). We acquired the original source code used by Gao (2014) and found that multiple image copies allow the reconstruction of images that are much less sparse, which led us to determine that this technique shows promise for capturing data from time-varying phenomena of interest to DOE missions.

In our first year we designed the patterned x-ray photocathode and an optical imaging system to replicate the results presented by Gao (2014) (Marks 2017). In our second year we tested our x-ray photocathode with static and dynamic imaging and found that the contrast between the aluminum and gold layers was much less than anticipated, so a new photocathode was designed with no aluminum layer. This new photocathode was tested with static imaging and found to have excellent contrast between the gold and non-gold regions of the pattern (Marks 2018).

PROJECT

In FY 2018 the project was divided between conducting the dynamic testing of the patterned x-ray photocathode described above and further developing the LiSens system originally proposed by Wang (2015). In the LiSens system, each line of the streak camera image encodes a single 2-D image, allowing the reconstruction of hundreds of low-resolution images.

Dynamic X-ray Imaging Using a Patterned Photocathode

To greatly increase contrast between the gold pattern and the substrate, we conceived a fully connected gold pattern applied directly to the polyimide with no aluminum layer. A diagram of the layers is shown in Figure 1, and the pattern we used is shown in Figure 2.

This new pattern is a radical departure from our original pattern—and all previous patterns used for compressed imaging—in that the pattern is composed of regions that are fully interconnected in order to

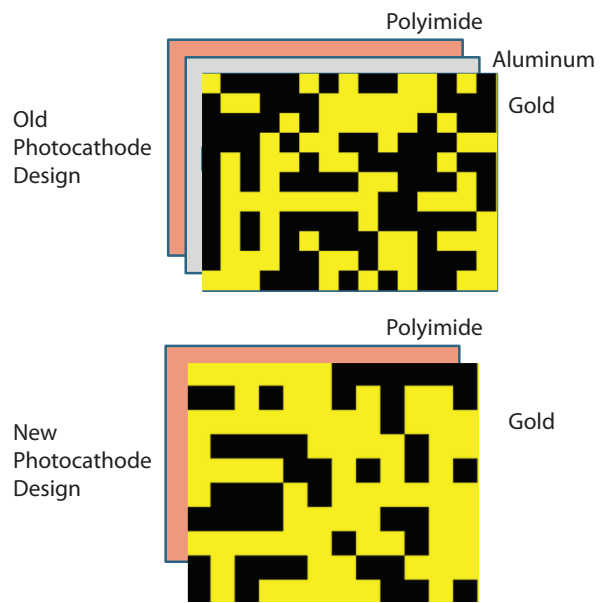


Figure 1. Old and new photocathode layers. In the new design, the gold pattern is continuously connected throughout to provide electrical conductivity without the aluminum layer.

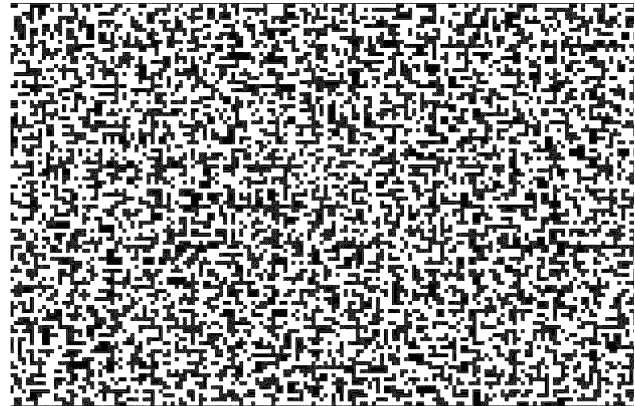


Figure 2. New photocathode pattern with the gold pattern shown in white on $150 \times 150 \mu\text{m}$ squares

allow current to flow throughout the pattern. In the original pattern, the aluminum layer provided the needed electrical conductivity so that a random pattern of gold blocks could be used. When we eliminated the aluminum layer, it became necessary to use a nonrandom pattern with fully connected blocks, but it needed to be as close to random as possible in order to get the uniform frequency response of a random pattern.

To generate this pattern, we created 10×10 random block regions and then added and subtracted blocks arbitrarily until the pattern within each region was fully connected. All of these 10×10 regions were

then connected together into the full pattern, and any remaining unconnected regions at the boundaries were connected with the most direct connection. The result in Figure 2 is a pattern that approximates a random pattern; in simulations this solution was found to have no discernable difference from a truly random pattern.

We performed dynamic imaging experiments at the Janus laser at the Lawrence Livermore National Laboratory Jupiter facility. These were laser-driven plasma experiments that had from 100 to 200 J, 1 ns laser pulses. We set up the experiments such that the plasma was viewed through a 50 μm pinhole to produce an image on the photocathode. The experimental setup is shown in Figure 3, and the one good dynamic image we were able to acquire is shown in Figure 4. We were unable to record additional images that could have assisted with calibrations; therefore, to analyze this image, we are in the process of backing out the calibrations from the image itself. The analysis is not yet complete.

Dynamic Optical Imaging Using a Regular Streak Camera with 1-D Slit

Imaging with a regular streak camera with 1-D input can be done with the LiSens configuration developed by Wang (2015). Each line of the streak camera image encodes a single 2-D image, allowing the

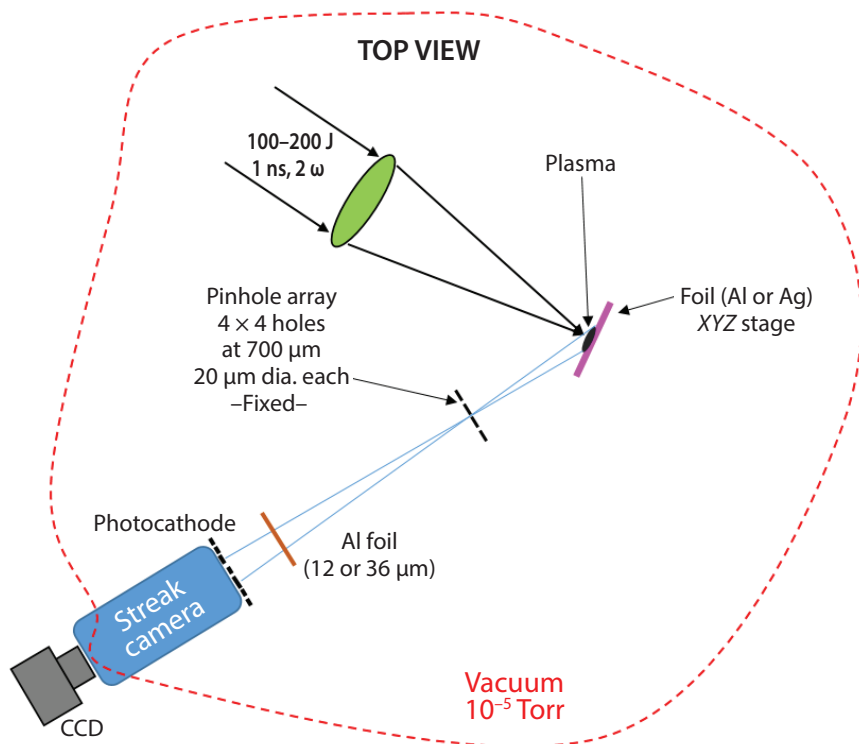


Figure 3. Diagram of dynamic experiments at the Janus laser

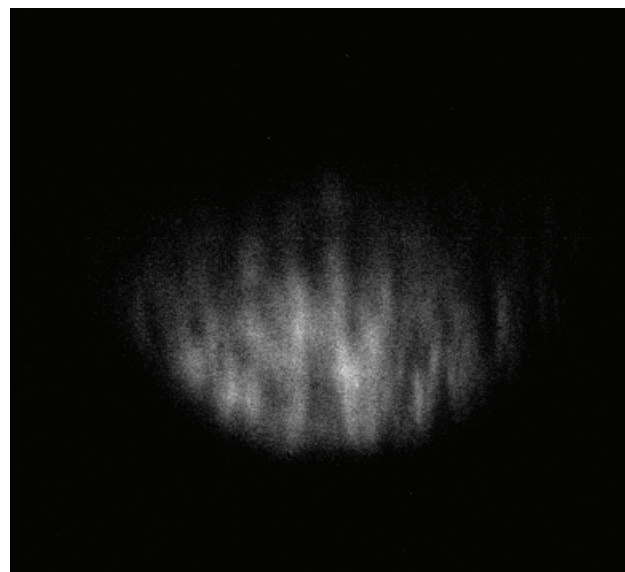


Figure 4. Dynamic image from plasma x-ray experiments that we are analyzing

reconstruction of hundreds of low-resolution images. We expect this new method and CUP to complement each other and be optimal for different applications. The LiSens method will function best when larger numbers of frames are needed and the system can tolerate a lower spatial resolution. LiSens will not be adversely affected by sudden changes in brightness, whereas with CUP a bright frame can swamp nearby dim frames.

We tested the LiSens system by conducting dynamic optical experiments using the 1.5 TW Zebra pulsed-power generator at the University of Nevada, Reno, Nevada Terawatt Facility (NTF). Zebra's Marx bank stores 150 kJ of energy; following pulse shaping and compression, it delivers ~ 1.0 MA of current to a plasma target with a rise time of ~ 100 ns. Initially, target material was ablated from the surface of a solid target mounted on the cathode by the use of the NTF Leopard laser (20 J at 0.8 ns Ti:sapphire/Nd:glass laser system). The ablation plume expanded across the gap between the anode and cathode in ~ 2 μs . Once the plume spanned the vacuum gap, it served as the load for the current from the Zebra pulsed-power generator to

travel through. As current passed through the ablation plume, it rapidly created a plasma cloud within the anode-cathode gap. As the current rose, the $\mathbf{J} \times \mathbf{B}$ force increased, causing the ionized material within the anode-cathode gap to implode and pinch along the vertical z -axis. The Z-pinch is our source for this configuration. Photons emitted from the source are transferred down.

We were able to get usable data only when we viewed a small section of the image through a 250 μm slit to narrow the field of view. The dynamic data are shown in Figure 5, and one of 80 reconstructed frames is shown in Figure 6. Little structure is visible in the narrow slit region.

Experimental conditions at the NTF made it difficult to acquire more data. We were unable to thoroughly adjust the conditions to match the random mask we had made. In comparison, we had much better results with tests we did at the Cordin Scientific Imaging facility. The mismatch between the input camera optics and the optics needed for our compressed imaging system prevented us from using a camera directly, so during imaging we used the rotating mirrors Cordin built to use with optical streak cameras and a benchtop setup. We used an LED flash to acquire a static image and then swept this image across a CCD to generate the data. A thorough calibration of the setup was possible, so we made a 20-line map to measure the system response.

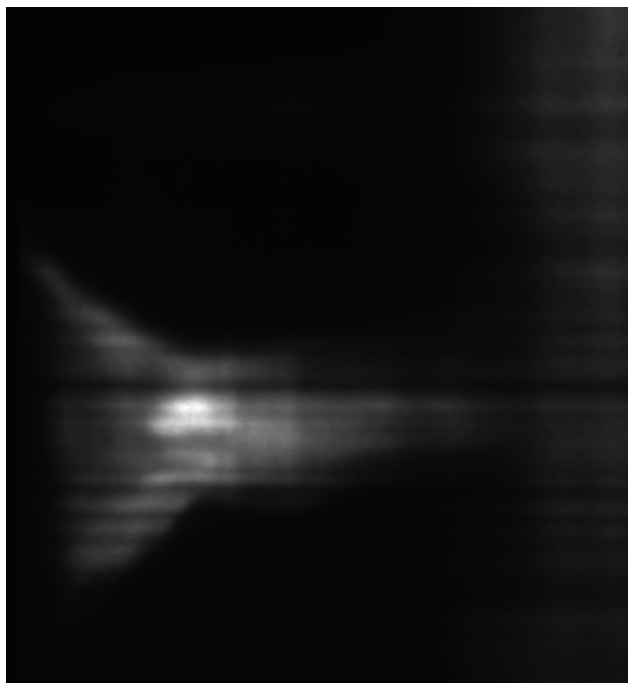


Figure 5. Dynamic image with 250 μm slit to narrow the field of view

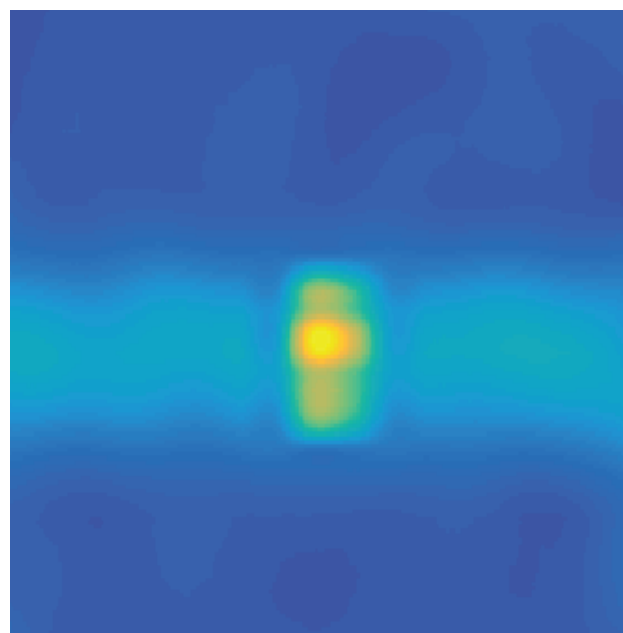


Figure 6. One of 80 frames of the reconstruction, showing the plasma seen through the 250 μm slit

We found that data quality was greatly improved if a narrower image was used. Images were printed onto a simple plastic sheet and illuminated with a 1 μs LED pulse. Figure 7 shows a large image and a shortened image; their reconstructions are shown in Figure 8.

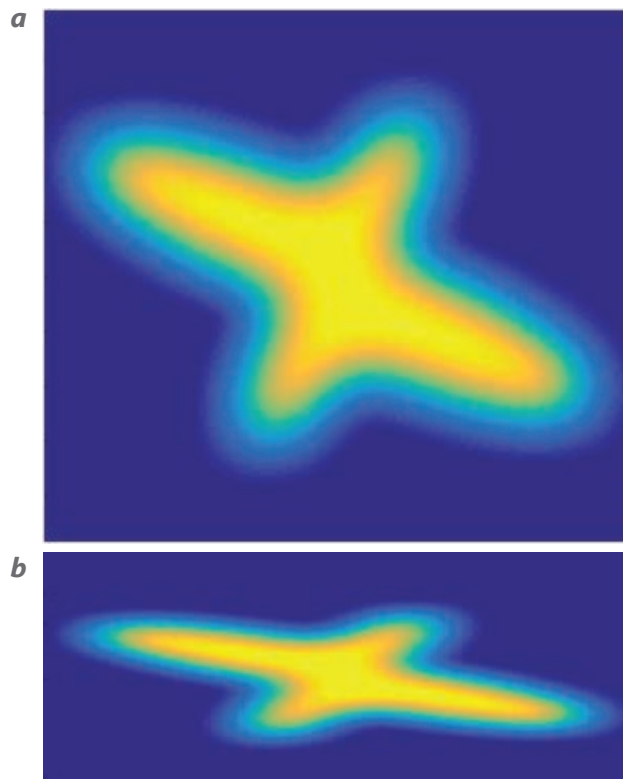


Figure 7. (a) Large and (b) shortened patterns used for testing the rotating mirror LiSens system

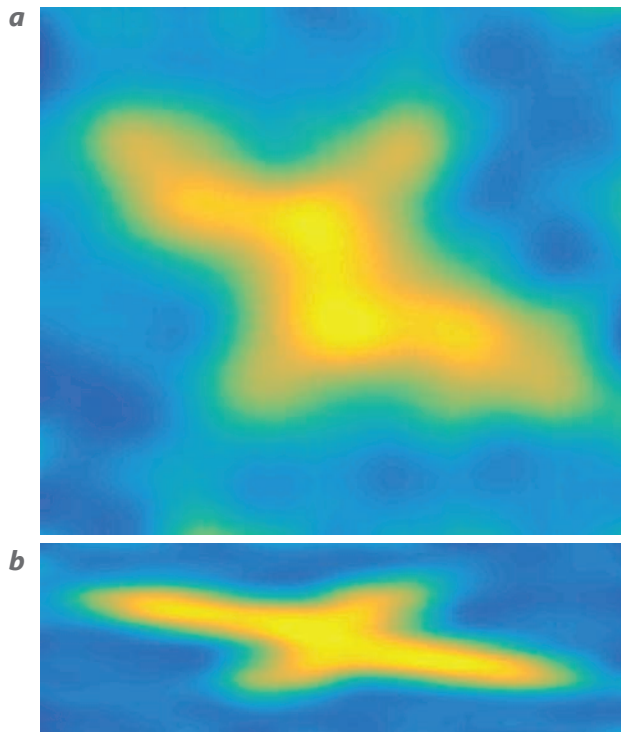


Figure 8. Reconstructions of (a) large and (b) shortened patterns from the rotating mirror data shown in Figure 7

CONCLUSION

The improved x-ray photocathode was demonstrated for the first time with dynamic x-ray imaging and was found to have excellent contrast between the patterned gold and the substrate. We are in the process of extracting missing calibration information to make the image we recorded usable. We demonstrated the LiSens streak imaging technique for the first time using a regular streak camera on a dynamic experiment and in benchtop tests done at Cordin Scientific Imaging with a rotating mirror. The rotating mirror data provided excellent results, demonstrating that compressed imaging can be done with a regular streak camera. We found that a shortened image produced better reconstructions, and likewise a full-size image with elongated pixels perpendicular to the image input should provide similar benefits.

ACKNOWLEDGMENTS

We would like to thank Professor Richard Baraniuk, who assisted us with algorithm development in our first year, and Cordin Scientific Imaging for providing us with the use of their facility and rotating mirrors to acquire data.

REFERENCES

- Frayner, D., G. Capelle, D. Marks, A. Bernstein, “Ultrafast all-optical framing technology,” in *Site-Directed Research and Development*, FY 2015, National Security Technologies, LLC, Las Vegas, Nevada, 2016, 205–211.
- Gao, L., J. Liang, C. Li, L. V. Wang, “Single-shot compressed ultrafast photography at one hundred billion frames per second,” *Nature* **516** (December 4, 2014) 74–77.
- Marks, D., J. A. Koch, R. Tiangco, J. O’Connor, M. Raphaelian, “Multi-frame x-ray imaging using a streak camera with a patterned photocathode,” in *Site-Directed Research and Development*, FY 2016, National Security Technologies, LLC, Las Vegas, Nevada, 2017, 189–195.
- Marks, D., C. Filip, J. A. Koch, “Multi-frame x-ray imaging using a streak camera with a patterned photocathode,” in *Site-Directed Research and Development*, FY 2017, National Security Technologies, LLC, and Mission Support and Test Services, LLC, Las Vegas, Nevada, 2018, 207–212.
- Wang, J., M. Gupta, A. C. Sankaranarayanan, “LiSens—A scalable architecture for video compressive sensing,” *2015 IEEE International Conference on Computational Photography*, Houston, Texas, April 2015, 1–9.

This page left blank intentionally

Site-Directed Research and Development

Appendixes

SDRD Performance Metrics

Mission Support and Test Services–Operated Sites

Acronyms and Abbreviations

This page left blank intentionally

SDRD Performance Metrics

The SDRD program uses quantifiable metrics to track the performance of our R&D investment from year to year. Metrics such as intellectual property, technology transfer to our programs, addressing R&D needs and requirements, and publications are some of the most common types of measureable outcomes. We also consider the importance of other factors, such as follow-on programmatic or external funding received, new methods developed that effectively reduce costs, and overall enhanced staff capabilities. These are further indicators of innovation productivity and are also a direct measure of investment return. SDRD provides our staff with opportunities to explore and exercise creative motivations that ultimately lead to new knowledge and realized technologies. Shown below are some of the more traditional metrics tabulated over the past ten-year period.



INVENTION DISCLOSURES & PATENTS

Invention disclosures are the first step in our intellectual property pursuit and are often followed by patent applications when deemed appropriate. SDRD has generated well over half of all inventions disclosed company-wide since FY 2002. On average about one-third of our projects generate new invention disclosures, which is a reasonably high ratio given that projects can vary widely from basic concept, low technical readiness to much

higher more applied development efforts. In fact, our programs benefit from a high rate of technology utilization precisely due to this diverse project mix. From FY 2016 to 2018 our patent applications and awarded patents actually increased; however, we note downward trend in disclosures due to contract transition and staffing changes. New planned enhancements to intellectual property are expected to increase our overall output in the following years.

	FY09	FY10	FY11	FY12	FY13	FY14	FY15	FY16	FY17	FY18
Number of projects	23	25	26	24	24	25	28	27	30	28
Invention disclosures	11	9	7	8	7	7	6	5	4	2
	48%	36%	27%	33%	29%	28%	21%	19%	13%	7%

TECHNOLOGY TRANSFER

A relatively high percentage of projects, approximately 1 in 3, produce technology that is subsequently adopted by a direct NNSC program. Another measure of program effectiveness and alignment with missions is how well projects address technology needs as identified in the annual *NNSC Technology Needs Assessment*. The ratio of needs addressed to total projects is also indicative of a trend that aligns efforts strategically with the NNSC mission. In addition, a number of projects, but still a small percentage, are targeting emerging fields (of the *Technology Needs Assessment*) and new initiatives intended to incorporate higher risk; these

projects explore opportunities for enhanced mission outside of traditional NNSC areas of expertise.

We continue to strive to have SDRD effectively contribute new technology into key programmatic efforts as quickly as possible. New strategic efforts are also providing greater emphasis on forward-looking needs efficiently coupled with long-term visionary goals. As always, SDRD looks to be “ahead of our time by design” and push for SDRD innovations to intersect future and evolving missions with the most impact possible.

	FY09	FY10	FY11	FY12	FY13	FY14	FY15	FY16	FY17	FY18
Number of projects	23	25	26	24	24	25	28	27	30	28
Technology adopted by programs	10	10	9	10	9	10	11	10	8	9
	44%	40%	35%	42%	38%	40%	39%	37%	27%	32%

TECHNOLOGY NEEDS ADDRESSED

The *NNSC Technology Needs Assessment* document continues to be an effective tool for proposal submitters and reviewers. It includes guidance regarding technology gaps and challenges facing mission areas. Our directed research emphasis areas this year were similar to last year, and they targeted key investment needs, including nuclear security, information security/assurance, high-energy density physics diagnostics, integrated experiments, advanced analysis, and safeguarded energy. The *NNSC Technology Needs Assessment* is developed from a broad base of input from the national security

complex, including laboratories, NNSA, and other external agencies. A minor refresh of the assessment was made again this year, building on the previous major revisions. The *NNSC Technology Needs Assessment* itself is now in the 14th year of revision, and its utility and effectiveness continues to improve year to year. Of note for 2018, we issued our second broad site announcement (BSA), which contained detailed information on strategic initiatives for our directed research, and also provided further guidance on exploratory research as underpinned by the *Needs Assessment*.

	FY09	FY10	FY11	FY12	FY13	FY14	FY15	FY16	FY17	FY18
Number of projects	23	25	26	24	24	25	28	27	30	28
Gap or need addressed	15	13	13	11	14	11	10	10	13	11
	65%	52%	50%	46%	58%	44%	36%	37%	43%	39%
“Emerging Area and Special Opportunity” effort*	--	--	--	--	3	5	5	3	5	6
	--	--	--	--	13%	20%	18%	11%	17%	21%

*per *NNSC Technology Needs Assessment*

PUBLICATIONS

Publications are another indicator of R&D output and provide an archival record of the investments made, which are then available to the broader scientific and technical community. We place a strong emphasis on high-quality, high-impact journal publications. We

generally expect about half of all SDRD projects will publish in a given year. An increase in follow-on and co-authored publications has been noted and future prospects for enhanced publishing look promising.

	FY09	FY10	FY11	FY12	FY13	FY14	FY15	FY16	FY17	FY18
Journal publications	6	6	5	7	9	8	7	7	8	8

This page left blank intentionally



Mission Support and Test Services— Operated Sites

LIVERMORE OPERATIONS (LO)

P.O. Box 2710
Livermore, California 94551-2710

NEVADA NATIONAL SECURITY SITE (NNSS)

P.O. Box 98521
Las Vegas, Nevada 89193-8521

NEW MEXICO OPERATIONS (NMO) (LOS ALAMOS AND SANDIA OFFICES)

2900 East Road
Los Alamos, New Mexico 87544

NEVADA OPERATIONS, NORTH LAS VEGAS (NLV)

P.O. Box 98521
Las Vegas, Nevada 89193-8521

REMOTE SENSING LABORATORY—ANDREWS (RSL—A)

P.O. Box 380
Suitland, Maryland 20752-0380
(Andrews Air Force Base)

REMOTE SENSING LABORATORY—NELLIS (RSL—N)

P.O. Box 98521
Las Vegas, Nevada 89193-8521
(Nellis Air Force Base)

SPECIAL TECHNOLOGIES LABORATORY (STL)

5520 Ekwil Street
Santa Barbara, California 93111-2352

This page left blank intentionally

Acronyms and Abbreviations

1-D	one-dimensional
2-D	two-dimensional
2DEG	2-D electron gas
2DHG	2-D hole gas
3-D	three-dimensional
3S-LiPo	three-cell lithium polymer
4G LTE	fourth generation long-term evolution (telecommunications)
10 DOF	ten degrees of freedom

A	ABS	acrylonitrile butadiene styrene
	AC/DC	alternating current/direct current
	ACE	adaptive coherence estimator
	ACF	antenna correction factor
	ADC	analog-to-digital converter
	Ag	silver
	AGC	automatic gain control
	Al	aluminum
	AlGaN	aluminum gallium nitride
	AlN	aluminum nitride
	Al ₂ O ₃	aluminum oxide
	APS	Advanced Photon Source
	Ar	argon
	AR	augmented reality
	ASC	Advanced Simulation and Computing
	ASE	amplified spontaneous emission
	ASI	Applied Spectra Incorporated
	ASIC	application-specific integrated circuit
	ASK	amplitude shift keying
	ASTER	Advanced Spaceborne Thermal Emission and Reflection Radiometer
AU	arbitrary units	
AVIRIS	Airborne Visible/Infrared Imaging Spectrometer	

B	B3LYP	Becke, 3-parameter, Lee-Yang-Parr, a density functional theory code
	Ba	barium
	bct	body-centered tetragonal
	Be	beryllium
	Bi	bismuth
	BIM	beam intensity monitor

BNC Bayonet Neill–Concelman
Br bromine
BSA broad site announcement

C C-4 common composition C plastic explosive
C₂H₂ acetylene
C₂H₄ polyethylene
CAD computer-aided design
CaO calcium oxide
CARS Coherent anti-Stokes Raman spectroscopy
CCD charge-coupled device
Cd cadmium
CD₂, C₂D₄ deuterated polyethylene
Ce cerium
CERN Conseil Européen pour la Recherche Nucléaire, or European Organization for Nuclear Research
CFD computational fluid dynamics
CG center of gravity
CH₂, C₂H₄ polyethylene
CINT Center for Integrated Nanotechnologies
CMS Compact Muon Solenoid (detector)
CNN convolutional neural network
Co cobalt
CO₂ carbon dioxide
COTS commercial off the shelf
CPU central processing unit
CRADA cooperative research and development agreement
Cs cesium
CsI cesium iodide
CTH multi-material, large deformation, strong shock wave, solid mechanics code developed at Sandia National Laboratories
Cu copper
CUP compressed ultrafast photography
CW continuous wave
CZT cadmium zinc telluride

D D₂ deuterium gas
DAC diamond anvil cell
DAC digital-to-analog converter
DAG Dry Alluvium Geology
DAQ data acquisition
DC direct current
DCM dichloromethane
DD deuterium-deuterium

DFT	density functional theory
DIXI	dilation x-ray imager
DNN	deep neural network
DNN	deep neural network
DOE	U.S. Department of Energy
DOF	degree of freedom
DPF	dense plasma focus
DSP	digital signal processing
DTRA	Defense Threat Reduction Agency

E	ECP	effective core potential
	EDFA	erbium-doped fiber amplifier
	EOS	equation of state
	ESC	electronic speed controller
	Eu	europium
	Exp	exponential moving average

F	FC	fixed connection
	Fe	iron
	Fe ₂ O ₃	iron oxide
	FFT	fast Fourier transform
	FHSS	frequency hopping spread spectrum
	FIR	finite impulse response
	FMCIO	FPGA Mezzanine Card Input/Output
	FPGA	field-programmable gate array
	FSK	frequency shift keying
	FWHM	full width at half maximum
FY	fiscal year	

G	GaN	gallium nitride
	GC-MS	gas chromatograph–mass spectrometer
	Ge	germanium
	GMT	Greenwich Mean Time
	GNU	“GNU not Unix”
	GPIO	general purpose input output
	GPS	global positioning system
	GPU	graphics processing unit
	GSD	ground sample distance
	GUI	graphical user interface

H	H	hydrogen
	HDI	high-density interface
	HDMI	high-definition multimedia interface

HDPE	high-density polyethylene
He	helium
HED	high energy density
HE	high explosive
HEA	high-entropy alloy
HED	high energy density
HEDP	high-energy density physics
HEL	Hugoniot elastic limit
HEP	high-energy physics
HEU	highly enriched uranium
HiPSEC	High Pressure Science and Engineering Center
HMX	cyclothramethylenetetranitramine
HPCAT	High Pressure Collaborative Access Team (Carnegie Science)
HTML	hypertext markup language
HV	high voltage

I	I	in phase
	IDE	integrated development environment
	IDEA	Interferometric Data Evaluation Algorithms
	I/Q	in phase/quadrature
	ILC	International Linear Collider
	IM-MS	ion mobility-mass spectrometer
	InGaN	indium gallium nitride
	InSb	indium antimonide
	I/O	input/output
	IP	internet protocol
	IR	infrared

J	JASPER	Joint Actinide Shock Physics Experimental Research
----------	--------	--

K	K	potassium
	Kr	krypton
	KZ	Kolmogorov-Zurbenko (filter)

L	LANL	Los Alamos National Laboratory
	LAZE	laser ablation Z-pinch experiments
	LED	light-emitting diode
	LEMAS	Leeds Electron Microscopy and Spectroscopy Centre
	Li	lithium
	lidar	light detection and ranging

LiF	lithium fluoride
LIGO	Laser Interferometer Gravitational-Wave Observatory
LLNL	Lawrence Livermore National Laboratory
LO	Livermore Operations
LSP	large scale plasma
LTE	local thermal equilibrium

M	MagLIF	magnetized liner inertial fusion
	MCPI	microchannel plate intensifier
	MCS	multichannel scaler
	MDT	Mountain Daylight Time
	MEMS	microelectromechanical systems
	MHD	magnetohydrodynamic (code)
	MINER	mobile imager of neutrons for emergency responders
	ML	machine learning
	MLL	mode-locked laser
	Mn	manganese
	Mo	molybdenum
	MSI	multispectral imagery
	MSTS	Mission Support and Test Services, LLC
	MWIR	mid-wave infrared
	M-Z	Mach-Zehnder

N	NaI	sodium iodide
	NaI:Tl	thallium-doped sodium iodide
	Nd	neodymium
	Nd:YAG	neodymium-doped yttrium aluminum garnet
	Ne	neon
	NEA	negative electron affinity
	NH ₄ ClO ₄	ammonium perchlorate
	NH ₄ NO ₃	ammonium nitrate
	NI	National Instruments
	NIF	National Ignition Facility
	NIST	National Institute of Standards and Technology
	NLSF	nonlinear least squares fitting
	NLV	North Las Vegas
	NMEA	National Marine Electronics Association
	NNSA	National Nuclear Security Administration
	NNSS	Nevada National Security Site
	NORM	naturally occurring radioactive material
	NTF	Nevada Terawatt Facility

O	O ₂	oxygen
	OBI	optical beam interrupt
	OC	output coupler
	OH	hydroxyl
	ORNL	Oak Ridge National Laboratory
P	PC	personal computer
	PCB	printed circuit board
	PCI	phase contrast imaging
	PDT	Pacific Daylight Time
	PDU	protocol data unit
	PDV	photonic Doppler velocimetry
	PES	potential energy surface
	PETN	pentaerythritol tetranitrate
	PHP	hypertext preprocessor (scripting language)
	PIR	passive infrared
	PM	polarization-maintaining (fiber)
	PMT	photomultiplier tube
	PNNL	Pacific Northwest National Laboratory
	PSK	phase shift keying
	PSNR	peak signal-to-noise ratio
PTW	Preston-Tonks-Wallace	
Q	Q	quadrature
	QE	quantum efficiency
R	RC	Rowland Circle
	RDX	cyclo-1,3,5-trimethylene-2,4,6-trinitamine (explosive)
	RF	radio frequency
	RGD	radiation-generating device
	RMS	root mean square
	ROI	region of interest
	RRTR	Radiological Response Training Range (Idaho National Laboratory)
	RSL	Remote Sensing Laboratory
	Ru	ruthenium
	Rx	receive
S	SA	saturable absorber
	SBC	single-board computer
	SCE	subcritical experiment

SDR	software-defined radio
SDRD	Site-Directed Research and Development
SG	Savitzky-Golay (filter)
SGL	Steinberg-Guinan-Lund
Si	silicon
SiO ₂	silicon dioxide
SKIROC	Silicon Kalorimeter Integrated Read-Out Chip
Sn	tin
SNL	Sandia National Laboratories
SNM	special nuclear material
SOB	start of burst
SOR	strategic opportunity research
SPE	Source Physics Experiment
SPIDER	Streaked Polar Instrumentation for Diagnosing Energetic Radiation
SR	super-resolution
SSH	Secure Shell
STL	Special Technologies Laboratory
sUAS	small unmanned aerial system
SWIR	short-wave infrared

T

Ta	tantalum
TEC	thermoelectric cooling
TEM	transmission electron microscopy
Ti	titanium
TL	transfer learning
TNT	2,4,6-trinitrotoluene
TTL	transistor–transistor logic
Tx	transmit
TXD	Talbot-Lau x-ray deflectometry

U

U	uranium
UAS	unmanned aerial system
UHD	universal hardware driver
UNLV	University of Nevada, Las Vegas
UNR	University of Nevada, Reno
USAXS	ultrasmall-angle x-ray scattering
USB	universal serial bus
USI	Unmanned Systems, Inc.
USRP	Universal Software Radio Peripheral
UV	ultraviolet

V	Virginia Tech	Virginia Polytechnic Institute and State University
	VISAR	velocity interferometer for any reflector system
	VNIR	visible-near infrared
	VOC	volatile organic compound
W	WAP	wireless access point
	WDM	wavelength division multiplexer
X	XDV	x-ray Doppler velocimetry
	XWFP	X-ray WaveFront Propagation (code)
Y	Y	yttrium
Z	ZBL	Z-Beamlet Laser Facility (SNL)
	Zn	zinc